Plenary Lecture

Antimicrobial azobenzene – a review

Leonard, Estelle[*a], Fayeulle, Antoine[a], Franche, Antoine[a], Sagadevan, Suresh[b], Billamboz, Muriel [c]

[a]Université de technologie de Compiègne, ESCOM, TIMR (Integrated Transformations of Renewable Matter), Centre de recherche Royallieu - CS 60 319 - 60 203 Compiègne Cedex, France

[b]Nanotechnology & Catalysis Research Centre, University of Malaya, Kuala Lumpur , Malaysia

[c]Laboratoire de chimie durable et santé, Junia, HEI, 13 rue de Toul, 59046 Lille Cedex, France

E-mail: e.leonard@escom.fr

Abstract

Amongst the photochromes superfamily, azobenzene subgroup is the most extensively produced and used for many applications. However, the emergence of MDR (Multi-Drug Resistant) bacterial strains brought to light the urgent need of efficient antimicrobial molecules. In that context, this presentation aims to compile the different approaches coupling azobenzene and antimicrobial activity.

Keywords: Azobenzenes, Antibacterial, Antifungal, Biocides

References

Léonard, E.; Fayeulle, A.; Franche, A.; Sagadevan, S. ; Billamboz, M. *J. Iranian Chem. Soc.*, **2021.** Antimicrobial Azo-Molecules – a review
DOI : 10.1007/s13738-021-02238-4

Invited Lecture

Constructing a Directional Ion Acceleration Layer at WO₃/ZnO Heterointerface to Enhance Li-ion Transfer and Storage

Chuanbao Tu, Ze Zhang, Zhenyu Yang[*]

College of Chemistry, Key Laboratory of Jiangxi Province for Environment and Energy Catalysis, Nanchang University, 999 Xuefu Rd. Nanchang, Jiangxi, 330031, China.
[*]Corresponding author: Z.Y.Yang, zyyang@ncu.edu.cn

Abstract

Rechargeable lithium ion batteries (LIBs) are considered as the dominant energy storage devices due to their high energy density and prolonged cycle life. However, LIBs suffer from severe interfacial issues of the slow transport of Li-ions in electrode materials and electrolyte/electrode interface. Such a weakness induces poor rate performance for most electrode materials, which is far behind the requirement of future electric vehicles and hybrid electric vehicles. In this aspect, constructing heterostructures for electrode materials are confirmed as a useful way to accelerate the charge transportation driven by the internal electric field at the interface and realize high rate capability of electrode materials. In this presentation, tungsten trioxide/zinc oxide (WO_3/ZnO) heterostructure film electrode with directional built-in electric field have been fabricated by WO_3 hexagonal flower arrays with a deposited layer of ZnO QDs supported by conductive carbon cloth substrate. The planar heterojunction and directional built-in electric fields will help to speed up Li-ion transport during the charge and discharge processes. As a result, when used as the anode material of LIBs, as-prepared WO_3/ZnO heterostructure electrode showed high reversible capacity (~1500 mAh/g at 0.2 C), excellent rate capability (~500 mAh/g at 9C), and cycling stability (1210 mAh/g at 1C after 200 cycles). Therefore, this work provides an effective strategy for constructing heterostructure film and make it become a promising candidate material for high-performance anode of lithium ion battery.
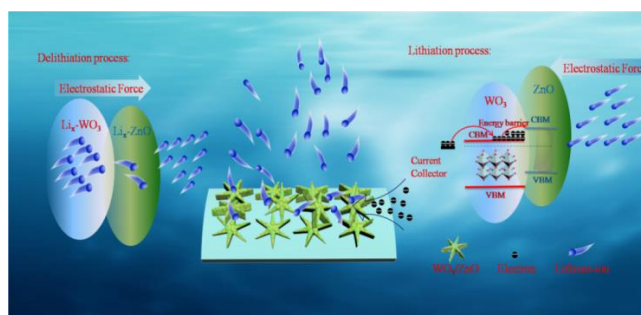
Reference:

[1] C. Tu, Z. Zhang, Z. Yang*, *Chemical Engineering Journal*, 2021, 425, 130648.
[2] C. Tu, Z. Zhang, Z. Yang*, *Composites Part B: Engineering*, 2021, 205: 108511

Improvement of spectral resolution and signal to noise ratio in the spatially modulated Fourier transform spectrometer

Ju Yong Cho[1], Hyoung Jin Kim[1], and Won Kweon Jang[1,*]

[1]Department of Aeronautic Electricity, Hanseo University, 46, Hanseo 1-ro, Seosan-si 31962, South Korea; *jwk@hanseo.ac.kr

Abstract

In a spatially modulated Fourier transform spectrometer comprised of a modified Sagnac interferometer, we report the improvement for the signal to noise ratio and spectral resolution, which could be obtained by synthesizing two spatially modulated interferograms. Conventional Fourier transform spectrometers has provided many advantages of wide spectrum measurement in a relatively short time, but at the same time, suffered from disadvantages of weak seismic resistance and strict operation environment. The spatially modulated Fourier transform spectrometer, recently reported as a strong substitutional candidate [1], has been expected that can overcome those drawbacks, if its spectral resolution and signal to noise ratio can be comparable to the conventional Fourier transform spectrometer. Those drawbacks come from the limited number of data points and low sensitivity of array detector. Though those drawback are intrinsic due to spectrometric structure for spatial modulation, in this paper, we introduce a synthesizing method of two interferograms for improving the spectral resolution and signal to noise ratio, in the spatially modulated Fourier transform spectrometer comprised of modified Sagnac interferometer. Though the spectral resolution and signal to noise ratio are in the relation of trade-off, those properties could be improved by applying the synthesizing method, that we propose in this paper.
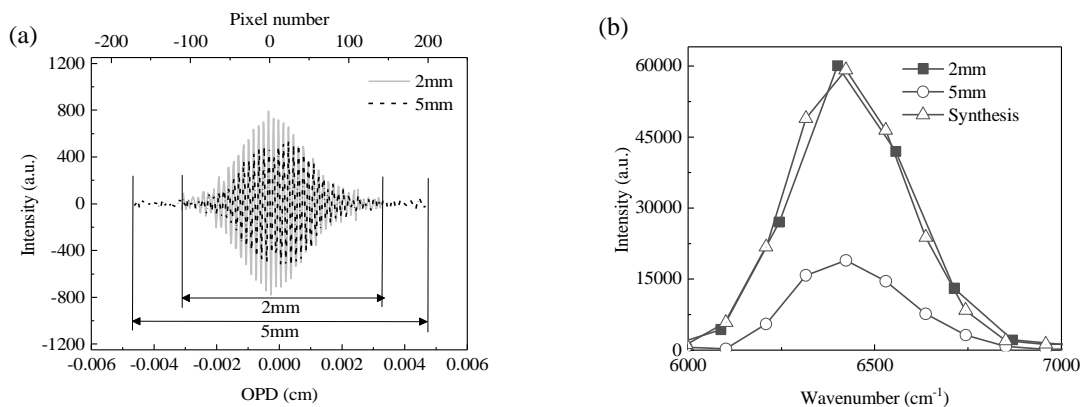
Figure 1. (a) The measured interferograms at displacement of 2 mm and 5 mm. (b) Fourier transformed spectra for comparison.

Figure 1(a) shows the measured interferograms, that were obtained when the one mirror dispalcement are 2 and 5 mm from the symmetric position. The interferogrm of 2 mm displacement shows higher visibility than the interferogram of 5 mm, but has shorter maximum optical path difference than the interferogram of 5 mm. Figure 1(b) shows the Fourier transformed spectra of those interferograms. The spectrum of the synthesized interferogram shows 3% improved signal to noise ratio, when it is compared to that of the spectrum at 5mm

displacement, and also shows 31% improved spectral resolution, when it is compared to that of the spectrum at 2 mm displacement.

Synthesizing method for the measured interferograms could provide the higher visibility and better spectral resolution than any interferogram can produce. We report the details of this method with newly developed algorithm, which is effective to solve the intrinsic problems in the spatially modulated Fourier transform spectrometer.

Keywords: Spectral resolution; Fourier transform; Spectrometer; Static modulation; Signal to Noise Ratio

References

[1] M. H. Köheler, M. Schardt, M. Müller, P. Kienle, K. Wang, X. Dong, C. Giebeler, B. R. Wiesent, M. Jakobi, and A. W. Koch, "Static Fourier transform mid-infrared spectrometer with increased spectral resolution using a stepped mirror," *OSA Continuum*, **3**(8), 2134-2142(2020).

Sunlight responsive photocatalyst based on CdS/BiOBr heterojunction for detoxification of ciprofloxacin and norfloxacin antibiotics in wastewater

Teeradech Senasu, <u>Suwat Nanan</u>*

Materials Chemistry Research Center, Department of Chemistry and Center of Excellence for Innovation in Chemistry (PERCH-CIC), Faculty of Science, Khon Kaen University, Khon Kaen 40002, Thailand suwatna@kku.ac.th

Abstract

Solar-light-driven CdS/BiOBr photocatalyst was prepared by a facile solvothermal route. In this talk, I will focus on the decoration of the hexagonal CdS nanoparticles on the surface of the tetragonal BiOBr micro-flowers for the creation of a heterostructure photocatalyst used for the removal of the antibiotics. The CdS/BiOBr-1:3 heterojunction exhibited 100% removal of norfloxacin and ciprofloxacin under visible light illumination. In addition, complete degradation of the antibiotics under natural solar light irradiation was also achieved. Construction of the CdS/BiOBr heterojunction is a promising strategy for the improvement of photocatalytic performance due to a decrease in the charge carrier recombination rate at the interface, an increase in the visible light absorption range, and an enhancement of the surface area of the resultant product. The removal of the pollutants fit very well with the first-order reaction. The photogenerated hole played a crucial role in the removal of the antibiotics. Confirmation of the stability of the CdS/BiOBr heterojunction was also elucidated. The photoactivity of the photocatalyst remained the same after five times of use suggesting the excellent cycling ability of the sample. The research demonstrates the promising potential of the prepared CdS/BiOBr photocatalyst for detoxification of antibiotics presented in water.

Keywords: CdS/BiOBr; Photodegradation; Antibiotics; Solar light; Visible light

Cobalt Oxide nanostructured for electrochemical and photocatalytic applications

Suresh Sagadevan[*]

Nanotechnology & Catalysis Research Centre, University of Malaya, Kuala Lumpur 50603, Malaysia

Abstract

In recent years, nano metal oxides are widely known for their potential applications in science and technology. This has led to progress in several processes for the preparation of nanoparticles, including anticipated physiognomies, corresponding dimensions, forms, morphology, imperfections in the crystal construction, and monodispersion, for potential use in medicament applications. The nanostructured materials received much attention due to their distinctive properties such as higher damping, mechanical stability, high strength, and good thermal conductivity. The nanostructured metal oxides, in general, maintains the high surface area and that developed much interest in the research due to its wide range of applications including optical electronics, sensing devices, and nanoelectronics. Photocatalysis technology offers excellent potentials for the complete removal of organic and other biochemical pollutants in an environmentally friendly and sustainable means where the outcome is without the involvement of greenhouse gas emissions. It has been found that under UV-Visible light irradiation, the nanostructured semiconductor metal oxide photocatalysts can easily degrade many different organic and biochemical pollutants. Since the photocatalysis is a process which involves the breaks down or decomposition of various dyes, organic dirt, and biological species like harmful fungi and viruses by making use of the UV or visible light in a sustainable manner. Herein we report on various surface morphological characteristics of the synthesized cobalt oxide (Co_3O_4) nanostructures obtained by means of facile one-step hydrothermal method for oxygen reduction reaction (ORR). The synthesized nanostructures of Co_3O_4 were adequately characterized by field emission scanning electron microscopy (FESEM) fitted with Energy-dispersive X-ray spectroscopy (EDX) elemental mapping, X-ray diffraction (XRD) and Raman techniques. The electrochemical studies were carried out to analyse the performance of as-synthesized catalysts for ORR by cyclic voltammetry (CV), and chronoamperometric (CA) techniques Further testing of the photocatalytic activity through the degradation of various dye confirmed for an effective and potential catalytic nature of the synthesized samples.

Keywords: Metal oxides, Nanoparticles, Optical properties, and photocatalytic activity

Miniaturized Sample Preparation for Trace Organic Compounds Analysis

Chongdee Thammakhet-Buranachai*[1,2], Nichapat Chunin[1,2], Warakorn Sukree[1,2], Proespichaya Kanatharana[1,2], Panote Thavarungkul[1,2], Morakot Kewapet[1,2], Dhassida Sooksawat[1,2], Panwadee Wattanasin[1,2], Kittirat Phooplub[1,2]

[1]Division of Physical Science, Faculty of Science, Prince of Songkla University, Hat Yai, Thailand
[2]Center of Excellence for Trace Analysis and Biosensor, Faculty of Science, Prince of Songkla University, Hat Yai, Thailand; *email: chongdee.t@psu.ac.th

Abstract

Sample preparation techniques play an important role in the analysis of trace organic compounds as they would assist the isolation, preconcentration and clean-up of target analytes from the complex sample matrices prior to instrumental analysis. Miniaturized sorbent based extraction is gaining much attention because it is more environmentally friendly compare to the conventional approach. It not only uses small volumes of sample and organic solvent, but also is cost effective since it requires only a small amount of sorbent and inexpensive devices. Two different developed platforms of SPE will be discussed in this presentation. Dumbbell-shaped stir-bar sorptive extraction was designed by adding a suitable amount of solid sorbent (XAD-2 resin) into a stainless-steel net that rolled into a tube and both ends were sealed with a larger size of Teflon caps. This simple extraction device was applied for the extraction of phthalate esters in food samples. The second work is the development of a microextraction device made with 3D printer uses SPME pencil lead fiber. A pencil lead fiber was modified with silver-incorporated polyaniline film. The SPME fiber was highly efficient, inexpensive and robust. The developed microextraction device was applied to detect trace phthalate esters in cosmeceutical products. The analytical performances of both developed miniaturize sample preparation techniques were investigated and their corresponded results will be discussed in the presentation.

Keywords: Miniaturized sample preparation, Dumbbell-shaped stir-bar sorptive extraction, Silver decorated polyaniline, Pencil lead fiber, Phthalate esters

Molten Salt-based Nitridation Synthesis of Metal Nitride Semiconductors

Gani Purwiandono

Department of Chemistry, Universitas Islam Indonesia, Indonesia

Abstract

The photoelectrochemical (PEC) water splitting can be a key potential solution to generate H_2 in an environmentally friendly way. Since discovering of PEC water decomposition using semiconductors, intensive research has been done to find new photocatalyst materials that generate H_2 more efficiently using sunlight. In the development of materials photocatalyst, III-nitrides are apparent due to unexpected properties such as wide-ranged direct bandgap (ranging from deep UV AlN (~6.01 eV) to far-infrared InN (~0.7 eV)), high thermal stability, and high electron mobility.

In conventional synthesis, the metal nitride semiconductors often required gas-phase nitridation of the metal oxide precursors at relatively high temperatures. One of the challenging issues in metal nitride synthesis is to explore reaction methodologies using another media of nitridation synthesis with low temperature, which would open up new avenues to create functional metal nitride materials.

Herein, we present the synthesis of GaN and InN as a material semiconductor in molten salt-based nitridation reactions. Molten salts can effectively control the crystallinity at relatively low temperatures. Moreover, molten salts have been shown to reduce the temperature and produce phase-pure nanoscale materials during the nitridation process. To investigate the further application of the synthetic method, this work focused on the effect of molten salt-based synthesis on the crystal growth of metal nitride and its photoelectrochemical properties.

Nanoparticles-functionalized Clay Based Materials for environmental remediation and medical applications

Is Fatimah[1], Ganjar Fadillah[1], Gani Purwiandono[1], Sheikh Ahmad Izaddin Sheikh Mohd Ghazali[2], Suresh Sagadevan[3,] Won-Chun Oh[4]

[1] Department of Chemistry, Faculty of Mathematics and Natural Sciences, Universitas Islam Indonesia, Kampus Terpadu UII, Jl. Kaliurang Km 14, Sleman, Yogyakarta, Indonesia, *email: isfatimah@uii.ac.id

[2]Faculty of Applied Sciences, Universiti Teknologi MARA Cawangan Negeri Sembilan, Kampus Kuala Pilah, Kuala Pilah 72000, Negeri Sembilan, Malaysia
[3]Nanotechnology & Catalysis Research Centre, University of Malaya, Kuala Lumpur 50603, Malaysia
[4]Department of Advanced Materials Science and Engineering, Hanseo University, Seosan-si, Chungnam 356-706, Republic of Korea

Abstract

Clay-based nanocomposites get interest in functional materials for many applications. The surface and structural modification of clay structure can be performed by various modifier such as polymer, metal oxide and metals nanoparticles. In this paper, the nanoparticles-modified clay structure and their applications are discussed. The key characteristics of the clay modification with nanoparticles and the influencing effects to the morphologies and physicochemical properties were evaluated. The supported silver nanoparticles, titanium dioxide nanoparticles, magnetic nanoparticles are the examples within these schemes. The correlation of functionalization to the physicochemical properties-correlated activities for environmental and medical applications that have been intensively studied is presented. The main focuses of this paper are to highlight the potencies of nanoparticles-modified clay materials and provide the challenge for developments, especially in environmental remediation and medical applications.

Self-Assembly and Phase Transition of Hydrous TiO$_2$ Colloidal Spheres for Photo/Electrochemical Applications

Jia Hong Pan

School of Environmental Science and Engineering, North China Electronic Power University, Beijing 102206, China; pan@ncepu.edu.cn

Abstract

Owning to their monodisperse nature, structural diversity at nano- and microscale, excellent structural stability, large surface area, and close-packing capability, mesoporous anatase TiO$_2$ spheres (MTS) have attracted increasing interest for photoelectrochemical applications. Traditional template and template-free (e.g. hydro/solvothermal) methods have been developed for the preparation of MAS with solid or hollow inner structure; however, mass production and textural property control have not well realized. Thanks to the colloidal science, monodisperse, amorphorse hydrous TiO$_2$ colloidal spheres (HTCS) derived from the forced hydrolysis of titanium alkoxides has been recently employed as a versatile self-template for the controllable synthesis of mesoporous TiO$_2$ spheres consisting of well-organized anatase nanocrystallites and possessing hierarchical structures and large surface area.

In this talk, synthetic technique and the underlying formation mechanism of HTCS will be first introduced. The key parameters, such as purity of titanium alkoxide (Ti(OR)$_4$), water dosage and the type of the structure-directing agents (SDAs), are discussed to achieve size-controllable synthesis. Phase transtion from HTCS to solid/hollow MTS and perovskite titanates by posttreatments such as hydro/solvothermal proces or UV irradiation is then addressed, together with the underlying structural transformations in outer surface and inner chamber of crystallized TiO$_2$ and titanate spheres. Photoelectrochemical applications of these elaborated mesoporous TiO$_2$-based spheres in the fields of semicondcutor photocatalysis and lithium-ion batteries will be discussed.
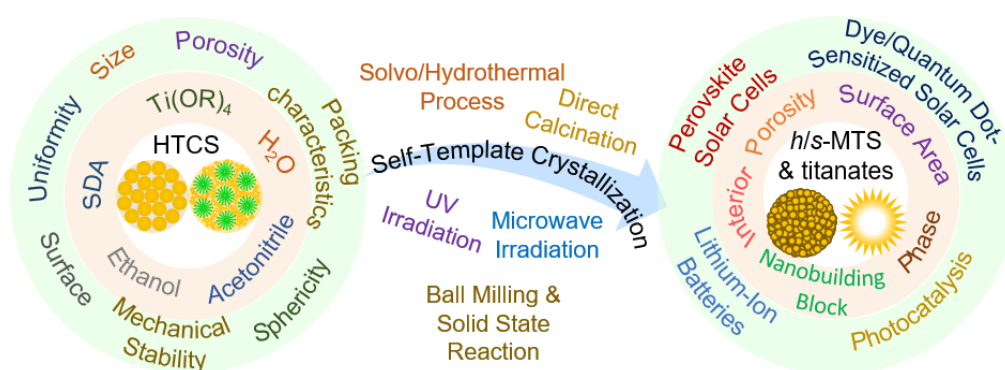
References

[1] J. H. Pan et al., *Adv. Colloid Interface Sci.* 2021, *295*, 102493
[2] J. H. Pan et al., *Cryst. Growth Des.* 2021, *21* (9), 5440−5450.
[3] J. H. Pan et al., *iScience* 2021, *24*, 102991.
[4] J. H. Pan et al., *Chemosphere* 2021, *263*, 128344.
[5] J. H. Pan et al., *ACS Appl. Energy Mater.* 2020, *3* (5), 4186−4192.
[6] J. H. Pan et al., *Langmuir* 2020, *36* (26), 7447−7455.
[7] J. H. Pan et al., *Prog. Mater. Sci.* 2020, *109*, 100620.

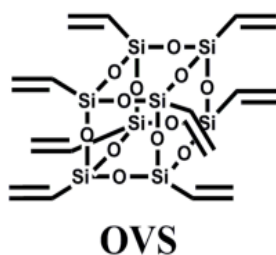# Silsesquioxanes-Based Functional Porous Polymers

Hongzhi Liu

School of Chemistry and Chemical Engineering, Shandong University, Jinan, China
e-mail:liuhongzhi@sdu.edu.cn

Abstract

Cage silsesquioxane has proven to be an ideal building block to prepare hybrid nanoporous polymers with enhanced thermal and mechanical properties in view of their rigidity and multifunctionality. Recently, octavinylsilsesquioxane(OVS) (Scheme) has been successfully used to prepare silsesquioxanes-based porous materials *via* Friedel-crafts reaction, Heck reaction or cationic polymerization by us.[1-4] Moreover, the bulky cage could prevent the aggregation of chromophores and enhance luminescence in silsesquioxanes-based porous materials.[5] These hybrid porous polymers exhibited high surface areas, thermal stabilities and excellent luminescence, which make them to be multifunctional and potentially apply in gas storage, water treatment, energy storage and sensors *etc.* [6,7]

OVS

References:

1. X. Yang; H. Liu, "Ferrocene-Functionalized Silsesquioxane-Based Porous Polymer for Efficient Removal of Dyes and Heavy Metal Ions", *Chem. Eur. J.*, **24**, 13504-13511 (2018).
2. M. Ge; H. Liu, "A silsesquioxane-based thiophene-bridged hybrid nanoporous network as a highly efficient adsorbent for wastewater treatment", *J. Mater. Chem. A., 4*, 16714-16722 (2016).
3. X. Yang; H. Liu, "Diphenylphosphine-Substituted Ferrocene/Silsesquioxane-Based Hybrid Porous Polymers as Highly Efficient Adsorbents for Water Treatment"，*ACS Appl. Mater. Interfaces,* **11**, 26474−26482 (2019).
4. Y. Du; M. Ge; H. Liu, "Porous Polymers Derived from Octavinylsilsesquioxane by Cationic Polymerization", *Macromol. Chem. Phys., 220*, 1800536-1800543 (2019).
5. Y. Yan; M. Laine; H. Liu, "In Situ Methylation Transforms Aggregation-Caused Quenching into Aggregation-Induced Emission: Functional Porous Silsesquioxane-Based Composites with Enhanced Near-Infrared Emission", *ChemPlusChem, 84*, 1630–1637(2019).
6. Y. Du; H. Liu, "Cage-like silsesquioxanes-based hybrid materials", Dalton Trans., *49, 5396-5405*(2020).
7. M. Soldatov, **H. Liu***, Hybrid porous polymers based on cage-like organosiloxanes: synthesis, properties and applications, *Progress in Polymer Science*, **2021**, *119*,101419.

Constructed Ultra-Sensitive SERS Probe towards Detection of Herbicide Paraquat and Diquat

Caiyu Ni, Jiadong Zhao, Xiaoxiao Zhao, Zhihui Wang, and Daming Gao[*]

Department of Chemical Engineering, School of Energy Materials and Chemical Engineering, Hefei University, Hefei 230601, Anhui, China; [*]To whom correspondence should be addressed. dmgao@hfuu.edu.cn, Tel: +86-551-62158047

Abstract

Herein, a strategy for the functional modification of silica nanoparticle surface encapsulated by free-tagged Ag nanoparticles is addressed together with their applications in the based-SERS detection and degradation of target species, including paraquat and diquat. The gap formed by two interparticles with SERS hot spots provides a gigantic amplification signal for the Raman scattering intensity of the analyte molecule located approximately the hot spots. The SPR effect was applicable to detect the trace paraquat and diquat through the enhanced intensity of Raman scattering. Meanwhile, the intrinsic properties of Ag nanoparticles were employed to degrade the target analytes, which are harmful to human health and deleterious to the ecological environment in soils and waters. A comparison between Ag nanoparticles and SiO_2@Ag nanoparticles was performed to detect the different herbicides using the sensors systems. The surface functional modification of silica contributed the most vigorous and effective technique as Ag nanoparticles SERS sensor, which enabled the SERS sensor detection of these target analytes down to 10^{-9} M in the aqueous solution for Raman spectra achieved by single Ag nanoparticle aggregates. Moreover, SERS spectra provided vital finger information about the interaction mechanism between herbicides and the Ag nanoparticles sensor, revealing the formation of a CT complex between the herbicides and Ag nanoparticles, and changes in the host conformation. The position of the ν(Ag-Cl) band and the SPR contribution assigned to Ag dimers were also utilized as spectral markers to monitor the host-guest interaction.
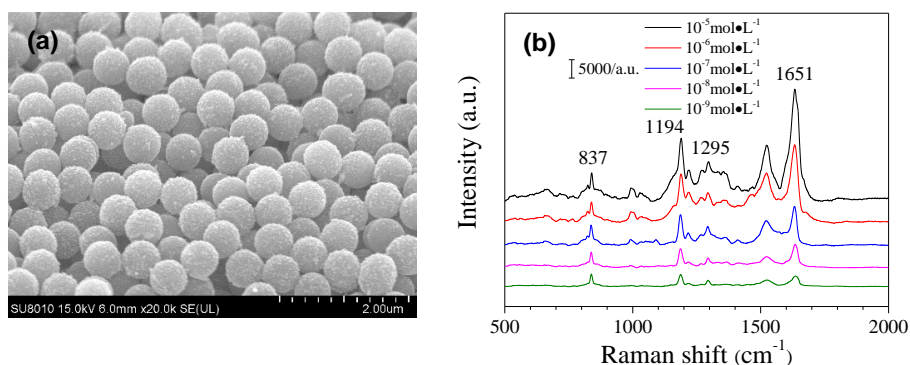
Figure 1 SEM image (a) of SiO_2@Ag nanoparticles with SERS active and Raman spectra evolution of paraquat (b) with the increase of four types of analytes concentration from bottom to top in order: 10^{-9}, 10^{-8}, 10^{-7}, 10^{-6}, and 10^{-5} mol•L^{-1}, respectively.

References

1. Botta R, Eiamchai P, Horprathum M, Limwichean S, Chananonnawathorn C, Patthanasettakul V, Maezono R, Jomphoak A, Nuntawong N (2020) 3D structured laser engraves decorated with gold nanoparticle SERS chips for paraquat herbicide detection in environments. Sens Actuator B: Chem, 304: 127327.

2. Linh VTN, Moon J, Mun C, Devaraj V, Oh JW, Park SG, Kim DH, Choo J, Lee YI, Jung, HS (2019) A facile low-cost paper-based SERS substrate for label-free molecular detection. Sens Actuator B: Chem 291:369-377.

3. Ge MH, Li P, Zhou GL, Chen SY, Han W, Qin F, Nie YM, Wang YX, Qin M, Huang GY, Li SF, Wang YT, Yang LB, Tian ZQ (2021) General Surface-Enhanced Raman Spectroscopy Method for Actively Capturing Target Molecules in Small Gaps. J. Am. Chem. Soc. 143:7769-7776.

Acknowledgements

Fluorescence-Tagged Recognition Sites SiO$_2$@MIPs with Nanoshell Layer Structure to the Ultra-Trace Detection of Heavy Metal Ions

En Yang, Xiaoxiao Xia,[*] Yue Cai, Fei Chang

Department of Biology Engineering, School of Biology, Food and Environment Engineering, Hefei University, Hefei 230601, Anhui, China; [*] To whom correspondence should be addressed. xia@hfuu.edu.cn, Tel: +86-551-62158453.

Abstract

Herein, a strategy for a metal ion-imprinted SiO$_2$@MIPs nanoparticles with fluorescence-tagged recognition sites was performed to construct the selective sites with sensitive optical response signal to specific metal ion. The surface of synthesized SiO$_2$ nanoparticles was functionally modified by the derivative residue group of APTS conjugated with NBD-Cl molecule through the hydrolysis and condensation reactions. The as-prepared SiO$_2$ nanoparticles were encapsulated by metal ions (Cu^{2+}, Cd^{2+}, Hg^{2+}, and Pb^{2+})-imprinted polymers with nanostructured shell layers through the copolymerization of EGDMA as crossing linker, AIBN as initiator, metal ions as template molecules, AA as functional monomer, and acetonitrile as solvent. The layers of SiO$_2$@MIPs nanoparticles with core-shell structure removed template molecules by EDTA-2Na to remain the cavities and spatial sizes to match the imprinted metal ions. The nanostructured-shell layers with fluorescence-tagged recognition sites rebound metal ions by the driving force of concentration difference demonstrates the high selective recognition and sensitive detection to heavy metal ions through the decline of fluorescence intensity. The LODs concentration for four metal ions is down to 10^{-9} mol•L^{-1}. The method will provide biomimetic synthesis, analyte screen, and detection of highly deleterious materials in the environment for theoretical foundation and technological support.
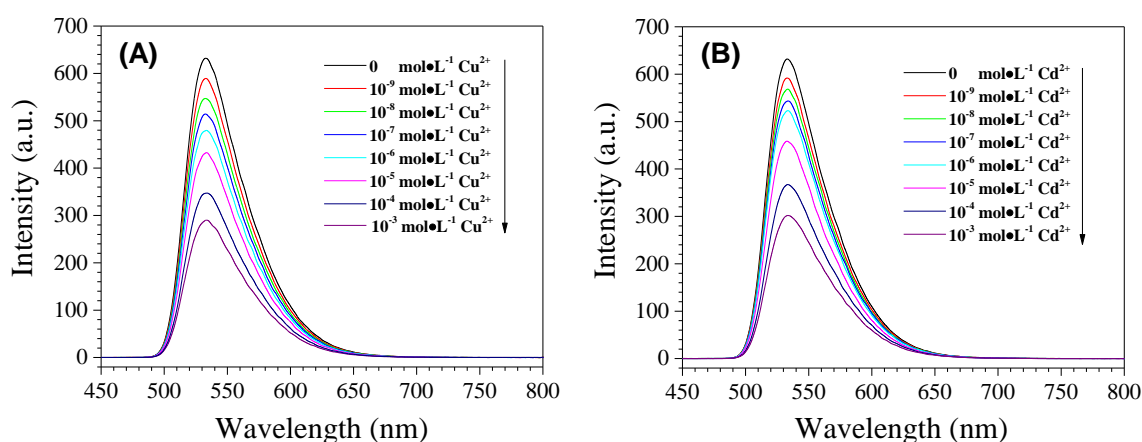
Figure 1 The limits of detection for the SiO$_2$@MIPs nanoparticles with fluorescence-tagged recognition sites to the different metal ion concentration from top to bottom in order: 0, 1×10^{-9}, 1×10^{-8}, 1×10^{-7}, 1×10^{-6}, 1×10^{-5}, 1×10^{-4} and 1×10^{-3} mol·L^{-1}, respectively. (A) and (B) represent the Cu^{2+} and Cd^{2+} different concentrations added into the fluorescence nanoparticles, individually.

References

1. Peng J.J, Li JY, Xu W, Wang L, Su DD, Teoh CL, Chang YT (2018) Silica nanoparticle-enhanced fluorescent sensor array for heavy metal Ions detection in colloid solution. Anal Chem 90:1628-1634.
2. Neupane LN, Oh ET, Park HJ, Lee KH (2016) Selective and sensitive detection of heavy metal ions in 100% aqueous solution and cells with a fluorescence chemosensor based on peptide using aggregation-induced emission. Anal Chem 88:3333-3340.
3. Kim J, Oh JS, Park KC, Gupta G, Lee CY (2019) Colorimetric detection of heavy metal ions in water via metal-organic framework. Inorg Chim Acta 486:69-73.

Acknowledgements

Sustainability in the synthesis of *N*- Heterocycles

K. L. Ameta *

Department of Chemistry, School of Liberal Arts and Sciences, Mody University of Science and Technology, Lakshmangarh-332311, Rajasthan, India

E-mail: klameta77@hotmail.com

Abstract

Pharmaceutical and chemical industries are facing the big challenge of finding adequate processes to produce large quantities of new products with special care of environment. Due to the crucial climate change issues, it is very important to focus on the novel developments for the organic synthesis in the areas such as catalysis, reagents, efficient synthetic methods and alternative energy sources having less impact on the environment and the risk of disasters. Azaheterocycles always played a vital role in biological processes and are widespread as natural products and the processes focused on the design and synthesis of such heterocycles are always in demand and the need of the present days.

High-Performance Nanocomposite of Metal Oxide and Reduced Graphene Oxide for Vanadium Redox Flow Battery

Daniel Manaye Kabtamu[1], Chen-Hao Wang[*1,2]

[1]Department of Materials Science and Engineering, National Taiwan University of Science and Technology, Taipei 106335, Taiwan

[2]Hierarchical Green-Energy Materials (Hi-GEM) Research Center, National Cheng Kung University, Tainan 70101, Taiwan

*Corresponding author: chwang@mail.ntust.edu.tw

Abstract

All vanadium redox flow battery (VRFB) is an electrochemical storage device with high efficiency, long cycle life, flexible design, and safety. In order to enhance its performance, the carbon-based electrodes need to be modified, and metal oxide and reduced graphene oxide nanocomposite are what we use in this study. We will report one or two methods to prepare metal oxide and reduced graphene oxide nanocomposite for enhancing the activity and reducing the production cost of VRFB. For instance, a MoO_2-reduced graphene oxide nanocomposite (MoO_2-rGO) electrode material shows excellent electrocatalytic activity for VO^{2+}/VO^{2+} and V^{3+}/V^{2+} than those of MoO_2 and rGO samples. The energy efficiency (EE) of the VRFB employing the MoO_2-rGO sample is 78.05% at 80 mA cm^{-2}, which is about 4% and 12% higher than using the rGO-coated graphite felt (GF) electrode and the GF electrode, respectively. We consider that the high activity of MoO_2-rGO electrode material is attributed to several reasons. First, the MoO_2 nanoparticles are uniformly distributed on the surface of rGO, suppressing nanoparticles aggregation and eluding the restacking of the rGO sheets. Second, oxygen vacancies of MoO_2 play the role of active sites to catalyze the redox reaction of the vanadium ions. Third, rGO has high conductivity and high oxygen-containing functional groups, which stabilize the MoO_2 nanoparticles and reduce the resistance of the electrode.

Keywords: Vanadium redox flow battery; reduced graphene oxide; MoO_2; MoO_2-rGO nanocomposite; graphite felt

Synthetic organic adsorbents for the removal of organic pollutants and heavy metal ions from water

Solhe F. Alshahateet[a,*], Salah A. Al-Trawneh[a], Anwar G. Jiries[a], Suresh Sagadevan[b]

[a]Department of Chemistry, Mutah University, P.O. Box 7, Mutah, Alkarak, Jordan
[b]Nanotechnology & Catalysis Research Centre, University of Malaya, Kuala Lumpur, 50603, Malaysia. *Email: s_alshahateet@mutah.edu.jo

Abstract

The utilization of synthetic organic adsorbents was investigated for organic pollutants and heavy metal ions elimination from water. The optimum adsorption conditions were included such as initial pollutant concentrations, reaction temperatures, and experimental duration. The adsorption process was studied by Langmuir, Freundlich, and Temkin isotherm models. Moreover, all essential thermodynamic variables such as Gibbs free energy ($\Delta G\circ$), enthalpy ($\Delta H\circ$), and entropy ($\Delta S\circ$) were calculated. The overall outcome shows the efficiency of our synthetic organic adsorbents in organic pollutants and heavy metal ions adsorption and it may become a viable solution in the near future.

References

1. Mohammed M. Al-Mahadeen, Anwar G. Jiries, Salah A. Al-Trawneh, Solhe F. Alshahateet, Ahmad S. Eldouhaibi and Suresh Sagadevan "Kinetics and equilibrium studies for the removal of heavy metal ions from aqueous solution using the synthesized C-4-bromophenylcalix[4]resorcinarene adsorbent" *Chemical Physics Letters,* 2021. 783. 139053.
2. Salah A. Al-Trawneh, Anwar G. Jiries, Solhe F.Alshahateet, Suresh Sagadevan "Phenol Removal from Aqueous Solution using Synthetic V-Shaped Organic Adsorbent: kinetics, isotherm, and thermodynamics studies" *Chemical Physics Letters*, 2021, 781, 138959.

Oral Lecture

The Nature on Electronic Spectra of Histidine "$N_{\varepsilon 2}$" and "$N_{\delta 1}$" Using A CASSCF/CASPT2 Method

Salmahaminati[1], and Daniel Roca-Sanjuán[2]

[1] Chemistry Department, Universitas Islam Indonesia, Kampus Terpadu UII, Jl. Kaliurang Km 14, Yogyakarta, Indonesia 5558422
[2] Instituto de Ciencia Molecular, Universitat de València, P.O. Box 22085, 46071 Valencia, Spain

Abstract

On the basis of ab initio quantum chemical calculations, we interpret the absorption spectra of two isomers histidine "$N_{\varepsilon 2}$" and "$N_{\delta 1}$" in the UV range of the electromagnetic spectrum and study the photochemistry of the lowest-lying excited states. We determined the molecular ground state geometries using CASSCF methods. The vertical electronic transition energies and associated oscillator strengths and dipole moments of the lowest excited states were computed at the CASPT2//CASSCF level. We found that the lowest-energy S1 state in histidine is of $n_{CO} \rightarrow \pi_{CO}*$ nature. The largest differences between both isomers is related to the (n, π*) excitations of nitrogen that is localized on the aromatic ring which is related to a different protonation of nitrogen on the aromatic ring. The computed absorption and emission energies are in good agreement with the experimental data.

Keywords: CASSCF, CASPT2, histidine

Influence of Operational Parameter on the Solar Light Driven Photocatalytic Degradation of Ofloxacin Antibiotic using Bismuth Ferrite (BiFeO₃) Nanoparticles

Ahmad Fadhil Rithwan[1], Muhammad Alif Abdul Khani[1], Noor Haida Mohd Kaus[1], Rohana Adnan[1], Sirikanjana Thongmee[2], Siti Fairus Mohd Yusoff[3], Takaomi Kobayashi [4]

[1]School of Chemical Sciences, Universiti Sains Malaysia, Gelugor 11800, Pulau Pinang, Malaysia; ahmadfadhil18@gmail.com; ashraftree2030@gmail.com; noorhaida@usm.my; r_adnan@usm.my

[2]Department of Physic, Faculty of Science, Kasetsart University, Bangkok 10900, Thailand; fscisjn@ku.ac.th

[3]Department of Chemical Sciences, Faculty of Science and Technology, Universiti Kebangsaan Malaysia, Bangi 43600, Selangor, Malaysia; sitifairus@ukm.edu.my

[4]Department of Materials Science and Technology, Nagaoka University of Technology, Nagaoka, Japan; takaomi@nagaokaut.ac.jp

Abstract

Photocatalysis is one of the advanced oxidation processes (AOP) which attract interest among the researchers to be utilized in the degradation of organic pollutants due to its mineralization and environmentally friendly approach. Ofloxacin was used as the model for this experiment since it is a prescription antibiotic that can be found at low concentrations in water bodies. Bismuth ferrite, BiFeO₃ is a multiferroic semiconductor with great potential in the photocatalysis field. However, obtaining the pure phase of perovskite BiFeO₃ throughout the synthesis process proved difficult. Thus, the pure BiFeO₃ was effectively synthesized using the sol-gel method via bio-templating in the presence of carrageenan. This multiferroic photocatalyst was utilized in the photocatalytic degradation of ofloxacin under natural solar light in different operational parameters such as photocatalyst dosage, the concentration of ofloxacin, pH of the solution, and effect of hydrogen peroxide, H_2O_2 as an oxidant. Scanning electron microscopy (SEM) image obtained shows the BiFeO₃ nanoparticle has a rhombohedral structure with an average size particle of ~170 nm. The pure phase of the BiFeO₃ was confirmed by the X-ray diffraction (XRD) analysis as the result exhibits rhombohedral distorted perovskite structure. Fourier transform infrared spectroscopy (FTIR) result shows absorption peaks at 568 and 457 cm^{-1} which are associated with the Fe-O and Bi-O bending vibration of BiFeO₃, respectively. The surface area, pore size and pore volume of BiFeO₃ identified are 4.67 m^2/g, 31.94 nm, and 0.041 cm^3/g, respectively. The calculated band gap energy based on the Kubelka-Munk theory for BiFeO₃ was 2.04 eV which is small and responds toward visible light. The optimum conditions for the photocatalytic activity of BiFeO₃ were found out to be 0.07 g/L of BiFeO₃ at pH 8 in 10 mg/L ofloxacin and 0.3 M H_2O_2 with the degradation of ~70 % and the reaction followed pseudo-first order kinetics. The observed results show that obtained BiFeO₃ nanoparticles are pure and a promising catalyst for the degradation of ofloxacin and other organic pollutants.

Keywords: Photocatalysis, Photo-functional materials, nano porous materials, ofloxacin, solar light driven

The Effect of Sulfation on Physicochemical Properties of ZrO$_2$ and TiO$_2$ Nanoparticles

Karna Wijaya [a,*], Edhita Rahmawati Fitri [a], Prisnu Fadilah Prabani [a], Yufinta Candrasasi [a], Remi Ayu Pratika [a], Wahyu Dita Saputri [b], Sri Mulijani [c], Aep Patah [d], and Arief Cahyo Wibowo [e]

[a] Chemistry Department, Faculty of Mathematics and Natural Sciences, Universitas Gadjah Mada, Yogyakarta, Indonesia
[b] Indonesian Institute of Sciences, Sasana Widya Sarwono (SWS), Jakarta 12710, Indonesia
[c] Chemistry Department, Faculty of Mathematics and Natural Sciences, Institut Pertanian Bogor, Bogor, West Java, Indonesia
[d] Chemistry Department, Faculty of Mathematics and Natural Sciences, Institut Teknologi Bandung, Bandung, West Java, Indonesia
[e] Chemistry Department, Faculty of Mathematics and Natural Sciences, Universitas Airlangga, Surabaya, East Java, Indonesia; Corresponding author: karnawijaya@ugm.ac.id

Abstract

The effect of sulfation process on the physicochemical properties of ZrO$_2$ and TiO$_2$ nanoparticles was properly studied. The SO$_4$/ZrO$_2$ and SO$_4$/TiO$_2$ catalysts were synthesized to identify each acidity character. The wet impregnation method was employed using H$_2$SO$_4$ with various concentrations of 0.5; 0.75; and 1 M followed by calcination at 400, 500, and 600 °C to obtain the optimum condition of the synthesis process. The highest total acidity of 2.642 mmol/g was found for 1 M SO$_4$/ZrO$_2$ with 500 °C calcination temperature and the highest total acidity of 6.920 mmol/g was obtained for 1 M SO$_4$/TiO$_2$ using similar calcination temperature. The sulfation impacted the increase in the size of the titania particles due to its agglomeration process. In contrast, the sulfation practically did not form a change in the size of the zirconia particles. However, the sulfation process caused the color of both catalyst particles to become brighter. An essential finding of this study was that 1 M SO$_4$/TiO$_2$ calcined at 500 °C was the best candidate as a heterogenous acid catalyst that have been synthesized in this work due to the highest total acidity.

Keywords: Sulfated zirconia, sulfated titania, acidity, calcination, impregnation

Acknowledgments

Green Synthesis of Silver Nanoparticles using Mangosteen (*Garcinia Mangostana* L.) Peels Waste and Its Colorimetric Performance for Pb^{2+} Detection

Khoirunisa[1], Hasna Azizah Zahra[1], Rahmania Audita[1], Wiyogo Prio Wicaksono[1,2*]

[1]Department of Chemistry, Faculty of Mathematics and Natural Sciences, Universitas Islam Indonesia, Sleman, Special Region of Yogyakarta, 55584, Indonesia
[2]Research Center for Materials and Electrochemistry, Faculty of Mathematics and Natural Sciences, Universitas Islam Indonesia, Sleman, Special Region of Yogyakarta, 55584, Indonesia
Corresponding author: wiyogo.prio@uii.ac.id

Abstract

Silver nanoparticles (AgNPs) have been successfully synthesized through facile green synthesis pathways. $AgNO_3$ was employed as the precursors, whereas the mangosteen (*Garcinia Mangostana* L.) peels extract (MPE) was used as both reducing and stabilizing agents. Initially, the MPE was prepared using a reflux system for a 3 h reaction, followed by the AgNPs preparation by mixing of the precursor and MPE, then left undisturbed for a 6 h reaction. The synthesized AgNPs showed a strong visible peak at 415 nm that indicated the AgNPs was successfully formed, whereas there was no peak observed at 415 m for the MPE. Further investigation, the IR spectra revealed that the OH-groups of polyphenols in the MPE has a main role in the AgNPs formation. The preliminary study of its colorimetric performance was evaluated for the detection of Pb^{2+} heavy metal ions. Interestingly, there was a color change from light yellow to orange when Pb^{2+} was added to the AgNPs solution and the UV-Vis spectra was also showed the decrease of the characteristic absorbance peak at 415 nm, revealing the potency of the green synthesized AgNPs for the colorimetric sensing probe.

Keywords: Ag nanoparticles, green synthesis, Pb^{2+} metal ions, colorimetric, mangosteen peels waste

Electrochemical Determination of Sulfadiazine at Fe-doped CeO$_2$ Solid Solution Nanoparticles Modified Carbon Paste Electrode

Chengbao LIU [1,2,3*], Junchao QIAN [1,2,3], Zhigang CHEN [1,2,3]

[1]Jiangsu Key Laboratory for Environment Functional Materials, Suzhou University of Science and Technology, Suzhou 215009, China; [2]School of Materials Science and Engineering, Suzhou University of Science and technology, Suzhou 215009, China; [3]Jiangsu Collaborative Innovation Center of Technology and Material for Water Treatment, Suzhou University of Science and Technology, Suzhou 215009, China

Abstract

The Fe-doped CeO$_2$ solid solution nanoparticles are successfully prepared by the hydrothermal method on the biotemplate. Sodium caseinate is used as gel skeleton for ceria growth in aqueous solution. It forms casein submicelles through self-assembly with a diameter of about 10 nm. In these micro-environment, Fe-doped CeO$_2$ solid solution nanoparticles are constantly growing and exhaust the metal ions surrounding to effectively avoid agglomeration. The confinement effect provided by the protein caves makes the particles uniform in shape and uniformly dispersed. Glassy carbon electrodes chemically modified with this novel solid solution nanoparticle to determine sulfadiazine are developed. Cyclic voltammetry (CV), differential pulse voltammetry (DPV) and electrochemical impedance tests are employed to analyze the electrocatalytic performance of sulfadiazine. The results show that under the optimal experimental conditions, the modified carbon paste electrode exhibit strong electrocatalytic performance for sulfadiazine. The linear response range of peak current and sulfadiazine test solution was 1×10^{-8}~1×10^{-4}. The standard curve equation can be expressed as y=1.3451x+2.9759 (R^2=0.9978) and the detection limit is 3.73 nM (S/N=3). In addition, it shows good detection performance in anti-interference test and actual sample detection.

Development of gel electrolyte from agar for using in Ag/AgCl electrode

Peerapon Jarungklin[1,*], Paiboon Sreearunothai[1] and Korakot Sombatmankhong[2]

[1]Master of Engineering (Engineering Technology), Sirindhorn International Institute of Technology, Thammasat University (Rangsit Campus), 99 Moo 18, Khlong Nueng, Khlong Luang, Pathum Thani 12120, Thailand

[2]National Science and Technology Development Agency (NSTDA), National Energy Technology Center (ENTEC), 114 Thailand Science Park, Phaholyothin Road, Klong Nueng, Klong Luang, Pathum thani, 12120, Thailand;

e-mail: markbo9555@gmail.com

Abstract

Ag/AgCl reference electrode (Ag/AgCl) is frequently employed among the reference electrodes due to its simplicity, low cost, environmental-friendly with non-toxic components. Normally, Ag/AgCl reference electrode is filled with liquid electrolyte, which makes the electrode prone to leakage or evaporation loss, and is also difficult to maintain. Gel polymer electrolyte (GPE) is an alternative for use as electrolyte in reference electrode that can provide high flexibility, low maintenance, and possibility for miniaturization. In this paper, an alternative fabrication of the Ag/AgCl reference electrode using agar as gel polymer electrolyte is presented. Agar, glutaraldehyde (GA), and potassium chloride (KCl) were used for preparation of GPE. The gel prepared has low evaporation loss, good mechanical strength, maintain the conductivity value and can be stored without salt creep, or moldy for over 3 months. A prototype reference electrode was also constructed by using a pipette tip installed with silver wire that has been applied with 3V current in 0.05M KCl for 10 min to coating a layer of AgCl and also installed the PTFE porous junction at the end of pipette tip. This prototype Ag/AgCl reference electrode was used to test the potential stability and difference in 0.1M, 1M, 2M and pH 4, 7, 10 solution for 5min and 10 hours. The results showed variation of potential stability average of 5 min and 10 hours test are less than 15 mV and potential difference average are less than 0.6 mV.

Keywords: Agar/Glutaraldehyde/Reference Electrode/Potential Stability and Difference/ Gel Electrolyte

Introduction

Ag/AgCl reference electrode (Ag/AgCl) was recommended among the reference electrodes due to simplicity, low cost and nontoxic components. This commercial reference electrode was typically constructed by immersing an Ag wire coated with AgCl in KCl or other chloride ion-rich solution contained in glass liquid junction [1]. Normally, Ag/AgCl reference electrodes are filled with liquid electrolyte but this has some disadvantages such as the electrode is prone to leakage or evaporation of the electrolyte as well as safety-related issues.

Gel polymer electrolyte is an alternative to use as electrolyte in reference electrode for solving the disadvantage. For example, Hassel et al. modified miniaturized Ag/AgCl reference electrode filled with gel electrolyte for use in micro-chemistry [2]. Zhao et al. developed flexible Ag/AgCl reference electrode based on perylene tube [3]. Compared with liquid electrolyte, gel polymer electrolyte (GPE) provides good flexibility, high safety, little or no

leakage with potential for miniaturization. GPE can be formulated using a polymer, salt, solvent and additives [4].

Agar is a heterogeneous mixture of two polysaccharides: agaropectin and agarose, which have been used as gel-forming polysaccharides and can be found naturally such as in seaweed. Agar chain consists of alternating 1,3-linked D-galactopyranose and 1,4-linked 3,6 anhydro-Ị-L-galactopyranose units [5, 6]. Agar may be used as gel electrolyte due to its cost effective, environmentally friendly, and is also easy to fill in the electrode upon heating into the liquid state [6, 7]. Glutaraldehyde (GA) has been widely used in many applications due to its high reactivity and ease of reaction. has also been used in literature as a preservative, disinfectant and also an additive to improve the shelf-life of the product [8, 9]. In this work, an alternative fabrication of the Ag/AgCl reference electrode using agar as gel polymer electrolyte is presented. Agar, glutaraldehyde (GA), and potassium chloride (KCl) were used for preparation of GPE and were filled in the fabricated reference electrodes that were then tested for their physical and electrochemical properties.

Experimental

1. Preparation and physical characterizations of gel electrolyte

1.1 Preparation of agar gel

KCl solution (1M, 20 mL) was poured in a glass bottle and boiled at 60-80°C on a hot plate. Agar powder (3%w/v) was then added into the heated KCl solution. The mixture solution was kept stirred using magnetic stirrer until agar was completely dissolved. Glutaraldehyde (1, 2.5 and 5% v/v) was then added and kept stirring for another 10 min. The temperature was then decreased and 20 ml of the solution was poured into a petri dish with a micro pipette. The solution was left at room temperature until solidification. There were four agar gel compositions: "Blank", "1% GA", "2.5% GA" and "5% GA".

1.2 Evaporation loss analysis

Evaporation loss was analyzed by weighting a petri dish before and after pouring agar gel without a petri dish lid. Agar gel was poured into petri dish and kept at 40°C in an oven to analyze the evaporation loss. Usually, a gel was kept for 30 days and the percent evaporation loss is calculated by the following equation:

$$\% Evaporation\ Loss = \frac{(Weight\ of\ GPE\ (Day\ 0) - Weight\ of\ GPE\ (Day\ n))}{Weight\ of\ GPE\ (Day\ 0)}\ x\ 100 \qquad (1)$$

1.3 Shelf-life analysis

The shelf life of agar gels was determined by incubating agar gel at 25°C for up to several months and inspecting the mold and salt creep that developed. The result was compared between pure agar gel and agar gels with GA additives.

1.4 Compression and 3-points bending tests

Compression and 3-points bending test were used to evaluate mechanical properties using a universal testing machine (UTM). Measurements were carried out at room temperature and gel samples were cut with a dimension of 1cm x 1cm x 1cm for compression test and with a dimension of 3cm x 1cm x 1cm for the 3-points bending test. For compression test, gel samples were placed on two parallel plates, where a compression force was applied at the rate of 5 N/min to the sample until the gel breaks. The results were reported as the average values from five samples and calculated by the following equations:

$$CS = \frac{F}{A} \qquad\qquad (2)$$

$$\sigma = \frac{3FL}{2wd^2} \qquad\qquad (3)$$

where CS is compression strength (MPa), F is force (N) and A is surface area (mm^2). For the 3-points bending test, the gel bar was placed on the two legs with a separation distance of 2.5 cm. A tip was then applied to press the gel bar in the middle with the rate of 5 N/m. The flexural strength was then calculated where σ is flexural strength (Pa), F is the maximum force applied before the gel breaks (N), L is the separation distance between two legs of the probe (m), w is width (m) and d is depth (m).

2. Preparation of Ag/AgCl reference gel electrode

2.1 Coating of Ag wire with AgCl

An Ag wire (99%) was scrubbed with sandpaper, cleaned with DI water, and immersed in 0.1 M HNO$_3$ for a few seconds and washed again with DI water. The Ag wire was then coated with AgCl layer by connecting the wire to a positive terminal of the potentiostat set at 3V and immersed into a 50 mM KCl solution. The current was allowed to pass through for 10 min when the shiny Ag wire was completely covered with a gray-black layer as shown in (Fig. 1).
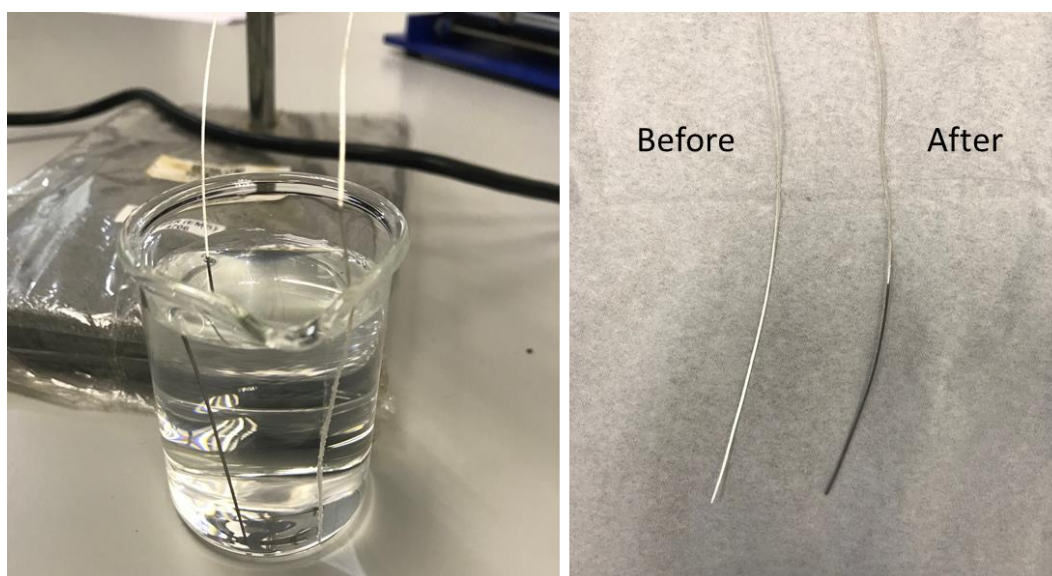
Fig. 1. The coating of the AgCl layer onto the Ag wire

2.2 Construction of Ag/AgCl reference electrode

A simple homemade chamber of the reference electrode was constructed from a 10 mL micropipette tip. A porous junction made from PTFE was installed at the end of the tip. The tip was filled with a hot solution of agar gel electrolyte and let it cool down and solidified inside the tip. After cooling and solidification, Ag wire coated with the AgCl layer was pricked into the gel electrolyte. Finally, the tip was sealed with parafilm to prevent evaporation loss (Fig. 2). There were four different types of Ag/AgCl

reference electrode model which named "PTFE – Blank", "PTFE – 1% GA", "PTFE – 2.5% GA" and "PTFE – 5% GA".
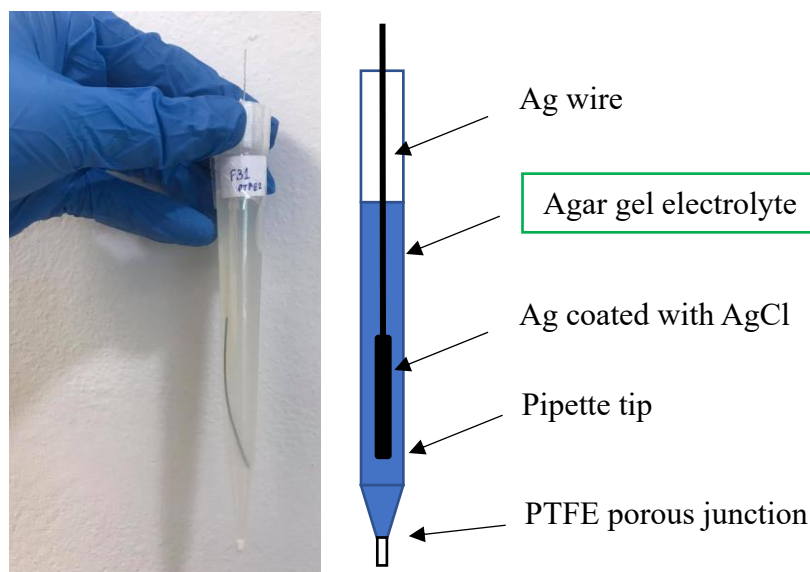
Fig. 2. Model of fabricated Ag/AgCl reference electrolyte.

3. Electrochemical characterization of the gel

3.1 Conductivity analysis

The conductivity was analyzed by using a conductivity probe (LF 1100T+, SI Analytics) and conductivity cell (Z 461, SI Analytics). A 20 g of gel samples placed in petri dish were connected to Pt reference electrode by pricking 5 mm down into the gel samples. The AC impedance was collected using the potentiostat with Pt electrodes. The applied voltage was set to 0.01-Vrms in the frequency range of $10^6 – 10$ Hz. The AC impedance data was conducted to conductivity value using Z-view program. The conductivity value was calculated from the equation:

$$K = \frac{I}{A} \tag{4}$$

$$\sigma = \frac{K}{Z'} \tag{5}$$

where K is cell constant (cm^{-1}), I is a distance between two electrodes (cm), A is a surface area of electrode (cm^2), σ is conductivity value (mS/cm) and Z' is a resistance from Nyquist plot (Zview program) at the interception of Z'' at 0 Ω.

#### 3.2 Potential stability and difference measurement

The potential stability and difference of fabricated Ag/AgCl reference electrode was compared with commercial Ag/AgCl reference electrode by immersing together in 0.1, 1 and 2M KCl and pH 4, 7 and 10 solutions and tested by potentiostat for 5 min and 10 hours. All electrochemical characterizations were performed by using the potentiostat (Autolab, PGSTAT 204, Metrohm) (Fig. 3).
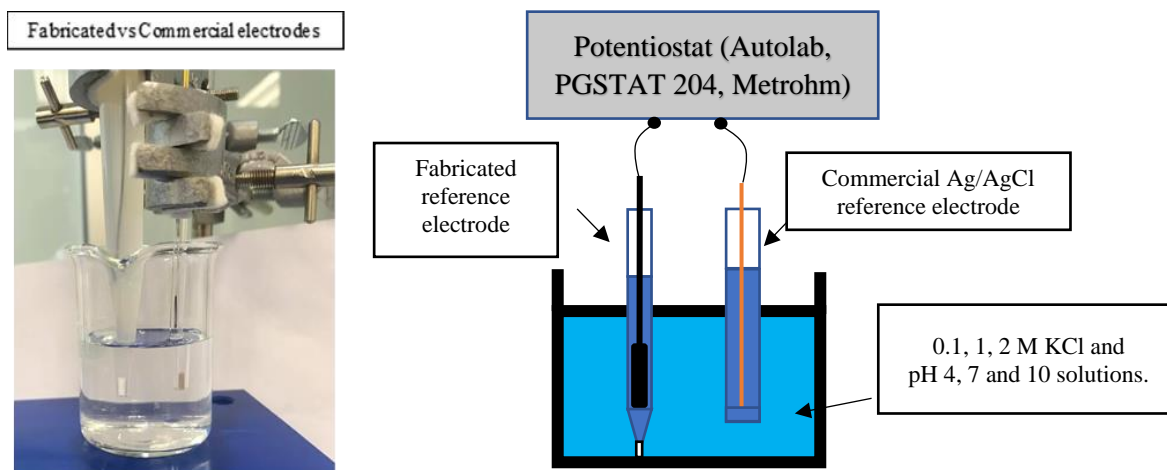
Fig. 3. Setup used for potential stability and difference measurement.

Results and discussion

From Fig. 4, evaporation loss of agar gels for 90 days showed that the increasing of 2.5% and 5% glutaraldehyde (GA) concentration increased evaporation loss of agar gel electrolyte and only 1% GA added decreased the evaporation loss of agar gels. The results were obtained from average of three samples for each %GA concentrations. The gel samples were also placed in randomized positions in the oven. This result indicates that there is an optimum %GA where the evaporation loss is minimum. GA can induce cross-linking in the gel, which was also reflected from increase compression and flexural strengths. The cross-linked gel may be able to hold water within the structure better than the blank gel. However, adding too much GA content may decrease the percent agar in the final gel product, and may affect the water holding ability of the final gel.
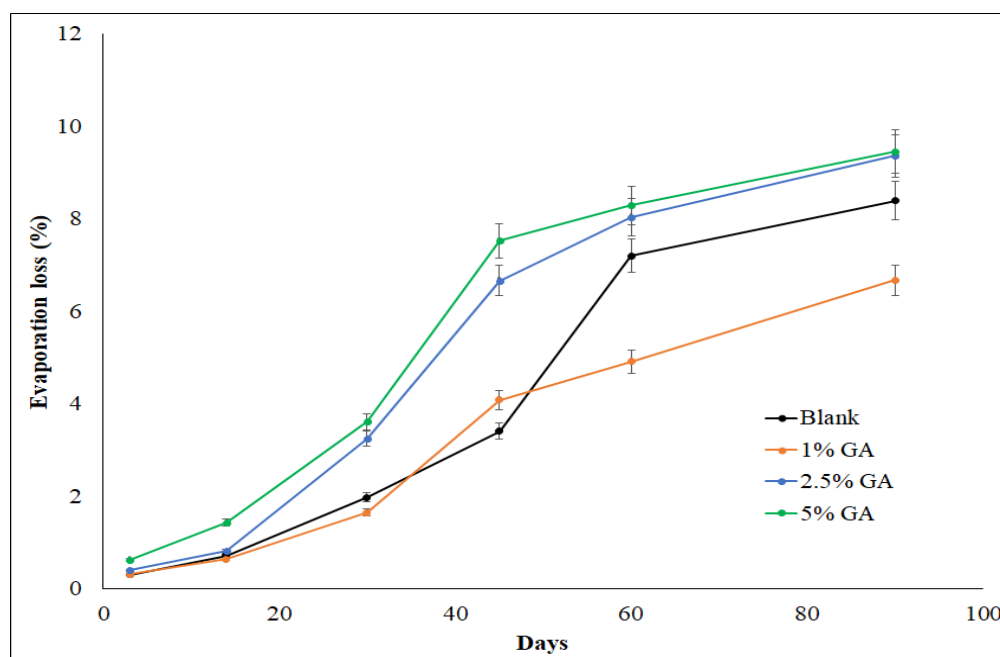
Fig. 4. Evaporation loss (%) of Blank, 1% GA, 2.5% GA and 5% GA agar gel for 90 days.

One of the main points of adding GA is to improve the storage times of agar gel electrolyte. The shelf-life of agar gel was analyzed. In this work, it was found that adding of GA solution improved the shelf-life of agar gels. The agar gels sample with GA added showed storage times more than 90 days without salt creep or any mold observed compared to the pure agar gel which can be stored for only around 15 days at room temperature when the mold can be observed on the gel.

The mechanical strengths of gel samples measured by the compression and 3-points bending tests are shown in Table 1. The addition of 1%, 2.5% and 5% GA concentration showed the improvement of compression and flexural strength. Adding 1% GA concentration can already lead to 41.28% and 51.72% (85.9 kPa and 43.8 kPa) increase in the compression and flexural strengths compared to the pure agar gel. The 2.5 and 5% GA gel samples show similar strengths to that of the 1%GA.

Table 1. Summary of compression test, 3-points bending test and conductivity value of agar gels.

| Agar gels	Compression test (kPa)	3-Point bending test (kPa)	Conductivity (mS/cm)
Blank	60.8±7.3	29.0±1.0	115.1±7.0
1% GA	85.9±8.8	43.8±1.5	120.9±12.5
2.5% GA	81.9±10.2	44.2±2.3	102.5±3.2
5% GA	82.7±6.6	42.7±4.3	119.9±11.2

From the state of electrolyte, gel electrolyte has the advantage of higher safety, prevent the lekage and possible for miniaturuzed devices but the conductivity value is the barrier because compare to the liquid electrolyte gel electrolyte has lower conductivity value than liquid electrolyte. From the conductivity results, it was found that pure agar gel electrolyte and agar gels with 1%, 2.5% and 5% GA concentration has conductivity around 115.1, 120.9, 102.4 and 119.9 mS/cm. The results showed that GA does not seem to affect the conductivity of gel electrolyte because it still showed an accpetable conductivity value if compare to liquid electrolyte that has conductivity value around $10^{-3} – 10^{-2}$ S/cm [4].

Fig.2 showed a model of fabricated Ag/AgCl reference electrode and Fig.3 showed the experimental set-up for the potential stability and potential difference measurement compared to that of the commerical Ag/AgCl reference electrode. The fabricated electrodes were immersed in test solutions which are: 0.1, 1 and 2M KCl and pH 4, 7 and 10 solutions for 5 minute and electrodes were taken in and out of the solutions for twelve times. The potential difference of PTFE-Blank, PTFE – 1% GA, PTFE – 2.5% GA and PTFE – 5% GA are 10.24, 11.35, 12.79 and 11.27 mV and potential stability calculated from the standard deviations of the 12 measurements, which are 0.43, 0.28, 0.30 and 0.25 mV (Fig. 5). The potential difference with average of 10 hours testing are 12.20, 13.68, 17.88 and 15.50 mV and potential stability are 0.89, 0.60, 0.65 and 0.44 mV in all solutions (Fig. 6).
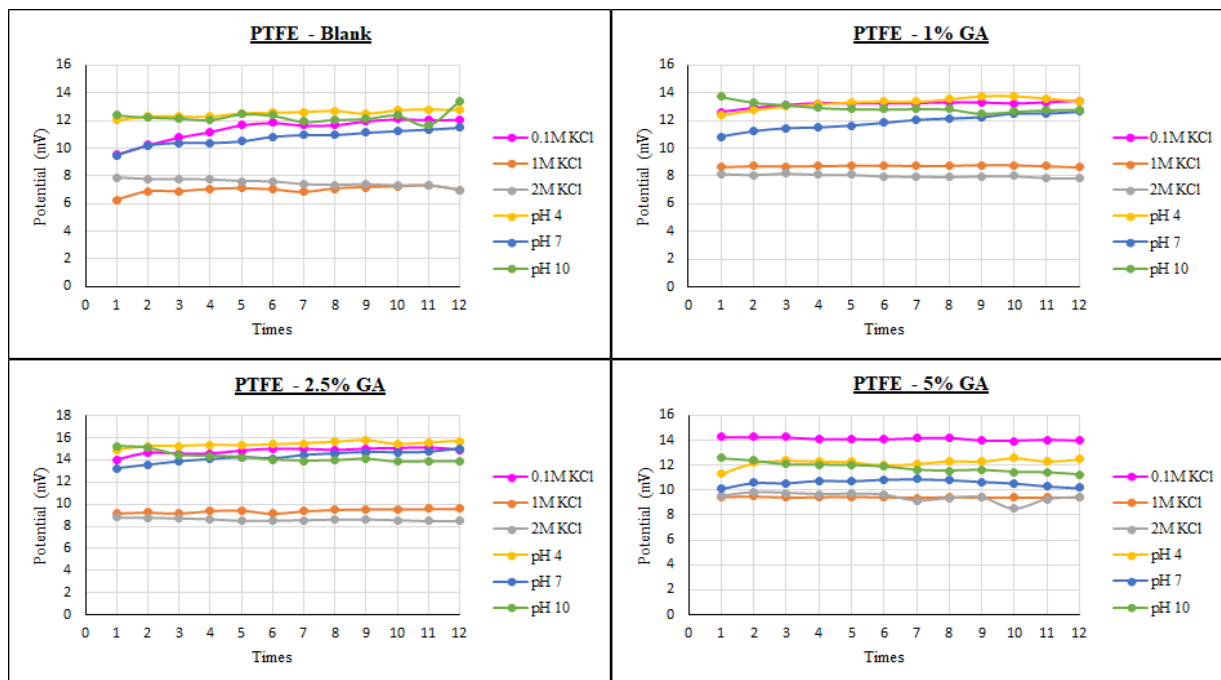
Fig. 5. Summary of potential stability and difference measurement of fabricated Ag/AgCl reference electrode for 5 min tested
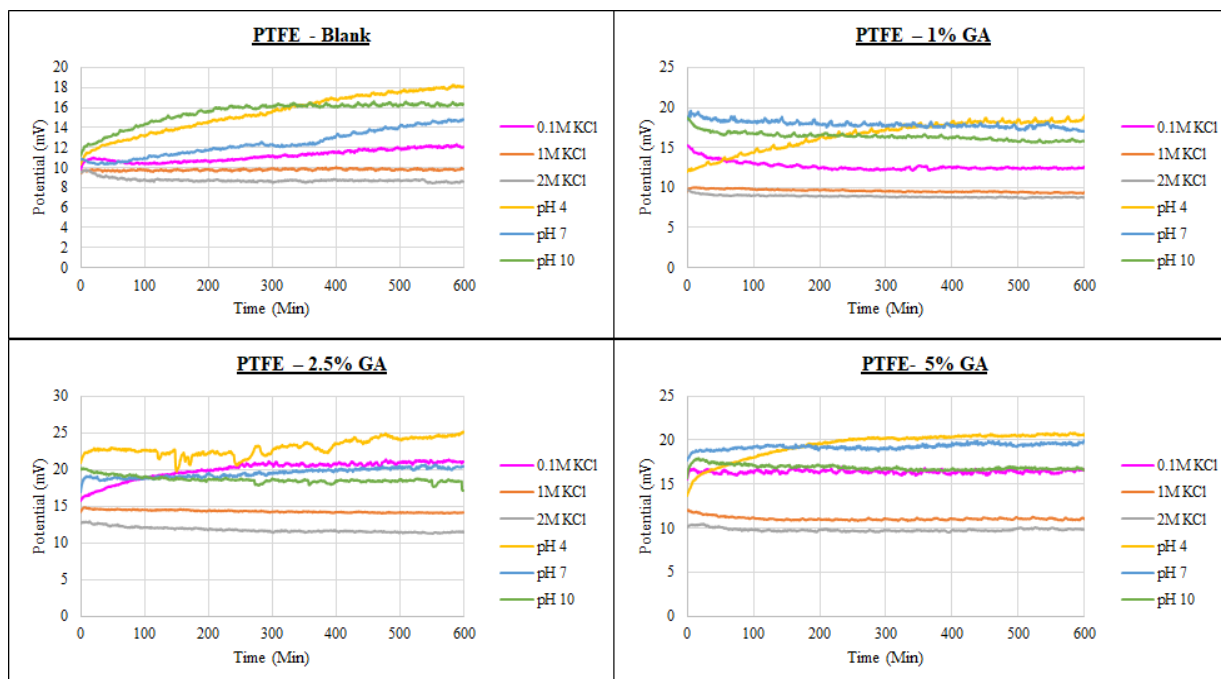
Fig. 6. Summary of potential stability and difference measurement of fabricated Ag/AgCl reference electrode for 10 hours tested

Conclusion

In this work, we present alternative fabrication of the Ag/AgCl reference electrode using agar as gel polymer electrolyte. The results showed an effect of GA concentration to agar gel electrolyte. Agar gels with 1% GA concentration is the best component in this work. The fabricated Ag/AgCl reference electrode filled with GA agar gels electrolyte were tested a potential stability and difference in various solution of KCl and pH and it also shows long operation time test has less stable than short operation time test. 5 minute test shows good potential stability with small drift over when 10 hours test is around 1-2 mV. Compare to pure agar gel GA the results shows that GA reduced evaporation loss value, maintained a electrochemical properties, improved gel strength and storage time without salt creep, or moldy for over 3 months.

Acknowledgments

References

[1] M. Komoda, I. Shitanda, Y. Hoshi, M. Itagaki, Fabrication and Characterization of a Fully Screen-Printed Ag/AgCl Reference Electrode Using Silica Gel Inks Exhibiting Instantaneous Usability and Long-Term Stability, Electrochemistry 87 (2018). https://doi.org/10.5796/electrochemistry.18-00075.
[2] A.W. Hassel, K. Fushimi, M. Seo, An agar-based silver|silver chloride reference electrode for use in micro-electrochemistry, Electrochemistry Communications 1(5) (1999) 180-183. https://doi.org/https://doi.org/10.1016/S1388-2481(99)00035-1.
[3] Z. Zhao, H. Tu, E.G. Kim, B.F. Sloane, Y. Xu, A flexible Ag/AgCl micro reference electrode based on a parylene tube structure, Sens Actuators B Chem 247 (2017) 92-97. https://doi.org/10.1016/j.snb.2017.02.135.
[4] X. Cheng, J. Pan, Y. Zhao, M. Liao, H. Peng, Gel Polymer Electrolytes for Electrochemical Energy Storage, Advanced Energy Materials 8(7) (2018) 1702184. https://doi.org/https://doi.org/10.1002/aenm.201702184.
[5] S. Arnott, A. Fulmer, W.E. Scott, I.C.M. Dea, R. Moorhouse, D.A. Rees, The agarose double helix and its function in agarose gel structure, Journal of Molecular Biology 90(2) (1974) 269-284. https://doi.org/https://doi.org/10.1016/0022-2836(74)90372-6.
[6] A. Nwanya, I. Amaechi, A. Udounwa, R. Osuji, M. Maaza, F. Ezema, Complex impedance and conductivity of agar-based ion-conducting polymer electrolytes, Applied Physics A 119 (2015). https://doi.org/10.1007/s00339-014-8979-x.
[7] S.Y. Liew, J.C. Juan, C.W. Lai, G.-T. Pan, T.C.K. Yang, T.K. Lee, An eco-friendly water-soluble graphene-incorporated agar gel electrolyte for magnesium-air batteries, Ionics 25(3) (2019) 1291-1301. https://doi.org/10.1007/s11581-018-2710-4.
[8] W. Wang, X. Jin, Y. Zhu, C. Zhu, J. Yang, H. Wang, T. Lin, Effect of vapor-phase glutaraldehyde crosslinking on electrospun starch fibers, Carbohydr Polym 140 (2016) 356-61. https://doi.org/10.1016/j.carbpol.2015.12.061.
[9] H.Y. Fan, D. Duquette, M.-J. Dumont, B.K. Simpson, Salmon skin gelatin-corn zein composite films produced via crosslinking with glutaraldehyde: Optimization using response surface methodology and characterization, International Journal of Biological Macromolecules 120 (2018) 263-273. https://doi.org/https://doi.org/10.1016/j.ijbiomac.2018.08.084.

High surface area mesoporous BiZnSbV-G-SiO$_2$ based electrochemical biosensor for quantitative and rapid detection of microalbuminuria

Kamrun Nahar Fatema[1] · Chang Sung Lim[1] · Won-Chun Oh [1,2]*

[1] Department of Advanced Materials Science & Engineering, Hanseo University, Seosan-si, Chungnam, Korea, 356-706

[2] Anhui International Joint Research Center for Nano Carbon-based Materials and Environmental Health, College of Materials Science and Engineering, Anhui University of Science & Technology, Huainan 232001, PR China

Abstract

In this work, we synthesized a mesoporous BiZnSbV-G-SiO$_2$ electrode-based sensor to detect microalbumin in urine, due to graphene-based sensor system has a high electrocatalytic movement, electrical conductivity, abundance, and low cost. The synergistic effects of BiZnSbV-G-SiO$_2$ nanocomposites advanced the electrochemical reaction and the affectability of the sensor. The synthesized active materials were characterized with surface morphology techniques, electron behavior controlling spectroscopy and electrochemical performance instrument, individually. Especially, chronoamperometric electrochemical evaluation system was used for the quantitative detection of microalbumin. We did electrochemical evaluations with a few possible compounds that regularly appear in urine (ascorbic acid, uric acid, glucose), which showed the good sensitivity and selectivity for the microalbumin detection. Under ideal conditions, the sensor can distinguish urinary microalbumin in a wide straight run from 0.01 to 0.1 μl with a location constraint of 0.01 μl. The excellent sensing performance of the mesoporous BiZnSbV-G-SiO2 active material was confirmed by analyzing microalbumin obtained from urine. The biosensor proposed here is specified in terms of simplification, low-cost, quick response, and precise screening for the microalbuminuria detection. This approach gives a promising stage for creating clinical point-of-care demonstrative applications. Additionally, the manufactured sensor had good selectivity, great reproducibility, great soundness, and good recuperation, which showed potential for applications in the clinical field.

*Corresponding author
E-mail: wc_oh@hanseo.ac.kr
Tel: +82-41-660-1337, Fax: +82-41-688-3352

Advance studies for semiconducting material for sonocatalytic hydrogen evolution under visible light irradiation with scavenger effect

Md Nazmodduha Rafat and Won-Chun Oh *,

[1]Department of Advanced Materials Science & Engineering, Hanseo University, Seosan-si, Chungnam, Korea, 356-706; wc_oh@hanseo.ac.kr

Abstract

To solve the global energy problem, hydrogen has been getting enormous attention because of its zero-carbon content. A promising strategy for producing clean and carbon-neutral hydrogen fuel is photocatalytic water splitting. Although different kinds of semi-conductive materials have been invented, modification of a solar-light-driven impressive material with low cost is the main goal in this decade. The goal of our research is to make a novel material with low band-gap energy. In this regard we used sonication for preparing quaternary material. The homogeneous structure is the main advantage of using ultrasonic a method, which causes it to have nanoparticles with high reactivity. In our lab, we are trying to design combined semiconducting material to get efficient photocatalysts. In our work, we find out that as a photocatalyst LaCdSe-GO-TiO$_2$ (LCS) has shown a good potential in photoelectrochemical water splitting for hydrogen evolution. In this work, LCS nanoparticles were synthesized by ultrasonic process under ambient pressure. The small particle size plays a key role in suppressing the recombination of photo-induced carriers, and thus promoting the photocatalytic activity. In the presence and absence of 20% methanol as a sacrificial agent, its show good photocatalytic activity. This work provides a good example on size control, low-cost synthesis and photocatalysts' design. Small size particles or low-dimension materials enable shorter diffusion distance of electrons and holes which could facilitate the surface redox reaction as compared to their bulk counterparts. Various synthetic techniques have been applied in controlling particle size, including solvothermal, sonochemical and wave-assisted hydrothermal methods in recent years. It is well-known that most of these methods demand harsh reaction conditions such as good quality equipment, high temperature or high pressure. Therefore, for the purpose of meeting the requirements of industrial application, it is highly competitive to make use of ultrasonic process under ambient pressure conditions. Our group has demonstrated that LaCdSe-GO-TiO$_2$ (LCS) can be prepared by ultrasonic method. We reckon, in the future it will be applicable for synthesizing novel materials.
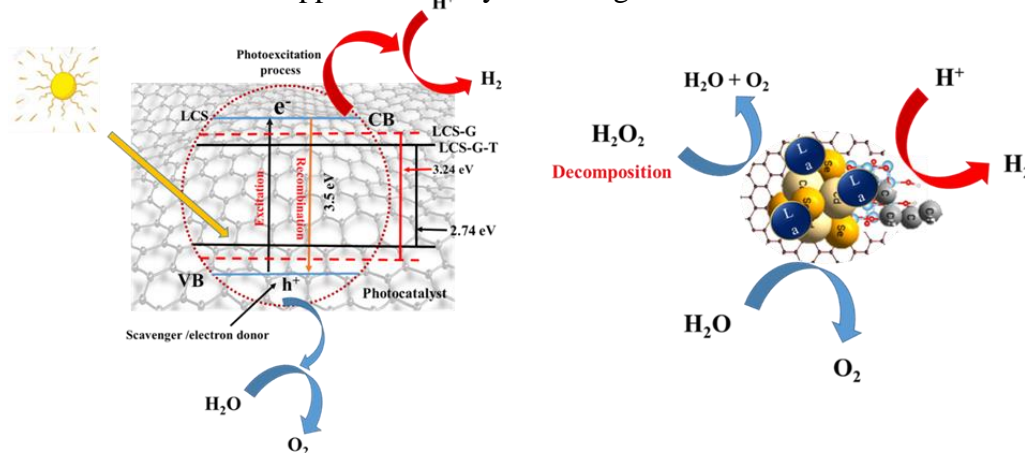
The synthesis of Fe_3O_4/Chi/Cyc for tetracycline adsorption

Channon Silaparaya[1], Hattakarn Keawmanee[1], Sucheewin Chotchatchawankul[1], Piyada Jitangprasert[1], Itthipol Sungwienwong[1], Phitchan Sricharoen[2] and Nunticha Limchoowong[1]*

[1]Department of Chemistry, Faculty of Science, Srinakharinwirot University 114 Sukhumvit 23 Rd., Wattana, Bangkok, 10110 Thailand
[2]Nuclear Technology Research and Development Center, Thailand Institute of Nuclear Technology (Public Organization), Nakhon Nayok 26120, Thailand
*e-mail: nunticha@g.swu.ac.th

Abstract

This study was planned to synthesize a novel magnetite chitosan cyclodextrin nano-composite (Fe_3O_4/Chi/Cyc). The Fe_3O_4/Chi/Cyc was developed as an adsorbent for the adsorption of tetracycline (TC) prior to determination by ultraviolet-visible spectrophotometry at the wavelength of 356 nm. The magnetite nano-composite was prepared by using co-precipitation method of Fe(II)/Fe(III), the conditions for adsorption using these particles for instant pH, adsorption time, temperature of adsorption, weight of Fe_3O_4/Chi/Cyc and concentration of tetracycline. Moreover, the nano-composite was characterized by Fourier transform infrared spectroscopy (FT-IR) and X-ray diffraction technique (XRD). The optimum conditions for the TC adsorption were investigated including an acid-base of solution (pH 5.0), adsorption time (30 mins), adsorbent dosage (5 mg) and initial concentration of TC at ambient temperature. This maximum adsorption was 26.74 mg g-1 demonstrate that this output gives a great deal to step forward for a huge scale elimination of antibiotic.

Keywords: Chitosan; Cyclodextrin; Magnetic nanocomposite; Tetracycline

References

Sricharoen P, Chanthai S, Lamaiphan N, Sakaew C, Limchoowong N, Nuengmatcha P, & W.-C. Oh. (2021). Sono-synthesized Fe_3O_4–GO–NH_2 nanocomposite for highly efficient ultrasound-assisted magnetic dispersive solid-phase microextraction of hazardous dye Congo red from water samples. *Journal of the Korean Ceramic Society* 58 : 201-11.

Photocatalytic CO₂ reduction with new band gap energy evaluation from spectroscopic relationship of graphene-Mg₂CuSnCoO₆ composite bridged with organics

Won-Chun Oh[1]*, Yonrapach Areerob[2]

[1]Department of Advanced Materials Science & Engineering, Hanseo University, Chungnam 356-706, South Korea
[2]Department of Industrial Engineering, School of Engineering, King Mongkut's Institute of Technology Ladkrabang, Bangkok, 10520, Thailand
Corresponding E-mail: wc_oh@hanseo.ac.kr

Abstract

A new structure of graphene-$Mg_2CuSnCoO_6$ composite bridged with gallic acid (GMG) was synthesized with a novel method. Band gap energy of the newly synthesized nanocomposite was evaluated with a laser-wavelength region and DRS method. Evaluation and analysis were based on the relationship among XRD, HRTEM, XPS, Raman scattering, and computer simulated model structure. Changes in the structure of graphene or graphene- based composite were associated with location changes of the valence band and the conduction band. Electron density was used to confirm the number of electrons by computer simulation. Finally, such graphene- $Mg_2CuSnCoO_6$ -gallic acid nanocomposite was used for photocatalytic CO_2 reduction into methanol. Under UV- light irradiation, the highest methanol yield was 5.576% with 0.6 g of scavenger. This work might offer a promising strategy for measuring band gap energies of different types of semiconductors.
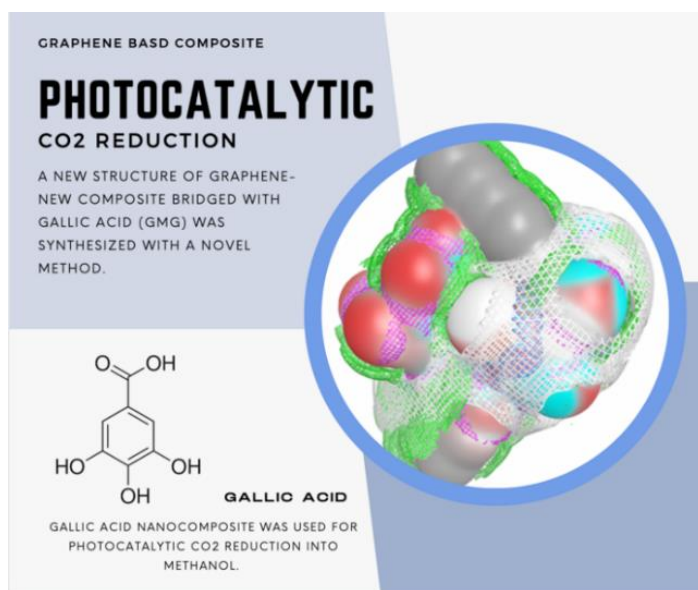
Keywords: CO₂ reduction, Photocatalyst, Band gap, Graphene composite Methanol
References: 1. W.C. Oh, and Y. Areerob, *Physica E 134 (2021) 114864*

The optical of liquid crystal molecules assisted biomolecular detection

Pemika Hirankittiwong[1*], Sirikanjana Thongmee[2], Praphat Kawicha[3],
Ladawan Rattanapolsan[3], Jariya Nitayaros[3]

[1] Department of General Science, Faculty of Science and Engineering, Kasetsart University,
Chalermphrakiat Sakon Nakhon Province Campus, Sakon Nakhon 47000, Thailand
[2] Department of Physics, Faculty of Science, Kasetsart University, Bangkok 10900, Thailand
[3] Plant Pest and Biocontrol Research Unit, Department of Agriculture and Resources, Faculty of
Natural Resources and Agro-Industry, Kasetsart University, Chalermphrakiat Sakon Nakhon Province
Campus, Sakon Nakhon 47000, Thailand
*e-mail: pemika.hi@ku.ac.th

Abstract

Optical of liquid crystals (LCs) molecules has been widely used in biosensors and other applications because of its potential for sensitive and real time detection. Self-assemble orientational mechanism of LCs molecules can respond at a specific location. We used nematic LCs (5CB) to rapidly detect specific DNA of plant pathogenic bacteria; *Erwinia* sp., *Xanthomonas* sp. and *Ralstonia solanacearum*, respectively. Optical images of LCs filled in the transmission electron microscopy (TEM) grid cell exhibited their changing planar to homeotropic orientation. The speed of planar-homeotropic configuration for *R. solanacearum* is faster perfect dynamic (19.47 s) than *Xanthomonas* sp. For *Erwinia* sp., it shows the imperfect changing in mechanism. Therefore, the grayscale intensity of optical image can detect the DNA of plant pathogenic bacteria. These results suggest that the LC based biosensor is a simple, reliable and accurate method.

Keywords: biosensor; liquid crystal; plants pathogen; responsibility.

References

Chonglin L., Haipei L. & Dawei, L. (2020). Application and Technique of Liquid Crystal-Based Biosensors. *Micromachines* 11, 176.
Mashooq K., Abdur R. K., Jae-Ho S. & Soo-Young P. (2016). A liquid-crystal-based DNA biosensor for pathogen detection. *Scientific Reports* 6, 22676.

# CNTs Doped Graphene/polyaniline Composite Material With In Situ Polymerization

Ye Ge, Guotao Dong, Tianhao Hu, Jing Wang[*]

College of Materials Science and Engineering, Anhui University of Science And Technology, Huainan, Anhui 232001

*Corresponding author (Phone and WeChat: + 0086 (13855418833); jingwang@aust.edu.cn

Abstract

We prepared Graphene with modified Hummers' method, and used the in situ polymerization to prepare graphene/polyaniline composites and different proportions of carbon nanotube doped graphene/polyaniline composites. To investigate the structure and surface morphology were investigated by X-ray diffraction, Fourier transform infrared spectroscopy, scanning electron microscopy. And electrical properties was tested. The results show that carbon nanotubes doped graphene improve interface binding ability with polyaniline and not obviously reduce the electrical properties of the composite material.
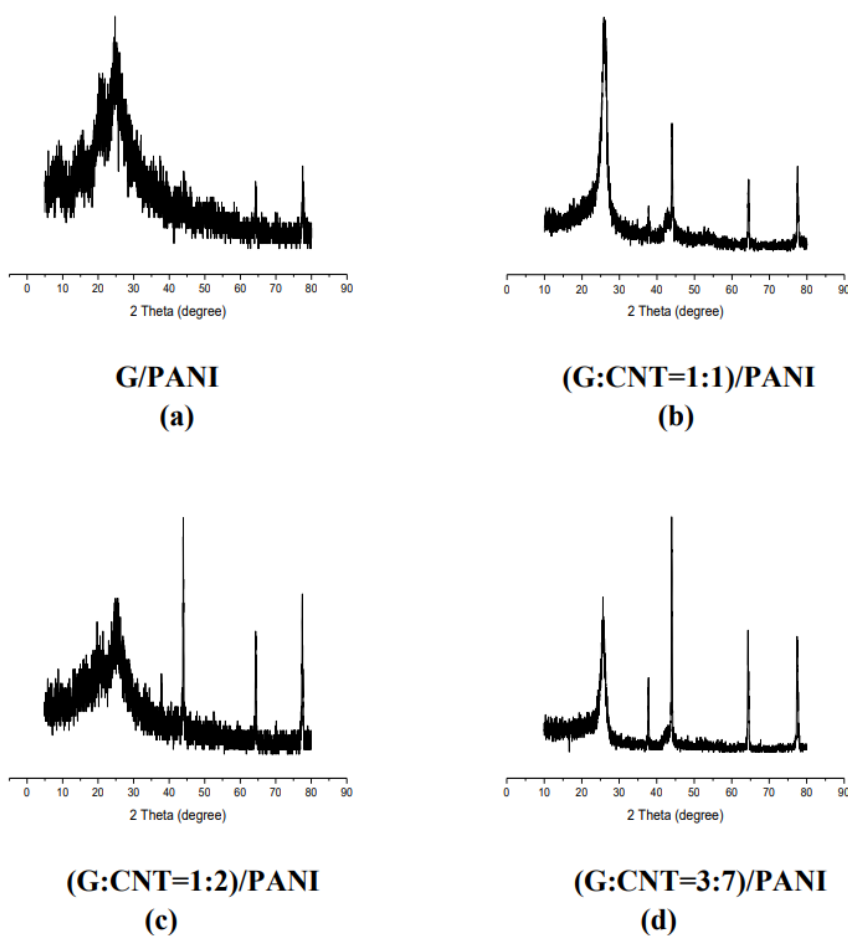
Figure 1 graphene / carbon nanotubes doped polyaniline and its composites XRD patterns

Table 1 Composite resistivity (unit: $[\Omega \cdot cm]$)

Sample value	1	2	3	average
(G/PANI)	0.815	0.958	0.877	0.883
(G:CNT=1:1)	2.450	2.350	2.390	2.397
(G:CNT=1:2)	1.218	1.300	1.172	1.230
(G:CNT=3:7)	1.192	2.720	3.270	2.394

Keywords: Graphene, CNTs, Polyaniline Composite

References

[1] Novoselov K S, Geim A K, Morozov S V, et al. Electric field effect in atomically thin carbon films[J]. science, 2004, 306(5696): 666-669.

[2] Geim A K, Novoselov K S. The rise of graphene[J]. Nature materials, 2007, 6(3): 183-191.

[3] Lee C. XD Wei, JW Kysar, J[J]. Hone, Sc ienc e, 2008, 321: 385.

[4] Stoller M D, Park S J, Zhu Y W, et al. Impermeable atomic membranes from graphene sheets[J]. Nano Lett, 2008, 8: 3498.

[5] Balandin A A, Ghosh S, Bao W, et al. Superior thermal conductivity of single-layer graphene[J]. Nano letters, 2008, 8(3): 902-907.

[6] Zhang Y, Tang Z R, Fu X, et al. TiO_2- graphene nanocomposites for gas-phase photocatalytic degradation of volatile aromatic pollutant: is TiO_2- graphene truly different from other TiO_2- carbon composite materials[J]. ACS nano, 2010, 4(12): 7303-7314.

[7] Zhang Y, Tang Z R, Fu X, et al. Engineering the unique 2D mat of graphene to achieve graphene-TiO_2 nanocomposite for photocatalytic selective transformation: what advantage does graphene have over its forebear carbon nanotube[J]. ACS nano, 2011, 5(9): 7426-7435.

[8] Cao Y, Mallouk T E.Morphology of template-grown polyaniline nanowares and its effect on poly(ionic liquid)-modified capaciteance of nanoware arrays. ACS Nano, 2011,5:436-442.

[9] Palaniappan S,Devi S L. Novel chemically synthsized polyaniline electrodes containing a fiuoroboric acid dopant for supercapacitors. J Appl Polyme Sci, 2008, 107:1887-1892.

[10] Prasad K R,Munichandraiah N.Fabrication and evaluation of 450F/g electrochemical redox supercapcitors using inexpensive and high-performance polyaniline coated,stainless-steel electrodes.J Pow Sources, 2002, 112:443-451.

[11] Wang H,Hao Q,Yang X.et al. Effect of graphene oxide on the properties of tis composite with polyaniline. ACS AppL Mater Inter, 2010, 2:821-828.

[12] Yang C M,Kim Y J, Endo M, et al, Nanowindow-regulated specific capacitance of supercapacitor electrodes of signle-wall carbon nanohorns. J Am Chem Soc, 2007,129:20-21.

[13] Futaba D N, Hata K,Yamada T, et al.Shape-engineerable and highly densely packed signle-wall carbon nanotubes and their application as super-capacitor electrodes. Nat Mater, 2006, 5:987-994.

[14] Frackowiak E,Khomenko V,Jurewicz K,et al.Supercapatitors based on conducting polymers/nanotubes composites.J Pow Source,2006,153:413-418.

[15] Camila Zequine Sanket Bhoyate Felipe de Souza Ravi Arukula Pawan K. Kahol Ram K. Gupta. Recent Advancements and Key Challenges of Graphene for Flexible Supercapacitors. 2020, 49-77.

[16] Gao, X., Du, X., Mathis, T.S. et al. Maximizing ion accessibility in MXene-knotted carbon nanotube composite electrodes for high-rate electrochemical energy storage.Nat Commun 11, 6160 (2020)

[17] Jiuxing Jiang et al. Graphene/polyaniline composite sponge of three-dimensional porous network structure as supercapacitor electrode[J]. Chinese Physics B, 2016.

Selective Photocatalytic and electrochemical CO₂ reduction to Methanol on Graphene-based Ternary nanocomposite

Zambaga Otgonbayar [1], Chang Sung Lim [1], Won-Chun Oh [1, 2*]

[1] Department of Advanced Materials Science & Engineering, Hanseo University, Seosan-si, Chungnam, Korea, 356-706

[2] Anhui International Joint Research Center for Nano Carbon-based Materials and Environmental Health, College of Materials Science and Engineering, Anhui University of Science & Technology, Huainan 232001, PR China; E-mail: wc_oh@hanseo.ac.kr

Abstract

The evolution of carbon dioxide into hydrocarbon fuels has been nominated as a green method to mitigate global warning. . Of all the methods, photocatalytic and electrochemical reduction methods are widely used in CO_2 conversion experiments. The advantages of the photocatalytic method are the conventional low-energy CO_2 conversion technology, and it can efficiently convert and stores solar energy into chemical energy and allows carbon to be recycled. Moreover, the electrochemical CO_2 reduction method has been studied latitudinal due to the operational parameters, faradaic efficiency and simple. The novel structured photocatalyst is a promising material for the CO_2 reduction in photocatalytic and electrochemical method, which can suppress the recombination of electron-hole pairs and effectively transfer the electrons to the surface for chemical rection of CO_2 reduction. Recently, ternary nanocomposite material studied as burgeoning nanocomposite for CO_2 reduction and production of hydrocarbon fuel. The ternary nanocomposite had high stability, better activity than binary and unary nanocomposite, and each semiconductor in the ternary nanocomposite has specific physical and chemical properties. In addition, the size of the nanoparticle affects to the performance of the catalyst material, especially, nano-sized particle had more active sites and large fraction of edge can provide different catalytic interface between catalyst and reductant molecule. Above-mentioned factors depend on the synthesis method and other parameters of the nano-sized photocatalyst. Mainly, sol-gel method, hydrothermal method, combustion and ultrasonic-assisted method are used for the synthesis process.

In our study, we mainly studied about the graphene-based nanocomposite for the manufacturing of ternary photocatalyst. 2D-structured graphene has 0-eV bandgap and unique sp^2 character of graphene serves to promote the efficient absorbance of CO_2, which can lead to better photocatalytic reactions due to graphene in composites can act as a fast electron transfer channel, thus reducing the recombination of the photo-generated electron–holes. The surface functional groups and abundant surface area can be the active field that metal-semiconductor can be chemically bonded and loaded. 2D structured graphene could function as a better catalyst than 0-D and 1-D nanomaterials. The successful structure of the catalyst presents an effective and raid charge transfer and abundant interaction area for CO_2, it can lead to high methanol production. Our study research presents a prototype for ternary nanocomposite for practical application of the CO_2 reduction and production of solar fuel.
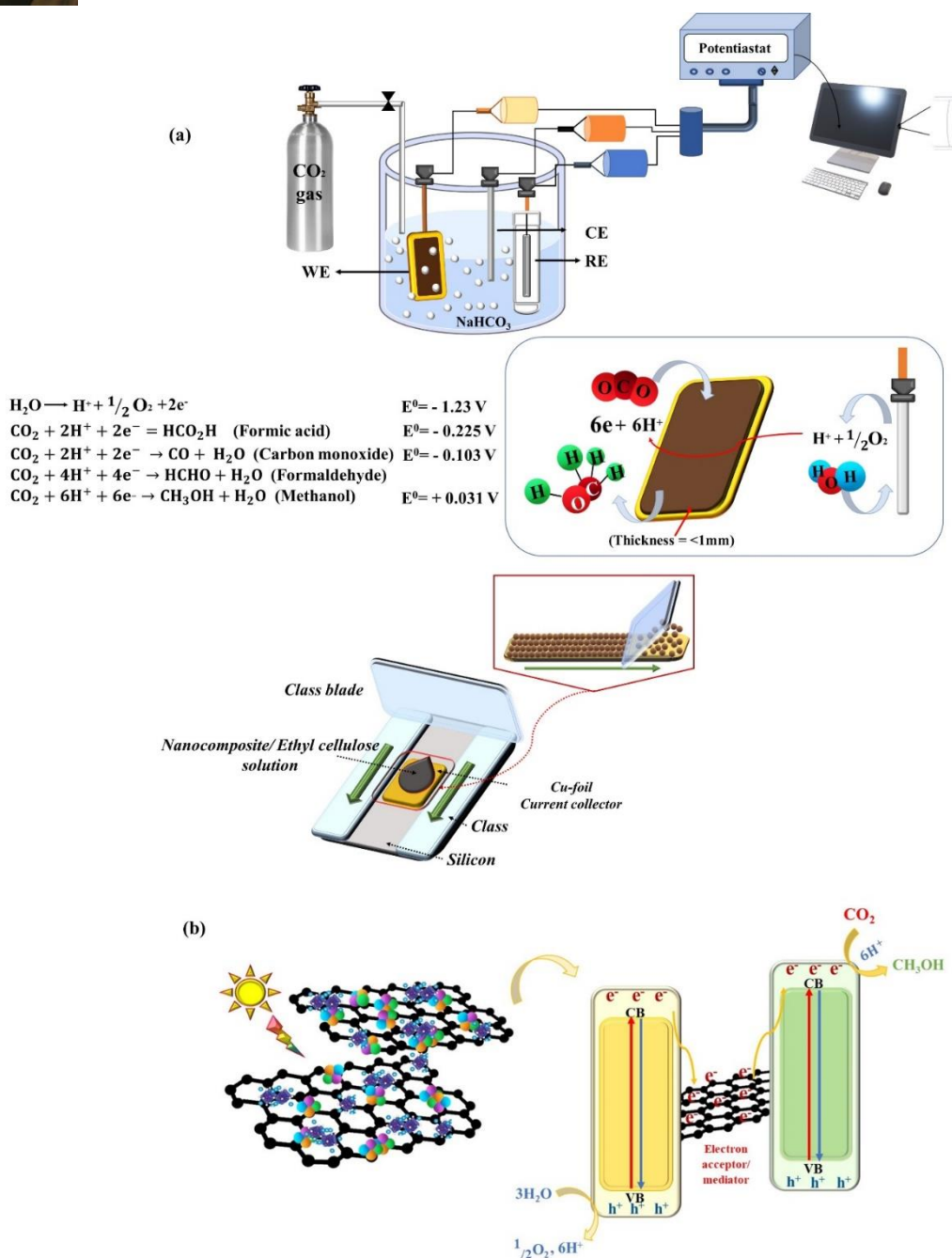
Keywords: Metal-semiconductor, 2D-graphene, new-modelled ternary nanocomposite, reduction of CO_2, methanol.

References : Zambaga, O.; Kwang, Y.C.; Oh, W.C. Enhanced photocatalytic activity of CO_2 reduction to methanol through the use of a novel-structured $CuCaAg_2Se$–graphene–TiO_2 ternary nanocomposite, *New J. Chem.*, 2020,**44**, 16795-16809.

Prof. Dr. Won-Chun Oh

Department of Advanced Materials Science & Engineering, Hanseo University, South Korea, fields: Nano chemistry and nanomaterials based on graphene and application

$$H_2O \longrightarrow H^+ + {}^1/_2 O_2 + 2e^- \qquad E^0 = -1.23\ V$$
$$CO_2 + 2H^+ + 2e^- = HCO_2H \quad (Formic\ acid) \qquad E^0 = -0.225\ V$$
$$CO_2 + 2H^+ + 2e^- \rightarrow CO + H_2O \quad (Carbon\ monoxide) \quad E^0 = -0.103\ V$$
$$CO_2 + 4H^+ + 4e^- \rightarrow HCHO + H_2O \quad (Formaldehyde)$$
$$CO_2 + 6H^+ + 6e^- \rightarrow CH_3OH + H_2O \quad (Methanol) \qquad E^0 = +0.031\ V$$

Schematic illustration of (a) electrochemical and (b) photocatalytic CO_2 reduction on Graphene-based new-modeled Ternary nanocomposite.

Importance of Graphene based composites as anode material for Li Ion batteries

Kefayat Ullah*

Department of Applied Physical & Material Sciences, University of Swat, Pakistan;
*Corresponding author E-mail: kefsayed@uswat.edu.pk ; Tel: +92-3459207686

Abstract

The increased demand for electric vehicles, as well as advancements in charging technologies, are turning points in the development of next-generation Lithium ion batteries. The performance, lifetime, capacity, and cycle stability of LIBs are determined by their electrodes. New electrode materials must be developed in order to increase the electrochemical performance of LIBs. It has been experimentally observed as the most useful unit for the construction of numerous nanocomposite materials in environmental and energy applications. We will observe such composites and their importance in advancement towards lithium ion battery technologies.

The effect of preparative pH on BiOCl morphology and photocatalytic activity on degradation of tetracycline hydrochloride wastewater

Nguyen-Thao-Trinh, Do[1,2] and <u>Minh-Vien Le</u>[1,2]

[1]Faculty of Chemical Engineering, Ho Chi Minh city University of Technology, Ho Chi Minh City, 700000, Vietnam
[2]Vietnam National University Ho Chi Minh City, Ho Chi Minh City, 700000, Vietnam
* E-mail: lmvien@hcmut.edu.vn

Abstract

In the present study, BiOCl hierarchical microsheets were successfully fabricated by simple precipitation-calcination method. The prepared photocatalysts were systematically investigated by the XRD, SEM, BET, and DRS techniques. By manipulating the pH of the precursor, the size, thickness, and morphologies over BiOCl microsheets were well controlled which can improve the photocatalytic activities of the sample toward tetracycline hydrochloride (TCH) degradation under simulated sunlight. The sample obtained at pH6 exhibited the outstanding photocatalytic performance, 92% of TCH (10 mg L^{-1}) degraded within only 90 min under stimulated sunlight irradiation, with the rate constant of 0.077 min^{-1} and high stability after five test cycles. This excellent photocatalytic activity in the visible range is attributed to the efficient separation and transfer efficiency of photogenerated electron-hole pairs as well as the high amount of reactive oxygen species (ROS) induced by OVs. Furthermore, the prevalent free radicals in the present system were identified by trapping experiments. As results, the free superoxide radicals (O_2^{-} •) are main key active species for the photocatalytic degradation of TCH, whereas contribution of hydroxyl radicals (•OH) and photogenerated holes (h^{+}) is minor. Finally, the BiOCl synthesized via morphological control and defect technique is promising visible light active and an efficient photocatalyst with lower environmental impact for degaradation of TCH from wastewater.
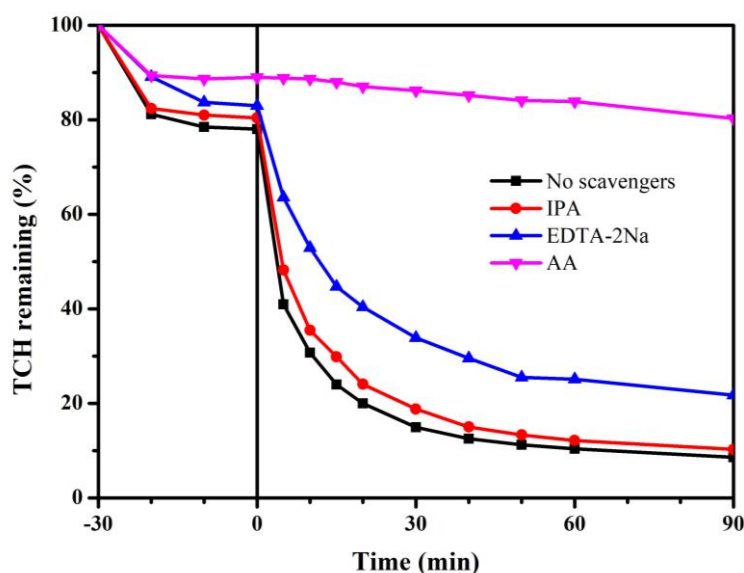
Fig.1. Photocatalytic degradation of TCH over BiOCl microsheets in the presence of various scavengers under simulated sunlight irradiation (IPA – isopropyl alcohol, EDTA-2Na – ethylenediamine tetraacetic acid disodium, AA – ascorbic acid).

Keywords: BiOCl hierarchical microsheets, Tetracycline hydrochloride degradation, Photocatalyst.

Study Plant Riboflavin luminescent (*Euphorbia tirucalli Linn.*) fingerprint powder for Forensic Science

Suranarong rattanakosoom[1*] and Rachadaporn Benchawattananon[2*]

[1*]Scientist Level 4 Crime Scene investigation sub division Police Forensic Science Center4,Khon Kaen ,Thailand 40000

[2*]Integrated Science Forensic Science Faculty of Science Khon Kaen University Khon Kaen 40002.Thailand.

Corresponding Author: Rachadaporn Benchawattananon: rachadaporn@kku.ac.th

Abstract

Forensic science have many evident in daytime and night time. Dyes is widely used to improve fingerprints identification test. Natural dyes is another interesting way that be used instead of chemical dyes because of its non-toxicity and lower cost. In this research, the development of plant powder from indian-tree spurge tree (*Euphorbia tirucalli Linn.*) was applied for fingerprints identification due to its fluorescence property under UV. Were applied to detect hidden fingerprints on non-porous surfaces in dried condition. Material and Methods: Check Riboflavin quality by plant was weighed and extracted with 100 mL boiling water for 30 minutes. 10 mLs of the plant extract was used for analysis. The standard addition method was used, then the polarogram were recorded from -300 mV to -700 mV vs. Ag/AgCl reference electrode. The method was simple and reproducible. The recoveries were in the range 98.80-99.69% with %RSD of 1.56-1.87 respectively. Green powder from indian-tree spurge tree was washed and dried by 70 degree Celsius 2 days then grinded, dried and use Powder dust monitored in dried condition. The samples were then place in UV cabinet with 254 and 365 nm excitation. The fluorescent photographs were then captured. Finding Plant Riboflavin luminescent (*Euphorbia tirucalli* Linn.) can be a good fingerprint powder in night time for Forensic Science.

Keywords : Riboflavin luminescent, *Euphorbia tirucalli* Linn., Fingerprint

Green Synthesis Carbon Dots (CDs) Coconut Water by Hydrothermal Method's for Finger Print Detection on nonporous surface

David Nugroho[1], Rachadaporn Benchawattananon[1], Saksit Chanthai[2], Chayanee Keawporm[2]

[1]Department Forensic, Faculty of Science, Khon Kaen University, Khon Kaen 40002, Thailand
[2]Department Chemistry, Faculty of Science, Khon Kaen University, Khon Kaen 40002, Thailand

Abstract

This study aims to synthesize environmentally-friendly carbon dots from coconut water which is then developed into carbon dots powder to detect latent fingerprints on nonporous surface material, studying the characteristics and optical property of carbon dots and carbon dots powder compounds, which have been synthesized from several variations of temperature, time. and the concentration of carbon dots mixed with commercial starch to become carbon dots powder. In addition, this study also examines the application of carbon dots of various non-porous surface materials, and the effect of time and temperature of storage on the surface were investigated. In this research was found the latent fingerprints on the non-porous surface gave a good performance and were easy to see under UV light. Therefore, the study of the natural fluorescent carbon dots mixed with commercial tapioca flour powder is a potential method to detect latent fingerprints in forensic processes.

Keywords: Carbon Quantum Dots; latent fingerprints; Coconut Water; Tapioca Flour; Green Synthesis; Forensic Science

Active different molecular weight of chitosan-konjac glucomannan edible film coating: physicochemical and aflatoxin binding properties in peanuts

Akkaracha Hanwattanakul[1], Anyanee Mokkran[1], Thanjira Intanasak[1], Benya Cherdhirunkorn[1], Surachet Toommee[3], Chiravoot Pechyen[1,2,*]

[1]Department of Materials and Textile Technology, Faculty of Science and Technology, Thammasat University, 12120, Thailand
[2]Thammasat University Center of Excellence in Modern Technology and Advanced Manufacturing for Medical innovation, Thammasat University, 12120, Thailand.
[3]Department of Industrial Arts, Faculty of Industrial Technology, Kamphaeng Phet Rajabhat University, 62000, Thailand
*e-mail: chiravoot.p@gmail.com.

Abstract

In this study, konjac glucomannan (KGM) and chitosan (CS) are researched and tested in the process of edible film production for consumption purposes. Currently there are significant drawbacks for the use of synthetic fungicides to control pathogenic fungi in grains, and it has increased the interest in exploring new alternatives to control the occurrence of fungal infections in these dried peanuts. The edible films were prepared by blending 1% w/v of KGM with 1% w/v of CS in acetic acid aqueous solution. In the preparation stage, the incorporation of chitosan in edible films are used by different molecular weights; (Lower molecular weight of chitosan (L-M_w), Medium molecular weight of chitosan (M-M_w) and Higher molecular weight of chitosan (H-M_w). Then, Glycerol was added as a plasticizer in the mixture ratio. The solutions of konjac glucomannan and chitosan are mixed together with different ratios [KGM:CS] at 100:0, 0:100 and 80:20 (CS of CS-L-M_w, CS-M-M_w, CS-H-M_w), respectively. The different mixture ratios leads to the change in structure and properties of the films which were investigated by FTIR, XRD, SEM, Tensile Strength (TS) and Elongation at break (%E). As a result, the film has a very broad peak at 2θ around $20°$ when the content of KGM blended into the films increases. Furthermore, the CS-M-M_w film shows the maximum tensile strength (39.23 MPa). The KGM/CS-L-M_w, KGM/CS-M-M_w and KGM/CS-H-M_w films were 17.87 MPa, 15.90 MPa and 10.33 MPa, respectively. The KGM/CS-L-M_w film showed the greatest inhibition of aflatoxin produced by fungi in peanuts. Therefore, the application of the tested coatings preserved the quality of peanuts as measured by some physicochemical attributes. From this, composite edible film coatings containing KGM and CS offer a promising alternative to control infection caused native fungal in peanuts without negatively affecting their quality over storage.

Keywords: Edible film coating; Konjac glucomannan; Chitosan; Aflatoxin; Peanuts

Eco-Synthesis of Platinum Nanoparticles (PtNPs) Using Thai Herb Leaves Extract as Capping and Reducing Agent : Effect of Reaction Times

Khanittha Ponsanti[1], Benchamaporn Tangnorawich[1,4], Nipaporn Ngernyuang[2,4], Chiravoot Pechyen[3,4]*

[1] Department of Physics, Faculty of Science and Technology, Thammasat University, 12120, Thailand
[2] Chulabhorn International College of Medicine, Thammasat University, 12120, Thailand
[3] Department of Materials and Textile Technology, Faculty of Science and Technology, Thammasat University, 12120, Thailand
[4] Thammasat University Center of Excellence in Modern Technology and Advanced Manufacturing for Medical innovation, Thammasat University, 12120, Thailand
*e-mail: chiravoot.p@gmail.com

Abstract

This study reports the synthesis of platinum nanoparticles (PtNPs) with biological method by using Kaffir Lime leaves (Citrus hystrix DC), Common Basil leaves (Ocimum basilicum Linn) and Fragrant Pandan leaves (Pandanus amaryllifolius Roxb), (resulted as Ka-PtNPs, Co-PtNPs, and Fr-PtNPs respectively) with different timeframe. The plant leaves contain sugars, terpenoids, polyphenols, alkaloids, phenolic acids, and proteins, which play an important role in act as reducing agents in the synthesis of platinum nanoparticles by reducing $H_2PtCl_6.6H_2O$ to platinum nanoparticles (PtNPs). As for the attributes, the platinum nanoparticles were extensively characterized by using Transmission Electron Microscopy (TEM), X-ray Diffraction (XRD), Energy dispersive X-ray spectroscopy (EDS), UV-Visible Spectrophotometer, Fourier Transform Infrared (FTIR), Thermogravimetric (TGA) and Particle Size Analyzer. The TEM images show the shape of synthesized platinum nanoparticles as spherical, and the particle size distributions of the synthesized platinum nanoparticles from Kaffir Lime leaves, Common Basil leaves and Fragrant Pandan Leaves are in the ranges of 20-80 nm. As shown by the UV-Visible Spectroscopy, the maximum absorption of platinum nanoparticles is at 256 nm. Therefore, this study uses the benefits from plant leaves which can be used in platinum nanoparticles synthesis, and the result of the synthesis can be applied in various fields.

Keywords: Platinum nanoparticles; Kaffir Lime leaves; Common Basil leaves; Fragrant Pandan leaves; Biological method

Measurement of stress in single-crystal diamond by Raman microscopy

Xiulin Shen[1,2,3], Meiyong Liao[2], Zhaohui Huang[3], Zhenfei Lv[1,*]

[1]School of Materials Science and Engineering, Anhui University of Science and Technology, Huainan, Anhui 232001, China
[2]Research Center for Functional Materials, National Institute for Materials Science, Namiki 1-1, Tsukuba, Ibaraki 305-0044, Japan
[3]School of Materials Science and Technology, China University of Geosciences (Beijing), Beijing 100083, China

Abstract

The stress characterization of cantilever structure has always been a focus issue in the related MEMS manufacturing. In this paper, the authors report single crystal diamond cantilevers fabricated by a smart-cut method with high quality factor up to 1.4×10^4. The Raman shift of the SCD cantilever clearly distinguishes from those of the SCD substrate, which is mostly centered at 1332.4 cm^{-1}. Along the cross-section of the SCD cantilevers, the Raman shift increased from 1332.6 cm^{-1} to 1332.9 cm^{-1} with stress 225.4-563.5 MPa. The origin of the stress might be from the ion implantation process.

Key words: Diamond; Cantilever; Stress; Raman microscopy

Introduction

Single-crystal diamond (SCD) has attracted much attention and extensive application potential to produce microelectromechanical system (MEMS) sensors with high reliability and sensitivity due to its excellent mechanical, chemical, and electronic properties [1, 2]. In general, the residual stress resulted from the sum of lattice mismatch, thermal mismatch, and crystal defects affects the MEMS devices properties and is a non-negligible obstacle in practical applications [3]. Therefore, the evaluation of stress details counts for a great deal in optimizing the structure design, improving the growth and process conditions and predicting the MEMS devices' reliability.

There are several methods to characterize the residual stress in films, such as x-ray diffraction (XRD) [4, 5], Raman spectroscopy [6-8], in situ microelectromechanical stress measuring structures [9], indentation fracture, and curvature measurements [10, 11] and other modified methods. Among all these approaches, actually, Raman spectroscopy is neither the most sensitive nor most accurate, but within micrometer scale, it is the most rapid and non-destructive stress measurement currently and has great application potential.

In this work, we report on the stress in the SCD cantilevers fabricated by a smart-cut method. We analyzed the cantilevers in depth by Raman spectroscopy. The thickness of the SCD cantilevers was around 1.44 μm and the length was from 60-160 μm. The quality factors

---

* * Corresponding author. Tel: +86-0554-6601251 E-mail: zflv@aust.edu.cn (Zhenfei Lv);

of the SCD cantilevers were up to 1.4×10^4. The Raman shift of the SCD cantilever clearly distinguishes from those of the SCD substrate, which is mostly centered at 1332.4 cm^{-1}. Along the cross-section of the SCD cantilevers, the Raman shift increased from 1332.6 cm^{-1} to 1332.9 cm^{-1}. Therefore, the existence of residual stress in the cantilevers were revealed. The stress in the cantilever beam was calculated to be around 125-312 GPa. The origin of the residual stress might be from the ion implantation process.

Experimental

The fabrication of SCD cantilevers bases on a modified ion implantation assisted lift-off (IAL) technique, which is named 'smart-cut' method, and has been experimentally proven to be reproducible in SCD MEMS/NEMS with controlled dimension[12, 13]. The length of SCD cantilevers were measured by 3D laser optical microscopy. The quality factors (Q) of the SCD resonators were measured through a laser Doppler vibrometer in a high-vacuum (10^{-3} Pa) chamber at room temperature, and were fitted by Lorentz function. Raman shifts of cantilevers and substrate were measured by Raman spectroscopy used for the calculation of residual stress.

Results and discussion

Figure 1(a-b) shows the images of prepared cantilever beams by 3D laser optical microscopy. Figure 1(c) is a schematic of a single cantilever established by COMSOL. The visible color change can be seen in all images in Figure 1, indicating the bending state of fabricated cantilever beams, which indicates the surface stress difference between the upper and bottom of cantilevers.
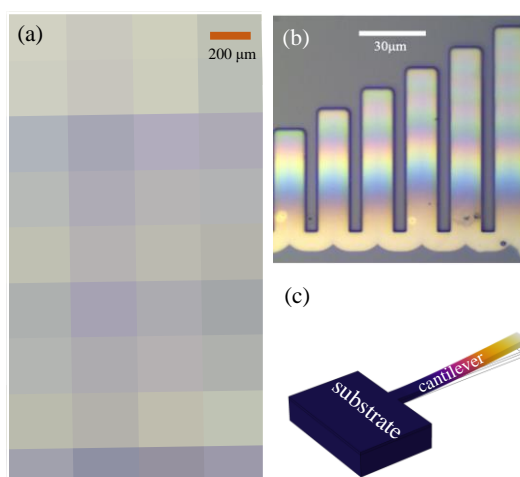
Figure 1. (a) 2D image of all prepared cantilever beams and arrays with length from 30 μm - 160 μm; (b) higher resolution of one cantilever group; (c) schematic of a single cantilever

Figure 2(a-b) shows the Raman shifts of SCD substrate and epilayer, which both locate around 1332.4 cm^{-1}, and Figure 2(c-g) exhibits the Raman shifts of cantilever beams with different length. It comes with Raman shift peak between 1332.6-1332.9 cm^{-1} after cantilever beams fabricated. With the cantilever length increasing, the area of surface stress distribution becomes larger, and there is a more obvious pixels increase near 1332.9cm^{-1}, indicating a rising

proportion of high stress distribution over the cantilever beams. The residual stress around 125-312 MPa, which is calculated by the following equation:

$$\sigma \ (GPa) = -0.625\Delta\omega \ (cm^{-1}) \quad (\Delta\omega = \omega_1 - \omega_0, \ \omega_0 = 1332.4 \ cm^{-1}) \tag{1}$$

where σ is the cantilever stress, ω is the Raman shift of cantilever beam. Figure 2(h) gives the quality factors and stress of cantilever beams with length of 60 μm - 140 μm. The quality factor increases with cantilever length and keep it around 14000 as cantilever length over 100 μm.
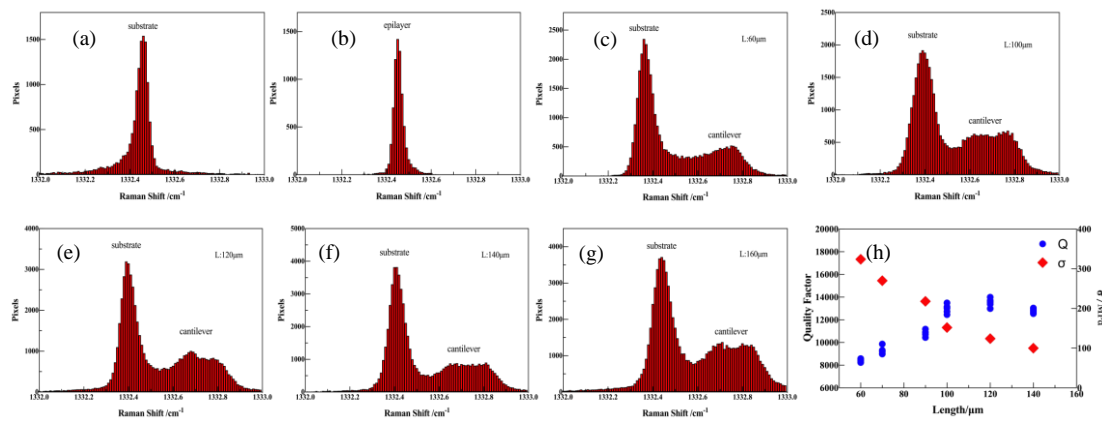
Figure 2. (a-g) Raman shifts of SCD substrate, epilayer and SCD cantilever beams with different length; (h) quality factors and calculated stress of cantilever beams with different length

Conclusion

In this study, cantilever beams were fabricated by a smart-cut method. For Raman shift on SCD cantilever beams, a large proportion of stress is concentrated in the bending direction of the cantilever beam, displaying compressive stress around 125- 312 MPa with high quality factor between 8000-14000. It is worth noting that based on valid analysis, only normal stress is taken into consideration in the case of slender beams with large aspect ratio. Considering different design of devices, uniaxial and biaxial stress usually exist at the same time, resulting in a more complex analysis and calculation for stress. Whatever, this study absolutely provides some valuable reference and research ideas for cantilever fabrication and stress analysis.

References

[1] M. Liao, M. Toda, L. Sang, T. Teraji, M. Imura, Y. Koide, Improvement of the quality factor of single crystal diamond mechanical resonators, Japanese Journal of Applied Physics. 56 (2017).

[2] M. Liao, L. Sang, T. Teraji, S. Koizumi, Y. Koide, Ultrahigh Performance On-Chip Single Crystal Diamond NEMS/MEMS with Electrically Tailored Self-Sensing Enhancing Actuation, Advanced Materials Technologies. 4 (2019) 1800325.

[3] K. Chen, Y. Lai, J. Lin, K. Song, L. Chen, C. Huang, Micro-Raman for diamond film stress analysis, Diamond Relat. Mater. 4 (1995) 460-463.

[4] E. Bemporad, M. Brisotto, L. Depero, M. Gelfi, A. Korsunsky, A. Lunt, M. Sebastiani, A critical comparison between XRD and FIB residual stress measurement techniques in thin films, Thin Solid Films. 572 (2014) 224-231.

[5] T. Namazu, A. Hashizume, S. Inoue, Thermomechanical tensile characterization of Ti–Ni shape memory alloy films for design of MEMS actuator, Sensors and Actuators A: Physical. 139 (2007) 178-186.

[6] M. Gurtin, X. Markenscoff, R. Thurston, Effect of surface stress on the natural frequency of thin crystals, Appl. Phys. Lett. 29 (1976) 529-530.

[7] J. Qian, T.-X. Yu, Y.-P. Zhao, Two-dimensional stress measurement of a micromachined piezoresistive structure with micro-Raman spectroscopy, Microsystem technologies. 11 (2005) 97-103.

[8] I. De Wolf, Micro-Raman spectroscopy to study local mechanical stress in silicon integrated circuits, Semicond. Sci. Technol. 11 (1996) 139.

[9] R.K. Gupta, Electrostatic pull-in test structure design for in-situ mechanical property measurements of microelectromechanical systems (MEMS), Massachusetts Institute of Technology, 1997.

[10] G.G. Stoney, The tension of metallic films deposited by electrolysis, Proceedings of the Royal Society of London. Series A, Containing Papers of a Mathematical and Physical Character. 82 (1909) 172-175.

[11] K.-S. Chen, K.-S. Ou, Modification of curvature-based thin-film residual stress measurement for MEMS applications, Journal of Micromechanics and Microengineering. 12 (2002) 917-924.

[12] M. Liao, Y. Koide, L. Sang, Single Crystal Diamond Micromechanical and Nanomechanical Resonators, Novel Aspects of Diamond, Springer2019, pp. 91-121.

[13] X. Shen, K. Wu, H. Sun, L. Sang, M. Liao, Temperature dependence of Young's modulus of single-crystal diamond determined by dynamic resonance, Diamond Relat. Mater. 116 (2021) 108403.

Influence of Magnetic Field on the Properties of Aqueous Solution and CaCO₃ precipitate

Xin Rong[1], Ming Gao[1], Jianjun Li[1,2*], Xujie Peng[1], Yin Liu[1,2], Changguo Xue[1]

[1]Department of Materials Science and Engineering, Anhui University of Science and Technology, Huainan, China, 232001; [2]Anhui International Joint Research Center for Nano Carbon-based Materials and Environmental Health, Huainan 232001, China; *E-mail*: lijj3@aust.edu.cn

Abstract

Magnetic water has attracted tremendous interest due to its unique physical and chemical properties, anti-scaling effect and memory effect. However, the effect of magnetic field on the properties of aqueous solution and the mechanism of scale formation have not been determined. In this paper, deionized water and calcium hydroxide solution were treated by a uniform magnetic field. The structures and properties of the solutions and the CaCO₃ precipitate were investigated. It is found, compared with regular water, the magnetic water has a smaller contact angle and higher UV absorbance, which is owing to the change of molecular structure and cluster configuration. Magnetic treatment also has a significant influence on the morphology and structure of the CaCO₃ precipitate. In the magnetic aqueous solution, CaCO₃ tends to form a lot of smaller crystal nuclei, which is aragonite structure, instead of the calcite structure in regular water. These CaCO₃ crystal nuclei grow slowly into a loose needle-like structure along a certain direction. While those in regular water grow fast into a dense scaly structure and finally form a spherical structure. This study is helpful to understand the mechanism of water magnetization scale prevention.

Keywords: Magnetic water; Contact angle; Calcium carbonate crystallization; Scale prevention

Introduction

Magnetic water has hottly studied owing to its unique physical and chemical properties, anti-scaling effect and memory effect. When water or an aqueous solution passes through or is exposed to a magnetic field at a certain flow rate, its physical and chemical properties will be changed. This was named as magnetic water effect. Modern magnetic water research began in 1945. Vermeiren discovered the anti-scaling and descaling effects of magnetic water in this year, and obtained patent authorization[1]. As a result, the scale removal and anti-scaling effects of magnetized water have been widely used in industrial water circulation systems. Since the second half of the 20th century, a large number of studies on the anti-scaling mechanism of magnetic water have been carried out all over the world. In 1993, Higashitani et al. found that when a magnetized Na₂CO₃ solution reacted with CaCl₂, the nucleation rate of CaCO₃ decreases, but the nucleus growth rate increased significantly[2]. However, in 1995, Madsen et al. proved that under the action of a magnetic field, the nucleation rate of CaCO₃ crystals is increased, while the particle growth rate was reduced. Too many nuclei hinder the size growth of the precipitate[3]. In 2003, Chibowski et al.

carefully studied the nucleation process of calcium carbonate by magnetically treating the Na_2CO_3 solution under static conditions, and found the sedimentation rate slowed down[4]. In 2006, Fathi et al. found that circulating an aqueous solution in a fixed magnetic field could reduce the nucleation efficiency and increase the precipitation of $CaCO_3$. They believed that the magnetic field accelerated the nucleation of calcium carbonate by affecting the binding process of ions in the aqueous solution[5]. In 2013, Liu Xin et al. also confirmed that the magnetization pretreatment accelerated the nucleation rate of $CaCO_3$ crystals. They found that the magnetization treatment triggered a change in the crystal form of calcium carbonate, thereby inhibiting the rapid growth of $CaCO_3$ crystals[6]. In 2016, Kong Chuixin et al. found that the magnetization effect of alternating magnetic field was different from that of constant magnetic field [7]. In general, the anti-scaling of magnetized water is achieved by controlling the nucleation process of $CaCO_3$ crystals by a magnetic field. But more research is needed to fully understand the anti-scaling mechanism.

Recently, more physical and chemical properties of magnetic water have been reported. The properties of magnetized water, including magnetism, surface tension, memory effect, dissolution enhancement effect, and changes in hydration properties,were all recieved extensive study[8-11]. Interestingly, it is found that the result of these researches seems closely related to the magnetization process, test methods and detection methods. It is well known that factors such as the magnetic field strength, magnetic field gradient, magnetization time, aqueous solution properties, flow speed, different solid-liquid interfaces and other factors all have impacts on the properties of magnetized water. Thus, even a slight change in test conditions can affect the results. In addition, the property change in magnetic water is very small, thus it is difficult to characterize directly. The research of magnetized water was faced with challenges due to multiple influencing factors and difficulty in direct characterization. As a results, the repeatability of the reported works was not good, and some research results even appeared to be contradictory[12, 13]. In recent years, researchers made continuous efforts to improve experimental accuracy by optimizing research method and adopting advanced characterization technique. On the other hand, computer simulation techniques such as density functional theory were introduced into the study of magnetic water [14]. Although the physical and chemical properties and the scale prevention effect of magnetized water became more and more clear, the microscopic mechanism and theoretical model of the water magnetization and the calcium carbonate crystallization is not determined.

In this article, the contact angle and UV absorbance of water under various magnetic field were carefully studied. The morphology and structure of the calcium carbonate in magnetized solution were investigated. And the effect of magnetic field on the crystallization of calcium carbonate was discussed.

Materials and methods

1. **Materials**

Calcium hydroxide ($Ca(OH)_2$), sodium bicarbonate ($NaHCO_3$), trisodium citrate dihydrate ($C_6H_5Na_3O_7$) were all purchased from Sinophenol Chemical Reagent Co., Ltd. (China). All the reagents were analytical reagent-grade.

2. Equipments

Structural characterization equipments used in this work include scanning electron microscopy (SEM, ZEISS SUPRA 40, Germany), UV visible spectrophotometer (UV-5100, Shanghai Yuan analysis instrument Co., Ltd.), electronic balance (FA1004, Shanyu Hengping instrument) and standard type contact angle meter (JY-PHa, China).

3. Magnetization experiment

The magnetization experimental device is shown in Figure.1. In a typical magnetization, 500 ml of deionized water was placed in the circulating device and was circulated in the device at a speed of 2 m/s. The pipe of the circulation device was be placed on the electromagnet so that the deionized water in the pipe could pass through the uniform magnetic field generated by the electromagnet vertically. The magnetic water was prepared under different magnetic field strengths. The strength magnetic field of the electromagnet was set so that the deionized water was magnetized in a magnetic field of 50 mT, 100 mT, 200 mT, 300 mT, and 400 mT for 1 hour. Then its contact angle on the silicon wafer were detected and UV absorbance across the entire wavelength range were tested.

To study the crystallization of calcium carbonate, 1 g of calcium hydroxide was dissolved in 500 ml of deionized water to make a supersaturated solution of calcium hydroxide. Then the supersaturated calcium hydroxide solution was cyclically magnetized in a 0 mT magnetic field for 1 hour. At the same time CO_2 gas was slowly introduced during the cycle to completely precipitate the calcium carbonate in the solution. Repeat the above steps to test under a magnetic field of 200 mT. The precipitate was collected and was dried under vacuum at 80 degrees Celsius.
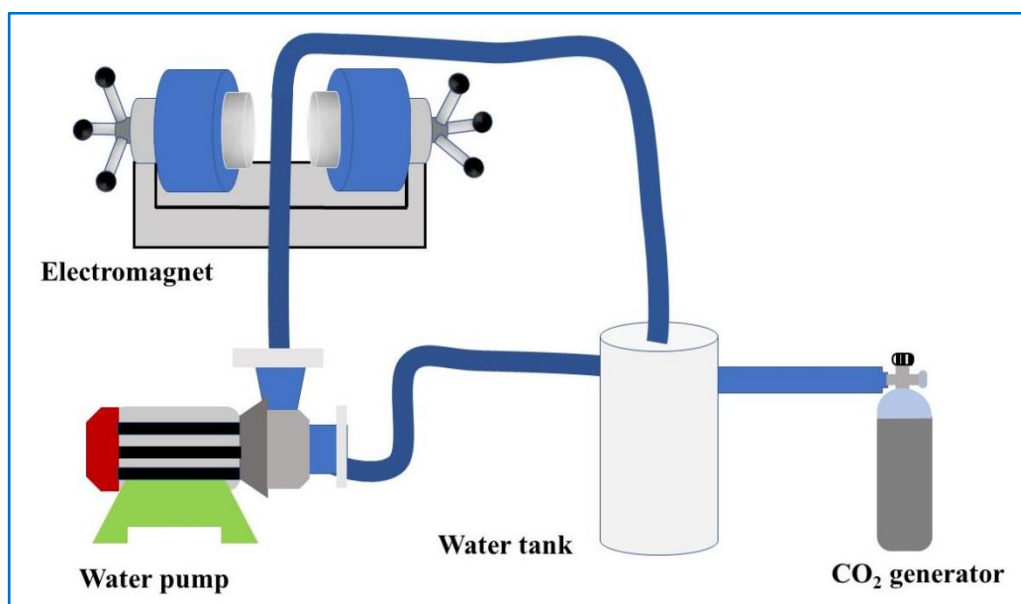
Figure. 1 Magnetic water circulation device

Results and discussion

Magnetization affected the contact angle of water significantly. As shown in Figure.2, after deionized water was magnetized for 1 hour under different magnetic field strengths, the contact angles formed on the silicon wafer were different. On the same substrate, the affinity of the magnetic water to the surface of the substrate gradually increases with the increase of the magnetic field intensity. The higher the magnetic field strength, the smaller the contact angle formed by the magnetic water. When the magnetic field is 0 mT, the contact angle of deionized water on the silicon wafer is 74.1 °. When the magnetic field strength is 50 mT, there is no significant change as shown in Figure. 2 (b). When the magnetic field is increased to 100 mT, the average contact angle decreases to 70.2° as shown in Figure.2 (c). When the magnetic field is 200 mT, the average contact angle is 68.75°, and the change is not obvious. When the magnetic field is increased to 300 mT, the contact angle decreased significantly. When the magnetic field is increased to 400mT, as shown in Figure.2 (f), the average value of the contact angle is 54.25°, which reaches the minimum. Figure. 3 shows that the absorbance of full-wavelength UV absorbance. It shows that the intensity of the magnetic field affects the absorbance of deionized water. The stronger the magnetic field, the higher the peak absorbance. The change in absorbance curve is roughly similar to the change in contact angle. From the absence of a magnetic field to 50 mT and 100 mT, the absorbance value rises slightly in the wavelength range. When the magnetic field reaches 200mT, the peak absorbance does not change significantly compared to 100 mT. When the magnetic field rises to 300 mT, the peak absorbance appears abruptly. Continue to increase the magnetic field to 400 mT, although the peak value increases, the change tends to be stable. The change in contact angle and absorbance of deionized water indicates that the microstructure of water molecules changes under the action of different strength magnetic fields. Since no chemical was added during the magnetization process, the change in the nature of deionized water should be due to the change of the water molecules or their cluster structure.
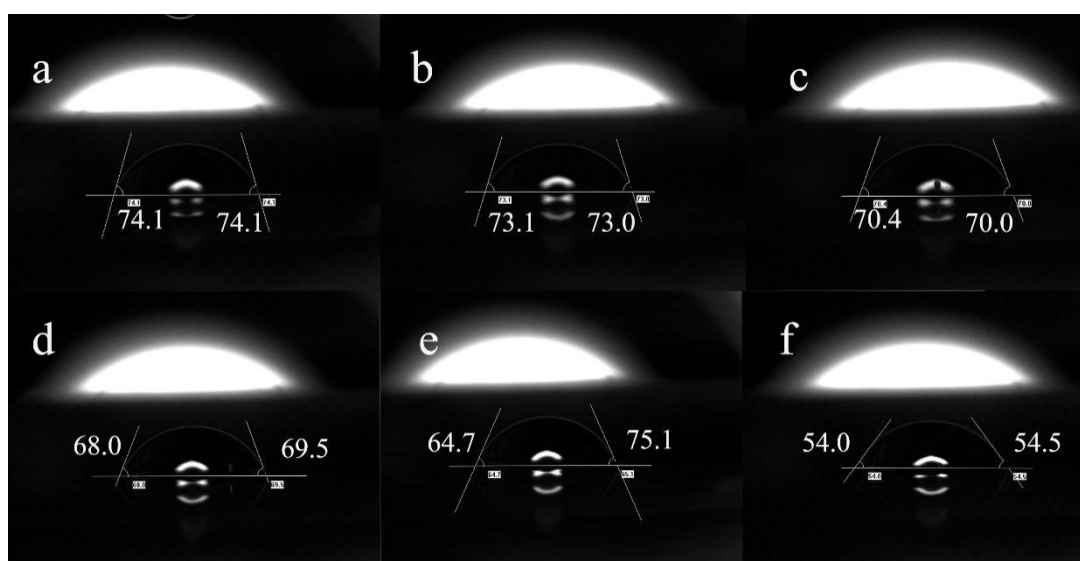
Figure. 2 Contact angle under different magnetic field strength. (a)0 mT, (b)50 mT, (c)100 mT, (d)200 mT, (e)300 mT, (f)400 mT

Scanning electron microscopy (SEM) results indicates the structure of calcium carbonate precipitates changed significantly under 400 mT. When the magnetic field is 400 mT, the overall morphology of the precipitate is a pinpoint structure, as shown in Figure.4 (a-c). While calcium carbonate precipitates into spherical particles at no magnetic field condition, as shown in Figure. 4 (d-f), Large magnification SEM graphics show that when the magnetic field is 400mT, calcium carbonate is more likely to form a loose rod-like aggregate structure.
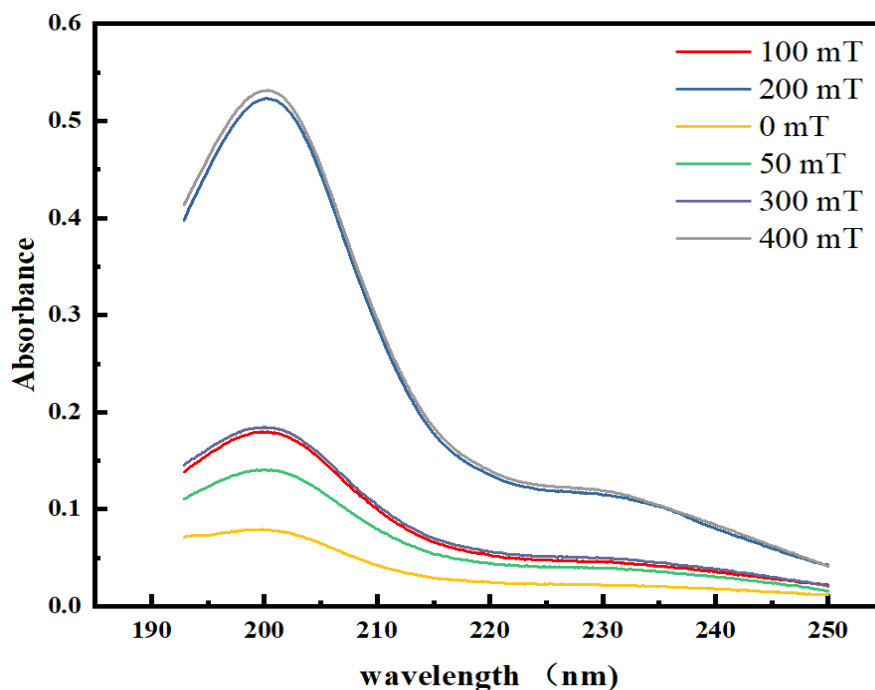
Figure. 3 UV absorbance under different magnetic field strength
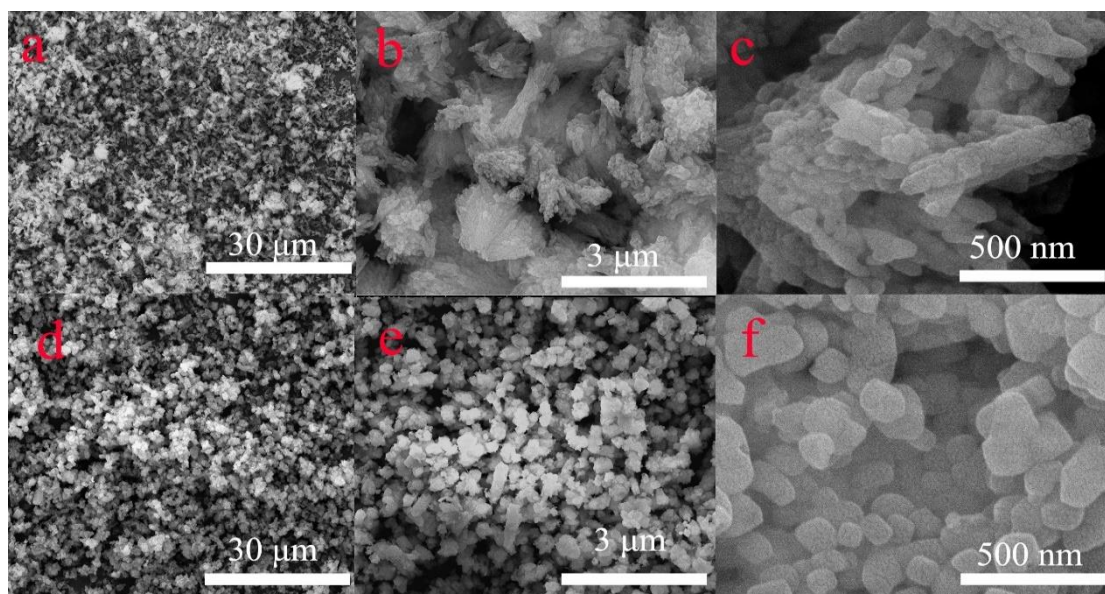
Figure. 4 SEM of the calcium carbonate precipitate produced ((a)、(b)、(c) under the magnetic field 400 mT. (d)、(e)、(f) under no magnetic field.)

Conclusions

In this work, the contact angle of magnetic water on the silicon wafer was detected and UV absorbance across the entire wavelength range were tested. The precipitation of calcium carbonate in a magnetic field was investigated. As the intensity of the magnetic field was increased, the contact angle of deionized water on the silicon wafer was decreased and the absorbance of deionized water was increased. It can indicate the microstructure of water molecules is changed due to the action of the magnetic field. The precipitation of calcium carbonate in a magnetic field will form more and smaller crystal nuclei, and at the same time grow into a loose needle-like structure along a certain direction.

This work proved that the magnetic field can effectively change the macroscopic properties of water and aqueous solutions.

Acknowledgments

References
1   Gehr R, Zhai Z A, Finch J A, et al. *Water Research,* 1995, 29(3), 933-940.
2   Higashitani K, Kage A, Katamura S, et al. *Journal of Colloid and Interface Science,* 1993, 156(1), 90-95.
3   Madsen H E L. *Journal of Crystal Growth,* 1995, 152(1), 94-100.
4   Chibowski E, Hołysz L, Szcześ A, et al. *Colloids and Surfaces A: Physicochemical and Engineering Aspects,* 2003, 225(1), 63-73.
5   Fathi A, Mohamed T, Claude G, et al. *Water Research,* 2006, 40(10), 1941-50.
6   Liu X,Wang L,Zhang Z H, et al. *Industrial Water Treatment*, 2013, 33(011), 29-32.
7   Kong C X. Experimental Study on the Anti-scaling Mechanism of the Alternating Electromagnetic Field.   Master's thesis, Shandong University, China, 2016(in Chinese).
8   Colic M, Morse D. *Colloids and Surfaces A: Physicochemical and Engineering Aspects,* 1999, 154(1), 167-174.
9   Oshitani J, Yamada D, Miyahara M, et al. *Journal of Colloid and Interface Science,* 1999, 210(1), 1-7.
10   Holysz L, Szczes A, Chibowski E. *Journal of Colloid and Interface Science,* 2007, 316(2), 996-1002.
11   Liu Z C, Song W Y, Yang L F, et al. *Science Technology and Engineering*, 2015, 15(19), 102-105.
12   Fujimura Y, Iino M. *Journal of Applied Physics,* 2008, 103(12), 6459.
13   Amor H, Elaoud A, Ben Salah N, et al. *International Journal of Advance Industrial Engineering,* 2013, 5(3), 119-124.
14   Toledo E J L, Ramalho T C, Magriotis Z M. *Journal of Molecular Structure,* 2008, 888(1-3), 409-415.

Synthesis and Characterization of 4-Chlorophenoxyacetic Acid Herbicide Intercalated with Calcium-Aluminium Layered Doble Hydroxide Through Co-Precipitation Method

Farah Liyana Bohari[1], Muhammad Alinsan Kamil Mukamil Hamzah[1], Sheikh Ahmad Izaddin Sheikh Mohd Ghazali[1*], Nur Nadia Dzulkifli[1] and Is Fatimah[2]

[1]School of Chemistry and Environment, Faculty of Applied Sciences, Universiti Teknologi MARA Cawangan Negeri Sembilan Kampus Kuala Pilah, 72000, Negeri Sembilan, Malaysia
[2] Department of Chemistry, Faculty of Mathematics and Natural Sciences, Universitas Islam, Indonesia, Kampus Terpadu UII, J1. Kaliurang Km 14, Sleman, Yogyakarta, Indonesia
*Corresponding author: sheikhahmadizaddin@uitm.edu.my

Abstract

Layered double hydroxide (LDH) or hydrotalcite-like compound is a material that can be used as a support for controlled release formulation for herbicide such as 4-Chlorophenoxyacetic acid (4-CPA) in agriculture. In this study, Calcium-Aluminium (Ca-Al) LDH host is prepared as a new herbicide delivery system by intercalating 4-CPA with Ca-Al LDH through co-precipitation method. The synthesis was performed at the pH 12 with different concentrations of $Al(NO_3)_3.9H_2O$ which were 0.025 M and 0.10 M. The successful intercalation was obtained at 0.025 M and had been confirmed through several analyses. Firstly, the result obtained from the Powder X-Ray Diffraction (PXRD) pattern showed that the basal spacing for the 0.025M nanocomposites was increased from 8.54 Å to 9.98 Å which indicate the intercalation of 4-CPA into the Ca-Al LDH were presence, but for 0.10 M, the basal spacing remain unchanged. This result supported by the ATR-FTIR band showed that the nitrate peak disappeared and carboxylate ion (COO^-) band present at 1634 cm^{-1} unlike the nitrate peak for 0.10 M nanocomposite which remains at 1365.30 cm^{-1}. The nanocomposite synthesized has shown mesoporous-type material with H3 hysteresis loop in the Brunauer-Emmett-Teller (BET) analysis. This study has signified the potential of Ca-Al LDH as a safer agent of agrochemicals by reducing the dosage of herbicide in the agriculture field and protect the herbicide through leaching and runoff into water system.

Keywords: 4-Chlorophenoxyacetic Acid (4-CPA), intercalation, co-precipitation, LDH, Nanoparticles

In Situ Growth of CdS Spherical Nanoparticles / Ti$_3$C$_2$ MXene Nanosheet Heterojunction with Enhanced Photocatalytic Hydrogen Evolution

Guo-Qing Wang[a] , Chun-Mei Kai[a], Cui Kong[a], Feng-Jun Zhang[a,b*]

[a] Key Laboratory of Functional Molecule Design and Interface Process, Anhui Jianzhu University, He fei Anhui, 230601, P. R. China.
[b] Anhui Key Laboratory of Advanced Building Materials, Anhui Jianzhu University, Hefei Anhui, 230 022, P. R. China; [*] Corresponding author: Zhang Feng-Jun, E-mail: fjzhang@ahjzu.edu.cn

Abstract

The current global energy is very urgent, solar photocatalytic hydrogen production is a potential solution. In this work, a novle CdS spherical nanoparticles / Ti$_3$C$_2$ MXene nanosheet (CM) heterostructure photocatalyst was prepared by in-situ growth method, which has the characteristics of high efficiency and stability. The results showed that the successfully prepared CM sample has a more regular morphology. Compared with pure CdS, its specific surface area increased and the hydrogen evolution performance also greatly improved. Among them, the hydrogen evolution of CM-0.06 is 1295μmol·g^{-1}·h^{-1} ($\lambda>420$ nm), which is 7 times that of spherical CdS, and it also showed stronger stability. Close interface contact can promote the transfer of photo generated carriers, and the effective separation of electron hole pairs can enhance the absorption of visible light. In addition, Ti$_3$C$_2$ MXene acts as an electron trap can further accelerate the separation of photogenerated electrons and holes. The synergistic effect between semiconductor CdS and Ti$_3$C$_2$ MXene nanosheets, which provides a new idea for the design of more stable and efficient CdS-based photocatalysts.

Key word: CdS/Ti$_3$C$_2$T$_x$ MXene, in-situ growth, photocatalyst, hydrogen evolution

Reference:
[1]   Xiao Rong, Zhao Chengxiao, Zou zhaoyong, et al. Appl. Catal. B, 2020, 268:118382-118393.
[2]   Li Jingyu, Li Yuehua, Zhang Fan, et al. Appl. Catal. B, 2020, 269:118783-118792.

Oxidative Degradation of Norfloxacin Antibiotics by Peroxymonosulfate Activated with Co$_3$O$_4$/Uio-66-NH$_2$ Composites

Xun Fang[1], Shibiao Wu[1,*], Xia Chen[2], Yaru Li[2], Jianli Chen[2], Yaqin Wang[2], Haiyan Xu[2]

[1]Anhui Province Key Laboratory of Advanced Building Materials, Anhui Jianzhu University, Hefei, Anhui, 230601, China

[2]Key Laboratory of Functional Molecule Design and Interface Process, Anhui Jianzhu University, Hefei, Anhui, 230601, China

Abstract

Norfloxacin (NOR) is one of the most widely used antibiotics in animal farming and hospital. With the mass production and consumption, the large amounts of NOR was discharged into the water environment which caused severe pollution problems. Advanced oxidation processes (AOPs) can decompose, mineralize most organic compounds, including NOR. In this paper, a novel AOPs catalyst based on peroxymonosulfate (PMS), Co$_3$O$_4$/Uio-66-NH$_2$ composites were prepared. The morphology and structure of the composites were shown in this paper. Degradation experimental results show that Co$_3$O$_4$/Uio-66-NH$_2$ composites have better degradation efficiency than Co$_3$O$_4$ nanoparticles, and the leaching concentration of cobalt ions is lower, indicating that the composite material has better stability than Co$_3$O$_4$ alone. Under the conditions of 1.0mM PMS and 0.2g/L Co$_3$O$_4$/Uio-66-NH$_2$ dosage at neutral pH, about 90% of norfloxacin (NOR) can be degraded within 30 min. In addition, the mechanism of PMS activation by Co$_3$O$_4$/Uio-66-NH$_2$ composites were studied through the free radical identification by quenching experiments and electron paramagnetic resonance (EPR) technology. In addition, the Co$_3$O$_4$/ Uio-66-NH$_2$ composites material has good regeneration efficiency, which has a certain application prospect for the removal of NOR from drinking water, and this work will also provide a potential contribution to the removal of NOR from the environment.

High supercapacitive performance on a 2D Ni-MOF material

Chao Feng

School of materials and chemical engineering, Bengbu University, 233030, China
E-mail: fchg042@163.com

Abstract

A layered structural MOF $[Ni(Hppza)_2]_n$ (**1**) was synthesized and characterized by single-crystal X-ray diffraction, elemental analyses and IR spectroscopy. For MOF **1**, the crystal structure is extended into 3D structure through N–H···O hydrogen bond. And for the first time, this complex used as an electrode material for a supercapacitor. It exhibited large specific capacitance of 184 F g^{-1} can be achieved at rates of 5 mVs^{-1}. Thevalue demonstrated the best performance of all the MOF materials in supercapacitor at present. Such an excellent electrochemical property may be attributed to the intrinsic characteristics of Ni-MOF material including its crystal structure and morphology.

Keyword MOF; Crystal structure; Electrochemical property; Supercapacitor
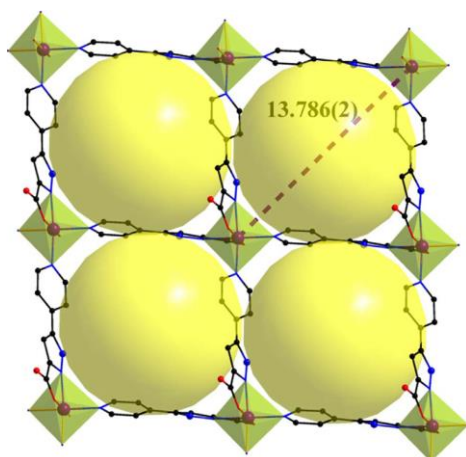
Figure 1 Structure of Ni-MOF
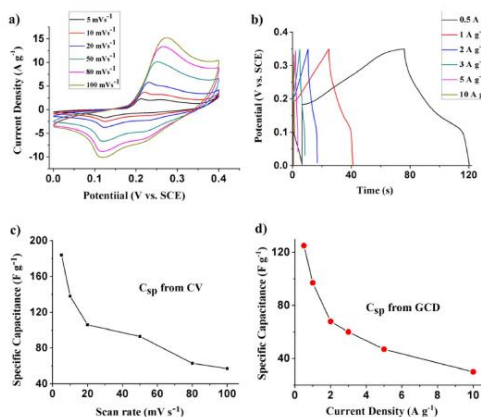
Figure 2 Supercapacitive performance of Ni-MOF

Acknowledgements

Microwave promoted synthesis of MOFs enhanced ceramic membrane for heavy metal removal

YIN Na,WANG Ke, LI Zongqun，

Anhui Provincial Engineering Technology Research Center of Silicon-Based Materials, Bengbu University，China 233000

Abstract

Heavy metal ion of lead in water pollution has caused great harm to human health, and irreparable damaged to people's nervous system and brain. MOFs (metal organic framework materials), as a new kind of porous materials with excellent structural diversity, chemical stability and high specific surface area, have a broad application prospect in the removal of heavy metal in wastewater. Four kinds of MOFs were synthesized from terephthalic acid, 1, 4-naphthalene dicarboxylic acid, 2-amino-terephthalic acid and 2, 5-dihydroxyterephthalic acid with microwave promoted synthesis. The structures of the MOFs were analyzed by X-ray diffraction (XRD).The adsorptive removal of heavy metal lead ion in water were studied using the above MOFs under the same conditions. The MOFs from terphthalic acid showed better performance than those of the other MOFs. The adsorption reached the peak value at 30min. And the MOFs could be a good candidate to enhance ceramic membrane for the removal of heavy metals from wastewater.

Influences of breakdown voltages on arc erosion of a Ti$_3$AlC$_2$ cathode in air atmosphere

Xiaochen Huang[1,2,*], Zongqun Li[1,2] , Jinlong Ge[1,2], Ming Ding[1,2]

[1] School of Material and Chemical Engineering, Bengbu University, Bengbu, Anhui 233030, People's Republic of China
[2] Engineering Technology Research Center of Silicon-based Materials, Anhui, 233030, People's Republic of China
E-mail address: 460140536@qq.com

Abstract

The influences of breakdown voltage on arc erosion of Ti$_3$AlC$_2$ have been investigated in experiments in detail. After 3-10 kV arc erosion in air, the cathode surface becomes uneven with pits, cracks and ejected particles. The arc columns can be recorded by a high-speed camera. With increasing the breakdown voltages, the breakdown currents and erosion areas increase, meanwhile, breakdown strengths decrease accordingly. Experimental results demonstrate that after high-energy arc erosion in air, Ti$_3$AlC$_2$ will be oxidized to TiO$_2$ and Al$_2$O$_3$. Remarkably, crystal transformation from anatase to rutile TiO$_2$ can be found when the breakdown voltage is higher than 3 kV, and this transformation process will be completed when the breakdown voltage reaches to 9 and 10 kV. The results in this work are helpful to understand the erosion dynamics of Ti$_3$AlC$_2$ cathode in air atmosphere, which is significant to the real applications of Ti$_3$AlC$_2$.

Keywords: Ti$_3$AlC$_2$; arc discharge; high-speed camera; Raman; oxidation; crystal transformation;

Poster

Adsorptive decontamination of malachite green contaminated water by GQDs-doped FeOH$_3$ /chitosan composite beads

Wararat Saisom[1], Nattaporn Keanjun[1], Phitchan Sricharoen[2] and Nunticha Limchoowong[1]*

[1]Department of Chemistry, Faculty of Science, Srinakharinwirot University114 Sukhumvit 23 Rd., Wattana, Bangkok, 10110 Thailand
[2]Nuclear Technology Research and Development Center, Thailand Institute of Nuclear Technology (Public Organization), Nakhon Nayok 26120, Thailand
*e-mail: nunticha@g.swu.ac.th

Abstract

This research presents a novel strategy for one step synthesis of iron (III) hydroxide dope chitosan (FeOH$_3$/chitosan) without using acidic solvent via graphene quantum dots as gelation, namely, GQDs-dope FeOH$_3$/chitosan composite bead. The GQDs-dope FeOH$_3$/chitosan composite bead is developed as an adsorbent for the adsorption of malachite green (MG) prior to determination by ultraviolet-visible spectrophotometry at wavelength of 618 nm. The bead properties were analyzers using FTIR, EDX, XRD and SEM. The optimum conditions for the dye adsorption were investigated including acid-base of a solution (pH 6), adsorption time (30 mins), adsorbent dosage (30 mg) and initial concentration of malachite green at ambient temperature. This GQDs-dope FeOH$_3$/chitosan composite bead was superb high adsorption efficiency demonstrate that this output gives a great deal to step forward for a huge scale elimination of toxic dye.

Keywords: GQDs; FeOH$_3$; Chitosan; Composite beads; Adsorption; Malachite green

References

Limchoowong N, Sricharoen P, & Chanthai S (2019). A novel bead synthesis of the Chiron-sodium dodecyl sulfate hydrogel and its kinetics-thermodynamics study of superb adsorption of alizarin red S from aqueous solution. *Journal of Polymer Research* 26 : 12.

Selective catalyst of ZnO-supported rice husk ash for glucose conversion

Gridsana Wannasri[1], Piyathida Prawsri[1], Chayut Sommit[1], Nichapha Senamart[1], Jatuporn Wittayakun[2], Pimrapus Tawachkultanadilok[2], Yingyot Poo-arporn[3], Surangrat Tonlublao[3] and Sirinuch Loiha[1*]

[1]Department of Chemistry, Faculty of Science, Khon Kaen University, Khon Kaen, 40002, [2]School of Chemistry, Institute of Science, Suranaree University of Technology, Nakhon Ratchasima, [3]Synchrotron Light Research Institute, Nakhon Ratchasima, 30000, Thailand
*e-mail: sirilo@kku.ac.th

Abstract

Zinc oxide supported on rice husk ash (RHA) plays a role of acidic catalyst for glucose conversion to fructose and 5-hydroxymethylfurfural (5-HMF). An acidic property is attributed to Brønsted and Lewis acid sites containing on silica and carbon surfaces of the RHA support. In this work, rice husk was soaked in 5 and 10 w/w% Zn^{2+} solution at room temperature for 10 h. The Zn-adsorbed rice husk was dried and calcined at 550°C for 5h to form 5ZnO/RHA and 10ZnO/RHA catalysts. The structures and element composition of the catalysts were characterized by XRD, FTIR and SEM-EDS. Catalytic testing of glucose conversion was carried out by hydrothermal method with and without applying reaction pressure at 50 bars of N_2 gas. Zn amount contained in the catalysts increased with increasing Zn^{2+} concentration. The highest Zn/Si ratio of 2.5 was observed on 10ZnO/RHA. Zn containing in the catalysts showed enhancing of the catalytic activity and selectivity of glucose conversion over RHA. Without applying pressure, 10ZnO/RHA showed the highest glucose conversion and selectivity to fructose product of 63 and 34%, respectively. Besides, high pressure reaction, the main product of 5-HMF was observed. 10ZnO/RHA showed the highest glucose conversion and 5-HMF yield of about 84% and 30%, respectively. In addition, percent yields of levulinic acid (LA) and acetic acid (AC) products achieved by the 10ZnO/RHA catalyst were higher that of 5ZnO/RHA and RHA. Thus, an addition of appropriate amount of ZnO on RHA could improve catalytic activity and product selectivity of glucose conversion under low and high pressure conditions.

Keywords: Zinc oxide, rice husk, glucose, 5-HMF

References

Lau, K.S., Chia, C.H., Chin, S.X., Chook, S.W., Zakaria, S & Juan, J.C. (2018). Conversion of glucose into lactic acid using silica-supported zinc oxide as solid acid catalyst. *Pure and Applied Chemistry*. 90(6) : 1035-1043.

Based on the Study on Preparation and Properties of Co(II) and La^{3+}-Doped TiO$_2$ Electrochromic Film

XU Zifang*, DAI Yan , YE Dongdong, JIANG Yujie

School of Material Science and Engineering, Anhui university of Science and Technology,

AnHui Huainan 232001, China

*Corresponding author: E-mail: zhfxubao@163.com

Abstract

In order to improve the optical properties and coloration effect. Co(II) and La^{3+} doped TiO$_2$ thin films were synthesized via a sol−gel, by using butyl titanate as precursor on the surface of ITO conductive glass substrate.Several techniques were used to characterize produces. Adopting the Sol-gel technology, [CH$_3$CH$_{23}$O]$_4$Ti、La$_2$O$_3$、CoC$_{12}$•6H$_2$O as the precursor, the composite membranes with different molar ratio of Ti、Ti/La、Ti/Co to be prepared on the ITO glass substrate, the optimum technological parameters for preparation of the base material of the electro-induced discoloration glass are determined. The structure and surface morphology optical and electrochromic properties of Co(II) and La^{3+}-doped TiO$_2$ films were examined with X-ray diffraction (XRD) analysis, energy dispersive spectrometer(EDS), scanning electron microscopy (SEM), and ultraviolet-visible spectrophotometer(UV-vis). DTA-TG analysis. It was found that：

(1) The sintering temperature coating number, [CH$_3$（CH$_2$）$_3$O]$_4$Ti content of the TiO$_2$ film sample, and the doping category are the main factors that affect the structure and properties of the membrane based material;

(2) Using two alcohol amine as chelating agent can effectively inhibit the formation of Ti (OH)$_4$ precipitation;

(3) The properties of the TiO$_2$ glass film prepared by La$_2$O$_3$ and CoCl$_2$·6H$_2$O are fine;

(4) Materials based on the preparation of a radiochromic film transmittance, high cyclic reversibility, cyclic voltammetry characteristics significantly ,the results of the study for the electric induced radiochromic film based material development and application provide a theoretical and experimental basis.

Keywords: Membrane based material preparation; Sol-gel; CH$_3$（CH$_2$）$_3$O]$_4$Ti; Doping category; Electro induced discoloration

Morphology control of glassy carbon coating layer to ethylene glycol / phenolic resin

Sang Hyun Joo[a], Young Jun Joo[a], Kwang Yeon Cho[a]*

[a]Fibrous Ceramics & Aerospace Materials Center, Korea Institute of Ceramic Engineering and Technology, 101, Soho-ro, Jinju-si, Gyeongsangnam-do, 660-031 Korea
E-mail: kycho@kicet.re.kr

Carbon has excellent thermal and electrical conductivity, and processability, as well as excellent chemical resistance. However, carbon has the disadvantage of causing defects and scattering dusts on the surface by physical stimulation. To improve this problem of graphite material, there is an impregnation method in which a carbonizable material such as glass or coke, various resins, etc. penetrates through the open pores of carbon. In the impregnating solution, the phenolic resin forms a glassy carbon layer via a thermal decomposition reaction, so that it is possible to form a carbon-based coating layer capable of maintaining the high-temperature thermal stability and electrical properties of carbon. Therefore, in this study, to optimize the control of the coating layer on the glassy carbon layer through the phenol resin, the mixing ratio and curing conditions were optimized, and then the glassy carbon coating layer generated through pyrolysis at 1000°C was observed

Keywords: carbon, glassy carbon, phenolic resin, phenolic coating

Experimental procedure

The selected materials were prepared at a ratio of phenol resin 1, Methyl benzene sulfonic acid 0.1, Methanol 1, Ethylene Glycol 0-0.4. The mixed phenolic resin was mixed for 2 hours. The carbon block was impregnated in the mixed phenolic resin solution for about 5 minutes. The solution impregnated with the liquid phenolic resin was dried by standing at room temperature for about 24 hours. After drying, the carbon block was carried out at 100°C for 2 h and 200°C for 2 h for surface hardening, Then, the cured carbon blocks were subjected to pyrolysis up to 1000°C (+3.3°C/min) under 1 atm and in Ar condition.

Results and discussion

The carbon block was successfully coated with a mixed phenolic resin. The SEM image result confirmed that the coating layer had a flat shape without bubbles through the phenol resin, and that the pores and rough surfaces of the existing carbon block surface were impregnated. In addition, a carbon block was fractured for coating layer analysis. It was observed that a uniform coating layer of about 20 μm was formed on the surface. As a result, through the impregnation solution with ethylene glycol added to the phenol resin, It will be possible to form a flat, pore-free glassy carbon coating layer.
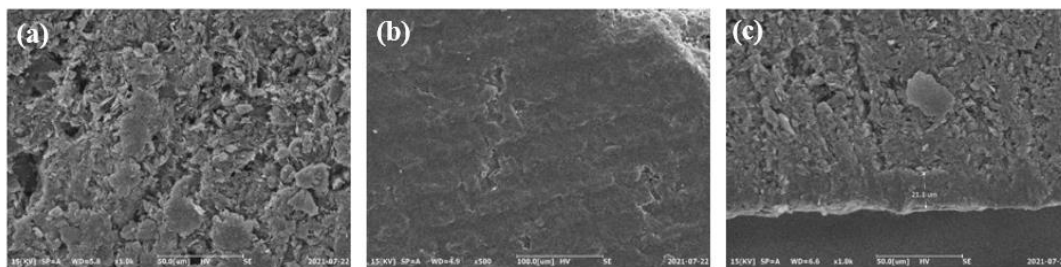
Fig. SEM image of carbon block coated by mixed phenolic resin (a) non-coated carbon block (b) coated carbon block (c) fractured surface of coated carbon block

References

[1] Zhang, Y., Zhang, Z., Tang, Y., Jia, D., Huang, Y., Guo, Y., & Zhou, Z. (2020). *Journal of Materials Chemistry A*, 8(46), 24393-24400.
[2] Zhang, J., Wang, C., & Zhou, C. (2012). *ACS nano*, 6(8), 7412-7419.

The crystallization behavior and microstructural analysis of polymer-derived SiC fibers fabricated via the control of impurity contents

Young Jun Joo, Sang Hyun Joo, Hyuk Jun Lee, Young Jin Shim, Kwang Youn Cho*

aFibrous Ceramics & Aerospace Materials Center, Korea Institute of Ceramic Engineering and Technology, 101, Soho-ro, Jinju-si, Gyeongsangnam-do, 660-031 Korea
E-mail: kycho@kicet.re.kr

The polymer-derived SiC fibers can be largely divided into amorphous SiC fibers and polycrystalline SiC fibers depending on the oxidation resistance at high temperature. Various manufacturing methods have been studied to fabricate high-performance polycrystalline SiC fibers. Various additives have been added to PCS to fabricate polycrystalline SiC fibers while suppressing degradation due to oxygen impurities present in SiC fibers. In this study, an amorphous SiC fibers with reduced oxygen content were fabricated using the iodine curing method and controlled pyrolysis conditions, and then pyrolyzed at 1800°C to investigate the crystallization behavior of the polymer-derived SiC fibers.

Keywords: *Polycarbosilane, SiC fiber, Crystallization, Microstructure, Impurity control*

Experimental procedure

PCS was melt-spun into green fibers having a diameter of 15–20 μm at 180–190°C in N_2 atmosphere. The chemical vapor curing method using iodine was adopted to fabricated the infusible PCS fiber. To control the content of oxygen impurities during the pyrolysis, the infusible PCS fibers were pyrolyzed at 1400°C for 2, 4, and 6 h. Finally, the cured PCS fibers and amorphous SiC fibers were heat-treated at 1800°C in an inert atmosphere to analyze the crystallization behavior according to the oxygen impurity content. The amorphous and polycrystalline SiC fibers containing Al content fabricated using PCS-Al precursor in the same method as described above.

Results and discussion

The polymer-derived SiC fibers fabricated at different times showed smooth cross-sectional surface without pores. Also, as the heat-treatment time increased, the iodine content introduced during the curing process was hardly observed in all samples, and the oxygen content decreased continuously.

In the polycrystalline SiC fiber heat-treated at 1600°C, coarsening of crystal grains was observed on the fiber surface as the heat treatment time increased in the fabrication stage of amorphous SiC fibers. On the other hand, the polycrystalline SiC fiber fabricated at 1800°C showed a dense surface due to the control effect of the impurity content in the fabrication stage of amorphous SiC fibers.

The X-ray diffraction pattern of SiC fiber fabricated at 1800°C showed that densified SiC fibers were poly-crystallized by optimized grain growth.
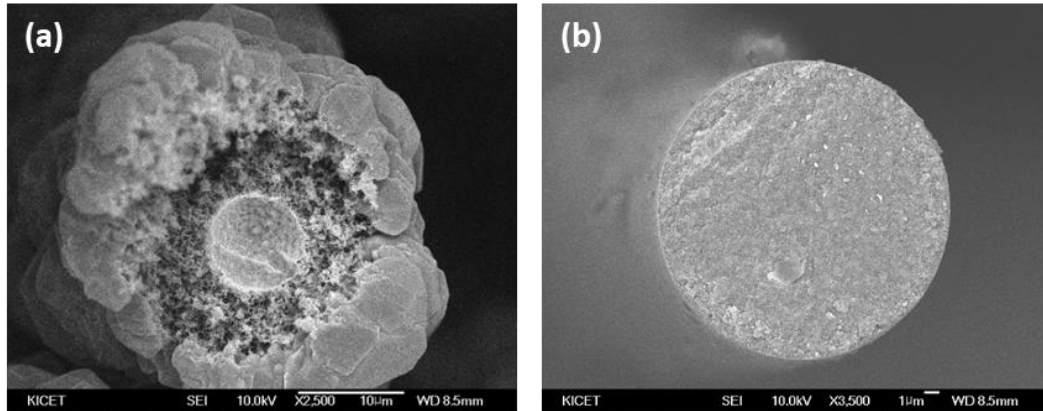
Fig. 1 SEM images of polymer-derived SiC fiber fabricated at 1600°C and 1800°C

References:

[1] Usukawa, R. and Ishikawa, T., *International Journal of Applied Ceramic Technology,* **18** (2021) 6-11

[2] Amir, H., Gerstel, P., Golczewski, J.A. and J. Bill, *Journal of Materials Research*, **25**

(2010)   2150-2158.

Z-scheme TiO$_2$/SnS$_2$ Heterojunctions with Enhanced Visible-light Photocatalytic Performance for Refractory Contaminants and Mechanistic Insight

Juan Gao[1*], Lingcheng Zheng[1], Yanfen Wang[2], Yin Liu[2]

[1]School of Mechanics and Photoelectric Physics, Anhui University of Science and Technology, Huainan 232001, P. R. China

[2]School of Materials Science and Engineering, Anhui University of Science and Technology, Huainan 232001, PR China

[*]Corresponding author's E-mail address: gaojuanphys@126.com.

Abstract

In this work, two-dimensional (2D) TiO$_2$/SnS$_2$(TOSS) nanosheet heterojunction with a novel face-to-face structure was fabricated by two-step hydrothermal method. The morphology, microstructure, chemical components, as well as optical features, photocatalytic activity, photoelectrochemical (PEC) performance and catalytic mechanism of TOSS were systematically investigated. Results certify that 2D TOSS sheet-like heterojunction can enhance the photocatalytic activity for refractory contaminants, including methyl orange (MO), methylene blue (MB), rhodamine B (RhB), and Tetracycline antibiotics (TCs). The TOSS with a mole ratio of Sn:Ti=0.15:1 possesses the best photocatalytic activity and PEC performance. The corresponding photocurrent density ($\sim$3.79 μA/cm^2) is 3.4 and 2.6 times higher than that of TiO$_2$ ($\sim$1.11 μA/cm^2) and SnS$_2$ ($\sim$1.45 μA/cm^2). Enhanced photocatalytic activity and PEC performance is ascribed to the synergistic effect of TOSS heterostructure, including (i) the Z-scheme band alignments, which can effectively inhibit the photogenerated carrier recombination, (ii) the modulation of the narrow band SnS$_2$, which can broaden the visible photoabsorption region, and (iii) the face-to-face structure, which can provide a convenient transport channel for photoinduced carriers. And active species tests demonstrated that $\bullet$OH oxidation procedure and $\bullet$O$_2^-$ oxidation procedure are the main degradation mechanism in TOSS-MO and TOSS-RhB reaction system under the simulated sunlight.

Keywords: TiO$_2$/SnS$_2$, Visible-light photocatalysis, Photoelectrochemistry, Z-scheme
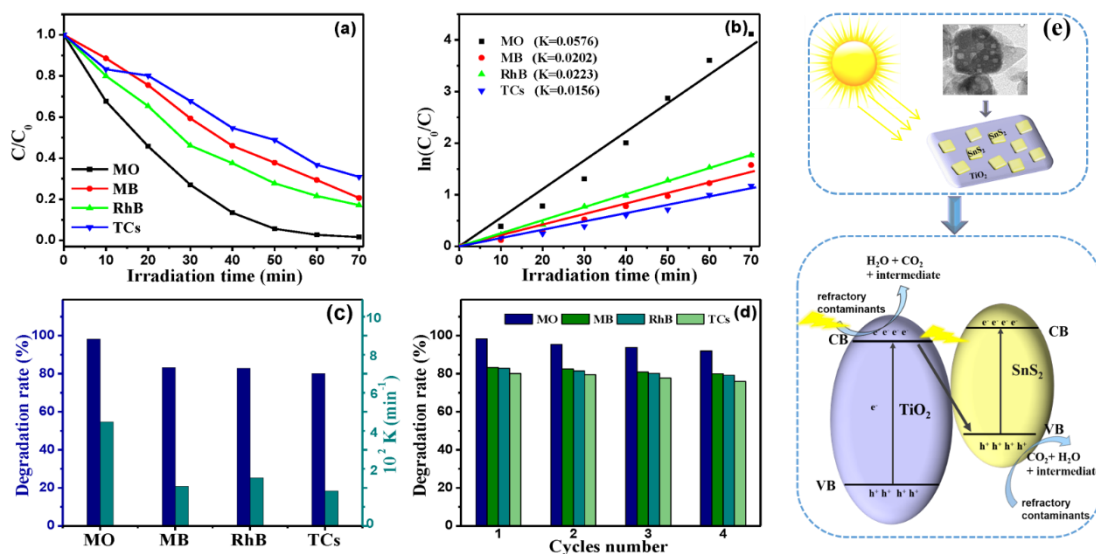
Figure (a) Photocatalytic efficiency, (b) pseudo first order reaction kinetics, (c) degradation ratio and rate constants K, and (d) repeatability tests of MO, MB, RhB and TCs for $TOSS_{0.15}$, (e) the photocatalytic mechanism for TiO_2/SnS_2 composite.

Microwave sol-gel derived Ho^{3+}/Yb^{3+} co-doped NaCaGd(MoO$_4$)$_3$ yellow phosphors and their upconversion photoluminescence properties for optoelectronic devices

Chang Sung Lim[1*], Won-Chun Oh[1], Aleksandr S. Aleksandrovsky[2,3], Victor V. Atuchin[4,5], Maxim S. Molokeev6,[7,8], Aleksandr S. Oreshonkov[7,9]

[1]Department of Aerospace Advanced Materials Engineering, Hanseo University, Seosan 31962, Korea
[2]Laboratory of Coherent Optics, Kirensky Institute of Physics Federal Research Center KSC SB RAS, Krasnoyarsk 660036, Russia
[3]Institute of Nanotechnology, Spectroscopy and Quantum Chemistry, Siberian Federal University, Krasnoyarsk 660041, Russia
[4]Laboratory of Optical Materials and Structures, Institute of Semiconductor Physics, SB RAS, Novosibirsk, 630090, Russia
[5]Research and Development Department, Kemerovo State University, Kemerovo 650000, Russia
[6]Laboratory of Crystal Physics, Kirensky Institute of Physics, Federal Research Center KSC SB RAS, Krasnoyarsk 660036, Russia
[7]Siberian Federal University, Krasnoyarsk 660041, Russia
[8]Department of Physics, Far Eastern State Transport University, Khabarovsk 680021, Russia
[9]Laboratory of Molecular Spectroscopy, Kirensky Institute of Physics Federal Research Center KSC SB RAS, Krasnoyarsk 660036, Russia
*E-mail: cslim@hanseo.ac.kr

Abstract

Rare earth-doped upconversion (UC) particles have attracted great interest in recent years due to the luminescent properties and potential applications in such products as lasers, three-dimensional displays, light-emitting devices, and biological detectors[1]. The known double molybdate compounds with general composition of MR$_2$(MoO$_4$)$_4$ (M = Ca^{2+}, Sr^{2+}; R = La^{3+}, Gd^{3+}, Y^{3+}) belong to a family of complex scheelite-type molybdates. It is possible that the trivalent rare earth ions in the disordered tetragonal phase could be partially substituted by Er^{3+}/Yb^{3+}, Ho^{3+}/Yb^{3+} and Ho^{3+}/Yb^{3+}/Tm^{3+} ions, and the ions are effectively doped into the crystal lattice of the tetragonal phase due to the similar radii of trivalent rare earth ions R^{3+}, inducing the excellent UC photoluminescence properties[2-4]. In this study, microwave sol-gel derived NaCaGd(MoO$_4$)$_3$:Ho^{3+}/Yb^{3+} ternary molybdates were successfully synthesized. Well-crystallized particles formed after heat-treatment at 850°C for 16 h showed a fine and homogeneous morphology with particle sizes of 3-5 μm. Under the excitation at 980 nm, the doped samples exhibited strong UC yellow emissions based on the combination of strong

emission bands at 520 and 630 nm in the green and red spectral regions, respectively. The strong 545 nm emission band in the green region corresponds to the $^5S_2/^5F_4 \rightarrow {}^5I_8$ transition of Ho^{3+} ions, while the strong 655 nm emission band in the red region appears due to the $^5F_5 \rightarrow {}^5I_8$ transition of Ho^{3+} ions. The optimal $Yb^{3+}:Ho^{3+}$ ratio was found to be 9:1, as indicated by the composition-dependent quenching effect of Ho^{3+} ions. The pump power dependence of the upconversion emission intensity, Raman spectroscopy, and the Commission Internationale de L'Eclairage chromaticity coordinates of the phosphors were evaluated in detail.

References

1. M.V. DaCosta, S. Doughan, U.J. Krull, Analyca Chimica Acta, **832**, 1-33 (2014).

2. Chang Sung Lim, Aleksandr Aleksandrovsky, Maxim Molokeev, Aleksandr Oreshonkov, Victor Atuchin,, Physical Chemistry Chemical Physics, **17**, 19278-19287 (2015).

3. Chang Sung Lim, Aleksandr Aleksandrovsky, Maxim Molokeev, Aleksandr Oreshonkov, Victor Atuchin, J. Solid State Chemistry, **228**, 160-166 (2015).

4. Chang Sung Lim, Materials Research Bulletin, **75**, 211-216 (2016).

Scheelite type microcrystalline AgGd(MoO$_4$)$_2$:Yb^{3+}/Ho^{3+} upconversion yellow phosphors by MES based synthesis and their spectroscopic properties for biomedical applications

Chang Sung Lim[1*], Won-Chun Oh[1], Aleksandr S. Aleksandrovsky[2,3], Victor V. Atuchin[4,5], Maxim S. Molokeev[6,7,8], Aleksandr S. Oreshonkov[7,9]

[1]Department of Aerospace Advanced Materials Engineering, Hanseo University, Seosan 31962, Korea
[2]Laboratory of Coherent Optics, Kirensky Institute of Physics Federal Research Center KSC SB RAS, Krasnoyarsk 660036, Russia
[3]Institute of Nanotechnology, Spectroscopy and Quantum Chemistry, Siberian Federal University, Krasnoyarsk 660041, Russia
[4]Laboratory of Optical Materials and Structures, Institute of Semiconductor Physics, SB RAS, Novosibirsk, 630090, Russia
[5]Research and Development Department, Kemerovo State University, Kemerovo 650000, Russia
[6]Laboratory of Crystal Physics, Kirensky Institute of Physics, Federal Research Center KSC SB RAS, Krasnoyarsk 660036, Russia
[7]Siberian Federal University, Krasnoyarsk 660041, Russia
[8]Department of Physics, Far Eastern State Transport University, Khabarovsk 680021, Russia
[9]Laboratory of Molecular Spectroscopy, Kirensky Institute of Physics Federal Research Center KSC SB RAS, Krasnoyarsk 660036, Russia
*E-mail: cslim@hanseo.ac.kr

Abstract

In recent years, rare earth-doped upconversion (UC) nanoparticles have attracted great interest due to their luminescent properties and potential applications in products such as lasers, three-dimensional displays, light-emitting devices, and biological detectors[1]. It is possible that the trivalent rare earth ions in the disordered tetragonal phase could be partially substituted by Er^{3+}/Yb^{3+}, Ho^{3+}/Yb^{3+} and Ho^{3+}/Yb^{3+}/Tm^{3+} ions, and the ions are effectively incorporated into the crystal lattice of the tetragonal phase due to the similar radii of trivalent rare earth ions, resulting in the excellent UC photoluminescence properties[2-4]. In this study, scheelite type microcrystalline AgGd(MoO$_4$)$_2$:Ho^{3+}/Yb^{3+} double molybdates with five concentrations of Ho^{3+} and Yb^{3+} were synthesized by mictowave employed sol-gel (MES) based process, and the crystal structure variation, concentration effects and spectroscopic characteristics were investigated. The crystal structures of AgGd$_{1-x-y}$Ho$_x$Yb$_y$(MoO$_4$)$_2$ (x = 0, 0.05; y = 0, 0.35, 0.4, 0.45, 0.5) at room temperature were determined in space group $I4_1/a$ by Rietveld analysis. Pure AgGd(MoO$_4$)$_2$ has a scheelite type structure with mixed occupations of (Ag,Gd) sites and cell parameters a = 5.24782 (11) and c = 11.5107 (3) Å, V = 317.002 (17) Å^3, Z = 4. In doped

samples, the sites are occupied by (Ag,Gd,Ho,Yb) ions and it provide a linear cell volume decreasing on the doping level increase. Under the excitation at 980 nm, the AGM:0.05Ho,yYb phosphors exhibited a yellowish green emission composed of red and green emission bands according to the strong transitions $^5F_5 \rightarrow {}^5I_8$ and $^5S_2/^5F_4 \rightarrow {}^5I_8$ of Ho^{3+} ions. The up-conversion intensity behavior dependent on the Yb/Ho ratio is explained in terms of optimum number of Yb^{3+} ions at the characteristic energy transfer distance around Ho^{3+} ion. The optimal concentration ratio $Yb^{3+}:Ho^{3+}$ was revealed to be 9:1. The room temperature Raman spectra were analyzed to obtain information on the AGM:xHoyYb crystal structure. The nature of extra bands was explained in framework of local distortions of MoO_4 tetrahedra. The results led to superior emitting efficiency and $AgGd(MoO_4)_2:Ho^{3+}/Yb^{3+}$ yellow phosphors can be considered as potentially active PL materials in new optoelectronic devices and in the field of biomedical applications.

References

1. M.V. DaCosta, S. Doughan, U.J. Krull, Analyca Chimica Acta, **832**, 1-33 (2014).

2. Chang Sung Lim, Aleksandr Aleksandrovsky, Maxim Molokeev, Aleksandr Oreshonkov, Victor Atuchin,, Physical Chemistry Chemical Physics, **17**, 19278-19287 (2015).

3. Chang Sung Lim, Aleksandr Aleksandrovsky, Maxim Molokeev, Aleksandr Oreshonkov, Victor Atuchin, J. Solid State Chemistry, **228**, 160-166 (2015).

4. Chang Sung Lim, Materials Research Bulletin, **75**, 211-216 (2016).

Evaluation for the fluorescence property of an energy transferred polymeric solid dye mixture in a spatially modulated Fourier transform spectrometer

JU YONG CHO[1], HYOUNG JIN KIM[1], AND WON KWEON JANG[1,*]

[1]Department of Aeronautic Electricity, Hanseo University, 46, Hanseo 1-ro, Seosan-si 31962, South Korea
*jwk@hanseo.ac.kr

Abstract

We introduce a spatially modulated Fourier transform spectrometer comprised of a modified Sagnac interferometer to monitor the temporal behavior of the energy transferred polymeric solid dye mixture. We report the fast and real time remote sensing spectrometry with improved spectral resolution.

Keywords: Solid dye mixture; Spectrometry; Fourier transform; Static modulation; Real time

Fast and remote sensing spectrometry can provide a real time spectral information. To date, however, any interferometers couldn't provide a real time changing wide spectral information with fast measurement on site. Dispersive spectrometry using diffraction optic can't provide wide spectral information, and the conventional Fourier transform spectrometers can't provide fast and real time spectral information on site. And most of others have the strict operation environment limitation, that is quite unsuitable under unstable mechanical operating conditions.

We suggest a fast and remote sensing spectrometry, that is spatially modulated Fourier transform spectrometer, comprised of modified Sagnac interferometer. It can provide a very fast measurement within several microseconds, with covering wide spectral range [1].

We synthesized an energy transferred polymeric solid dye mixture, for lasing at orange color wavelength. The emission peak and absorption peak wavelengths of acceptor dye, rhodamine 6G, were 590 nm and 530nm, respectively. However, there is not a suitable laser diode for pumping source. Therefore, we mixed a donor dye, C-545, to absorb the pump light at 450nm. C-545 has the absorption and fluorescence peak wavelengths at 450 nm and 530 nm, respectively. If we use the 450 nm laser diode as a pumping light source for polimeric solid ye mixture, the pumping light can be absorbed by a donor dye of C-545, that is mixed with rhodamine 6G. And then the absorbed power can be transferred to rhodamine 6G, acceptor dye, by producing the fluorescence at 530nm.

The lasing operation, sometimes, should be monitored in output power and spectral information, in the application to spectroscopic research. Furthemore, it should be done real time and remote sensed on site. The solid dye laser has a wide spectral tuning range. We noticed this point, and suggested the spatially modulated Fourier transform spectrometer for this kind of fast and remote sensing spectrometry.

In this paper, we report the real time monitoring about the temporal behavior of the energy transferred polymeric solid dye mixture. The remote sensing measurement was performed by a spatially modulated Fourier transform spectrometer, that is developed in our

laboratory [2]. The spectral resolution of the energy transferred polymeric dye mixture was 49 cm^{-1}, which was comparable to that of the diffraction distributed spectrometry, though it was performed in a very short time.

Solid-state dye with 1×10^{-4} mol/l and 3×10^{-4} mol/l for C-545 and Rh-6G

Solid-state dye with 1×10^{-4} mol/l and 1×10^{-4} mol/l for C-545 and Rh-6G
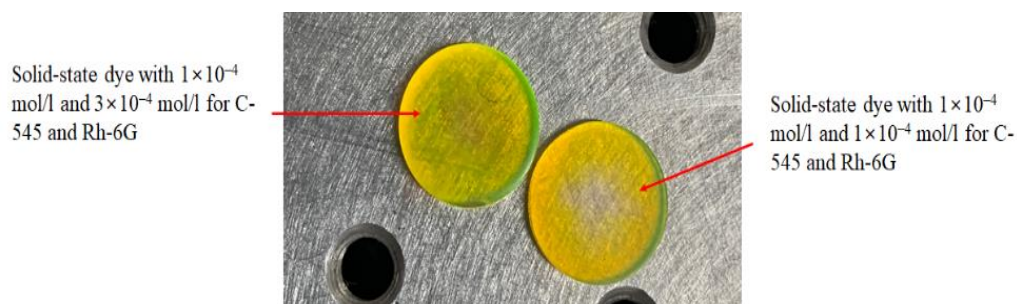
References

[1] J. Y. Cho, S. H. Lee, and W. K. Jang, "Improvement of spectral resolution by signal padding method in the spatially modulated Fourier transform spectrometer based on a Sagnac interferomter", Appl. Opt., 58(25), 6755-6761(2019).

[2] S. Singh, V. R. Kanetkar, G. Sridhar, V. Muthuswamy, and K. Raja, "Solid-state polymeric dye lasers" J. Lumin., 101, 285-291(2003).

Vinetting in a spatially modulated Fourier transform spectromter

Ju Yong Cho[1], Hyoung Jin Kim[1], and Won Kweon Jang[1,*]

[1]*Department of Aeronautic Electricity, Hanseo University, 46, Hanseo 1-ro, Seosan-si 31962, South Korea*
*[*jwk@hanseo.ac.kr](mailto:jwk@hanseo.ac.kr)*

Abstract

Vinetting effect is one of major problems that induce the distortion of the signal and the deterioration of signal to noise ratio, in a spatially modulated Fourier transform spectrometer. We discuss the dependent factors such as total optical path, throughput, and divergence angle limit to prevent the vinetting effect.

Keywords: Vinetting; Spectrometer; Fourier transform; Static modulation; Divergence limit

Spatially modulated Fourier transform spectrometers have been reported as an alternative for the conventional Fourier transform spectrometers, that have disadvantages of seismic resistance and strict operation environment. However, in the spatially modulated spectrometer, one or two dimensional sensor array is required to detect the spatially modulated interferogram. Therefore, the spatially modulated Fourier transform spectrometers are also suffered from low signal to noise ratio, due to low detected signal intensity on each pixel element. An optical power detected on each pixel can be insufficient, compared to that of the conventional spectrometers. And the interferogram is in the overlapped sector of two beams, that have different optical path length. In order to obtain better spectral resolution, the separation between two beams should be long, but it induce the degraded signal to noise ratio.

In this paper, we discuss some dependent factors of total optical path length, throughput, and divergence angle limit in the spatially modulated spectrometer comprised of a Sagnac interferometer to analyze and lessen the vinetting effect [1-2].

Figure 1(a) shows the unfolded layout of the spatially modulated Fourier transform spectromter comprised of the modified Sagnac interferometer. L is total optical path, S is a slit size, and θi is the indicence angle. If θi is larger than the allowed range, the incident light cannot exit the interferometer. Therefore, the incidence angle should be kept smaller than the allowed value. Otherwise, the measured signal would be severely deteriorated.

The splitted two beams in the interferometer have different optical path. Hence, each beam would have different values of L and limit of θi. Figure 1(b) shows the variation of limit of θi for each beam according to the mirror displacement. S was assumed to be a width of 50 mm. Mirror displacement cannot be longer than the width of S. Maximum displacement was calculated to be 33 mm. At this displacement, the allowed valsue of θi for transmitted and reflected beams was 5.4˚ and 6.3˚, respectively. This result shows that the optical path length of the transmitted beam is longer than that of the reflected beam. Therefore, the allowed limit value of θi was determined by the optical path of transmitted beam.
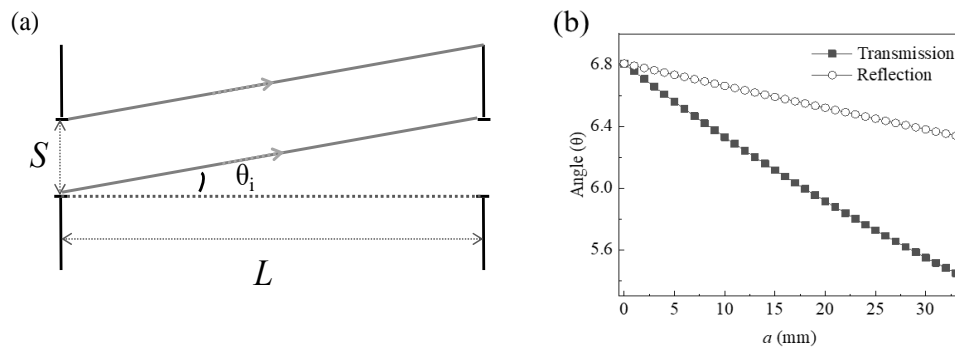
Figure 1. (a) The unfolded optical path scheme to inspect the vinetting effect in the spatially modulated Fourier transform spectrometer comprised of the modified Sagnac interferometer. (b) Allowed value for the incident angle according to the mirror displacement.

In the spatially modulated Fourier transform spectrometer comprised of modified Sagnac interferometer, the larger mirror displacment, the longer optical path difference. Though the longer optical path difference provide the better spectral resolution, the allowed value of incident angle for the transmitted beam should be monitored to avoid the vinetting effect. And the allowed value of the incident angle, θ_i, was limited by that of the transmitted beam.

References

[1] R. Glenn Sellar and Glenn . Boreman, "Limiting aspect ratios of Sagnac interferometer," *Opt. Eng.*, **42**(11), 3320-3325(2003).
[2] Jingjing Ai, Chunmin Zhang, Peng Gao, and Chenling Jia, "Signal-to-noise ratio of the spatially modulated imaging spectrometer on modified Sagnac interferometer," *Opt. Commun.*, **287-299**, 46-53 (2013).

A simple method for fabricating an external light extraction composite layer with random nanostructures to improve the optical properties of OLEDs.

Geun Su Choi[1], and Young Wook Park[1]*

[1] Nano and Organic-Electronics Laboratory, Department of Display and Semiconductor Engineering, Sun Moon University, Asan, Chungcheongnam-do 31460, Republic of Korea
Corresponding author, Email: zerook@sunmoon.ac.kr

The light extraction technology is a technology required for organic light-emitting diodes (OLEDs) in which light loss occurs due to the difference in the refractive index of the multilayer thin film. However, the light extraction technology of OLEDs has difficulty in implementing the technology in the process due to the complicated process and the high temperature/high-pressure process.[1-3] In this study, we fabricated a random nanostructures (RNSs) external light extraction composite layer containing high-refractive-index nanoparticles through a simple and inexpensive solution process and a low-temperature mask-free process. We focused on varying the shape and density of the RNSs and adjusting the concentration of high-refractive index nanoparticles to control the optical properties. As a result, our film exhibited ~ 85% direct transmittance at a wavelength of 550 nm. Therefore, these films can be used as a scattering layer to reduce the loss of OLED substrate mode. RNSs made in low-temperature mask-free process can use the distance between nanostructures and various forms to control diffraction and scattering effects in the visible wavelength range. In addition, the randomly distributed high-refractive-index nanoparticles on the polymer film can contribute to the reduction of waveguide mode and total reflection at the substrate/air interface.

References
1. Shim, Y. S., et al. *Nanoscale*, 8(7), 4113-4120 **(2016)**
2. Song, H. J., et al. *Organic Electronics*. 52, 230-236 **(2018)**
3. Wang, L., et al. *AIP Advances*. 8(5), 055030 **(2018)**
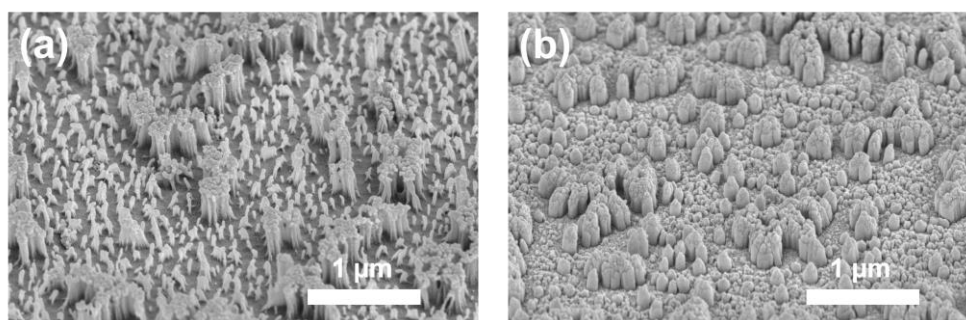
Figure. 1 scanning electron microscopy images of random nanostructure (RNS) obtained under different plasma etching conditions: (a) RNSs 1, (b) RNSs 2

Comparison of Carbon Dots Derived from Sugarcane Bagasse and WasteTea Residue for the Detection of Tetracycline

Dhanapat Kerdkok, Paphavee Rujichansiri, Panyapat kitivoranunnakul,
Sucheewin Chotchatchawankul, Nunticha Limchoowong, Piyada
Jittangprasertand Itthipol Sungwienwong*

Department of Chemistry, Faculty of Science, Srinakharinwirot
University114 Sukhumvit 23 Rd., Wattana, Bangkok, 10110 Thailand
*e-mail: itthipol@g.swu.ac.th

Abstract

Carbon dots (CDs) were synthesized from different biowaste including sugarcane bagasse and waste tea residue by the hydrothermal technique. The performance of CDs from sugarcane bagasse and waste tea residue were compared for determination of tetracycline (TC). The stability test result showed that the synthesized CDs had dispersion stability within 7 days for the sugarcane bagasse source and 15 days for the waste tea residue source. The sugarcane bagasse CDs were capable of reacting rapidly with TC at pH 6 and pH 8 for waste tea residueCDs. The intensity of fluorescence quenching increased at higher concentrations of the TC solution. The results also showed that a linear calibration curve were obtained with good correlation coefficients ($r^2 > 0.99$) over the concentration range of 22.5-225 µM for the sugarcane bagasse CDs and 50-200 µM for the waste tea residue CDs. The limit of detection (LOD) was 6.52 µM and 12.48 µM for the sugarcane bagasse and waste tea residue CDs, respectively. The limit of quantitation (LOQ) was identified at 21.8 µM for the sugarcane bagasse CDs, 41.6 µM for waste tea residue CDs. The proposed method using CDs from bothcarbon sources demonstrated good precision for both inter-day and intra-day results. The developed method was successfully applied for the quantitative determination of TC intetracycline tablets. The analytical results obtained from proposed method were in agreement with the content on the drug label.

Keywords: Carbon dots, Sugarcane bagasse, Waste tea residue, Tetracycline

References

Gunjal, D. B., Naik, V. M., Waghmare, R. D., & Patil, C. S. (2019). Sustainable carbon nanodots synthesised from kitchen derived waste tea residue for highly selective fluorimetric recognitionof free chlorine in acidic water: A waste utilization approach. *Journal of the Taiwan Institute of Chemical Engineers* 95 : 147-154.

The flexible PDMS with random porous structure for external light extraction of OLEDs

Eun Jeong Bae[1], Dong-Hyun Baek[2*], and Young Wook Park[1*]

[1] Nano and Organic-Electronics Laboratory, Department of Display and Semiconductor Engineering, Sun Moon University, Asan, Chungcheongnam-do 31460, South Korea
[2] Center for Next Generation Semiconductor Technology, Department of Display and Semiconductor Engineering, Sun Moon University, Asan, Chungcheongnam-do 31460, South Korea

*Corresponding author: Prof. Young Wook Park and Dong-Hyun Baek
Email: zerook@sunmoon.ac.kr, dhbaek@sunmoon.ac.kr

Abstract

In this study, we propose a flexible porous polydimethylsiloxane (PDMS) film formed by a high-pressure steam process to improve the external light extraction of organic light-emitting diodes (OLEDs). The fabricated flexible PDMS film exhibits a randomly distributed micro-sized porous structure and is used as the external light scattering layer of OLEDs. The porous PDMS film was produced by mixing the PDMS pre-polymer and curing agent in various ratios and then using a high-pressure steam process. The size and distribution of the formed pores can be controlled by the mixing ratio of the PDMS pre-polymer and curing agent. By applying a film made with an optimized PDMS mixing ratio to OLEDs, the EQE and viewing angle characteristics of the device are improved. This result is expected to affect the light extraction characteristics of the device because the internal scattering effect was increased.

We believe that the flexible porous PDMS film can provide another opportunity to achieve high efficiency in wearable light sources and flexible OLEDs.

Highly efficient blue phosphorescent OLEDs with undoped ultra-thin emission layer structure

Shin Woo Kang[1,2], Byeong-Kwon Ju[1*], and Young Wook Park[2*]

[1] *Display and Nanosystem Laboratory, Department of Electrical Engineering, Korea University, 145, Anam-ro, Seongbuk-gu, Seoul 02841, Republic of Korea*
[2] *Nano and Organic-Electronics Laboratory, Department of Display and Semiconductor Engineering, Sun Moon University, Asan, Chungcheongnam-do 31460, Republic of Korea*
Corresponding author, E-mail address: bkju@korea.ac.kr[1], zerook@sunmoon.ac.kr[2*]*

In this study, the highly efficient ultra-thin emission layer (EML) based blue phosphorescent organic light-emitting diodes (OLEDs) were fabricated. The ultra-thin EML structure referred to the structure of the very thin (being under 1nm) dopant thin film that was inserted into the EML position between the electron transport layer and hole transport layer, and it has a difference from the conventional doping structure, which has a co-deposit host and dopant. The ultra-thin EML structure has advantages as a simple structure and simple fabrication process compared with the conventional doping process[1]. In previously, we reported the ultra-thin EML structure-based green phosphorescent OLEDs with 24% external quantum efficiency (EQE), and ultra-thin EML structure-based white OLEDs using blue and yellow dopants[2-3]. Here, we report the high-efficiency ultra-thin EML based blue phosphorescent OLEDs. The thickness of the HTL and the ETL were precisely controlled and applied using finite-difference time-domain method, and the thickness of the ultra-thin EML layer was also precisely controlled to fabricate the device. As a result, the maximum EQE of 19.1%, the maximum current efficiency of 41.5cd/A, and the maximum power efficiency of 38.3lm/W were achieved.

References
1. Zhao, Y., Chen, Y. & Ma, D. *ACS Appl. Mater. Interfaces* 5(3), 965–971 **(2013).**
2. S. W. K., D-H. B., B-K. J. & Y. W. P. *Sci. Rep.* 11(8436), **(2021).**
3. S. W. K., D-H. B., B-K. J. & Y. W. P. *J. Nanosci. Nanotechnol* 21(8), 4719-4184 **(2021).**

High quality 3-dimensional structure based on polymeric material for enhancing the external quantum efficiency

Dong-Hyun Baek[1], Eun Jeong Bae[2], Ho Seob Kim[1], and Young Wook Park[2]

[1] Center for Next-Generation Semiconductor Technology, Sun Moon University, Asan Chungcheongnam-do, South Korea, 31460
[2] Nano and Organic-Electronics Laboratory, Department of Display and Semiconductor Engineering, Sun Moon University, Asan, Chungcheongnam-do, South Korea, 31460

E-mail: dhbaek@sunmoon.ac.kr

Abstract

The Organic Light-Emitting Diodes (OLEDs) have high potential for development as a lightweight, ultra-thin, low-cost, and flexible device in order to expand to flexible displays and wearable devices. Although the OLEDs have made it possible to achieve 100 % internal quantum efficiency, the 70 ~ 80% of lights are trapped because the difference in refractive indices of conventional OLEDs structure. In this study, we need a random scattering layer consisting of a random micro/nano structure based on a polymeric material for function a low haze and external extraction structure (EES). so that the random scattering layer was fabricated by using a Breath Figure (BF) and a replica process. The proposed method can form the high-quality 3D structure with polymeric material which has excellent flexibility such as polydimethylsiloxane (PDMS). The replicated PDMS as external scattering layer effect to the trapped light direction in the glass substrate and it is influenced by the scattering effect, so that the External Quantum Efficiency (EQE) is increased over 20 %. Afterward, the external scattering layer based on PDMS can offer an effective film as light extraction layer.

Preparation of porous geopolymers depending on foaming agents

Kyung won Kim, Hyung Mi Lim*

ªFibrous Ceramics & Aerospace Materials Center, Korea Institute of Ceramic Engineering and Technology, 101, Soho-ro, Jinju-si, Gyeongsangnam-do, 660-031 Korea
E-mail: lim@kicet.re.kr

Geopolymers are aluminosilicate that are typically composed at low temperatures below 100º. It is an inorganic polymer that is synthesized by the chemical reaction of an aluminosilicate precursor and an alkali polysilicate to form an Al-O-Si bond. Depending on the pH of the alkaline solution, the amount of the reaction varies. Since the early 2000s geopolymers have been mainly considered as an alternative to ordinary Portland cement, primarily due to their lower CO_2, but also to performance advantages (e.g. early compressive strength; greater chemical and heat resistance). Recently, the use of porous geopolymers intentionally including pores for high value-added applications such as insulation and sound insulation, fireproofing, and moisture-absorbing materials are being considered.

Keywords: *Geopolymer foam; Porosity; Alkalis leaching; Composites matrix*

Experimental procedure

Kaolin is a starting material for the geopolymer reaction, was calcined at 800 °C (10°C/min elevated temperature) to obtain metakaolin. As alkali activators, aq. potassium hydroxide(KOH) and liquid potassium silicate(K_2SiO_3) were used. In addition, carbon fibers with a diameter of 15-20 μm and a length of 5 mm were added as reinforcing materials in the matrix. Then, 3 kinds of foaming agents (propyl gallate, hydrogen peroxide (H_2O_2), citric acid) were added to the mixture of metakaolin and alkali activators and further combined. The foam contents were recorded for 3days intervals of 6h at room temperature to check the stability of the foam. Thereafter, a flexural strength test was also performed to confirm the mechanical strength. Microstructure was observed by SEM.

Results and discussion

When the amount of H_2O_2 added increases, the air content is excellent and the density is the lowest. This is due to the formation of pores in the structure, and it is confirmed through the flexural strength value. However, foam stability is poor. On the other hand, when citric acid was added, the air content slightly increased, and therefore the density was also relatively high, indicating that pore formation was not achieved. Propyl gallate had lower air content and flexural strength than the other two additives but confirmed foam stability and homogeneous pore distribution.
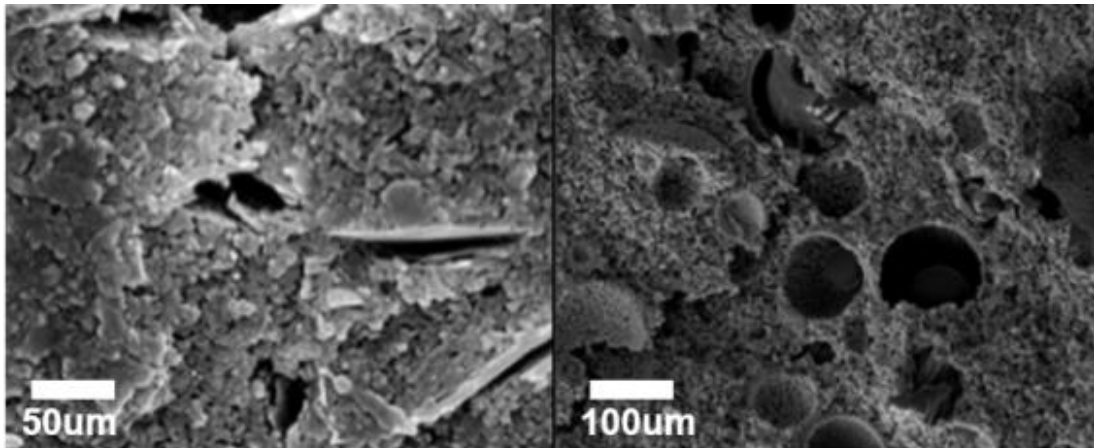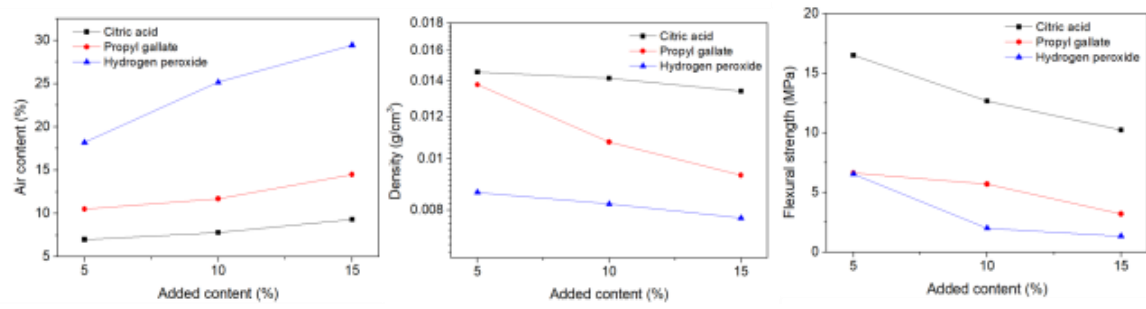
Fig. Flexural strength and SEM image of fractured surface of porous geopolymer with forming agent of H_2O_2

References

[1] Novais RM, Seabra MP, Labrincha JA. Porous geopolymer spheres as novel pH buffering materials. Journal of Cleaner Production. 2017;143:1114-22.

Changes in the shape of silica sol particles depending on the difference in aging time

Seong Yoon Kim, Seong Hoon Lee, Hyung Mi Lim*

ªFibrous Ceramics & Aerospace Materials Center, Korea Institute of Ceramic Engineering and Technology, 101, Soho-ro, Jinju-si, Gyeongsangnam-do, 660-031 Korea
E-mail: lim@kicet.re.kr

Colloidal silica is a material in which solid amorphous silica particles are stably dispersed in a solvent without precipitation. Colloidal silica is produced by ion exchange method, oxidation and neutralization method, peptization method, electrodialysis method, Sol-gel method. In this study, the Stöber method using hydrolysis and condensation reactions was carried out as a well-known method for producing colloidal silica. A mixed solution of EtOH and TEOS (Tetraethyl orthosilicate), which is an alkoxide, is added to a mixed solution of EtOH, H_2O, and NH_4OH, and the reaction proceeds. After mixing TEOS and EtOH at room temperature, the time until the time of input was set as a variable for synthesis, and the difference in the shape of the silica sol was confirmed.

Keywords: Colloidal silica, Aging, Nano silica, TEOS, Stöber method

Experimental procedure

To synthesize colloidal silica, mix EtOH, H_2O, NH_4OH to make a mixed solution and raise the temperature to 40°C. After reaching 40°C, a mixed solution of TEOS and EtOH is added to proceed with the reaction. After mixing TEOS and EtOH, the time to the time of input was set with a difference of 0, 6, 12, 18 and 24h. After adding a mixed solution of TEOS and EtOH, the reaction was carried out at 40 °C for 2 h, and then the size and shape of the silica particles was confirmed through TEM and particle size analysis by electrophoretic light scattering method.

Results and discussion

When the aging time 0h, the size of the primary particles is 32nm, and the size of the secondary particles is also 32nm, When the aging time 24h, the size of the primary particles is 12nm and the size of the secondary particles is 60nm or more. It was confirmed that the size of the primary particles decreased while the size of the secondary particles increased as the aging time increased from 0h to 24h. In other words, it shows that the degree of aggregation of the particles increases with the passage of aging time.
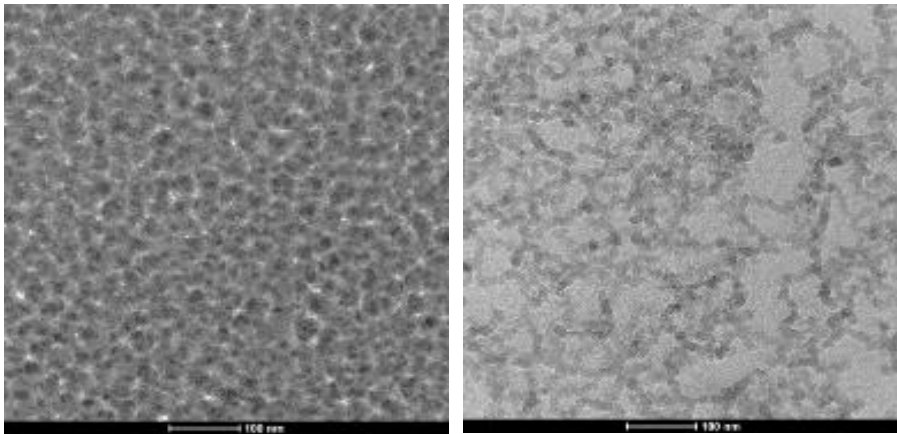
Fig. TEM image of Colloidal silica particles according to aging time 0 and 24h

References:

[1] X Jiang, X Tang, L Tang, B Zhang, H Mao, Synthesis and formation mechanism of amorphous silica particles via sol–gel process with tetraethyl orthosilicate, Ceram. Int. **45** (2019) 7673-7680.

Removal of Cr (VI) ions from aqueous solution by zinc impregnated cellulose composites in a fixed-bed column

Supattra Tangtubtim[1] Natthawut Potprarinya[2] and Kongsak Pattarith[1]*

[1]Department of Chemistry, Faculty of Science, Buriram Rajabhat University, 31000, Thailand
[2]Department of Electrical Engineering Technology, Faculty of Industrial Technology, Buriram Rajabhat University, Buriram 31000, Thailand
*e-mail: kongsak.pr@bru.ac.th

Abstract

This study was carried out to the preparation, characterization, and applications of adsorbent obtained from cellulose and ZnO/cellulose composites in a fixed bed column for the removal of Cr (VI) ions from the synthetic waste water. The characterization of the materials was examined using Fourier transform infrared spectroscopy (FTIR) and Scanning electron microscopy (SEM). For the column sorption study conducted at various parameters including bed height (1.0, 2.0 and 3.0 cm), flow rate (1, 1.5 and 2 mL/min), influent Cr (VI) ions concentrations (150, 300 and 500 mg/L) and an influent pH (2, 3, 4, 5 and 6). It was found that the exhaustion time increased with the increase of bed depth, the decrease of flow rate and initial concentration. The performance stability of the adsorbent was tested by continuous adsorption–desorption studies.

Keywords: Zinc impregnated cellulose; Zine Oxide; Fixed-bed column; Cr (VI) removal

References

Ahmed, M. J., & Hameed, B. H. (2018). Removal of emerging pharmaceutical contaminants by adsorption in a fixed-bed column: A review. Ecotoxicology and Environmental Safety, 149: 257–266.

Aleksandra, T., Patryk, O., & Ryszard, D., (2015). Sorption and desorption of Cr (VI) ions from water by biochars in different environmental conditions. Environ. Sci.Pollut. R 22, 5985–5994.

Chen, S., Yue, Q., Gao, B., Li, Q., Xu, X., & Fu, K., (2012). Adsorption of hexavalent chromium from aqueous solution by modified corn stalk: a fixed-bed column study. Bioresour. Technol. 113, 114–120.

Hyder, A.H., Begum, S.A., & Egiebor, N.O., (2014). Sorption studies of Cr (VI) from aqueous solution using bio-char as an adsorbent. Water. Sci. Technol. 69,2265–2271.

Naked-eye detection of KCN based on intramolecular charge transfer of azo compound in aqueous solution

Suphawarat Thupsuri and Sukanya Tongkhan[*]

Department of Chemistry, Faculty of Science, Buriram Rajabhat University, 31000, Thailand
*e-mail: sukanya.tk@bru.ac.th

Abstract

Cyanide is extremely toxic ions which can be harmed the brain and heart to cause coma and death. The toxicity of cyanide is depends on the chemical form especially free cyanide including hydrogen cyanide and water-soluble cyanide such as sodium cyanide (NaCN) and potassium cyanide (KCN). In this study, the azo compound (3) was synthesized and studied the response to KCN in aqueous solution by UV-vis spectrophotometer. Compound 3 showed high selectivity response to cyanide ion over other anions (F^-, Cl^-, Br^-, I^-, CH_3COO^-, $H_2PO_4^-$, HSO_4^- and SCN^-) in 60% $EtOH/H_2O$. The UV-vis spectrum was observed; the absorbance at 360 nm decreased and new absorbance at 550 nm appeared upon the addition of cyanide ion. A color change from yellow to purple was immediately observed. The job curve indicated that compound 3 and cyanide ion formed a 1:1 reaction. The ^{1}H NMR experimental and DFT investigation confirmed the reaction of compound 3 with cyanide ion and the intramolecular charge transfer (ICT) process. We expected that this sensor could be developed as test strips based on compound 3 for the rapid monitoring of cyanide ion in real water samples.

Keywords: Potassium cyanide; Cyanide; Sensor; Azo compound

References

Lee, J.H., Jang, J.H., Velusamy, N., Jung, H.S., Bhuniya, S., & Kim. J.S. (2015). An intramolecular crossed-benzoin reaction based KCN fluorescent probe in aqueous and biological environments. *Chemical Communications* 51 : 7709-7712.
Udhayakumari, D. (2018). Chromogenic and flourogenic chemosensors for lethal cyanide ion. A comprehensive review of the year 2016. *Sensors and Actuators B* 259 : 1022-1057.

Preparation of *Cymbopogon nardus* (L.) Rendle oil nanocapsule by encapsulation process for embedding into cotton fibers

Rungnapa Pimsen[1*], Paweena Porrawatkul[1], Naengnoi Sangsane[1],
and Montakarn Thongsom[2]

[1]Nanomaterials Chemistry Research Unit, Department of Chemistry, Nakhon Si Thammarat Rajabhat University, 80280, Thailand.

[2] Department of Biology Nakhon Si Thammarat Rajabhat University, 80280, Thailand.

*Corresponding author. e-mail : rpimsen@gmail.com; Tel. +66-7537-7443, Fax +66-7537-7443

Abstract

Encapsulated *Cymbopogon nardus* (L.) Rendle oil nano-capsule have been developed in nano-emulsion form. CS was incorporated as a thickener and fabric binder for embedding into cotton fibers. The interaction between cotton fibers and gel was investigated by FTIR. Wash durability of nano-capsules were evaluated using SEM. The SEM analyses revealed that CS containing nano-capsules retains on fabric after a series of washing. The optimum conditions for the synthesis were determined to be a frequency of 60 Hz for 45 minutes, a CS content of 100 ppm, and a SDS concentration of 0.02 M. The spherical shape of nano-capsules with uniform particle size was shown by a scanning electron microscope. As the concentrations of CS (positively charged) and SDS (negatively charged), which stabilize the oily portion, increase, a complex or chi-complexion arises by electrostatic interaction between CS and SDS. The stability investigations of the nano-emulsions produced yielded electrifying results. The percentage of Creaming Index value demonstrated that increasing the amount of SDS reduced the percent Creaming Index. The embedding of nano-capsules into cotton fabric was successfully developed using a technique Dipping-Coating with optimal ratio between the nano-capsules and the chitosan binder was 5:3. the wash durability of the nano-capsule into cotton fabrics was found to have nano-capsules on the fabric for 20 wash cycles.

Keywords: *Cymbopogon nardus* (L.) Rendle, nano-capsule, encapsulation, cotton fibers

Introduction

Mosquitoes represent one of the most significant threats to human and veterinary health around the world[1]. The worldwide incidence of dengue fever has increased 30-fold in the past 30 years, and more countries are reporting their first outbreaks of the disease (WHO, 2019)[2]. The use of mosquito repellents has become one of the most effective ways to prevent disease transmission and the discomfort associated with mosquito bites.

Natural products, including essential plant oils, have been used due to their repellent properties. In recent decades, interest in natural repellents has been increasing since they are considered safer, more effective, environmentally friendly, biodegradable, cheaper and more easily accessible[3]. Essential oils of citronella, *Cymbopogon nardus* (L.) Rendle has been reported its repellent activity due to sesquiterpene, citronellal, citronellol, compounds marketed with great success[1], [4].

The incorporation of insect repellents in an apparel fabric gives it mosquito repellent or anti-mosquito finishing is one of the strategies to provide long lasting protection against mosquito bites. Fabric finished with mosquito repellent may reduce the possibility of mosquito biting either by repelling or knockdown effects. Anti-mosquito finished fabric may be preferred because of their extended effectiveness and outdoor applicability. As apparel, cellulosic fabrics such as cotton are preferred, because of their ecofriendly nature, comfortability, and air permeability

Although, essential oils are reported to be potential mosquito repellent, however, because of volatility issues they are not effective for longer duration [5], [6]. Encapsulation can reduce the evaporation rate of the essential oils [7]–[9]. There are several reports on the encapsulation of essential oils for mosquito repellent finishing of fabric. Micro-encapsulation of citronella oil and limonene oil has been reported for fabric coating [1], [4]. Chitosan is a biopolymer which has confirmed to be an efficiency carrier with essential characteristics such as its biodegradability, biocompatibility, availability, safety, and innate antimicrobial potential[8], [10], [11].

This study was aimed to encapsulate the citronella oil nano-capsule by encapsulation process using sodium dodecyl sulfate and chitosan stabilized as shell material for embedding into cotton fibers. Moreover, the wash durability of the nano-capsule into cotton fabrics was also evaluated.

Materials and methods

Analytical reagents used in the study were of analytical grade and were purchased from Merck. Nutrient agar for bacterial culture and Mueller–Hinton broth and agar for antimicrobial activity were purchased from Hi-Media, Mumbai, India. Chitosan was purchased from Bonafides marketing, Thailand. The degree of deacetylation was ca. 85%. SDS was purchased from GFS, USA ($\geq$98.5%). *Cymbopogon nardus* (L.) Rendle oil or citronella oil was purchased from Thai-China Flavours & Fragrances industry Co., Ltd. Acetic acid (Sigma Aldrich, Germany, 99.9%) of 1% v/v was utilized as a medium. Distilled water was used throughout this study.

CS/SDS-stabilized emulsions of citronella essential oil preparation

The mixtures of preset amount of CS, SDS, and citronella essential oil, in 1% acetic acid solution with the total volume of 50 ml were charged into the glass bottle. Then, the mixtures were ultrasonicated (ultrasonicator, Elma S 60 H Elmasonic) for 5 min with 37 kHz frequency.

Citronella essential oil nano-emulsions characterization

The functional groups of the prepared Citronella essential oil emulsions were evaluated using an attenuated total reflection (ATR)-FTIR spectrophotometer (Tensor 27, Bruker). The spectra were recorded at a resolution of 4 cm−1 in the range between 4000 and 600 cm−1. The particle size of the formulated Citronella essential oil emulsions was evaluated using a dynamic light scattering (DLS) method with a laser particle size analyzer at 25 ∘C. The significance of the electrostatic or charge repulsion of the prepared Citronella essential oil emulsions which known to affect stability. The surface charge of prepared emulsions was determined by zeta potential analyzer, Model ZetaP ALS, Brookhaven, USA. The morphology of emulsion was characterized by scanning electron microscope (SEM) SEM-Hitachi SU8020.

Citronella essential oil emulsions stability

The Citronella essential oil emulsion was transferred into a glass bottle. The height of Citronella essential oil emulsions was fixed at 10 cm. Then, the bottle of Citronella oil emulsion was left at room temperature for 15 days. The emulsion was separated into a milky layer (cream) at the top and a translucent layer (serum) at the bottom. The total height of the emulsion of each bottle (E) and the height of the serum layer (S) were determined. The creaming index was calculated by following equation:

$$\text{Creaming index} = S/E \times 100 \ldots\ldots \quad (1)$$

Embedding of nano-capsules into cotton fibers

The synthesized nano-capsules was mixed with 1 %w/v chitosan binder at the ratio of 1:3, 3:3 and 5:3. The fabric was cut approximately of 10 x 10 cm and soaked in the mixture for 15 minutes. The chemically soaked cloth is subjected to periodic compression by hand for approximately 30 minutes, then heated to 130 °C for 2 minutes, and then ironed on the highest heat for 5 minutes, dry at room temperature.

Wash durability

The clothes that have been fixed with nano capsules were washed with detergent formulated for children. The fabric was washed with 1 g/L non-ionic detergent at 30 °C for 10 min, then rinsed with clean water and dried. The washing was tested 0, 5, 10, 15 and 20 times to achieve desired series of wash cycles, modified to the standard AATCC Test Method. After drying prepared samples were used for durability studies and further analysis of scanning electron microscopy (SEM).

Results and discussion

Attenuated total reflection (ATR)-FTIR analysis of Citronella essential oil nanocapsules

The prepared nanocapsules was characterized by FTIR spectroscopy. The spectra of Citronella essential oil nanocapsules was recorded (Figure 1).
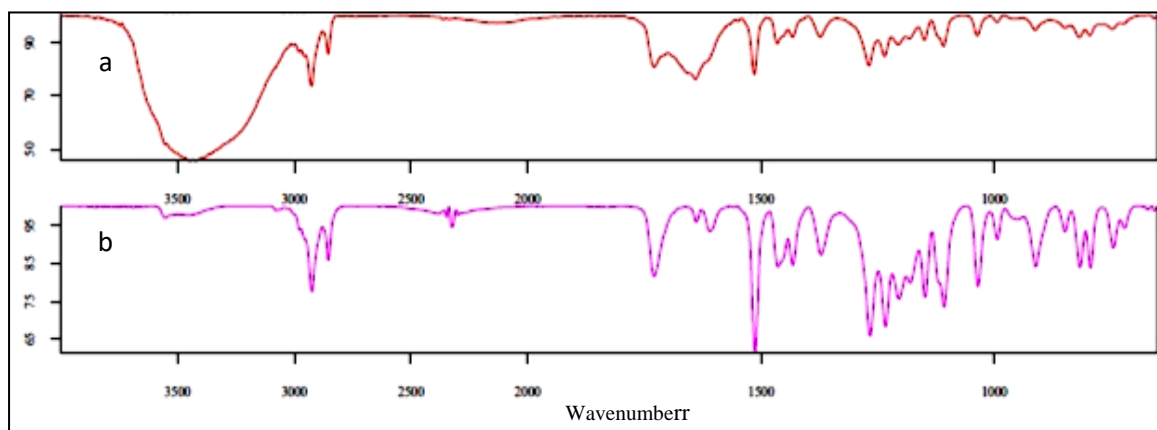
Figure 1. ATR-FTIR spectra of a) Citronella essential oil nanocapsules and b) Citronella essential oil

The spectrum of CS exhibited the characteristic signal OH and NH stretching around 3419 cm^{-1}, CH stretching (2922 cm^{-1}), and NH bending (amide II, 1514 cm^{-1}). Moreover, the signal of SDS displayed the characteristic S=O stretching at 1084 cm^{-1}. The spectrum of Citronella oil displayed CH, and C=C stretching bands at 2922, and 1641 cm^{-1}, respectively. As a result, the IR spectrum of Citronella oil emulsion comprised of signals from CS, SDS, and Citronella oil, which contained in the oil emulsion [4], [12]. The sharp one is corresponded to the π-π*transition of carbon-carbon bonds, whereas the rest ones arise from the n-π* transition of carbon-oxygen bonds.

Citronella essential oil nanocapsules stability (%Creaming index)

The stability of nanoemulsion was investigated using the creaming index under phase separation of stabilized emulsions within 15 days. The results of creaming occurrence were reported under the form of creaming index (see Eq.1) which was monitored by the total height of the emulsion of each bottle (E) and the height of the serum layer (S).
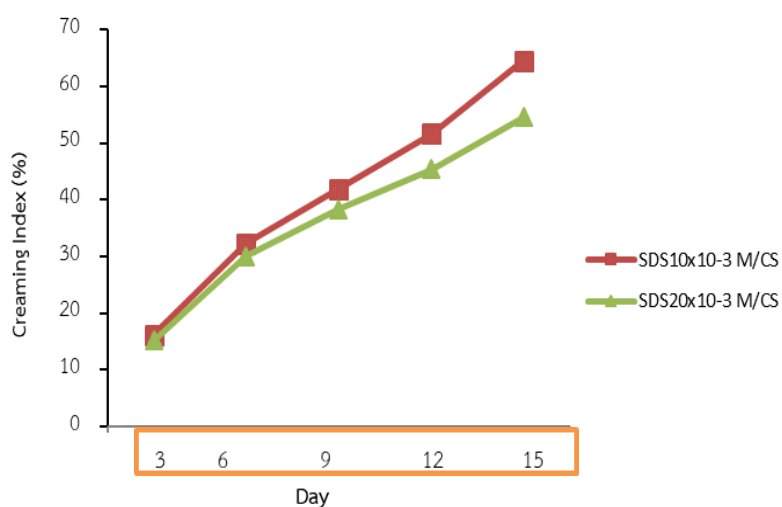
Figure 2. Creaming index percentage of Citronella essential oil nanocapsules using ChS 100 ppm and Citronella essential oil 1 g

It found that the increasing of CS can cause the percentage of creaming index reducing (Figure 2). As a result, it was possible that the complex of CS and SDS stabilized Citronella oil in water emulsion presented a superior resistance to droplet combination accordingly diminishing the droplet size and creaming progression [13].

Zeta potential analysis and particle size of Citronella essential oil nanocapsulation

The zeta potential of the synthesized nanocapsules revealed that the increasing of CS concentration (positively charged) and SDS (negatively charged), which is a stabilizer for the oily part, it becomes a complex or a complex between CS and SDS via electrostatic interaction. Electrostatic interaction results in a less negative or more positive of zeta potential shown in Table 1. Furthermore, when considering the chemical structure of the major constituents in essential oils comprised of a functional group with a high electron density, resulting in a negative zeta potential of the nanocapsules prepared from this condition[14], [15].

Table 1. Zeta potential of the nanocapsules in the various CS concentration

CS (ppm)	SDS(M)	Zeta potential (mv)		
		Oil (g)		
		1	2	3
100		-69.29	26.39	0.76
200	0.02 M	-73.51	-50.71	0.12
300		-63.26	-43.82	3.51

The particle size distribution of the nanoemulsion was investigated using dynamic light scattering (DLS) to determine the average particle size and particle size distribution. At 0.02 M of SDS provided a particle size of nanoemulsion about 160 nm shown in Figure 3. The appropriated CS/SDS complexes effected to nanoemulsion stability and particle size. Moreover, the nanoemulsion may possibly be disrupted by either coalescence or combination led to decrease the surface area of the nanoemulsion.
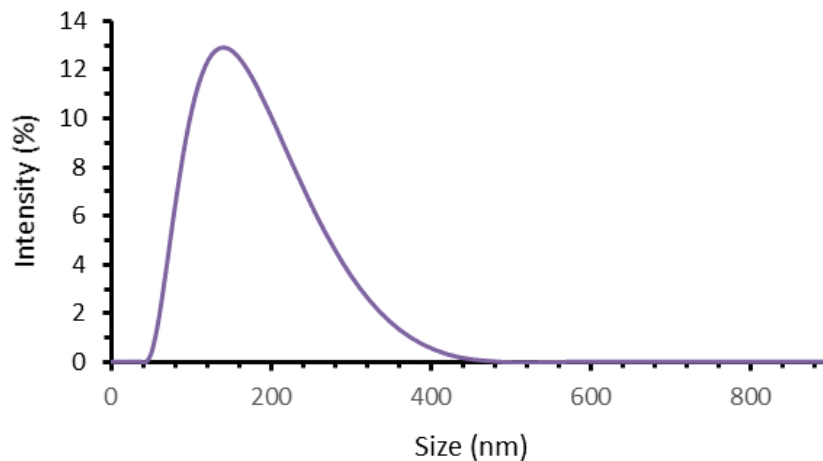
Figure 3. Particle size of citronella essential oil nano-capsule at a frequency of 60 Hz for 45 min.

Citronella essential oil nanocapsules morphology

A morphological study of Citronella essential oil nanocapsules with 100 ppm CS and 1 g of Citronella oil were obtained from a scanning electron microscope (SEM) images. The nanocapsules was found that the obtained nanocapsules regular spherical particles of nanoemulsion as shown in Figure 4 because of the electrostatic interaction between ChS and SDS adequately to stabilized the nanoemulsion.
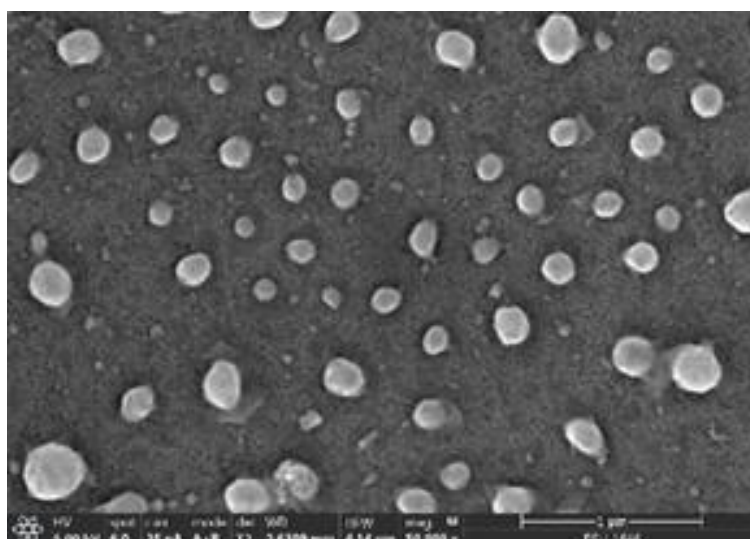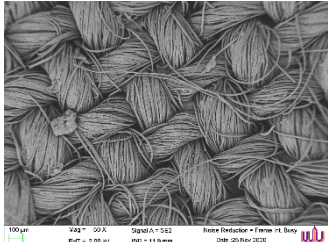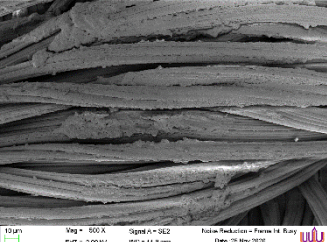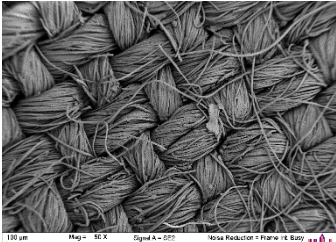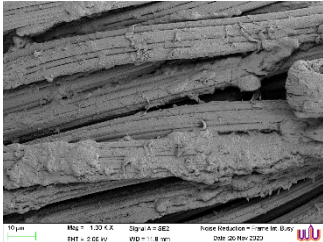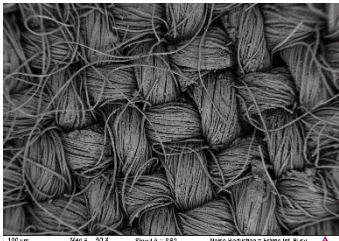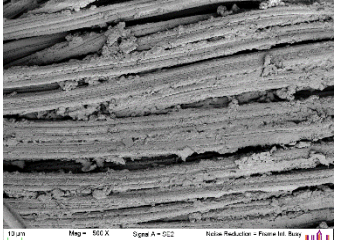
Figure 4 SEM image of Citronella essential oil ChS 100 ppm with SDS 0.02 M

Surface morphology and washing fastness of treated cotton fabric

The citronella nano-capsules were evaluated the odor fastness. Table 2 showed SEM image of cotton fibers coated with a 5:3 ratio of nano-casules and CS. It clearly observed that the amounts of nano-capsules in the fabric was reduced through the washing process. Until after washing 20 times, it was found that there were still some nano-capsule particles stuck on the fabric fibers as shown in Table 2. Moreover, there is a light smell, so it can be concluded that the smell can last for 20 wash cycles.

Table 2 SEM image of cotton fibers coated with a 5:3 ratio of nanocasules and CS

Washing cicles (cicle)	SEM image of cotton fibers coated with a 5:3 ratio of nanocasules and CS at 60X magnification	SEM image of cotton fibers coated with a 5:3 ratio of nanocasules and CS at 500X magnification
0		
5		
10		

15		
20		

Conclusion

We successfully prepared *Cymbopogon nardus* (L.) Rendle oil nano-capsule by encapsulation process for embedding into cotton fibers. It was found that the optimum condition for the nano-emulsion synthesis was the frequency of 60 Hz for 45 min, the chitosan content was 100 ppm, and the SDS was 0.02 M. Scanning electron microscope showed the spherical shape of nano-capsules with uniform particle size. The increasing the concentration of CS (positively charged) and SDS (negatively charged), which stabilize the oily part, it forms a complex or a chi-complexion occurs via electrostatic interaction between CS and SDS. The stability studies of the produced nano-emulsion revealed electrostatic interactions. The percentage of Creaming Index value demonstrated that increasing the amount of SDS reduced the percent Creaming Index. Fixation of nano-capsules onto cotton fabric was successfully developed using a technique Dipping-Coating. The optimal ratio between the nano-capsule and the chitosan binder was 5:3. The fabrics that were morphed by the nano-capsule by SEM technique were found to have nano-capsules on the fabric for 20 wash cycles.

Acknowledgements

References

[1] M. R. M. da Silva and E. Ricci-Júnior, "An approach to natural insect repellent formulations: from basic research to technological development," *Acta Trop.*, vol. 212, no. September 2019, p. 105419, 2020, doi: 10.1016/j.actatropica.2020.105419.

[2] S. Ghayempour and M. Montazer, "Micro/nanoencapsulation of essential oils and fragrances: Focus on perfumed, antimicrobial, mosquito-repellent and medical textiles," *J. Microencapsul.*, vol. 33, no. 6, pp. 497–510, 2016, doi: 10.1080/02652048.2016.1216187.

[3] A. P. B. Balaji, A. Ashu, S. Manigandan, T. P. Sastry, A. Mukherjee, and N. Chandrasekaran, "Polymeric nanoencapsulation of insect repellent: Evaluation of its bioefficacy on Culex quinquefasciatus mosquito population and effective impregnation onto cotton fabrics for insect repellent clothing Polymeric nanoencapsulation of insect repellent," *J. King Saud Univ. - Sci.*, vol. 29, no. 4, pp. 517–527, 2017, doi: 10.1016/j.jksus.2016.12.005.

[4] M. M. M. Specos *et al.*, "Microencapsulated citronella oil for mosquito repellent finishing of cotton textiles," *Trans. R. Soc. Trop. Med. Hyg.*, vol. 104, no. 10, pp. 653–658, 2010, doi: 10.1016/j.trstmh.2010.06.004.

[5] J. Hu, Z. Xiao, R. Zhou, S. Ma, M. Wang, and Z. Li, "Properties of aroma sustained-release cotton fabric with rose fragrance nanocapsule," *Chinese J. Chem. Eng.*, vol. 19, no. 3, pp. 523–528, 2011, doi: 10.1016/S1004-9541(11)60016-5.

[6] M. Montazer and T. Harifi, "Nanoencapsulation techniques for textile finishing," *Nanofinishing Text. Mater.*, pp. 295–310, 2018, doi: 10.1016/b978-0-08-101214-7.00019-4.

[7] D. França, Â. F. Medina, L. L. Messa, C. F. Souza, and R. Faez, "Chitosan spray-dried microcapsule and microsphere as fertilizer host for swellable − controlled release materials," *Carbohydr. Polym.*, vol. 196, pp. 47–55, 2018, doi:

10.1016/j.carbpol.2018.05.014.

[8]   S. Kala *et al.*, "Chitosan-acrylate nanogel for durable anti mosquito finishing of cotton fabric and its dermal toxicity profiling on Swiss albino mice," *Colloids Surfaces B Biointerfaces*, vol. 181, no. May, pp. 789–797, 2019, doi: 10.1016/j.colsurfb.2019.06.022.

[9]   S. Garzoli *et al.*, "Lavandula x intermedia essential oil and hydrolate: Evaluation of chemical composition and antibacterial activity before and after formulation in nanoemulsion," *Ind. Crops Prod.*, vol. 145, no. December 2019, p. 112068, 2020, doi: 10.1016/j.indcrop.2019.112068.

[10] S. Noppakundilograt, P. Buranagul, W. Graisuwan, C. Koopipat, and S. Kiatkamjornwong, "Modified chitosan pretreatment of polyester fabric for printing by ink jet ink," *Carbohydr. Polym.*, vol. 82, no. 4, pp. 1124–1135, 2010, doi: 10.1016/j.carbpol.2010.06.040.

[11] D. Alonso, M. Gimeno, R. Olayo, H. Vázquez-Torres, J. D. Sepúlveda-Sánchez, and K. Shirai, "Cross-linking chitosan into UV-irradiated cellulose fibers for the preparation of antimicrobial-finished textiles," *Carbohydr. Polym.*, vol. 77, no. 3, pp. 536–543, 2009, doi: 10.1016/j.carbpol.2009.01.027.

[12] M. R. M. da Silva and E. Ricci-Júnior, "An approach to natural insect repellent formulations: from basic research to technological development," *Acta Trop.*, vol. 212, 2020, doi: 10.1016/j.actatropica.2020.105419.

[13] H. Cui, M. Bai, M. M. A. Rashed, and L. Lin, "The antibacterial activity of clove oil/chitosan nanoparticles embedded gelatin nanofibers against Escherichia coli O157:H7 biofilms on cucumber," *Int. J. Food Microbiol.*, vol. 266, no. November 2017, pp. 69–78, 2018, doi: 10.1016/j.ijfoodmicro.2017.11.019.

[14] I. Simionato, F. C. Domingues, C. Nerín, and F. Silva, "Encapsulation of cinnamon oil in cyclodextrin nanosponges and their potential use for antimicrobial food packaging," *Food Chem. Toxicol.*, vol. 132, no. January, p. 110647, 2019, doi: 10.1016/j.fct.2019.110647.

[15] D. Zhao *et al.*, "Preparation of high encapsulation efficiency fragrance microcapsules and their application in textiles," *RSC Adv.*, vol. 6, no. 84, pp. 80924–80933, 2016, doi: 10.1039/c6ra16030a.

Microwave assisted synthesis of Ag/ZnO nanoparticles using *Averrhoa carambola* fruit extracts as reducing agent for antibacterial finishing over cotton fabrics

Paweena Porrawatkul[1,2*] and Prawit Nuengmatcha[2]

[1]Creative Innovation in Science and Technology, [2]Nanomaterials Chemistry Research Unit, Department of Chemistry, Faculty of Science and Technology, Nakhon Si Thammarat Rajabhat University, 80280, Thailand
*e-mail: paweena_por@nstru.ac.th

Abstract

The present study reported a green route for synthesis of silver/zinc oxide (Ag/ZnO) nanocomposite using *Averrhoa carambola* fruit extract by microwave assisted method. The synthesized Ag/ZnO nanocomposite was characterized by using UV–visible spectroscopy, X-ray diffraction (XRD), scanning electron microscopy (SEM), transmission electron microscopy (TEM), energy dispersive X-ray spectroscopy (EDS) techniques. The XRD pattern revealed wurtzite crystalline structure of Ag/ZnO nanocomposite. Electron microscopy images showed agglomeration of Ag/ZnO nanocomposite having spherical shaped structure with size in the range of 30–50 nm. The antibacterial activity of uncoated cotton, *Averrhoa carambola* fruit extract and Ag/ZnO NPs coated cotton fabrics were investigated against Gram positive (*S. aureus*) and Gram negative (*E. coli*) via using agar well diffusion method. It showed that Ag/ZnO NPs coated cotton fabric has higher antibacterial activity than other test samples against both bacteria's. Finally, the modified cotton fabrics were washed through a certain number of laundering cycles and their surfaces and antibacterial performances were investigated. It was found that the modified cotton fabrics remains has antibacterial activity for *E. coli* and *S. aureus* even after 20 washing cycles.

Keywords: Antibacterial, Averrhoa carambola, Cotton fabric, Ag/ZnO nanoparticles

References

Example

Mansoor, F., Leila, S., & Ameneh, A. (2021). A novel synthesis of Ag@ZnO yolk-shell and ZnO hollow sphere nanostructures and comparison of their photocatalytic performances. *Physica B* 613, 412729.

Preethi, S., Abarna, K., Nithyasri, M., Kishore, P., Deepika, K., Ranjithkumar, Bhuvaneshwari, R., & Bharathi, V.D. (2020). Synthesis and characterization of chitosan/zinc oxide nanocomposite for antibacterial activity onto cotton fabrics and dye degradation applications. *International Journal of Biological Macromolecules* 164, 2779–2787.

Sagadevan, S., Selvaraj, V., Anita Lett, J., Is, F., Faruq, M., Hamad A., Al-Lohedan, Solhe, F., Alshahateet, M.A., Motalib, H., & Mohd Rafie, J. (2021). Star fruit extract-mediated green synthesis of metal oxide nanoparticles. Inorganic and Nano-Metal Chemistry https://doi.org/10.1080/24701556.2021.1880437.

Effect of Gamma Chitosan/ZnO composites on Antifungal Properties

Arnannit Kuyyogsuy[*1], Prawit Nuengmatcha[1] and Wilaiwan Chaisorn[2]

[1]Nanomaterials Chemistry Research Unit, Department of Chemistry, [2] Department of Biology
Faculty of Science and Technology, Nakhon Si Thammarat Rajabhat University, 80280, Thailand.
[*]Corresponding author. e-mail: arnannit.k@gmail.com; Tel. +66-7537-7443, Fax +66-7537-7443

Abstract

In this study, we synthesized the gamma chitosan/ZnO composites for antifungal. *Phytophthora palmivora* is a major pathogen of rubber tree, which is the causative agent of leaf fall. The morphology, composition, and optical absorption properties of the synthesized gamma chitosan/ZnO composites were investigated by various methods. The scanning electron microscopy (SEM) displayed clusters of rod shaped particulate morphology. UV–vis absorption spectra showed a shift in the optical absorption towards lower wavelength for gamma chitosan/ZnO composites when compared to ZnO particles. The antifungal activity results (against *P. palmivora*) showed that the greater inhibit the potential of gamma Chitosan/ZnO composite. SEM analysis results showed the substantial change in the external morphology of *P. palmivora* after treatment with gamma chitosan/ZnO composites due to the fungal cell membrane damage. It is expected that gamma Chitosan and ZnO complement each other and exhibit synergistic effects, potential for antifungal and agricultural applications.

In vitro antimicrobial activity of extracts obtained from *Syzygium gratum* against the fish pathogenical bacteria *Streptococcus agalactiae*

Sunanta Khongsai[1*] Uton Charoendat[2] and Luksamee Vittaya[1]

[1] Department of Physical Science, Faculty of Science and Fisheries Technology, Rajamangala University of Technology Srivijaya, Trang Campus.
[2] Department of Fisheries Technology, Faculty of Science and Fisheries Technology, Rajamangala University of Technology Srivijaya, Trang Campus

Abstract

The purpose of this study would be how efficient *Syzygium gratum* extracts are at preventing microbial pathogens in fish. Hexane, ethyl acetate, ethanol, and methanol were used to extract the dried leaf, flower, and fruits samples. The antibacterial activities of crude extracts on *Streptococcus agalactiae* infection in fish were evaluated using the hole – plate diffusion method with oxytetracycline as the positive control and DMSO as the negative control. The results revealed that *S. gratum* hexane leaf, flower, and fruit extracts would have the highest efficiency against *S. agalactiae* with average inhibition zones of 18.38 ± 0.12, 22.57 ± 0.06, and 27.50 ± 0.07 mm, respectively. The minimum inhibitory concentration (MIC) and minimum bactericidal concentration (MBC) were determined to be 195.31, 48.83, and 0.01 µg/ml, respectively, using a broth microdilution susceptibility test and microbicidal activity test. Positive control, oxytetracyclin, would have the average inhibition zone of *S. agalactiae* 31.38 ± 0.03 mm with MIC and MBC of 0.1953 µg/ml. As a result, *S. gratum* extracts in organic aquaculture may be more beneficial for both preventive and therapeutic applications. As a consequence of the results of this study's screening, *S. gratum*, may be utilized as a source of antibacterial substances in the future.

Keywords: *Syzygium gratum*, fish pathogenical bacteria, *Streptococcus agalactiae*

.

Introduction

Thailand is a global fisheries industry leader. Both freshwater and saltwater animals are important economic resources. Fish are great valuable economic animals that provide significant revenue for both the government and the aquarist. It is popular throughout Thailand, particularly in the east, middle, and southern provinces. According to statistics, due to fish pathogenical bacteria, the overall volume of aquatic produce in the country began to change at a slower rate and result in a slew of issues, including disease outbreaks. Streptococcus is the most common genus of bacteria found in fish. The majority of them are caused by bacterial infections as a result of the pond cramps and the unsuitable environment. Because the fish in the pond are weak and stressed, germs are readily affected.

Streptococcus spp., in particular *Streptococcus agalactiae* is a pathogenic bacteria that has caused an outbreak in commercial aquaculture operations. Streptococcosis causes the neurological system to malfunction, as well as spots and bleeding on the fins, leading the fish to become ill or die. Reports of anomalous swimming behavior, frequently described as spiraling or spinning, should be included in documented evidence indicating streptococcal

infection as the source of sickness in a population of fish [1]. Freshwater and saltwater outbreaks have been discovered, with the potential to spread to other aquatic species in the environment as a result of harm to fish farming, particularly tilapia growth in Asia, notably Thailand. As a result, *S. agalactiae* is vital in inducing infected fish, such as stress or transport injuries, low oxygen content movement, poor quality feeding, and parasite wounds. *S. agalactiae* outbreaks have been identified in Thailand's tilapia farms, espectially, in the central and southern regions [2].

Antibiotics such as ampicillin, penicillin, erythromycin, oxytetracycline, nalidixic acid, oxyolinic acid, sulphamethoxazol, chloramphenical, and nitrofurans are the most popular treatments for *S. agalactiae* infection in fish. Sulfamerazine and oxytetracycline, which block the synthesis of bacterial proteins, are commonly employed in fish farms. Pathogenic bacteria are growing increasingly resistant to the most regularly used antibiotics and chemicals, which is causing problems in medicine. Antibiotic drug resistance can be overcome by using probiotics, immunostimulants, and bioactive compounds from terrestrial medicinal plants and aquatic macrophytes [3]. Some herbal plants, such as *Azadirachta indica*, *Butea superba Roxb*., as well as many plants from the family of Papaveraceae, Basellaceae, Solanaceae, Krameriaceae, and Caprifoliaceae have been shown to be effective antibacterials against *S. agalactiae* including some from Myrtaceae [4,5,6,7]. The most important phytochemicals in the Myrtaceae family as anthraquinones, terpenoids, flavonoids, saponins, tannins, and alkaloids [8]. Essential oils from plants in the Myrtaceae family are widely employed in a variety of industries. This is due to the fact that the essential oils of this group of plants have an unique chemical composition and pharmacological activity that is related to biological activity [9]. *Syzygium gratum*, one of plants in the Myrtaceae, was utilized to make the extract for this study. To see if the extracts are effective at inhibiting pathogenic bacteria in fish and to learn more about them.

Material and methods

Chemicals

Sodium chloride, Hexane, Ethyl acetate, Ethanol and Methanol were purchased from Labscan. *P* – iodonitrotetrazolium chloride was purchased from Biochemica. Brain Heart Infusion Agar, Brain Heart Infusion Broth, Mueller Hinton Agar, Mueller Hinton Broth were purchased from Hi-media.

Plant Materials

Fresh leaves, flowers, and fruits of *S. gratum* was collected from germinate naturally surrounding Rajamangala University of Technology Srivijaya, Mai Fad Sub-district, Sikao District, Trang province, Thailand, between January and March 2019 around 6.00 – 9.00 a.m. The Forest Herbarium in Bangkok, Thailand, accepted voucher specimens (Specimen BKF no. 194869).

Preparation of Samples

Fresh materials were air – dried for 5 days at 30°C, weighed, coarse ground, and immersed in hexane (1:2, g/ml) for 7 days at room temperature with occasional shaking, then filtered through a Whatmann filter paper No.1 and the extraction was repeated twice. After

that, the residue was soaked in ethyl acetate, ethanol, and methanol, in that order. Finally, using a rotary evaporator (Heidolph, Switzerland) at decreased pressure and controlled temperature (40°C), the 24 supernatants of the various extracts were concentrated to dryness.

Determination of antibacterial activity

The antibacterial activity of *S. gratum* crude extracts were measured in quadruplicate using the hole-plate diffusion method, and the zone of inhibition was calculated in quadruplicate [10]. To begin, the tested inoculums were gently swabbed onto Mueller-Hinton agar (MHA) to achieve a homogeneous dispersion of microorganisms with a bacterial concentration of 1×10^8 CFU/ml. The agar plates were dried in a laminar flow for 5 minutes before sterile piercing was used to create wells with a diameter of 6 mm. Then 40 µl of 10 mg/ml crude extracts dissolved in DMSO were added to the four wells that had been formed. Similarly, oxytetracyclin antimicrobial susceptibility disc and DMSO were used as positive and negative controls, respectively, in the other wells. Finally, the agar plates containing crude extracts were incubated at 35°C for 24 hours. The antibacterial activity, which appeared as an inhibitory zone surrounding the well after incubation, was measured at time check and interpreted as millimeter in diameter.

Determination of minimal inhibitory concentration (MIC)

The MIC value of 12 crude extracts were evaluated using the modified broth microdilution susceptibility test [11,12]. In a sterile 96 - well microplates, the stock solution of extracts dissolved in DMSO with an initial concentration of 50 mg/ml were serially two – fold diluted with Mueller Hinton broth (MHB). This was duplicated four times. Following that, 50 µl of tested inoculums with a bacterial concentration of 1×108 CFU/ml were gently re – mixed with a multichannel auto – pipette. The 96-well microplates were then covered with a sterile lid, sealed with parafilm, and incubated for 24 hours at 35°C. The turbidity of the solutions were tested after incubation, and p – iodonitrotetrazolium chloride (INT) was added to each well to confirm bacterial growth from the mixture's coloring. The well with the pink mixture revealed the presence of live microorganisms, whereas the well with no precipitate and discoloration of the mixture suggested that the extracts' diluted concentration could inhibit bacterial growth in the well. The MIC value in this example was determined as the lowest concentration of extracts that completely inhibited bacterial growth

Determination of minimal bactericidal concentration (MBC)

A broth microdilution test was used to determine the MBC value. In a brief, one loopful of antibacterial solutions was scattered onto Mueller Hinton agar (MHA) plates to prevent bacterial growth. The agar plates were then incubated for 24 hours at 35°C. Based on the formation of bacterial colonies on agar plates, the bactericidal concentration of the tested extracts was determined. The MBC value was the lowest concentration of diluted extracts that did not produce any bacterial colonies [12].

Statistical analysis

The antibacterial activity data obtained using the hole – plate diffusion method were statistically analyzed using one – way analysis of variance (ANOVA) in a statistical program (IBM SPSS Statistics 23) with Duncan's multiple range test (DMRT) used to determine

significant differences between the means. The comparisons were made at a 0.05 significance level.

Results and Discussion

The hole – plate diffusion method was used to evaluate the primary properties of *S. gratum* crude extracts obtained from extraction with different solvents against *S. agalactiae* and the results of this testing are provided in Table 1. The results from the 24 hour evaluation showed that the hexane crude extract of *S. gratum* leaves, flowers, and fruits inhibited the growth of the tested bacterial strains slightly better than the crude extracts obtained from extraction with other solvents. Furthermore, the crude extracts of ethanol and methanol seemed to have the lowest activity against *S. agalactiae*.

Table 1 Inhibition zone of *S. gratum* crude extracts against *S. agalactiae* at 24 hours.

Extracts	Inhibition zone (mm. in diameter)		
	Leaves	**Flowers**	**Fruits**
Hexane	18.38 ± 0.12 [a]	22.57 ± 0.06 [a]	27.50 ± 0.07 [a]
Ethyl acetate	14.00 ± 0.14 [b]	22.19 ± 0.12 [b]	18.75 ± 0.10 [b]
Ethanol	12.13 ± 0.07 [c]	18.31 ± 0.02 [c]	12.38 ± 0.09 [d]
Methanol	12.25 ± 0.10 [c]	18.13 ± 0.09 [d]	12.56 ± 0.08 [c]
Oxytetracyclin	31.38 ± 0.03		
DMSO	0.00 ± 0.00		

Data are shown as mean ± SD from quadruplicate analysis of all samples; superscripts a–d indicate that the difference between the other samples (in the same column) is significant at the 0.05 level from higher to lower values.

As shown in Table 2 and 3, the hexane crude extract of *S. gratum* showed satisfactory bacteriostatic activity with the lowest MIC and MBC values equal to 0.01, 48.83, and 195.31 µg/ml for fruits, flowers, and leaves, respectively.

Table 2 Minimal inhibitory concentration (MIC) of *S. gratum* crude extracts against *S. agalactiae*.

Extracts	Minimal inhibitory concentration (µg/ml)		
	Leaves	**Flowers**	**Fruits**
Hexane	195.31	48.83	0.01
Ethyl acetate	1,562.50	390.63	97.66
Ethanol	390.63	781.25	3,125.00
Methanol	390.63	390.63	1,562.50
Oxytetracyclin	0.1953		
DMSO	ND		

Note: ND was no detection

Table 3 Minimal bactericidal concentration (MBC) of *S. gratum* crude extracts against *S. agalactiae*.

Extracts	Minimal bactericidal concentration (μg/ml)		
	Leaves	**Flowers**	**Fruits**
Hexane	195.31	48.83	0.10
Ethyl acetate	25,000.00	390.63	97.66
Ethanol	6,250.00	781.25	50,000.00
Methanol	6,250.00	6,250.00	25,000.00
Oxytetracyclin		0.3906	
DMSO		ND	

Note: ND was no detection

The plant's secondary metabolites necessary correlate for the extract's antimicrobial activities. Antimicrobial activity is considered to be conferred by a wide range of bioactive constituents from various phytochemical groups, including alkaloids, phenols, flavonoids, glycosides, saponins, and terpenes. The presence of a wide range of phytochemical components in plants is considered responsible for their therapeutic properties [12]. According to the phytochemical screening of *S. gratum*, which revealed the presence of alkaloids and flavonoids in hexane extracts, the extract's antibacterial activity is obviously related to the presence of flavonoid compounds [8]. Since hexane has a lower polarity than other solvents, the antibacterial substances are non – polar molecules in the refining process. Microbial membranes may possibly be affected by lipophilic flavonoids.

Conclusions

Many plant species are capable of generating antibacterial substances. The results demonstrate *S. gratum* is interesting antibacterial efficacy against *S. agalactiae* and provides a scientific validity for the species traditional usage. The results indicate that all parts of *S. gratum* exhibited intermediate antibacterial activity against *S. agalactiae* in vitro. Hexane extract of all of parts have the highest antibacterial activity against *S. agalactiae*. The fruit's parts have a lot of biological ability for possible treatment and might be utilized as natural antimicrobials in veterinary science. Further research is needed to validate this efficacy against other pathogenic bacteria common in aquaculture, as well as to clarify immune response involvement and virulence factor inhibitor potential. These substances can be utilized in aquaculture as antimicrobial therapeutic and preventive compounds against fish pathogens. According to the results of this study, *S. gratum* extracts investigated might be potential sources of novel antibacterial agents. Finally, more research is need to identify bioactive compounds that can be submit to specific pharmacological studies and clinical application development.

Acknowledgements

References

[1] Amal, M.N.A. and Zamri-Saad, M. 2011. Streptococcosis in Tilapia (*Oreochromis niloticus*). **Journal of Tropical Agriculture Science**. 34 (2) : 195 – 206.

[2] Abuseliana, A. F., Daud, H. H. M., Aziz, S. A., Bejo, S. K. and Alsaid, M. 2011. Pathogenicity of *Streptococcus agalactiae* isolated from a fFish farm in Selangor to Juvenile Red Tilapia (*Oreochromis sp.*). **Journal of Animal and Viterinary Advances**. 10(7) : 914 - 919.

[3] Charoendat, U., Khongsai, S., Vittaya, L. and Tep – Ubon, C. 2019. Antibacterial activity of *Caulerpa racemosa* var. *Corynephora* crude extracts against pathogenic bacteria of aquatic animals. **Rajamangala University of Technology Srivijaya Research Journal**. 11(1): 30 – 40.

[4] Dhayanithi, N.B., Ajith Kumar, T.T. and Kathiresan, K. 2010. Effect of neem extract against the bacteria isolated from marine fish**. Journal of Environmental Biology**. 31: 409 – 412.

[5] Pirarat, N., Rodkhum, C., Ponpornpisit, A. and Suthikrai, W. 2012. *In vitro* efficacy of red Kwao Krua *(Butea superba Roxb.)* extract against streptococcal bacteria isolated from diseased Tilapia (*Oreochromis niloticus*). **Thai Journal of Veterinary Medicine**. 42(1): 101 – 105.

[6] Delfani, S., Bahmani, M., Mohammadrezaei-Khorramabadi, R., Kopaei, M. R. 2017. Phytotherapy in *Streptococcus agalactiae*: An overview of the medicinal plants effective against *Streptococcus agalactiae*. **Journal of Clinical and Diagnostic Research**. 11(6): DE01 - DE02.

[7] Castro, S.B.R., Leal, C.A.G., Freire, F.R., Carvalho, D.A. Oliveira, D.F. and Figueiredo, H.C.P. 2008. Antibacterial activity of plant extracts from Brazil against fish pathogenic bacteria. **Brazilian Journal of Microbiology**. 39. 756 – 760.

[8] Khongsai, S. and Vittaya, L. 2020. Solvent effect on phytochemical screening of *Melaleuca leucadendra Linn*. and *Syzygium cinerea*. **Rajamangala University of Technology Srivijaya Research Journal**. 12(1): 112 – 119.

[9] Luiz, C. A., Cleber, J., Róbson, R. T. and Antônio, L. P. 2013. Chemistry and biological activities of essential oils from *Melaleuca* L. species. **Agriculturae Conspectus Scientificus**. 78(1): 11 – 23.

[10] Brantner, A., Pfeiffer, K., Brantner, H. 1994. Applicability of diffusion methods required by the pharmacopoeias for testing antibacterial activity of natural compounds. **Pharmazie**. 49(7): 512 - 516.

[11] Eloff, J. N. 1998. A sensitive and quick microplate method to determine the minimal inhibitory concentration of plant extracts for bacteria. **Planta Method**. 64. 711 - 713.

[12] Clinical and Laboratory Standards Institute. 2006. Method for dilution antimicrobial susceptibility tests for bacterial that grow aerobically; Approved standards 7th edition. Clinical and Laboratory Standards Institute, USA.

[13] Tkachenko, H., Buyun, L., Terech-Majewska, E. and Osadowski, Z. 2016. *In vitro* antimicrobial activity of ethanolic extracts obtained from *Ficus spp*. leaves against the fish pathogen *Aeromonas hydrophila*. **Archives of Polish Fisheries**. 24: 219 – 230.

Natural pigments from Malabar spinach berries using as colorimetric detection of potassium cyanide in aqueous solution

Thayapan Hobanthad and Sukanya Tongkhan[*]

Department of Chemistry, Faculty of Science, Buriram Rajabhat University, 31000, Thailand
*e-mail: sukanya.tk@bru.ac.th

Abstract

Malabar spinach (*Basella alba* L.) berries has been reported in food applications as the red-violet natural colorant which mostly compose of betalains. In this research, we have extracted natural pigments from Malabar spinach berries by ethanol, methanol and water. The response of the Malabar spinach berries extract (MSBE) to potassium cyanide (KCN) was studied in aqueous solution including other anion interferences. The MSBE solution exhibits high sensivity and good selectivity for cyanide ion in pure water. The pink solution of MSBE was immediately changed to purple when added a cyanide anion. It causes spectral changes in the UV-vis spectrum of MSBE solution by the red shift. Other monovalent anions tested such as; F^-, Cl^-, Br^-, I^-, CH_3COO^- and SCN^- caused no significant color or spectra changes. Notably, this natural sensor promised to detect water-soluble cyanide in real sample.

Keywords: Potassium cyanide; Cyanide; Natural pigment; Malabar spinach berries

References

Kumar, S.S., Manoj, P., Nimisha, G. & Giridhar, P. (2016). Phytoconstituents and stability of betalains in fruit extracts of Malabar spinach (Basella rubra L.). *Journal of Food Science and Technology* 53(11) : 4014–4022.

Kim, I.J., Ramalingam, M. & Son, Y. (2017). A reaction based colorimetric chemosensor for the detection of cyanide ion in aqueous solution. *Sensors and Actuators B: Chemical* 246 : 319-326.

Antioxidant activity and total phenolic content of different parts of *Nelumbo nucifera Gaertn.*

Naengnoi Saengsane, Apitsara Intaratat, Yanisa Thepchuay[*]

Nanomaterials Chemistry Research Unit, Department of Chemistry, Faculty of Science and Technology, Nakhon Si Thammarat Rajabhat University, Nakhon Si Thammarat 80280, Thailand.
*e-mail: yanisa_tep@nstru.ac.th

Abstract

This study aimed to evaluate antioxidant activity and determine total phenolic contents (TPC) from ethanolic extract of petal, leaf and pod of two flower colors of *N. nucifera* including white flower and pink flower lotuses. The antioxidant activity determined by ferric reducing antioxidant potential (FRAP) method ranges from 14.67 to 5.70 mgFe/g dry wt. for white flower lotus and from 14.76 to 4.90 mgFe/g dry wt. for pink flower lotus. Total phenolic contents determined by the Folin-Ciocalteu method, thus providing its correlation with the mentioned antioxidant activity, are in the range of 30.46 to 90.25 mgGAE/g dry wt. for white flower lotus and of 31.41 to 91.65 mgGAE/g dry wt. for pink flower lotus. A linear regression fitted to the antioxidant activity and total phenolic provides the correlation coefficient (r^2) of 0.9154, suggesting that total phenolic compounds are attributed to antioxidant activity. The comparison between different parts of the lotus demonstrates that the most potent antioxidant activity is leaves, followed by pods and petals, respectively. Taken together, these results provide useful information about lotus leaves could be served as antioxidant ingredients. Furthermore, besides leaves, pods and petals are suggested as rich sources for antioxidant activity.

Keywords: Total phenolic compound, Antioxidant, *Nelumbo nucifera Gaertn.,* Lotus.

References

Jarmkom, K., Wisidsri, N., Eakwaropas, P., & Khobjai, W. (2019). Total Phenolic Content and Free Radical Scavenging Activity of Nelumbo nucifera Gaertn. *Applied Mechanics and Materials, 886*, 52-55. doi:10.4028/www.scientific.net/AMM.886.52

Wang, Z., Cheng, Y., Zeng, M., Wang, Z., Qin, F., Wang, Y., He, Z. (2021). Lotus (Nelumbo nucifera Gaertn.) leaf: A narrative review of its Phytoconstituents, health benefits and food industry applications. Trends in Food Science & Technology, 112, 631-650. doi:https://doi.org/10.1016/j.tifs.2021.04.033

Heating preconcentration system for determination of metal ions using distance-based paper device, colorimetric and electrochemical assay

Benjawan Ninwong[1,2] and Wijitar Dungchai[1,3*]

[1]Organic Synthesis, Electrochemistry & Natural Product Research Unit, Department of Chemistry, Faculty of Science, King Mongkut's University of Technology Thonburi, Bangkok, 10140, Thailand.
[2]Nanomaterials Chemistry Research Unit, Department of Chemistry, Faculty of Science and Technology, Nakhon Si Thammarat Rajabhat University, Nakhon Si Thammarat, 80280, Thailand.
[3]Applied Science & Engineering for Social Solution Unit, Faculty of Science, King Mongkut's University of Technology Thonburi, Bangkok, 10140, Thailand
*e-mail: wijitar.dun@kmutt.ac.th

Abstract

The heating system has been developed for preconcentration of metal ions on paper devices by different applications. The design of heating preconcentration can evaporate off the large volume of sample solutions to concentrate the metals ions and easily continue to the next step of detection process. This approach was demonstrated by determining Hg^{2+} with nitrogen-doped carbon dots (NCDs) on distance-based paper devices. The results were obtained from the distance signals of turned-off fluorescence under a black light in a black box. Another application of preconcentration process was presented by simultaneous detection of Pb^{2+}, Cd^{2+}, Fe^{3+} and Ni^{2+} using a combination of electrochemical and colorimetric detection methods. The current signals of Pb^{2+} and Cd^{2+} were measured from stripping voltammetry, whereas Fe^{3+} and Ni^{2+} concentrations were quantified from color intensities. Assay conditions were optimized by evaluating performance when changing the concentration of colorimetric reagent, pH, NCDs concentration, eluent volume, electrolyte concentration and electrochemical parameters. The limits of detection (LOD) were obtained at concentrations as low as 5.00 µg L^{-1}, 0.97 µg L^{-1}, 2.33 µg L^{-1}, 0.03 mg L^{-1} and 0.04 mg L^{-1} for Hg^{2+}, Pb^{2+}, Cd^{2+}, Fe^{3+} and Ni^{2+}, respectively. The comparison of with and without heating preconcentration system was shown the high enrichment greater than 13-fold. The application of this method was successfully investigated in water samples which provides convenient, inexpensive material, portability for on-field monitoring, high sensitivity and selectivity for quantification of metals ions.

Keywords: Carbon dots; Heating preconcentration; Metal ions; Paper device

References

Ninwong, B., Sangkaew, P., Hapa, P., Ratnarathorn, N., Menger, R. F., Henry, C. S. & Dungchai, W. (2020). Sensitive distance-based paper-based quantification of mercury ions using carbon nanodots and heating-based preconcentration. *RSC Advances*. 10(17) : 9884-9893.

Wong, S. Y., Cabodi, M., Rolland, J. & Klapperich, C. M. (2014). Evaporative concentration on a paper-based device to concentrate analytes in a biological fluid. *Analytical Chemistry* 86(24) : 11981-11985.

Development of sunscreen using Na doping ZnO nanoparticals capped *Caulerpa racemosa* extract

Paweena Porrawatkul[2], Nichapa Rattanakomon[2], Montakarn Thongsom[3] Luksamee Vittaya[1] and Sunanta Khongsai[1*]

[1]Faculty of Fisheries Science and Technology, Trang Campus, Rajamangala University of Technology Srivijaya, 92150, Thailand.
[2]Nanomaterials Chemistry Research Unit, Department of Chemistry, [3]Department of Biology,Faculty of Science and Technology, Nakhon Si Thammarat Rajabhat University, 80280, Thailand.
*e-mail: Ta047@hotmail.com

Abstract

Metal oxide can be employed in sunscreen applications due to its physical and chemical stability, as well as its transparency in the visible area and ultraviolet protective action. In this work the production of zinc oxide (ZnO) nanoparticles and sodium doped zinc oxide (Na/ZnO) from *Caulerpa racemosa* extract was investigated in this study. Na/ZnO nanoparticles derived from *Caulerpa racemosa* extract were reported to have higher DPPH antioxidant activity than ZnO nanoparticles. In a research on methylene blue dye degradation, Na/ZnO nanoparticles were found to be more effective in blocking UV light than ZnO nanoparticles. The slope of the linear equation suggested this 0.1605 h^{-1} and 0.4860 h^{-1} were the evaluations, respectively. The antibacterial activity of *S. aureus* and *E. coli* was studied, and it was discovered that none of the nanoparticles could inhibit *E. coli*. As a result, ZnO nanoparticles and Na/ZnO make them ideal for use as sunscreen components in the pH range of 7.1–7.5, which is suitable for skin application and absorbs effectively. All of the sunscreens were found to inhibit *S. aureus* and *E. coli* bacterials.

Keywords: *Caulerpa racemosa*, Sunscreen, Zinc oxide nanoparticle,

Introduction

Beachgoers all over the world use sunscreen for skin protection and some of it is likely to end up in the coastal marine environment. The two forms of ultraviolet (UV) filters that are usually found in sunscreen active ingredients are organic chemical absorbents and inorganic physical blockers. Organic molecules absorb UVR and convert it to heat energy, whereas inorganic substances deflect or scatter UV radiation. These filters aren't as popular as organic filters since their bulk particles scatter visible light and make sunscreens appear opaque on the skin. Micronized substituents (e.g., nano metal oxides) have expanded their popularity since the nanoparticles in these advanced inorganic filters may effectively reflect and scatter UVR while reflecting far less visible light, resulting in a more visually beautiful shape. Titanium dioxide (TiO_2) and zinc oxide (ZnO) are the most common inorganic UV-blocking filters today. Because its damaging effects are not represented in the current Sun Protection Factor (SPF) measurement technique, which is based on the erythema induced by UVB alone, ZnO can give protection in the UVA band, which is also deadly solar radiation.

ZnO is appealing for sunscreen formulation due to a number of factors, including its low refractive index (2.0), absorption of only a small fraction of solar radiation in the UV range, high likely recombination of photogenerated carriers (electrons and holes), large direct band gap, high exciton binding energy, non-hazardous nature, and high tendency toward chemical

and p-type recombination. Because of these advantages, ZnO nanoparticles are transparent in the visible range and have UV protective activity, hence ZnO's UV-blocking capacity is crucial. Because of its photocatalytic activity, ZnO can create ROS in the presence of UV radiation, which is a serious concern for its application in sunscreens. As a result, it's critical to create a non-photocatalytic ZnO material by doping it with other metals. Several attempts have been made to use inorganic surface modifiers to disable ZnO's photocatalytic activity. Another technique to change the photocatalytic activity of ZnO is to dope it with various metals. Successful doping of ZnO with various metals such as Ce, La, Co, Mn, Al, Li, Na, K, and Cr has recently been reported using a variety of approaches including a simple and easy one-pot water bath, co-precipitation, hydrothermal, solvothermal, combustion, and sol gel methods. These compounds outperform undoped ZnO when it comes to boosting ZnO's photocatalytic activity in visible light. For therapeutic reasons, ZnO has been discovered to be potentially beneficial and more efficient than other metals in the production of NPs. Several investigations have shown that different plant extracts can be used to synthesize ZnO NPs. Flower extracts of the medicinal plant *Cassia fistula* and *Melia azedarach* (Minha Naseer, *et al*., 2020) and leaf extracts of *Cayratia pedata* (Ashwini J.,   *et al*., 2021) were utilized as zinc nitrate reducing agents in the production of ZnO NPs.

Herein, ZnO NPs were synthesized via a green process using *Caulerpa racemose* extract and show that using the right doping and synthesis procedures, it change the photocatalytic characteristics of ZnO in the UVA region and make UV filters with less photocatalytic activity. The UV photocatalytic activity of Na-doped ZnO synthesized by co-precipitation techniques has been reduced, according to the current study. In this article, We report a decrease in UV photocatalytic efficiency via co-precipitate synthesis of Na-doped ZnO activity as well as hydrothermal techniques.

Materials and methods

To produce Na-doped ZnO, Sigma-Aldrich provided sodium nitrate, NaNO$_3$, purity >99.0%, commercial ZnO nanopowder, ethanol amine (C$_2$H$_7$NO, purity >99.5%), and ethanol. We focused on low-cost procedures that can be scaled up for industrial use when it came to sample preparation. Commercial ZnO nanoparticles were employed in this study, as well as Na-doped ZnO nanoparticles made by co-precipitation techniques.

Preparation of Na-ZnO using co-precipitation method

To begin, 0.25 M of each starting material, zinc acetate dehydrate, and sodium nitrate, were produced, then mixed and dissolved in DI water separately before adding 1 ml of *Caulerpa racemose* extract. Second, a solution of NaOH 2 M was dropped dropwise until the pH reached 9, then stirred continuously on a hot plate at 70 °C for 90 minutes. Finally, the gelatin product was calcined for two hours at 600°C before being crushed for characterization.

A sunscreen cream based on oil in water (O/W) emulsion (semisolid formulation) was developed. In the oil phase (Phase B), the emulsifier (stearic acid) and other oil soluble components were dissolved and heated to 50 °C. In the aqueous phase (Phase A), the preservatives and other water soluble components were dissolved and heated to 50 °C. The aqueous phase was added in parts to the oil phase after heating, with continuous stirring until the oil phase cooled. After that phase C and phase D were added with continuous stirring until homogenous cream occurred. The ingredients in each phase showed in Table 1.

Table 1 Composition of sunscreen cream.

Ingredients	Amount (g)
Phase A	
DI Water	Up to 50 mL
Glycerin	2.00
Xanthan gum	0.15
Triethanolamine (TEA)	0.05
Phase B	
Glycerol	5.00
Coconut oil	1.00
Squalane	1.00
Cetearyl alcohol	1.00
Glyceryl stearate	1.00
Stearic acid	0.50
Eumulgin B2	1.00
Vitamin E dl-alpha tocopherol	0.50
Phase C	
Titanium dioxide (TiO$_2$)	0.50
Squalane	2.50
Phase D	
ZnO or Na-ZnO	1.50
Triethanolamide (TEA)	1.00
Phenoxyethanol	1.00
DI Water	1.50
Coconut oil	0.07

Antioxidant activity by DPPH assay

The antioxidant activity of the leave extract and was studied by using 2,2-diphenyl-1-pieryl-hydrazyl (DPPH) assay. Briefly, 1 mL of the samples with varied concentrations received 2 mL of 2×10^{-4} mM DPPH in 95 percent ethanol. After 5 minutes, the absorbance was measured at 518 nm against a blank of 95 percent ethanol at room temperature in the dark. The standard compound was ascorbic acid.

Antibacterial study

Using the agar well diffusion method, *Caulerpa racemose* extract and sunscreen cream were tested for antibacterial activity against *Escherichia coli* (*E. coli*) and *S. epidermidis* (*S. aureus*). A sterile cotton swab was used to disseminate the bacteria culture evenly across the nutrient agar plate. Agar plates were used to make wells. Standard antibiotic disc (chloramphenicol) was added to these well. The diameter of the inhibitory zones around herbal cream was measured and compared to that around commercial standard antibiotics chloramphenicol and *Caulerpa racemose* extract after incubation at 37 °C for 24 hours.

Photocatalytic activity study

In a confined room with varying visible light intensities, the photocatalytic performance of all catalysts was examined (40, 60, 100 and 130 W). Various amounts of catalysts (0.1, 0.2, 0.5, 1.0, 2.0, and 5.0 g/L) were added to 100 mL of varying concentrations (5, 10, 20, 30, and 40 mg/L) of methylene blue, indicated as the starting concentration, for the photocatalytic test

done at room temperature (Co). To achieve the adsorption-desorption equilibrium, the mix trues were mixed and kept in a dark environment for 2 hours before being irradiated. After that, the mixture was irradiated for 180 minutes. After 10, 20, 30, 40, 60, 90, 120, 150, and 180 minutes, 3 mL of the reaction solution was removed from the reactor flask. After that, an external magnet was used to separate the mixes from any suspended solids. A UV-vis spectrophotometer was used to examine the produced supernatant at a wavelength of 665 nm, which corresponded to the dye solution's maximum absorption.

Results and discussion

Characterization of the ZnO NPs and Na-ZnO

X-ray diffraction (XRD)

All of the as-prepared ZnO samples had a polycrystalline structure and excellent crystallinity, according to the XRD examination. The XRD spectra of undoped and Na-doped ZnO nanoparticles synthesized by the co-precipitation technique are shown in Figures 1. All of the peaks can be traced back to hexagonal wurtzite ZnO [(space group P63mc or (186)/amd, JCPDS No. 96-230-0114] zinc oxide, exhibiting great purity and crystallinity. The samples are polycrystalline in nature and have the hexagonal wurtzite structure, as shown in the picture. It's also worth noting that there isn't an impurity phase that corresponds to Na.
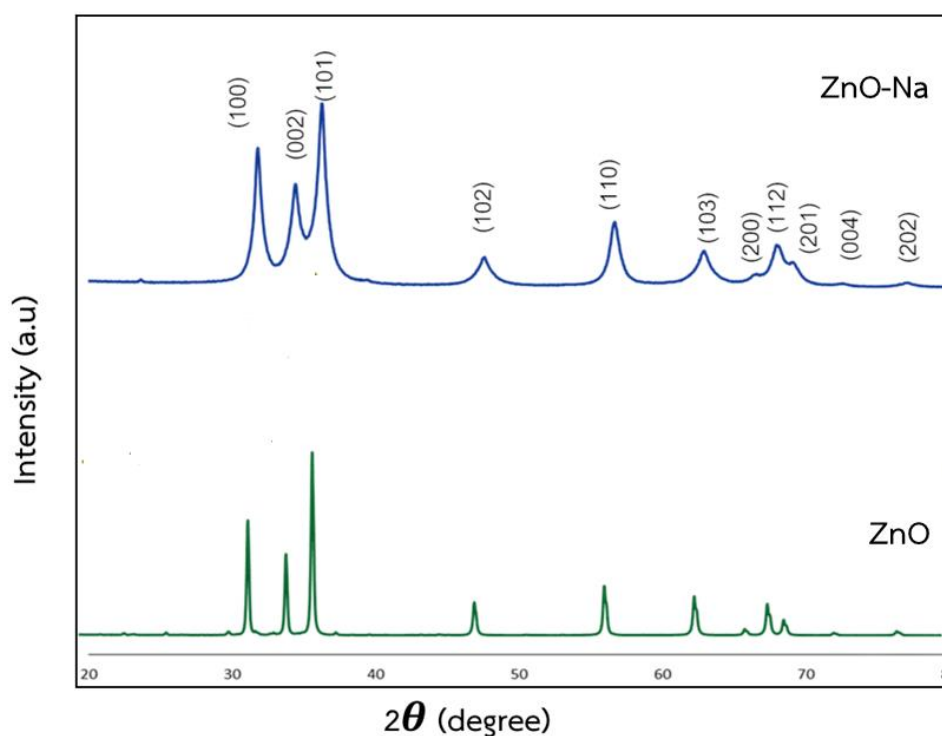
Figure 1 XRD pattern of ZnO and Na-ZnO.

Scanning electron microscope (SEM)
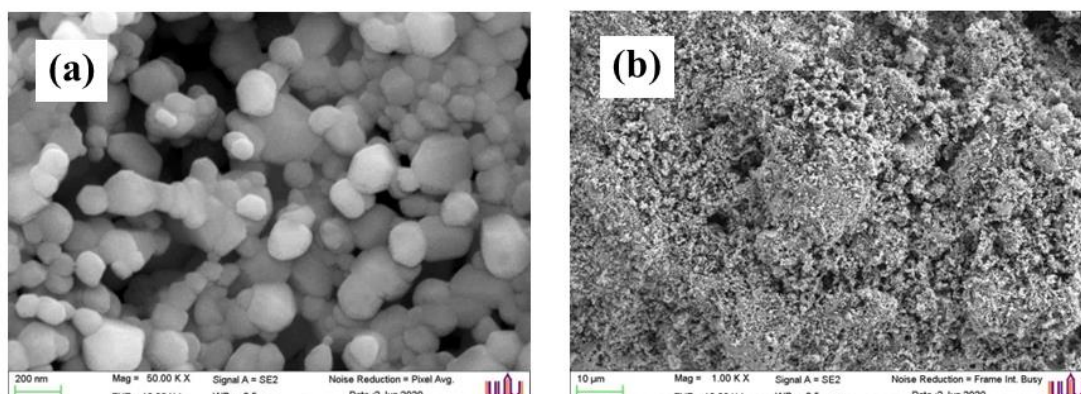
Figure 2 SEM image of (a) ZnO and (b) Na-ZnO.

SEM imaging was used to analyze the shape of ZnO nanoparticles, as shown in Figure 2 at two different magnifications for the ZnO nanoparticles. The resulting morphologies of ZnO NPs are highly clear and homogeneous spherical, as seen in SEM photos. Na-ZnO particle's form, on the other hand, it has a spherical shape, but the particle distribution is superior as well as smaller.

Antioxidant activity study

The free radical scavenging activity was studied in terms of electron donating or radical scavenging ability, using the stable radical, DPPH. The report in the literature showed that plant mediated nanoparticles synthesis includes reduction followed by capping with these constituents of plants. These results showed that the antioxidant activity of ZnO and Na-ZnO capped with important functional group of possessing free radical scavenging activity.   As displayed in the results, capped ZnO and Na-ZnO of *Caulerpa racemose* extract were found to be a strong free radical scavenger when compared to the standard ascorbic acid. This antioxidant activity may be caused by the capping constituents present in plant extract and present on the surface of materials.

Table 2 Antioxidant activity of *Caulerpa racemose* extract and metal oxide materials.

Sample	DPPH assay IC_{50} (mg/L)
Ascrobic acid	4.30
Caulerpa racemose extract	4.67
ZnO NPs	4.29
Na-ZnO NPs	4.55

The IC_{50} value of the *Caulerpa racemose* extracts, ZnO NPs and Na-ZnO were 4.67 mg/L, 4.29 mg/L and 4.55 mg/L, respectively. When compared to the free radical scavenging

activity of ascorbic acid, which has an IC_{50} value of 4.30 mg/L, the *Caulerpa racemose* extracts, ZnO NPs, and Na-ZnO displayed good antioxidant activity.

Antibacterial activity study

The efficiency of synthesized ZnO NPs and Na-ZnO as antibacterial agent was tested focus on gram positive (*Staphylococcus aureus*) and gram negative (*Escherichia coli*) bacteria by well diffusion method. The mean inhibitory zone diameter in mm was measured (Table 3). The inhibition zone around the well shows the synthesized ZnO NPs and Na-ZnO have more antibacterial activity than extract and starting compounds. The *E. coli* which is the gram negative bacterium displayed maximum zone of inhibition which may owing to the cell wall of gram positive bacteria composed of a thick peptidoglycan layer, thus founding more inflexible structure leading to difficult penetration of the ZnO NPs and Na-ZnO compared to the gram negative bacteria where the cell wall has thinner peptidoglycan layer.

Table 3 Inhibitory action of *Caulerpa racemose* extract and metal oxide materials against *S. aureus* and *E. coli* bacteria.

Sample	Solvent	Inhibition Zone (mm)	
		S. aureus	*E. coli*
Caulerpa racemose extract	H_2O	3.7 ± 0.62	5.2 ± 0.51
ZnO NPs	H_2O	9.5 ± 2.12	11.3 ± 1.41
Na-ZnO NPs	H_2O	13.5 ± 2.12	16.5 ± 1.41

*NI = no inhibition

Sun screen cream
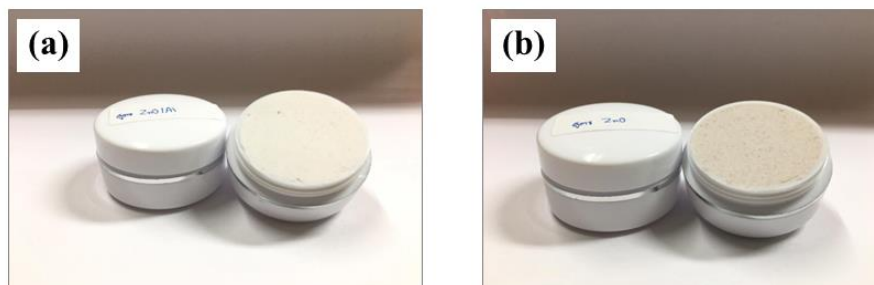
Figure 3 Sunscreen cream formulation with inorganic absorber (a) ZnO (b) Na-ZnO.

The completed sunscreen cream formulations appear to be smooth and uniform. When applied to the skin, all of the developed formulations had pH values ranging from 7.1 to 7.5, which are deemed appropriate for avoiding skin irritation. The pH values of the compositions are within the normal pH range of human skin. The pH of the cream remained unchanged as a result of the investigation.

Photocatalytic activity

The photocatalytic MB bleaching method was used to test the UV-induced photocatalytic activity of undoped and metal doped ZnO samples. Under UV light irradiation, Figure 4 contrasts the time-dependent profiles of MB bleaching on different materials and shows that the net decomposition of MB in the aqueous solution followed the pseudo-first order kinetic model.
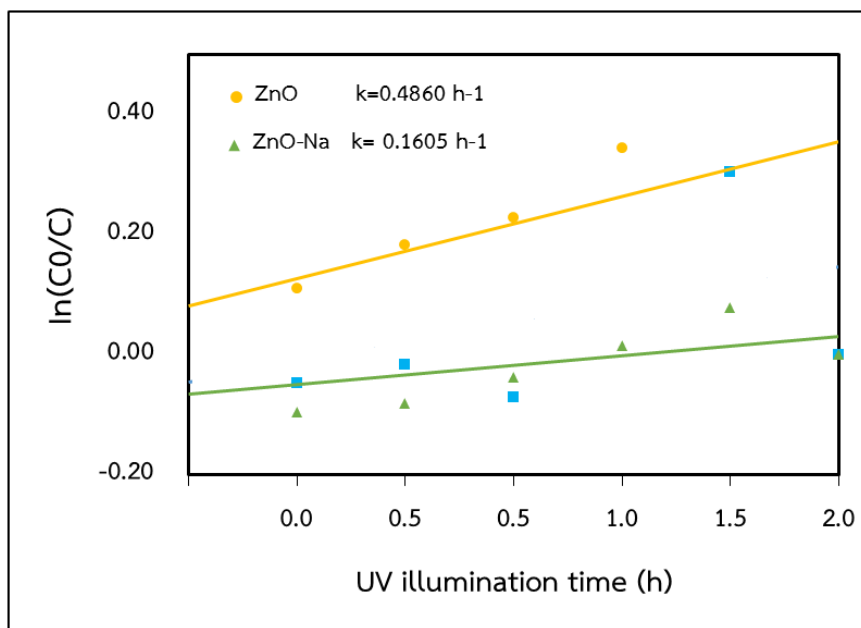
Figure 4 ln(C_0/C) versus time plot of MB bleaching under UV irradiation on undoped and metal ion doped ZnO samples. C is the MB concentration (mol·L^{-1}) at time t and C_0 is the initial MB concentration (mol·L^{-1}).

The rate constant (k) of MB bleaching for undoped ZnO is 0.486 h^{-1}, demonstrating high photocatalytic activity under UV illumination. The MB bleaching rate was drastically lowered when ZnO was doped with Na metal. For Na doping, the rate constant was reduced by a factor of, as compared to undoped ZnO. These findings reveal that metal doping can effectively deactivate ZnO's photocatalytic properties. It should be noted that the metal doping in our study resulted in a reduction in ZnO particle size, which leads to an increase in powder specific area, which increases photocatalytic activity in general. These changes could lead to a rise in structural flaws in bulk ZnO. The structural flaws, according to the literature could operate as recombination sites, promoting the recombination of photogenerated electron–hole pairs and so limiting the photocatalytic activity.

Conclusion

Finally, we used low-cost nanotechnologies to create Na-doped zinc oxide nanoparticles with extremely low photoactivity, which might be used as UVA filters in sunscreens. The co-precipitate technique was used to dope zinc acetate dehydrate with sodium in various quantities. As a function of doping concentration, the experimental results reveal a rise in cell parameters and a decrease in particle size. These changes could result in a considerable change in photocatalytic activity of ZnO toward deactivation under UV light.

References

Ashwini J., Aswathy, T.R., Achuthsankar S. N., (2021). Green synthesis and characterization of zinc oxide nanoparticles using Cayratia pedata leaf extract. *Biochemistry and Biophysics Reports*. 26, 100995.

Brittany, C., Cristina, T. D., Gary, C., Nikki, A. (2020). Effects of three zinc-containing sunscreens on development of purple sea urchin (Strongylocentrotus purpuratus) embryos. *Aquatic Toxicology*. 218 : 105355.

Borra, SK., Gurumurthy, P., Mahendra, J., Jayamathi, K. M., Cherian, C. and Chand, R. (2013). Antioxidant and free radical scavenging activity of curcumindetermined   by   using different in vitro and exvivo model Plans
Reearch, 7(36), 2680-2690

D. Vu DaO, M. Bremt, Z. Koeller, T. Khoa Le. (2014). Effect of Fe ion doping on the suppression of photocatalytic activity of ZnO nanopowder for application
in sunscreens. Powder Technology, 268, 173-176.

D. Vu DaO, M. Bremt, Z. Koeller, T. Khoa Le. (2016). Effect of matal ion doping on the optical properties and the deactivation of photocatalytic activity of ZnO nanopowder for application in sunscreens. Powder Technology 288, 366-370.

Ishwaryaa, R., Vaseeharana, B., Kalyania, S., Banumathia, B., Govindarajanb, M., Alharbid, N. S., Kadaikunnand, S., Al-anbrd, M. N., Khaledd, J. M., Benellie, Giovanni. (2018). Facile green synthesis of zinc oxide nanoparticles using Ulva lactuca seaweed extract and evaluation of their photocatalytic, antibiofilm and insecticidal activity. *Journal of Photochemistry & Photobiology, B: Biology*. 178 : 249 – 258.

Khongsai, S., Chareondat, U., Chalad, C. (2017). The performance of Caulerpa racemosa extracts on inhibition of some pathogenic skin bacteria. *Rajamangala University of Technology Srivijaya Research Journal*. 9(1) : 68 – 75.

Minha Naseer, Usman Aslam, Bushra Khalid & Bin Chen, (2020). Green route to synthesize Zinc Oxide Nanoparticles using leaf extracts of Cassia fstula and Melia azadarach and their antibacterial potential. *Scientific Reports*. 10: 9055.

Preparation of BaFe$_{12}$O$_{19}$ magnetic nanoparticles using CMC as chelating agent for photocatalytic degradation of methylene blue

Parintip Rattanaburi[1*], Prawit Nuengmatcha[1,2]

[1]Creative Innovation in Science and Technology, [2]Nanomaterials Chemistry Research Unit, Department of Chemistry, Faculty of Science and Technology, Nakhon Si Thammarat Rajabhat University, 80280, Thailand.
*e-mail: parintip_rat@nstru.ac.th

Abstract

The purpose of this work is to assess the role of carboxymethyl cellulose (CMC) as a chelating agent in the synthesis of barium hexaferrites (BaFe$_{12}$O$_{19}$: BaF) with various concentrations of CMC via the sol gel auto-combustion method for green chemistry synthesis. The formation of BaF nanoparticles in this work was confirmed using XRD, SEM, VSM, FTIR and UV-Vis-NIR techniques. The XRD peak indicates the formation of good crystalline quality of the prepared sample at 6% (w/v) of CMC concentration. SEM exhibited that synthesized BaF is spherical with sizes ranging from 10-15 nm. The *M-H* hysteresis loops of obtained samples showed soft and hard magnetic behavior due to their M-H hysteresis loops. When increasing the CMC content leads to the magnetism becoming harder, the increasing *Ms* value can be observed. UV-Vis-NIR techniques reveal that the band gab energy of synthesized BaF increased with increasing content of CMC.

Keywords: Carboxymethyl Cellulose (CMC); Barium hexaferrite; Green synthesis; Nanoparticles

References

Lalegani, Z., & Nematil, A. (2017). Influence of synthesis variables on the properties of barium hexaferrite nanoparticles. *Journal of Materials Science: Materials in Electronics* 28 : 4606-4612.

Thirupathy, C., Cathrin Lims, S., John Sundaram, S., Mahmoud, A. H., & Kaviyarasu, K. (2020). Equilibrium synthesis and magnetic properties of BaFe$_{12}$O$_{19}$/NiFe$_2$O$_4$ nanocomposite prepared by co precipitation method. *Journal of King Saud University – Science* 32 : 1612-1618.

Hashim, A., (2021). Synthesis of SiO$_2$/CoFe$_2$O$_4$ Nanoparticles Doped CMC: Exploring the Morphology and Optical Characteristics for Photodegradation of Organic Dyes. *Journal of Inorganic and Organometallic Polymers and Materials* 31 : 2483-2491.

Charoensuk, T., Thongsamrit, W., Ruttanapun, C., Jantaratana, P., & Sirisathitkul, C. (2021). Synthesis of SiO$_2$/CoFe$_2$O$_4$ Nanoparticles Doped CMC: Loading Effect of Sol-Gel Derived Barium Hexaferrite on Magnetic Polymer Composites. *Nanomaterials* 11(558) : 1-12.

Biological synthesis of hybridized silver nanoparticle-graphene quantum dots for anti-*Vibrio* bacterial activity

Worrakul Teewawech[1], Saitharn Nuanseang[1], Wanwisa Chairit[1] Montakarn Thongsom[2] and Rungnapa Pimsen[1*]

[1]Nanomaterials Chemistry Research Unit, Department of Chemistry,
Nakhon Si Thammarat Rajabhat University, 80280, Thailand.
[2]Department of Biology Nakhon Si Thammarat Rajabhat University, 80280, Thailand.
*e-mail: rungnapa_pim@nstru.ac.th

Abstract

Vibrio can cause a disease of Early Mortality Syndrome (EMS) or Acute Hepatopancreatic Necrosis Syndrome (AHPNS) in a white shrimp *Litopenaeus vannamei* (*L. vannamei*). As a result, the production of a white shrimp has declined worldwide. In this work, we have synthesized a silver nanoparticle-graphene quantum dots (AgNPs-GQDs) using *Barringtonia acutangula* (L.) Gaertn leaf extract and graphene quantum dots as reducing agents and stabilizers. The characterization of synthesized GQDs and AgNPs-GQDs were investigated by ultraviolet–visible spectroscopy (UV-Vis), X-ray diffraction (XRD) and transmission electron microscopy (TEM). Results indicated that mono-dispersed AgNPs were obtained with particles size around 6–16 nm, and the lattice spacing is 0.234 nm, which corresponds to the (1 0 0) lattice fringes of graphene. Several influencing parameters for the synthesis process, such as reaction temperature, reaction time, amount of extract, and amount of GQDs, were discovered to result in a gradual drop in absorbance at 425 nm as those factors were increased. Furthermore, GQDs can improve AgNPs-GQD dispersion, resulting in less particle agglomeration. The antibacterial activity of AgNPs-GQDs displayed the good activity of AgNPs/GQDs against *V. Alginolyticus*, *V. Harveyi*, and *V. parahaemolyticus*.

Keywords: Biological synthesis; silver nanoparticle-graphene quantum dots; *Vibrio*.

References

Mei, L., Cao, F., Zhang, L., Xu, J., Xu, Z., Yu, Y., Zhang, X., Shi, Y., Li, X., Cheng, K., & Li, X. (2020). Ag-Conjugated graphene quantum dots with blue light-enhanced singlet oxygen generation for ternary-mode highly-efficient antimicrobial therapy. *Journal of Materials Chemistry B*, *8*(7), 1371–1382.

Meneses-Marquez, J.C., Hamdan-Partida, A., Del Carmen Monroy-Dosta, M., Castro-Mejia, J., Faustino-Vega, A., Soria-Castro, E., & Bustos-Martínez, J. (2019). Use of silver nanoparticles to control Vibrio fluvialis in cultured angelfish Pterophyllum scalare. *Diseases of Aquatic Organisms*, *137*(1), 65–72.

Efficient degradation of dye pollutant from wastewater via photocatalysis using a magnetic ZnO/graphene/Fe₂O₃ catalyst

Teerachot Bunsong, Sarawut Puttasuk, Paweena Porrawatkul, Amnuay Noypha,
and Prawit Nuengmatcha[*]

Nanomaterials Chemistry Research Unit, Department of Chemistry, Faculty of Science and
Technology, Nakhon Si Thammarat Rajabhat University, 80280, Thailand
*e-mail: pnuengmatcha@gmail.com

Abstract

In this research, study on the optimum conditions for ZnO/graphene/Fe₂O₃ (ZGF) catalysis synthesis by solvothermal method as catalyst for dye degradation via photocatalysis process. Various parameters were studied including $Zn(NO_3)_2$ concentration, temperature and heating time. All of synthesized samples were characterized by SEM, EDX, XRD, VSM and UV-Vis DRS techniques. From the results, the suitable conditions were 0.10 mol/L, 600°C and 1 h for $Zn(NO_3)_2$ concentration, temperature and heating time, respectively. The synthesized ZGF showed XRD pattern of 2θ which according to the XRD patterns of graphene, iron oxide and zinc oxide indicating that the ZGF catalyst was successfully synthesized. In addition, when the obtained ZGF was applied for dye degradation from wastewater. It was found that the optimum conditions for dye degradation were 90 min, 10 mg/L, 0.03 g and 100 watts for irradiation time, dye concentration, catalyst dosage and irradiation intensity, respectively. From the above results confirm that the synthesized ZGF can be applied as catalyst for dye degradation from real wastewater samples. The present work demonstrates that this ZnO/graphene/Fe₂O₃ hybrid nanocomposite can also be applied as a highly potent photocatalyst degrader for other dye pollutants.

Keywords: ZnO/graphene /Fe₂O₃; Photocatalysis; Dye pollutants; Catalyst

References

Noypha, A., Areerob, Y., Chanthai, S., & Nuengmatcha, P. (2021). Fe₂O₃-graphene anchored Ag nanocomposite catalyst for enhanced sonocatalytic degradation of methylene blue. *Journal of the Korean Ceramic Society* 58(3) : 297-306.

Nuengmatcha, P., Porrawatkul, P., Chanthai, S., Sricharoen, P., & Limchoowong, N. (2019). Enhanced photo-catalytic degradation of methylene blue using Fe₂O₃/graphene/CuO nanocomposites under visible light. *Journal of Environmental Chemical Engineering* 27(6) : 103438.

Nuengmatcha, P., Chanthai, S., Mahachai, R., & Oh, W.C. (2016). Visible light driven photocatalytic degradation of rhodamine B and industrial dyes (texbrite BAC-L and texbrite NFW-L) by ZnO-graphene-TiO₂ composite. *Journal of Environmental Chemical Engineering* 4(2) : 2170-2177.

Total phenolic content and Antioxidant activity of
Syzygium gratum extracts

Sunanta Khongsai[1*] and Luksamee Vittaya[1]

[1] Department of General Education, Faculty of Science and Fisheries Technology,
Rajamangala University of Technology Srivijaya, Trang Campus.

Abstract

The purposes of this research was to study on active substance of leaves, flowers and fruits of *Syzygium gratum* extracts. The dried samples were extracted with four solvents according to polarity of solvents such as hexane, ethyl acetate, ethanol and methanol, respectively in order to study on total phenolic contents, DPPH and ABTS radical scavenging activity of twelve extracts. The methanolic of *S. gratum* flowers and leaves extract showed the highest of total phenolic contents with not significantly difference (P<0.05) aqua to 537.64 ± 1.41 and 527.07 ± 4.88 mgGAE/DW, respectively according to the highest DPPH radical scavenging activity with IC_{50} of 1.01 ± 0.01 and 1.02 ± 0.02 µg/ml, respectively including to the highest ABTS radical scavenging activity with IC_{50} of 0.65 ± 0.01 and 1.30 ± 0.01 µg/ml, respectively. The part of flowers and leaves of *S. gratum* showed the highest of antioxidant activity in methanol indicated that antioxidant substance in flowers and leaves of *S. gratum* dissolved in the higher polar solvent instead of the extracts of *S. gratum* fruits showed the highest of antioxidant activity in the lower polar solvent. A weaker correlation was observed between the total phenolic contents and the antioxidant activities, which demonstrated that the presence of a considerable amount of these compounds in a plant does not always imply a corresponding antioxidant potential. Since the present studies suggest that *S. gratum* has shown potential as sources of natural antioxidants, further studies need to be directed to isolate and characterize antioxidant active compounds from the extracts which could be responsible for the high antioxidant activities.

Keywords : *Syzygium gratum*, Total phenolic contents, Antioxidant activities

Introduction

A large number of dietary plants in Southeast Asian countries such as Thailand are important source of traditional medicine consist of potentially beneficial bioactive phytochemicals [1]. Presently, the dietary plants have been used for preventing diseases caused by pathogens, fungi, protecting against the action of free radicals, developing of the ageing process, reduces the risk of diseases involving cardiovascular, diabetes, neurodegenerative diseases and cancer.[2-4]. Phytochemicals in dietary plants possess a variety of substance containing of phenolic compounds which acted as sources of natural antioxidants [3]. Phenolic-rich dietary with antioxidant activity have been interested due to phenolic compounds are secondary metabolites with good electron donors because their hydroxyl groups can directly contribute to antioxidant action and exhibit free radical inhibition, peroxide decomposition, metal inactivation or oxygen scavenging and prevent oxidative disease burden [4].

Syzygium gratum is a dietary and herbal plant belonging to the Myrtaceae family, one of approximately 1200 – 1800 species of myrtaceous genus is widely distributed in Africa, Asia and Pacific regions [5]. Its leaves has been reported to contain a high content of protein, beta-carotene, and iron [6]. The shoot and young leaves of *S. gratum* consumed eatable as edible leafy plants including traditional medicine and helpful for several disorders including arthralgia, dyspepsia, indigestion, peptic ulcer, diarrhea, bacterial infection, asthma, and cardiovascular diseases [7-8]. The previous substantial data was found that the beneficial effects of *S. gratum* can induce cytoprotective enzyme in mice by exhibits potent direct antioxidant properties and has strong antioxidant property including improved vascular function in phenylhydralazine-induced circulatory shock [1,3]. In addition, the preliminary phytochemical screening has indicated the presence of anthraquinones, terpenoids, flavonoids, saponins, tannins, and alkaloids in the leaves, flowers and fruits of *S. gratum* in various solvent extracts [2]. Several plants from *Syzygium* species contain high total phenolic contents, which suggest they are rich sources of antioxidant compounds.

According to the literature research, there is no report about total phenolic contents and antioxidant activities varies between different parts of *S. gratum*. Many different methods have been reported for the antioxidant capacity evaluation of plant samples. 2,2-diphenyl-1-picrylhydrazyl (DPPH) method and 2,2´-azino-bis(3-ethylbenzthiozoline-6-sulphonic acid) diammonium salt (ABTS) method were numerous methods to estimate the antioxidant activities. The purpose of this study was to evaluated the total phenolic contents and antioxidant activities of different *S. gratum* parts (leaves, flowers, fruits), especially those of 12 crude extracts were estimated the relationship between the antioxidant activities evaluated by DPPH and ABTS free radical methods and the total phenolic contents. The results will provide important information for the future study and use of *S. gratum*.

Material and methods
Chemicals
Gallic acid, Folin-Ciocalteu reagent, 2,2-diphenyl-1-picrylhydrazyl (DPPH), 2,2´-azino-bis(3-ethylbenzthiozoline-6-sulphonic acid) diammonium salt (ABTS), L-Ascorbic acid, Potassium persulfate were purchased from Sigma - Aldrich. Sodium carbonate was purchased from Loba Chemie. Hexane, Ethyl acetate, Ethanol and Methanol were purchased from Labscan. All chemicals and reagents used in the study were of analytical grade.

Plant Materials
Fresh leaves, flowers and fruits of *S. gratum* were collected between January – March 2011 at 6.00 – 9.00 A.M. from local agricultural around Rajamangala University of Technology Srivijaya, Mai Fad Sub-district, Sikao District, Trang province, Thailand. Voucher specimens were deposited at the Forest Herbarium, Bangkok, Thailand (Specimen BKF no. 194869).

Preparation of Samples
The fresh samples were air-dried at room temperature (30 ˚C) for 5 days, weighed, coarse grinding and immersed in hexane (1:2, g/ml) for 7 days at room temperature with occasionally shake, then filtered through a Whatmann filter paper No.1 and the extraction was repeat twice. The resultant residue was then immersed in ethyl acetate, ethanol and methanol, respectively. Finally, the 12 supernatants of the different extracts were concentrated to dryness using a rotary evaporator (Heidolph, Switzerland) under reduced pressure and controlled temperature (40℃).

Determination of Total Phenolic Contents (TPC)

The total phenolic content (TPC) of *S. gratum* extracts were determined by the spectrophotometric method. The assay for TPC was conducted using the Folin - Ciocalteu reaction with gallic acid as standard by modification [2]. In brief, 0.2 mL of methanolic sample (0.1 mg/ml) were mixed with 2.5 mL of distilled water. After that, 0.2 mL of Folin – Ciocalteu reagent was added to the mixture followed by the addition of 2 mL of 7% sodium carbonate solution and mixed thoroughly. The mixture was kept in the dark for 90 min at room temperature. The absorbance was measured at 765 nm. The TPC was determined from extrapolation of calibration curve (y = 0.0041x - 0.0121 ; R^2 = 0.9965) which was prepared using 0, 20, 40, 60, 80 and 100 ppm gallic acid solution. The estimation of the TPC was carried out in triplicate and expressed as milligrams of gallic acid equivalents per gram dried weight (mg GAE/g DW).

Antioxidant Activity

DPPH Radical Scavenging Assay

The 2,2-diphenyl-1-picrylhydrazyl (DPPH) radical scavenging activity of the crude extracts was determined according to a previous described method with some modification [4]. The reaction mixture was prepared by adding 1 mL of 0.1 mM of DPPH in absolute methanol to 1 mL of methanolic extract solution at various concentrations (0.01 – 100 µg/mL). The mixture was left for 30 min in the dark at room temperature and the absorbance at 517 nm was measured against methanol as a blank. L-Ascorbic acid was used as positive control. The percentage of radical scavenging effect was calculated by the following equation as:

$$\text{scavenging effect (\%)} = [\ (A_{control} - A_{sample}) / A_{control}\ ] \times 100$$

where $A_{control}$ = absorbance of the control (DPPH and methanol)
  A_{sample} = absorbance of the sample (DPPH and methanolic extract solution)

The scavenging percentage of the crude extract was plotted, and the final result was interpreted as the effective concentration (µg/mL) of the extract required to scavenge 50% of DPPH (IC_{50}). All measurements were performed in triplicates and expressed as mean ± SD.

ABTS Radical Scavenging Assay

The 2,2´-azino-bis(3-ethylbenzthiozoline-6-sulphonic acid) diammonium salt (ABTS) radical scavenging activity of the crude extracts was determined according to a previous described method with some modification [10]. The reaction mixture was prepared by adding 7 mM of ABTS in distilled water to 2.45 mM potassium persulfate at a ratio of 1:1. The mixture was allowed to stand in the dark at room temperature for 16 h before use. The $ABTS^{.+}$ solution was diluted with ethanol to an absorbance of 0.70 ± 0.02 at 743 nm was measured against ethanol as a blank. After that, 1 mL of diluted $ABTS^{.+}$ was added to 0.5 mL of ethanolic extract solution at various concentrations (0.01 – 1,000 µg/mL). The absorbance reading at 734 nm was taken exactly 5 min after initial mixing. L-Ascorbic acid was used as positive control. The percentage of radical scavenging effect was calculated by the following equation as:

$$\text{scavenging effect (\%)} = [\ (A_{control} - A_{sample}) / A_{control}\ ] \times 100$$

where $A_{control}$ = absorbance of the control ($ABTS^{.+}$ and ethanol)
  A_{sample} = absorbance of the sample ($ABTS^{.+}$ and ethanolic extract solution)

The scavenging percentage of the crude extract was plotted, and the final result was interpreted as the effective concentration (µg/mL) of the extract required to scavenge 50% of ABTS (IC_{50}). All measurements were performed in triplicates and expressed as mean ± SD.

Statistical analysis

The data were presented as means ± SD for triplicate and quadruplicate determinations of TPC and antioxidant activity. Statistical analysis was carried out using ANOVA. The correlation between phenolic and antioxidant activity (DPPH and ABTS) was determined using one way ANOVA and the Pearson correlation coefficient (r) at the significant levels of 0.05.

Results and Discussion

Total Phenolic Contents (TPC)

The TPC of *S. gratum* extracts were measured using the Folin - Ciocalteu reaction and values were between 40.08 ± 3.73 to 537.64 ± 1.41 mgGAE/g DW. The results have indicated significant differences (p<0.05). The extracts of flower in methanol contained greater amounts of phenolics (Table 1). Wherewith, the phytochemical can be polar or non-polar in nature, so the extraction solvents are responsible for dissolving the compounds of plants. In other findings, phenolic compounds are more soluble in polar organic solvents because of the presence of a hydroxyl group, the solvents with different polarity have significant effect on TPC in higher content in more polar solvents [4]. Therefore, the effect of different solvents on TPC are very considerable and indicate the highest content of phenolic [14].

Antioxidant Activity

The radical scavenging effect were obtained by two free radical antioxidant methods (DPPH and ABTS), an analysis of the scavenge 50% of DPPH and ABTS of leaves, flowers and fruits extracts of *S. gratum* can be observed in Table 1. The best results obtained from the DPPH and ABTS radical scavenging assay were those for the extracts of flower in methanol aqual to IC_{50} of 1.01 ± 0.01 and 0.65 ± 0.01 µg/ml, respectively.

Table 1. Total phenolic contents and antioxidant activity of leaves, flowers and fruits extracts of *S. gratum*

Plant Part	Extracts	TPC (mgGAE/g DW)	DPPH IC_{50} (µg/ml)	ABTS IC_{50} (µg/ml)
Leaves	Hexane	62.03 ± 2.82 [c]	928.04 ± 8.66 [g]	697.88 ± 6.00 [f]
	Ethyl acetate	144.15 ± 4.88 [g]	48.06 ± 2.57 [c,d]	22.97 ± 0.63 [b]
	Ethanol	485.61 ± 2.44 [i]	7.53 ± 0.09 [a,b]	56.06 ± 1.56 [d]
	Methanol	527.07 ± 4.88 [j]	1.02 ± 0.02 [a]	1.30 ± 0.01 [a]
Flowers	Hexane	54.72 ± 3.73 [b]	1610.06 ± 24.15 [h]	768.13 ± 8.98 [g]
	Ethyl acetate	73.41 ± 2.44 [d]	89.11 ± 1.56 [e]	31.86 ± 1.16 [b,c]
	Ethanol	153.09 ± 1.41 [h]	35.43 ± 0.39 [b,c]	42.58 ± 0.94 [c,d]
	Methanol	537.64 ± 1.41 [k]	1.01 ± 0.01 [a]	0.65 ± 0.01 [a]
Fruits	Hexane	40.08 ± 3.73 [a]	1729.11 ± 64.69 [i]	782.38 ± 27.46 [h]
	Ethyl acetate	115.69 ± 5.08 [f]	77.05 ± 1.51 [d,e]	24.12 ± 0.23 [b]
	Ethanol	65.29 ± 3.73 [c]	232.22 ± 1.00 [f]	108.22 ± 2.22 [e]
	Methanol	85.61 ± 4.88 [e]	88.80 ± 1.32 [e]	46.64 ± 1.23 [d]
Ascorbic acid		-	0.05 ± 0.00 [a]	0.03 ± 0.00 [a]

Data are presented as mean ± SD from analysis of all samples in triplicate; superscripts a – k indicate the difference compared with the others (in the same column) is significant at 0.05 level TPC and IC$_{50}$ from higher to lowest values.

It could be seen that the scavenging effect detected by the DPPH method was different from the results detected by ABTS method because of the different reaction mechanisms which the antioxidant capacity among the different genotypes varied could be explained by different kinds or contents of antioxidants insides [14].

Correlation between TPC and antioxidant activities
Pearson's correlation coefficient, which quantifies the linear association between two quantitative variables, it was possible to estimate the relationships between the different antioxidant activities of the extracts and their contents of phenolic compounds [13]. There were weak negative correlations between the TPC of the different extracts and their antioxidant activities in DPPH radical scavenging assays (r= - 0.484) and ABTS radical scavenging assays (r= - 0.475) at significant levels of 0.05. The negative correlation coefficient indicates that the lower is the TPC, the higher is the value of IC$_{50}$, as they are inversely proportional. The Folin - Ciocalteu reaction gives a approximate of the TPC in an extract, whereas the free radical scavenging assay in not only specific to polyphenols. In addition, all kinds of phenolic compounds affect to differently in DPPH and ABTS assay with depending on the number of phenolic groups [17].

The phytochemical investigation on *S. gratum* leaves, flowers and fruits showed that the ethanol and methanol extracts of leaves and flowers showed the presence of all phytochemicals, anthraquinones, terpenoids, flavonoids, saponins, tannins and alkaloids [9]. So, the ethanol and methanol extracts of leaves and flowers has attributed the high TPC and antioxidant activity according to the presence of different phytochemicals [16].

Conclusions

The TPC and antioxidant activity of different parts of *S. gratum* are reported in this study. It was found that leaves, flowers and fruits containing of phenolic composition and have antioxidant scavenging effect. Among of 12 extracts that were studied, the part of flowers and leaves in methanol showed the highest of antioxidant activity indicated that the antioxidant substance in flowers and leaves of *S. gratum* dissolved in the higher polar solvent. A weaker correlation was observed between the TPC and the antioxidant activities, which demonstrated that the presence of a considerable amount of these compounds in a plant does not always imply a corresponding antioxidant potential. However, the exact phenolic compounds or other compounds responsible for the antioxidant activities of the extracts are still unknown. Since the present studies suggest that *S. gratum* has shown potential as sources of natural antioxidants, further studies need to be directed to isolate and characterize antioxidant active compounds from the extracts which could be responsible for the high antioxidant activities.

Acknowledgements

References

[1]   Kukongviriyapan, U., Luangaram, S., Leekhaosoong, K., Kukongviriyapan, V. and Preeprame, S. 2007. Antioxidant and Vascular Protective Activities of *Cratoxylum formosum*, *Syzygium gratum* and *Limnophila aromatic*. Biological and Pharmaceutical Bulletin. 30(4): 661-666.

[2]   Vittaya, L., Na Ranong, S., Charoendat, U., Janyong, S. and Leesakul, N. 2020. Bio-Activity Investigations of Extracts of Different Parts of *Lumnitzera littorea Voigt*. Tropical Journal of Natural Product Research. 4(8): 365-371.

[3]   Senggunprai, L., Kukongviriyapan, V., Prawan, A. and Kukongviriyapan, U. 2010. Consumption of *Syzygium gratum* Promotes the Antioxidant Defense System in Mice. Plant Foods for Human Nutrition. 65: 403-409.

[4]   Aryal, S., Baniya, M. K., Danekhu, K., Kunwar, P., Gurung, R. and Koirala, N. 2019. Total Phenolic Content, Flavonoid Content and Antioxidant Potential of Wild Vegetables from Western Nepal. Plants. 8(96): 1-12.

[5]   Rocchetti, G., Lucini, L., Ahmed, S. R. and Saber, F. R. 2019. In Vitro Cytotoxic Activity of Six *Syzygium* Leaf Extracts as Related to Their Phenolic Profiles: An Untargeted UHPLC-QTOF-MS Approach. Food Research International 126 (2019) 108715. 1-8.

[6]   Pakdeechote, P., Meephat, S., Sakonsinsiri, C., Phetcharaburanin, J., Bunbupha, S. and Maneesai, P. 2020. *Syzygium gratum* Extract Alleviates Vascular Alterations in Hypertensive Rats. Medicina. 56(509): 1-12.

[7]   Meephat, S., Maneesai, P., Bunbupha, S., Prachaney, P., Kukongviriyapan, U. and Pakdeechote, P. 2018. Effect of *Syzygium gratum* Extract on Blood Pressure and Endothelium-Dependent Vasorelaxation in Nitric Oxide-Deficient Rats. Srinagarind Medical Journal. 33(1): 38-42.

[8]   Suttisansanee, U. and Kruawan, K. 2019. Cholinesterase-inhibiting Potential and Anti-BACE1 Activities of Edible Leaves of Selected Thai Local Plants. Walailak Journal of Science and Technology. 16(3): 155-163.

[9]   Sunanta, K. and Vittaya, L. 2020. Solvent Effect on Phytochemical Screening of *Melaleuca leucadendra* Linn. and *Syzygium cinerea*. Rajamangala University of Technology Srivijaya Research. 12(1): 112-119.

[10]   Re, R., Pellegrini, N., Proteggente, A., Pannala, A., Yang, M. and Rice-Evans, C. 1999. Antioxidant Activity Applying An Improved ABTS radical Cation Delocarization Assay. Free Radical Biology and Medicine. 26(9/10): 1231-1237.

[11]   Sriket, P. 2014. Chemical Components and Antioxidant Activities of Thai Local Vegetables. KMITL Science and Technology Journal. 14(1): 18-23.

[12]   Saeed, N., Khan, M. R. and Shabbir, M. 2012. Antioxidant Activity, Total Phenolic and Total Flavonoid Contents of Whole Plant Extracts *Torilis leptophylla* L. BMC Complementary and Alternative Medicine. 12(221): 1-12.

[13]   Teixeira, T.S., Vale, R.C., Almeida, R.R., Ferreira, T.P.S. and Guimaraes, L.G.L. 2017. Antioxidant Potential and its Correlation with the Contents of Phenolic Compounds and Flavonoids of Methanolic Extracts from Different Medicinal Plants. Revista Virtual de Quimica. 9(4); 1546-1559.

[14]   Mazandarani, M., Zarghami, M.P., Zolfaghari, M.R., Ghaemi, E.A., Bayat, H. 2012. Effects of Solvent Type on Phenolics and Flavonoids Content and Antioxidant Activities in *Onosma dichroanthum Boiss*. Journal of Medicinal Plants Research. 6(28); 4481-4488.

[15]   Brighente, I.M.C., Dias, M., Verdi, L.G. and Pizzolatti, M.G. 2007. Antioxidant Activity and Total Phenolic Content of Some Brazilian Species. Pharmaceutical Biology. 45(2); 156-161.

[16] Bharathi, B. and Prasad, NBL. 2021. Phytochemical Screening and Antioxidant Potential of *Pterocarpus Santalinus* L.F. Plant Parts. Asian Journal of Pharmaceutical and Clinical Research. 14(3); 75-83.

[17] Azlim, A.A.A., Ahmed, J.K.C., Syed, Z.I., Mustapha, S.K., Aisyah, M.R. and Kamarul, R.K. 2010. Total Phenolic Content and Primary Antioxidant Activity of Methanolic and Ethanolic Extracts of Aromatic Plants' Leaves. International Food Research Journal. 17: 1077-1084.

Gas Chromatography-Mass Spectrometry (GC-MS) of volatile oil in Siam Cardamom

Mayoon Lamsub[1]*, Sirirat Phaisansuthichol[2], Paramee Chumsri[3], Natyada Lamsub[4]

[1]Nanomaterials Chemistry Research Unit,Department of Chemistry, Faculty of Science and Technology, Nakhon Si Thammarat Rajabhat University, 80280, Thailand
[2]Program in Chemistry, Faculty of Science, Maejo University, Chiang Mai 50290, Thailand
[3]Department of Food science and nutrition, Faculty of Science and Technology, Nakhon Si Thammarat Rajabhat University, 80280, Thailand
[4]Songsermsasana Vittaya School, Songkhla, 90110, Thailand
*e-mail: mayoon105@gmail.com

Abstract

Siam cardamon (Amomum Krervanh), one of the most common spices and herbs, plants in Southeast Asia and can be found in the mountains in Nakhon Si Thammarat Province, south of Thailand. The local people like Siam cardamom for cooking, medicine and insect repellant because of its essential oil. Therefore, the researcher is interested in studying Gas Chromatography-Mass Spectrometry (GC-MS) of volatile oil in Siam Cardamom. The essential oil is produced from the stems by extraction steam. The result of GC-MS analysis showed that Siam cardamom essential oil consists of 25 components.

Keywords: Siam Cardamom; Gas Chromatography-Mass Spectrometry; volatile oil

References

Wannakrairoj, S., & Tefera, W. (2019). Thidiazuron and Other Plant Bioregulators for Axenic Culture of Siam Cardamom (Amomum krervanh Pierre ex Gagnep.). *Journal of Kasetsart - Natural Science* 46 : 335 - 345

Formulation and evaluation of herbal cream from *Elateriospermum tapos Blume* oil

Naengnoi Sangsane [1]*, Paweena Porrawatkul[1], Rungnapa Pimsen[1], Prawit Nuengmutcha[1], Nongyao Teppaya[1], Arnannit Kuyyogsuy [1], Yanisa Thepchuay[1], Nichapa Rattanakomon[1] and Montakarn Thongsom[2]

[1]*Nanomaterials Chemistry Research Unit, Department of Chemistry, [2]Department of Biology, Faculty of Science and Technology, Nakhon Si Thammarat Rajabhat University, 80280, Thailand.*
*Corresponding author. e-mail: s.saengsane@gmail.com

Abstract

Natural skin care products are gaining popularity in today's market since everyone wants healthy, beautiful skin. The major goal of this study was to assess the antioxidant effectiveness of a herbal cream prepared with *Elateriospermum tapos Blume* oil, whose omega 3, 6, and 9 concentrations were measured by using GC-MS. Physical tests such as color, odor, homogeneity, and pH were performed on the two produced formulations. The ferric reducing antioxidant potential (FRAP) method and the vitro 2,2-diphenyl-1-picrylhydrazyl (DPPH) assay were used to assess the antioxidant activity of herbal cream prepared with *Elateriospermum tapos* Blume oil. The oil and formulation cream showed strong antioxidant activity. *Elateriospermum tapos* Blume oil had an IC_{50} of 59.13 ± 1.3 mg/L and the formulation cream had an IC_{50} of 42.67 ± 1.7 mg/L, whereas ascorbic acid had an IC_{50} of 39.72 ± 0.95 mg/L. The FRAP value corresponded to the DPPH data with good results. The created *Elateriospermum tapos* Blume oil herbal cream was discovered to be natural and may be used topically to treat skin infections further.

Keywords: Antioxidant activity; *Elateriospermum tapos* Blume oil; Herbal cream

Introduction

Improper blood circulation, pollutants in the blood, and an individual's lifestyle are all factors that contribute to skin disorders. Inflammations, acne, and rashes are examples of skin concerns. Cosmetics are used to protect skin from exogenous and endogenous harmful agents, as well as to enhance skin beauty and attractiveness. However, cosmetics contain a variety of synthetic compounds, chemicals, dyes, and derivatives that have been shown to cause a variety of skin diseases and have a number of side effects (Nirmala kumari, D. *et al*., 2016). Herbal medicine is gaining popularity among the general public. Patients and doctors employ a wide range of herbal preparations used to treat a variety of illnesses, including skin problems the standard the treatment of dermatologic problems by applying creams or lotions to the skin medicines made from plants have been used since the dawn of time. In today's industrialized world, it's still important (Kumar, R. *et al*., 2013). Treatments using herbs Things that have been used for hundreds of years are now being investigated. Scientifically,

As a result, the value of herbs in cosmeceutical formulation has greatly increased in the personal care system, and herbal cosmetics are in high demand. As a result, we make extensive use of herbal cosmetics. The *Elateriospermum tapos Blume* (*E. tapos*) oil was tested as a herbal cream in this study. The monoecious tropical canopy species *E. tapos* can be found in Southeast Asia's tropical rain forest. It belongs to the *Euphorbiaceaceae* family and belongs to the *Crotonoideae* and *Elateriospermeae* tribes. *E. tapos* is more often known as look-pra among natives in Nakhon Si Thammarat province (Thailand). *E. tapos* oil has been shown to be

efficient against bacterial and fungal species in recent investigations (Ooi Yong Yong, Jumat Salimon, 2006). The goal of this current study was to determine the antioxidant and antibacterial (*Staphylococcus epidermidis* and *Propionibacterium acnes*) properties of *E. tapos* oil in prepared cream.

Materials and methods

E. tapos was collected in the Tambon Krungching, Amphoe Nopitum, Nakhon Si Thammarat Province, Thailand, from the surrounding area of Nakhon Si Thammarat Rajabhat University. The study's analytical reagents were all acquired from Merck and were of analytical quality. Hi-Media in Mumbai, India, provided nutrient agar for bacterial culture as well as Mueller–Hinton broth and antimicrobial activity agar.

Preparation of *Elateriospermum tapos Blume* oil and cream formulation

Bring in the *Elateriospermum tapos* Blume beads to be cleaned thoroughly. Remove the peel from the meatballs and ground them thoroughly. After that, squeeze the oil out. To obtain brown semisolid extract for use in herbal cream, the solvent was evaporated using a rotary evaporator. A cream based on an oil in water (O/W) emulsion (semisolid formulation) was developed. In the oil phase (Phase B), the emulsifier (stearic acid) and other oil soluble components were dissolved and heated to 50 °C. In the aqueous phase (Phase A), the preservatives and other water soluble components were dissolved and heated to 50 °C. The aqueous phase was added in parts to the oil phase after heating, with continuous stirring until the oil phase cooled.

Table 1 Composition of herbal cream

Ingredients	Amount (g)	
	Formulation 1	Formulation 1
Phase A		
DI water	Up to 100 mL	Up to 100 mL
EDTA	0.50	0.50
Glycerin	2.00	2.00
Carbomer (Carbopol 940)	1.00	1.00
Phase B		
Cetearyl alcohol	4.00	4.00
Stearic Acid	6.00	6.00
Squalane	3.00	3.00
E. tapos oil	3.00	3.00
Eumulgin B1	3.00	3.00
Vitamin E di-alpha tocopherol	1.00	1.00
Phase C		
Triethanolamine	1.00	1.00
Phenoxyethanol	2.00	2.00
Fragrance	1.00	1.00
Total	100	100

Diagnosing the omega components by Gas Chromatography technique connected with mass spectrometry (GC-MS)

A chromatography equipment is coupled to a mass spectrometry apparatus in a gas-using fish. Before being injected into the GC, 0.1 ml oil was transformed to methyl ester using 1 ml NaOMe (1 M) in 1 ml hexane. Shimadzu gas chromatography with flame ionization detector and capillary column (30 m 0.25 mm 0.25 m film) was used for the analysis. With a flow rate of 0.3 ml/min, the detector temperature was set to 280–340 C. The temperature of the injector was fixed at 250 degrees Celsius. As a carrier gas, nitrogen was employed. Retention periods were used to identify the peaks, which were then compared to authentic standards examined under the same conditions.

Antioxidant activity
:DPPH assay

The antioxidant activity of the oil extract was studied by using 2 2-diphenyl-1-pieryl-hydrazyl (DPPH) assay. Briefly, 1 mL of the samples with varied concentrations received 2 mL of 2×10^{-4} mM DPPH in 95 percent ethanol. After 5 minutes, the absorbance was measured at 518 nm against a blank of 95 percent ethanol at room temperature in the dark. The standard compound was ascorbic acid.

:The Ferric reducing antioxidant power (FRAP) assay

E. tapos oil's ferric reducing antioxidant potential (FRAP) was investigated. In two separate tubes, two microliters of sample and 100 mL of standard were taken. FRAP reagent (3 mL) was added. At zero minutes after vortexing, the absorbance at 593 nm was measured. After 4 minutes, the samples were placed in a water bath at 37 °C and the absorption was measured again. The same procedure had to be followed for ascorbic acid standards (100 M-1000 M). The contents of the tubes above were thoroughly combined. At zero minutes and 4 minutes, the absorbance of the standard and test were measured at 593 nm.

Antibacterial study

Using the agar-well diffusion method, *E. Tapos* oil and herbal cream were tested for antibacterial activity against *P. acnes* and *S. epidermidis*. A sterile cotton swab was used to disseminate the bacteria culture evenly across the nutrient agar plate. Agar plates were used to make wells. Standard antibiotic discs (chloramphenicol and clindamycin) were added to these wells. The diameter of the inhibitory zones around herbal cream was measured and compared to that around commercial standard antibiotics chloramphenicol, clindamycin, and *E. tapos* oil after incubation at 37 °C for 24 hours.

Physical evaluation of formulated herbal cream

The ointments and creams were evaluated physically over a 30 day period using the following criteria: appearance, scent test by smelling, color test by naked sight, and homogeneity test by physical contact with hands. A digital pH meter was used to determine the pH of various mixtures. The pH was determined after dissolving 0.5 g of the weighed formulation in 50 mL of pure water.

Results and discussion

(a)   (b)   (c)

Fig. 1 (a) *E. tapos* (b) *E. tapos* oil (c) Formulattion of *Elateriospermum tapos* Blume oil cream.

Omega-3, omega-6 and omega-9 amount of *E. tapos* oil were determined using gas chromatography technique connected with mass spectrometry (GC-MS). The results showed the percentage and the amount of omega–3, omega-6 and omega-9 is 45.28%, 100% and 92.61%, respectively.

Antioxidant activity

Atherosclerosis, arthritis, ischemia and reperfusion injury of many tissues, central nervous system injury, gastritis, cancer, and AIDS are only a few of the illnesses caused by free radicals in humans. The main players in lipid peroxidation are these free radicals. Antioxidants may exert their action by interacting directly with reactive oxygen species (ROS), quenching them, and/or chelating the catalytic metal ions. Natural antioxidants, particularly phenolics and flavonoids, are both safe and effective at absorbing and neutralizing free radicals, quenching singlet and triplet oxygen, and decomposing peroxides. The identification of plants has recently gotten a lot of attention. The antioxidant activity of the *E. tapos* oil was evaluated using DPPH scavenging assay and FRAP assay. The oil and formulation cream showed strong antioxidant activity. Elateriospermum tapos Blume oil had an IC_{50} of 59.13 ± 1.3 mg/L and the formulation cream had that of 42.67 ± 1.7 mg/L, whereas ascorbic acid 39.72 ± 0.95 mg/L. These results showed good antioxidant activity versus with this property of ascorbic acid as standard reagent.

Antibacterial activity

The antibacterial efficacy of the *E. tapos* oil cream formulation against S. epidermidis was outstanding. The following was the order of antibacterial activity of *E. tapos* in the topical bases: *E. tapos* oil cream formulation. The *E. tapos* oil integrated into the cream bases also exhibited better action than the *E. tapos* oil, according to the findings (Table 2). The action against *S. epidermidis* is of particular importance because it is regularly found on the hands, face, and in deep layers of the skin, and is one of the most common and dangerous bacteria. *S. epidermidis* is difficult to eradicate, particularly in the deeper layers of the skin, sweat glands, sebaceous glands, and hair.

Table 2 Preliminary *in vitro* antibacterial activity of *E. tapos* oil and formulation cream.

Test oganism	Zone of Inhibition (mm)			
	Formulation cream	*E. tapos* oil	Chloramphenicol	Clindamycin
S.epidermidis	26.25 ± 1.4	20.0 ± 0.7	42.38 ± 1.2	No
P. acnes	NA	15.65 ± 1.2	-	19.36 ± 0.3

NA : no activity

The finished formulations (Table 3) appear to be smooth and homogeneous. All of the developed formulations had pH values ranging from 7.1 to 7.5, which are considered adequate for avoiding skin irritation when applied to the skin. The compositions' pH values are within the typical pH range of human skin (7.2±1). The cream's pH did not change as a result of the investigation.

Table 3 Evaluation parameters of the formulations

Formulation	color	odour	pH	homogeneity
E. tapos oil cream	Light-yellow	*E. tapos* oil	7.2±1	homogenous

Conclusion

E. tapos oil has been found to be an effective antibacterial and anti-inflammatory agent in studies. The antibacterial efficacy of cream formulations including *E. tapos* oil was tested in vitro against *S. epidermidis*. The antibacterial activity inhibition zones were compared to those of conventional chloramphenicol. Furthermore, the manufactured *E. tapos* oil creams had a uniform appearance, a pleasant odor, and a neutral pH. The prepared herbal cream using *E. tapos* oil was discovered to be natural and may be used topically to treat skin infections.

Acknowledgements

References

[1] Abubacker, M. N., Ramanathan, R., Senthil, K. T. (**2008**). In vitro antifungal activities of *Cassia alata* Linn. Flower extract. *Natural product Radiance*. 7(1): 6-9.

[2]. Agarkar, S.V., Jadge, D. R. (**1999**). Phytochemical and pharmacological investigations of genus Cassia: a Review. *Asian J. Chem.*11: 295-299.

[3]. Amao, S.Y., Ajani, R.S., Oladapo, O. (**2010).** *Cassia alata* alters Liver Structure in Rat Afr. *J. Biomed. Res*. 13: 231 – 233.

[4]. Ibrahim, D., Osman, H. (**1995**). Antimicrobial activity of Cassia alata from Malaysia. *J. Ethnopharmacol*. 45(3): 151-156.

[5] Kumar, R., Bhagat, S. K., Kumar, V., Nirmala, A. (**2013**). AntioxidentActivtiy & Cytotoxic Analysis of Seed Extract of *Punica Granatum. Asian J. Biochem. and Pharm*. 3(1): 225-236.

[6] Ooi, Y. Y., Jumat, S. (2006). Characteristics of *Elateriospermum tapos* seed oil as a new source of oilseed. *Industrial Crops and Products*. 24,146–151.

[7]. Panigrahi, L., Jhon, T., Shariff, A., Shobanirani, R. S. **(1997)**. Formulation and evaluation of lincomycin HCL gels. *Ind. J. Pharm. Sci*. 59: 330-332.

[8] Nirmala kumari, D., Satyanarayana, T., Sai kumar, CH., Moulabi, SK., Pullarao, B., Gavamma, A., Nagamani, K. **(2016)**. Formulation and evaluation of herbal vanishing cream containing Punica Granatum. *Indo American J. Pharm. Res***.,** 6: 4938-4944.

[9]. Villasenor, I. M., Canlas, A. P., Pascua, M. P. I., Sabando, M. N., Soliven, L. A. **(2002)** Bioactivity studies on studies on *Cassia alata* Linn. leaf extract. *Phytother Res.* 16: 93-96.

Lead (II) removal from wastewater using a magnetic magmesium oxide/graphene/iron oxide adsorbent

Teerachot Bunsong[1], Namtip Saetang[1], Sarawut Puttasuk[1],
Amnuay Noypha[2] and Prawit Nuengmatcha[1*]

[1]Department of Applied Physical and Material Sciences, University of Swat, Pakistan
[2]Nanomaterials Chemistry Research Unit, Department of Chemistry, Faculty of Science and Technology, [3]Department of Physic, Nakhon Si Thammarat Rajabhat University, Nakhon Si Thammarat, Thailand

Abstract

A magnetic magmesium oxide/graphene/iron oxide adsorbent (MMGF) was produced and used to remove Pb^{2+} from aqueous solutions in this work. Energy-dispersive X-ray spectroscopy (EDX), scanning electron microscopy (SEM), fourier-transform infrared spectroscopy (FTIR), X-ray powder diffraction (XRD), and vibrating sample magnetometry (VSM) techniques were used to characterize the adsorbent. The Langmuir isotherm model was used to match the Pb^{2+} adsorption data of the adsorbent. The maximum Pb^{2+} adsorption capacity of 212.82 mg/g was reached under optimized conditions, which included a 30 minute incubation time, a pH of 7, a contact time of 60 minutes, and an adsorbent dosage of 0.02 g. When 0.1 mol/L HNO_3 was utilized as the desorbing agent, the MMGF still had 80.0 percent of its original Pb^{2+} sorption capacity after five successive sorption–regeneration cycles. These findings clearly show that the MMGF is a high-stability adsorbent with prospective applications in the removal of hazardous metal ions from wastewater.

Keywords: Lead (II) removal, Waseater treatment, Adsobent

References:

Rezania, S., Mojiri, A., Park, J., Nawrot, N., Wojciechowska, E., Marraiki, N., Zaghloul, N.S.S. (2022). Removal of lead ions from wastewater using lanthanum sulfide nanoparticle decorated over magnetic graphene oxide. *Environmental Research* 204: 111959.

Wong, S., Ngadi, N., Inuwa, I.M., Hassan, O. (2018). Recent advances in applications of activated carbon from biowaste for wastewater treatment: a short review. *Journal of Cleaner Production* 175: 361-375.

Nuengmatcha, P., Mahachai, R., Chanthai, S. (2014). Thermodynamic and kinetic study of the intrinsic adsorption capacity of graphene oxide for malachite green removal from aqueous solution. *Oriental Journal of Chemistry* 30(4): 1463-1474.

Removal of methylene blue and Cr (VI) using activated carbon derived from waste rubber seed shell

Suphawarat Thupsuri, Kongsak Pattarith and Supattra Tangtubtim*

Department of Chemistry, Faculty of Science, Buriram Rajabhat University, Buriram 31000, Thailand
*e-mail: supattra.tt@bru.ac.th

Abstract

Rubber seed shell (RSS) from agricultural waste was extensively utilized as a low-cost and effective adsorbent for removals of methylene blue and Cr(VI). Chemical activation was performed using zinc chloride ($ZnCl_2$) carried out at 600 °C. The characterization of rubber seed shell charcoal (RSS-CH) and rubber seed shell activated carbon (RSS-AC) were performed by scanning electron microscopy (SEM), fourier transform infrared spectroscopy (FTIR), surface area and pore size analyzer (BET). The adsorption process was found to influenced by parameters such as pH, initial MB and Cr (VI) concentration and temperature. The adsorption of methylene blue onto RSS-CH and RSS-AC adsorbents could be described by the pseudo-second-order kinetic model and fitted to Langmuir adsorption. The maximum adsorption capacities of 336 and 86 mg/g was found for MB and Cr(VI), respectively. Reusable performance tests indicated that RSS-AC could be potentially reused with maintaining high adsorption efficiency.

Keywords: activated carbon; Cr(VI); methylene blue

References

Ma, J., Li, J., Guo, Q., Han, H., Zhang, S., & Han, R., (2020). Waste peanut shell modified with polyethyleneimine for enhancement of hexavalent chromium removal from solution in batch and column modes. *Biresourse Technology Reports* 12(2020) : 100576.

Yagmur, HK. & Kara, I. Synthesis and characterization of magnetic $ZnCl_2$-activated carbon produced from coconut shell for the adsorption of methylene blue. *Journal of Molecular Structure* 1232 : 130071.

Lead (II) removal from synthetic wastewater using activated carbon derived from mangosteen peel

Piyawan Nuengmatcha[1*], Piyakan Khongsaiya[1], Jiraporn Chaithip[1], Nichapa Rattanakomon[2], Anusorn Banluepuech[3], Amnuay Noypha[4]

[1]Department of Environmental Science, [2]Department of Chemistry, [3]Science Center, Faculty of Science and Technology, [4]Department of Physic, Faculty of Education, Nakhon Si Thammarat Rajabhat University, 80280, Thailand

Abstract

Lead (Pb^{2+}) is a well-known metalloid and fund in the earth's crust which is a toxic pollutant. In the recent past, a variety of biosorbents have been synthesised using different parts of plants for removing Pb^{2+} or other heavy metals from waste water. The present investigation deals with removal of Pb^{2+} ions from wastewater using activated carbon prepared from mangosteen peel (ACMP). The optimum conditions include the initial concentration of Pb^{2+}, contact time, adsorbent dose, and temperature. According to the results, the optimal conditions (Pb^{2+} concentration 70 mg/L, contact time 60 minutes, adsorbent dose 0.05 g, and temperature 30°C) resulted in Pb^{2+} removal of 90%. The adsorption capacity has been found to be 49.35 mg/g. The obtained ACMP presents an effective adsorbent material compared to others, so it should be further applied to several heavy metals in wastewater.

Keywords: Lead (II) removal, Waseater treatment, Adsobent

Introduction

Because lead (Pb^{2+}) ions are a very hazardous heavy metal at low quantities, they can cause a variety of environmental problems [1]. Mining activity may be one of the Pb^{2+} polluted sources of soil, groundwater, and surface water in natural sources of Pb^{2+}. Through bio-accumulation and biomagnification of living species, it can be harmful to ecosystems [2,3]. Because lead is employed in a range of sectors, including batteries, pigments, paints, gasoline, cables, steels, alloys, and plastics [4], polluted Pb^{2+} discharged in wastewater is harmful to aquatic habitats [2]. Lead can build up in a variety of human systems, including the muscles, neurological system, blood, reproductive, renal, brain, and tissue systems, resulting in a variety of disorders, including human carcinogens [5]. As a result, Pb^{2+} polluted wastewaters must be treated to a concentration of less than 0.01 mg/L before being discharged to receiving waters for safety reasons.

Various strategies for removing Pb^{2+} ions from aqueous systems have been used in recent decades, including bioremediation, photocatalytic, membrane, polymer, electro-coagulation, oxidative degradation, and adsorption [6]. Adsorption is an excellent technology for removing Pb^{2+} ions from water samples because it is ecologically benign, simple to run, easy to recover, low cost, and rapid. Activated carbon is a carbonaceous substance with a high porosity, large specific surface area, and higher mechanical strength that is utilized as the primary adsorbent in the adsorption process [7].

For the reported work, the activated carbon derived from mangosteen peel (ACMP) using strong oxidizing agents including sulfuric acid (H_2SO_4), potassium permanganate ($KMnO_4$), sodium nitrate ($NaNO_3$), hydrogen peroxide (H_2O_2) as the activating agent was synthesized. The obtained activated carbon was characterized for its morphology and used to study its divalent lead (Pb^{2+}) adsorption ability in batch mode. Different adsorption factors, namely initial Pb^{2+}concentration, contact time, adsorbent dosage, and operational temperature were studied to understand their effects on Pb^{2+} separation by ACMP adsorbent.

Experimental

Reagents and materials

Sulfuric acid (H_2SO_4), potassium permanganate ($KMnO_4$), sodium nitrate ($NaNO_3$), hydrogen peroxide (H_2O_2), nitric acid (HNO_3), and lead nitrate ($Pb(NO_3)_2$). All chemicals were of analytical grade and used without further purification. All experiments were carried out with deionized (DI) water.

Synthesis of ACMP adsorbent

The conditions of our earlier study [8] were used to manufacture ACMP adsorbent from mangosteen peel. In a beaker at 0 °C, 30 g mangosteen peel and 300 mL concentrated H_2SO_4 were combined for 30 minutes with vigorous magnetic swirling. After that, 3.0 g of $NaNO_3$ was added to the mixture in portions, and it was agitated for another 30 minutes. Then a solid $KMnO_4$ powder was gently added to the beaker, and the temperature was held below 15 °C. The mixture was agitated at 35°C until it turned brown, then diluted with 200 mL deionized water, which was gradually added to the mixture and swirled for another 30 minutes. 40 mL of 30% H_2O_2 was sloshed after being heated to 80 °C for 6 hours.

Adsorption experiments

The effects of experimental parameters such as initial Pb^{2+} concentration (10-120 mg/L), contact time (30-180 min), adsorbent dose (0.05-1.00 g) and temperature (20-70°C) on the adsorptive removal of Pb^{2+} ions were studied in a batch mode of operation for a specific period of Pb^{2+} concentration of 20 mg/L. All adsorption experiments were conducted in 125 mL conical flask, adsorbent (0.05 g) was accurately weighed into a conical flask. Then, 25 mL of Pb^{2+}solution was added and shaken by an orbital shaker at approximately 150 rpm at ambient temperature. After a period of shaking, the adsorbent was separated from the solution mixture by centrifugation for 5 min and Pb^{2+} in the supernatant solution was determined by atomic absorption spectrophotometer (AAS; Analytikjena, ContrAA800, Germany). All experiments were conducted in triplicate under the same conditions. The adsorption capacity (q_e, mg/g) of Pb^{2+}at an equilibrium state was determined as follows: $q_e = [V(C_0-C_e)]/m$ where, C_o is the initial concentration (mg/L) of Pb^{2+} in the solution, C_e is the Pb^{2+} concentration (mg/L) at the equilibrium state, V is the volume (L) of the solution, and m is the mass (g) of the adsorbent. Langmuir and Freundlich adsorption models were used to describe the equilibrium nature of Pb^{2+} adsorption onto the ACMP adsorbent.

Results and Discussion

Morphology and major elements of adsorbent

The morphology and major elements of the bare mangosteen peel and ACMP adsorbent were analyzed by SEM and EDX techniques. Figure 1 shows the SEM image of mangosteen peel and ACMP adsorbents. It can be seen that the porosity of the ACMP adsorbent increases after being activated with strong oxidizing agents. From Fig. 2. It was found that the EDX spectrum of ACMP shows strong peaks of C, O, and K, which are the main elements. The weight percentages of C, O, and K were 88.8, 9.6, and 1.6 wt%, respectively.
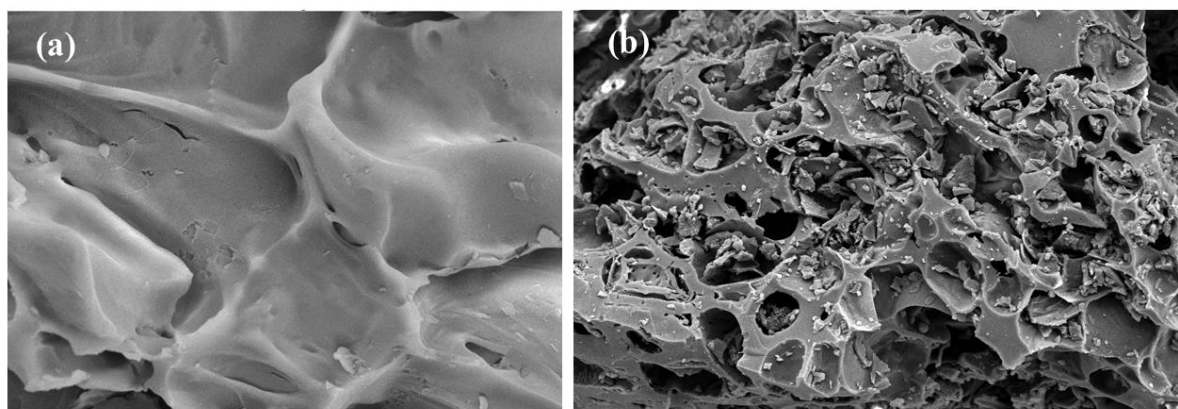
Fig. 1 SEM images of (a) mangosteen peel and (b) ACMP adsorbents
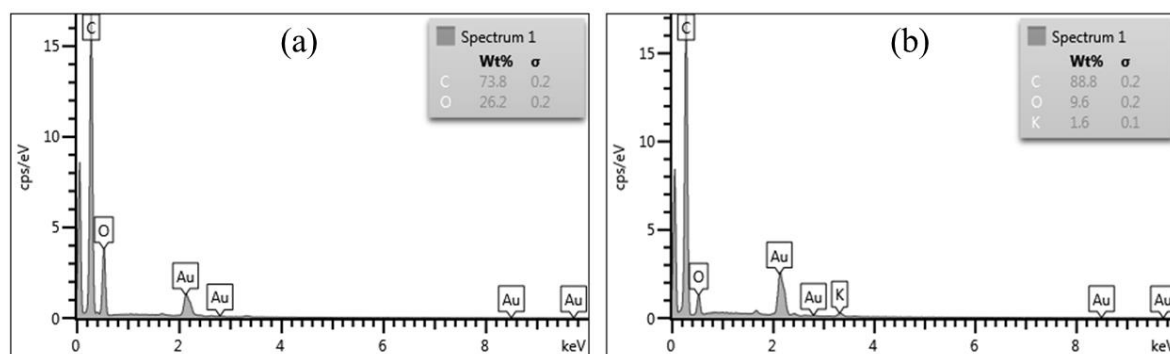
Fig. 2 EDX spectrums of (a) mangosteen peel and (b) ACMP adsorbents

Adsorption experiment

The influence of the starting concentration on the ACMP adsorbent's adsorption capability was investigated. The adsorption capacity increased with the Pb^{2+} concentration in the range of 10 mg/L (0.32 mg/g) to 70 mg/L (1.56 mg/g) due to an increase in the chance of collision between Pb^{2+} ions and ACMP particles, as shown in Fig. 3 (a). Moreover, in the initial stage, all active sites of the ACMP surface were vacant, and the Pb^{2+} concentration gradient

was relatively high [9]. For contact time is a crucial factor. The influence of contact time on the efficiency of the produced ACMP adsorbent for Pb^{2+} removal from synthetic wastewater is shown in Fig. 3 (b). After 60 minutes, equilibrium Pb^{2+} adsorption was achieved with a 1.67 mg/g adsorption capacity. The existence of unoccupied sites on the ACMP surface, significant concentration gradients between the ACMP surface and bulk solution, and direct electrostatic attraction between the negatively charged ACMP surface and Pb^{2+} resulted in rapid uptake of Pb^{2+} over the first 0 to 30 minutes. However, after 60 minutes, the adsorption level remained steady. As a result, a 60-minute incubation time was chosen as the best equilibrium time for Pb^{2+} elimination. In addition, the effect of adsorbent dosage on Pb^{2+} removal was investigated throughout a dosage range of 0.05 to 1.00 g. The ACMP adsorbent's Pb^{2+} adsorption capability is shown in Fig. 3 (c). As the adsorbent dosage is increased from 0.05 g (7.69 mg/g) to 0.6 g (0.79 mg/g), the adsorption capacity declines. This can be described as follows: as the dosage was increased, the number of active surface sites and functional groups on the ACMP surface increased, enhancing the adsorption process [10].
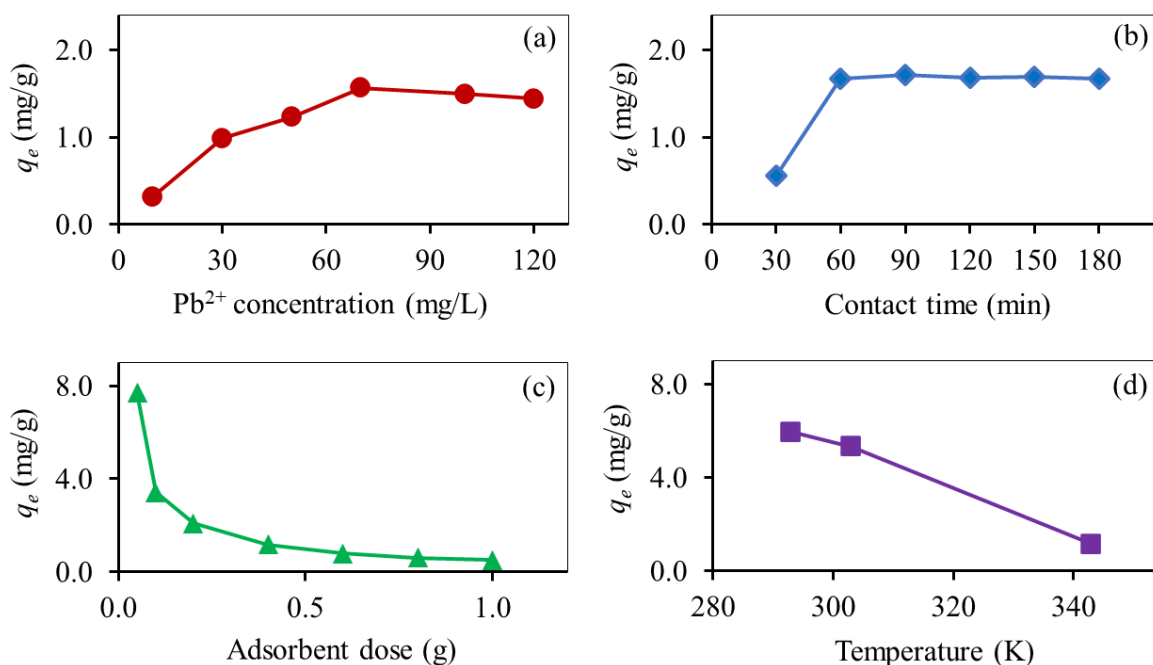
Fig. 3 Effect of (a) initial Pb^{2+} concentration, (b) contact time, (c) adsorbent dose, and (d) temperature on adsorption performance of ACMP adsorbent

The removal of pollutant species from aqueous solutions is influenced by temperature, with most adsorption mechanisms being exothermic in nature. The present procedure was also discovered to be exothermic, as illustrated in Fig.3 (d). The adsorption capabilities of ACMP adsorbent were observed to decrease as the temperature rose. The common thermal influence on their binding energy generated by the collision principle, in particular for weak physisorption of the adsorption capacity, is the reason for this appearance. The findings show that the circumstances that favor the removal of Pb^{2+} by the adsorption process are exothermic at lower temperatures. When the temperature is high.
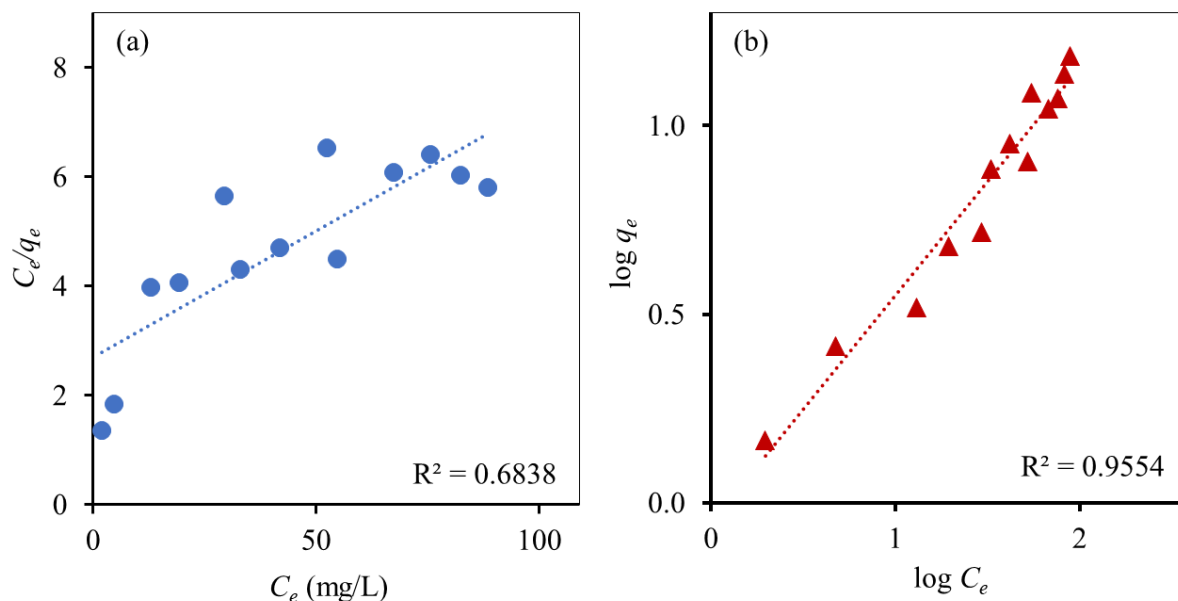
Fig. 4 (a) Langmuir isotherm model and (b) Freundlich isotherm model of the adsorption of Pb^{2+} ions on the surface of ACMP adsorbent

The adsorption was described using the Langmuir and Freundlich adsorption isotherms. When adsorption occurs only at adsorbent-specific locations, the Langmuir adsorption isotherm is employed to explain monolayer sorption onto the adsorbent surface. The Freundlich adsorption isotherm, on the other hand, is used to characterize the adsorption properties of a heterogeneous surface. Figures 4 (a) and 4 (b) show the Langmuir and Freundlich adsorption isotherms, respectively. Because the R^2 values are high, the Freundlich equation (0.9554) fits the adsorption data better than the Langmuir equation (0.6838). The maximum adsorption capacity (q_m) of ACMP adsorbent is 49.35 mg/g.

Conclusion

ACMP adsorbent was effectively obtained and characterized using SEM and EDX techniques in this study. These were used to remove Pb^{2+} from synthetic wastewater as adsorbents. The ACMP adsorbent had a high capacity for adsorption of Pb^{2+}. The Freundlich isotherm with a maximum adsorption capacity of 49.35 mg/g fit the isotherm data well. The synergistic action of functional groups on ACMP could explain its high adsorption affinity for Pb^{2+}. The ACMP adsorbent was quite stable. As a result, the ACMP produced is promising for heavy metal ion removal from wastewater.

Acknowledgements

References

[1] Tchounwou, P.B., Yedjou, C.G., Patlolla, A.K., Sutton, D.J. (2012). Heavy metal toxicity and the environment, molecular, clinical and environmental toxicicology. *Environmental Toxicology* 101(3): 133-163.

[2] Ali, H., Khan, E., Ilahi, I. (2019). Environmental chemistry and ecotoxicology of hazardous heavy metals: environmental persistence, toxicity, and bioaccumulation, *Journal of Chemistry*: 6730305.

[3] Panichayapichet, P., Nitisoravut, S., Simachaya, W. (2007). Spatial distribution and transport of heavy metals in soil, ponded-surface water and grass in a pb-contaminated watershed as related to land-use practices. *Environmental Monitoring and Assessment* 135: 181-193.

[4] Amin, M.T., Alazba, A.A., Amin, M.N. (2017). Absorption Behaviours of Copper, Lead, and Arsenic in Aqueous Solution Using Date Palm Fibres and Orange Peel: Kinetics and Thermodynamics. *Polish Journal of Environmental Studies* 26(2): 543-557.

[5] Mason L.H., Harp J.P., Han D.Y. (2014). Pb neurotoxicity: Neuropsychological effects of lead toxicity. *BioMed Research International*: 840547.

[6] Rezania, S., Mojiri, A., Park, J., Nawrot, N., Wojciechowska, E., Marraiki, N., Zaghloul, N.S.S. (2022). Removal of lead ions from wastewater using lanthanum sulfide nanoparticle decorated over magnetic graphene oxide. *Environmental Research* 204: 111959.

[7] Wong, S., Ngadi, N., Inuwa, I.M., Hassan, O. (2018). Recent advances in applications of activated carbon from biowaste for wastewater treatment: a short review. *Journal of Cleaner Production* 175: 361-375.

[8] Nuengmatcha, P., Mahachai, R., Chanthai, S. (2014). Thermodynamic and kinetic study of the intrinsic adsorption capacity of graphene oxide for malachite green removal from aqueous solution. *Oriental Journal of Chemistry* 30(4): 1463-1474.

[9] Ebisike, K., Okoronkwo, A.E., Alaneme, K.K. (2019). Adsorption of Cd (II) on chitosan-silica hybrid aerogel from aqueous solution. *Environmental Technology & Innovation* 14: 100337.

[10] Al-Malack, M.H., Dauda, M. (2017). Competitive adsorption of cadmium and phenol on activated carbon produced from municipal sludge. *Journal of Environmental Chemical Engineering* 5: 2718-2729.

Instability of FFLO states in multiply connected superconductor-ferromagnet hybrid geometry

Noppasin Chamnan

Department of Physics, Faculty of Science, Burapha University, Chonburi, 20131, Thailand

e-mail: noppasinchamnan@gmail.com

Abstract

We study the instability of the Fulde‐Ferrell‐Larkin‐Ovchinnikov (FFLO) states in multiply connected hybrid superconductor‐ferromagnet structures that consist of a ferromagnetic core surrounded by a superconducting shell within the framework of linearized Usadel equations. The Little‐Parks (LP) effect is a phenomenon that displays the oscillations of the superconducting critical temperature Tc as the fluxoid varies, in the presence of an axial magnetic field applied to the proximity system. The FFLO states are the typical inhomogeneous superconducting states which represented by a modulation wavevector along the cylinder axis in our model. Examining such states through the LP effect using the Usadel equations to calculate the Tc formula in the thin-walled superconducting shell condition allow us to analyse their possibilities to exist in the system.

Keywords: Little-Parks (LP) effect; FFLO states; Critical temperature; Exchange interaction

References

Krunavakarn, B. (2016). Little–Parks effect in proximity superconductor-ferromagnet coaxial cylinders. *Physica C: Superconductivity and its Applications, 527*, 63-67.

Samokhvalov, A. (2017). Screening properties of multiply connected ferromagnet–superconductor hybrid structures. *Journal of Experimental and Theoretical Physics, 125*(2), 298-309.

Samokhvalov, A., Mel'nikov, A., Ader, J.-P., & Buzdin, A. I. (2009). Little-Parks oscillations in hybrid ferromagnet–superconductor systems. *Physical Review B, 79*(17), 174502.

Facile Synthesis of g-C$_3$N$_4$ modified Bi$_2$MoO$_6$ Nanocomposite with

Improved Photoelectronic Behaviors

Lei Zhu[1†], Jia-Yao Tang[1], Jia-Yi Fan[1], Chen-Sun[1], Ya-Xuan Tang[1], Shi-Yu Lu[1], Heng-Yang Zhu[1], Won-Chun Oh[2†]

[1]Key Laboratory for Advanced Technology in Environmental Protection of Jiangsu Province, Yancheng Institute of Technology, Yancheng, 224051, P.R. China
[2]Department of Advanced Materials Science & Engineering, Hanseo University, Seosan 31962, Republic of Korea

Abstract

Herein a series of g-C$_3$N$_4$ modified Bi$_2$MoO$_6$ nanocomposites using Bi$_2$MoO$_6$ and melamine as original materials were fabricated via sintering process. The as-prepared g-C$_3$N$_4$/Bi$_2$MoO$_6$ composites (BMC 5-9) are selected and investigated by SEM analysis, which inhibits special morphology consisting of Bi$_2$MoO$_6$ nanoparticle and some g-C$_3$N$_4$ nanosheet. The introduction of small sized g-C$_3$N$_4$ nanosheet in sample BMC 9 was effective to improve the charge separation and transfer efficiency, resulting in the enhancing the photoelectric behavior of Bi$_2$MoO$_6$. The improved photoelectrochemical (PEC) properties of the g-C$_3$N$_4$/Bi$_2$MoO$_6$ may attribute to enhanced charge separation efficiency, photocurrent stability and fast electrons transport pathways for some energy applications.

Key words: Bi$_2$MoO$_6$, g-C$_3$N$_4$, charge separation, photoelectrochemical property.
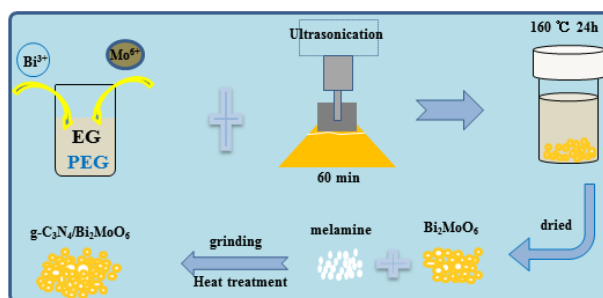
Schematic 1. Facile fabrication process for g-C$_3$N$_4$/Bi$_2$MoO$_6$ nanocomposite.

Rapid screening of formaldehyde in food using spectrophotometric assay

Yanisa Thepchuay, Wannisa Chairit, Naengnoi Saengsane,
Paweena Porrawatkul, Rungnapa Pimsen[*]

Nanomaterials Chemistry Research Unit, Department of Chemistry, Faculty of Science
and Technology, Nakhon Si Thammarat Rajabhat University, Nakhon Si Thammarat 80280, Thailand.
*e-mail: rungnapa_pim@nstru.ac.th

Abstract

We present a colorimetric approach for the rapid detection of formaldehyde in food samples. The detection was relied on the reaction of formaldehyde with excess hydrogen peroxide in alkaline media to produce formic acid which causes a bromothymol blue indicator to change color from blue to yellow. A change of indicator color can be detected by a UV-Vis spectrophotometer or even by the naked eye. Under the optimal parameters, a linear calibration graph in the range of 0.1 – 150 ppb was obtained with a correlation coefficient (r^2) of 0.9907. The LOD and LOQ were found to be 0.18 and 0.60 ppb, respectively. Moreover, the total analysis process can be completed within five minutes. The developed method validated against a commercial formalin test kit also shows similar formaldehyde contents between them, indicating a high degree of accuracy of the developed method. This demonstrates that the proposed method could be a promising tool for rapid, inexpensive, and point-of-use screening of formaldehyde in food samples.

Keywords: Rapid screening; Formaldehyde; Food sample; Bromothymol blue

References

Noor Aini, B., Siddiquee, S., & Ampon, K. (2016). Development of Formaldehyde Biosensor for Determination of Formalin in Fish Samples; Malabar Red Snapper (Lutjanus malabaricus) and Longtail Tuna (Thunnus tonggol). *Biosensors, 6*(3), 32.

Yasri, N., Seddik, H., & Mosallb, M. (2015). Spectrophotometric determination of formaldehyde based on the telomerization reaction of tryptamine. *Arabian Journal of Chemistry, Arabian J Chem, 2015*, 487–494.

Highly stable and active PtP$_2$-based electrocatalyst for oxygen reduction in high temperature polymer electrolyte membrane fuel cell

Jeong-Hoon Yu, Jong-Sung Yu[*]

Department of Energy Science and Engineering, Daegu Gyongbuk Institute of Science & Technology (DGIST), Daegu 42988, Republic of Korea
Email: jsyu@dgist.ac.kr

Abstract

Platinum (Pt) is known to be the best and most effective electrocatalyst for the oxygen reduction reaction (ORR). However, given its high surface energy, it tends to lose its excellent catalytic activity after an unacceptably short period of usage. The stability of Pt has always been a bottleneck in commercializing the polymer electrolyte membrane fuel cell (PEMFC) technology. In high temperature-polymer electrolyte membrane fuel cells (HT-PEMFC), the activity loss has been traced back to the chemisorption of phosphate anions, irreversibly poisoning the active sites. Herein, we present an alternative platinum phosphide-based (PtP$_2$/C) electrocatalyst for the application under high temperature conditions. The prepared PtP$_2$/C catalyst shows surprisingly excellent long-time stability and catalytic activity in phosphoric acid. The improved stability is shown to be the product of lower adsorption strength of PtP$_2$ compared to Pt and better oxidation resistance of the carbon support in the presence of PtP$_2$.

Fabrication of Ag/ZnO coated on cotton fabric with improved UV protection and antibacterial activity using *Caulerpa racemosa* extract as reducing agent

Paweena Porrawatkul[1], Montakarn Thongsom[2], Prawit Nuengmatcha[1*]

[1]Nanomaterials Chemistry Research Unit, Department of Chemistry, [2]Department of Biology, Faculty of Science and Technology, Nakhon Si Thammarat Rajabhat University, 80280, Thailand.

*Corresponding author. e-mail: pnuengmatcha@gmail.com; Tel. +66-7537-7443, Fax +66-7537-7443

Abstract

Recent years have observed the explosive progress of functional materials, which are made by padding various metal oxides onto fabrics. Here, the fabrication of the multifunctional Ag/ZnO coated on cotton fabrics is demonstrated using Caulerpa racemosa extract as reducing agent. The Ag/ZnO nanoparticles were subjected to X-ray diffraction, scanning electron microscope and energy-dispersive X-ray spectroscopy to ascertain its structure/morphology. The synthesized Ag/ZnO NPs has spherical particles and good dispersed on cotton fiber. The modified cotton fabric coated Ag/ZnO NPs more excellent inhibited Gram-negative bacterium and Gram-positive bacterium than uncoated cotton fabric. The UV reflectivity of Ag/ZnO cotton fabric is higher than the raw fabric and UPF value of treated fabric was 29. These results suggest that the modified cotton fabrics may find potential applications in a wide variety of areas such as sports wears, socks, and medical textiles.

Keywords: UV protection, Antibacterial activity, *Caulerpa racemosa*, Cotton fabric

Introduction

Cotton fibers are the most extensively used natural fibers for the manufacturing of comfortable textiles and garments due to its great qualities such as flexibility, comfortability, water absorption, and air permeability. Initial research on functionalized cotton fibers enhanced with nanoparticles widened the range of applications for cotton garments [1-5]. Due to the advantages of ZnO nanoparticles, such as UV-shielding, antibacterial activity, biocompatibility, biodegradability, and biosafety for environmental applications, the use of ZnO nanoparticles to textiles has gotten a lot of interest [6]. Several investigations have been carried out to boost ZnO's antibacterial efficacy by combining various metal dopants with other metal ions and other repulsive agents. There are no publications on the thermal, UV protection, photocatalytic, or antibacterial capabilities of Ag/ZnO nanoparticles produced with biosurfactants, based on the information above [7-8].

Normally, synthesis of metal oxide nanomaterials can be recognized by various methods such as hydrothermal, thermal decomposition, microwave assisted, co-precipitation, ultrasonic synthesis, electrochemical and sol-gel methods [9–11]. Toxic chemicals and solvents are used in all of these processes, which are detrimental to human health and the environment. Green synthesis composites of Ag/ZnO NPs, particularly those made using plants, have recently gotten a lot of attention because of their eco-friendly, low-cost, and simple synthesis techniques. Flavonoids, alkaloids, carotenoids, terpenoids, and tannins are among the chemical compounds found in plants. For the manufacture of Ag/ZnO NPs, the presence of these chemical compositions in plants can be exploited as a reducing and capping agent [12].

In this research, we interested to study in bio-synthesis of Ag/ZnO NPs by using the ethanoic *Caulerpa racemose* extract as reducing agent, because *Caulerpa racemosa* showed the potential antibacterial activity against pathogenic skin bacteria such as *Staphylococcus aureus*, *Staphylococcus epidermidis* and *Pseudomonas aeruginosa*. In the Southeast Asian, *Caulerpa racemosa* is green seaweed that is spread widely throughout tropical regions along in the Andaman coastal area such as Trang, Satun, Krabi and Pang-nga province, Thailand. Normally, *Caulerpa racemosa* was usually used as food [13]. In this work, antibacterial cotton textile with a Ag/ZnO NPs was successively prepared by applying *Caulerpa racemosa* onto cotton fiber surface under microwave irradiation. The antibacterial activity of Ag/ZnO nanofluids and modified cotton fabric were tested against *S. aureus* and *E. coli* via agar-well diffusion method. Furthermore, the UV protection of modified cotton fabric was investigated and measured in ultraviolet protection factor (UPF).

Materials and methods

Caulerpa racemosa was collected in Thailand's Trang province's Had-Sam-Ran district. All of the analytical reagents used in this study were purchased from Merck and were of analytical quality. Hi-Media, Mumbai, India, provided nutrient agar for bacterial growth and Mueller–Hinton broth and agar for antimicrobial activity.

Collection of seaweeds

Caulerpa racemosa was collected in Thailand's Trang province's Had-Sam-Ran district. The seaweed was thoroughly cleansed with seawater to remove all contaminates and inessential debris. The samples were then completely rinsed with tap water, followed by 95 percent ethanol solvent, and kept under a sunshade until dry, before being dried in an oven at 50 degrees Celsius for 8 hours and powdered with a mixer grinder.

Synthesis of zinc oxide nanoparticles (ZnO NPs) and silver doping zinc oxide nanoparticles (Ag/ZnO NPs)

2.5 grams of dried *Caulerpa racemosa* were combined with 25 milliliters of 95 percent ethanol. The solution was heated to 50 degrees Celsius for 30 minutes before being filtered through Whatman filter paper no. 1. The ZnO NPs were made from freshly processed Caulerpa racemosa extract. After that, a magnetic hot plate was used to keep a 0.1 M 50 mL zinc acetate hexahydrate solution at 80 °C for 20 minutes. It was then given 5 mL of newly produced extract and agitated for 10 minutes. Dropwise additions of 2 M NaOH were used to alter the pH of the reaction mixture until the pH reached 12. After The colorless solution became white. Microwave irradiation at 600 W was used for 12 minutes to incubate the resulting sample. ZnO NPs were centrifuged for 10 minutes at 10,000 rpm and then washed twice with deionized water and 95 percent ethanol. Ag/ZnO NP production is nearly identical to that of ZnO NPs. In this case, however, the incubated solution included silver nitrate and zinc acetate hexahydrate.

Characterization of zinc oxide nanoparticles (ZnO NPs) and silver doping zinc oxide nanoparticles (Ag/ZnO NPs)

The production of ZnO NPs and Ag/ZnO NPs processes were studied using visual observation. The maximum absorbance of surface Plasmon resonance peaks of ZnO NPs and Ag/ZnO NPs was measured using UV–Visible Spectrophotometry in the 300–700 nm range. SEM (Scanning electron microscope), XRD (X-Ray Diffractometer), and EDX (Energy Dispersive X-Ray Diffractometer) were used to investigate their structure and content (Energy-dispersive X-ray spectroscopy).

Coating of Ag/ZnO NPs on cotton fabrics

Surface micro-dissolution and in situ synthesis of nanoscale Ag/ZnO on the surface of cotton fabrics were used to create Ag/ZnO NPs coated cotton fabrics. 1 g of Ag/ZnO NPs was dissolved in 50 mL of chitosan solution (2 g of chitosan in 100 mL of 2 percent acetic acid) and agitated at room temperature for 30 minutes with a magnetic stirrer. To promote the dispersion of Ag/ZnO NPs particles in the solution, the mixture was sonicated for 30 minutes. Approximately 4 g of bio-scoured cotton fabric was submerged in Ag/ZnO NPs in chitosan solution for 30 minutes before being padded in the padding mangle and squeezed between two squeezing rollers for an 80 percent wet pick-up. The padded fabric was dried for 10 minutes at 70°C and then cured for 10 minutes at 120°C. The cured cloth was thoroughly washed in a 1% sodium hydroxide solution, neutralized with 1% acetic acid, washed again, and air-dried.

Antibacterial activity assessment

Antimicrobial activity of cotton fabrics was tested. Using the agar well diffusion method, the antibacterial activity of the *Caulerpa racemosa* extract and modified cotton fabric was determined against S. aureus and E. coli. With the help of a sterile cotton swab, the bacteria culture was evenly disseminated on the nutrient agar plate. On agar plates, wells were drilled. Antibiotic discs (chloramphenicol) were placed in these wells as a control. The diameter of the inhibition zones surrounding samples was measured and compared to the diameter of the inhibition zones around the commercial standard antibiotic chloramphenicol and ethanoic extract after incubation at 37 °C for 24 hours.

UV light protection measurement

UV light responses of treated and untreated cotton fabrics were examined utilizing UV-Vis spectroscopy for UV light protection evaluation. UV absorption and transmission were measured to determine the effectiveness of the UV shielding. According to formulae, the transmission data was utilized to compute the ultraviolet protection factor (UPF) and the % of UV transmission. The UPF is the ratio of the computed average effective irradiance for skin to the calculated average UV irradiation for skin shielded by the investigation fabric. It was estimated using the UV region's mean % transmission (280–400 nm).

$$UPF = \frac{\sum_{280}^{400} E_\lambda S_\lambda \Delta_\lambda}{\sum_{280}^{400} E_\lambda S_\lambda T_\lambda \Delta_\lambda}$$

where E_λ is the relative erythemal spectral effectiveness, S_λ is the solar spectral irradiance in W m^{-2} nm^{-1}, and T_λ is the UV spectrometric spectral transmission specimen E_λ and S_λ were taken from a database maintained by the National Oceanic and Atmospheric Administration.

Result and discussion

Synthesis of ZnO nanoparticles

Zinc oxide nanoparticles were previously made from Caulerpa racemosa ethanolic extract, which was obtained from healthy plants and contains phytochemical elements such as alkaloids, tannins, saponins, phenols, glycosides, steroids, terpenoids, and flavonoids. The hue of the reaction mixture changed from light yellow-green to white after adding ethanolic Caulerpa racemosa extract to zinc nitrate solution under alkalinity conditions. The color shift is caused by the activation of surface plasmon resonance in metal nanoparticles, indicating the production of ZnO nanoparticles, and it could be Cau's electron-rich functional groups. The hue of the reaction mixture was changed from light yellow-green to a dark brown color in the

case of Ag/ZnO produced revealed surface plasmon resonance phenomena like this. The SEM image of Ag/ZnO particles, on the other hand, revealed globular or spherical shaped particles in both dispersed and agglomerated states. As a result, the *Caulerpa racemosa* extract appears to operate as a capping and stabilizing agent for the production of ZnO NPs. Figure 1 shows the shape of ZnO NPs and Ag/ZnO NPs.

Fig. 1 Morphology of (a) ZnO NPs and (b) Ag/ZnO NPs synthesis by using *Caulerpa racemosa* extract

X-ray diffraction analysis of ZnO nanoparticles

The crystalline phase-structural information of the nanoparticles was obtained using an X-ray diffraction analysis. The XRD pattern of ZnO NPs produced at pH 12 is shown in Figure 2. The production of strong peaks at diffraction angles of 31.69°, 34.35°, 36.18°, 47.56°, 56.54°, 63.00°, 68.05°, and 77.04°, corresponding to (100), (002), (101), (102), (110), (103), (200), and (202) planes, respectively, demonstrates the crystalline character of ZnO NPs. The hexagonal phase of produced ZnO NPs is thought to be responsible for the peak patterns. *Caulerpa racemosa* extract produced ZnO NPs had a same lattice plane [14]. Sharp diffraction peaks in the XRD pattern indicate a high degree of crystallinity in ZnO NPs. The observed pattern matched the data on JCPDS card no. 36–1451. The pure nature of ZnO NPs was demonstrated by the absence of any random peak in the XRD pattern [15]. When compared to the JCPDS number 040783 values, three additional peaks in Ag-ZnO NPs with 2q values of 38.09, 44.38, and 64.51, respectively, imply face-centered cubic of Ag. The additional dopant peaks reflect elemental Ag growth in the ZnO lattice, and the peak's intensity is always determined by the Ag concentration used in the experiments. The majority of the peaks were lowered in dopant, indicating a reduction in the element's structural property due to generation flaws generated by Ag ions during doping. There was also no evidence of any other impurity peaks.

SEM image and EDX analysis

Scanning electron microscopy was used to examine the surface morphology of ZnO NPs and Ag/ZnO NPs. Synthesized ZnO NPs and Ag/ZnO NPs have a spherical form in SEM pictures (Fig. 3). The EDX spectrum of ZnO NPs reveals peaks of Zn, O, and C elements, while the EDX spectrum of Ag/ZnO NPs shows peaks of Zn, O, C, and Ag elements, confirming the element composition of the obtained ZnO and Ag/ZnO NPs and confirming that they were free of impurities. The carbon 54.0 percent, oxygen 16.5 percent, and zinc 78.1 percent in these EDX patterns of ZnO NPs, and the carbon 7.3 percent, oxygen 20.3 percent, zinc 58.9%, and silver 13.4 percent in these EDX patterns of Ag/ZnO NPs. ZnO NPs and Ag/ZnO N's EDX spectrum
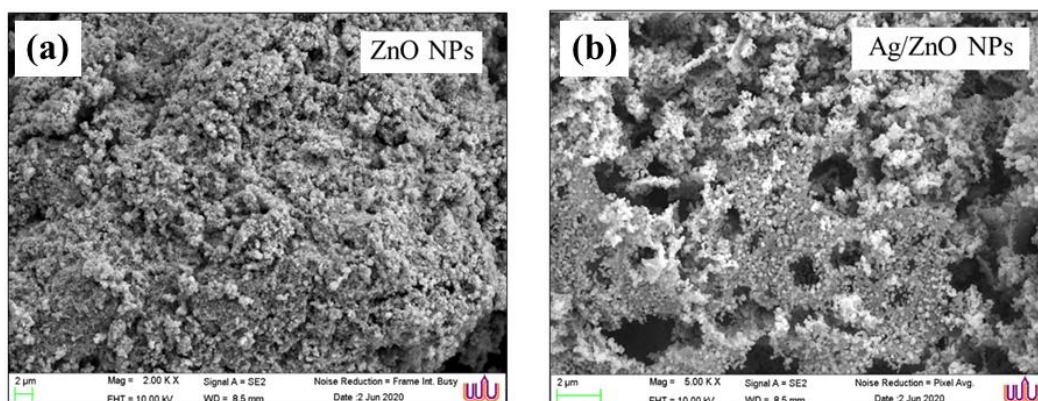
Fig. 3 (a) SEM image of ZnO NPs, (b) SEM image of Ag/ZnO NPs.

Surface morphology of the unmodified and modified fabrics

SEM was used to examine the surface morphologies of untreated cotton fabrics and cotton fabrics treated with *Caulerpa racemosa* extract capped ZnO-NPs and Ag/ZnO NPs, as shown in Fig. 4. Clearly, the surface of cotton fiber appears relatively smooth at low magnification and displays obvious grooves at high magnification in the SEM picture of the unmodified cotton fabrics (Fig. 4a). The surface morphology of cotton fabrics treated with ZnO NPs and Ag/ZnO NPs is similar to that of cotton fabrics treated with ZnO NPs (Fig. 4b). The antibacterial properties of cotton fabric were affected by the ZnO NPs that were coated on the fiber fabric. The Ag/Zno NPs are more uniformly distributed in this finding.
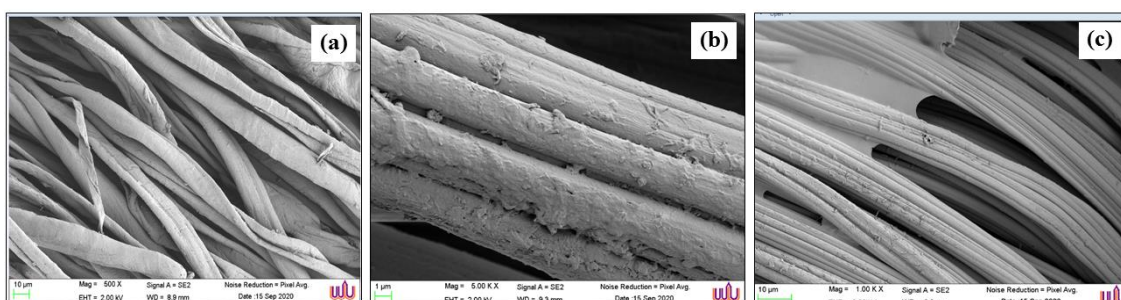
Fig. 4 SEM image of (a) unmodified fabric (b) modified fabric with ZnO NPs and (c) modified fabric with Ag/ZnO NPs

Antibacterial activities test

Staphylococcus aureus (Gram positive) and *Escherichia coli* (Gram negative) pathogens were used to test the bacterial resistance activities of *Caulerpa racemosa* extract functionalized Ag/ZnO nanoparticles. The presence of an inhibitory zone around the sample in the discs was used to assess the bactericidal action. Figure 5 depicts the results. ZnO NPs and unmodified cotton fabric had no inhibition zones (N), whereas coated cotton fabric with ZnO NPs and Ag/ZnO NPs had zones of inhibition diameter for antibacterial S. aureus and E. coli. Furthermore, Ag/ZnO NPs had a greater diameter of the inhibition zone than ZnO NPs, much as coated cotton fabric with Ag/ZnO NPs had a greater diameter of the inhibition zone than coated cotton fabric with ZnO NPs. The discrepancies in the organization of the cells and their existing functional groups can be attributed to this result. The Ag^+ ion, which binds strongly to

electron donor groups on biological molecules, is responsible for antibacterial effect of Ag. [16].

Sample	Zone inhibition diameter (mm) [mean±SD]	
	S. aureus	*E. coli*
ZnO NPs	5.6 ± 2.83	N
Ag/ZnO NPs	13 ± 2.83	11 ± 1.41
Uncoated fabric	N	N
Fabric coated ZnO	3.5 ± 0.07	N
Fabric coated Ag/ZnO	12 ± 1.25	8 ± 1.21
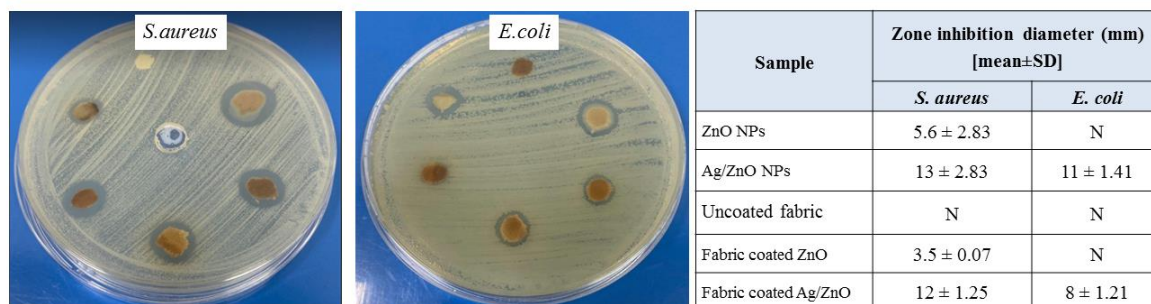
Fig. 5 Antibacterial of materials, unmodified and modified fabric.

UV radiation was effectively blocked by cotton textiles treated with Ag/ZnO NPs in both locations. The UPF rating for the control cotton fabric is 29, whereas the ZnO NPs coated cotton fabric and uncoated cotton fabrics have UPF factors of 22 and 11, respectively (Table 1). The homogeneous distribution of Ag/ZnO NPs (as observed in the SEM micrograph) and greater absorption of Ag/ZnO nanoparticles in the UV-A and UV-B regions are responsible for the improved UV protection efficiency.

Table 1. UV protection values of uncoated and coated cotton fabric

Sample	UPF value	Protection value
Uncoated fabric	11	Not considerable
Fabric coated ZnO	22	Good
Fabric coated Ag/ZnO	29	Very good

Conclusion

In conclusion, the Caulerpa racemose extract-derived Ag/ZnO NPs were successfully coated on cotton fabric to suppress bacterial growth. The modified cotton fabric had good Gram-negative (*E. coli*) and Gram-positive (*S. aureus*) bacteria inhibition while still maintaining the basic features of cotton fabric. The findings of this work could be used to create cotton textile materials with significant antibacterial characteristics for use in practical applications, such as biomedical textiles. The UV tests show that the Ag/ZnO treated fabrics have significantly improved UV absorption activity. These findings can be used to safeguard the environment.

Acknowledgements

References

[1] Li, L., Fan, T. & Hu, R. (2017). Surface micro-dissolution process for embedding carbon nanotubes on cotton fabric as a conductive textile. *Cellulose* 24: 1121–1128.

[2] Tao, F., Zhao, Z. & Jing, Z. (2018). Fabrication of magnetic cotton fabrics using surface micro-dissolving technology in ZnCl2 aqueous solution. *Cellulose* 25: 1437–1447.

[3] Hu, R., Zhao, Z. & Zhou, J. (2019). Ultrasound assisted surface micro-dissolution to embed nano TiO_2 on cotton fabrics in $ZnCl_2$ aqueous solution. *Ultrasonic Sonochemistry* 56: 160–166. https://doi.org/10.1016/j.ultsonch.2019.04.006

[4] Salat, M., Petkova, P. & Hoyo, J. (2018). Durable antimicrobial cotton textiles coated sonochemically with ZnO nanoparticles embedded in an in-situ enzymatically generated bioadhesive. *Carbohydrate Polymer* 189: 198.

[5] Thi, V.H.T., Lee, B.K. & Ngo, C.V. (2017). Durable superhydrophobic cotton filter prepared at low temperature for highly efficient hexane and water separation. *Journal Taiwan Institution of Chemistry Engineering* 71: 527–536.

[6] Ruimin, H. Jinlong, Y. Pu, Y. Ziqin, W. Hang, X. Yiping, L. & Ming, L. (2020). Fabrication of ZnO@Cotton fabric with anti-bacterial and radiation barrier properties using an economical and environmentally friendly method. *Cellulose* 27: 2901–2911. https://doi.org/10.1007/s10570-019-02965-1.

[7] Xie, X., Mao, C., Liu, X. L., Tan, Z., Cui, X., Yang, S., Zhu, Z., Li, X., Yuan, Y., Zheng, K.W.K., Yeung, P.K., Chu, S. & Wu. (2018). Tuning the bandgap of photo-sensitive polydopamine/Ag_3PO_4/graphene oxide coating for rapid, noninvasive disinfection of implants. ACS Central Science 4: 724–738.

[8] Jin, C., Liu, X., Tan, L., Cui, Z., Yang, X., Zheng, Y., Yeung, K.W.K., Chu, P.K. & Wu, S. (2018). Ag/AgBr-loaded mesoporous silica for rapid sterilization and promotion of wound healing. Biomaterials Science 6: 1735–1744.

[9] Gan, L., Shang, S., Yuen, C.W.M. & Jiang, S.X., (2015). Graphene nanoribbon coated flexibleand conductive cotton fabric. *Composites Science and Technology* 117: 208-214.

[10] Samat, N.A. & Nor, R.M. (2013). Sol–gel synthesis of zinc oxide nanoparticles using Citrus aurantifolia extracts. *Ceramics International* 39: S545–S548.

[11] M. Hasanpoor, M., Aliofkhazraei, H. & Delavari, (2015). Microwave-assisted synthesis of zinc oxide nanoparticles. *Procedia Materials Science* 11: 320–325.

[12] Noypha, A., Areerob, Y., Chanthai, S., & Nuengmatcha, P. (2021). Fe_2O_3-graphene anchored Ag nanocomposite catalyst for enhanced sonocatalytic degradation of methylene blue. *Journal of the Korean Ceramic Society* 58 (3): 297-306.

[13] Khongsai, S., Chareondat, U. & Chalad, C. (2017). The performance of Caulerpa racemosa extracts on inhibition of some pathogenic skin bacteria. *Rajamangala University of Technology Srivijaya Research Journal*. 9 (1): 68 – 75.

[14] Noah, A.Z., El Semary, M.A., Youssef, A.M. & El-Safty, M.A. (2017). Enhancement of yield point at high pressure high temperature wells by using polymer nanocomposites based on ZnO and $CaCO_3$ nanoparticles. *Egyptian Journal of Petroleum* 26: 33–40.

[15] Park, H.J., Park, S., Roh, J., Kim, S., Choi, K., Yi, J., Kim, Y. & Yoon, J. Biofilm-inactivating activity of silver nanoparticles: a comparison with silver ions. *Journal of Industrial and Engineering Chemistry*. 19 (2013) 614–619.

[16] Zhang, S., Lu, M., Li, Y., Sun, F., Yang, J., Wang, S., (2013). Synthesis and electrochemical properties of Zn_2SiO_4 nano/mesorods. *Materials Letters* 100: 89–92.

Potentiometric Titration Analysis of Cerium(IV) in Foam Decontaminant

Chong-Hun Jung*, W. K Choi, S. B. Kim, B. K. Seo

Decommissioning Technology Research Division, Korea Atomic Energy Research Institute,
11, Daedeok-daero 989 beon-gil, Yuseong-gu, Daejeon, 34057,Korea
*Corresponding author:E-mail:nchjung@kaeri.re.kr

Abstract

A nanoparticle-based foam decontaminant is composed of a surfactant and nanoparticles for the generation and maintenance of foam, and a chemical decontamination agent made of Cerium(IV) dissolved in nitric acid. Ce(IV) will be reduced to Ce(III) through the decontamination process. Oxidizing the cerium (III) can be reused as a decontamination agent, Ce(IV). Oxidation treatment technology by ozone using its strong oxidizing power, can be regarded as an environmentally friendly process. A concentration analysis of Ce(IV) in foam decontaminant containing a surfactant is necessary prior to the derivation of optimal conditions for the regeneration of Ce(III) through ozonation treatment.

A traditional UV spectrometric method has a problem receiving the influence of the surfactant, and a potentiometric method is difficult to use because of the problem of an insignificant change in the potential difference value of the Ce(III)/Ce(IV). Thus, the study was undertaken to determine whether the potentiometric titration method using Fe (II) can be used for an analysis of the Ce(IV) concentration in the nanoparticle-based foam decontaminant containing surfactant. The potential change value was measured in a surfactant concentration range of 0.5 to 1.5% in order to search whether the potentiometric titration method is valid for an analysis of Ce(IV) concentration in nanoparticle-based foam decontaminant containing TBS surfactant.

Potentiometric titration with Fe(II) was able to effectively analyze the concentration of Ce(IV) in the nanoparticle-based foam decontaminant containing surfactant regenerated through ozonation treatment. Also it was confirmed that a Ce(IV) concentration analysis is valid by this potentiometric titration method since it exhibits the same behavior in the different acid medium. Therefore, it will be effectively used for the Ce(IV) concentration measurement, in relation to the subsequent study on the derivation of optimal conditions for the regeneration of Ce(III) through ozonation treatment.

Key words: Decontamination, Cerium, Potentiometic titration, Foam

Novel synthesis of nano needle-like Cu$_2$O-GO-TiO$_2$ and CuO-GO-TiO$_2$ for the high photocatalytic performance of anionic and cationic pollutants

Jingjing Zhao[1], Won-Chun Oh[2]*

[1]School of Pharmacy, North China University of Science and Technology, Tangshan 063210, Hebei, Peoples R China

[2]Department of Advanced Materials Science & Engineering, Hanseo University, Seosan-si, Chungnam 31962, Korea

Abstract

Novel nano needle-like Cu$_2$O-GO-TiO$_2$ (Cu$_2$OGT-A) and CuO–GO-TiO$_2$ (CuOGT-B) composites with superior photocatalysis were successfully synthesized via a self-assembly process at a low temperature. It was found that the use of different base sources had a great effect on the pore structure. The microporous Cu$_2$O-GO-TiO$_2$ (Cu$_2$OGT-A) was obtained by using NaOH as base source. The mesoporous CuO-GO-TiO$_2$ (CuOGT-B) was obtained by using triethylamine (TEA) as a base source. The structural and morphological characterizations of the synthesized compounds were analyzed using a series of analytical techniques. The nitrogen adsorption/desorption isotherm speculated that the CuOGT-B has a mesoporous structure. The photocatalyst showed excellent activity under visible light and was used for the photodegradation of safranine O (SO), reactive black B (RBB), and gallic acid (GA) as target anionic and cationic pollutants. The removal capacity of CuOGT-B is slightly higher than that of Cu$_2$OGT-A, and the removal rates of SO, RBB, and GA reach up to 82.91%, 81.51%, and 83.87%, respectively. The photocatalytic oxidation of SO, RBB and GA all accords with the first order kinetic equation. After five cycles of photocatalytic oxidation, the photocatalytic performance was not significantly reduced. Furthermore, the excellent morphologies of Cu$_2$OGT-A and CuOGT-B composites, e.g., needle-like structure, monodisperse, and grapheme sheets drastically improve their dispersion in solution, light harvesting, charge separation and transportation, which might do some contributions to improve their photocatalytic activities accordingly. The photocatalytic efficiency of mesoporous structure is better than that of microporous structure. The mesoporous structure reduces the transmission distance of photo-generated holes and enhances the conduction of photo-generated carriers. Mesoporous structure enhances light absorption by reducing light reflection and increasing optical transmission path. The Cu$_2$OGT-A and CuOGT-B prepared under the conditions reported herein could be promising materials in water purification.

*Corresponding author
E-mail: wc_oh@hanseo.ac.kr
Tel: +82-41-660-1337, Fax:+82-41-688-3352

Improvement of UV Protection of Indigo Textiles
with Zinc Oxide Nanoparticles

Waraporn Chuekuna, Chulaporn Peartuapu and Thitiya Sripakdee[*]

Department of Chemistry, Faculty of Science and Technology, Sakon Nakhon Rajabhat University,
47000, Thailand
*e-mail: thitiya_1020@snru.ac.th

Abstract

The objective of this research was to improve the ultraviolet protection and antibacterial properties of indigo textile with zinc oxide nanoparticles. The ZnO nanoparticles were prepared by chemical precipitation method and characterized by scanning electron microscopy (SEM) and X-ray diffraction (XRD). The result showed that it matched well with ICDD No.00-036-1451. SEM image showed the particle size of 50-150 nm. The antibacterial activity of the ZnO-coated cotton and ZnO-coated indigo textile were investigated against Gram-positive (*Staphylococcus aureus*) and Gram-negative (*Escherichia coli*) bacteria. The result indicate that coated fabric with 2% zinc oxide nanoparticles had high antibacterial activity, while the ZnO-coated indigo textile non-inhibited. A UV protection properties of the ZnO-coated indigo textile is increase according to the concentration of ZnO nanoparticles. Finally, the durability of UV protection properties was analyzed after 3 washing cycles, it was observed that the UV protection of ZnO-coated indigo textile decreased.

.

Keywords: Zinc oxide nanoparticles; Indigo textiles; modified cotton fabric; UV protection; Antibacterial activity

References

Nooriana, S.A., Hemmatinejad, N. & Navarro, Jorge A. R. (2020) Ligand modified cellulose fabrics as support of zinc oxide nanoparticles for UV protection and antimicrobial activities. *International Journal of Biological Macromolecules* 154(1): 1215-1226

Pandimurugan, R., & Thambidurai, S. (2017). UV protection and antibacterial properties of seaweed capped ZnO nanoparticles coated cotton fabrics. *International Journal of Biological Macromolecules* 105(1): 788-795.

Design and preparation of basic magnesium sulfate cement-based high-strength coral concrete

Wang Aiguo*, Chu Yingjie, Sun Daosheng, Liu Kaiwei, Ma rui, Guan Yanmei

Anhui Key Laboratory of Advanced Building Materials, Anhui Jianzhu University, Hefei Anhui, P. R. China, 230022; *Corresponding author: Wang Aiguo, E-mail: wag3134@126.com

Abstract

Crushing coral coarse aggregate into coral fine aggregate can weaken its size effect and reduce the adverse effect on concrete properties brought by the porous characteristics of coral aggregate. However, the special particle morphology and surface configuration of coral sand can also affect the grading and void ratio of coral fine aggregate, which in turn affects the workability, mechanical properties and compactness of concrete and limits the development of coral concrete. In this paper, the morphological parameters of coral sand particles in six particle size ranges from 0.075 mm-4.75 mm were firstly determined and statistically analyzed with the goal of the closest packing theory, and then the artificially crushed coral sand was sieved and directionally compounded into coral fine aggregates of different gradations to investigate the intrinsic relationship between coral sand particle gradation and concrete properties. Finally, the coral fine aggregates with suitable gradation were compounded with alkali-magnesium sulfate cement to prepare alkali-magnesium cement-based coral concrete, and the preparation parameters were optimized by response surface method. The results show that mechanical crushing of large size coral aggregate can weaken its size effect and reduce its angularity and porosity. With the decrease of coral sand particle size, the coral sand is closer to spherical shape. The reasonable particle gradation is easier to make the coral sand reach the most compact stacking state, and the optimized ratio (molar ratio of M is 8.5-9.5, sand-cement ratio is 1.1-1.3, and admixture dosing is 1.6 %-2.2 %) can make the 28d flexural and compressive strength of alkali magnesium sulfate cement-based coral concrete exceed 13MPa and 80MPa.

Keywords: Coral aggregate; Morphological parameters; Basic magnesium sulfate cement; Mechanical properties; Pore structure

Antibacterial Activity of *Nypa frutican* Vinegar-Graphene Quantum Dots Against Gram-Positive and Gram-Negative Bacteria

Nongyao Teppaya[1] and Prawit Nuengmatha[2*]

[1]Creative Innovation in Science and Technology, Faculty of Science and Technology, Nakhon Si Thammarat Rajabhat University, Nakhon Si Thammarat 80280, Thailand

[2]Nanomaterials Chemistry Research Unit, Department of Chemistry, Faculty of Science and Technology, Nakhon Si Thammarat Rajabhat University, Nakhon Si Thammarat 80280, Thailand

*Corresponding author: Tel./Fax: +66 7 5377443; E-mail ele9594218@yahoo.co.th

Abstract

Nypa frutican vinegar–graphene quantum dots (NFV-GQDs) were successfully synthesized using a pyrolysis method with *Nypa frutican* vinegar (NFV) as the precursor. All samples were characterized using ultraviolet-visible spectrophotometry (UV-Vis), scanning electron microscopy (SEM), and energy-dispersive X-ray spectroscopy (EDX). The antibacterial activities of NFV-GQDs against strains of Gram-positive bacteria (*Staphylococcus aureus*) and Gram-negative bacteria (*Escherichia coli*) were determined using the agar well diffusion method for preliminary screening, while minimum inhibitory concentration (MIC) and minimum bactericidal concentration (MBC) were determined using the broth macro-dilution method. The zones of inhibition were compared with those of citric acid–graphene quantum dots (CA-GQDs). It was observed that the inhibition zones for the diameter of the antibacterial rings of *Staphylococcus aureus* and *Escherichia coli* reached to 29.30 mm and 23.50 mm respectively. The MIC of NFV-GQDs against *S. aureus* was 6.25 mg/mL, and *E. coli* was 12.50 mg/mL, whereas the MBC of NFV-GQDs against *S. aureus* and *E. coli* were 50.00 mg/mL.

Keywords: Nipa palm vinegar; Graphene quantum dots; Antibacterial activity

Research on butt submerged arc welding technology of 09MnNiDR plate

Binquan Cao，Ye Ge，Tianhao Hu, Guotao Dong, Jing Wang *

College of Materials Science and Engineering, Anhui University of Science And Technology,
Huainan, Anhui 232001
*Corresponding author (Phone and WeChat: + 0086 (13855418833);
jingwang@aust.edu.cn)

Abstract

After entering the 21st century, China's petrochemical industry has developed rapidly, among which the manufacture of low-temperature pressure vessels for storing nitrogen, ethylene and other gases has made great progress. 09MnNiDR is a very suitable material for manufacturing low-temperature pressure vessels. Compared with the American Standard low-temperature container plate sa537cl1, the low-temperature impact requirements of 09MnNiDR produced in China are - 70 °C, both mechanical properties and application scope are better than sa537cl1. Therefore, the submerged arc welding technology of 09MnNiDR is a very worthy subject.

Through the analysis of welding parameters, this experiment selects specific submerged arc welding parameters (welding wire brand and diameter, welding current and voltage, welding speed), obtains a series of welding finished products, and then carries out process qualification tests on the welding joints: tensile test, bending test, impact test. The results of the post weld test show that the weld and the heat affected zone samples are in accordance with the process standards, and the welding parameters selected in this experiment can be used for the plate butt submerged arc welding of 09MnNiDR steel.

Keywords: 09MnNiDR steel; welding parameters; process qualification test; weld and heat affected zone

Purpose and significance

09MnNiDR is a new type of steel plate material. It is the main manufacturing material of low-temperature pressure vessel. The carbon content of this material is very low. It is a typical low-carbon alloy structural steel. The main structural composition of 09MnNiDR steel is ferrite + a small amount of pearlite. The chemical composition is shown in Table 1-1. 09MnNiDR steel has excellent strength and low temperature impact toughness due to the action of alloying elements and nickel. Compared with sa537cl1 produced in the United States, 09MnNiDR produced in China has better mechanical properties and application range [1] .

In this paper, 09MnNiDR plate is welded by submerged arc welding machine, and then the weld is observed and studied to evaluate whether the welding results obtained by the selected welding conditions meet the standards.

Table 1.1 Chemical composition of 09MnNiDR steel

-	Chemical composition (mass fraction) Wt%								
	C	Si	Mn	Ni	V	Nb	Alt	P	S
								≤	
09MnNiDR	≤0.12	0.15～0.50	1.20～1.60	0.3~0.8	—	≤0.04	≥0.020	0.020	0.008

Material selection and research route and method

09MnNiDR steel produced by Wugang is selected. Delivery status: normalizing or normalizing + tempering, quenching + tempering [2] . In this experiment, the butt submerged arc welding process of 09MnNiDR plate with plate thickness of 9mm is studied, and the reasonable welding parameters are formulated [3, 4] .Carry out submerged arc welding to obtain the samples of post welding weld and heat affected zone. Then the post weld qualification test is carried out on the obtained samples, including tensile test, bending test and impact test, to test whether these samples meet the process standards.

Introduction and advantages of submerged arc welding

The full name of submerged arc welding is automatic arc welding under flux layer or submerged arc automatic welding. Submerged arc welding is an efficient welding method, which has the following advantages: high quality weldment, strong mechanical properties and stable composition of weld, and obvious wind protection effect of slag; The production efficiency of submerged arc welding is high. Due to the shortening of the conductive length of submerged arc welding wire and the increase of current density, the deposition efficiency of welding wire and the penetration depth of arc have been significantly improved[5,6]; Submerged arc welding has a good operating environment and is not prone to accidents. See table 3-1 for submerged arc welding. parameters.

Table 3-1 Submerged arc welding parameters

Weld bead/ Welding layer	method	Filling material		welding current		arc voltage (V)	Speed (cm/min)
		Brand	diameter	Polarity	electric（A）		
1-2	SAW	H09MnNiDR /SJ208DR	Φ4	DC	550-650	30-34	50-54

Welding plate 09MnNiDR / submerged arc welding. In this submerged arc welding test, we choose 550-650a welding current, 30-34v arc voltage and 50-54cm / min welding speed.

Welding process

Prepare welding wire and flux. After decontaminating, oiling and derusting the welding wire, coil it in the welding wire coil. The flux shall be baked at 250 ℃ for more than one hour. The welding joints of workpieces shall be cleaned of oil, dirt and water[7]. The distance between the welding gun head and the workpiece shall not be less than 15mm, and the length of welding wire shall not be less than 30mm.

After the submerged arc welding machine is started, the welding wire will be automatically pulled up by the machine and then supplied in a downward direction. The welding wire and the workpiece will rub against each other to produce an arc, and the welding process can be carried out normally.

During welding, we pay attention to the changes of ammeter and voltmeter at any time and make corresponding adjustments. After welding the second layer, the water must be cooled and the voltage and current can be increased to form welding slag.

Stop welding and close the flux hopper door. Press the stop button on the submerged arc welding machine to stop the power transmission of the welding wire, but still burn the arc to fill the metal molten pool and repair welding. The welding surface must be cleaned before the second welding[8].

Post weld test and analysis

Table 5.1 Tensile test data

-	width(mm)	thickness(mm)	Tensile strength(MPa)	Fracture location and characteristics
B97-1	25	9.5	522	Plastic fracture in base metal
B97-2	25	9.6	504	Plastic fracture in base metal

Table 5.2 TTest data of bending test

-	Sample type	thickness(mm)	Bending center diameter(mm)	Bending angle (°)	result
B97-1	Lateral bending	10	40	180°	Intact without crack
B97-2	Lateral bending	10	40	180°	Intact without crack
B97-3	Lateral bending	10	40	180°	Intact without crack
B97-4	Lateral bending	10	40	180°	Intact without crack

Table 5.3 impact test data

-	Sample size	Notch type	Notch position	Test temperature (℃)	Impact absorption energy（J）	-
B97-1	10×10×55	V	weld line	-70	80	qualified
B97-2	10×10×55	V	weld line	-70	74	qualified
B97-3	10×10×55	V	weld line	-70	70	qualified
B97-4	10×10×55	V	Heat affected zone	-70	36	qualified
B97-5	10×10×55	V	Heat affected zone	-70	41	qualified
B97-6	10×10×55	V	Heat affected zone	-70	47	qualified

In the bending experiment, four specimens were under bending conditions; The side bending is 180 ° and the bending center diameter is 40mm °, and there is no crack. In the tensile test, the two samples did not break under tensile stress, the ultimate tensile strength was 500-530mpa, plastic fracture occurred, and the fracture position was located in the base metal. In the impact test, the test condition is - 70 ℃, and the six weld samples are V-notch. The impact absorption energy of weld samples b97-1, b97-2 and b97-3 are 80, 74 and 70 respectively. All the welded joints meet the standard. The corresponding impact absorption energies of heat affected zone samples b97-4, b97-5 and b97-6 are 36j, 41j and 47j respectively. The test results show that the test samples meet the standard.

Conclusion

In this experiment, the welded joint obtained from the welding of 09MnNiDR plate meets the process standard. Submerged arc welding is used as process. The welding parameters are 550-650a welding current, 30-34v arc voltage and 50-54cm / min welding speed.The toughness of welded joints can be improved by reasonably selecting the electrode diameter, controlling the thickness of single pass and avoiding welding swing as far as possible. The arc height and weld cleanliness can improve the toughness of welded joints.

References

[1] Ram G D, Mitra T K J, Raju M K, et al. Use of inoculantsto refine weld solidification structure and improve weldabliltyin type 2090Al-Li alloy [J]. Materials Science andEngineering A, 2000, 276(1): 48 57.

[2] Wang F, Han X. Influence of vibration and shock on thecrystal g rowth during solidification [J]. Journal ofMaterials Science , 2000, 35(8): 1907 1910.

[3] Alireza R, Kenji M. Effects of the intensity and frequency ofelectromag netic vibrations on the microstructural refinementof hypoeutectic Al-Si alloys [J]. Metallurgical and MaterialsTransactions A: Physical Metallurgy and Materials Science,2000, 31(3): 755 762.

[4] Sundaresan S, Janaki R G D, Madhusudhan R G.Microstructural refinement of weld fusion zones in α-βtitanium alloys using pulsed current welding [J]. MaterialsScience & Engineering A, 1999, 262(1): 88 100.

[5] Safronov I I, Leurda I A. Emission of ultrasound into theweld pool and its role during solidification [J]. Physics andChemistry of Materials Treatment, 1990, 24(4): 410 414.

[6] ZHANG Chunlei, WU Minsheng, DU Jinglei. Improvingweld quality by arc-excited ultrasonic treatment[J].Tsinghua Science and Technology , 2001, 6(5): 475 478.

[7] Inclusion behavior and microstructure of weld metal with Ce in twin wire high heat input submerged-arc welding， 2017-01-05

[8] Effect of Mn and Ni on Microstructure and Impact Toughness of Submerged Arc Weld Metals，Tianjin University，2015

MoO₃/g-C₃N₄ heterostructure for degradation of organic pollutants under visible light irradiation: high efficiency, general degradation and Z-scheme degradation mechanism

Yuanzhi Li, Changzhao Chen[*], Xinxin Chen, Jiyuan Zang

School of Mechanics and Optoelectronics Physics, Anhui University of Science and Technology,

Huainan 232001, China, Correspondence author, E-mail: czch68@163.com.

Abstract

The development of semiconductor photocatalyst with simple and controllable components, high catalytic efficiency and cycle stability as well as diversified degradation goals is important conditions for achieving large-scale commercial applications for environmental remediation. The achievement of these important performance indicators requires not only the precise modulation of the components, but also the clarification of the photocatalysis process and charge transfer mechanisms. In this work, we fabricate a heterostructured photocatalyst composed of graphite carbon nitride (g-C₃N₄) nanosheets and MoO₃ nanoparticles through a simple mixing and annealing process, which exhibits effective visible light photocatalytic activity for both rhodamine (RhB) and methyl orange (MO). In the evaluation of RhB catalytic performance, the optimized heterojunction photocatalyst achieves extremely high visible light photocatalytic performance with a small amount of catalyst (0.1g/L), characterized by nearly 100% degradation rate within 24 minutes, the kinetic constant k as high as 0.11 min^{-1}, as well as almost 100% cycle stability after four cycles. Based on the measurement of energy level positions, free radical scavenging experiment and electrochemical analysis, direct Z-scheme charge transfer is established. Electrons accumulate in g-C₃N₄ conduction band while holes remain in the MoO₃ valence band, which maintains a high redox potential and promotes effective carrier separation. Superoxide radicals and holes play a dominant role in photocatalytic degradation, and the role of hydroxyl radicals cannot be ignored.

Keywords: g-C₃N₄; MoO₃ nanoparticles; Photocatalytic; Degradation; Z-scheme
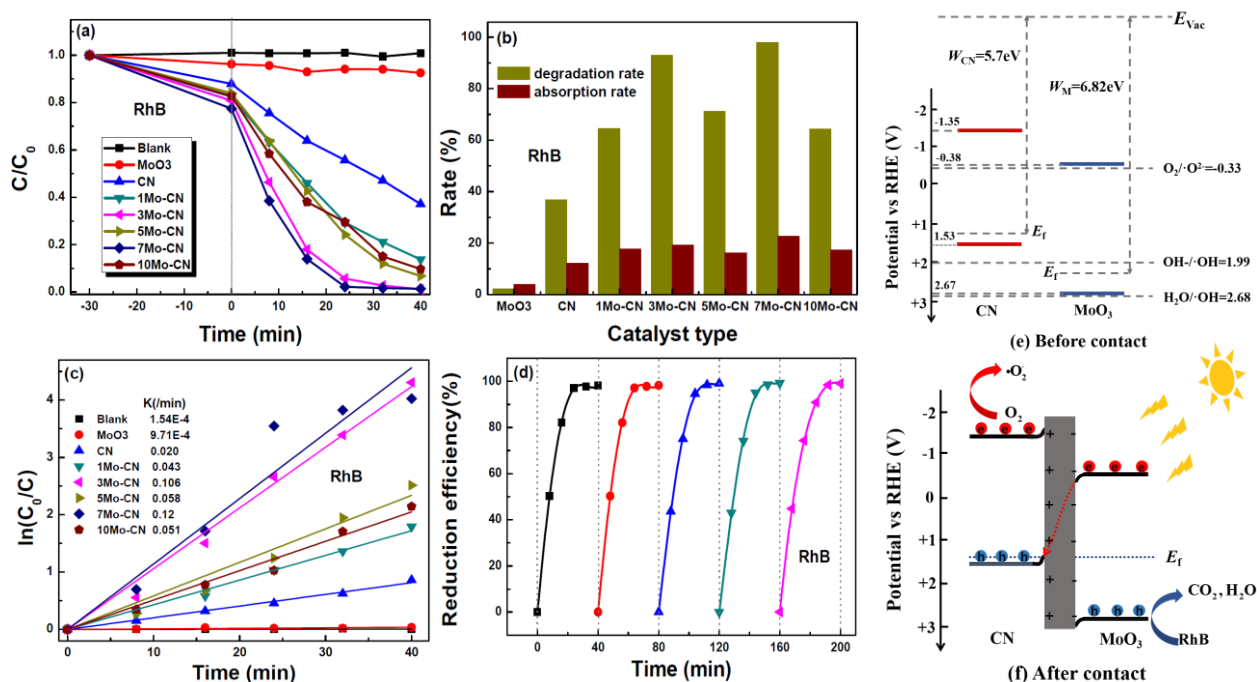
Fig.1 (a) Photodegradation curves, (b) photodegradation and adsorption histograms, and (c) the corresponding first-order kinetic plots for RhB degradation of the pure $g\text{-}C_3N_4$, MoO_3, and all $MoO_3/g\text{-}C_3N_4$ binary heterojunctions, (d) Recyclability test of 7Mo-CN degradation of RhB, (e)-(f) Brief diagram of photogenerated carriers transfer route for $MoO_3/g\text{-}C_3N_4$ heterojunction.

ZnO Bilayer Thin Film Transistors Using H$_2$O and O$_3$ as Oxidants by Atomic Layer Deposition

Xue Chen[1], and Chang Liu[2]*

[1]School of Mechanics and Optoelectronics Physics, Anhui University of Science and Technology, Huainan 232001, China
[2]Key Laboratory of Artificial Micro- and Nano-structures of Ministry of Education, and School of Physics and Technology, Wuhan University, Wuhan 430072, China.

Abstract

This work demonstrates a novel design of thin film transistors composed of a bilayer structure of ZnO thin films (O$_3$ as oxidant/H$_2$O as oxidant) prepared by atomic layer deposition. Based on this structure, a large I_{ON}/I_{OFF} ratio of 10^8 at $V_{DS} = 0.1$ V, a high field-effect mobility of 31.1 ± 0.26 cm^2 V^{-1}s^{-1}, a low threshold voltage of 0.14 ± 0.07 V and a proper subthreshold swing of 0.21 ± 0.02 V/decade as well as an excellent positive bias stress stability have been obtained. The improved performance of the bilayer structured devices is attributed to the first channel layer of ZnO (H$_2$O as oxidant) decreasing the interfacial trap density and providing high mobility, and the second channel layer of ZnO (O$_3$ as oxidant) suppressing the off-state current as well as a newly formed sub-channel at the interface between the the two channel layers.

Preparation and flame retardancy of bromine Modified Hyperbranched waterborne Polyurethane

Fen Li [1], Xiang Wang [1], Haifeng CAO [1], Jinbo ZHU [1]

[1]School of Materials, Anhui University of Science and Technology

Abstract

Firstly, hyperbranched waterborne polyurethane (WHPU) was prepared with 2, 4-toluene diisocyanate (TDI), polypropylene glycol (PPG-1000), diethanolamine (DEOA) and dihydroxymethyl propionic acid (DMPA), and then modified by dibromoneopentyl glycol. Bromine modified hyperbranched polyurethane (Br-WHPU) was obtained. Infrared characterization of WHPU was carried out. WHPU and Br-WHPU were calcined in muff furnace and their residues were tested by SEM. The oxygen index of polyester fabric was measured by Br-WHPU. The experimental results show that the infrared spectrum analysis shows the formation of hyperbranched polyurethane. The surface of carbon residue of Br-WHPU is smoother and tighter than that of WHPU. The oxygen index of polyester fabric is 19.4%, and the oxygen index of polyester fabric finished by Br-WHPU with 15% content of dibromo-neopentyl glycol is 21.2%. The bromo-modified hyperbranched water polyurethane has remarkable flame retardant effect.

Keywords: hyperbranched polyurethane, flame retardant modification, waterborne, dibromoneopentyl glycol

Introduction

Hyperbranched polyurethane is a kind of highly branched macromolecule with a large number of functional groups at the end of the branched chain, which is suitable for various modification. These excellent properties enable hyperbranched polyurethane to be used in high technology fields such as photocurable coatings, phase change energy storage materials, synthetic leather and biological materials[1-2]. Therefore, more and more attention has been paid to the study of hyperbranched waterborne polyurethane. Polyurethane material is flammable in the air, so the direct application of polyurethane material is greatly limited. Therefore, improving the flame retardant performance of polyurethane has always been a hot topic in the research of polyurethane. Brominated flame retardants have the advantages of low price, good flame retardancy, low dosage and little influence on product performance, and will remain the main flame retardants for a long time in the future.

Experimental Part

1. Raw reagent

   Toluene diisocyanate (TDI), industrial pure, Shanghai Reagent Factory; Polyether polyol (PPG-1000), industrial pure, Jiangsu Hai 'an Petrochemical Plant; Diethanolamine (DEOA), chemical pure, Sinopharm Chemical Co., LTD.; Triethylamine (TEA), chemical pure, Sinopharm Chemical Reagent Co., LTD.; Dihydroxymethylpropionic acid (DMPA), industrial pure, Beijing Lin Refined New Materials Co., LTD. Acetone, analytically pure, Yangzhou Lubao Chemical Reagent Co., LTD. Dibromoneopentyl glycol (DBNPG), chemically pure; Polyester cloth.

2. Main instruments and equipment

   Oxygen index tester, JF-3, Xi 'an Minx Testing Equipment Co., LTD. Fourier Transform infrared spectrometer, VEVTOR33, Bruck GMBH, Germany; Scanning electron microscope, S-3000N, Hitachi High-tech Nako Business Institute, Japan; Shear emulsifier, FA25, Gongyi Yuhua Instrument Co., LTD.

3. Preparation of WHPU

   A certain amount of polyether polyol (PPG), toluene diisocyanate and 2,2 dihydroxyacetic acid (DMPA) were poured into a four-way flask and reacted at 80℃ for 3h. Diethanolamine was added into the flask for a period of time at -5℃. The temperature was raised and the reaction continued for 3h.

4. Preparation of Br-WHPU

   Dibromoneopentyl glycol was added into the WHPU in proper proportion, and then Br-WHPU was prepared by cutting and stirring with emulsified shear machine.

5. Performance Test

   5.1   Determination of WHPU by INFRARED spectroscopy

      WHPU is repeatedly cleaned with cyclohexane and acetone to obtain a polymer solid and then dissolved with acetone. Determination by Fourier transform infrared spectrometer.

   5.2   SEM determination of carbon residue

      Appropriate amounts of WHPU and Br-WHPU were calcined in muffle furnace under air atmosphere, and the residues were tested by SEM at 500℃. The electron beam energy was 15keV, the sample was fixed with conductive tape, and the sample was sprayed with gold before scanning.

   5.3   Oxygen index test

      The oxygen index of polyester fabric was measured by Br-WHPU.

Results and analysis

1. **Infrared analysis of hyperbranched waterborne polyurethane**

   Figure 1 is the infrared spectrum of WHPU membrane.
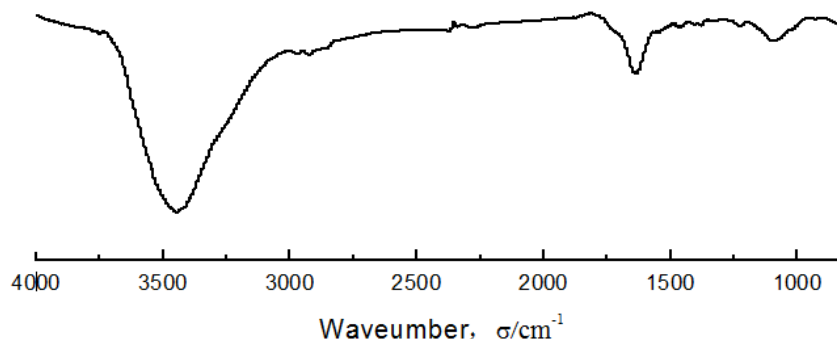
Figure 1. infrared spectrum of WHPU

In Figure 1, 3300cm^{-1} is the n-H stretching vibration absorption peak in carbamate bond, 2972cm^{-1} is the asymmetric stretching vibration peak of methyl, 2272cm^{-1} isocyanate-NCO antisymmetric stretching vibration peak, 1372cm^{-1} is the symmetric stretching vibration peak of -NCO. 1712cm^{-1} is the absorption peak of carboxyl group in carbamate, 1600cm^{-1} is the absorption peak of stretching vibration of benzene ring skeleton, 1538cm^{-1} is the deformation vibration peak of N-H in -NH-CO-, 1412cm^{-1} is the in-plane bending vibration of C-OH in C(O)-OH. The stretching vibration peak of C-O-C in 1222cm^{-1} ammonia ester group, and the absorption peak of tertiary amine group at 1600cm^{-1}. The peak at 1620cm-1-1640cm^{-1}, which should be the amide peak, indicates the formation of hyperbranched structure.

2. **SEM analysis of carbon residue**

   The SEM of carbon residue of WHPU is shown in Figure 2.
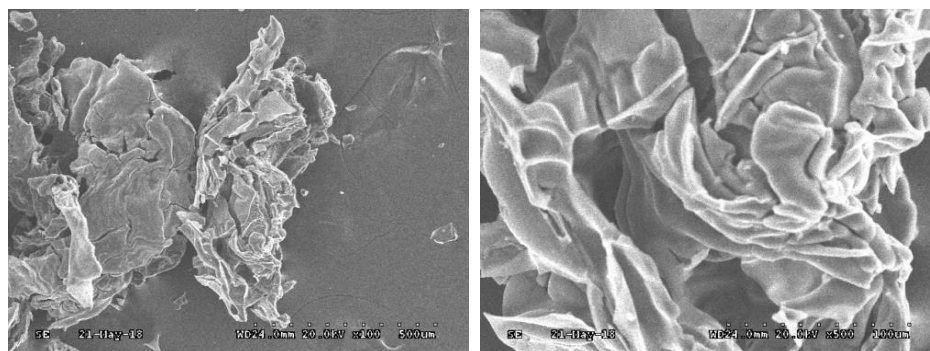
(a) 200 times   (b) 500 times

Figure 2. SEM of WHPU carbon residue

According to Figure 2, it can be seen that the surface of blank hyperbranched waterborne polyurethane is not smooth and full of many honeycomb pores. It shows that during combustion, not only will a lot of oxygen come in, but also a lot of combustion gas will be released during combustion, so it is not conducive to flame retardant.

The Br-WHPU with 15% dibromoneopentyl glycol content was burned, and the SEM of its carbon residue was shown in Figure 3.

(a) 200 times   (b) 500 times
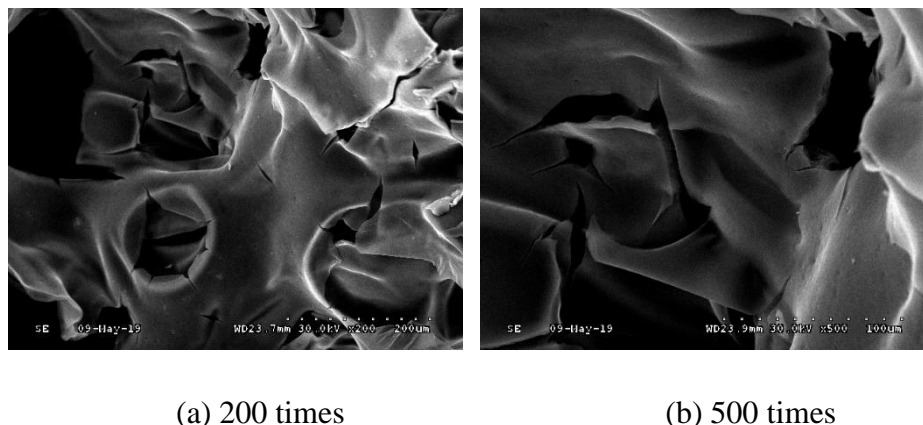
Figure 3.   SEM of Br-WHPU carbon residue

As can be seen from figure 3, the carbon layer formed after combustion of Br-WHPU is complete, with large and uniform particles. From Figure 3(a), the formation of carbon layer can be seen more intuitively in the figure. The structure is complete, very continuous, smooth and with few voids. As the carbon accumulates, a smooth, uniform, dense and complete carbon layer is formed. Such a carbon layer can act as a good protective layer, not only playing the role of heat insulation, but also can prevent oxygen from entering and the release of combustible gas inside the material, so as to achieve the purpose of stopping combustion.

3.   The LOI analysis

The oxygen index of polyester cloth treated with Br-WHPU was tested, and the data are shown in the following table:

Table 1   Oxygen index values of polyester fabrics treated with Br-WHPU

Dibromoneopentyl glycol/%	0	5	10	15	20
LOI	19.4%	20.2%	20.8%	21.2%	21.4%

It is generally believed that the material whose oxygen index is lower than 22 is flammable, the material whose oxygen index is between 22 and 28 is combustible, and the material whose oxygen index is greater than 28 is non-combustible. It can be seen from Table 1 that the oxygen index of polyester fabric is 19.4, which is less than 22, and is flammable. With the increase of the proportion of dibromoneopentyl glycol, the oxygen index value of treated polyester cloth increases gradually, which increases the flame retardant property of polyester.

Conclusion

(1) Hyperbranched waterborne polyurethane was synthesized from toluene 2, 4-diisocyanate (TDI) and polypropanediol (PPG-1000), 2, 2-dimethylpropionic acid (DMPA) as hydrophilic chain extender, diethanolamine (DEA) as small molecule chain extender, acetone as solvent and triethylamine (TEA) as salt forming agent. Bromo-modified hyperbranched polyurethane was prepared from modified hyperbranched polyurethane using dibromo-neopentyl glycol as flame retardant.

(2) Infrared spectrum analysis showed the formation of hyperbranched polyurethane. The results of SEM showed that the carbon residue of Br-WHPU was smoother and tighter than that of WHPU. When the content of dibromoneopentanediol is 15%, the oxygen index of the polyester fabric finished by Br-WHPU is 21.2%. The Br-WHPU can effectively play the role of flame retardant.

References

[1] LanqingFang, Tingtian Qiu, QuanYang,et al. A novel hyperbranched polyurethane/ nTiO$_2$ waterborne sizing agent for improving UV-resistance and interfacial properties of SCF/PA6 composites. Composites Communications,2021,23:1-5.

[2] Reihaneh Farajollah, Mir MohammadAlavi Nikje, EbrahimSaadat, et al. Star-hyperbranched waterborne polyurethane based on D-glucose-poly(ε-caprolactone) core as a biomaterial candidate. European Polymer Journal, 2021,147:1-5.

Synthesis and characterization of porous MXene Ti_3C_2Tx with high microwave absorption properties

Chongmei Wu, Zhenying Liu, Yan Wang, Guiyang Xian, Yin Liu*

School of Materials Science and Engineering, Anhui University of Science and Technology, Huainan 232001, Anhui, China, *Corresponding authors: yinliu@aust.edu.cn (Yin Liu)

Abstract

The increasingly serious electromagnetic pollution urgently requires the development of light and strong absorption of electromagnetic wave absorber. Therefore, in this work, the modified LiF-HCl method and freeze-drying technology were used to prepare porous MXene Ti_3C_2Tx, and XRD and SEM respectively characterized the phase and microstructure of MXene Ti_3C_2Tx. The microwave absorption properties of MXene Ti_3C_2Tx were measured by a vector network analyzer. The results showed that the minimum reflection loss (RL) of MXene Ti_3C_2Tx was -43.93 dB, the frequency bandwidth was 3.04 GHz, and the thickness was only 2.1 mm, which provides a reference for the preparation of other efficient MXene-based absorbing materials.

Keywords: MXene Ti_3C_2Tx; freeze-drying; microwave absorption

Introduction

With the rapid development of wireless communication and electronic equipment in recent years, electromagnetic pollution is increasingly serious[1, 2]. Therefore, electromagnetic absorption materials have been widely concerned due to their ability to convert electromagnetic energy into heat energy[3]. However, traditional electromagnetic wave absorbing materials such as ferrite, carbonyl iron[4] and metal oxide are limited in microwave absorption applications due to their high density and high filling ratio. Therefore, it is urgent to develop new absorbing materials with light weight and strong absorption capacity. Herein, in this study, Ti_3AlC_2 was used as raw material to prepare the popular new two-dimensional MXene material by modified LiF-HCl etching method in recent years. Then the porous shape MXene Ti_3C_2Tx was synthesized by simple freeze-drying technology. The results of vector network analyzer measurement and Matlab simulation showed that MXene Ti_3C_2Tx with porous structure had excellent microwave absorption performance.

Experimental

First, 1 g LiF was added to 40 mL 9 M HCl and stirred for 2 h. After LiF was fully reacted, 1 gTi_3AlC_2 was added to the above solution and reacted at 45 °C for 32 h. Then, centrifuged with deionized water at 3500 rpm for 5 min until the pH value was close to 6-7. Finally, put the black precipitate into a freezing drying oven at -80 °C for 24 h.

Results and discussion

1. Phase and morphology of MXene Ti_3C_2Tx

It can be observed from Fig.1a that the strong diffraction peak of Ti_3AlC_2 at 39° disappears and the peak at 9.59° moves to a lower peak (6.24°), indicating that Al atom was etched successfully and Ti_3C_2Tx was formed[5]. In Fig.1b, it can be observed that porous MXene Ti3C2Tx is obtained after etching and freeze drying, which made the prepared MXene lighter and enlarged the specific surface area, which was conducive to multiple dissipation of electromagnetic wave energy.
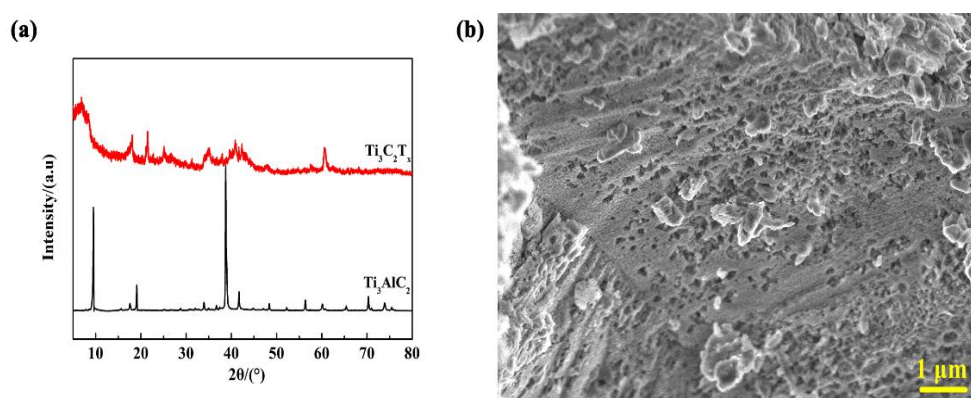
Fig.1(a) and (b) XRD and SEM images of Ti3C2Tx

2. Microwave absorption property

Microwave absorption performance was usually evaluated by the value of RL. When the value of RL is below -10 dB, the corresponding frequency range is the effective absorption bandwidth (EAB), indicating that more than 90% of the electromagnetic wave is absorbed. In Fig.2a, the prepared MXene Ti_3C_2Tx has an excellent RLmin of -40.93 dB at 10.8 GHz, the EAB of 3.04 GHz (9.2-12.24 GHz), and a thickness of only 2.1 mm, which was attributed to the porous structure of MXene Ti_3C_2Tx to increase dipole polarization and specific surface area, thus improving microwave absorption performance. In addition, the relationship between RL value, frequency and thickness is revealed in Fig.2b.
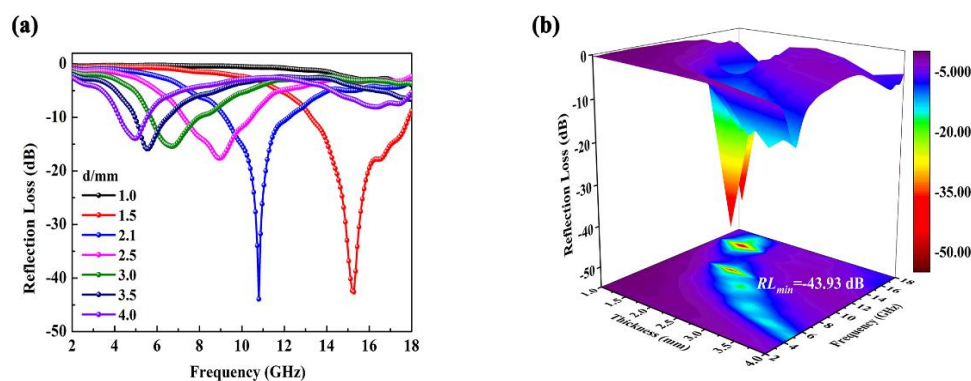
Fig.2(a) and (b) RL curve of Ti3C2Tx and 3D representation and contour mapping

Conclusions

In conclusion, porous MXene Ti3C2Tx has been successfully prepared by simple freeze-drying technology, and MXene Ti3C2Tx with this structure had rich specific surface area. It can produce a large amount of dipole polarization, thus enhancing microwave absorption performance. The results showed that the RLmin of porous MXene Ti3C2Tx was -40.93 dB, and the thickness was only 2.1 mm. Herein, this study provides a way for the preparation of other MXene-based porous microwave absorption materials.

Acknowledgements

References
[1] G. Cui, L. Wang, L. Li, W. Xie, G. Gu, Synthesis of CuS nanoparticles decorated Ti3C2Tx MXene with enhanced microwave absorption performance, Progress in Natural Science: Materials International, 30 (2020) 343-351.
[2] G. Cui, X. Zheng, X. Lv, Q. Jia, W. Xie, G. Gu, Synthesis and microwave absorption of Ti3C2Tx MXene with diverse reactant concentration, reaction time, and reaction temperature, Ceramics International, 45 (2019) 23600-23610.
[3] H. Wu, M. Qin, L. Zhang, NiCo2O4 constructed by different dimensions of building blocks with superior electromagnetic wave absorption performance, Composites Part B: Engineering, 182 (2020) 107620.
[4] W. Dai, F. Chen, H. Luo, Y. Xiong, X. Wang, Y. Cheng, R. Gong, Synthesis of yolk-shell structured carbonyl iron@void@nitrogen doped carbon for enhanced microwave absorption performance, Journal of Alloys and Compounds, 812 (2020) 152083
[5] J. Zhang, W. Xue, X.Y. Chen, Ti3C2Tx MXenes as thin broadband absorbers, Nanotechnology, 31 (2020) 275301.

Effect of Different Modifiers on Dispersion of Nano-TiN in Organic System

Guojun Cheng [a,b,c], Feixiang Sha [a], Ziyue Xuan [a], Meng Liu [a], Longxuan Zhou [a], Shen Tian [a]

[a] School of Materials Science and Engineering, Anhui University of Science and Technology, Huainan 232001, China

[b] Institute of Environment-friendly Materials and Occupational Health of Anhui University of Science and Technology (Wuhu), Wuhu 241003, China

[c] Anhui Province Key Laboratory of Environment-friendly Polymer Materials, Anhui University, Hefei 230601, China

Corresponding author: Guojun Cheng and _chengguojun0436@126.com_

Abstract

The dispersion of nanofillers in organic system has always been a focus of attention. In this work, two kinds of modified nano-TiN were obtained by wet modification with traditional γ-methacryloyloxy propyltrimethoxysilane (CA) and macromolecular interfacial modifier styrene/acrylonitrile/γ-methacryloyloxy propyltrimethoxysilane (MCA, which was designed and synthesized based on CA in the laboratory). The dispersibility and thermal stability in organic solvents and SBR were compared. As the results of high-resolution transmission electron microscope (HRTEM) showed that TiN nanoparticles modified had better dispersibility in organic solvent and SBR matrix, especially the effect of MCA was more prominent. At the same time, the Tg of SBR was increased by nearly 7 °C due to the addition of MCA. Which were attributed to the higher effective grafting rate of MCA than that of CA.

Keyword: Titanium nitride nanomaterials, Macromolecular interfacial modifier, Surface modification, Thermal performance

Introduction

Adding nanoparticles within a certain size range as an additive to the polymer matrix at a low level of addition amount to synthesize nanocomposites is a common method to enhance the performance of the polymer matrix [1-3]. Generally, nanocomposites often exhibit better physical, mechanical or thermal properties than uncomposited materials [4]. During the past few decades, nanoparticle polymer composites have received extensive attention from many researchers in the academic and industrial fields. Many researchers have studied the effects of different nanofillers such as clay [5], graphene [6], and titanium dioxide [7] nanoparticles on the properties of different polymers.

Titanium nitride (TiN) is a relatively popular ceramic nano-material in recent years, which shows excellent corrosion resistance, abrasion resistance, heat resistance, mechanical strength and hardness [8, 9]. The surface of TiN nanoparticles adsorbs a large number of hydroxyl

groups (-OH) and amino groups (-NH2), which causes the surface weak alkaline. Previous research on nano-TiN mainly focused on using it as a coating to enhance the corrosion resistance and friction resistance of materials [10, 11]. It is worth mentioning that the weak alkalinity of the TiN surface can not only make surface modification easier and more convenient but also reduce the adverse effects of rubber vulcanization. Therefore, TiN nanoparticles as a rubber reinforcing phase may have development prospects. Using inorganic TiN nanoparticles as a new filler to reinforce rubber can reduce the need for traditional fillers (such as carbon black) as a reinforcing filler. Moreover, due to the unique surface and structural properties of TiN nanoparticles, it is expected to further improve the comprehensive performance of rubber materials and even obtain functions unavailable in traditional rubber.

Familiarly, nano fillers will agglomerate in the matrix for their high surface energy, which may affect the performance of composite materials [12, 13]. TiN nanoparticles are the same. Therefore, the TiN nanoparticles need to be modified. The existing literature indicates that the ceramic nano-powders modified by silane coupling agent may have a better dispersion in the matrix leading to better performance of the composite system [14, 15]. In this paper, the common silane coupling agent γ-(methacryloyloxy) propyltrimethoxysilane (CA) and macromolecular interfacial modifier styrene/acrylonitrile/γ-methacryloxytrimethoxysilane (MCA) synthesized in the previous work was used as modifiers to TiN nanoparticles[16]. On the one hand, the macromolecular modifier MCA retains pendant siloxane groups that can react with active hydrogen such as hydroxyl and amino groups adsorbed on the surface of TiN nanoparticles. On the other hand, the flexible long chain of macromolecular modifier has good compatibility with the styrene butadiene rubber (SBR) matrix (The formula composition is shown in Table 1.) . In our work, the effects of small molecule modifiers and macromolecular modifier on the dispersion and thermal properties of nanofillers in the organic system were investigated.

Table. 1. Basic recipes for TiN nanoparticles filled SBR composites.

Samples	SBR/ g	Sulfur/ g	SA/ g	ZnO/ g	CZ/ g	TiN-0/g	TiN-CA/g	TiN-MCA/g
R0	100	1.75	1.0	3.0	1.0	0	0	0
R1	100	1.75	1.0	3.0	1.0	2.0	0	0
R2	100	1.75	1.0	3.0	1.0	0	2.0	0
R3	100	1.75	1.0	3.0	1.0	0	0	2.0

Results and discussion

1. Dispersion of TiN nanoparticles
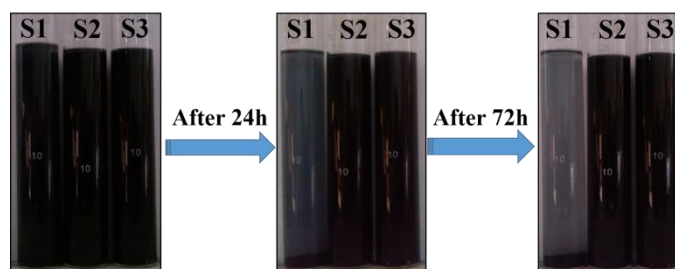
Fig 1. Photos of (S1) TiN-N, (S2) TiN-CA and (S3) TiN-MCA dispersed in ethyl acetate at different times

The dispersion stability experiment of the nano-TiN was tested by the sedimentation experiment. As shown in Fig 1, the modified nano-TiN maintained stable dispersion state in the ethyl acetate solution while the unmodified nanoparticles almost completely precipitated after 3 days. This phenomenon indicated that the addition of modifier was beneficial to the dispersibility of nano-TiN. The surface hydroxyl group (-OH) of the nanoparticle and the silanol group ($-Si-OCH_3$) of the modifier react with each other on the surface of the nano-TiN to form a complex. These anchored or grafted coupling agent molecular chains formed a certain steric hindrance, which restricted the nanoparticles from contacting with each other to form aggregates. Therefore, the modified nanoparticles can maintain a stable dispersion state in ethyl acetate for a long time. In the respect of maintaining the dispersibility of nano-TiN in ethyl acetate solution after modification, macromolecular modifiers and small molecule modifiers also have excellent effects.

2. HRTEM analysis
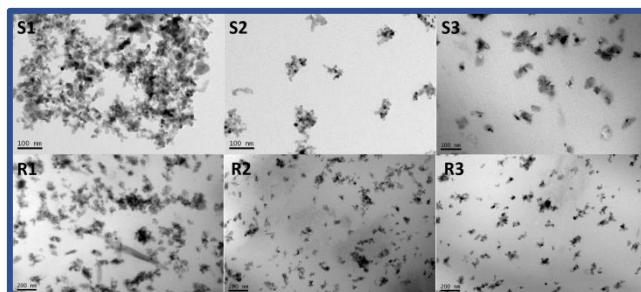
Fig 2. TEM photo of TiN nanoparticles suspended in ethyl acetate (a: TiN-0, b: TiN-CA, e: TiN-MCA).

The difference of the dispersion stability of nano-TiN in ethyl acetate organic solvent had been analyzed by sedimentation experiments. The HRTEM was used to further visually analyze the morphology and dispersion state of nano-TiN in in ethyl acetate solution. From Fig 2S1, TiN-0 nanoparticles condensed into a cluster state with a size of more than 800 nm. While, the TiN-CA and TiN-MCA nanoparticles with significantly reduced agglomeration and uniform dispersion can be clearly observed in the Fig 2S2 and 2S3. The average particle size of the modified nano-TiN was all below 100nm. It indicated that modified TiN has better dispersibility in ethyl acetate solution. The difference of the dispersion for TiN-CA and TiN-MCA is not obvious in ethyl acetate solution. The dispersion for TiN-CA and TiN-MCA in SBR were excellent as shown in Fig 2R2 and 2R3, and the effect of MCA was better.
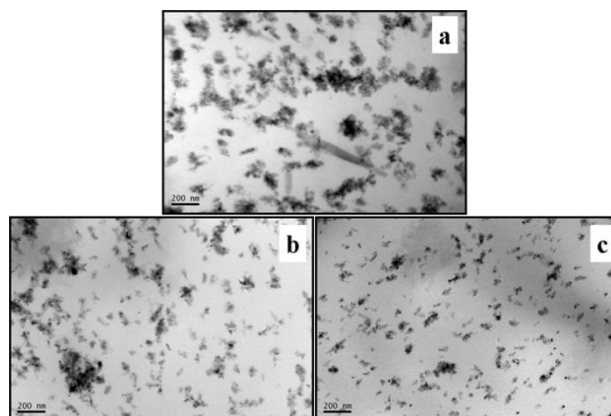
Fig 3. TEM photos of ultrathin section of TiN/SBR nanocomposites (a: TiN-0, b: TiN-CA, e: TiN-MCA).

Fig 3 showed the TEM photos of ultrathin sections of TiN-filled SBR rubber nanocomposites at a vulcanization temperature of 180 ℃ and 2 parts per hundreds of rubber (phr). From Fig 3a, the TiN-N nanoparticles agglomeration phenomenon was more obvious in SBR. While, the TiN-CA and the TiN-MCA nanoparticles can be relatively uniformly dispersed in the SBR matrix and the nanoparticles size was mostly below 200nm from Fig 3b and 3c. Besides, the TiN-MCA nanoparticles had better dispersibility in SBR. TiN-MCA nanocomposites have lower molecular interaction forces due to the larger molecular chains of MCA. Under the strong shearing of the dense mixing and double-crushing, the TiN-MCA nanoparticles tended to be more dispersed and the TiN-MCA/SBR nanocomposites may have better performance.

3. Thermal analysis

The glass transition temperature (Tg) of the TiN/SBR nanocomposites was directly related to the strength of the interface bonding [17, 18]. If the interface bonding was strong, the movement of the rubber molecular chain was restricted and the Tg increases; otherwise, the Tg decreases. Fig 4 showed DSC curve of SBR filled with nano-TiN modified by different

interfacial modifiers. It can be seen from the Fig 4 that the addition of interfacial modifier can appropriately increase the Tg of SBR. The main reason was that the nanoparticles coated with interfacial modifier molecules own reduced agglomeration improving the compatibility of nanoparticles and rubber, which improved the interface performance [19]. Compared with TiN-CA/SBR, the Tg of TiN-MCA/SBR was increased about 3.7 %. It indicated that the macromolecules of MCA in the vulcanization of rubber macromolecular chains improving the crosslink density of SBR, which further improved the interfacial adhesion of nanoparticles and SBR thus increased the Tg of TiN-MCA/SBR.
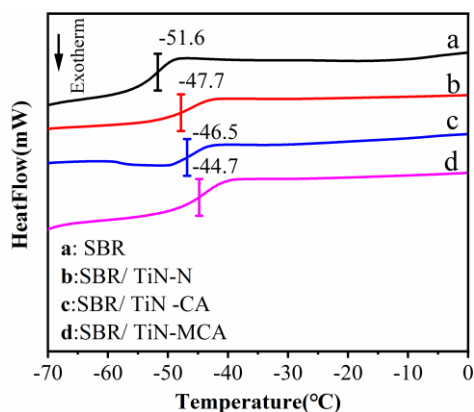
Fig 4. DSC curve of TiN/SBR nanocomposite.
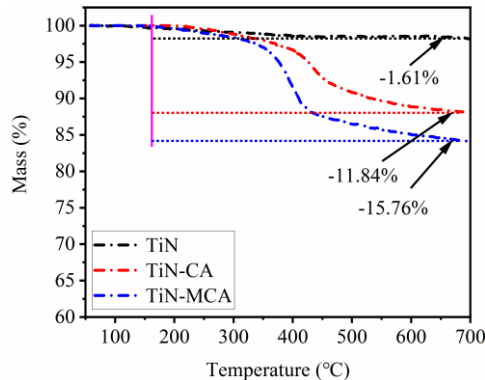
Fig 5. TG curve of TiN/SBR nanocomposite ((a: TiN-0, b: TiN-CA, c: TiN-MCA).

In order to further compare the modification effects of two interfacial modifiers on nano-TiN, TGA was used to analyze and compare the thermal decomposition behavior of TiN/SBR nanocomposites with the optimal dosage of interfacial modifier [16, 17]. Fig 5 showed the TG curves for TiN-0/SBR, TiN-CA/SBR and TiN-MCA/SBR. From the TG curve of TiN-0/SBR (Fig 5a), it can be seen that the thermal decomposition of TiN-0/SBR occurred continuously between 180 ℃ and 320 ℃ and there was almost no mass loss after 320 ℃. The total thermal mass loss was about 0.88%. These thermal mass losses were mainly due to the water adsorbed and bound by the high surface energy of nano-TiN and some small molecular impurities [20-23]. From Fig 5b, the thermal mass loss process for TiN-CA/SBR continued continuously from

185 ℃ to 580 ℃. In addition to the adsorbed water and small molecular impurities on the surface of thenano-TiN, the thermal mass loss also included the molecular chain of the CA that reacts with the nanoparticles. The overall thermal mass loss rate was about 8.9 %. Fig 5c showed the TG curve of the TiN-MCA/SBR. The curve showed that the thermal mass loss was relatively slow in the temperature range of 185 ℃ to 320 ℃. It mainly due to the loss of adsorbed water and small molecular impurity components and the thermal mass loss trend was comparable to that of TiN-0/SBR in this temperature range. However, the speed of thermal mass loss from 320 ℃ to 580 ℃ was accelerated, which mainly caused by the decomposition of the chain of the macromolecular modifier. The overall thermal mass loss rate of TiN-MCA/SBR was about 7.4 % and approximately 1.5 % less than that of TiN-CA/SBR. The decrease in thermal mass loss and the increase in thermal decomposition temperature indicated that the macromolecular modifier was superior to the small molecule modifier in terms of improving thermal stability of nanocomposites.

Conclusion

In this paper, TiN nanoparticles were modified by CA and MCA to improve its dispersibility in the organic system. The difference of the dispersion of TiN-CA and TiN-MCA in ethyl acetate and SBR matrix was very obvious. The Tg of TiN-MCA/SBR was increased by approximately 3.7% while thermal mass loss rate of it decreased by approximately 1.5% compared with TiN-CA/SBR. The above all illustrated the advantages of macromolecular interfacial modifier. This work demonstrated the potential of nano-TiN as fillers to enhance SBR rubber and also provided important information for the design of high-performance composite rubber materials.

Acknowledgments

Reference

[1] HA C S. Chem Rec, 2018, 18(7-8): 759-775.

[2] XU X F, CHEN J, ZHOU J, et al. Adv Mater, 2018, 30(17): 10.

[3] ZHANG X, LI B W, DONG L J, et al. Adv Mater Interfaces, 2018, 5(11): 28.

[4] GILIOPOULOS D, ZAMBOULIS A, GIANNAKOUDAKIS D. Molecules, 2020, 25(1): 28.

[5] CHEN H B, SCHIRALDI D A. Polym Rev, 2019, 59(1): 1.

[6] WANG J F, JIN X X, LI C H, et al. Chem Eng J, 2019, 370: 831.

[7] CHEN S N, AI J, CHEN J W, et al. J Appl Polym Sci, 2020, 137(20): 7.

[8] KAN X Q, DENG C J, YU C, et al. J Mater Sci-Mater Electron, 2018, 29(12): 10624.

[9] LIU Z Q, LIU G Q, HUANG Z P, et al. Sol Energy Mater Sol Cells, 2018, 179: 346.

[10] ELAGINA O Y, KOMADYNKO A C, POLESHCHUK E D. J Frict Wear, 2020, 41(1): 25.

[11] SUGISAWA H, KITAURA H, UEDA K, et al. Dent Mater J, 2018, 37(2): 286-292.

[12] YEAP S P. Powder Technol, 2018, 323: 51.

[13] SPYROGIANNI A, KARADIMA K S, GOUDELI E, et al. J Chem Phys, 2018, 148(6): 18.

[14] RUSU C L, BRODIN M, HAUSVIK T I, et al. Coatings, 2018, 8(6): 12.

[15] WANG Z Q, LIU Y F, LV H Q, et al. Polym Compos, 2018, 39(9): 3040.

[16] CHENG G J, SONG R J, MIAO J B, et al. Asian J Chem, 2013, 25(10): 5585.

[17] CHENG G J, QIAN J S, XIA R, et al. Micro Nano Lett, 2014, 9(7): 441.

[18] WANG H, SONG L Y, MA Y S, et al. Acta Polym Sin, 2018, 3: 419.

[19] ZHANG J W, LU J M, SU K, et al. J Appl Polym Sci, 2019, 136(45): 10.

[20] ZHU J H, WEI S Y, LI Y T, et al. Macromolecules, 2011, 44(11): 4382.

[21] PARLINSKA-WOJTAN M, MEIER S, PATSCHEIDER J. Thin Solid Films, 2010, 518(17): 4890.

[22] TAI Y L, QIAN J S, MIAO J B, et al. Mater Des, 2012, 34: 522.

[23] XIA R, LI M H, ZHANG Y C, et al. J Appl Polym Sci, 2011, 119(1): 282.

Preparation and properties of hydroxyethyl cellulose crosslinked membrane

Hao Cui[a], Yanfeng Qian[a], Meiling Gao[a], Zhibo Chen[a], Mingyue Zhang[a], Xianglong Wan[a,b], Yin Liu[a,b]

a. School of Materials Science and Engineering, Anhui University of Science and Technology, Huainan, Anhui 232001, China；
b. Anhui International Joint Research Center for Nanocarbon-based Materials and Environmental health, Huainan 232001, China

Abstract

The application of hydroxyethyl cellulose is affected by its poor film-forming and water resistance. In this paper, the effects of different chemical crosslinking agents on the film formation of 2wt% hydroxyethyl cellulose hydrogels were studied, and the contact Angle, swelling degree, microstructure and infrared properties of the crosslinking films were tested. The results show that the film modified by glutaraldehyde has good comprehensive properties, in which the water contact Angle is increased from 18.2° to 40.3°, and the swelling degree is controlled at about 40%. The film formation and water resistance of hydroxyethyl cellulose hydrogel films were improved by crosslinking method, which has a good application prospect.

Keywords: hydroxyethyl cellulose, crosslinking agent, film-forming, water contact Angle, swelling degree

Introduction

Hydroxyethyl cellulose (HEC) is a cellulose ether environment friendly, but it is poor film formation and water resistance which is not conducive to its industrial application. Utilizing chemical crosslinking [1], HEC molecular chain was transformed from linear structure to three-dimensional network structure, which improved the film formation and water resistance of HEC [2]. D Babiker et al. [3] selected HEC and polyacrylic acid (PAA) to form composite films by the layer-by-layer assembly on the surface of polyethylene terephthalate (PET) non-woven fabric. Employing thermally induced crosslinking and chemically induced crosslinking modification, functional films with rejection rates of oil-in-water emulsion both over 99.4% were prepared. Gomaa F et al. [4] studied adding zinc oxide with different concentrations to HEC and using citric acid as a crosslinking agent to prepare antibacterial films.

In this paper, the method of chemical crosslinking was tried to improve the film formation and water-resistance of the crosslinking membrane. The swelling rate, contact Angle, morphology and IR spectrum were measured to analyze the properties of the crosslinked membrane.

Materials and method

Hydroxyethyl cellulose (HEC): analytically pure, Shanghai Herister Chemical Co., LTD. Glycol: Analytical pure, Baijia Chemical Company; Citric acid: analytical pure, Aladdin reagent; Glutaraldehyde: analytical pure, Aladdin's reagent; Copper sulfate: Analytical pure, Aladdin's reagent. Electronic balance: UTP-313; Analytical balance: F1204N; I-coater: 1000 μm; Multimeter: UT-804; Air blast drying oven: DGX-9143B; 10. Yidu Qiafan Substrate Membrane: 4R [110 x 160] mm; Water contact Angle tester: TY2017003142; Microscope: DMM-900C.

The preparation process of hydroxyethyl cellulose crosslinking solution and film was used crosslinking agents such as ethylene glycol, citric acid, glutaraldehyde and polyvalent cation solution. With the ratios 0%, 5%, 10%, 15%, 20% and 25% crosslinking agent contents to HEC solutions were prepared in this study. The film formation and water-resistance of the dry thin films were measured by microscope, contact angle and swelling degree. The functional group properties of the film were analyzed by infrared spectroscopy, and the functional group information of hydroxyethyl cellulose film and the crosslinking film was compared to analyze the crosslinking effect.

Results and discussion

Film formation analysis was shown in Fig. 1. The results were showed that the cross-linking agent can improve the formation of the film.
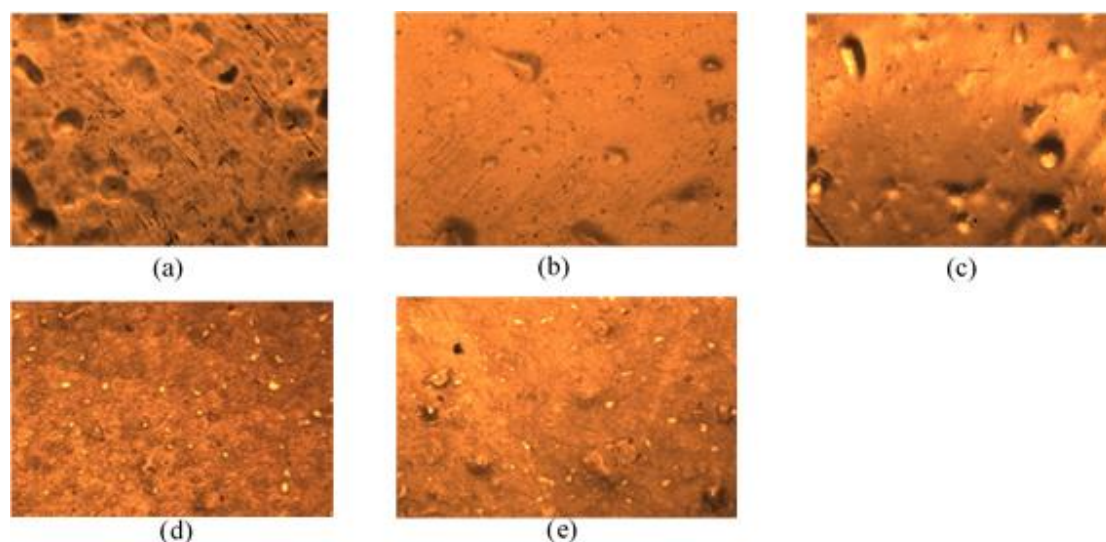
Fig. 1 Micrograph of crosslinked film for HEC ((a) 2%HEC film; (b) 5% ethylene glycol crosslinking membrane; (c)5% citric acid crosslinked membrane; (d) 5% glutaraldehyde crosslinked membrane; (e) 5% copper sulfate crosslinked membrane)

The swelling ratio and contact angle showed that the four crosslinking agents can enhance water resistance. The results were shown in Fig 2.
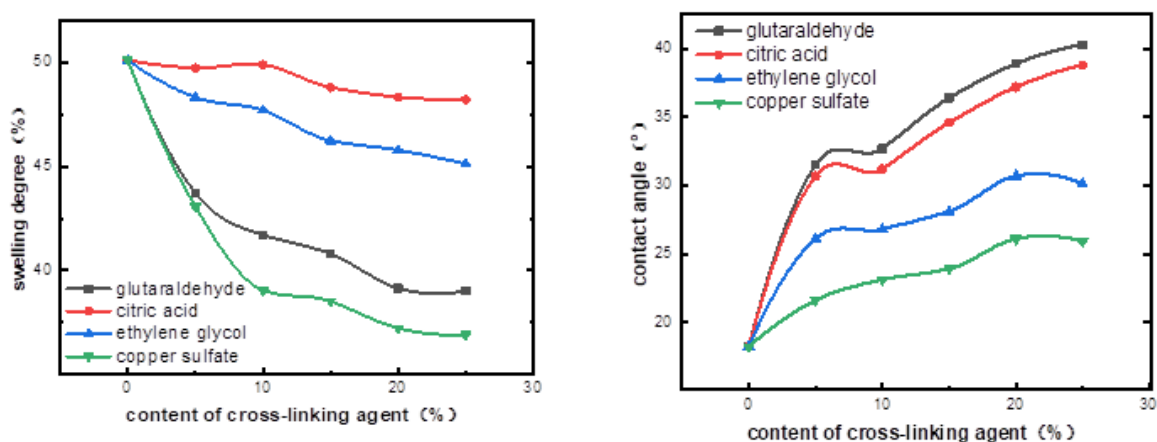
Fig. 2 Relationship between swelling rate and crosslinking agent /HEC membrane

According to the infrared spectrum in fig. 3, intermolecular hydrogen bonds are generated in the film modified by cross-linking agents, After the film was modified by glutaraldehyde, the hydrophilic group was reduced. A few intramolecular hydrogen bonds were reduced after the film was modified by the four crosslinking agents.
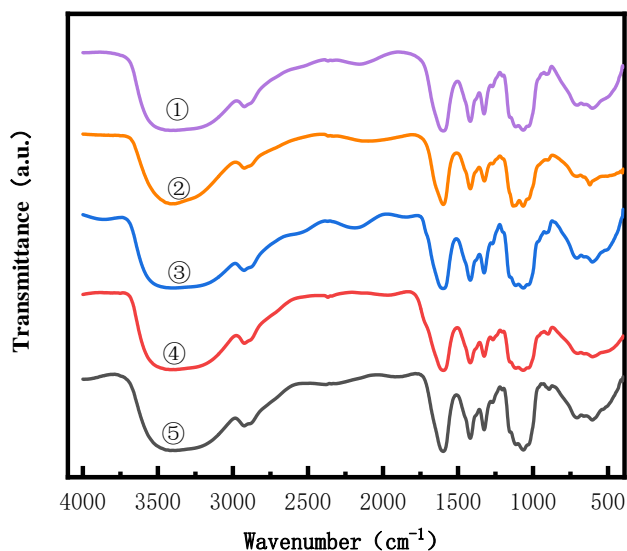
Fig. 3 FT-IR of HEC film (①2%HEC film; ② Ethylene glycol crosslinked film; ③ Citric acid crosslinking film ④ glutaraldehyde crosslinking film; ⑤ Copper sulfate cross-linked film)

Conclusion

The property of film-forming of HEC was improved to a certain extent through crosslinking, especially after crosslinking with glutaraldehyde. The swelling degree of glutaraldehyde /HEC crosslinked film is 39%, which improves the water-resistance of the film. The contact Angle of glutaraldehyde /HEC crosslinked membrane is as high as 40.3°, showing good water resistance. The water-resistance of HEC film can be effectively improved by crosslinking agents.

Acknowledgments:

References

[1] Islam M M, AbuSamra D B, Chivu A, et al. Optimization of Collagen Chemical Crosslinking to Restore Biocompatibility of Tissue-Engineered Scaffolds.[J]. Pharmaceutics, 2021,13(6):832.

[2] Qijun Z, Xinxin S, Dongyin L, et al. Modification of hydrophilic amine-functionalized metal-organic frameworks to hydrophobic for dye adsorption[J]. Journal of Solid State Chemistry, 2019,275:23-29.

[3] Babiker D M D, Zhu L, Yagoub H, et al. The change from hydrophilicity to hydrophobicity of HEC/PAA complex membrane for water-in-oil emulsion separation: Thermal versus chemical treatment.[J]. Carbohydrate polymers, 2020,241:116343.

[4] Gomaa E F, Huoyan H, Xinran S, et al. Fabrication of antimicrobial films based on hydroxyethylcellulose and ZnO for food packaging application[J]. Food Packaging and Shelf Life, 2020,23:100462.

Improvement of Sedimentation Clay Sewage by Micron Magnetic seed Addition

Hu Mengyuan, Gao Ming, Hu Tianyu, Li Jianjun*

Department of Materials Science and Engineering,Anhui University of Science and Technology,Huainan，Anhui 232001，China

Abstract

High turbidity wastewater is one of the difficulties in water treatment field because it is difficult to efficiently clarify. The fineness of suspended particles and surface charge are the main factors that hinder the efficient settlement of high turbidity sewage. Flocculation technique, which constructs large flocs by adding coagulants and flocculants, is employed to accelerate the particle settling. Currently, flocculation is the most common method to treat high turbidity wastewater. However, floccules settle mainly by their own gravity. Thus, when the water quality of high turbidity wastewater is very complicated, it is often difficult to clarify efficiently because of insufficient settling power. To improve the settling power, magnetic separation technique was introduced in. However, most of the suspended particles are not magnetic. Therefore, magnetic seeds are needed. In this paper, magnetic flocculation using processed coal-fly-ash magneticspheres (CMS) was employed to improve the settlement of high turbidity sewage.

Keywords ： magnetic flocculation; coal-fly-ash magnetic spheres; settlement rate; clarification quality; mechanism

Table 1. Average particle size, Fe content and surface properties of Coal fly ash, original CMS and CMS magnetic seeds.

Samples	CFA	Original CMS	CMS magnetic seeds
average particle size (μm)	31.26	29.61	12.03
Fe content (%)	8.17	34.80	51.77
Specific surface area (m^2/g)	4.18	2.33	10.42
Micropores surface (t-plot; m^2/g)	1.82	1.17	3.31
Micropores volume (t-plot; cm^3/g)	0.0004	0.0003	0.0012

The high-turbidity water with a mass concentration of 4% used in this study was prepared in the laboratory. The original pH value and electrokinetic ζ- potential were examined as 8.09 and -22.40 mV, respectively. The CMS magnetic seeds were prepared by a

three-step processing. The original CMS was magnetically separated from coal-fly-ash. Then it was ball-milled carefully to reduce the average particle size to about 12 μm. Finally, CMS magnetic seeds were obtained by a further magnetical separation for the obtained CMS particles[1]. The investigation results of laser particle size analysis, scanning electron microscope (with EDS) analysis and nitrogen adsorption analysis show that the average particle size, Fe content and specific surface area of CMS magnetic seeds changed significantly, as shown in Table 1.

In the magnetic flocculation experiment, APAM solution and $CaCl_2$ were used as flocculant and coagulant, and different amounts of magnetic seeds were added. The magnetic flocculation results indicate that the addition of CMS magnetic seeds could significantly speed up the sedimentation rate of clay particles. As shown in Fig.1(a), the sedimentation rate increased gradually with the increase of magnetic-seeding addition. When adding 0.2, 0.4, 0.6, 0.8 and 1.0 g CMS magnetic seeds, the final volume of tailing mud is tested as 86, 70, 62, 54 and 52 mL, respectively. The fastest settling rate is obtained when the magnetic seed dosage is 0.8 g. Further adding magnetic seeds does not help to accelerate sedimentation. The addition of magnetic seeds also affected the quality of clarification. As shown in Fig.1(b), the transmittance of the supernatant increased gradually with the increase of magnetic-seeding addition. But when the magnetic seed doseage exceeds 0.6 g, the transmittance of the supernatant tends to be stable. The highest transmittance (83.4%) was obtain at 0.8 g magnetic seed addition. Considering the variation of both settling velocity and transmittance, the optional addition amount of magnetic seed could be determined as 0.8 g.

The increase of sedimentation rate under magnetic flocculation could be due to two factors. Firstly, the inclusion of magnetic species in the floc increases the gravity, which is also the power of the floc settlement and the tail mud compression. Secondly, The magnetic force of the magnetic flocs in a gradient magnetic field is much larger than the gravity itself. The magnetic force could be expressed as Equation (1).

$$ \tag{1} $$

Where   is the vacuum permeability, k is the volume susceptibility of floc, H is the intensity of external magnetic field and is the magnetic field gradient. The increase of transmittance is closely related to the coagulating nucleus effect of CMS magnetic seeds. It suggests the addition of magnetic seeds could increase the probability of suspended solids collision and promote the coagulation of clay particles[2].

The research shows that the addition of CMS magnetic seeds in the flocculation could not only accelerate the settlement rate of the clay wastewater, but also improve the quality of clarification. It is a efficient, clean and promising method to treat high turbidity sewage.
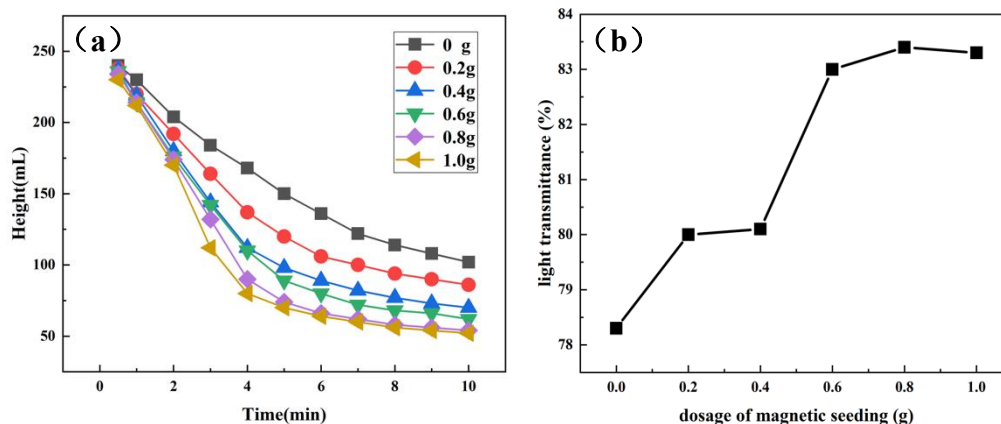
Fig.1 (a)Effect of the dosage of magnetic seed on the tailing mud volume; (b) Effect of the magnetic seeds dosage on the transmittance of the supernatant.

Acknowledgments

References

1. Jianjun Li,Jinbo Zhu,Shangyuan Qiao,Zhenwei Yu,Xiaolin Wang,Yin Liu,Xiangrui Meng. Processing of coal fly ash magnetic spheres for clay water flocculation[J]. International Journal of Mineral Processing,2017,169.
2. Miao Lv,Zhaohan Zhang,Jiayue Zeng,Junfeng Liu,Muchen Sun,Ravi S. Yadav,Yujie Feng. Roles of magnetic particles in magnetic seeding coagulation-flocculation process for surfacewater treatment[J]. Separation and Purification Technology,2019,212.

Role of P and La co-doped SrTiO₃ visible light photocatalytic activity for water splitting: a first-principles study

Jingyu Wang[a], Ximing Zhang[a], Yang Fan[a], Yueqin Wang[b], Yin Liu[a] *

[a]School of Materials Science and Engineering, Anhui University of Science and Technology, Huainan 232001, Anhui, China
[b]School of Mechanics and Optoelectronic Physics, Anhui University of Science and Technology, Huainan 232001, Anhui, China.
**Corresponding authors: yinliu@aust.edu.cn (Yin Liu)

Abstract

In this work, a +5 valence P and +3 valence La co-doped SrTiO₃ photocatalyst that can simultaneously improve photocatalytic performance and magnetic properties is reported. The band structure, and photocatalytic activity of the P and La co-doped system were systematically investigated using GGA+U method. P has a high electronegativity and small ionic radius, and when it is introduced as an acceptor dopant, significant lattice distortion and electron transfer appear in the system. This leads to a change in the properties of the La half-metal. which facilitates photogenerated carrier transfer and thus improves photocatalytic activity. The energy band edge alignment of (P+La) co-doped SrTiO₃ are desirable for water-splitting.

Keywords: Perovskite; First-principle; Co-doped SrTiO₃;

Industrial development has brought booming productivity and convenience to modern life, it has also made the degradation of pollutants and the need for renewable energy more and more urgent. In solving these two crises, photocatalytic degradation of organic pollutants and photocatalytic hydrogen production are highly expected.[1-2] SrTiO₃ (STO) is a typical wide band gap semiconductor with a large enough band width for photocatalytic reactions, but the wide band gap width also prevents it from absorbing visible light. Herein, we present a work on the electronic structure and photocatalytic activity of V and P co-doped STO using the first-principles calculations.

For doping strategy, a 2 × 2 × 2 supercell with 40 atoms of STO is taken into account, as shown in Fig.1. In mono-doping, La replaces one of the eight Ti atoms at the Ti site with a doping concentration of 12.5%. And when co-doping, the P atom and the La replace one Ti atom at a concentration of 12.5% each, while the doping concentration of the system is 25%.
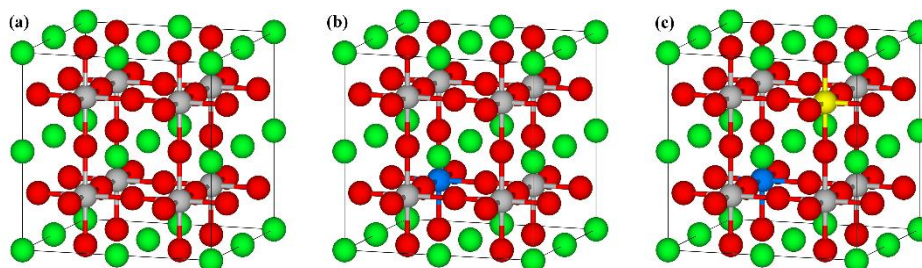
Fig.1 The 2×2×2 supercell of (a) pure, (b) P mono-doped and (c) (P+TM) co-doped STO (The blue balls indicate P atom and the yellow balls indicate La atom).

All the calculations carried out were performed using density functional theory (DFT) with Cambridge Sequential Total Energy Package (CASTEP) software package in Materials

Studio 8.0. The exchange and correlation interaction is treated with generalized gradient approximation (GGA) of Perdew-Burke-Ernzehof (PBE). In order to meet the experimental band gap of 3.20eV in STO as close as possible, the GGA+U approach is adopted to describe the correlation effects, which can predict the corrected electronic structure and optical properties.
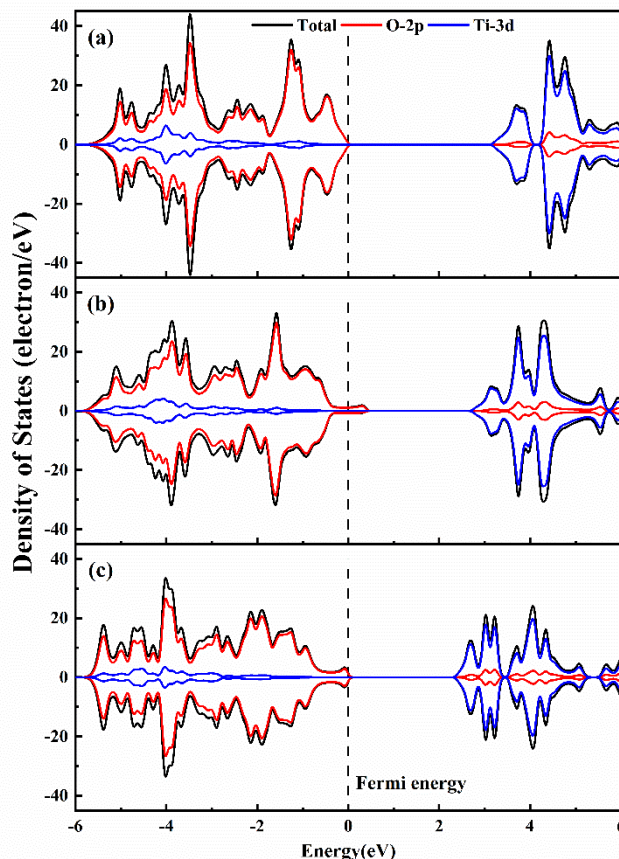
Fig.2 The density of states of (a) pure, (d)La doped, (f) (P+La) doped SrTiO$_3$.

The calculated DOS diagram is shown in Fig. 2. The VBM of pure STO is shown in Fig. 2(a) to consist mainly of O-2p orbitals, while the CBM consists mainly of Ti-3d orbitals. This composite has been reported in the published. It can be seen that La mono-doped STO shows a half-metallic nature, which would be detrimental to the migration and separation of photogenerated carriers. It can be seen in Fig. 2(c) that the introduction of P makes the La-doped STO no longer show half-metallic properties and turns into a semiconductor. And the band gap width is reduced without magazine band generation. This is beneficial to both enhancing the visible light absorption performance and suppressing the generation of photogenerated carrier recombination centers. [3-4]

To confirm whether the photocatalyst can photocatalytically crack water to hydrogen, we calculated band edge alignment of according to the following equation:[5]

$$E_{CB} = X - E_0 - 1/2E_g \tag{1a}$$
$$E_{VB} = X - E_0 + 1/2E_g \tag{1b}$$

where E_g is the band gap width, X is the absolute electronegativity of the catalyst, and E_0 is the energy of the free electron on the hydrogen scale (~4.5 eV). The results show that both pure and doped STO satisfy the conditions for hydrogen production from cracked water.
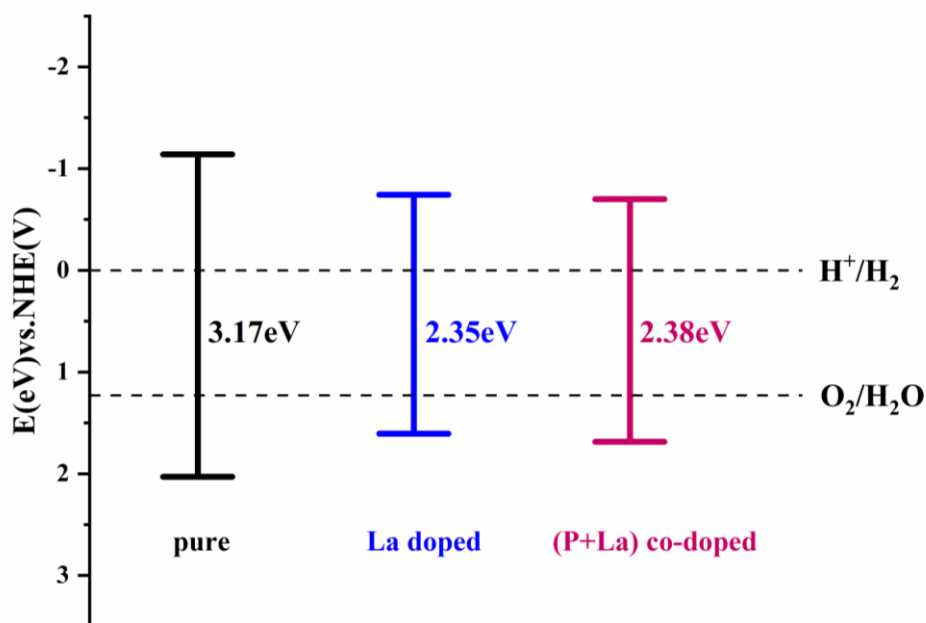
Fig.3 Band edge alignment of pure SrTiO$_3$ and doped SrTiO$_3$ respect to water redox potentials.

Conclusion

In conclusion, we used a first-principles approach to predict the feasibility of (P+La)-doped STO photocatalysts for hydrogen production. The results indicate that the (P+La) co-doped photocatalyst not only satisfies the band edge control condition for photocatalytic hydrogen production, but also reduces the band gap of STO and suppresses the generation of photogenerated carrier recombination centers.

Acknowledgments

References

(1) Shi, J.; Guo, L., ABO$_3$-based photocatalysts for water splitting. *Prog Nat Sci-Mater* **2012**, *22*, 592-615.
(2) Modak, B.; Ghosh, S. K., Insight into the enhanced photocatalytic activity of SrTiO$_3$ in the presence of a (Ni, V/Nb/Ta/Sb) pair. *Phys Chem Chem Phys* **2018**, *20*, 20078-20087.
(3) Liu, J.; Weng, M.; Li, S*., et al.*, High-throughput HSE study on the doping effect in anatase TiO$_2$. *Phys Chem Chem Phys* **2019**, *22*, 39-53.
(4) Moss, B.; Wang, Q.; Butler, K. T*., et al.*, Linking in situ charge accumulation to electronic structure in doped SrTiO$_3$ reveals design principles for hydrogen-evolving photocatalysts. *Nat Mater* **2021**, *20*, 511-517.
(5) Wang, Y. Q.; Wang, J. Y.; Lian, W*., et al.*, Insight into the enhanced photocatalytic activity of Mo and P codoped SrTiO$_3$ from first-principles prediction. *RSC Adv* **2020**, *10*, 40117-40126.

Novel lithium-based sorbents from diatomite for high temperature CO$_2$ capture

Jinxiang Wang[1], Xiaobo Peng[2]

[1]School of Materials Science and Engineering, Anhui University of Science & Technology, Huainan, 232001,Anhui ,China
[2]China Triumph International Engineering Co-Ltd, Bengbu, 233018,Anhui, China

Abstract

In this work, the cost-effective diatomite as silicon source, high efficient Li$_4$SiO$_4$ sorbents for high temperature CO$_2$ capture were prepared by solid-state reaction method at lower temperature (650℃). Analytical pure SiO$_2$ was used to synthesize Li$_4$SiO$_4$ sorbents for comparison. Phase composition was analyzed by X-ray diffraction. The CO$_2$ absorption capacity and adsorption-desorption performance were tested by the thermo-gravimetric analyzer (TG-DSC) in CO$_2$ atmosphere. The results showed that Li$_4$SiO$_4$ sorbent from diatomite had high CO$_2$ absorption capacity of 32.12%, 87.6% of the theoretical uptake capacity.

Keywords: Diatomite; Li$_4$SiO$_4$ sorbent; CO$_2$- absorption

Introduction

In recent years, the increasing CO$_2$ concentration in the atmosphere due to fossil fuel burning is identified as a major contributor to climate change, energy crisis and other health hazards. Consequently, the separation, recovery and utilization of CO$_2$ have attracted global attention [1-5]. Recently, CO$_2$ capture at high temperature with regenerable solid sorbents has received increasing attention, such as metal oxides adsorbent、Calcium sorbents、Lithium sorbents [6-8]。 Among the various solid sorbents , lithium orthosilicate (Li$_4$SiO$_4$）seem to have higher adsorption-desorption capacity, which can theoritically absorb CO$_2$ in amounts up to 36.7 of its own weight, according to the following reactions:

$$Li_4SiO_4 + CO_2 \leftrightarrow Li_2CO_3 + Li_2SiO_3 \qquad (1)$$
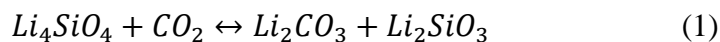
The solid phase reaction is the most common synthesis route for Li$_4$SiO$_4$. By this method, some researchers usually prepare Li$_4$SiO$_4$ with high absorption properties with analytically pure SiO$_2$ as silicon source, which needs harder preparation conditions (900℃ -1000℃) and increases the preparation cost.

Taking into account the significant content of SiO$_2$ of diatomite and in order to increase its use and decrease the cost of Li$_4$SiO$_4$ preparation, this work was focused on the solid-state preparation of Li$_4$SiO$_4$ with cheap porous diatomite(with 5um pore size) for high temperature CO$_2$ capture at lower preparation condition 650℃. Pure Li$_4$SiO$_4$ with analytically

pure SiO_2 was also prepared for comparison purposes. The influence of different sorption parameters, such as sorption temperature on CO_2 sorption capacity, have been investigated. In the following paper, P-Li_4SiO_4 and D-Li_4SiO_4 stand for Li_4SiO_4 from analytical pure SiO_2 and diatomite respectively.

Experimental

Li_2CO_3 (99%, A.R., Tianjin Chemical Reagent Co.Ltd., China), diatomite (92%SiO_2, C.R., Fujian Chemical Reagent Co.Ltd., China) and SiO_2 (99%, A.R., Tianjin Chemical Reagent Co.Ltd., China) were used as the starting powders.

In the work, Li_4SiO_4-based sorbents were prepared using the common solid-state method. Powders of Li_4SiO_4 were synthesized by mixing powders of Li_2CO_3 and diatomite in the molar ratio of nLi_2CO_3: $nSiO_2$=2:1 with a suitable amount of ethanol by using an agate mortar. The mixed powders were dried and calcined in a box-type furnace at 650℃ for 6h. The resultant powders were named D-Li_4SiO_4. For comparison, pure lithium silicate (named P-Li_4SiO_4) was also prepared. P-Li_4SiO_4 was prepared following the same solid-state method described above from Li_2CO_3 and SiO_2 at 700℃ for 6h.

Results and discussion

1. Sorbent characterization

Fig.1 compares the XRD patterns of P-Li_4SiO_4 with D-Li_4SiO_4. It can be seen that P-Li_4SiO_4 and D-Li_4SiO_4 show clearly the crystalline structure of pure Li_4SiO_4 in the pattern . The results show that the synthesis temperature can be reduced by using diatomite as silicon sources.
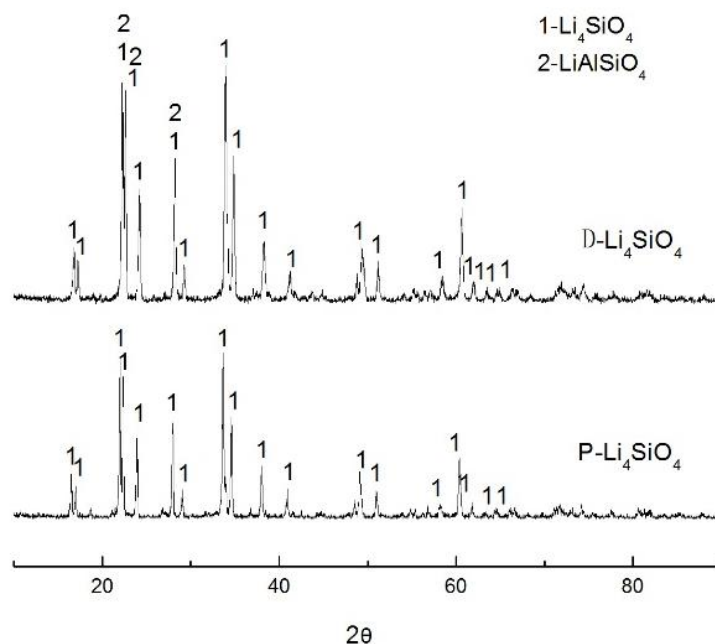
Fig.1. XRD patterns of samples P-Li_4SiO_4 and D-Li_4SiO_4

2. CO₂ sorption performance

Once Li_4SiO_4-based sorbents were characterized, these materials were thermally treated under a CO_2 flux to analyze the dynamic thermograms. Figure 2 shows the dynamic thermograph of Li_4SiO_4-based sorbents. All the sorbents show the typical CO_2 chemisorption, while the variations were also observed for the two sorbents.
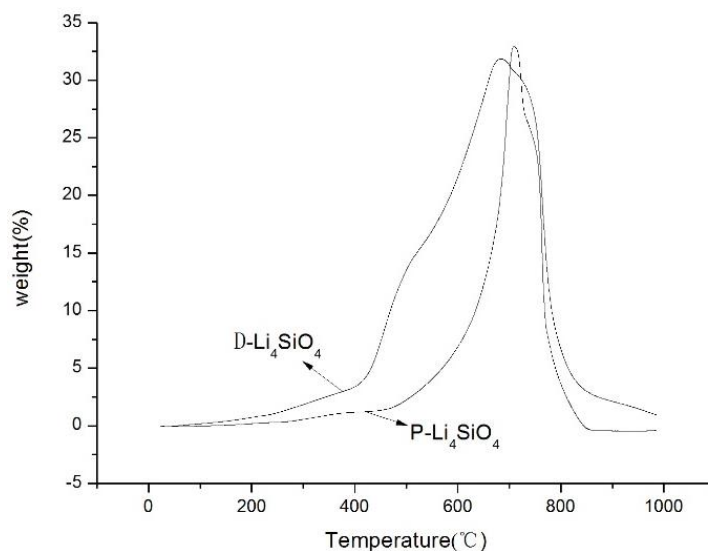
Fig.2. Dynamic thermograms of D-Li_4SiO_4 and P-Li_4SiO_4

At temperatures lower than 450℃, the thermograph of P-Li_4SiO_4 sorbent was stable, which showed no reaction between Li_4SiO_4 and CO_2. The sorbent began to absorb CO_2 at about 450℃, finishing the process at around 710℃.The maximum adsorption capacity for the sorbent was equal to 32.93%. Later , at temperatures higher than 710℃, the sorbent presented desorption process. While for D- Li_4SiO_4, the chemisorption range changed, which began to absorb CO_2 at about 250℃, finished the process at around 680℃.The maximum increase in mass equals to 31.85%. The little lower adsorption capacity was due to its poor purity of D-Li_4SiO_4 sorbent.
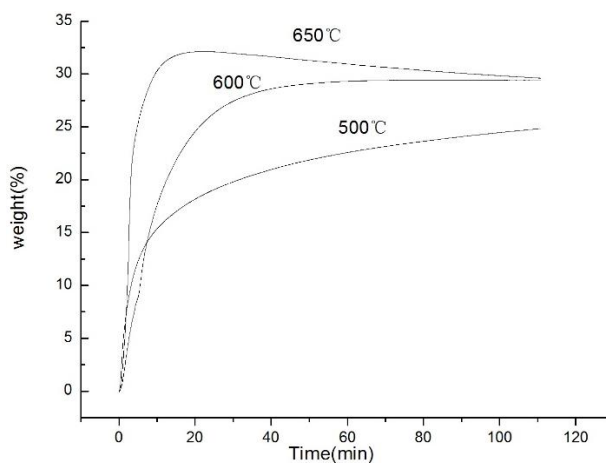
Fig.3. Isotherms of D-Li_4SiO_4 sorbent

199

To further understand the CO_2 adsorption on Li_4SiO_4-based sorbent, some extra experiments were performed. Figure 3 shows the experimental results of the mass uptake of D-Li_4SiO_4 sorbent as it changes over time at different temperatures. Obviously, the CO_2 sorption capacity increases as a function of the temperatures. When the temperature is 500℃, the mass uptake of Li_4SiO_4 for 100min reaches 24.46%, without showing a sorption-desorption balance. The curve obtained at 600℃ reaches a sorption-desorption balance within 70min with a mass uptake of 29.40%. While the curve obtained at 650℃ shows a sharp increment within 20min with a mass uptake of 32.12% before it reaches a sorption-desorption balance. This means that when heat-treated at 650℃,the Li_4SiO_4-based sorbent had a final efficiency of 87.6% of the theoretical uptake capacity, displaying significantly increased CO_2 chemisorption in comparison to samples treated at lower temperatures.

Conclusions

Novel Li_4SiO_4-based sorbents from lower cost diatomite as silicon source for high temperature CO_2 capture were prepared through solid-state reaction method at lower temperature(650℃).The CO_2 absorption capacity was investigated by the thermo-gravimetric analyzer (TG-DSC) in CO_2 atmosphere. D-Li_4SiO_4 sorbent from diatomite had high CO_2 absorption capacity of 32.12%, 87.6% of the theoretical uptake capacity, which nearly reached the amount of P-Li_4SiO_4 sorbent from analytical pure SiO_2.

References
[1]Bermúdez JM, Ruisánchez E, Arenillas A, et al. New concept for energy storage: microwave-induced carbon gasification with CO_2[J]. Energy Convers Manage, 2014, 78:559-564.
[2] Liu J, Gao S, Jiang X, et al. NO emission characteristics of superfine pulverized coal combustion in the O_2/CO_2 atmosphere [J]. Energy Convers Manage, 2014, 77:349-355.
[3] Gao S, Wang Y, Jia L, et al. CO_2–H_2O–coal interaction of CO_2 storage in coal beds [J]. Int J Min Sci Technol, 2013, 23:525-529.
[4] Broberg Viklund S, Johansson MT. Technologies for utilization of industrial excess heat: potentials for energy recovery and CO_2 emission reduction[J]. Energy Convers Manage, 2014, 77:369-379.
[5] Ge YT, Tassou SA. Control optimizations for heat recovery from CO_2 refrigeration systems in supermarket[J]. Energy Convers Manage, 2014, 78:245-252.
[6] Chen H, Zhao C. Development of a CaO-based sorbent with improved cyclic stability for CO_2 capture in pressurized carbonation[J]. Chem Eng J, 2011, 171:197-205.
[7] Chen H, Zhao C, Duan L, et al. Enhancement of reactivity in surfactant-modified sorbent for CO_2 capture in pressurized carbonation[J]. Fuel Process Technol, 2010, 92:493-499.
[8] Yang YD, Chen QJ, Liu WQ, et al. Mineral-derived Li_4SiO_4-based adsorbent for post-combustion CO_2 capture: An experimental and kinetic investigation [J]. P Combust Inst, 2021, 38: 5339-5346.

Preparation of Nano Montmorillonite Modified Polypropylene Films

Junshan Gao, Jianxun Gong, Xin Chen

School of Materials Science and Engineering, Anrui University of Science and Tecnology, Huainan, 232001, PR China.

Abstract

Nanocomposite films of polypropylene with montmorillonite were prepared via simple solution method. The montmorillonite modified polypropylene films were characterized by fourier transform infrared spectroscopy (FTIR). The results shown that the films had good transparency and film forming properties.

Keywords: montmorillonite, nanocomposite, polypropylene Films.

Introduction

With the rapid development of modern science and technology, the requirements for materials are increasingly high, and the development of plastics in the field of engineering is more and more rapid, and even plastic instead of steel has a certain possibility. Polyethylene has superior mechanical properties, and because of its simple composition and structure, it is very feasible to analyze and change its structure. And PE films in various fields also have a lot of applications[1-2]. In this paper, the nano montmorillonite modified polypropylene films were obtained by a simple solution method. And the films had good transparency and film forming properties.

Experimental

Firstly, the nano-montmorillonite(MMT) was modified with cetyl trimethyl ammonium bromide (CTAB) by the methods in the literature[3]. Then, 0.8g polyethylene（PE） was dissolved in decahydronaphthaline, heated to 135°C and stirred for 2 h to make the PE completely dissolved, and the modified MMT was evenly dispersed in the solution. Then, the solution was poured into a flat-bottomed glass dish preheated at 120°C, dried in the oven at 120°C for 15-20 min, and then quenched in water, the MMT-PE films with montmorillonite mixed were obtained.

Results and Discussion

The infrared spectra of purified MMT (a), and CTAB-MMT (b) are shown in Fig. 1. Compared with the IR spectra of purified MMT, the absorption band at 3450cm^{-1}, corresponding to –OH stretching vibration of H_2O of MMT, shifted to the lower wave number 3628cm^{-1}. In addition, the characteristic absorption bands of the symmetric and asymmetric stretching vibrations of the –CH$_2$ (2849 cm^{-1}) and –CH$_3$ (2927 cm^{-1}), were observed on the IR spectra of CTAB-MMT. The characteristic absorption bands of the stretching vibrations of the -C-O- (1196 cm^{-1} and 1037 cm^{-1}) were observed on the IR

spectra of surfactant modified MMT. Compared with the IR spectra of purified MMT, the absorption band of –OH bending vibration of H_2O of MMT ($1635 cm^{-1}$) moved to 1662 cm^{-1}. The vibration peak of Si-O-Al (824 cm^{-1}) was completely weakened after modification[4].
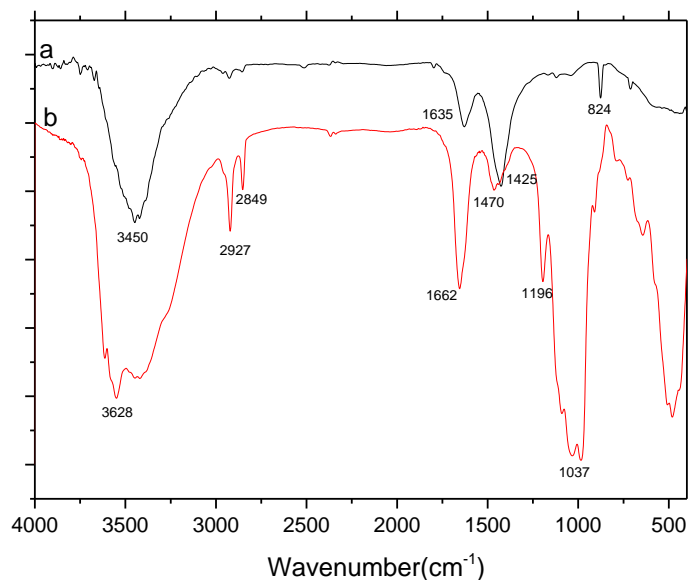
Fig.1. IR spectra of purified MMT(a) and CTAB-MMT(b)

Fig.2. The photo of CTAB-MMT modified PE film

The photo of CTAB-MMT modified PE film is shown in Fig.2. It can be seen from the picture, the film is smoothly, without bubbles and whitening, and has good transparency. The thickness of the film measured by the film thickness tester is about 50-60 mm.

Conclusion

In this study, the CTAB-MMT modified PE films were obtained. The structure of CTAB modified MMT was characterized by IR spectra. In addition, the modified MMT –PE films were prepared by a simple solution method. In this way, the films have good film forming performance and high transparency, which is suitable for the preparation of small-scale personalized film products.

Acknowledgments

References

[1]P. Wang, H.Wang, J. Liu, et al. Montmorillonite@chitosan-poly (ethylene oxide) nanofibrous membrane enhancing poly (vinyl alcohol-co-ethylene) composite film[J]. *Carbohydrate Polymers* 2018, 181: 885-892.

[2]J. Gou, L. Zhang, C. Li. A new method combining modification of montmorillonite and crystal regulation to enhance the mechanical properties of polypropylene[J]. *Polymer Testing* 2020, 82: 106236.

[3]L. Wang, A. Wang. Adsorption properties of Congo Red from aqueous solution onto surfactant-modified montmorillonite[J]. *Journal of Hazardous Materials* 2008, 160: 173-180.

[4]Z. Ceylan, D. Mustafaoglu, E. Malkoc. Adsorption of phenol by MMT-CTAB and WPT-CTAB: Equilibrium, kinetic, and thermodynamic study[J]. *Particulate Science and Technology* 2018, 36(6): 716-726.

Preparation of electromagnetic wave absorbing material by co-processing lignin and coal

Li Zongru, Shi Qiong, Wen Minyue, Zhao Yan*, Liu yin

School of Material Engineering and Science, Anhui University of Science and Technology, Huainan, Anhui 232000, China

Abstract

In this work, a high-performance electromagnetic wave absorbing carbon material was prepared by using lignin and coal to join KOH for co-thermal activation. When the thickness is 4.21mm, the reflection loss can reach -51.67dB. It has the advantages of good absorbing performance, simple preparation method, and lightweight.

Keywords：lignin; coal; carbon material; electromagnetic wave absorption; activate

With the development of science and technology, there are more and more electronic equipment appearing in human life. However, electromagnetic interference caused by electromagnetic waves generated by various electronic devices is becoming more and more serious, which will not only interfere with the operation of electronic devices but also cause harm to the human body[1]. Therefore, it is very urgent to explore high-performance electromagnetic wave absorbing materials. The traditional electromagnetic wave absorbing materials are mainly ferrite, magnetic metals, and alloys, which mainly use magnetic loss to show strong electromagnetic wave absorption performance[2]. However, these materials have the disadvantages of high density and require thicker coatings, which cannot meet the requirements of low-weight thin coatings for absorbing materials[3, 4].
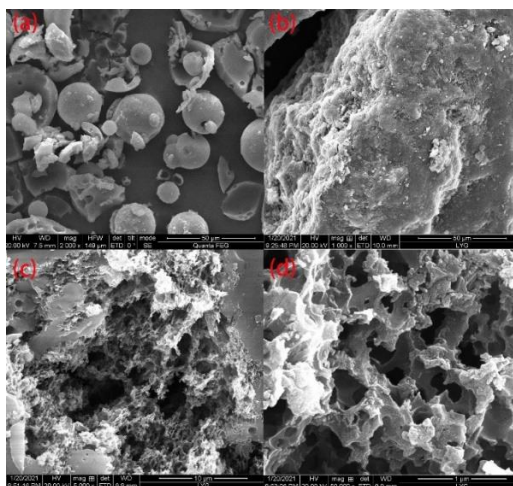
Fig.1 SEM image of lignin (a), coal (b) and PC (c, d)

Carbon absorbing materials have received extensive attention in this field due to their low density and good electrical conductivity. Lignin, as a compound widely derived from biomass, has limited its application due to its low calorific value, high volatile content, and high transportation cost. Because coal has a high fixed carbon content and contains a large amount of oxygen-containing functional groups, it can provide dipolar polarization, so it can promote microwave absorption. At the same time[5], the co-heating of coal and biomass has a synergistic effect, so the co-heating of coal and lignin to prepare electromagnetic wave absorbing carbon materials is a very promising method.

In this work, the carbon absorbing material was prepared by a simple co-thermal activation one-step method. The electromagnetic wave absorbing carbon materialswere prepared by co-thermal activation of lignin and coal through KOH (named PC). The experiment process was simple and easy. System characterization shows that the obtained PC has a three-dimensional porous structure. The SEM image of the raw material and the sample as shown in Fig 1. Fig 1 (c) and (d) showed SEM images of PC at different resolutions, showing a three-dimensional porous structure. This morphological change of PC is mainly caused by the synergistic effect of coal and lignin and the activation of KOH.
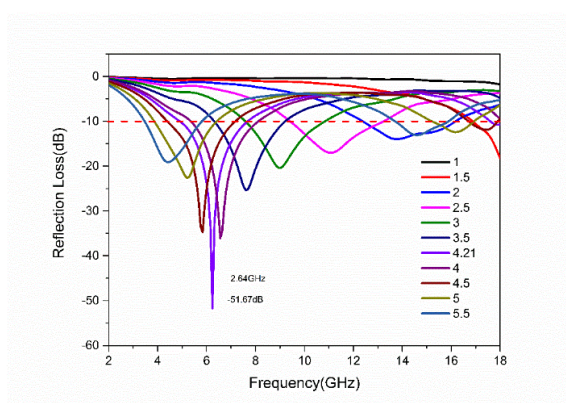
Fig.2 Reflection loss performance of PC
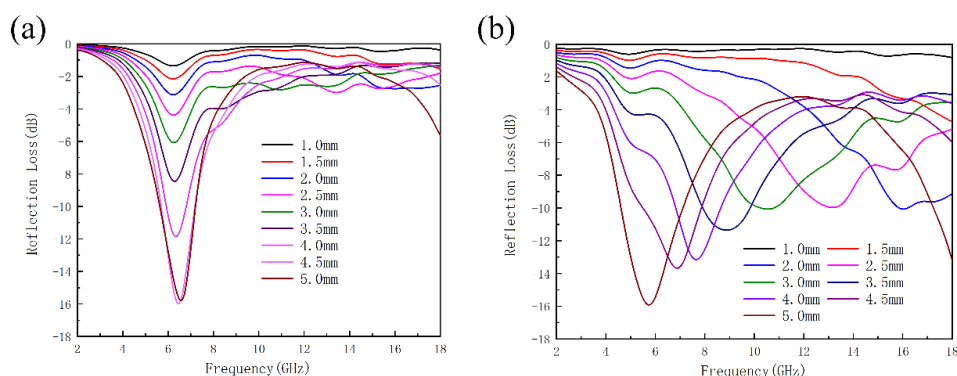
Fig.3 Reflection loss of coal(a) and lignin(b)

The results of the absorbing experiment show that PC has a strong electromagnetic wave absorbing ability. The reflection loss result of PC was shown in Fig 2. It is generally believed that when the reflection loss was less than -10dB, more than 90% of the electromagnetic waves are completely absorbed[6]. When the thickness of the PC absorber is 4.21mm, the reflection loss of the electromagnetic wave at 6.24GHz was as high as -51.67dB, and the bandwidth reaches 2.64GHz. The absorbing performance of PC was far superior to pure lignin and coal (as shown in Fig 2 and Fig 3).

We attribute the difference in absorbing performance between PC, coal, and lignin to the changes in electromagnetic parameters caused by changes in the pore structure. Due to the increase of the pore structure, more defects are generated in the PC and the interface polarization was increased.

In conclusion, we prepared a high-performance carbon absorbing material PC by co-thermal activation of lignin andcoal. PC has the advantages of good microwave absorbing effect, low density, simple preparation method. It is a relatively promising new type of carbon absorbing material.

Acknowledgements

Reference

[1] Y. Ding, Q.L. Liao, S. Liu, H.J. Guo, Y.H. Sun, G.J. Zhang, Y. Zhang, *Scientific Reports* **2016**, *6*.

[2] L.Y. Liu, S. Yang, H.Y. Hu, T.L. Zhang, Y. Yuan, Y.B. Li, X.D. He, *Acs Sustainable Chemistry & Engineering* **2019**, *7*, 1228-1238.

[3] X. Qiu, L.X. Wang, H.L. Zhu, Y.K. Guan, Q.T. Zhang, *Nanoscale* **2017**, *9*, 7408-7418.

[4] Z.C. Wu, K. Tian, T. Huang, W. Hu, F.F. Xie, J.J. Wang, M.X. Su, L. Li, *Acs Applied Materials & Interfaces* **2018**, *10*, 11108-11115.

[5] X.Y. Chen, L. Liu, L.Y. Zhang, Y. Zhao, P.H. Qiu, *Energy & Fuels* **2019**, *33*, 1267-1278.

[6] H.T. Guan, Q.Y. Wang, X.F. Wu, J. Pang, Z.Y. Jiang, G. Chen, C.J. Dong, L.H. Wang, C.H. Gong, *Composites Part B-Engineering* **2021**, *207*.

Structure and Microwave Dielectric Properties of the $Li_{2/3(1-x)}Ti_{1/3(1-x)}Mg_xO$

(x=1/7 to 5/8) Systems

Li Chang, Zhonyi Yang, Qing Cheng

School of Mechanics and Optoelectronic Physics, Anhui University of Science & Technology,
Huainan, 232001, China
E-mail address:971985803@qq.com(C.Li).

Abstract

In this paper, the $Li_{2/3(1-x)}Ti_{1/3(1-x)}Mg_xO$ (LTMO, x = 1/7 to 5/8) ceramic systems were prepared by solid-state reaction sintering. The effects of extra magnesium content on the phase evolution, crystal structure and microwave dielectric properties of $Li_{2/3(1-x)}Ti_{1/3(1-x)}Mg_xO$ (LTMO) ceramics were systematically investigated. The Li_2MgTi_3O8 and Li_2TiO_3 coexisted for x = 1 / 7, and three phases coexist at x = 1/4、 x = 2/5、 x = 4/7 and x = 5/8, including $Li_2Mg_3TiO_6$ phase. Pure $Li_2Mg_3TiO_6$-like phase with cubic rock salt structure in Fm-3m space group was obtained for x = 1/2. All samples showed well-dense and smooth microstructures. The microwave dielectric properties are highly dependent on phase composition, average grain size and octahedral distortion. The LTMO ceramics sintered at 1300°C for 4 h possessed excellent comprehensive properties of ε_r= 20.89， $Q\times f$= 68,908 GHz and τ_f= -8.4 ppm/°C for x=1/7. Typically, the LSMO ceramics sintered at 1350°C for 4 h showed a maximum $Q\times f$ of 119,072 GHz for x=4/7.

Keywords: Microwave Dielectrics Ceramics; Microstructures; Sintering;

Magnetic zeolite synthesized from Gangue by ball-milling method

Linlin Song, Tianyu Hu, Xujie Peng, Xin Rong, Jianjun Li *

Department of Materials Science and Engineering,Anhui University of Science and Technology,Huainan，Anhui 232001，China

Abstract

Excessive phosphorus content of phosphorus has been confirmed as one of the main causes of water eutrophication, which leads to a variety of environmental problems of surface water bodies. Therefore, removing phosphate (P) from water becomes an urgent task for water environmental protection. Adsorption technique is supposed as one of the most important P removal methods for its advantages, including high efficiency, low cost, and suitability for treating low-concentration phosphorus-containing wastewater[1]. A lot of adsorbents, eg. zeolite, were fabricated for P adsorption. However, most of the adsorbents were not used in in industrial water treatment practices owing to the low solid-liquid separation. To address this problem, magnetic separation technique was introduced. In this way, adsorbent was made magnetic. With the aid of magnetic field, the magnetic adsorbent could be efficiently separated from water.

Keywords：magnetic zeolite; energetic ball milling method; phosphorous adsorption; coal gangue
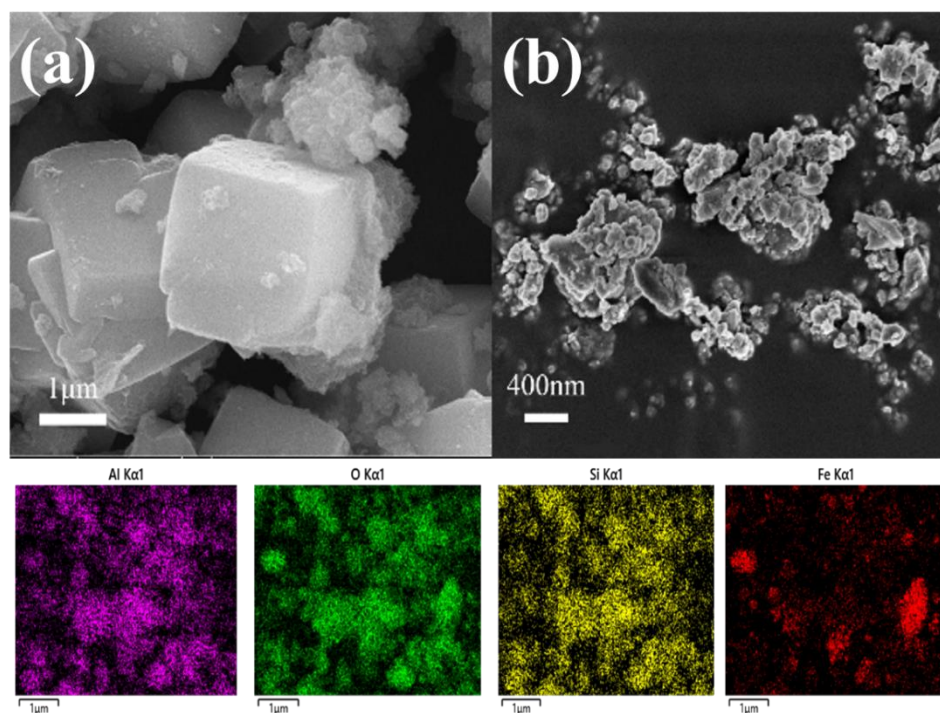
Fig.1 SEM image of (a) zeolite; (b) MZ and EDS mapping of MZ.

In this work, the magnetic zeolite (MZ) was synthesized by a simple ball-milling method, using zeolite from gangue and magnetite as raw materials. SEM results show that the as prepared zeolite particles are all cube in shape, which is a typical characteristic of Na-A zeolite, as shown in Fig. 1(a). The Na-A zeolite structure is further proved by X-ray diffraction. After the energetic ball-milling, the morphology of MZ changed a lot from that of the as prepared zeolite. As displayed in Fig. 1(b), the cubic shape of the zeolite is totally destroyed, all the samples became irregular particles. Meanwhile, the average size was reduced to 150 - 800 nm. The corresponding EDS mappings of Fig. 2(b) proves the combination of zeolite and magnetite.
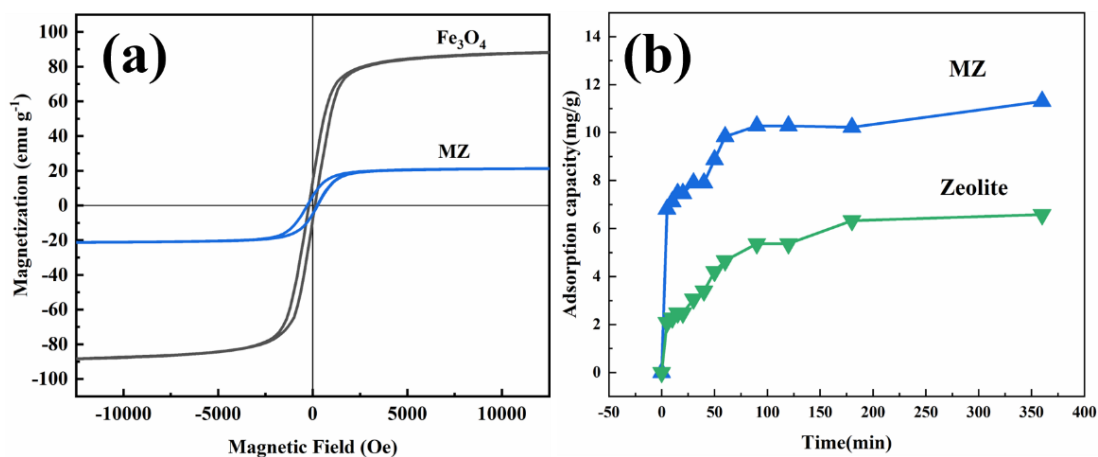
Fig.2 (a)Magnetic hysteresis loops of zeolite and MZ; (b) Time effect of zeolite and MZ for P adsorption capacity.

Fig. 2(a) shows the magnetic hysteresis loop of the MZ and Fe_3O_4. The saturation magnetization of the MZ and Fe_3O_4 are detected as 88.5 and 20.1 emu·g^{-1}, respectively. Although the magnetism of MZ decreased compared with the magnetite, it still has relative high ferromagnetism, which is strong enough for an effective magnetic separation. Adsorption experimental results show that the MZ have strong P adsorption, almost twice of that of zeolite. The adsorption data can be fitted well by the Langmuir model and pseudo-second-order kinetic model. The significant increase of P adsorption could be owing to the introduction of Fe_3O_4 and the increase of the S_{BET}[2]. It is well known that iron oxides have chemical affinity for phosphate. Since Fe_3O_4 is uniformly distributed in MZ, it could adsorb more P ions. As suggested by the EDS, the adsorbed phosphorus element is evenly distributed on the MZ surface, Compared with pure zeolite, the specific surface area of zeolite after ball milling increased from 5.58 m^2·g^{-1} to 21.88 m^2·g^{-1}. The increase of the specific surface area enhanced the physical adsorption.

The obtained magnetic P adsorbents is environmentally friendly, cheap, and have an effective P adsorption. Since the adsorbents are ferromagnetic, they could be effectively separated by the external magnetic. MZ combines the advantages of magnetic material and adsorption material, making coal gangue recycle, which is a new type of environmental adsorption material.

Acknowledgments

Refferences

[1] S. Shan, W. Wang, D. Liu, Z. Zhao, W. Shi, F. Cui, Remarkable phosphate removal and recovery from wastewater by magnetically recyclable La2O2CO3/γ-Fe2O3 nanocomposites, J. Hazard. Mater. 397 (2020) 122597.
[2] P. Wang, A. Armutlulu, W. Jiang, B. Lai, R. Xie, Facile synthesis of novel 3D flower-like magnetic La@Fe/C composites from ilmenite for efficient phosphate removal from aqueous solution, RSC Adv. 9 (2019) 28312–28322.

Controlled Semimetallic 1T ' -Phase As Cocatalysts and Boron-Doped Nitrogen-Deficient g-C3N4 Composite for Photocatalytic Hydrogen Evolution

Mei Liu, Juan Gao*, Lingcheng Zheng, Jiale Deng

School of Mechanics and Photoelectric Physics, Anhui University of Science and Technology, Huainan 232001, P. R. China
Correspondence author, E-mail: gaojuanphys@126.com.

Abstract

Graphitic carbon nitride (g-C3N4) is widely used in the field of photocatalytic hydrogen generation due to its relatively narrow band gap and low cost. However, the practical application of g-C3N4 is still limited by the low separation efficiency of photogenerated carriers. An effective strategy to overcome the above drawback is to load suitable co-catalysts on g-C3N4. MoS_2 is an effective co-catalyst because of its abundant exposed edges and low overpotential. The boron-doped and nitrogen-deficient g-C3N4 also has abundant unsaturated sites and induces strong interlayer C-N interactions, leading to effective electronic excitation and accelerated charge transport. Moreover, the energy band structure is exceptionally modulated to achieve effective light absorption in visible light. In this paper, 1T'-MoS_2/g-C3N4 and 1T'-MoS_2/BDCNN composites prepared by hydrothermal method can effectively accelerate charge transfer and thus produce high photocatalytic activity. The photocatalytic hydrogen production rate of 1T'-MoS_2/g-C3N4 composites with the mass ratio of 1T'-MoS_2 to g-C3N4 set to be 1:10(489.172 $\mu mol \cdot h^{-1} \cdot g^{-1}$) was higher than pure g-C3N4 (12.947 $\mu mol \cdot h^{-1} \cdot g^{-1}$). The photocatalytic hydrogen production rate was significantly higher with good stability.

Keywords: 1T'-MoS_2, Graphic carbon nitride, Photocatalytic H_2 evolution, Boron-doped nitrogen-deficient

Acknowledgments

Multilayer Ti₃CTₓ impregnated polyurethane foam, with improved conductivity and flame retardancy

Longxuan Zhou [a], Guojun Cheng [a,b,c,*], Ziyue Xuan [a], Meng Liu [a], Feixiang Sha[a], Shen Tian [a]

[a] School of Materials Science and Engineering, Anhui University of Science and Technology, Huainan 232001, China

[b] Institute of Environment-friendly Materials and Occupational Health of Anhui University of Science and Technology (Wuhu), Wuhu 241003, China

[c] Anhui Province Key Laboratory of Environment-friendly Polymer Materials, Anhui University, Hefei 230601, China

Corresponding author: Guojun Cheng and *chengguojun0436@126.com*

Abstract

In this work, polyurethane was used as a template to prepare polyurethane through simple foaming. Then, with the aid of ultrasound, the liquid Ti_3CT_x is immersed in the polyurethane sample, and then heat-treated to prepare the polyurethane containing Ti_3CT_x. Polyurethane composites containing Ti_3CT_x show better electrical conductivity than pure polyurethane. For example, the volume resistivity of a PU composite containing 5% by mass of Ti_3CT_x is 3.82×10^6 ω·cm, which is significantly lower than that of pure polyurethane by 5 orders of magnitude. The flame retardant properties of polyurethane composites containing Ti_3CT_x are also increased to 22%, which is about 5 levels higher than that of pure polyurethane. In addition, the composite material also shows a significant improvement in compressive strength and mechanical properties.

Keywords: conductivity, flame retardant, soak, Ti_3CT_x

Introduction

Recently, the advancement of electronic technology has brought many conveniences to our lives, and electronic devices have become an indispensable part of modern life [1–3], such as TVs, laptops and mobile phones. Any electronic equipment will produce static electricity, which will cause harmful effects on the performance of the equipment and the surrounding environment [4-6]. Therefore, there is an urgent need to meet an anti-static material, which has a certain effect on the protection of electronic products [7-9].

MXene is a relatively novel two-dimensional material [10-13], it provides a wide range of ingredients and excellent performance, good electrical conductivity [14-16], flame retardancy [17],

energy storage performance [18- 19]. In composite materials, lubricants, electromagnetic shielding, batteries, capacitors, catalysis, sensors, antibacterial, etc. have potential value [20-21]. These characteristics make them become fillers in polymer nanocomposites and have good application prospects. Among them, Ti_3AlC_2 is one of MXene. Polyurethane (PU) containing Ti_3CT_x has excellent performance in modification, so it is widely used in the fields of sound, heat, force, electricity, antibacterial, corrosion resistance, and flame retardant, reflecting the versatility of polyurethane. Especially in the packaging and transportation of electronic products, there will be movement, which leads to the generation of electrostatic charges. If it is not eliminated in time, the charge will produce sparks, and there is even a danger of explosion [22-23]. In order to effectively reduce the accumulation of these charges, the packaging of electronic products needs conductive treatment. Polyurethane containing Ti_3CT_x can provide moderate conductivity and act as a reinforcing agent to improve overall strength, modulus, hardness and wear resistance. These characteristics make them particularly suitable as high-performance sealing products in the automotive, electronics, construction and chemical industries.

In this work, a combination of Ti_3CT_x and polyurethane was used to prepare a polyurethane material containing Ti_3CT_x by the immersion method, so that the surface of the material can form a uniform network with better conductivity and act as a protective layer on the PU. The results show that compared with pure PU, the conductivity, flame retardancy, compressive strength and Young's modulus of polyurethane composites containing Ti_3CT_x are significantly improved. Therefore, the preparation of polyurethane composite materials containing Ti_3CT_{x2} may provide a feasible solution to eliminate static electricity generated by electronic products due to friction during transportation and reduce the risk of fire or explosion.

Experimental

1. Improve the preparation of Ti_3CT_x

Take 15.5ml of 36% hydrochloric acid and 4.5ml of deionized water to prepare hydrochloric acid; then take 1g of LiF and put it into hydrochloric acid to react, start the magnetic stirrer, set the speed to 50r/min, and slowly Add 1g Ti_3AlC_2, react for 5 minutes, and heat to 40°C. Then wrap the beaker with hydrochloric acid in a film and seal it with tape. Use a needle to make two holes in the film. One is used for nitrogen gas and the other is for removing oxygen. After that, it is sealed with tape. Under the condition of 40°C, set the rotation speed to 50r/min, and take the time of one day. Centrifuge in a centrifuge for 7 times, ultrasonic for 1h, and centrifuge for 1 time, separate layers, and collect the precipitate.

2. Preparation of foaming

First, pour 3g of concentrated sulfuric acid into a beaker containing deionized water. Pour the sulfuric acid slowly along the wall of the cup while stirring with a glass rod to dissipate heat. The stirring range should not be too large or the speed is too fast to cause the liquid to splash out. Security incident. After the diluted sulfuric acid is cooled to room temperature, add 0.5 g of L-aspartic acid, and stir to dissolve. Then put 6g of polyether polyol into the beaker, start the magnetic stirrer, set the rotation speed to 100r/min, add 0.35g of calcium oxide under stirring, react for 1h, heat to 120°C, remove the residual moisture until No small bubbles are generated; then add a certain amount of MDI, magnetically stir for 1h, set the rotation speed to 150r/min, under stirring, add 0.1g of triethylenediamine and 0.1g of dodecyldimethyl in the beaker Base siloxane, 0.1g KH-550, 0.1g ethylene glycol, set the stirring speed to 300r/min, and become milky yellow; then first add 7g diisocyanate and 0.1g L-aspartame dissolved in sulfuric acid Amino acid, under stirring at 500r/min for about 10s, there will be milky white, then stop stirring, the obtained material is poured into the mold, and it is naturally foamed at hot room temperature, solidified and demolded, and cooled overnight. A rigid polyurethane foam is obtained. Finally, stir the reaction at a speed of 6000r/min until the milky white phenomenon appears, stop the stirring, and transfer the material into the mold, foam naturally at room temperature, and demold after curing to obtain a rigid polyurethane foam.

3. Synthesis of polyurethane containing Ti_3CT_x

The polyurethane is made into a sample, put into ethanol and water solution, ultrasonic for 1.5h, and then in an oven at 70°C overnight, put the sample in Ti_3AlC_2, and sonicated for 2h, dry overnight in an oven at 70°C, you can get the conductive polyurethane hard Quality foam.

Results and discussion

1. Microstructure and phase evolution

Scanning electron micrographs (shown in Figure 1a) clearly show irregular particle shapes, and the average size of these particles is 300 μm. On the other hand, the photographic PU foam template shown in Figure 1b clearly shows the interconnected open-cell structure. It can be noticed that the pores are almost spherical, with almost complete cell wall edges. Therefore, during the polyurethane foaming process, the pores are completely opened with interconnected pores. Obviously, these pillars have a completely open pore structure with an average pore diameter in the range of 300–400 μm. The pore size distribution and the edge thickness of the entire skeleton structure depend on the foaming degree of the polyurethane template. It is also noticed that compared with the original polyurethane template, the improved pore size is slightly reduced. This may be due to the fact that the foaming agent in the foaming process is

better than the yeast (as shown in Figure 1c, the left is the improved , The right is before improvement). Using a mixed solution of LiF and HCl instead of HF as an etchant, Ti_3CT_x was etched at 40°C. Although the Ti_3CT_x layer prepared by this method is not obvious, and there are many small pieces of fallen products attached to the surface (as shown in Figure 1d), high quality, high yield and high yield can be obtained in the subsequent ultrasonic stripping. Multi-layer Ti_3CT_x nanosheets with large lateral dimensions.
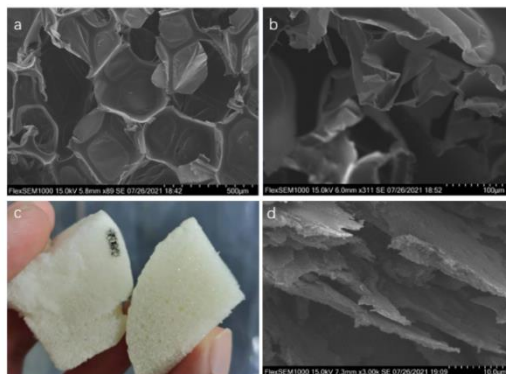
Figure 1 a and b are scanning electron micrographs of polyurethane; c is a comparison of polyurethane before and after improvement; d is a scanning electron micrograph of Ti_3CT_x

2. Conductivity of polyurethane composites containing Ti_3CT_x

The volume resistivity of pure PU is $10^{11}\omega\cdot cm$, which corresponds to the value of the insulator. When adding 5% by weight of Ti_3CT_x to PU, the volume resistivity of the polyurethane composite containing Ti_3CT_x is significantly reduced by 5 orders of magnitude. The volume resistivity of polyurethane composites containing Ti_3CT_x gradually increases with the loading of Ti_3CT_x. In general, these changes are almost in the order of magnitude. The small volume resistivity means that the formation of Ti_3CT_{x2} provides an effective path for electron transport. The conductivity of composite materials containing Ti_3CT_x has also been reported in other documents. When the filler content is 5 wt%, the resistivity of the composite material can reach 3.82×10^6 $\omega\cdot cm$ (as shown in Figure 2).
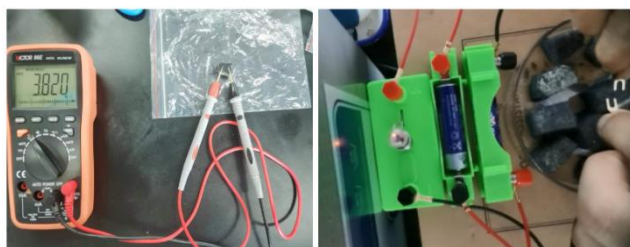
Figure 2 When the filler content is 5 wt%, the resistivity of the composites

3. Mechanical properties of polyurethane composites

The mechanical properties of polyurethane composites were studied through compression tests. The compressive strength of the composite material and its degree of slag drop are shown in Figure 3. It can be clearly seen that under the same force, the degree of slagging before and after the improvement is different. The slagging and fragile before the improvement is easy, and the mechanical properties of the polyurethane after the improvement are obviously improved. The reason is that as the added amount of polyol and isocyanate tends to be average, the compressive strength and Young's modulus of the polyurethane composite gradually increase. This is because the pre-built frame effectively prevents defects caused by the uneven dispersion of isocyanate in the matrix. In addition, the compressive strength of the improved polyurethane composite material is almost several times higher than before, indicating that the improved polyurethane will have improved mechanical properties.

Figure 3 Deslagging degree of composite materials

4. Flame retardancy of polyurethane composites containing Ti_3CT_x

The flammability of the foam samples was evaluated by the LOI test. The LOI value is obtained according to the JF-3 type. When the PU foam containing Ti_3CT_x, the LOI of the treated PU sample increased from 16% (untreated foam) to 22.0%. As the concentration of Ti_3CT_x continues to increase, the flame retardant effect increases in turn. When Ti_3AlC_2 reaches 32%, its LOI value does not increase and maintains a stable state. It is worth mentioning that when the alcohol lamp is not burning, the flame retardant effect will increase. The polyurethane stopped burning. This phenomenon may mean that Ti_3CT_x has a synergistic flame-retardant effect on LOI. When the surface of the synergistic system is burned, the surface is carbonized to form a layer of carbon, which prevents the flame from extending to the inside, and phosphorus acts as a flame retardant inside(as shown in Figure 4).
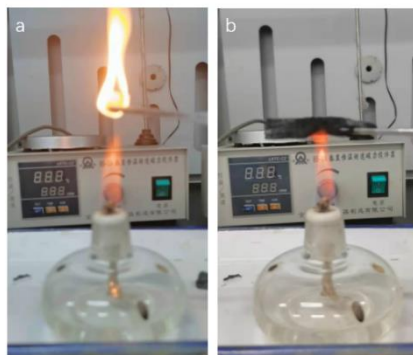
Figure 4 Picture a is before polyurethane improvement, b is after polyurethane improvement

Conclusion

Usually, polyurethane foam is used as a template to prepare polyurethane through simple foaming. Then, with the aid of ultrasound, the liquid Ti_3CT_{x2} is immersed in the polyurethane sample, and then heat-treated to prepare the polyurethane containing Ti_3CT_x. The results show that compared with pure PU, the electrical conductivity, flame retardancy, compressive strength and Young's modulus of the polyurethane composite containing Ti_3CT_x are significantly improved. In this work, the preparation of polyurethane composites containing Ti_3CT_x may provide a feasible solution to eliminate static electricity generated by electronic products and packaging boxes, thereby protecting electronic products.

Acknowledgments

References:

[1] Abeykoon C, Mcmillan A, Dasanayaka C H, et al. International Journal of Lightweight Materials and Manufacture, 2021,4: 434.

[2] Qu H, Fu S, Pang L, et al. Applied Thermal Engineering, 2018, 138: 83.

[3] Chen X, Sun L. Microprocessors and Microsystems, 2020, 81(8):103784.

[4] Frank, Huess, Hedlund. Biomass & Bioenergy, 2018, 108: 113.

[5] Qian W, Sz A, Gl A, et al. Journal of Alloys and Compounds, 2020, 820: 153184.

[6] Chan K, Pham D Q, Demir B, et al. Composites Part B Engineering, 2020, 201: 108375.

[7] Wang X, Jin T, Wang H W, et al. Wood material ence & engineering, 2015, 12(1-5):63.

[8] Gao W, Bie M, Liu F, et al. Acs Appl Mater Interfaces, 2017, 9(18): 15798.

[9] Shen X, Wang Z, Wu Y, et al. Carbon, 2016, 108: 412.

[10] Meng W X, Liu X J, Song H Q, et al. Nano Today 2021, 40: 101273.

[11] Luo Y, Xie Y H, Geng W, et al. Journal of Colloid and Interface Science, 2022, 606: 223.

[12] Lin H J, Mo Q L, Xu S, et al. Journal of Catalysis, 2020, 391: 485.

[13] Woo J H, Kim N H, Kim S I, et al. Composites Part B Engineering, 2020, 199: 108205.

[14] Mao M, Yu K X, Cao C F, et al. Chemical Engineering Journal, 2021, 427: 131615.

[15] Zhang Q, Chen S, Fu Z, et al. Nano Energy, 2020, 76: 105060.

[16] Yang G, Lei W, Chen C, et al. Nano Energy, 2020, 75: 104954.

[17] Zhang L, Huang Y B, Dong H R, et al. Composites Part B: Engineering, 2021, 223: 109149.

[18] Jamil F, Ali H M, Janjua M M. The Journal of Energy Storage, 2021, 35: 102322.

[19] Aslfattahi N, Saidur R, Arifutzzaman A. et al. Journal of Energy Storage, 2020, 27: 101115.

[20] Wang X W, Zhang D Z, Zhang H B, et al. Nano Energy, 2021, 88: 106242.

[21] Tahir K, Miran W, Jang J, et al. Chemosphere, 2021, 268: 1287846.

[22] Tao W J, Zeng S H, Xu Y, et al. Composites Part A: Applied Science and Manufacturing, 2021, 143: 106293.

[23] Bai S C, Guo X Z, Zhang X Y, et al. Composites: Part A, 2021, 149: 106545.

Preparation of crosslinked membrane based on PVA and its application

Meiling Gao[a], Zhibo Chen[a], Hao Cui[a], Yanfeng Qian[a], Mingyue Zhang[a],

Ruobin Li[a], Xiaorui Wang[a], Xianglong Wan[a,b], Yin Liu[a,b]

[a.] School of Materials Science and Engineering, Anhui University of Science and Technology, Huainan, Anhui 232001, China；
[b.] Anhui International Joint Research Center for Nanocarbon-based Materials and Environmental health, Huainan 232001, China)

Abstract

Membrane filtration is one of the commonly used technologies in water treatment. Its high cost and poor effect on high concentration wastewater treatment restrict the application of membrane filtration technology in high concentration organic wastewater treatment. In this paper, PVA composite crosslinking membrane was prepared for the pretreatment of high concentration organic wastewater. The infrared spectrum, hydrophilicity, swelling and thermogravimetric properties of composite crosslinking PVA film were analyzed, and the film-forming property was analyzed with SEM. The feasibility of pretreatment of industrial wastewater was analyzed by investigating ion permeability. This method not only reduces the cost of membrane treatment but also promotes membrane treatment technology to the treatment of high concentration industrial wastewater.

Keywords: PVA composite crosslinking membrane, high concentration wastewater, water flux, transport mechanism

Introduction

Membrane technology takes advantage of the selective permeability of the membrane to purify water by specific separation of impurities [1]. It is generally divided into the organic membrane and inorganic membrane. According to the separation mechanism, it can be divided into a membrane, ion exchange membrane, selective membrane and non-selective membrane [2]. Membrane treatment technology in general membrane cost is high, but also easy to cause membrane pollution, thus affecting the membrane separation efficiency [3]. Cleaning the membrane system, the membrane system can work normally and the separation performance can return to a normal level. Most of the organic pollutants are toxic, difficult to degrade, poor biodegradability, for organic wastewater problems, the traditional wastewater treatment is difficult to directly meet the industrial standards. This study intends to use membrane separation technology for organic wastewater treatment to launch a new attempt to reduce the cost of the membrane, for high concentration.

Materials and methods

Styrene-acrylic emulsion (RS-998A): Beijing Jiasheng Building Materials Co., LTD. Polyvinyl alcohol (PVA): analytical pure, Henan Yuheng Chemical Co., LTD. Fourier Transform Infrared spectrometer (NICOLET 380), Multimeter (UNI-T UT804): Changsha Exp Instrument Co., LTD. Scanning electron microscope (FlexSEM 1000): Hitachi Corporation, Japan. Different ratios of PVA in RS-998A and wet thicknesses films were prepared by a Mayer tool and dried in a dryer cabinet. Performance and characterization tests of the crosslinked membrane were measured by FT-IR, SEM, contact angle, swelling degree, TG/DSC, and resistance change of composite film.

Results and discussion

FT-IR spectrum of the composite crosslinked membrane was shown in Fig. 1. The result showed that with the increase of PVA, a few intramolecular hydrogen bonds were reduced after the film was modified by the four crosslinking agents.
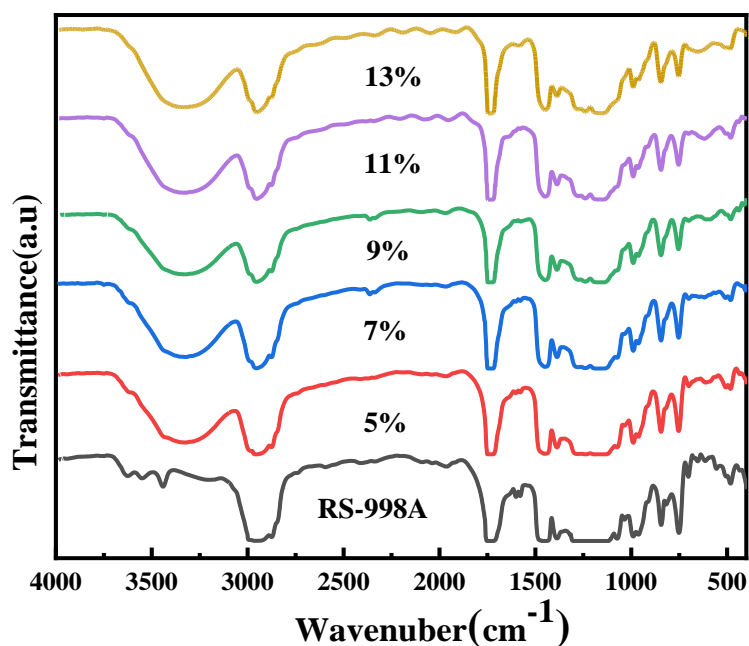
Fig.1 FT-IR of RS-998A /PVA composite crosslinked films with different PVA contents

The SEM of RS-998A/PVA composite film was shown in Figure 2.
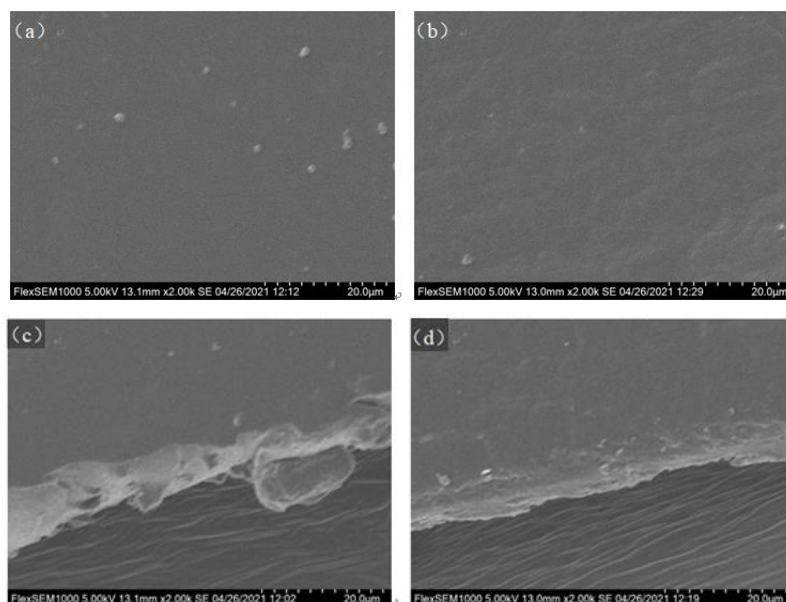
Fig. 2. SEM of RS-998A and RS-998A /PVA (a,c. RS-998A; b,d. RS-998A /PVA)

From Fig. 2, the film-forming is not changed visibly which can be used for the treatment for high concentration waster water. The contact angle and solubility of the film were shown in Fig. 3. With the increasing contents of PVA, the contact angle decreased clearly, which will help enhance the permeability of water in films.
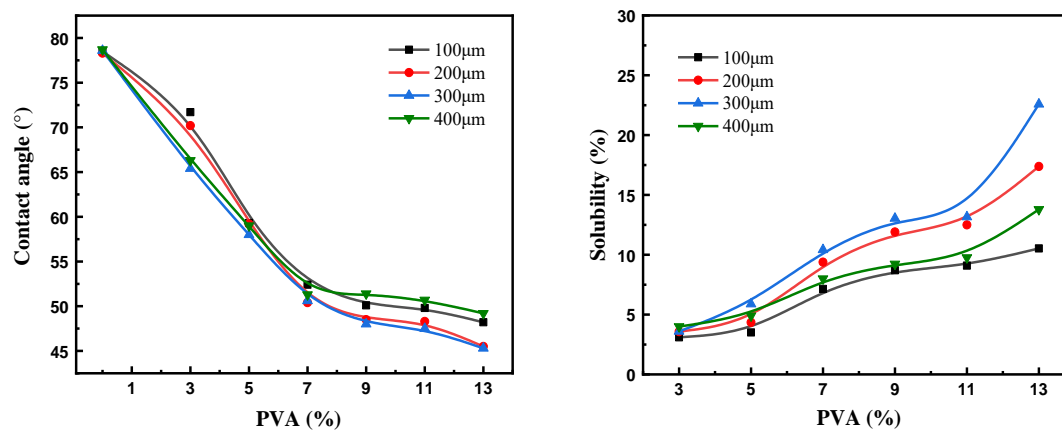
Fig. 3. The contact angle of composite crosslinked films with different PVA contents

The thermogravimetric and ion permeability of RS-998A/PVA composite crosslinked film was shown in Fig. 4. The results showed that the thermal stability and ion transport in the film are fit to the prospect well.
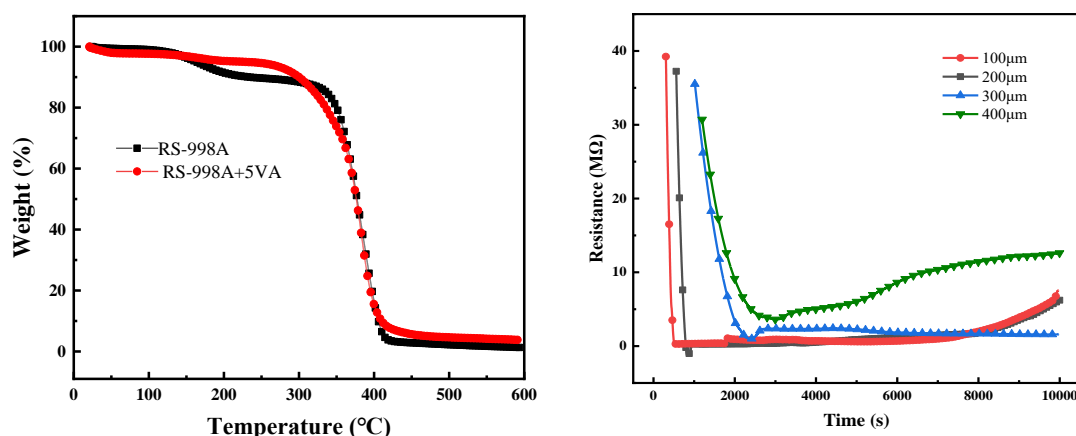
Fig. 4 Thermogravimetric and ion permeability of composite crosslinked films

Conclusion

The FT-IR, hydrophilicity, swelling and thermogravimetric properties of the composite film are shown the film-forming improvement by crosslinking of PVA. The thermal stability of the film is enhanced under 300℃. This method not only reduces the cost of the membrane but also has good potential for the treatment of high concentration industrial wastewater.

References:

[1] Peng L E , Yao Z , Chen J , et al. Highly selective separation and resource recovery using forward osmosis membrane assembled by polyphenol network[J]. Journal of Membrane Science, 2020, 611:118305.

[2] Kondrat'Eva L , Sverdlova O , Dobrynina N . Application of ion-exchange membrane systems in continuous flow analysis[J]. Scientific Papers, 2021, (1):45-50.

[3] Ma L , Y Chen, Zheng J . An efficient, stable and reusable polymer/TiO$_2$ photocatalytic membrane for aqueous pollution treatment[J]. Journal of Materials Science, 2021, 56(19):11335-11351.

Photocatalytic properties of TiO$_2$/SnS/MoS$_2$ heterojunction

Jiale Deng, Juan Gao*, Lingcheng Zheng, Mei Liu

School of Mechanics and Photoelectric Physics, Anhui University of Science and Technology, Huainan 232001, P. R. China
Correspondence author, E-mail: gaojuanphys@126.com.

Abstract

In this work, a new TiO$_2$/SnS/ MoS$_2$ (TSM) 3D heterostructure was prepared by hydrothermal method, and the three-element rod-liked composite photocatalyst was synthesized. The morphology, microstructure, chemical composition, optical properties, photoelectrochemical (PEC) performance, photodegradation ability and photocatalytic mechanism of TSM were systematically studied. RhB contamination reagent was used to study the photocatalytic performance of TSM. By adjusting the amount of MoS$_2$, when the weight percentage of MoS$_2$ is 12.5wt%, it has the best photocatalytic activity and PEC performance. The pseudo-first-order rate constants are 2.6 times that of TiO$_2$, 1.6 times that of TiO$_2$/MoS$_2$ and 1.4 times that of TiO$_2$/SnS. The corresponding photocurrent density is 1mA/cm^2, which is about 10 times higher than pure TiO$_2$ and significantly higher than TM and TS. The improvement of photocatalytic performance and PEC performance of TiO$_2$/SnS/MoS$_2$ is attributed to i) the construction of a new heterostructure conducive to carrier separation; ii) the introduction of SnS and MoS$_2$ constructs the nanonetwork, which is favorable the transport of carriers and increases the reaction sites; the introduction of narrow-band gap semiconductor expands the absorption region of visible light. Based on the band structure and free radical trapping experiments of photocatalyst, the mechanism of RhB removal by TiO$_2$/SnS/MoS$_2$ heterojunction was proposed and analyzed, and the main reaction species were identified as O^{2-} and h$^+$.

Keywords: TiO$_2$/SnS/MoS$_2$, photocatalysis, photoelectrochemistry
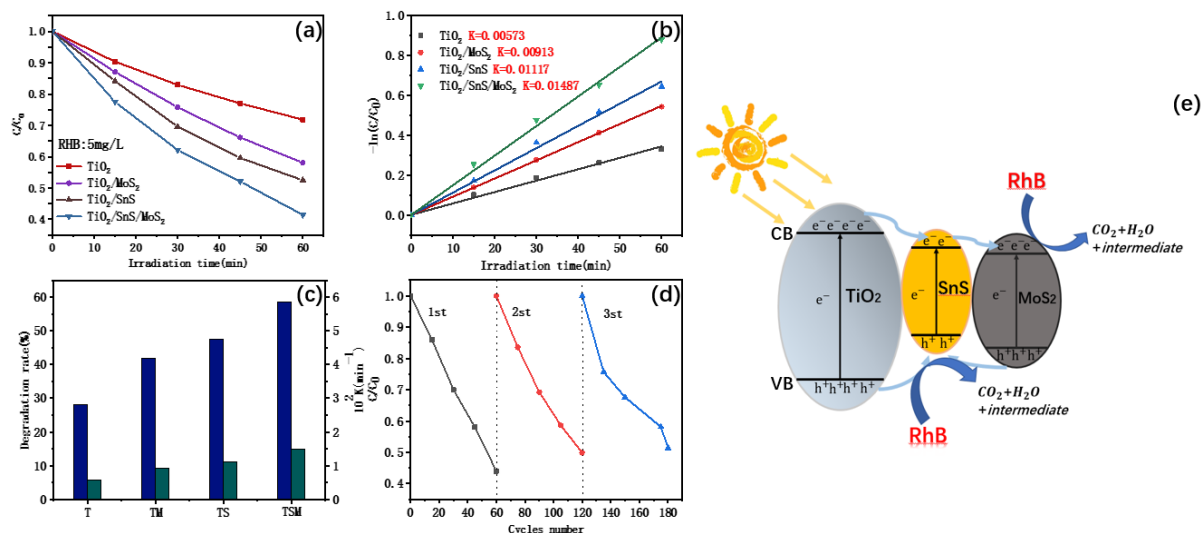
Figure (a) Photocatalytic efficiency, (b) pseudo first order reaction kinetics, (c) degradation ratio and rate constants K, and (d) repeatability tests RhB for TSM, (e) the photocatalytic mechanism for $TiO_2/SnS/MoS_2$ composite.

Acknowledgments

Research on settlement mechanism of fine grain with compound agent

Mengting Li, Longqian Ni, Xianglong Wan[1]*, Bohan Zhou[2], Chuyang Xu[1],
Yanfen Wang[1]

[1.]School of Materials Science and Engineering，Anhui University of Science and Technology，Anhui Huainan 232001，China;[2.]Huainan Institute of Standardization， Anhui Huainan 232001，China

Abstract

In this paper, the particle size composition and XRD analysis of the samples are carried out, and the existence of clay minerals is the main cause of coal slime. Through orthogonal experiment, the best compound conditions were determined. It can be seen from the analysis of the potential of the coal particle that the surface potential of the particle is effectively reduced, the electrostatic repulsion is reduced, and the process of the small particles can be promoted by the use of polymerization aluminum chloride. The comparison of infrared spectra before and after the action of the agents, and the slime showed that the coagulants and flocculants were adsorbed with the particle surface. Under the action of coagulant, the dual electric layer on the surface of slime particles is effectively compressed, and the flocculant plays the role of adsorption bridge, thus the flocculation and sedimentation process of slime water is accelerated.

Key words: Raw coal properties；Flocculant；Polycoagulant；ζ potential；FT-IR

Introduction

In recent years, China's coal-preparation industry level has made greatly improved, but the theoretical research on slime water treatment in China has been stagnating[1]. In this paper, the properties of raw coal are analyzed, and the optimal conditions of compound distribution are selected, and the action mechanism of coagulants and flocculants on the surface of coal particles is investigated.

Experimental Section

1. Nature of the raw coal

The coal sample provided by Wangfenggang coal preparation plant is taken as the research object of this study. The ash content of raw coal is 24.78%. According to China's national standards GB/T6003.1 and GB/T6005, the samples were subjected to small screening test, and the results are shown in figure 1. The results of laser particle size analysis are shown in Figure 2.

---

* Corresponding author. Tel: +86-0554-6668684; fax: +86-0554-6668643.

E-mail address: xlwan@aust.edu.cn
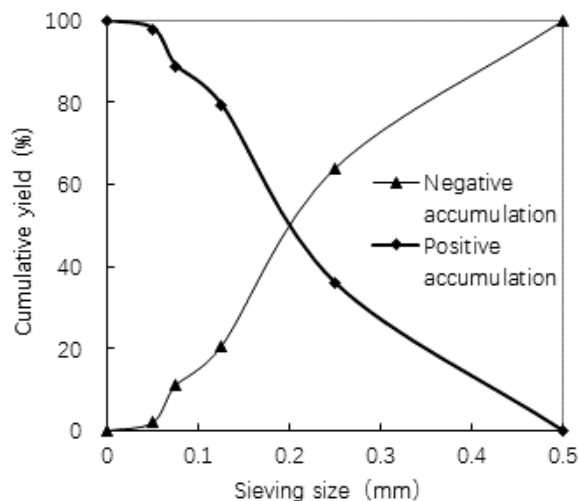
Fig.1 Curve of cumulative particle size on coal sample.
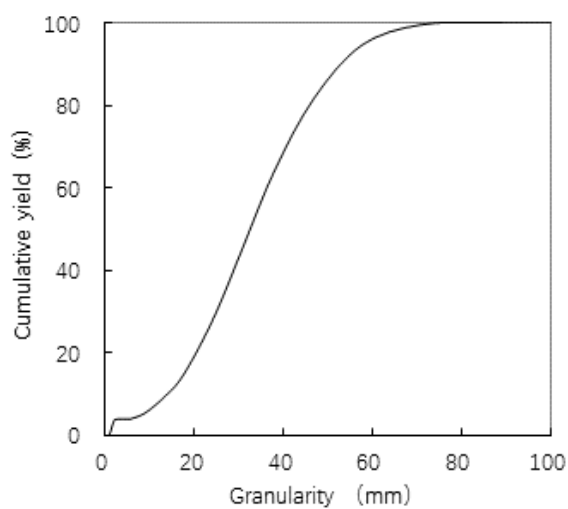
Fig.2 Curve of laser particle size on coal sample.

2. Mineral composition

XRD analysis was carried out on the samples in this paper，and the experimental results are shown in Figure 3
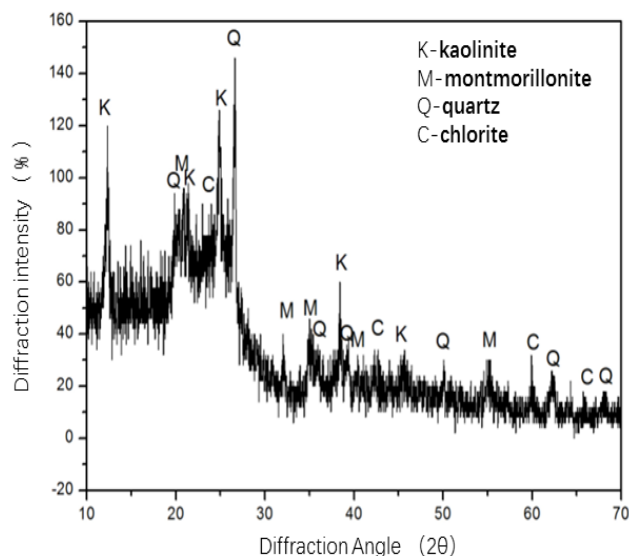
Fig.3 XRD analysis of coal sample.

3.   The Optimum formula selection

Three factors, namely, coagulant dosage, flocculant dosage, and slurry water concentration, were controlled during this experiment[2]. Then single-factor experiments were carried out, and the experimental results were shown in table 1.Orthogonal table L_{27}（3^{13}） was selected for complex test, and the best combination of compound experimental results is $A_1B_3C_1$. When slime water concentration is 50g/L, PAC addition amount is 60g/m^3, and APAM addition amount with molecular weight of 10 million is 4.8g/m^3, the flocculation sedimentation effect of slime water is the best. At this time, the light transmittance of coal slurry water is 86.7%, and the settling speed of coal slurry is as high as 710.46cm/min.

Table.1 Horizontal design of orthogonal factors.

Level	factor A: coagulant (g/m^3)	factor B: flocculant (g/m^3)	factor C: slime concentration (g/L)
1	60	1.8	50
2	70	2.6	75
3	90	4.8	100

Results and Discussion

1.   ζ potential analysis

In this section, the experimental conditions are as follows: the slurry water concentration is 50g/L, and the coagulant is PAC. The experimental results are shown in figure 4.
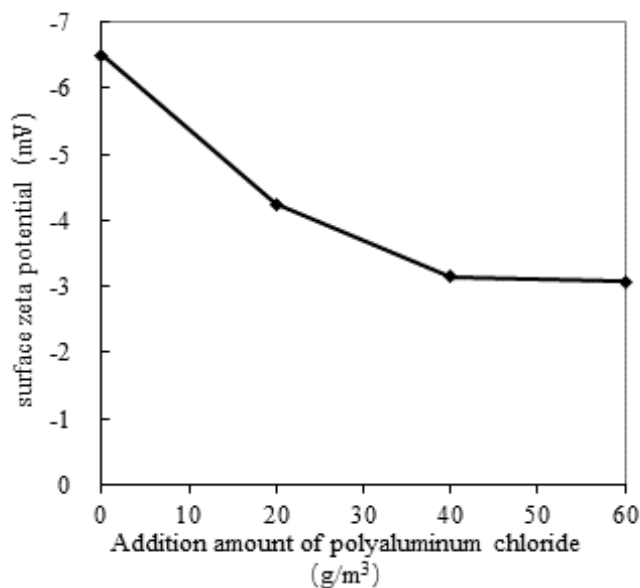
Fig.4 Influence of the addition of PAC on zeta potential

According to figure 4, the addition of PAC can effectively reduce the surface potential of coal slime particles. When no coagulant is added, the particle surface has more negative charge and greater surface potential absolute value. When two particles with the same electrical properties are close to each other, their double electric layers will overlap with each other, and the electric potential between the particle interfaces will increase, which will increase the electrostatic repulsion force, leading to the dispersed stable state of particles in the system. When the dosage of condensed matter gradually increases, the positively charged ions react with the negative charges on the surface of particles. The surface potential of particles decreases, and the electrostatic repulsion between particles becomes weaker. At this time, small particles may condense into large particles and settle.Therefore, adding PAC can effectively reduce the particle surface potential, and zeta potential is lower, the easier it is for fine particles to flocculation sedimentation.

2. Infrared spectroscopic analysis

In this paper, infrared spectrum analysis was carried out before and after the compound agent acted with coal, and the experimental results are shown in Figure 5. It can be seen from figure 5 that the infrared spectrum of coal changed to some extent after the compound agent. The peak values of wave number $3450.56 cm^{-1}$ (H_2O expansion) and $1650.21 cm^{-1}$ (C=O expansion) were significantly reduced，indicating that the adsorption of poly aluminum on the surface of coal particles occurs.

In conclusion, the mechanism of action of coagulants in treating slime water is to reduce the potential on the surface of slime particles and then reduce the electrostatic repulsion between particles, so that small particles will condense into large particles [3]. The main action mechanism of flocculant in treating coal slime water shows that the flocculant acts with coal slime fine particles through the active group on the molecular chain, generates mutual adsorption phenomenon and plays a bridging role. In addition, by comparing the infrared spectra of the surface of slime particles with the action of flocculant and compound

agent (coagulant and flocculant), it can be seen that the flocculant also adsorbs on the surface of solid particles, which may be hydroxyl complex adsorption.
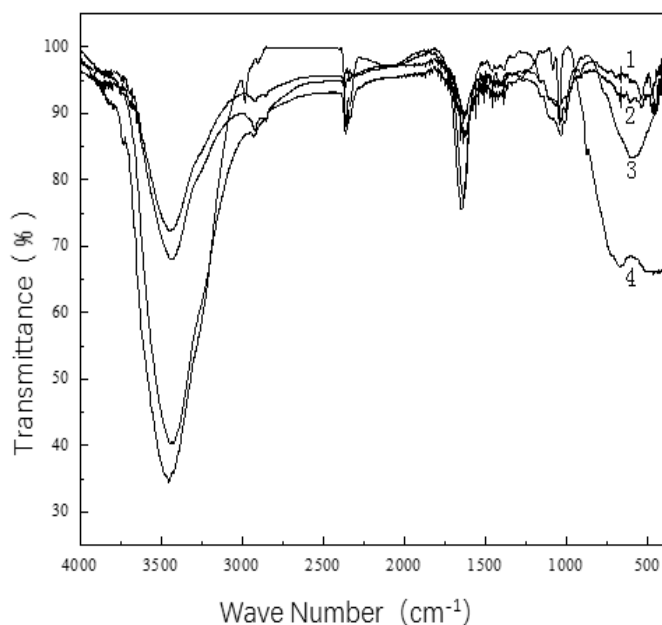
Fig.5 Infrared spectrogram before and after the action of compound agents and coal particles (1-compound agents interacts with coal samples, 2- raw coal;3- PAC, 4-APAM).

Conclusion

Through XRD analysis, it can be seen that the minerals contained in the coal slime are kaolinite, montmorillonite, quartz and chlorite, etc. The main components are clay minerals, which are easily sliming in water, thus increasing the difficulty of natural sedimentation of coal slime particles. By zeta potential and infrared spectrum analysis, the flocculant adsorption on the surface of coal particles, can effectively reduce the surface potential.When the amount of coagulant is gradually increased, the positively charged ions react with the negative charge on the surface of the solid particles in charge neutralization. As a result, the surface potential decreases and the small particles of coal slurry polymerize to form large particles, which is conducive to the sedimentation of coal slurry. Under the action of coagulants, the fine particles of coal slime become large particles, which can be adsorbed on many active groups on the molecular chain of flocculant. The coal slime particles in the system eventually form large flocs, thus accelerating their sedimentation. It can be seen that polymer flocculant plays a role of adsorption-bridge. This paper is about the study of the mechanism of coal slime concentration and settlement, which is helpful to the subsequent pressure filtration and dehydration effect of tailings.

References

[1] Lin Z , Wang Q , Wang T , et al. Dynamic floc characteristics of flocculated coal slime water under different agent conditions using particle vision and measurement[J]. Water Environment Research, 2020, 92.

[2] Smirnova A I , Dyagileva A B . Evaluation of the Effect of Temperature on the Efficiency of Wastewater Treatment with a Composite Coagulant-Flocculant Based on Nepheline Raw Materials[J]. Russian Journal of Applied Chemistry, 2021, 94(2):252-258.

[3] C. Peng, Y. Zhong, F. Min, Adsorption of alkylamine cations on montmorillonite (001) surface: a density functional theory study, Appl. Clay. Sci. 152 (2018) 249–258.

Preparation and electrochemical performance of NiCo$_2$O$_4$@Co$_3$O$_4$ nanomaterials by ball milling

NI Liang-liang, SHENG Shao-ding, TIAN Kong-hu

Material science and Engineering School, Anhui University of Science and Technology, Huainan 232001

Abstract

With the increasing concentration of sustainable development and energy crises, the efficiency of energy storage systems also urgent to be improved. Supercapacitor is a new type of energy storage element, with the advantages of higher capacity, higher power and higher charge and discharge efficiency than traditional batteries[1, 2]. At present, the development of capacitors is fairly mature and will be widely applied in automobiles, military equipment, and daily electronic equipment. Porous carbon materials, transition metal oxides, and conductive polymers are currently the most studied capacitor materials.

The spinel structure of NiCo$_2$O$_4$ has multiple states of metal oxides, and possesses higher specific capacitance and rate property for its better conductivity and electrochemical activity than single metal oxides (NiO or Co$_3$O$_4$)[3-5]. Therefore, it is a supercapacitor electrode material with good application prospects. Besides, NiCo$_2$O$_4$ has many other advantages, including low preparation cost, abundant raw material resources, etc. The electrochemical properties of the NiCo$_2$O$_4$ nanomaterials obtained are different due to different preparation conditions. In this paper, NiCo$_2$O$_4$@Co$_3$O$_4$ composites were prepared by high-energy ball milling of nickel carbonate and basic cobalt carbonate. And materials were characterized by the powder X-ray diffraction, X-ray photoelectron spectrometer, scanning electron microscope, and transmission electron microscope to identify phase, structure and morphology of the sample. The characterization results show that spherical composite materials can be obtained by ball milling and annealing, with a size of about 12 nm, as shown in Fig.1. The 70 wt% as-prepared NiCo$_2$O$_4$@Co$_3$O$_4$ with 20 wt% Acetylene black and 10 wt% Poly tetra fluoroethylene (PTFE) were mixed and painted on the stainless steel mesh (1cm×1cm) as as a current collector. The electrochemical performance is shown in Fig.2. The NiCo$_2$O$_4$@Co$_3$O$_4$ possesses a specific capacitance of 200F/g at a current density of 1A/g and a potential range of 0-0.45v, And after 500 charge-discharge cycles, 90.5% of the specific capacitance remains.
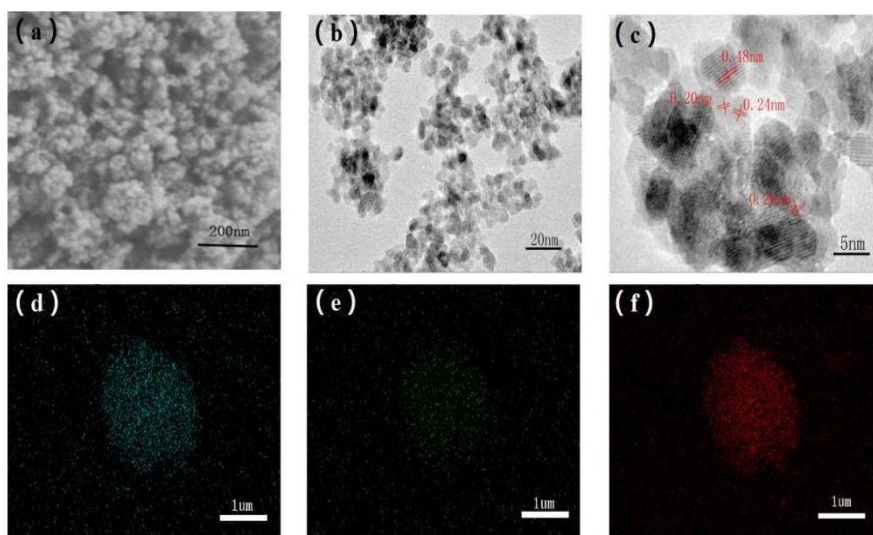
Fig.1 (a)SEM Picture;　(b)(c) TEM Pictures; (d)～(f) SEM-EDS Mapping photos
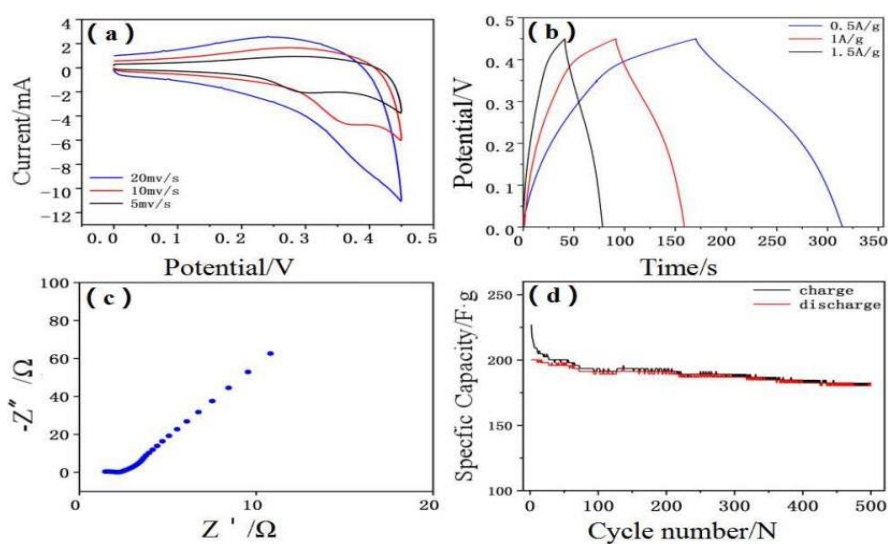
Fig.2 Graph of electrochemical performance of materials. (a) cyclic voltammetry curves; (b) Charge and discharge curves; (c) impedance spectrum;(d) Cyclic charge-discharge test curve.

Acknowledgments

References

[1] MILLER John R., SIMON Patrice. Electrochemical capacitors for energy management. Science Magazine, 2008, 321(5889): 651-652.

[2] LEE Seung Woo, et al. Nanostructured carbon-based electrodes: bridging the gap between thin-film lithium-ion batteries and electrochemical capacitors. Energy & Environmental Science, 2011, 4(6): 1972-1985.

[3] ZHANG Zai-lei, et al. Mesoporous $CoFe_2O_4$ nanospheres cross-linked by carbon nanotubes as high-performance anodes for lithium-ion batteries. Journal of Materials Chemistry A, 2013, 1(25): 7444-7450.

[4] PENG Sheng-jie, et al. In situ growth of $NiCo_2S_4$ nanosheets on graphene for high-performance supercapacitors. Chemical communications, 2013, 49(86): 10178-10180.

[5] XIE Qing-shui, et al. Template-free synthesis of amorphous double-shelled zinc–cobalt citrate hollow microspheres and their transformation to crystalline $ZnCo_2O_4$ microspheres. ACS applied materials & interfaces, 2013, 5(12): 5508-5517.

Properties of Radiation Cross-linked Polytetrafluoroethylene

Feixiang Sha [a,d], Guojun Cheng [a,b,c,*], Zhongfeng Tang [d,e,*], Ziyue Xuan[a], Meng Liu[a]

[a] School of Materials Science and Engineering, Anhui University of Science and Technology, Huainan 232001, China;

[b] Anhui Province Key Laboratory of Environment-friendly Polymer Materials, Anhui University, Hefei 230601, China;

[c] Institute of Environment-Friendly Materials and Occupational Health, Anhui University of Science and Technology (Wuhu), Wuhu, China;

[d] *Shanghai Institute of Applied Physics, Chinese Academy of Sciences, Shanghai 201800, China;*

[e] *Key Laboratory of Interfacial Physics and Technology, Chinese Academy of Sciences, Shanghai, 201800, China.*

Corresponding author: Guojun Cheng and Zhongfeng Tang

Email: *chengguojun0436@126.com* and *tangzhongfeng@sinap.ac.cn*

Abstract

Cross-linked polytetrafluoroethylene (XPTFE), which had a cross-linked network structure, was formed by polytetrafluoroethylene (PTFE) irradiated at a high temperature at a specific temperature. Compared with PTFE, XPTFE had significantly enhanced radiation and abrasion resistance, which effectively compensated for the deficiencies of PTFE and had a wider application range. The crystallization enthalpy, melting temperature, surface hardness and dynamic mechanics of XPTFE vary with the cross-linking degree were studied in this article. The results showed that the crystallinity and the melting temperature of XPTFE decreased and the surface hardness increased as the absorbed dose increased. By introducing crosslinking, the temperature of α relaxation shifted to lower temperatures while that of γ relaxation shifted to higher temperature and β relaxation disappeared.

Keyword: PTFE, Cross-linked PTFE, Differential scanning calorimeter, Surface hardness, dynamic mechanics

Introduction

Due to its excellent thermal properties, chemical stability and low dielectric constant, polytetrafluoroethylene (PTFE) is an ideal material for the encapsulation of corrosive chemicals or electronic components. However, due to its extreme sensitivity to ionizing radiation, only a few kGy doses can make it completely lose its mechanical properties [1, 2]. Therefore, PTFE has been widely used as a typical radiation cracking material for a long time. Until the last few decades, PTFE has been found to be

234

crosslinked when irradiated in the absence of oxygen and at a temperature slightly above the crystalline melting point [3, 4].

As an emerging material, cross-linked polytetrafluoroethylene (XPTFE) not only retains the excellent properties of PTFE but also has superior mechanical properties and radiation stability[5-9]. Therefore, XPTFE is expected to have a large prospect of application in the fields of artificial satellites, spacecraft and nuclear facilities. Tang [10, 11] et al. studied the structural changes of XPTFE using in situ SAXS and found that the grain size of cross-linked PTFE decreased with increasing irradiation dose. Li [12, 13] et al. studied the structural evolution pattern of XPTFE during deformation using in situ SAXS, and at low tensile stress, with increasing dose, the thin layer structure of XPTFE became more and more obvious and its long-period structure became weaker, and the mechanism during deformation was analyzed for XPTFE with different degrees of cross-linking.

In this experiment, three types of XPTFE with low, medium and high cross-linking degree (XPTFE90, XPTFE300 and XPTFE1500) were prepared by electron beam irradiation at high temperature, and their structures and properties were investigated. In this work, the crystallization enthalpy, melting temperature, surface hardness and dynamic mechanics of XPTFE vary with the cross-linking degree were studied.

Results and discussion

1. Differential scanning calorimeter (DSC) of XPTFE

Table 1. Crystallization enthalpy, melting temperature and number average molecular weight of PTFE and XPTFE.

Sample code	Dose (kGy)	Crystallization enthalpy (J/g)	Melting temperature (°C)	Number average molecular weight (g/mol)
PTFE	0	26.1	325.9	1.6×10^6
XPTFE90	90	40.0	322.9	1.8×10^5
XPTFE300	500	36.0	313.3	3.2×10^5
XPTFE1500	1500	15.1	273.5	2.8×10^7
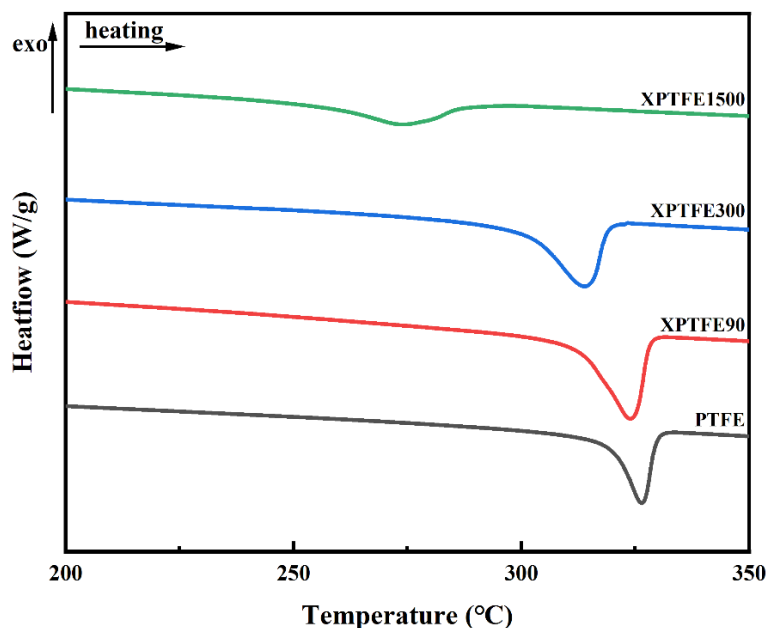
Fig 1. DSC thermograms of XPTFE with different degree of crosslinking.

The DSC thermograms of XPTFE with different degree of crosslinking was shown in Fig.1. The peak shown in this picture was related to the melting of polymers. The melting point and crystallinity of XPTFE cross-linked by different irradiation doses were different. The number average molecular weight ($\overline{Mn}$) of samples was measured by DSC and then calculated using the equation by Suwa [14] et al. The detailed data of the melting temperature, enthalpy of crystallization, crystallinity and molecular weight of samples could be found in Table 1. It can be seen from the Fig.1 that as the absorbed dose increased, the melting temperature and crystallization temperature of XPTFE gradually shift to low temperatures, and the heat of crystallization also decreased. This is due to XPTFE was cross-linked in the molten state under irradiation and a mesh structure was formed in this process, which led to the poor mobility of molecular chains and the formed crystals were not perfect during cooling and crystallization process. Therefore, as the degree of cross-linking increased, the crystallinity of XPTFE decreased. During the irradiation process, XPTFE was also degraded to some extent. When the absorbed dose was low, the heat of crystallization increased due to the presence of partial degradation. As the absorbed dose increased, for XPTFE, the proportion of crosslinking increased but that of degradation decreased. The ratio between the crystalline part and the amorphous part gradually decreased due to cross-linking, which destroyed the crystallinity and led to a decrease in its crystallization enthalpy.

2. Surface hardness of XPTFE
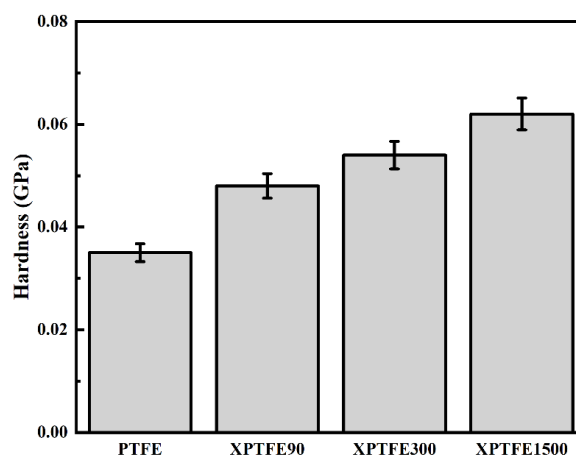
Fig 2. Surface hardness of XPTFE with different degree of crosslinking.

The Surface hardness of XPTFE with different degree of crosslinking was shown in Fig 2. As the absorbed dose increased, the surface hardness of XPTFE increased. Due to the extremely high electronegativity of fluorine atoms and the perfect symmetry of the PTFE monomer structure, the force between PTFE molecules was weak and the cohesive energy was low. With the occurrence of cross-linking, a cross-linked network structure was formed between XPTFE molecules, which in turn led to an increase in the force between XPTFE molecules and an increase in strength. As the absorbed dose increased, the degree of cross-linking of XPTFE increased, the force between XPTFE molecules increased, and the surface hardness increased slightly.

3. Dynamic thermomechanical analysis of XPTFE
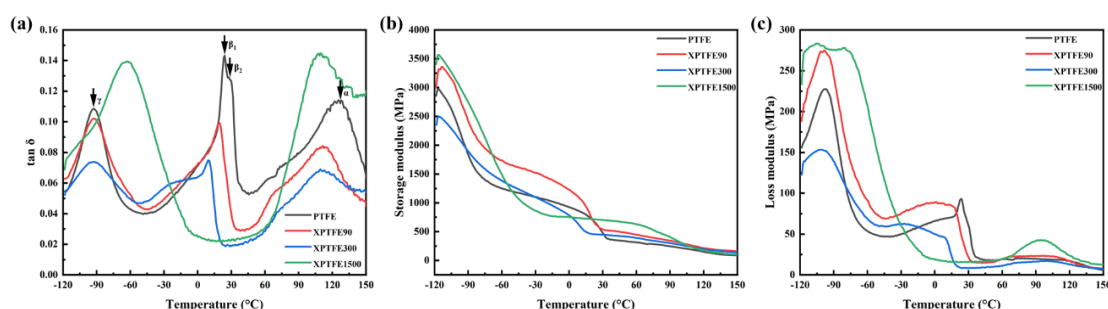
Fig 3. Dynamic thermomechanical analysis of XPTFE with different degree of crosslinking.

The loss factor (tanδ), storage modulus (E') and loss modulus (E") of XPTFE with different degree of crosslinking was shown in Fig 3. And Tanδ can be calculated from the ratio of E'' and E'. As shown in Fig 3a, for PTFE, four peaks associated with different patterns of molecular at the respective temperatures were marked by α, $β_1$, $β_2$ and γ, respectively. Sauer, McCrum et al. [15-18] attributed the transition at about -97 °C (γ relaxation)) and about 130 °C (α relaxation) to molecular motion in the amorphous

fraction, and the glass transition to α relaxation. Meanwhile, the two observed crystalline transitions at approximately 19 and 30 °C (β_1, β_2 relaxation) had been assigned to conformational changes of molecular chains in crystals. However, Oshima et al. [19] declared that the relaxation cannot be attributed to the glass transition and attributed the α relaxation to the molecular motion mode of polymer chains penetrating among crystallites. At present, there is no consensus on the ownership of the three secondary transition peaks, which needs further research. For XPTFE, it can be found that with the increase of cross-linking degree, the γ transition moved to high temperature, the β transition moved sharply to low temperature until disappeared and the α transition moved to low temperature. Oshima et al. [19] explained the disappearance of β transition was due to the small size of crystallites affected by the cross-linking, the shift of γ transition was attributed to the change of glass transition temperature to high temperature caused by cross-linking and the shift of α transition is due to the lateral structure of polymer chains becoming more disordered with increasing crosslinking.

Conclusion

In this paper, the thermal properties, surface hardness and dynamic mechanics of XPTFE have been studied. As the absorbed dose increased, the crystallinity and the melting temperature of XPTFE decreased and the surface hardness increased. By introducing crosslinking, the temperature of α relaxation shifted to lower temperatures while that of γ relaxation shifted to higher temperature and β relaxation disappeared. This work introduced some basic properties of XPTFE cross-linked by electron beam at high temperature. It also proved the application potential of XPTFE and provided important information for the subsequent design of XPTFE composite materials.

Acknowledgments

Reference

[1] LUNKWITZ K, BRINK H-J, HANDTE D, et al. Radiat. Phys. Chem., 1989, 33(523).

[2] KOCHERVINSKII V V, GLUKHOV V A, LEONT'EV V P. Polymer Science USSR, 1986, 28(4): 772-781.

[3] SUN J, ZHANG Y, ZHONG X, et al. Radiat. Phys. Chem., 1994, 44(6): 655-659.

[4] SUN J, ZHANG Y, ZHONG X. Polymer, 1994, 35(13): 2881-2883.

[5] OSHIMA A, TABATA Y, KUDOH H, et al. Radiat. Phys. Chem., 1995, 45(2): 269-273.

[6] OSHIMA A, IKEDA S, SEGUCHI T, et al. Radiat. Phys. Chem., 1997, 49(2): 279-284.

[7] TANG Z, WANG M, ZHAO Y, et al. Radiat. Phys. Chem., 2011, 80(3): 496-500.

[8] SEGUCHI T. Radiat. Phys. Chem., 2000, 57(3): 367-371.

[9] TANG Z, WANG M, ZHAO Y, et al. Wear, 2010, 269(5): 485-490.

[10] FENG T, ZHONGFENG T, HONGJIE X, et al. Polym. Polym. Compos., 2011, 19: 439-444.

[11] TANG Z, WANG M, TIAN F, et al. Eur. Polym. J., 2014, 59: 156-160.

[12] LI X, TIAN F, YANG C, et al. J. Appl. Polym. Sci., 2014, 131(4).

[13] LI X, TIAN F, TANG Z, et al. Eur. Polym. J., 2016, 83: 35-41.

[14] SUWA T, TAKEHISA M, MACHI S. J. Appl. Polym. Sci., 1973, 17(11): 3253-3257.

[15] SAUER J A, KLINE D E. J. Polym. Sci., 1955, 18(90): 491-495.

[16] MCCRUM N G. J. Polym. Sci., 1958, 27(115): 555-558.

[17] SAUER J A, WOODWARD A E. Rev. Mod. Phys., 1960, 32: 88.

[18] MCCRUM N G. J. Polym. Sci., 1959, 34: 355.

[19] OSHIMA A, IKEDA S, SEGUCHI T, et al. Radiat. Phys. Chem., 1997, 49(5): 581-588.

Synthesis of Co/C@PANI with high microwave absorption properties

Guiyang Xian, Zhaolin Zhu, Chongmei Wu, Yan Wang, Yin Liu[*]

School of Materials Science and Engineering, Anhui University of Science and Technology, Huainan 232001, Anhui, China
*Corresponding authors: yinliu@aust.edu.cn (Yin Liu)

Abstract

This paper introduces the preparation of Co/C material by calcination based on zif-67, one of MOFs materials. Taking Co/C material as the source material, the microwave absorption performance of the material is improved by in-situ synthesis of coated polyaniline. In this paper, pure phase Co/C@PANI is prepared, It is found that the microwave absorption performance of Co/C material coated with polyaniline is significantly improved.

Keywords: Co/C; PANI; Absorbing wave

Introduction

Metal/carbon composites are generally prepared by liquid-phase synthesis method, so that carbon materials with large specific surface area react with metal salts. After calcination in inert gas or reduction with strong reducing agent, metal/carbon composite microwave absorbing materials can be obtained [1].

With the continuous research on microwave absorbing materials, it is found that the preparation of magnetic metal/carbon composite microwave absorbing materials by metal organic framework derivation method can avoid the problem of uneven distribution of components in the materials, while metal organic framework complexes (MOFs) can be used not only as metal source but also as carbon source, and their morphology is easier to maintain in high-temperature pyrolysis reaction, The metal/carbon composites with uniform distribution of components can be obtained by one-step pyrolysis. During the pyrolysis of MOFs materials, magnetic metal nanoparticles are formed in the carbon matrix [2].

Conductive polymers have both the electrical properties of inorganic conductors and metals and the processability of polymer. Polyaniline (PANI) is a common conductive polymer. Ting et al [3] prepared polyaniline/multi wall carbon nanotube composites by in-situ polymerization. PANI was attached to the tube wall of multi wall carbon nanotube in needle shape. The reflection loss of the material decreases with the increase of PANI mass fraction. On this basis, polyaniline is coated on Co/C material to improve dielectric loss and magnetic loss, and work together to improve reflection loss [4].

Experiment

The preparation of composites by coating MOFs with polyaniline can improve the specific surface area of Polyaniline and the microwave absorption performance of MOFs.

Firstly, zif-67 precursor is prepared, and Co/C composites are obtained by calcination. Then, coated polyaniline is synthesized in situ at low temperature. After centrifugation, washing and drying, pure samples are obtained.

Results and Discussion

As shown in Figure 1, The steamed bread peak of Polyaniline and the peaks of Co and C can be seen obviously, indicating that the prepared composite is pure and free of impurities. With the increase of Co/C addition, the peak strength of polyaniline decreases and the peak strength of Co and C increases.
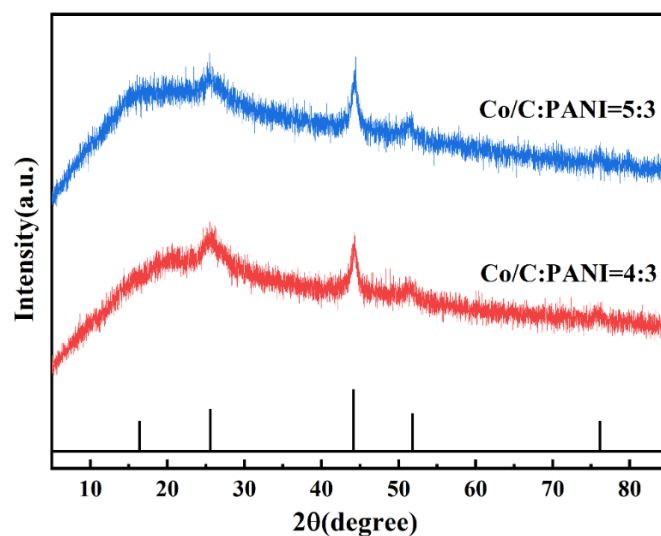
Figure 1. XRD pattern of obtained Co/C@PANI sample.

As can be seen from Figure 2, Zif-67 is a Co/C composite prepared after calcination, and polyaniline is coated on the composite. The coated polyaniline can be clearly seen on the surface. The coated polyaniline is relatively uniform, the particles maintain the dodecahedral shape, the structure is intact and the dispersion is good.
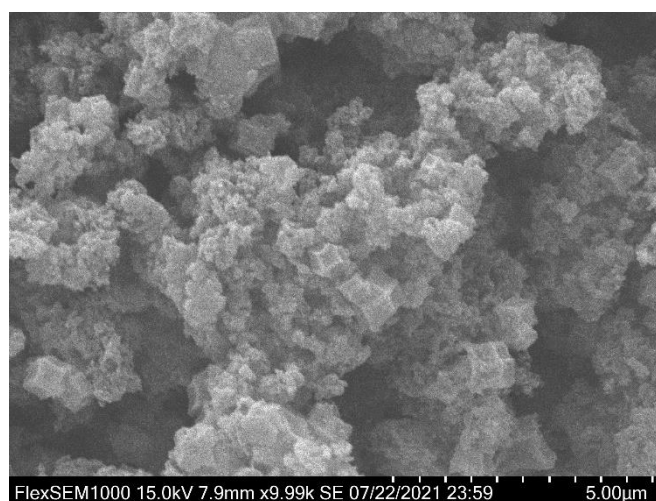
Figure 2. SEM image of Co/C@PANI sample.
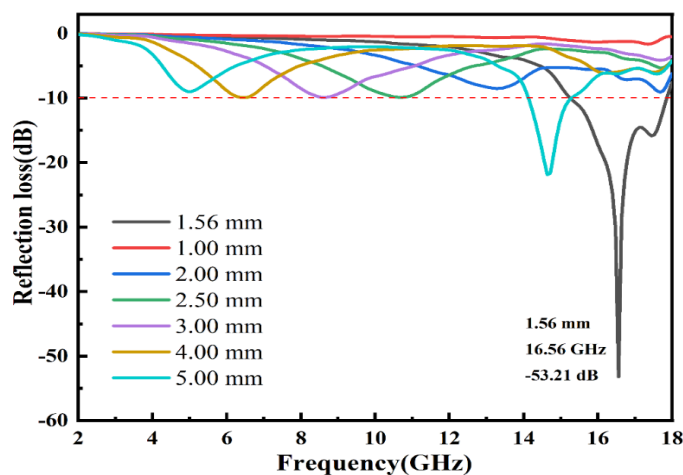
Figure 3. Reflection loss diagram of Co/C@PANI sample.

As can be seen from Figure 3, at 16.56ghz, the minimum reflection loss is -53.21db, the thickness is 1.56mm, and has a wide absorption bandwidth.

Conclusion

In this experiment, the pure phase zif-67 precursor was prepared. After calcination, the pure phase Co/C composite was prepared. After centrifugal washing and drying, PANI was synthesized in situ on the Co/C composite. It was seen by SEM that PANI was successfully coated on the Co/C composite, and Co/C@PANI was tested the reflection loss value of the composite has good microwave absorption performance.

Acknowledgments

References
[1] Zhao H B, Fu Z B, Chen H B, et al. Excellent Electromagnetic Absorption Capability of Ni/Carbon Based Conductive and Magnetic Foams Synthesized Via A Green One Pot Route[J]. ACS Applied Materials & Interfaces, 2016, 8(2): 1468-1477.
[2] Zhu L, Zeng X, Li X, et al. Hydrothermal Synthesis of Magnetic Fe_3O_4/Graphene Composites with Good Electromagnetic Microwave Absorbing Performances[J]. Journal of Magnetism and Magnetic Materials, 2017, 426: 114-120.
[3] Ting T H, Jau Y N, Yu R P. Microwave Absorbing Properties of Polyaniline/Multi-Walled Carbon Nanotube Composites with Various Polyaniline Contents[J]. Applied Surface Science, 2012, 258(7): 3184-3190.
[4] Wen S L, Liu Y, Zhao X C. Facile Chemical Synthesis, Electromagnetic Response, and Enhanced Microwave Absorption of Cobalt Powders with Controllable Morphologies[J]. The Journal of Chemical Physics, 2015, 143(8): 084707.

L-aspartic acid flame retardant polyvinyl alcohol composites membrane with high transparency

Meng Liu[a], Guojun Cheng [a,b,c], Ziyue Xuan [a], Longxuan Zhou [a], Shen Tian [a], Feixiang Sha[a]

[a] School of Materials Science and Engineering, Anhui University of Science and Technology, Huainan 232001, China

[b] Anhui Province Key Laboratory of Environment-friendly Polymer Materials, Anhui University, Hefei 230601, China

[c] Institute of Environment-Friendly Materials and Occupational Health, Anhui University of Science and Technology (Wuhu), Wuhu, China

Corresponding author: Guojun Cheng and *chengguojun0436@126.com*

Abstract

In recent years, it has been a challenge to maintain the transparency and excellent mechanical properties of Poly (vinyl alcohol) membrane with good flame retardant properties. In this paper, environment-friendly and biocompatible L-aspartic acid was used as flame retardant, and the uniform molecular dispersion of flame retardant in polyvinyl alcohol film was realized by one-pot method based on esterification reaction. By this method, high transparency of PVA/L-ASP composites film is obtained. The transparency, flame retardant property and tensile property of the composite film were tested. The results showed that the transparency of the film was very high, no crystallization was found in the film through the SEM picture. During the tensile test, it was found that the composite film could be stretched to three times the original length. In the fire retardant test, the film was not ignited within 10 seconds, it quickly carbonized to form a carbon layer, so that the film had a good flame retardant effect.

Key words: Esterification, L-aspartic acid, flame retardant, Poly (vinyl alcohol) membrane

Introduction

Polyvinyl alcohol is an extremely versatile water soluble polymer derived from the hydrolysis of Polyvinyl Acetate. Its unique properties, including hydroxyl groups in the repeating units, strong polarity, easy to form hydrogen bonds with each other, so that the polyvinyl alcohol has excellent water solubility, film formation, oil resistance and other properties. Thin films made from polyvinyl alcohol are characterized by excellent Biocompatibility, excellent mechanical properties, and excellent barrier properties, it is widely used in the fields of antibacterial and bacteriostatic [1-3] , flexible optoelectronic devices[4-6], gas barrier[7-9] and so on. However, as a membrane product with smaller thickness, its

flammability is much higher than that of the product with larger wall thickness, and it will release unsaturated Aldehydes, ketones and other harmful substances when burning[10-12].

At present, it is a conventional method to prepare flame retardant film by Casting PVA solution with flame retardant agent. Several flame retardants, such as phosphorus compounds [13-18] , layered inorganic [19-21] and hydroxide [22,23], have been reported to be used in PVA membranes. Although some of these flame retardants can achieve an ideal flame retarding effect through the synergistic action of one or more components, their incompatibility with PVA solution leads to agglomeration or precipitation, most of the flame-retardant fillers are difficult to disperse evenly in the film, especially Inorganic fillers with high addition (15% ~ 30%) . Poor dispersion will not only reduce the flame retardant efficiency and mechanical properties of PVA film, but also further reduce the transparency of PVA film. High transparency of PVA film is very important for its wide application.

It is difficult to maintain good transparency of the flame retardant film. In general, there are two ways to improve the transparency of the film. For the physical addition method, the particle size of the added flame retardant should be reduced to the nanometer scale, and the uniform dispersion should be achieved in the polymer film. Reactive grafting of flame retardants onto polymer chains is another method to improve the transparency of membranes. In fact, both of these approaches are uncontrollable, complex, and expensive. So far, it is still a challenge to prepare polyvinyl alcohol (PVA) membranes with good flame retardancy and high transparency by a simple and economical process.

In this research, there is an amino acid, L-Aspartic Acid, was introduced as a flame retardant. L-aspartic acid (L-ASP) , also known as-aminosuccinic acid, is an important Acidic amino acid, which is widely used in food, medicine, chemical and other fields[24]. In the food industry, L-Aspartic Acid is the dietary supplement of a variety of foods and is also used in the synthesis of the sweetener Aspartame[25]; in medicine, it is used as a liver promoter, an ammonia antidote, a fatigue restorer[26]. It is also a major raw material for the synthesis of L-alanine and a variety of pharmaceutical intermediates; in chemical engineering, it can be used as a list of synthetic polymers L-Aspartic Acid. L-ASP is non-toxic and contains nitrogen and two carboxyl groups. In this study, its carboxyl group was used to esterify with the hydroxyl group of polyvinyl alcohol to form transparent flame-retardant PVA film.

Experimental

1. Materials

PVA with a polymerization degree of 1680-1850 and an alcoholysis degree of 98.0-100.0%, is supplied by Anhui Wanwei Group CO., LTD. L-Aspartic Acid and and HCl are supplied by Sinopharm Chemical ReagentCo., Ltd.

2. Preparation of the flame retardant PVA/L-ASP composites membranes
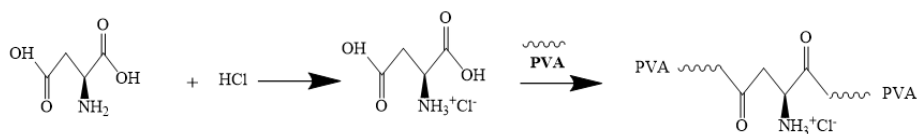
Scheme 1. synthetic procedure

The membranes are prepared by solution casting method and their preparation process is shown in Scheme 1. Put1g L-aspartic acid is dissolved in 10g 1 mol/L HCl solution, stir in oil bath at 70 °C for 1 hour, then add 2 g of PVA solution in oil bath for 2 hours, pour the mixture into acrylic model plate, put it at room temperature for 12 hours to volatilize part of the solvent. Then the transparent flame retardant film was obtained at 55 °C in an oven. The composites named PVA/L-ASP.

3. Characterization

The morphology and surface elements of the samples were observed by scanning electron microscope (SEM). The scanning voltage is 30kV. In addition, energy dispersive spectroscopy (EDS) and mapping of element distribution in the sample were performed to determine sample composition.

The dimensions of PVAfilm and PVA/L-ASP composite film for combustion test is 5cm×2.5cm×300μm

Tensile test PVA film and PVA/L-ASP composite film size is 5cm*1cm*300μm

Results and discussion

1. The morphology and surface elements and transparency of PVA/L-ASP membranes
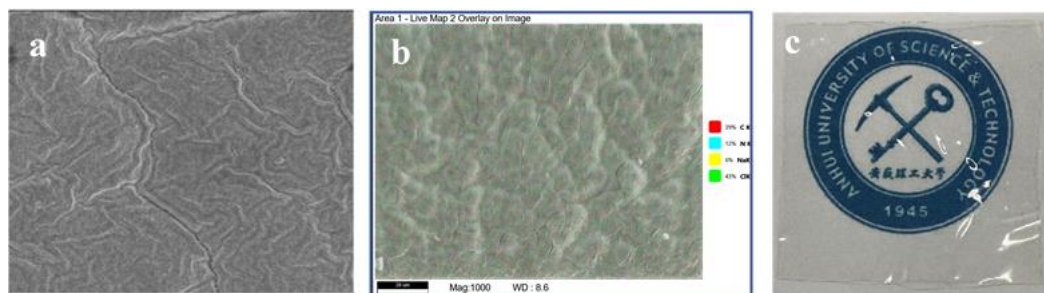
Fig. 1. Micro-morphology and transparency of PVA/L-ASP composite membrane (a. Sem of composite film, b. EDS of composite film，c. Transparency Photograph of composite film).

As shown in Fig. 1a, the surface of the PVA/L-ASP composite film is very smooth except for a few cracks, and the L-Aspartic Acid crystals are not visible. It is most likely that the L-ASP are all converted to a solution of hydrochloric acid with a lower melting point, which is

liquid at room temperature, good fusion with PVA membrane. As can be seen from fig. 1b, the nitrogen element representing the L-ASP is evenly distributed and does not gather, indicating a better fusion between the L-ASP and PVA. As can be seen from Fig. 1c, the resulting PVA/L-ASP blend membrane is transparent and colorless, thus showing the perfect fusion of L-Aspartic Acid and PVA.

2. Mechanical property
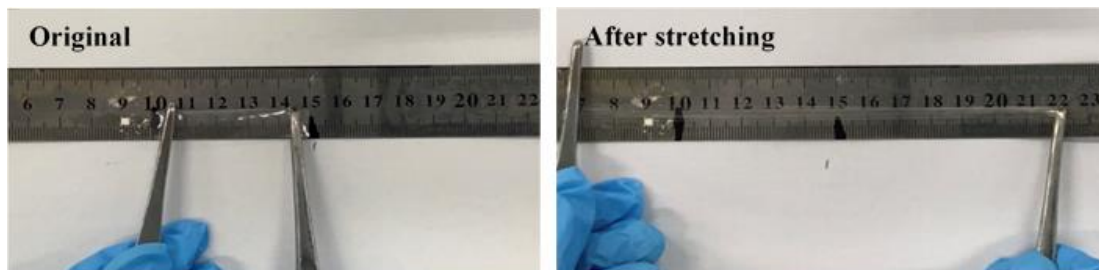
Fig. 2. Tensile properties of composite membrane.

Tensile properties were tested to investigate the mechanical properties of the PVA/L-ASP composite membrane. The detailed results are shown in Fig. 2. As shown in figure, the PVA/L-ASP composite film has good tensile property and can be stretched to 3 times its original length. The pure PVA membrane is not malleable, which may be due to the good compatibility between L-ASP and PVA, and the formation of soft ester bonds, hydrogen bonds in the reaction process. Pure PVA molecular chain is regular and easy to crystallize, destroying the crystal structure of PVA is one of the reasons for the higher flexibility of PVA/ L-ASP films[27].

3. Flame retardancy

As shown in Fig.3, the pure PVA membrane was ignited at 4s, burned rapidly at 6s, and almost burned completely at 10S. The prepared PVA/L-ASP composite membrane has not been burned, but has been carbonized, and the shape of the burning residue membrane is complete as shown in Fig. 4. The possible reason is that in the gas phase, the nitrogen in the L-ASP forms non-flammable ammonia and dilutes the concentration of flammable gases such as nitrogen, which causes the concentration of flammable gases to be lower than the concentration of flammable gases, thus inhibiting combustion. In the condensed phase, the overall acidity of the L-ASP causes the membrane to be carbonized rapidly during heating, forming a protective carbon layer that insulates the inner membrane from heat and thus inhibits combustion.
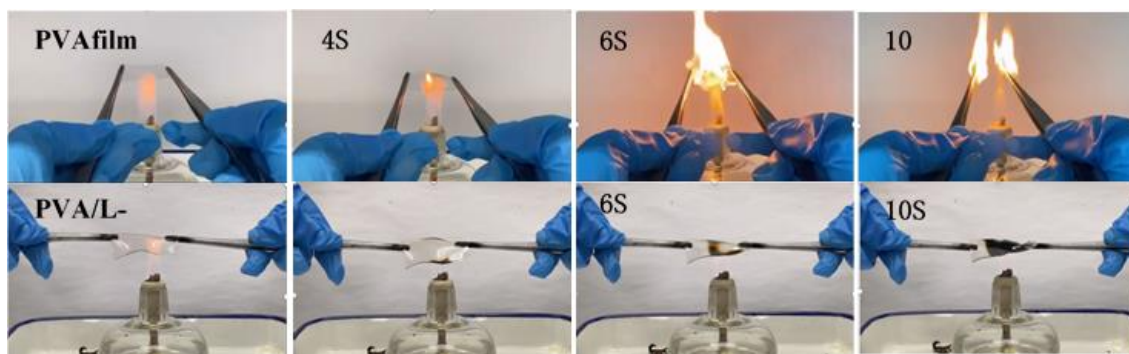
Fig. 3. Photos of Burning of pure PVA and PVA/L-ASP.
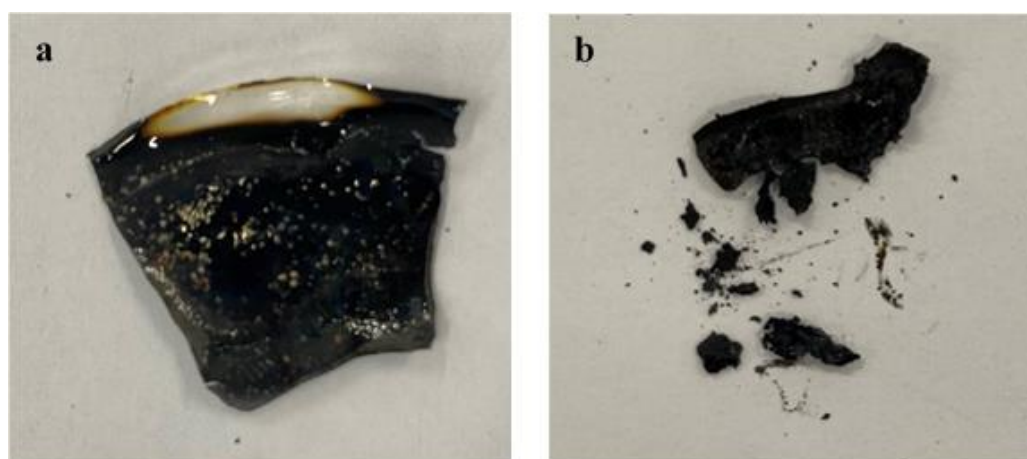
Fig. 4. Combustion residue of membrane (a. PVA/L-ASP composites film,b. PVA film).

Conclusions

In this paper, the excellent polyvinyl alcohol flame retardant film was prepared by a simple one-pot method, and the L-Aspartic Acid in the flame retardant film played the role of flame retardant, and the content of L- Aspartic Acid could be added to a very high level. The flame-retardant transparent film and the preparation method thereof have the advantages of simple implementation process, high efficiency, low cost and easy realization.

Acknowledgment

Reference

[1] Bhat S A, Zafar F, Mirza A U, et al. Arabian Journal of Chemistry, 2020, 13(6): 5724-5739.

[2] Youssef A M, El-Naggar M E, Malhat F M, et al. Journal of Cleaner Production, 2019, 206: 315-325.

[3] Min T T, Sun X L, Yuan ZH P, et al. LWT, 2021, 135: 110034.

[4] Saini I, Sharma A, Dhiman R, et al. Journal of Alloys and Compounds, 2017, 714: 172-180.

[5] Wang T, Wang Y Z, Jing L C, et al. Carbon, 2021, 172: 379-389.

[6] Ratan A, Kunchakara S, Dutt M, et al. Materials Science in Semiconductor Processing, 2020, 108: 104877.

[7] Li X Y, Guo M, Bandyopadhyay P, et al. Composites Part B: Engineering, 2021, 207: 108568.

[8] Zhang J, Lei W W, Schutz J, et al. Part B, Polymer physics, 2019, 57(7): 406-414.

[9] Zamanian M, Sadrnia H, Khojastehpour M, et al. Polymer, 2001, 42(16): 6775-6783.

[11] Xie W, Han ZH Q, Zhang ZH D, et al. Composites Part B: Engineering, 2019, 176: 107265.

[12] Wang P J, Zhang M Y, Liu Y, et al. Journal of Applied Polymer Science, 2019, 136(44): 48174.

[13] Wu K, Song L, Wang Z, et al. Polymers for Advanced Technologies 2008, 19: 1914–1921.

[14] Lu H, Wilkie CA, Ding M, et al. Polymer Degradation and Stability, 2011, 96:1219–1224.

[15] Huang G, Liang H, Wang Y, et al. Materials Chemistry and Physics, 2012, 132: 520–528.

[16] Pan H, Qian X, Ma L, et al. Polymer Degradation and Stability, 2014, 106: 47–53.

[17] Wang Y, Liao S, Shang K, et al. Acs Applied Materials&Interfaces, 2015, 7: 1780–1786.

[18] Peng S, Zhou M, Liu F, et al. Royal Society Open Science, 2017, 4: 170512.

[19] Lin J, Liu Y, Wang D, et al. Industrial& Engineering Chemistry Research, 2011, 50: 9998–10005.

[20] Huang G, Gao J, Wang X, et al. Materials Letters, 2012, 66: 187–189.

[21] Layek R, Das A, Park M, et al. Journal of Materials Chemistry, 2014, 2: 12158.

[22] Yuan B, Bao C, Guo Y, et al. Industrial& Engineering Chemistry Research, 2012, 51: 14065–14075.

[23] Ghanbari D, Salavati-Niasari M, Sabet M. Composites Part B-Engineering, 2013, 45: 550–555.

[24] Goetz K P, Chmielewski F M, Goedeke K, et al. Scientia Horticulturae. 2017, 222(5):

102-110.

[25] Jaime V C, Isabel A A, Jorge J H, et al. Materials Science & Engineering C-materials For Biological Applications. 2017, 77(3): 366-373.

[26] Mathur N, Goswami G K, Pathak A N. Journal of Molecular Graphics Modelling, 2017, 74(2): 337-343.

[27] Li J H, Li Y S, Song Y N, et al. Ultrasonics-Sonochemistry, 2017, 39: 853-862.

Comparison and Analysis of Synthesis of Bisphenol-A Polyarylates by Melt Polycondensation and Interfacial Polycondensation

Zhoufeng Wang*, Junwei Hu, Taoguo Ding, Bolin Wang, Yingying Liu, Danlei Huang

School of Materials Science and Engineering, Anhui University of Science and Technology, Huainan 232001, PR China

Corresponding author. E-mail address: zfwang@aust.edu.cn (Zhoufeng. Wang).

Abstract

Using bisphenol A, tere/isophthalic acid, and tere/isophthaloyl chloride as the main raw materials, bisphenol-A polyarylates was synthesized by melt polycondensation and interfacial polycondensation, respectively. The product was characterized by by Fourier transform infrared spectrometry (FTIR), X-ray diffraction (XRD), gel permeation chromatography(GPC), differential scanning calorimetry(DSC) and thermogravimetric analysis(TG), the structure and properties of the polyarylates obtained by the two methods are compared, and the influence of the content of m-phenylene structure on the structure and properties of polyarylates was also studied. The results show that the number average molecular weight of the polyarylates synthesized by melt polycondensation is 2190, and the M_n of the polyarylates synthesized by interfacial polycondensation is 7362. Polyarylates have good thermal properties. With the increase of the content of m-phenylene structure, the polyarylates obtained by the two methods are transformed into amorphous polyarylates, and the glass transition temperature is reduced, and the processing performance is improved.

Keywords: bisphenol-A polyarylates; melt polycondensation; interfacial polycondensation

Introduction

Polyarylate(PAR) is a high-performance thermoplastic with aromatic rings and ester bonds on the main chain.[1-3] Polyarylate's excellent comprehensive properties are given by its own rigid molecular structure. It has the characteristics of high modulus, high strength, good thermal and dimensional stability, good wear resistance and optical stability, etc.[4-7] It has a wide range of application prospects in 5G, aerospace, electronic appliances, medical equipment and other industrial fields.[8-10]

Experimental

1. Preparation of polyarylates by melt polycondensation

Bisphenol A and 3-4 times excess acetic anhydride were added to a four-necked flask equipped with a stirring device and a condenser, stirred at 70°C until the monomer was dissolved, and a few drops of concentrated sulfuric acid were added dropwise. The reaction was heated to 130°C for 4 hours, and the product is separated out in ice water and rinsed, dried in vacuum at 60°C, and purified to obtain bisphenol A diacetate.

The obtained product and different proportions of terephthalic acid/isophthalic acid/ were added to a four-necked flask, and nitrogen was introduced. The temperature was slowly raised to 235°C, and acetic acid was distilled out. Then the temperature was slowly increased to 270°C and reached the high-temperature polycondensation stage, and the temperature was kept for 2 hours to vacuumized the reaction until the acetic acid no longer distills out. The product was collected at the end of the reaction.

2. Preparation of polyarylates by interfacial polycondensation

Bisphenol A, sodium hydroxide, and benzyltriethylammonium chloride were added to a four-necked flask equipped with a mechanical stirring device, and then the dichloromethane solution with different proportions of terephthaloyl chloride/isophthaloyl chloride was slowly added dropwise to the three-necked flask, and stirred at 2000 rpm at 10°C. After reacting for 1 hour, the reaction mixture was poured into deionized water for precipitation and filtered. The precipitated product was dissolved in DMC, precipitated and purified in MeOH, and dried under vacuum at 100° C for 24 hours, bisphenol-A polyarylates is obtained.

A series of polyarylates with fixed bisphenol A ratios and different ratios of p-benzene structure and m-phenylene structure were prepared by the above methods as shown in Scheme 1. Named PAR-I-XX, or PAR-M-XX, XX is a number, where I and M represent interfacial polycondensation and melt polycondensation methods respectively, and the number represents the content of the m-phenylene structure of polyarylate. For example, PAR-I-30 means polyarylate with 30% m-phenylene structure synthesized by interfacial polycondensation method.

Melt polycondensation
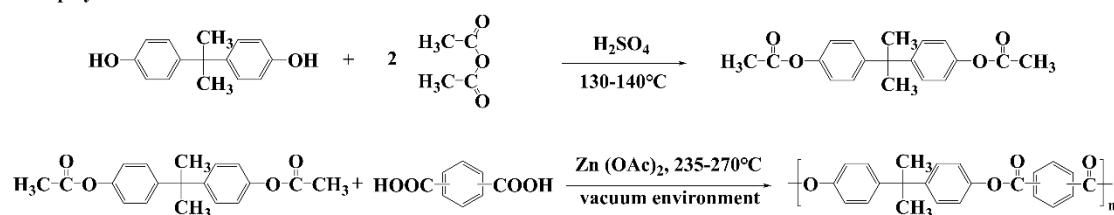
Interfacial polycondensation
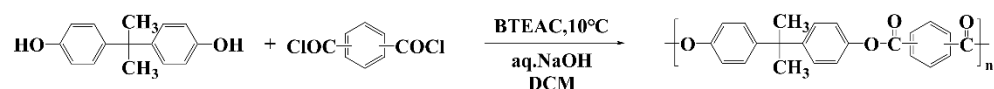
Scheme 1 The reaction equations for the synthesis of bisphenol-A polyarylates by melt polycondensation and interfacial polycondensation, respectively

Results and discussion

1. FT-IR of polyarylates
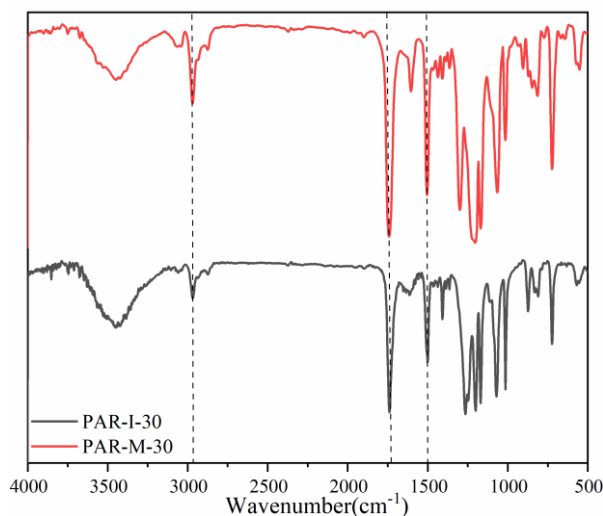
Figure 1 The FT-IR of polyarylates obtained by melting and interfacial polycondensation, respectively

As shown in

Figure **1**, The characteristic absorption peak at 2967cm^{-1} is attributed to C-H stretching of methyl group. The strong absorption peak at 1739cm^{-1} is caused by ester carbonyl group, the strong characteristic absorption peak at 1502cm^{-1} is attributed to the vibration of the polyarylates benzene ring skeleton, and the absorption band at 1200-1300cm^{-1} is attributed to C-O-C asymmetric stretching vibration. It shows that the bisphenol-A polyarylates has been successfully synthesized.

2. X-Ray diffraction diagrams of polyarylates
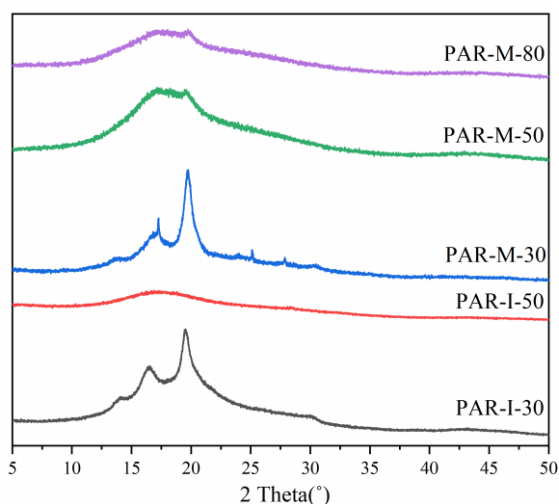
Figure 2 X-Ray diffraction diagrams of polyarylates with different content of m-phenylene structure obtained by melting and interfacial polycondensation, respectively.

As shown in Figure 2, With the increase of the content of m-phenylene structure, the sharp diffraction peaks of the polyarylates gradually disappear, showing a wider halo in the 2θ range of 10-25°. The introduction of an asymmetric m-phenylene structure into the polyarylate structure destroys the regularity of the molecular chain and hinders the close packing of polymer chains, resulting in the amorphous nature of the polyarylates.

3. GPC of polyarylates

Table 1 GPC of polyarylates

Sample	M_n	M_w	M_z	M_v	PD
PAR-I-30	7362	16250	35958	14348	2.20728
PAR-M-30	2190	2581	3069	2517	1.17854

It can be seen from Table 1 that the polyarylates obtained by melt polycondensation has a low molecular weight, The number average molecular weight (M_n) and the weight average molecular weight (M_w) are 2190 and 2581, respectively. This may be due to the cracking of the polymer under high temperature and high vacuum, which caused the molecular weight of polyarylates to be reduced. Post-processing such as solid-phase polycondensation is needed to increase the viscosity and the molecular weight.

4. Thermal analysis of polyarylates
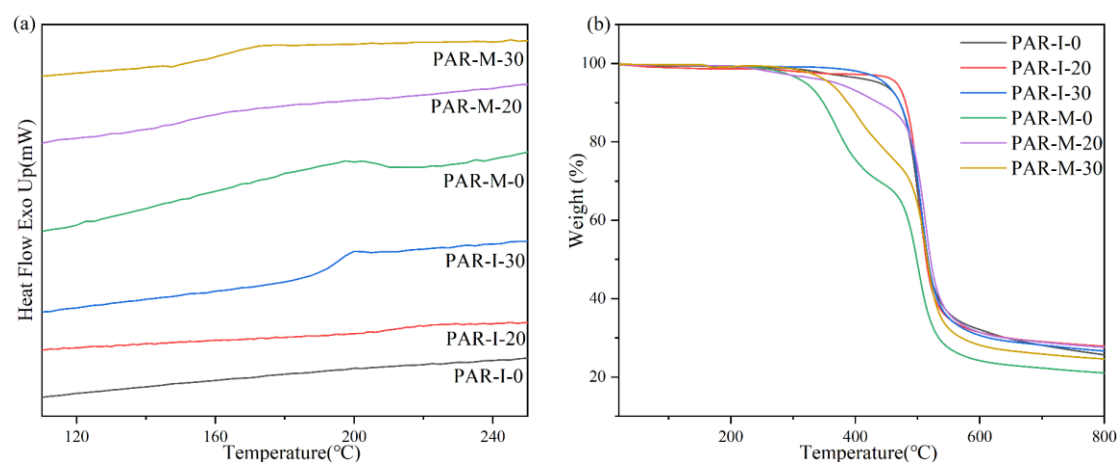
Figure 3 (a) DSC curves of polyarylates with different content of m-phenylene structure obtained by melting and interfacial polycondensation, respectively; (b) TGA curve of polyarylates with different content of m-phenylene structure obtained by melting and interfacial polycondensation, respectively.

In
Figure **3**(a), it can be observed that with the increase of the content of m-phenylene

structure, The T_g values of PAR-M decreases from 197°C to 164°C, and the T_g values of PAR-I decreases from 218°C to 199°C. This is due to the introduction of an asymmetric m-phenylene structure into the rigid molecular chain of the polyarylates, which destroys the regularity of the chain, thereby improving the processability of the polyarylates. At the same time, the T_g of the polyarylates obtained by melt polycondensation is generally lower than that of the interfacial polycondensation, which may be due to the low molecular weight of the melt polymerization product.

Figure **3**(b) shows that polyarylates have good thermal properties. The 5% and 10% weight loss temperatures ($T_{5\%}$, $T_{10\%}$) of the polyarylates obtained by the interfacial polycondensation method are 448-466°C and 471-481°C respectively. The residual carbon rate at 800°C is above 25%. The 5% and 10% weight loss temperatures ($T_{5\%}$, $T_{10\%}$) of the melt polycondensation method are within the range of 320-370°C and 340-440°C, respectively, and the residual carbon rate is 20-23%, which may be due to the low molecular weight of polyarylates obtained by melt polycondensation, and the decomposition of small molecules at high temperature leads to low thermal decomposition temperature and low carbon residual rate.

Conclusion

(1)The bisphenol-A polyarylates were successfully synthesized by melt polycondensation and interfacial polycondensation.

(2) GPC results show that the molecular weight of the product obtained by the melt polycondensation method is low, the number average molecular weight is 2190, and post-processing such as solid-phase polycondensation is needed to increase the viscosity and increase the molecular weight.

(3) Polyarylates have good thermal properties. With the increase of the content of m-phenylene structure, the polyarylates obtained by the two methods are transformed into amorphous polyarylates, and the glass transition temperature (T_g) is reduced, and the processing performance is improved.

Acknowledgements

Refferences
[1] Nechifor M. Aromatic polyesters with photosensitive side chains: Synthesis, characterization and properties[J]. Journal of the Serbian Chemical Society, 2016, 81(6): 673-685.
[2] Zhang Y, Lei Z, Yan G-M, et al. Syntheses and properties of novel polyarylates with ethyl units as a side group[J]. Materials Today Communications, 2021, 28: 102643.
[3] Zhang P, Wu L, Li B-G. Thermal stability of aromatic polyesters prepared from diphenolic acid and its esters[J]. Polymer Degradation and Stability, 2009, 94(8): 1261-1266.

[4] Wei P, Cakmak M, Chen Y, et al. Aromatic liquid crystalline copolyesters with lowTmand highTg: Synthesis, characterization, and properties[J]. Journal of Applied Polymer Science, 2014, 131(13): 1368-1380.

[5] Meng S, Sun N, Su K, et al. Novel organosoluble polyarylates based on diphenylamine-fluorene units: Synthesis, electrochromic, and electrofluorescent properties[J]. High Performance Polymers, 2018, 30(7): 864-871.

[6] Zhang Y, Yan G-M, Zhang G, et al. Synthesis of high transparency polyarylates containing cyclohexane group[J]. Polymer, 2020, 186: 122047.

[7] Asgari S, Koohmareh G A, Parsanasab G M. Synthesis and Characterization of Soluble Aromatic Polyesters with Side-Chain Azobeneze and Azothiazole Chromophores[J]. Polymer Science, Series B, 2018, 60(2): 218-230.

[8] Honkhambe P N, Avadhani C V, Wadgaonkar P P, et al. Synthesis and characterization of new aromatic polyesters containing biphenyl side groups[J]. Journal of Applied Polymer Science, 2007, 106(5): 3105-3110.

[9] Choi W S, Padias A B, Hall Jr H. LCP aromatic polyesters by esterolysis melt polymerization[J]. Journal of Polymer Science Part A: Polymer Chemistry, 2000, 38(19): 3586-3595.

[10] Chamkure Y K, Sharma R K. New organosoluble polyarylates containing pendent fluorene units: synthesis, characterization and thermal behaviour[J]. Journal of Polymer Research, 2019, 26(1): 17.

Preparation and properties of aromatic polyesters derived from

bisphenol-A / bishydroxyphenylbutane

Zhoufeng Wang*, Taoguo Ding, Junwei Hu, Bolin Wang, Yingying Liu, Bo Wang

School of Materials Science and Engineering, Anhui University of Science and Technology, Huainan 232001, PR China
Corresponding author. E-mail address: zfwang@aust.edu.cn

Abstract

Two aromatic polyesters with different structures were prepared by interfacial polymerization derived from bisphenol-A / bishydroxyphenylbutane and diacyl chloride. And the microstructure, morphology and thermal properties of the aromatic polyester were characterized by adjusting the proportion of reactants, so as to further study the effect of different bisphenol monomers on the properties of the polymer. The preparation of these two aromatic polyesters with different structures was confirmed by Fourier Transform Infrared spectra. X-ray diffraction analysis showed that bisphenol-A polyarylate had strong crystallinity, while romatic polyesters derived from bishydroxyphenylbutane had amorphous morphology. The 5% weight loss temperature of polyesters were 440°C–470°C, and the maximum thermal decomposition temperature was stable at 500°C, which showed good thermal stability. Compared with bisphenol-A polyarylate, aromatic polyesters derived from bishydroxyphenylbutane had lower thermal stability, but stronger chain fluidity, which was reflected in the decrease of glass transition temperature values.

Keywords: aromatic polyesters; bisphenol-A; bishydroxyphenylbutane; thermal properties

Introduction

After the traditional polyarylates were developed in the 1970s, it has been widely used in various fields of production and life because of its high-strength properties, among which the most representative is the commercialized U-100 product.[1-3] Due to Bisphenol-A (BPA) polyarylates highly symmetrical structure, it had high molecular chain rigidity, high thermal stability and excellent mechanical properties, so its melting point and glass transition temperature (T_g) were too high, and insoluble in common organic solvents, which limited its application.[4-5] In order to further expand the application of polyarylates, researchers have adopted a variety of strategies to modify the traditional polyarylate materials. And the introduction of flexible structural elements into the main chain of aromatic polyesters was one of the most effective methods.[6-8]

Bishydroxyphenylbutane is a chemical product with asymmetric structure, low price and easy access. Moreover, the similar structure between bishydroxyphenylbutane and BPA suggested similar reaction activity and would lead to a novel polyarylate was prepared by the original synthesis method of BPA polyarylates. As far as we know, there were few reports on the application of bishydroxyphenylbutane in the synthesis of polyarylates. In this paper, BPA / bishydroxyphenylbutane were prepared by interfacial polymerization to prepare aromatic polyesters with different structures, and their physicochemical properties were characterized to study the effects of different bisphenol monomers on the properties of the synthesized aromatic polyesters.

Experimental

The aromatic polyarylesters were described in Scheme 1. BPA / bishydroxyphenylbutane and BTEAC were dissolved in 1M NaOH solution. Isophthalic acid chloride (IPC) and p-Phthaloyl chloride (TPC) were dissolved in DCM as organic phase. The reaction temperature was controlled at 10°C and stirred at 2000r/min for 3h. Poured the reaction solution into methanol for precipitation, washed the obtained crude product with water, grinded it into powder with a mortar, and washed it repeatedly with methanol and water until it was washed. Finally, the product was dried in a vacuum drying oven at 80 °C for 12h.

To synthesize aromatic polyesters with side ethyl groups in the main chain, namely, BPA/BPB0, BPA/BPB10, BPA/BPB20 and BPA/BPB40 by adjusted the ratio of diacyl monomer (TPC: IPC) as 100:0, 90:10, 80:20 and 60:40, respectively.
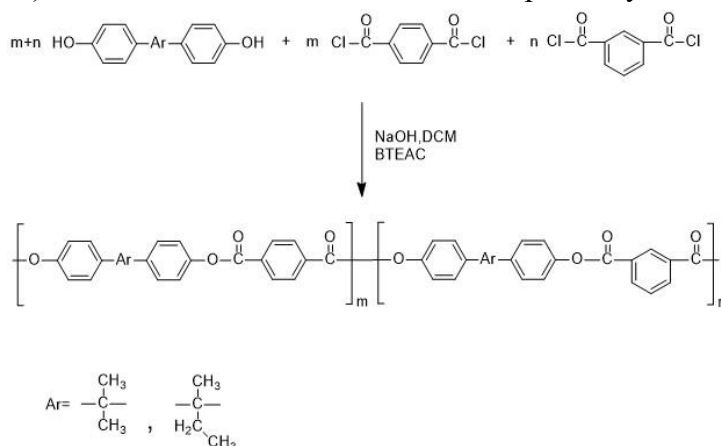
Scheme 1. Synthesis of aromatic polyesters derived from BPA/ bishydroxyphenylbutane

Results and discussion

As shown in the FT-IR spectrum in Fig. 1, a absorption peak was observed at 2930cm-1 in the infrared spectrum, which was derived from the homocarbon dimethyl group of bishydroxyphenylbutane. The other absorption peaks were corresponded to the groups of polyarylates one by one. This proved the successful preparation of aromatic polyesters with different structures.

As shown in the X-ray diffraction (XRD) patterns in Fig. 2(a), it can be observed in BPA polyarylates (BPA0/10/20/40) had sharp diffraction peaks in the range of 2θ=12-21°, indicating that the polyester had strong crystallinity, which was consistent with the properties of BPA

polyarylates.[4] On the contrary, BPB10/20/40 showed a wide halo in the pattern Fig. 2(b), which indicated that the polyesters were amorphous. The results showed that bishydroxyphenylbutane has asymmetric molecular structure, which destroyed the symmetry of molecular chain and greatly improved the flexibility of the molecular chain, thus inhibiting the crystallization of the polymer and making the aromatic polyesters in an amorphous form. Notably, BPB0 also showed sharp diffraction peaks in XRD pattern. This was because TPC had a highly symmetrical structure and the prepared polyarylesters had high rigidity.
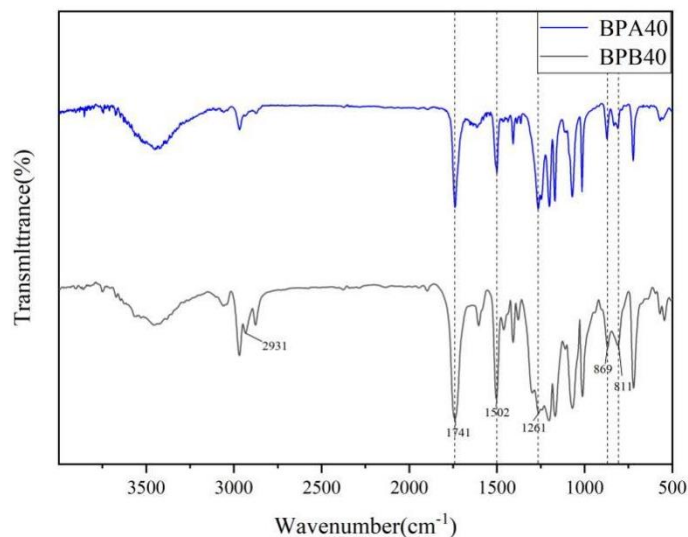
Figure 1. FT-IR spectrum of aromatic polyesters
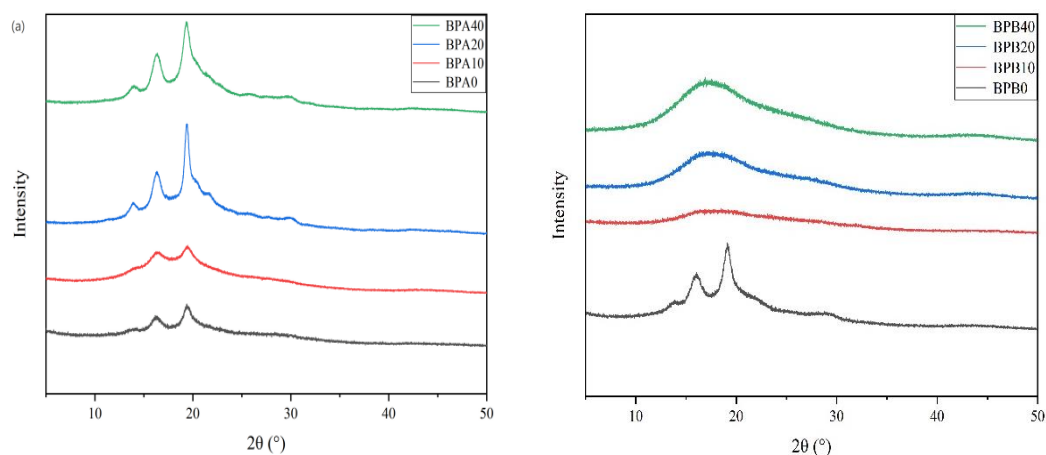
Figure 2. X-ray diffraction patterns of aromatic polyesters derived from (a) BPA and (b) bishydroxyphenylbutane

The thermal properties of aromatic polyesters were characterized by TGA and DSC in nitrogen atmosphere, and the results were summarized in Table 1. The $T_{5\%}$ of aromatic polyesters were in the range of 440-470°C, which indicated that the polymers had good thermal stability. And it can be observed that with polyarylatse derived from bishydroxyphenylbutane, $T_{5\%}$ value of BPA polyarylates were higher, which were due to BPA had structural symmetry, the prepared polyarylates had strong rigidity and stable structure. This can also be found from the T_{max} (maximum thermal decomposition temperature), the T_{max} of BPA0/10/20/40 was stable

at 503℃, while the fluctuation of BPB0/10/20/40 was large. Meanwhile, it was observed that the carbon residue rate of BPB0/10/20/40 were higher than that of BPA0/10/20/40 at 800℃, which were caused by the gradual increase of aromatic contents.

The T_g values of the samples BPA0/10/20/40 were in the range of 194.99-213.74℃, and the values of the samples BPB0/10/20/40 were in the range of 167.49-202.48℃. This was consistent with the previous test results, the asymmetric structure of bishydroxyphenylbutane reduced the rigidity of the polymers and the thermal stability of the molecular chain, increased the fluidity of molecular chain, which was manifested in the decrease of the T_g values.

Table 1. Thermal properties of aromatic polyesters

Polyester	T_g(℃)	$T_{5\%}$(℃)	T_{max}(℃)	RW(%)
BPA0	209.99	439.59	502.06	25.66
BPA10	212.48	471.32	503.62	28.37
BPA20	213.74	466.50	503.56	27.88
BPA40	194.99	291.16	503.61	24.94
BPB0	167.48	448.19	506.35	26.64
BPB10	197.46	447.53	497.88	29.48
BPB20	202.48	460.93	497.88	29.97
BPB40	167.49	456.01	503.60	30.73
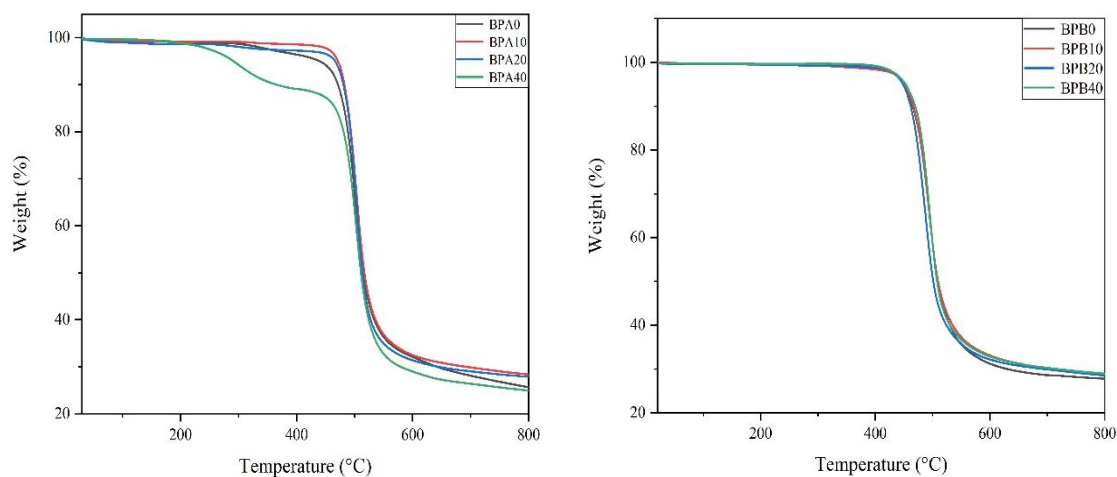
Figure 3. TG curves of aromatic polyesters derived from (a) BPA and (b) bishydroxyphenylbutane
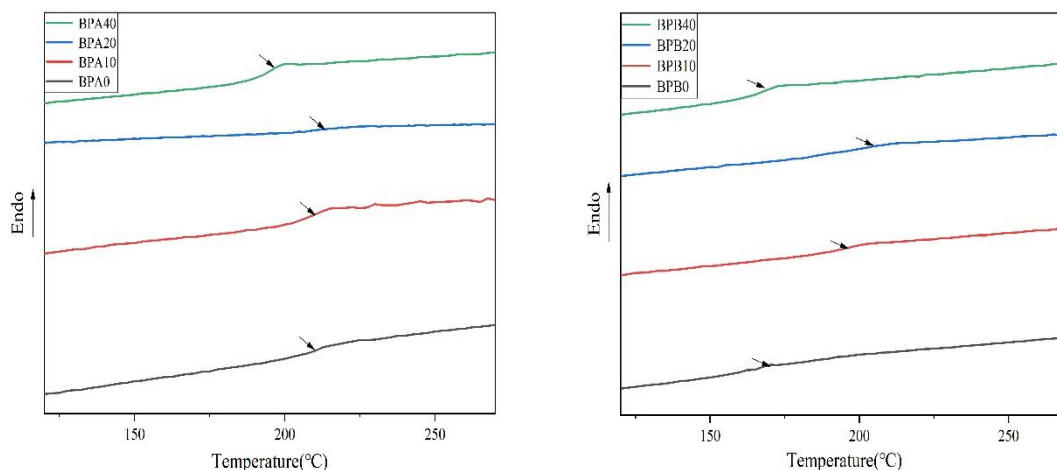
Figure 4. DSC curves of aromatic polyestersderived from (a) BPA and (b) bishydroxyphenylbutane

Conclusions

In summary, bisphenol-A and bishydroxyphenylbutane played different roles in the structure of polyarylates. The highly symmetrical molecular structure of bisphenol-A ensured the thermal stability and crystallinity of the polymer, and bishydroxyphenylbutane effectively reduced the rigidity and crystallinity of the polymer and improved the fluidity of the molecular chain, which was specifically reflected in the decrease of T_g values. When products with different structures are applied, different bisphenol monomers can be selected according to their own properties.

Acknowledgements

References

[1] Maresca LM, Robeson LM and Nargolis JM. . (1985). Engineering Thermoplastics: Properties and Applications. New York: Marcel Dekker Inc. p. 255–282.2.

[2] Arroyo M and Olabisi O. . (1997). Handbook of Thermoplastics.New York: Marcel Dekker Inc, pp. 599–608.

[3] Ivanov, M. V. , Storozhuk, I. P. , Dibrov, G. A. , Semyashkin, M. P. , & Kagramanov, G. G. . (2018). Fabrication of hollow fiber membrane from polyarylate–polyarylate block copolymer for air separation. Petroleum Chemistry, 58(4), 289-295.

[4] Liu, P. , Zeng, L. , Ye, G. , & Xu, J. . (2013). Bisphenol a-based co-polyarylates: synthesis, properties and thermal decomposition mechanism. Journal of Polymer Research, 20(10), 1-9.

[5] Wang, Jinggang, Xiaoqing, Zhen, Yuan, & Liyuan. Synthesis of bio-based poly(ethylene

2,5-furandicarboxylate) copolyesters: Higher glass transition temperature, better transparency, and good barrier properties.

[6] Liu, P. , Zeng, L. , Ye, G. , & Xu, J. . (2013). Bisphenol a-based co-polyarylates: synthesis, properties and thermal decomposition mechanism. Journal of Polymer Research, 20(10), 1-9.

[7] Manurkar, N. , More, S. , Mulani, K. , Ganjave, N. , & Chavan, N. . (2017). Thermotropic liquid crystalline polyesters derived from 2-chloro hydroquinone. Journal of Chemical Sciences, 129(9), 1-8.

[8] Zhu, Q. , & Han, C. C. . (2007). Synthesis and crystallization behaviors of highly fluorinated aromatic polyesters. Polymer, 48(13), 3624-3631.

Application of microcantilever sensing system in CNTs micro heat detection

TENG Yanhua, WANG Qiming, ZHOU Ninghong, FENG He, LI Gaohan, WANG Qingping

School of Materials Science and Engineering, Anhui University of Science and Technology, Huainan 232001, China

Abstract

It is difficult to detect the micro heat of carbon nanotubes (CNTs) by ordinary methods. This paper uses microcantilever sensors to detect CNTs micro heat based on the optical lever detection method. The heat dissipation of CNTs' photothermal conversion influence of deflection is studied on the microcantilever. The relationship between the temperature change of the CNTs film and the offset of the corresponding microcantilever was investigated by curve fitting. The results show that the temperature change has a linear relationship with the deflection of the microcantilever. The linear correlation coefficient of the fitting curve of the sample film in the area of 0.07 mm^2 is 0.9932. Compared with the fitting value of the experimental system, the results are consistent, which verifies the system's reliability.

Keywords: Microcantilever; Carbon nanotubes; Temperature detection; Photothermal spectroscopy; Thermal expansion

Introduction

Carbon nanotubes have excellent optical, thermal, and electrical properties[1] and high near-infrared light and thermal radiation source absorption efficiency[2, 3]. They have attracted more and more attention in photothermal therapy, nanomedicine, and flexible electronic devices. There are 3ω methods, self-heating DC current and Raman flash methods for temperature measurement of carbon nanotube films. DC current method and 3ω method require the sample to be tested to be conductive and have good resistance temperature characteristics; the pulse direction of the Raman flash method is not fixed, and the curve is more likely to appear. The above methods have a good effect on the heat measurement of conventional substances, but it isn't easy to measure the heat of trace substances. The static working mode of the microcantilever beam was adopted in this paper. When the sample film is used to absorb the laser of the characteristic peak of the photothermal absorption spectrum, the different mass film absorbs different light energy. The heat radiated to the environment changes the temperature. Then the temperature change is measured by the different thermal expansion coefficients of the surface of various materials above and below the microcantilever beam.

Experimental process

A sample solution of 10 mg/ml was prepared in the experiment, and the prepared sample solution was evenly divided into 10 equal parts. Then dilute the evenly distributed sample to prepare a standard concentration solution with a concentration of 1-10 mg/ml. After preparing the standard sample concentration, drop 1 μl solution of each concentration onto the glass slide. A natural air drying method is used to obtain a carbon nanotube film with 1-10 mg mass on a glass slide. The schematic diagram of the experimental device is shown in Fig 1. When the concentration of the standard concentration solution is greater than 10 mg/ml, the film is prone to deformation and cracking after natural air drying. Therefore, the experiment chose a standard solution with a concentration lower than 10mg/ml.
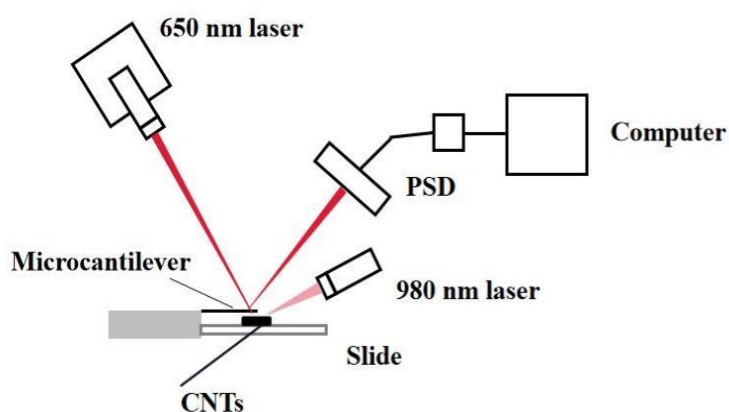
Fig. 1 Schematic diagram of the experimental device

Results and discussion

A 4 mg carbon nanotube film was placed on a glass slide and adjusted directly below the microcantilever. 980 nm laser directly irradiates the carbon nanotube film, and the thermal imager detects the temperature change in a short distance. The thermal imager takes photos every 30s. After the experiment, the data are recorded and analyzed. The data processing results are shown in Fig. 2. Fig. 2 shows the general trend of experimental temperature change. It can be seen that after the 980 nm laser is turned on, the CNTs film has a photothermal conversion effect, emits heat, and the temperature rises significantly to reach the threshold (38.2 ℃, converted into the heat of 0.887J); Turn off the laser, the photothermal conversion stops, and the temperature gradually returns to the initial position.
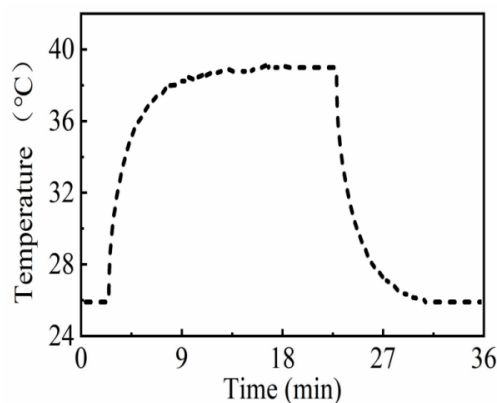
Fig. 2 Temperature change after 980 nm laser is turned on and off

As shown in Fig 2, the temperature test of the general trend of temperature change is carried out for three cycles, and the detection time of each cycle is controlled to be 12 minutes. The test results are shown in Fig 3. The temperature threshold measured in three cycles is 38.2 °C, which indicates from Fig. 4 that the temperature change curve is consistent. The results show that the measurement results of the system have high repeatability and can be used to detect the micro heat of CNTs films.
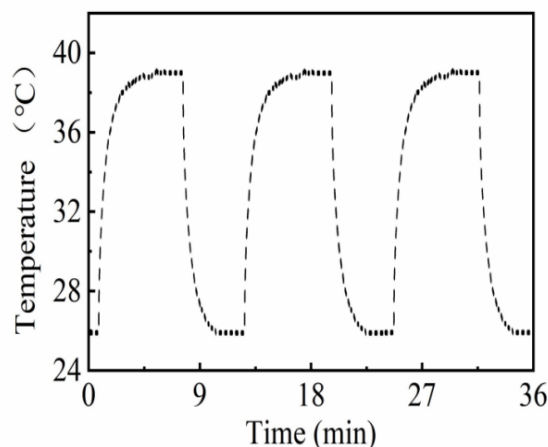
Fig. 3 Repeatability test of temperature detection

To prove the experiment's reliability, 2.5 mg,4.5 mg,6.5 mg,8.5 mg, and 9.5 mg of CNTs film were again placed on the glass slide and measured in sequence. The test data is compared with the fitted straight line calculation data of this quality tested above, and the results are shown in Table 1.

Table 1 Test data

Film quality （mg）	Measure the temperature value （°C）	The film quality is converted to the fitting temperature value （°C）	Actual value / measured value （%）
2.5	35.7	34.8	109.2
4.5	41.1	40.6	103.7
6.5	53.5	46.5	105.1
8.5	53.5	49.4	103.6
9.5	57.5	55.3	107.3

The above results show that the test data's recovery rate (actual value/measured value) is 103.6 % and 109.2 %. Within the measurement range, the error of the temperature measurement results is within 2.2 °C, and the measurement error does not exceed 5.6 %, which can indicate. The prediction model fitted by the experiment has high reliability, can effectively detect the micro-heat of the carbon nanotube film, and has broad application prospects and promotion value.

Reference

[1]   AJAYAN P M, TERRONES M, GUARDIA A. Nanotubes in a Flash-Ignition and Reconstruction [J]. Science, 2002, 296(5568): 705-706.

[2]   KOVATS E, PEKKER A, PEKKER S, et al. Carbon Nanotube Films For Optical Absorpton [J]. Nato Science, 2006, 222: 169-170.

[3]   GOKHALE V J, SHENDEROVA O A, MCGUIRE G E, et al. Infrared Absorption Properties of Carbon Nanotube/Nanodiamond Based Thin Film Coatings [J]. Journal of Microelectromechanical Systems, 2014, 23(1): 191-197.

Three-dimensional ZIF-derived hollow Co and N co-doped carbon bifunctional catalyst for Zn-air battery

Wenhan Zhou, Yang Li*, Kejian Shi, Yanyan Zhang

School of Mechanics and Optoelectronic Physics, Anhui University of Science and Technology,

Huainan 232001, P. R. China

Abstract

Considering the actual commercial large-scale application, the research on non-precious metal material catalysts gain much interest. Particularly, the zeolitic-imidazole framework (ZIF) is used as non-precious metal catalyst because of three-dimensional controllable, high surface area and rich N content. Herein, ZIF transformed into hollow and porous Co-N-C catalyst by a one-step synthesis method and the joint action of Zn and PVP is reported. The catalyst exhibits efficient oxygen reduction reaction (ORR) performance ($E_{1/2}$=0.83 V vs. RHE) and oxygen evolution reaction (OER) performance (E_{j10} =1.69 V vs. RHE). More meaningfully, the Zn-air battery (ZAB) assembled with the catalyst, exhibiting superior 3100 min cycling charging/discharging stability and high power density of 109.8 mW/cm^2, compared with the Pt-RuO$_2$ of 2600 min of cycling charging/discharging stability and power density of 96.1 mW/cm^2. In addition, the solid-state ZAB based on the catalyst shows excellent rechargeable flexible and stability. Undoubtedly, this work designs a bifunctional oxygen electrocatalytic catalyst of the practical application value.

Keywords: Hollow Porous Carbon, Zn/Co Ratio, Bifuctional, Zn-air Battery

---

* To whom correspondence should be addressed. Email: liyang800904@163.com; Post address: School of Mechanics and Optoelectronic Physics, Anhui University of Science and Technology, Huainan 232001, P.R.China.
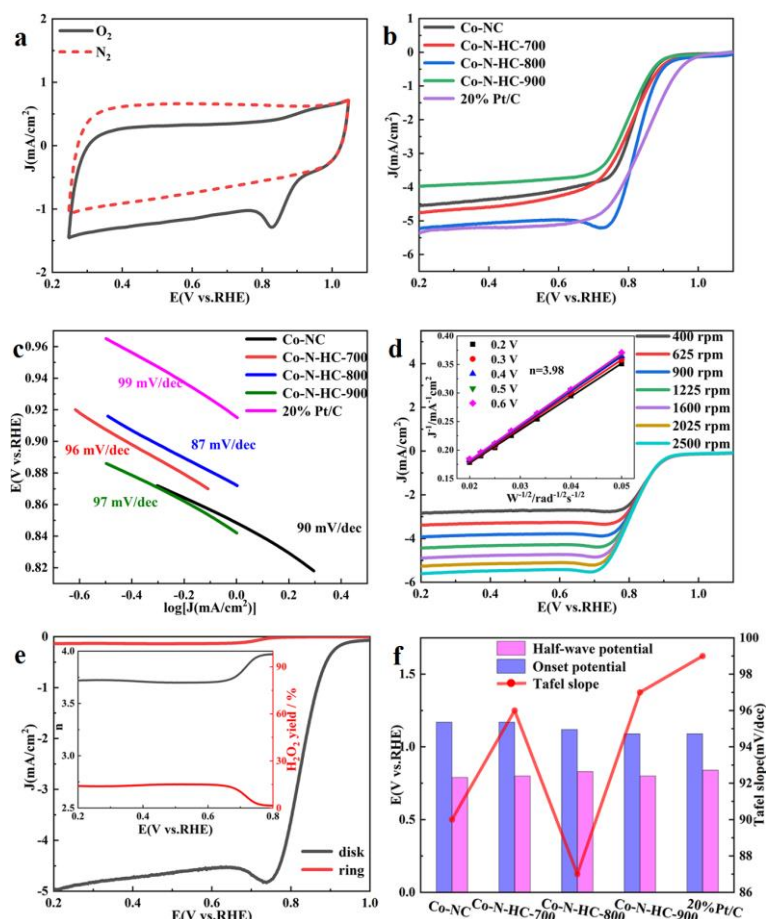
Figure 1. Electrocatalytic ORR of catalysts.   a)   CV curves of Co-N-PC-800 in N2   and O2-saturated 0.1 M KOH solution.   b) LSV of the ORR curves of Co-NC, Co-N-PC-900, Co-N-PC-800, Co-N-PC-700 and   20% Pt/C   in O2-saturated 0.1 M KOH solution at 1600 rpm. c) Tafel   slopes of   Co-NC,   Co-N-PC-700,   Co-N-PC-800,   Co-N-PC-900 and 20% Pt/C. d) LSV of the ORR of Co-N-PC-800 at different rotating rates,   The inset is   K-L curves.   e) RRDE   voltammograms of Co-N-PC-800,   The inset shows   the H2O2   yield   and   the electron transfer number (n) of Co-N-PC-800. f) Statistical comparison of th--e   half-wave potential, onset potential   and   Tafel   slope   of   Co-NC, Co-N-PC-900, Co-N-PC-800, Co-N-PC-700 and 20% Pt/C catalyst.

Ni$_{(1-x)}$Zn$_x$Fe$_2$O$_4$ with excellent electromagnetic wave absorption performance

Ximing Zhang, Jingyu Wang, Yang Fan, Yin Liu*

School of Materials Science and Engineering, Anhui University of Science and Technology, Huainan 232001, Anhui, China

*Corresponding authors: yinliu@aust.edu.cn (Yin Liu)

Abstract

Nanocrystalline NiZn ferrite was prepared by using spraying-coprecipitation method, for electromagnetic wave absorption. When the NiZn ferrite molar ratio is 7:3, optimal absorption performance is achieved, with reflection loss of -64.37 dB at 6.48 GHz while the thickness of 5.91 mm. The outstanding electromagnetic wave absorption performance is attributed to the magnetic losses, which greatly improves the impedance matching and increases the decay constants of the materials.

Keywords: NiZn ferrite; Electromagnetic wave absorption; spraying-coprecipitation method

Introduction

With the advent of wireless communication era, various electronic and electrical equipment have provided high efficiency for social production and brought great convenience to people's daily life [1,2]. At the same time, the electromagnetic radiation and interference produced in the work of the equipment have become a serious issue [3,4]. Therefore, it is necessary to develop high performance wave absorption materials to address this problem. In this work, nanocrystalline NiZn ferrite was prepared by using spraying-coprecipitation method. It is found that the doping Zn element significantly improves the electromagnetic wave absorption. The molar ratio of NiZn was 7:3 has the excellent electromagnetic wave absorption properties.

Experimental

NiZn ferrite nanoparticles were prepared by spraying-coprecipitation method. Namely, analytically pure nickel chloride (NiCl$_2$·6H$_2$O), zinc chloride (ZnCl$_2$) and iron chloride (FeCl$_3$·4H$_2$O) were first dissolved in a jar by preset-ration, then these metal ions and the sodium hydroxide solution were transferred and sprayed into a flask by using high pressure nitrogen. The mixture was vigorously stirred to obtain their precipitates, then they were washed several times with distilled water and dried at about 100°C for 24h. The precursors obtained were calcined at various temperature to form the spinel phase and alter its grain size.

Results and Discussion
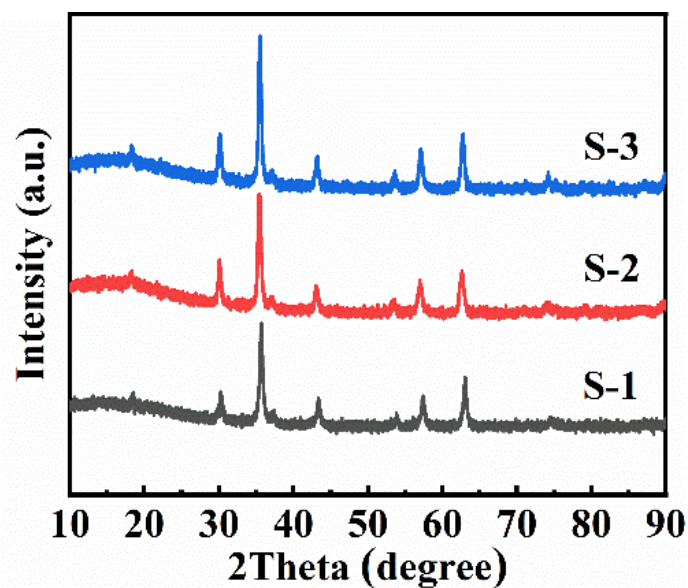
Fig. 1 XRD patterns of S-1, S-2 and S-3

The XRD pattern of all samples was shown in fig. 1. The peaks of the above S-2 and S-3 samples were in the middle of $ZnFe_2O_4$ and $NiFe_2O_4$, which indicates the synthesis of Ni-Zn ferrite. The pattern of S-1 demonstrate it was the pure ferrite. The three samples have similar peaks value indicating that they have similar crystallinity.
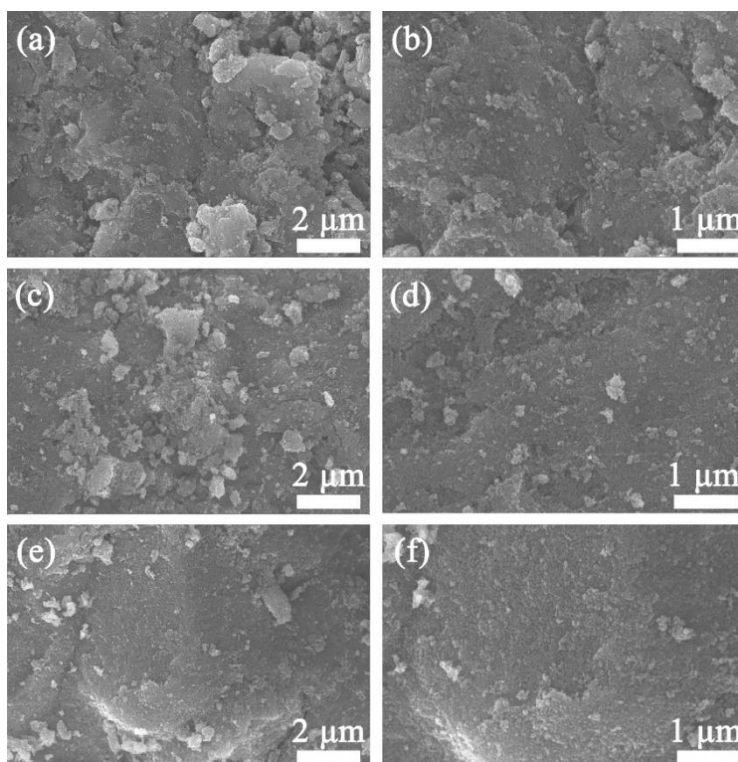
Fig. 2 FESEM images of (a, b) S-1, (c, d) S-2, (e, f) S-3

As shown in the fig. 2, it is obviously that the particle size of sample was uniform and there is no too big sample. It can see the size of sample was dispersed good and without As shown in fig. 2, it is clear that the sample has a uniform particle size with no obvious agglomeration, indicating that a uniform sample can be obtained by spray co-precipitation
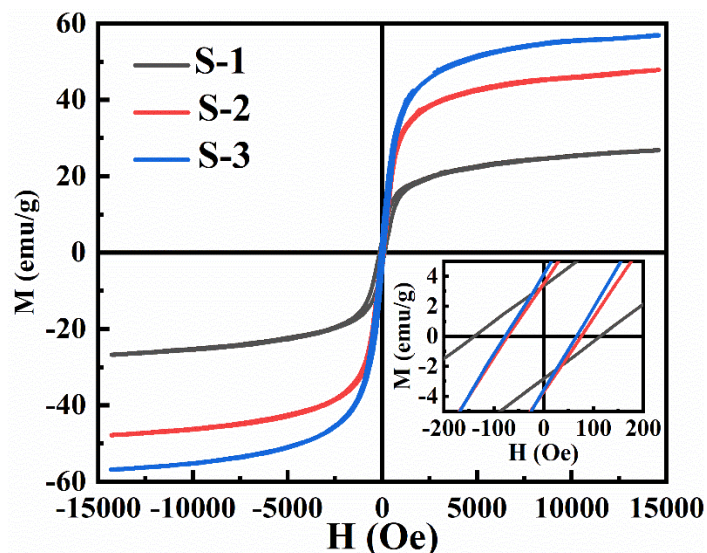
Fig. 3 M-H loops of all samples and zoom-in views.

To characterize the magnetic properties of the samples by using vibrating sample magnetometer (VSM). The hysteresis loops of all samples were traced at room temperature. As shown in the fig. 3, the M_S of samples is increase as the amount of Ni increase. The amount of Ni increase contributes to the increase of M_S because Ni has magnetic.
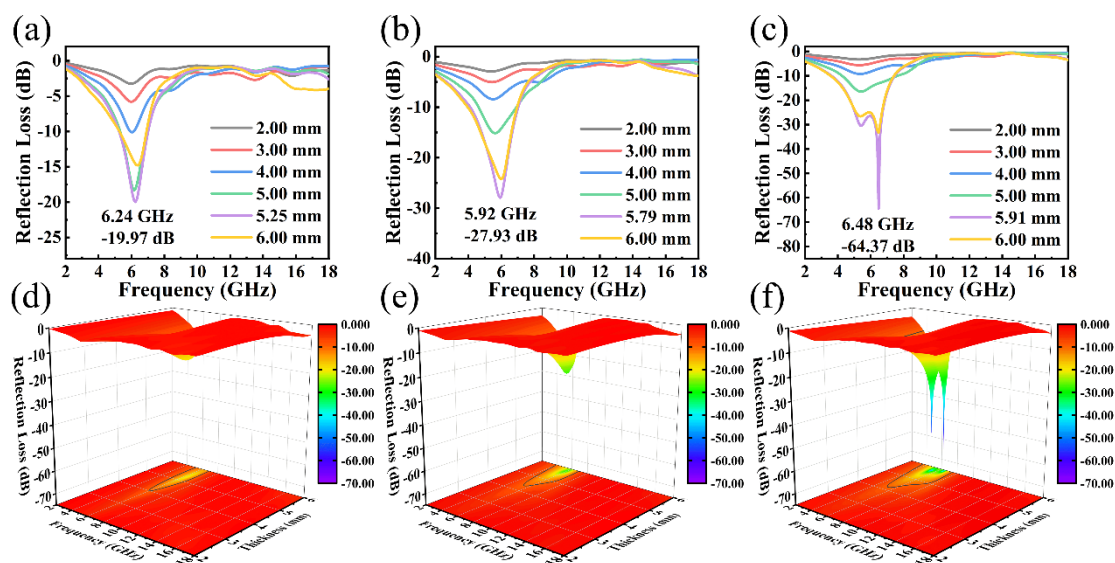
Fig. 4 RL at different thickness: S-1 (a), S-2 (b) and S-3 (c) and 3D reflection loss profiles: S-1 (a), S-2 (b) and S-3 (c)

Reflection loss of three samples at different thickness at the frequency range of 2-18 GHz were shown in fig. 4. It is obliviously that S-3 has the best reflection loss and impedance properties. S-3 has reach -64.37 dB at 6.48 GHz with the thickness of 5.91 mm. The effective absorption bandwidth of S-3 was 3.84 GHz (3.6 GHz – 7.44 GHz). The amount of Zn doping significantly changed the electromagnetic wave absorption properties of the samples.

Conclusions

$Ni_{(1-x)}Zn_xFe_2O_4$ composites were effective and low-cost electromagnetic wave absorber materials. The composites can be readily synthesized by using spraying-coprecipitation method. At optimal molar ratio, the composite exhibited the highest reflection loss of -64.37 dB at 6.48 GHz with a thickness of 5.91 mm. These NiZn ferrite composites can be used as a new type of electromagnetic absorption materials.

Acknowledgements

References

[1] ZHANG Y, RUAN K, SHI X, et al. Ti3C2Tx/rGO porous composite films with superior electromagnetic interference shielding performances [J]. Carbon, 2021, 175(271-280) https://doi.org/10.1016/j.carbon.2020.12.084.

[2] LIANG L L, SONG G, LIU Z, et al. Constructing Ni12P5/Ni2P Heterostructures to Boost Interfacial Polarization for Enhanced Microwave Absorption Performance [J]. ACS Appl Mater Interfaces, 2020, 12(46)(52208-52220) https://doi.org/10.1021/acsami.0c16287.

[3] HUANGFU Y, LIANG C, HAN Y, et al. Fabrication and investigation on the Fe3O4/thermally annealed graphene aerogel/epoxy electromagnetic interference shielding nanocomposites [J]. Composites Science and Technology, 2019, 169(70-75) https://doi.org/10.1016/j.compscitech.2018.11.012.

[4] DING J, WANG L, ZHAO Y, et al. Rutile TiO2 Nanoparticles Encapsulated in a Zeolitic Imidazolate Framework-Derived Hierarchical Carbon Framework with Engineered Dielectricity as an Excellent Microwave Absorber [J]. ACS Appl Mater Interfaces, 2020, 12(42)(48140-48149) https://doi.org/10.1021/acsami.0c12764.

[5] BAO S, TANG W, SONG Z, et al. Synthesis of sandwich-like Co15Fe85@C/RGO multicomponent composites with tunable electromagnetic parameters and microwave absorption performance [J]. Nanoscale, 2020, 12(36)(18790-18799) https://doi.org/10.1039/d0nr04615a.

Synthesis of high performance Ti$_3$C$_2$ electrode material doped with phosphorus and nitrogen diatoms based on guanidine salt

Ziyue Xuan [a], Guojun Cheng [a,b,c,*], Meng Liu [a], Feixiang Sha[a], Longxuan Zhou [a], Shen Tian [a]

[a] School of Materials Science and Engineering, Anhui University of Science and Technology, Huainan 232001, China；

[b] Anhui Province Key Laboratory of Environment-friendly Polymer Materials, Anhui University, Hefei 230601, China;

[c] Institute of Environment-Friendly Materials and Occupational Health, Anhui University of Science and Technology (Wuhu), Wuhu, China.

Corresponding author: Guojun Cheng and _chengguojun0436@126.com_

Abstract

A new type of PN–Ti$_3$C$_2$ electrode material was prepared for the first time through the aid of guanidine salt to achieve Ti$_3$C$_2$ phosphorus and nitrogen diatomic doping. Here, we report a controllable and simple strategy, using the weak reducing agent guanidine phosphate (CH$_6$N$_3$O$_4$P) as the phosphorus source and nitrogen source, hydrothermally preparing P–N doped Ti$_3$C$_2$ (PN–Ti$_3$C$_2$) and fabricating electrodes. At a scan rate of 2 mV s^{-1}, the PN–Ti$_3$C$_2$ electrode exhibits a high specific capacitance of 274.3 F g^{-1}, and there is no capacitance degradation after 1000 cycles in 1.0 M H$_2$SO$_4$ electrolyte. These results indicate that PN–Ti$_3$C$_2$ can be used as an outstanding electrode material for high-performance supercapacitors. Guanidine salt is a new heteroatom source, and its processing operation provides a broader and convenient experimental idea for heteroatom doping.

Keywords: P, N-doping; Ti$_3$C$_2$; Electrodes; Synthesis; Electrochemical capacitor.

Introduction

Due to the increasing and urgent demand for environmentally friendly high-power energy, supercapacitors have aroused great interest. Because they can provide fast charging and discharging process, relatively low cost, long cycle life and high power performance.[1-3] Electrode material is the key to supercapacitors. Among various electrode materials, MXene, a new two-dimensional early transition metal carbide/nitride family, has become a promising electrode material for supercapacitors due to its high electronic conductivity, large active surface area, and surface hydrophilicity.[4] It can be expressed as M$_{n+1}$X$_n$T$_x$, where M is an early transition metal, X is C or N, T is –O, –OH or –F, mainly by selectively etching the A layer in

the ternary layered compound material MAX.[1, 5] As the most typical representative of MXenes, $Ti_3C_2T_x$ nanosheets have received extensive attention.

In order to improve the conductivity and capacitance performance of MXene materials, heteroatom doping is a promising strategy. Among them, nitrogen is the most studied heteroatom, which can improve the electron transfer and ion diffusion kinetics in carbon by adjusting the electronic and/or crystal structure of the matrix.[6, 7] Compared with nitrogen, phosphorus doping is expected to adjust the surface structure of MXene to a greater extent, which is based on its larger atomic radius and different electronegativity.[8, 9] However, the doping process of MXenes is usually triggered under severe reaction conditions, such as high temperature and protective atmosphere.[10, 11] The sustainable hydrothermal doping under mild conditions will cause serious damage to the two-dimensional structure of MXene.[12] Therefore, it is necessary to give the hydrothermal process a reducing environment to prevent oxidation of MXene flakes.

This article reports for the first time a simple and controllable method of using guanidine salt to achieve Ti_3C_2 doping with phosphorus and nitrogen diatoms. As a weakly reducing dopant, guanidine phosphate not only provides phosphorus and nitrogen for Ti_3C_2, but also provides a reducing environment. The electrode material prepared by PN–Ti_3C_2 exhibits excellent electrochemical performance. At a scan rate of 2 mV s^{-1}, the PN–Ti_3C_2 electrode exhibits a high specific capacitance of 274 F g^{-1}, and there is no capacitance degradation after 1000 cycles in 1.0 M H_2SO_4 electrolyte. Therefore, guanidine phosphate as a new heteroatom doped raw material to prepare high-performance Ti_3C_2 electrodes will be successful.

Synthesis of PN–Ti_3C_2

Two-dimensional Ti_3C_2 flakes were successfully prepared by etching Al from Ti_3AlC_2 powder. Add 1.0 g of Ti_3AlC_2 powder to 20 mL of a premixed solution of 1.0 g LiF and 9.0 M HCl, and magnetically stir the solution at 40 °C for 24.0 hours. After that, deionized water is used for repeated washing until the pH value of the supernatant is greater than 6, and multi-layer Ti_3C_2 (abbreviated as Mult-Ti_3C_2) is obtained. In order to obtain 2D Ti_3C_2 flakes, 40 mL of deionized water was added to the precipitate and ultrasonicated in an ice water bath for 1.0 h. The supernatant, a colloidal solution of delaminated Ti_3C_2 flakes (abbreviated as Ti_3C_2), was collected and vacuum dried. To prepare Ti_3C_2 doped with phosphorus and nitrogen (abbreviated as PN-Ti_3C_2), 0.1 g of Ti_3C_2 flakes were added to a premixed solution of 1.0 g of guanidine phosphate and 30 mL of deionized water, and magnetically stirred for 5.0 min. Afterwards, put the mixture in a 50 mL reactor and keep it at 180 °C for 12.0 h. After the reaction, PN–Ti_3C_2 is obtained through washing and vacuum drying processes. A schematic diagram of the synthesis process of PN–Ti_3C_2 is shown in Fig. 1.
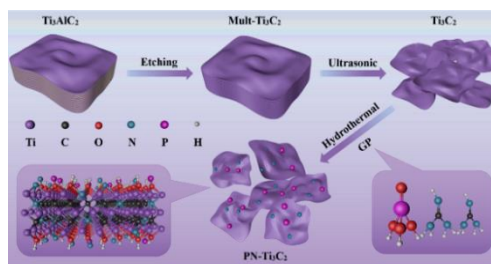
Fig. 1. Schematic illustration of the synthesis process of the PN–Ti$_3$C$_2$.

Results and discussion
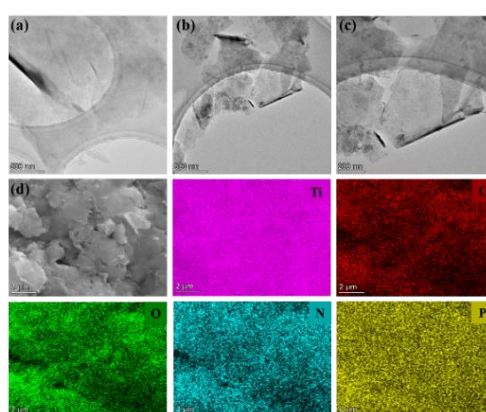
Fig. 2. Different magnification TEM images of Ti$_3$C$_2$ (a), PN–Ti$_3$C$_2$ (b) (c). SEM images of the PN–Ti$_3$C$_2$ (d) and the corresponding EDS elemental mappings of Ti，C, O, N and P.

Fig. 2 shows the patterns of Ti$_3$C$_2$ and PN–Ti$_3$C$_2$ observed by the electron microscope. Fig. 2a reveals the smooth and ultra-thin nano-chip structure of Ti$_3$C$_2$. The layer structure of Ti$_3$C$_2$ is preserved in PN–Ti$_3$C$_2$ in Fig. 2b and 2c, indicating that the auxiliary water heat treatment of phosphate does not destroy the two-dimensional appearance of Ti$_3$C$_2$.[6, 13] In addition, after nitrogen doping, many nanoparticles or small nanoplatelets can be observed on the thin Ti$_3$C$_2$ flakes, which may be due to an increase in surface defects in Ti$_3$C$_2$ due to the doping of phosphorus and nitrogen atoms.[8] Fig. 2d shows the SEM for PN–Ti$_3$C$_2$. The corresponding element mapping image shows the uniform distribution of elements Ti, C, O, N and P, indicating that P and N atoms are evenly dispersed on the Ti$_3$C$_2$ nanosheet.[12]
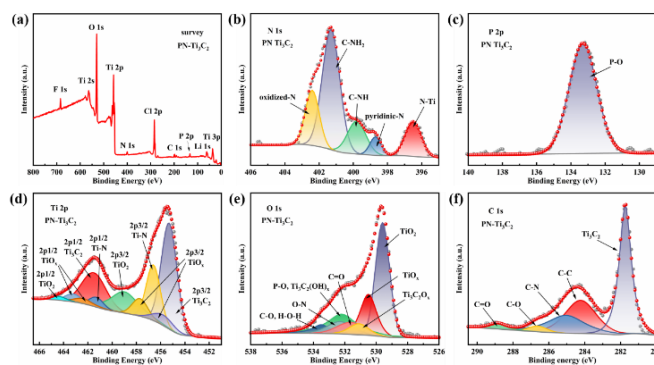
Fig. 3. (a) XPS survey spectrum of the PN–Ti$_3$C$_2$. (b-f) High-resolution XPS spectra of N 1s, P 2p, Ti 2p, O 1s and C 1s of the PN–Ti$_3$C$_2$, respectively.

The above analysis proves that the phosphorus and nitrogen atoms were successfully introduced into the Ti$_3$C$_2$ nanosheets, but the specific bonding method has not yet been clearly analyzed. The following further studies the valence state, element composition and bonding through X-ray photoelectron spectroscopy (XPS) analysis. The complete XPS measurement spectrum of the PN–Ti$_3$C$_2$ sample (Fig. 3a) shows a peak of 400.1 eV corresponding to N 1s and a peak of 133.1 eV at P 2p. This result confirms the successful combination of P and N elements into Ti$_3$C$_2$ using guanidine phosphate-assisted hydrothermal method, which is consistent with the EDS result. High-resolution spectroscopy can provide more information about the bonding configuration and chemical environment of P and N in Ti$_3$C$_2$. As shown in Fig. 3b, the N 1s peak can be deconvoluted into five different components located at about 396.5, 398.7, 399.8, 401.3 and 402.4 eV, which can be attributed to N–Ti, pyridinic–N, C–NH, C–NH$_2$ and oxidized–N, respectively.[14] The characteristic peak centred at 396.5 eV corresponding to the N–Ti bond confirmed that N was doped in the Ti$_3$C$_2$. Similarly, the high-resolution P 2p spectrum (Fig. 3c) shows that phosphorus is doped into Ti$_3$C$_2$ by means of P–O bonding, corresponding to a characteristic peak of 133.3 eV.[15] This is because at lower doping temperatures, P atoms are mainly bonded to the end of the Ti$_3$C$_2$ surface and produce more P–O configurations.[6] As shown in Fig. 3d and Fig. 3e (see Table S1 for detailed peak information), Ti 2p can be divided into 10 peaks. The two peaks of 456.6 eV and 461.3 eV correspond to N–Ti 2p$_{3/2}$ and N–Ti 2p$_{1/2}$, respectively. C 1s can be divided into 5 peaks, and 285.04 eV is attributed to C–N. The appearance of these characteristic peaks further proves the successful doping of N atoms into Ti$_3$C$_2$. The high-resolution O 1p spectrum (Fig. 3f) shows the O-N characteristic peak of 532.3 eV, which also confirms the above results. The assignment of 532.2 eV to O-H is also attributable to the existence of P–O, which is consistent with the results of the P 2p spectrum.[16] It can be expected that N and P doping will help improve the electrochemical performance of Ti$_3$C$_2$.
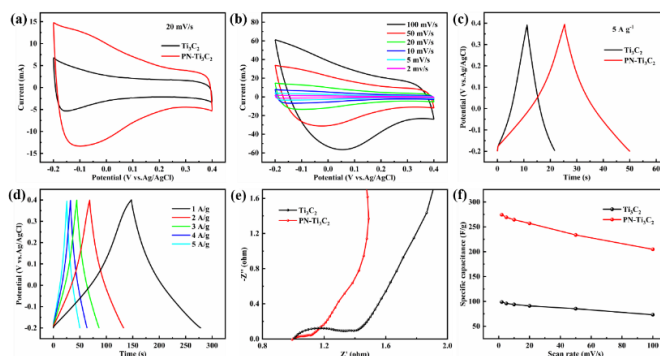
Fig. 4. (a) CV curves of the Ti_3C_2 and $PN–Ti_3C_2$ electrodes. (b) CV curves of the $PN–Ti_3C_2$ electrode at various scan rates. (c) GCD curves of the Ti_3C_2 and $PN–Ti_3C_2$ electrodes. (d) GCD plots of the $PN–Ti_3C_2$ electrode at various current densities. (e) Nyquist plots of the Ti_3C_2 and $PN–Ti_3C_2$ electrodes. (f) Specific capacitance of the Ti_3C_2 and $PN–Ti_3C_2$ electrodes at various scan rates.

The electrochemical performance of the $PN–Ti_3C_2$ electrode was evaluated by a three-electrode system. Fig. 4a shows the CV curves of Ti_3C_2 and $PN–Ti_3C_2$ electrodes in 1.0 M H_2SO_4 solution at a scan rate of 20 mV/s in the potential range of – 0.2V to 4.0V. The area of the CV curve of the $PN–Ti_3C_2$ electrode is significantly larger than that of the Ti_3C_2 electrode, and the large slope ($\triangle I/\triangle V$) at the beginning and end of the potential window. It shows that the $PN–Ti_3C_2$ electrode has a faster charge and discharge response to the applied voltage.[17] Fig. 4b shows the CV curve of the $PN–Ti_3C_2$ electrode at 2, 5, 10, 20, 50, and 100 mV s^{-1}. A small change in the shape of the CV curve indicates a good rate capability.[17] The GCD curves of $PN–Ti_3C_2$ and Ti_3C_2 electrodes at 5 A g^{-1} are shown in Fig. 4c. The discharge time of the $PN–Ti_3C_2$ electrode is significantly longer than that of the Ti_3C_2 electrode, revealing that its energy storage performance is better and can provide a larger capacitance, which is consistent with the result of the CV curve. Fig. 4d shows the charge and discharge curves of the $PN–Ti_3C_2$ electrode at different current densities. All charge and discharge curves are almost triangular. The insignificant voltage drop (iR drop) and linear symmetrical charging and discharging characteristics reflect the low overall resistance, fast charging and discharging response and electrochemical reversibility of the $PN–Ti_3C_2$ electrode.[11, 12] EIS can directly reflect the conductivity and charge transfer capability of the material. The semicircular arc of the high frequency part and the vertical line of the low frequency part constitute the Nyquist diagram of the electrode (Fig. 4e).[4] Generally, the semicircular arc is related to the electrode surface characteristics and the charge transfer resistance (Rct), while the vertical line reveals the Warburg impedance and capacitance characteristics of ion diffusion. The Rct values of Ti_3C_2 and $PN–Ti_3C_2$ electrodes are 0.39 Ω and 0.11 Ω, respectively. Rct originates from the electron transfer at the interface between the electrode material and the electrolyte. The greater the conductivity of the electrode material, the lower the Rct.[18] This is also consistent with the effect of P and N in the $PN–Ti_3C_2$ electrode on improving the conductivity. In contrast, the

slope of the low-frequency line of PN–Ti$_3$C$_2$ is larger, indicating that the electrode has a low diffusion resistance, and ions are more likely to penetrate between the layers of the active material. Fig. 4f shows the scan rate dependence of the specific capacitance calculated from Eq (1).[18]

$$C_m = \frac{\int IdV}{2 \cdot m \cdot v \cdot \triangle V} \qquad (1)$$

Here C$_m$ is specific capacitance (F g^{-1}), I is the response current (A), V is the potential, m is mass of the active materials (g), v is the scan rate (mV s^{-1}) and $\triangle$V is the potential window (V). Obviously, under the same scan rate, the Cm of the PN–Ti$_3$C$_2$ electrode is significantly higher than that of the Ti$_3$C$_2$ electrode. At 2 mV/s, the Cm of PN–Ti$_3$C$_2$ is 274.3 F/g, which is more than 2.7 times that of Ti$_3$C$_2$ (98.7 F/g). The results showed that guanidine phosphate assisted hydrothermal preparation of Ti$_3$C$_2$ doped with phosphorus and nitrogen diatoms, which significantly enhanced the energy storage performance of Ti$_3$C$_2$.

Conclusions

In summary, this article reports for the first time a convenient method for preparing Ti$_3$C$_2$ doped with phosphorus and nitrogen diatoms using guanidine salt-assisted hydrothermal method. Here, guanidine phosphate plays a very important role in the synthesis of PN–Ti$_3$C$_2$, providing Ti$_3$C$_2$ with phosphorus and nitrogen elements while creating a reducing environment. It can be expected that electrode materials prepared from PN–Ti$_3$C$_2$ will significantly improve the electrochemical performance of Ti$_3$C$_2$. At a scanning rate of 2 mV s^{-1}, the PN–Ti$_3$C$_2$ electrode exhibits a high ratio capacitor of 274.3 F/g, which is more than 2.7 times that of the Ti$_3$C$_2$ electrode, and no capacitor degradation after 1000 cycles in the 1.0 M H$_2$SO$_4$ electrolyte.

Acknowledgments

References

[1]ZHU Q, LI J, SIMON P, et al. Energy Storage Materials, 2021, 35:630-660.

[2]MENG W, LIU X, SONG H, et al. Nano Today, 2021, 40:101273.

[3]LI W, Lü H-Y, WU X-L, et al. RSC Advances, 2015, 5:12583-12591.

[4]LIU R, CAO W, HAN D, et al. Journal of Alloys and Compounds, 2019, 793:505-511.

[5]ZHAO Z, WANG S, WAN F, et al. Advanced Functional Materials, 2021, 2101302.

[6]WEN Y, LI R, LIU J, et al. Journal of Colloid and Interface Science, 2021, 604:239-247.

[7]LU C, YANG L, YAN B, et al. Advanced Functional Materials, 2020, 30:2000852.

[8]YOON Y, TIWARI A P, CHOI M, et al. Advanced Functional Materials, 2019, 29:1903443.

[9]WEN Y, WANG B, HUANG C, et al. Chemistry, 2015, 21:80-85.

[10]YOON Y, LEE M, KIM S K, et al. Advanced Energy Materials, 2018, 8:1703173.

[11]DAI S, LIU Z, ZHAO B, et al. Journal of Power Sources, 2018, 387:43-48.

[12]YU J, ZENG M, ZHOU J, et al. Chemical Engineering Journal, 2021, 426:130765.

[13]ZHAO N, YANG Y, YI D, et al. Chemical Engineering Journal, 2021, 422:130018.

[14]ZHANG T, XIAO J, LI L, et al. Ceramics International, 2020, 46:21482-21488.

[15]LI R, WEI Z, GOU X, et al. RSC Advances, 2013, 3:9978.

[16]LIU Z W, PENG F, WANG H J, et al. Angewandte Chemie International Edition, 2011, 50:3257-3261.

[17]LI L, ZHANG M, ZHANG X, et al. Journal of Power Sources, 2017, 364:234-241.

[18]WEN Y, RUFFORD T E, CHEN X, et al. Nano Energy, 2017, 38:368-376.

Adsorption mechanism of SA/PVA/GO aerogel spheres for MB

Xiuling Lin, Jieqi Zhang Huawei Feng

Department of Materials Science and Engineering, Anhui University of Science and Technology, Huainan 232001, China

Correspondence to: Xiuling Lin (E-mail: xiulinglin@126.com)

Abstract

Sodium alginate/polyvinyl alcohol (SA/PVA) aerogel spheres modified by graphene oxide (GO) was prepared, and the adsorption mechanism of SA/PVA/GO aerogels for methylene blue (MB) was studied by adsorption kinetics and isotherm models. Kinetic studies showed that the pseudo-second-order kinetics model and the particle internal diffusion model could calculate experimental data and the results are in good agreement with practice. Adsorption isotherm analysis indicated the monolayer adsorption produced between methylene blue and complex aerogels.

Keywords: aerogel; adsorption kinetics; adsorption isotherm; mechanism; SA/PVA/GO

Introduction

Aerogel consisting of biopolymers such as alginate and polyvinyl alcohol have been widely studied for wastewater treatment [1,2]. Graphene oxide (GO) has large quantities of oxygen-containing functional groups, including hydroxyl, epoxy and carboxyl groups [3], that can provide abundant active sites for functionalization and adsorption. Recently, GO aerogels have gained attention for applications in wastewater treatment [4]. Sodium alginate/polyvinyl alcohol aerogels modified by graphene oxide (SA/PVA/GO) have been considered as adsorbents and used for the adsorption of heavy metal ions [5,6], and methylene blue (MB) [7,8]. The effects of dosage of gel, pH of solution, initial MB concentration, and adsorption time on the adsorption behavior, and obtained the highest adsorption capacity of SA/PVA/GO hydrogels for MB are studied in these documents.

Based on the above researches, the adsorption mechanism of SA/PVA/GO aerogel spheres for MB was studied. SA/PVA and SA/PVA/GO aerogel spheres were fabricated by immersing in $CaCl_2$ and boric acid solution in this paper. To study the adsorption mechanism of the aerogel spheres with different GO content to dye, methylene blue was chosen as the model dye. The relationship between adsorption capacity and time was substituted into adsorption kinetic model and isotherm model to study the adsorption mechanism.

Experimental section
Materials

Sodium alginate (SA), polyvinyl alcohol (PVA), *N, N′*- methylene bisacrylamide (MBA), boric acid (H_3BO_3) and methylene blue (MB) were purchased from Sinopharm Chemical Reagent Co., Ltd (Shanghai, China). Graphene oxide (GO) was provided by Turing Evolution

Technology Co., Ltd (Shenzhen, China). Calcium chloride (CaCl$_2$) was purchased from Fuchen Chemical Reagent Co., Ltd (Tianjin, China). They were all analytical grade and used directly without further purification.

Preparation of aerogel spheres

The SA/PVA/GO mixed solution was dropped into CaCl$_2$ solution (5 wt%) by a peristaltic pump and obtained SA/PVA/GO hydrogel beads. The composite hydrogel spheres were soaked in saturated boric acid solution for 2 h. Finally, the hydrogel beads were immersed in CaCl$_2$-saturated boric acid mixed solution for 12 h to form steady morphology. The prepared composite hydrogel spheres were stored after freezing-drying. The composite aerogel spheres with different GO content 1, 2, 4, and 6 wt% were designated as SA/PVA/GO1, SA/PVA/GO2, SA/PVA/GO4, and SA/PVA/GO6, respectively.

Adsorption Experiments

Adsorption experiments were conducted in a 50 ml MB solution with the concentration 50 mg/L at 25 °C. The gel spheres (50 mg) were added into the MB solution and the adsorption capacity was measured at different time until the adsorption was completed. The capacities of MB adsorbed were determined at the wavelength of 664 nm. The UV absorbance of MB solution was detected and converted to the MB concentration through a calibration curve. The relationship between adsorption capacity and time was obtained. The equilibrium adsorption capacity (q_e) and adsorption capacity of gel spheres at different time (q_t) were calculated.

Study methods of mechanism

The adsorption mechanism was studied by kinetic and isotherm models and the equation was as follows:

Pseudo-first-order kinetic model equation: $\ln(q_e\text{-}q_t) = \ln q_e - k_1 t$ (1)

Pseudo-first-order kinetic model equation: $\dfrac{t}{q_t} = \dfrac{1}{k_2 q_e^2} + \dfrac{t}{q_e}$ (2)

Particle internal diffusion model equation: $q_t = k_i t^{1/2} + C$ (3)

where q_e and q_t (mg/g) were equilibrium adsorption capacity and adsorption capacity at time t, respectively. k_1 (h^{-1}) was the rate constant of the pseudo-first-order kinetics. k_2 (g/mg·h^{-1}) was the pseudo-second-order rate constant. k_i (mg/g·h^{-1}) was the particle internal diffusion rate constant, and C (mg/g) was the intercept which was related to the thickness of the boundary layer.

Langmuir isotherm model equation: $\dfrac{c_e}{q_e} = \dfrac{1}{K_L q_m} + \dfrac{c_e}{q_m}$ (4)

$$R_L = \dfrac{1}{1 + K_L c_0}$$ (5)

Freundlich isotherm model equation: $\ln q_e = \ln K_F + \dfrac{\ln c_e}{n}$ (6)

Temkin isotherm model equation: $q_e = \dfrac{R_T}{b_T} \ln(K_T c_e)$ (7)

where q_e (mg/g) was the equilibrium adsorption capacity, c_e (mg/L) was the concentration

of MB at equilibrium, K_L (L/mg) was the Langmuir adsorption constant, and q_m (mg/g) was the maximum adsorption capacity. K_F and n were Freundlich constants indicating adsorption capacity and intensity, respectively. R (8.314 J/mol·K) was the universal gas constant, T (K) was the absolute temperature, b_T was the Temkin isotherm constant and K_T represented the equilibrium binding constant corresponding to the maximum binding energy. c_0 (mg/L) was the initial concentration of MB. The value of R_L would indicate the adsorption process was irreversible ($R_L = 0$), favorable ($0 < R_L < 1$), linear ($R_L = 1$), and unfavorable ($R_L > 1$)

Results and discussion

Adsorption kinetic analysis

In order to study the adsorption kinetic principle of SA/PVA/GO (0, 1, 2, 4, 6) composite aerogels for MB, the pseudo-first-order kinetic model, pseudo-second-order kinetic model and particle diffusion model were used to calculate the data of adsorption capacity and time. The adsorption kinetic curves of SA/PVA/GO (0, 1, 2, 4, 6) aerogels for MB were shown in Fig. 1. The kinetic parameters of the three models were shown in Table 1.
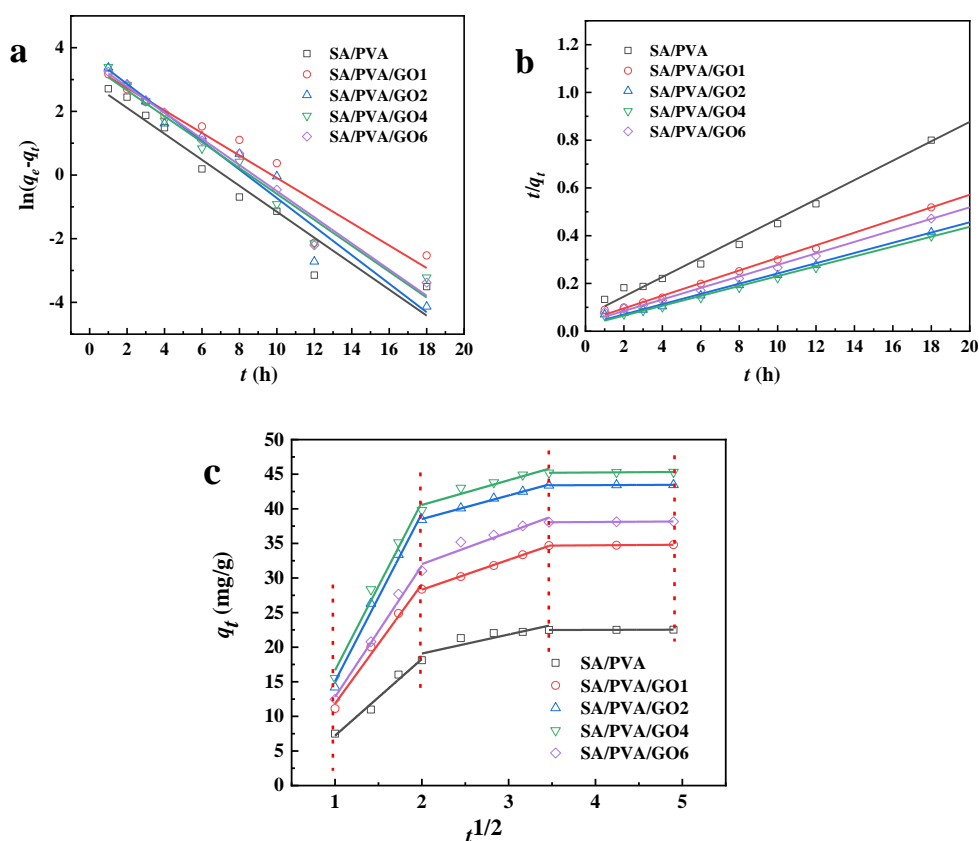
Fig. 1 The adsorption kinetic curves: (a) pseudo-first-order (b) pseudo-second-order and (c) particle internal diffusion

Fitting data showed the correlation coefficient (R^2) of the pseudo-second-order kinetic model was greater than that of the pseudo-first-order kinetic model. It indicated that the curves fitted by the pseudo-second-order kinetic model were closer to the experimental data. In addition, the equilibrium adsorption capacity calculated by the pseudo-second-order kinetic model was closer to the experimental equilibrium adsorption capacity. These results suggested that the adsorption process of SA/PVA/GO (0, 1, 2, 4, 6) aerogel for methylene blue accorded with the pseudo-second-order kinetic model and belonged chemical adsorption.

Fig. 1 (c) was the fitting result of the particle internal diffusion model. The adsorption curve was not linear during the entire adsorption time, and the adsorption of MB by SA/PVA/GO (0, 1, 2, 4, 6) aerogels could be divided into several stages. The whole adsorption process could be divided into three linear parts, and the particle internal diffusion rate constants were $K_{i1}>K_{i2}>K_{i3}$ in three parts.

Table 1 The adsorption kinetic parameters of SA/PVA/GO(0、1、2、4、6) aerogel spheres

Kinetic Models	Parameters	SA/PVA	SA/PVA /GO1	SA/PVA /GO2	SA/PVA /GO4	SA/PVA /GO6
Pseudo-first-order	k_1 (h^{-1})	0.940	0.813	1.031	0.935	0.946
	q_e (mg/g)	18.54	31.187	42.95	39.25	32.14
	R^2	0.938	0.925	0.958	0.969	0.974
Pseudo-second-order	k_2 (g/mg·h)	0.026	0.016	0.017	0.018	0.016
	q_e (mg/g)	24.39	37.87	46.73	48.54	41.49
	R^2	0.994	0.997	0.996	0.996	0.996
Intra-particle diffusion	k_{i1}	11.079	17.256	24.259	24.306	18.993
	k_{i2}	2.756	4.325	3.412	3.576	4.601
	k_{i3}	0.030	0.081	0.046	0.082	0.077

Adsorption isotherm analysis

The fitting curves of the Langmuir, Freundlich and Temkin isotherm models were shown in Fig. 2, and all relevant parameters were listed in Table 2. The correlation coefficient (R^2) of Langmuir model was better than that of Freundlich model. It indicated that Langmuir model was more suitable for explaining the current adsorption process of aerogels for methylene blue. The Langmuir isotherm model fitting results showed that the maximum theoretical adsorption capacity of methylene blue on SA/PVA/GO (0, 1, 2, 4, 6) aerogel spheres were 162.86, 119.90, 174.52, 209.20, 128.04 mg/g, respectively, which were close to the experimental values.
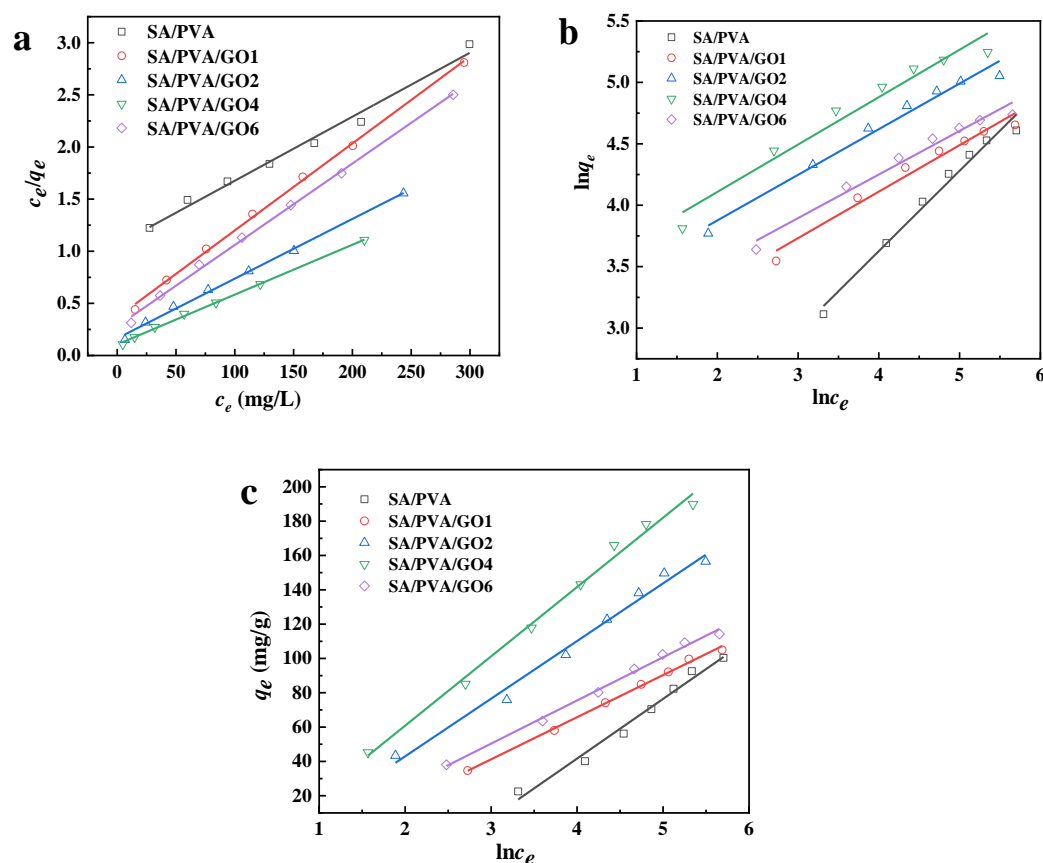
Fig. 2 The adsorption isotherm curves: (a) Langmuir, (b) Freundlich and (c) Temkin

Langmuir isotherm model adsorption parameter R_L value could be used to evaluate the degree of suitability of adsorption process. For example, in the 100 mg/L methylene blue solution, the R_L values of SA/PVA/GO (0, 1, 2, 4, and 6) aerogel spheres were 0.633, 0.304, 0.223, 0.181, and 0.264, respectively. The R_L values were all between 0 and 1 indicated that the adsorption process was favorable adsorption. In addition, the 1/n values in Freundlich isothermal model fitting results were found to be in the range of 0~1 by comparison, which further indicated that the adsorption process of SA/PVA/GO (0, 1, 2, 4, 6) aerogel spheres for MB was favorable.

Table 2 The adsorption isotherm parameters of SA/PVA/GO (0, 1, 2, 4, 6) aerogel spheres

Isotherm Models	Parameters	SA/PVA	SA/PVA/GO1	SA/PVA/GO2	SA/PVA/GO4	SA/PVA/GO6
Langmuir	K_L (L/mg)	0.006	0.023	0.035	0.045	0.028
	q_m (mg/g)	162.86	119.90	174.52	209.20	128.04
	R^2	0.988	0.999	0.997	0.998	0.998
Freundlich	K_F	2.75	13.42	22.94	28.11	16.95
	R_L	0.633	0.304	0.223	0.181	0.264
	R^2	0.982	0.971	0.978	0.960	0.975
	$1/n$	0.654	0.379	0.372	0.386	0.355
Temkin	K_T	0.060	0.267	0.486	0.61	0.369
	R^2	0.982	0.997	0.987	0.992	0.994
	B	34.76	24.54	33.59	40.39	25.16

Adsorption mechanism analysis

Preliminary experimental data showed that GO modified network structure of SA/PVA gel through physical crosslinking. And –COOH functional groups still were retained in the composite hydrogels. Adsorption kinetic analysis indicated cationic dyes and ion exchange between the functional groups on the aerogel or electrostatic interactions to control the adsorption process. The particle internal diffusion rate constant further confirmed that diffusion process was not the only "velocity control" step, but was also affected by boundary layer diffusion. In this process, methylene blue molecules rapidly combined the active groups on the surface of SA/PVA/GO aerogel, and then internally diffused into the complex aerogel network to bind to more adsorption sites. Subsequently, the adsorption rate decreased with the concentration of MB solution and the mass transfer force decreased. In the third stage, the adsorption reached dynamic equilibrium. Adsorption isotherm analysis indicated the monolayer adsorption produced between methylene blue and complex aerogels.

Conclusions

The fitting results of adsorption kinetic model showed that the adsorption process of SA/PVA/GO aerogels for MB was in accordance with the pseudo-second-order kinetic model and the particle internal diffusion model. The adsorption process of SA/PVA/GO aerogels for MB was controlled by chemical adsorption, which mainly used the ion exchange between cations dye and functional groups on the aerogels. The adsorption isotherm fitting results showed that the adsorption process conformed to the Langmuir isotherm model and the adsorption of SA/PVA/GO aerogels for MB was monolayer adsorption.

References
[1] Shalla A H, Bhat M A, Yaseen Z. Hydrogels for removal of recalcitrant organic dyes: A conceptual overview. Journal of Environmental Chemical Engineering, 2018, 6(5): 5938-5949.
[2] Wang A Q, Wu S S, Zhang Y N, et al. Preparation of modified sodium alginate aerogel and its application in removing lead and cadmium ions in wastewater. International journal of biological macromolecules, 2020, 157: 687-694.
[3] Nguang S Y, Wong S R, Law J S, et al. Enhancing adsorption property of Engelhard Titanosilicate-10 through incorporation of graphene oxide. Microporous and Mesoporous Materials, 2017, 252: 125–139.
[4] Wu Z J, Huang W X, Shan X G, et al. Preparation of a porous graphene oxide/alkali lignin aerogel composite and its adsorption properties for methylene blue. International Journal of Biological Macromolecules, 2020, 143: 325-333.

[5] Yi X F, Sun F L, Han Z H, et al. Graphene oxide encapsulated polyvinyl alcohol/sodium alginate hydrogel microspheres for Cu (II) and U (VI) removal. Ecotoxicology and Environmental Safety, 2018, 158: 309-318.

[6] Yu Y R, Zhang G, Lin Y. Preparation and adsorption mechanism of polyvinyl alcohol/graphene oxide-sodium alginate nanocomposite hydrogel with high Pb (II) adsorption capacity. Journal of Applied Polymer Science, 2019, 136(14): 47318.

[7] Liu C, Liu H, Xiong T, et al. Graphene Oxide Reinforced Alginate/PVA Double Network Hydrogels for Efficient Dye Removal. Polymers, 2018, 10(8): 835.

[8] Ma Y X, Li X, Shao W J, et al. Fabrication of 3D Porous Polyvinyl Alcohol/Sodium Alginate/Graphene Oxide Spherical Composites for the Adsorption of Methylene Blue. Journal of Nanoscience and Nanotechnology, 2020, 20(4): 2205-2213.

Fabrication and property investigation of epoxy nanocomposites reinforced by a nanohybrid of flower-like nickel phyllosilicate@znic sulfide

Xue-song Feng, Ji-nian Yang[*], Liu Jiang

School of Materials Science and Engineering, Anhui University of Science and Technology, Anhui Huainan 232001, P.R. China
Corresponding to Ji-nian Yang (yangjinian@163.com; jnyang@aust.edu.cn)

Abstract

Flower-like particles of nickel phyllosilicate (NiPS) were synthesized using a deposition-precipitation method, which were then decorated with abundant zinc sulfide (ZnS) nanoparticles through a hydrothermal technology, yielding the nanohybrids of NiPS@ZnS. Finally, the epoxy (EP)-based nanocomposites containing varied mass fraction of NiPS@ZnS were fabricated by blending physically, and the influences on the mechanical, tribological, thermal properties and fire safety were investigated carefully. Based on a series of measurements and analysis, the flower-like morphological structure of NiPS and binary architecture of NiPS@ZnS, as well as their chemical compositions are investigated, confirming the successful synthesis of the nanohybrids. Mechanical tests revealed that the added nanohybrids enhanced the mechanical properties of EP nanocomposites. With the elevated content of NiPS@ZnS, the elastic modulus increased monotonously while the tensile and compression strengths increased first and then decreased, showing the maximum values of 86.1 and 259.02 MPa, respectively, which were 11% and 25% higher than that of pure EP. Dry sliding measurements demonstrated the significantly positive influence of NiPS@ZnS on the tribological properties, and the lowest friction coefficient of 0.404 could be obtain when 5% filler was added, which was lowered by about 12%. However, a much more improvement on the anti-wear property could be achieved, showing the lowest wear rate of 0.494×10^{-5} mm^3/N·m, which is 93% lower than that of pure EP. Thermogravimetric tests found the added NiPS@ZnS could slightly increase the thermal decomposition temperature and remarkably decrease the mass loss rate, implying the enhancement in the thermal stability. Kinetics analysis emphasized that such nanohybrids would not change the thermal decomposition mode, still exhibiting the one-stage reaction, i.e. reaction order equaled to around 1. However, the activation energy decreased steadily along with the increased concentration of NiPS@ZnS. Besides, NiPS@ZnS nanohybrids also make EP nanocomposites be self-extinguished, shortening the duration of burning time to just 63 s, which was greatly lower than the 214 s for pure EP.

Keywords: nickel phyllosilicate; zinc sulfide; mechanical response; tribological property; thermal stability

Acknowledgements

Cu^{2+} Adsorption of Magnetic Chitosan: Kinetic and Thermodynamic Studies

Xujie Peng[1], Liting Zhang[1*], Ruichang Cao[1], Meng Li[1], Xin Rong[1], Jianjun Li[1,2], Yin Liu[1,2]

[1]Department of Materials Science and Engineering, Anhui University of Science and Technology, Huainan, China, 232001;
[2]Anhui International Joint Research Center for Nano Carbon-based Materials and Environmental Health, Huainan 232001, China
Corresponding author: Liting Zhang, *E-mail*: ljj.hero@126.com

Abstract

To improve the adsorption performance and solid-liquid separation of Cu^{2+} adsorbent, magnetic chitosan (MCS) adsorbent was fabricated via a chemical cross-linking method. The Cu^{2+} adsorption of MCS at 288, 298, and 308K was experimentally investigated and theoretically fitted by adsorption kinetic model, adsorption activation energy model, and adsorption isotherm model. The highest specific adsorption of the MCS for Cu^{2+} was tested as 38.7 mg/g. The kinetic model fitting result indicates that Cu^{2+} adsorption of MCS is more in consist with the pseudo-second-order kinetic model, suggesting that it is dominated by chemical adsorption. It is found that a two-step diffusion mechanism, the boundary layer diffusion followed by an intra-particle diffusion, may play an important role in Cu^{2+} adsorption. The adsorption activation energy is calculated as 10.05 kJ/mol, suggesting that physical adsorption has a significant effect on Cu^{2+} adsorption. From adsorption isotherm fitting the Cu^{2+} adsorption is found to belong to the Sips and Langmuir isothermal adsorption model. Based on all three fittings, it could be concluded that the Cu^{2+} adsorption of MCS is a composite adsorption process, which is dominated by chemical adsorption and supplemented by physical adsorption.

Keywords: Magnetic chitosan; Cu^{2+} adsorption; Adsorption kinetics; Adsorption activation energy; Adsorption isotherm

Introduction

With the rapid development of economic society and industrial production, the amount of industrial wastewater generated has increased significantly. As one of the main pollutants, industrial wastewater with heavy metal ions, including Cr^{6+}, Hg^{2+}, Cd^{3+}, Zn^{2+}, Ni^{2+}, and Cu^{2+}, poses a high threat to the environment and human beings[1]. Because heavy metals cannot be excreted from the human body through physiological metabolism, the accumulation of heavy metals in the body will increase the risk of liver cancer and affect the human central nervous

system[2]. To ensure human health and environmental safety, the heavy metal content in water must be strictly controlled below the safe concentration threshold. Eg., the safety standard for Cu^{2+} is less than 0.5 mg/L. Most of the heavy metal wastewater is discharged from mineral production, electroplating, semiconductor manufacturing, and lead-acid battery industry. For example, the chemical mechanical polishing process in the semiconductor manufacturing industry produces heavy metal wastewater with a Cu^{2+} concentration over 100 mg/L[3]. After several treatment processes, the Cu^{2+} content was diluted, resulting in the production of a large amount of low concentration (tens of mg/L) Cu^{2+} wastewater[4; 5]. This concentration is still much higher than the allowable emission value. Therefore, the effective elimination of heavy metals from surface water and drinking water becomes an urgent task for humankind.

Many technologies, including coprecipitation, electrodialysis, membrane filtration, and ion exchange, have been explored to remove Cu^{2+} from water[3; 4; 6-8]. Some of these technologies are widely used in the wastewater treatment industry. Each method has specific water treatment ranges and advantages. However, they also have significant disadvantages, such as high cost, low efficiency, sludge handling problems, and possible secondary pollution. In addition, the removal efficiency for trace concentrations of Cu^{2+} is low. In contrast, adsorption is a more economical and feasible heavy metal removal technology, especially for low Cu^{2+} concentration wastewaters treatment. Furthermore, in this way, the adsorbed Cu^{2+} can be easily retrieved. The adsorption technique for Cu^{2+} removal has attracted significant interest. Various Cu^{2+} adsorbents were fabricated and studied, including activated carbon, lignin, silica composite, and zeolite[9-11]. Chitosan is a natural biopolymer, which has functional groups such as -OH and $-NH_2$ in the molecular. These groups have a chemical affinity for Cu^{2+} ions, thus can selectively adsorb Cu^{2+} from water[12; 13]. Furthermore, chitosan has the advantages of low cost, renewable, perfect hydrophilicity, biocompatibility, biodegradability, and non-toxicity[14; 15]. Therefore, chitosan is supposed as one of the best candidates for Cu^{2+} adsorbents. The other difficulty of adsorption technology is the low solid-liquid separation efficiency due to the tiny diameter of the adsorbents. To address this problem, the magnetic separation technique was introduced in[16]. Since most materials for adsorbents have no magnetic, a magnetic core is needed to make the adsorbent magnetic[16; 17]. Efficient solid-liquid separation could be achieved by using magnetic adsorbents.

In this study, magnetic chitosan (MCS) adsorbent was fabricated by using industrial waste coal-fly-ash magnetic spheres (MS) as magnetic core and chitosan as the coating. The structure and Cu^{2+} adsorption of MCS was investigated. The adsorption mechanism was carefully studied by three theoretical fitting models: adsorption kinetic model, adsorption activation energy model, and adsorption isotherm model.

Materials and methods

1. Materials

The coal-fly-ash used in this study was obtained from Luohe power plant in Huainan, China. Chitosan ($C_{56}H_{103}N_9O_{39}$, deacetylation＞95%), Acetic Acid (CH_3COOH), Glutaraldehyde ($C_5H_8O_2$), tween-80 ($C_{46}H_{52}N_5O_8P$), Copper(II) sulfate pentahydrate

(CuSO₄·5H₂O), DDTC ($C_5H_{10}NNaS_2$), ammonium hydroxide ($NH_3 \cdot H_2O$), concentrated hydrochloric acid (HCl, 32-38%), and sodium hydroxide (NaOH, 98%) were all purchased from Sinophenol Chemical Reagent Co., Ltd. (China). All the reagents were analytical reagent-grade. The Cu-containing wastewater was prepared by dissolving $CuSO_4 \cdot 5H_2O$ in an appropriate amount of deionized water. The pH of the solution was adjusted by 0.1 M NaOH or HCl.

2. Equipments

CMS preparation equipment: Magnetic separation tube (GXG-08SD, Coal Research Institute, China), Planetary ball mill (XGB04, Nanjing Boyun Tong Co., Ltd.), Electronic balance (FA1004, Shanyu Hengping instrument). Cu^{2+} adsorption detection equipment: UV visible spectrophotometer (UV-5100, Shanghai Yuan analysis instrument Co., Ltd.), Constant temperature oscillator (ZQTY-70, Shanghai Zhichu Instrument Co., Ltd.). Structural characterization equipment: Scanning electron microscopy (SEM, ZEISS SUPRA 40, Germany), Fourier transform infrared (FT-IR) spectra in the range of 4000-400 cm^{-1} were recorded to determine the functional group of materials. Magnetic characterization equipment: HH-20 vibration sample magnetometer (VSM, Nanjing University Instrument Factory).

3. Preparation of MCS

The preparation of MS core includes multistage magnetic separation and ball milling. In short, MS were obtained from 100 mesh sieved coal fly ash by a magnetic separation under a 300 mT magnetic field. Then the MS was further separated under a low-intensity magnetic separation (100 mT), followed by a ball milling at 400 rpm for 10 h. The final MS particles were obtained by an additional low-intensity magnetic separation (100 mT).

The magnetic chitosan (MCS) was synthesized via a chemical cross-linking method. A certain amount of chitosan powder was dispersed in 80 mL 2% CH_3COOH solution and stirred for 10 min. Then tween-80 and a certain amount of CMS was added in proportion and stirred for 30 min. A certain amount of glutaraldehyde was added to the obtained gel and the solid content was separated by a permanent magnet, carefully washed with deionized water and ethanol. The product was dried at 60 °C in a vacuum drier for 12 h and sealed for later Cu^{2+} adsorption experiments.

4. Adsorption experiments

Cu^{2+} adsorption performance was investigated using homemade Cu-containing wastewater. 0.1 g MCS was added in iodide bottles containing 100 mL Cu^{2+} solution at concentrations in the range of 10-300 mg/L. The mixed solution oscillated in an oscillator under 288, 298, and 308 K, respectively, with a swing speed of 140 r/min. The supernatant was extracted every 5 min for the following color reaction and a UV-Vis absorbance at 451 nm was measured. According to the standard adsorption curve of the Cu^{2+} solution, the Cu^{2+} concentration could be calculated from the absorbance value. Three parallel samples were taken for detection in each group of samples, and the average value was taken for analysis. The Cu^{2+} adsorption q was calculated according to formula (1).

$$q = \frac{(C_0 - C_e)v}{m} \qquad (1)$$

where C_0 and C_e (mg/L) are the initial and final concentration of Cu^{2+}, respectively, v (L) is the volume of Cu^{2+} solution, and m (g) is the dosage of the adsorbent.

Results and discussion

1. Structural characterization and magnetic investigation

The structure of the MCS was characterized by SEM and FTIR. It is found the morphology of MCS changes a lot from that of CMS particles. As shown in Fig. 1(a) and (b), in the MCS sample, the CMS particles were fully covered by a certain substance. The FTIR investigation proves this substance is chitosan. As shown in Fig. 1(c), the absorption peaks at 1650 and 1080 cm^{-1} correspond to the C=O stretching vibration and the C-N axial bending vibration of amides in chitosan, indicating that chitosan has been coated on CMS. According to the VSM hysteresis loops, both CMS and MCS have a strong magnetism and small remanence and coercivity. The specific saturation magnetization of MCS is tested as 20.4 emu·g^{-1}. Although the magnetism is low than CMS, it is also strong enough for effective magnetic separation.
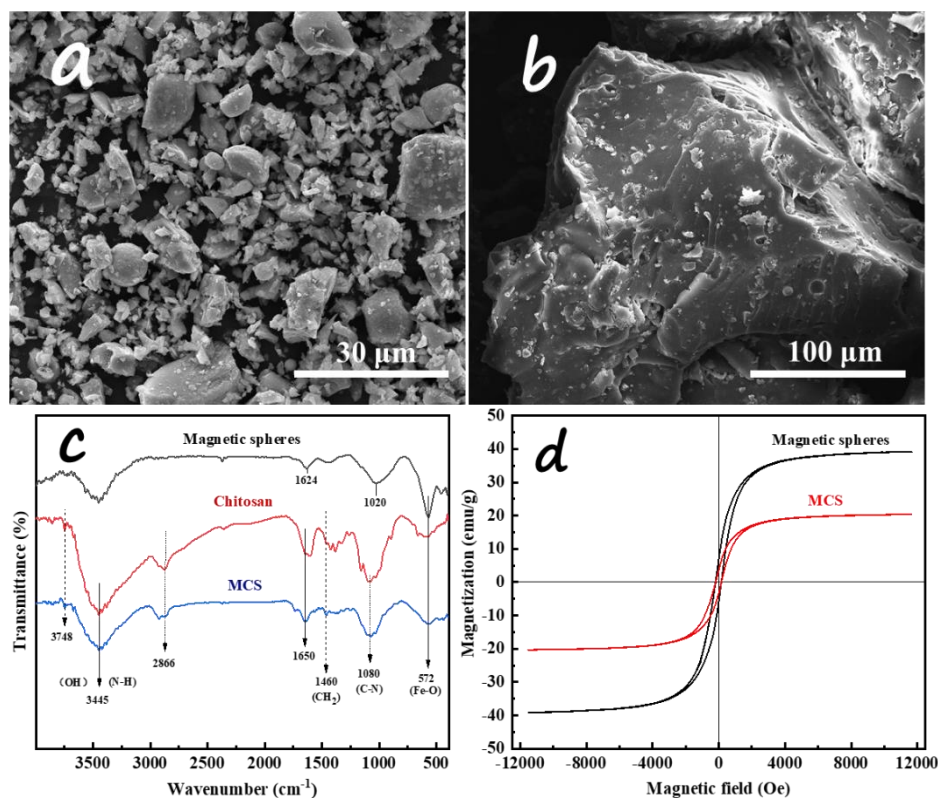
Figure.1 SEM of (a) CMS and (b) MCS, (c) FT-IR results of CMS, chitosan, and MCS, and (d) VSM hysteresis loop of CMS and MCS.

2. Adsorption kinetics

The Cu^{2+} adsorption performance of MCS was investigated by both experimental and theoretical fitting methods. Fig. 2 shows the Cu^{2+} adsorption performance and the kinetic fitting curve of the adsorption. The relevant fitting parameters are shown in Table. 1. The Cu^{2+} adsorption of MCS under 288, 298, and 308 K was tested as 13.3, 18.0, and 19.8 mg/g. It is found that the adsorption speed is first fast and then becomes slow gradually. In the first 5 minutes, more than 50% Cu^{2+} was removed from the solution. The Cu^{2+} adsorption capacity continued to increase slowly till saturating after 60 min around. The Cu^{2+} adsorption rate is closely related to the concentration of the surface chemical activity sites and the movement of Cu^{2+} ions. With the decrease of the reaction sites available for Cu^{2+} adsorption on the surface of the adsorbent, the adsorption reached equilibrium. The increase of adsorption with the rise of temperature may be due to the rise of the chemical activity sites and the increase of the collision chance between the adsorbents and the Cu^{2+} ions under higher temperatures.
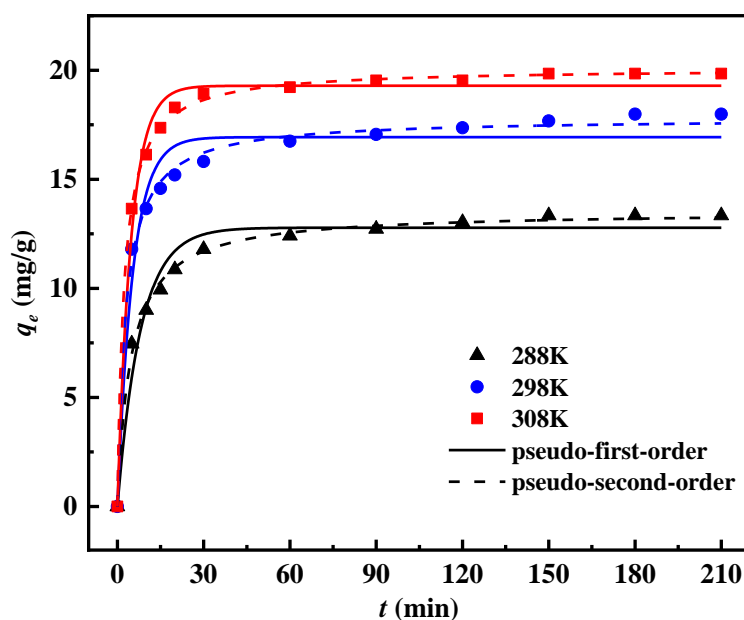
Figure. 2 Experimental Cu^{2+} adsorption performance and kinetic model fitting of CMS adsorbent.

The adsorption kinetics of Cu^{2+} on MCS was studied by using pseudo-first-order and pseudo-second-order kinetic models and intra-particle diffusion model. The pseudo-first-order and pseudo-second-order kinetic equations are respectively expressed as

$$q_t = q_e(1 - e^{-k_1 t}) \tag{2}$$

$$q_t = \frac{k_2 q_e^2 t}{1 + k_2 q_e t} \tag{3}$$

The initial adsorption rate v_0 (mg/g·min^{-1}) and half adsorption time $T_{1/2}$ (min) can be calculated using pseudo-second-order kinetic parameters. The relevant expressions are

$$v_0 = k_2 q_e^2 \tag{4}$$

$$t_{1/2} = \frac{1}{k_2 q_e} \tag{5}$$

The diffusion equation in the particle is shown in Equation (6):

$$q_t = k_{id} t^{1/2} + C_i \tag{6}$$

In equation (2)-(6), q_e and q_t (mg/g) are adsorption capacity at equilibrium concentration and predetermined time, k_1(min^{-1}), k_2 (g/mg·min^{-1}), and k_{id}(mg/g·min$^{1/2}$) are adsorption rate constants, and C_i is kinetic constant. As can be seen from Table. 1, the R^2 values of pseudo-second-order kinetics at 288, 298, and 308 K are 0.997, 0.995, and 0.999, respectively. Compared with those of pseudo-first-order kinetics, these values are closer to 1. It indicates that chemical adsorption plays a major role in adsorption, and physical adsorption also plays a certain role. With the increase of temperature, the initial adsorption rate (V_0) increased gradually (0.248, 0.343, and 0.567mg/g·min^{-1} for 288, 298, and 308 K, respectively), the semi-adsorption time ($T_{1/2}$) decreased significantly (11.62, 8.99, and 5.40min, respectively), and the equilibrium adsorption time shortened.

Table. 1 Kinetic parameters for adsorption of Cu^{2+} onto MCS composite.

T	$q_{e,exp}$	Pseudo-first-order			Pseudo-second-order				
		$q_{e, cal}$	k_1	R^2	$q_{e, cal}$	k_2	R^2	v_0	$t_{1/2}$
288	13.3	12.8	0.124	0.966	13.5	0.016	0.997	2.933	4.62
298	18.0	16.9	0.187	0.962	17.8	0.019	0.995	6.027	2.96
308	19.8	19.3	0.211	0.986	20.1	0.021	0.999	8.484	2.37

Fig. 3 is the three-segment line graph of q_t and $t_{1/2}$ for the intra-particle diffusion model. The adsorption process is divided into rapid surface adsorption, intra-particle diffusion, and the dynamic equilibrium of adsorption and desorption. Table. 2 shows that $k_{1d} > k_{2d} > k_{3d}$, indicating that the diffusion rate of the boundary layer is greater than the diffusion rate within the particle and the equilibrium dynamic rate. Since the relationship between q_t and $t_{1/2}$ is nonlinear, and C_i is not zero, the Cu^{2+} adsorption could be controlled by a composite mechanism. Both boundary layer diffusion and intra-particle diffusion play an important role.

Table. 2 Intra-particle diffusion model parameters for adsorption of Cu^{2+} onto MCS composite.

T	$q_{e,exp}$	Intra-particle diffusion model								
		k_{1d}	C_1	R^2	K_{2d}	C_2	R^2	K_{3d}	C_3	R^2
288	13.3	2.94	0.201	0.984	1.13	5.64	0.979	0.149	11.3	0.913
298	18.0	4.49	0.395	0.974	0.756	11.7	0.979	0.199	15.2	0.980
308	19.8	5.29	0.415	0.979	0.929	13.9	0.934	0.094	18.6	0.882

Figure. 3 Intra-particle diffusion model of MCS adsorption process.

3. Activation energy of adsorption

The adsorption activation energy (Ea) was obtained by using the fitted kinetic model rate constants and the Arrhenius formula (Eq. (7)).

$$ln\,(k) = ln\,(A) - \frac{E_a}{RT} \tag{7}$$

Where k is the adsorption rate constant, A is the pre-exponential influence factor, which is only related to the adsorption temperature. The rate constant used in this model is the rate constant k_2 of pseudo-second-order kinetics. Adsorption activation energy parameters are shown in Table.3.
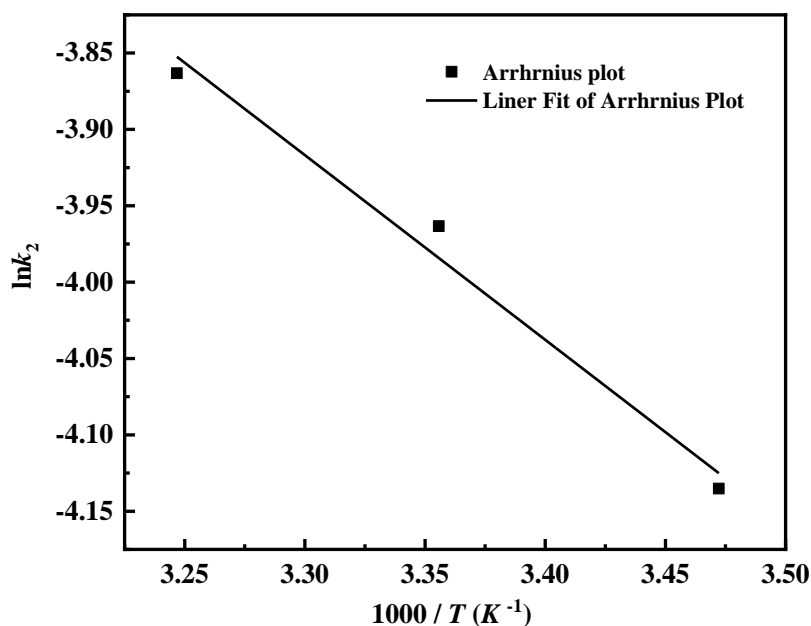
Figure. 4 Arrhenius equation fitting curve of MCS adsorption of Cu^{2+}.

As shown in Fig. 4, the activation energy of Cu^{2+} adsorption on MCS was 10.05 kJ/mol by calculating the slope of the fitting curve. The adsorption type can be judged by the strength of Ea: when 5＜Ea＜50 kJ/mol, it is a physical adsorption process; When 60＜Ea＜ 800 kJ/mol, it is a chemical adsorption process. Therefore, physical adsorption plays a major role in the Cu^{2+} adsorption of MCS.

Table. 3 Adsorption activation energy parameters of MCS adsorption of Cu^{2+}.

Arrhenius equation	R^2	Ea / (kJ·mol^{-1})
$\ln(k_2) = -1209.187\dfrac{1}{T} + 0.073$	0.983	10.1

4. Adsorption isotherm model

Fig. 5 shows the effect of Cu^{2+} initial concentration on adsorption capacity at 288, 298, and 308K, respectively. When the initial concentration of Cu^{2+} is in the range of 10-300 mg/L, the adsorption capacity increases with the increase of the initial concentration of Cu^{2+}, and the higher the temperature, the greater the adsorption capacity. The maximum adsorption capacity was 38.7 mg/g.
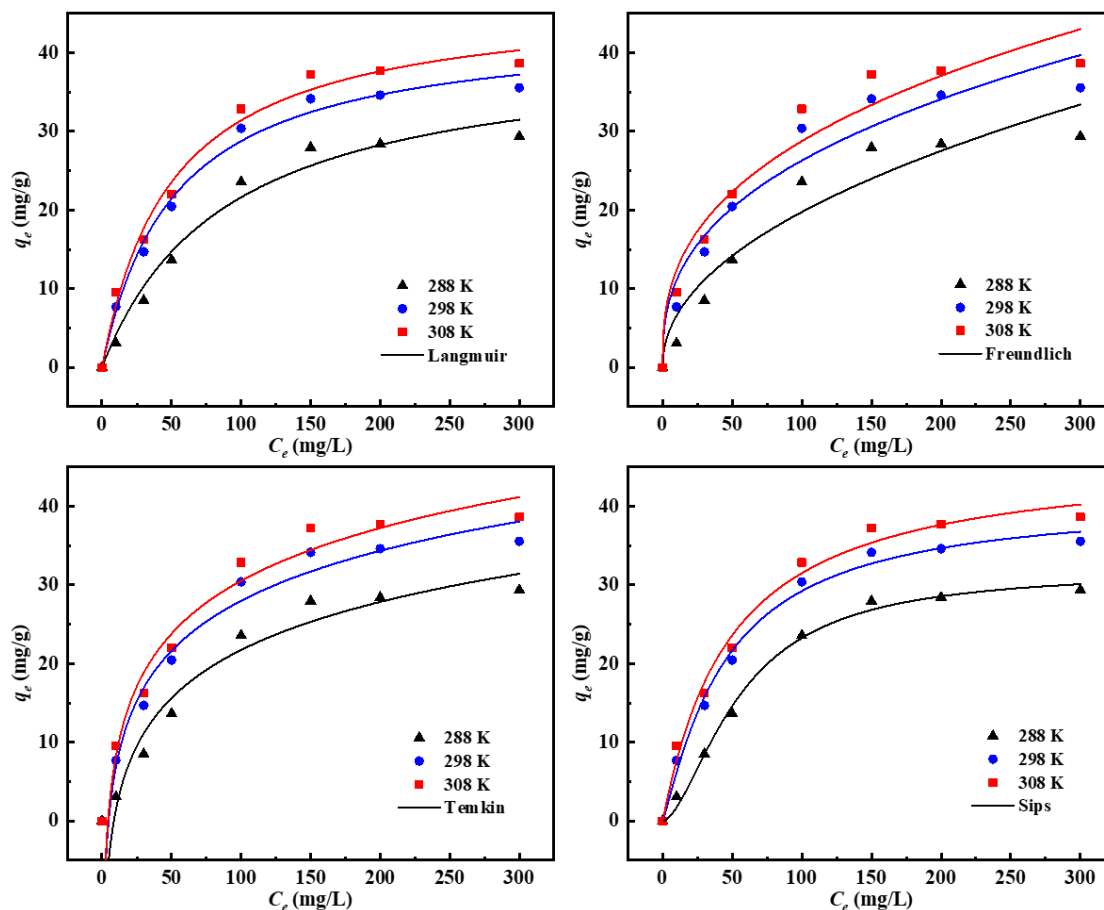
Figure. 5 Adsorption isotherms of Cu^{2+} on MCS at different temperatures.

Langmuir equation:

$$q_e = \frac{q_{max}k_L C_e}{1+k_L C_e} \tag{8}$$

Freundlich equation:

$$q_e = k_F C_e^{1/n} \tag{9}$$

Temkin equation:

$$q_e = A \ln (k_T c_e) \tag{10}$$

Sips equation:

$$q_e = \frac{q_m k_s c_e^{\gamma}}{1+k_s c_e^{\gamma}} \tag{11}$$

Where Ce (mg/L) is the concentration of Cu^{2+} in the solution at equilibrium, k_L (L/mg) is Langmuir adsorption coefficient, k_F (mg/g) and n are Freundlich adsorption isotherm constants, q_e and q_{max} (mg/g) represent the adsorption amount at equilibrium and the predicted maximum adsorption amount, respectively. The fitting curve of the adsorption model is shown in Fig. 5.

Table.4 Adsorption isotherm parameters of Cu^{2+} on MCS at different temperatures.

T	$q_{e,exp}$	Langmuir			Freundlich		
		q_m	k_L	R^2	k_F	$1/n$	R^2
288	29.4	40.8	0.0113	0.981	2.18	0.478	0.934
298	35.6	43.6	0.0194	0.991	4.68	0.375	0.952
308	38.7	47.0	0.0201	0.989	5.34	0.366	0.957

T	$q_{e,exp}$	Temkin			Sips			
		A	k_T	R^2	q_m	k_S	γ	R^2
288	29.4	8.82	0.118	0.972	31.9	1.21×10^{-3}	1.67	0.995
298	35.6	9.17	0.211	0.981	41.0	0.0124	1.15	0.992
308	38.7	9.69	0.234	0.979	46.3	0.0184	1.03	0.989

As shown in Table. 4, the validity of the isotherm model was tested according to the correlation coefficient (R^2). It can be seen that the adsorption process is in good agreement with Sips and Langmuir models, indicating that the adsorption process tends to be monomolecular adsorption and the surface of the adsorbent has a certain uniformity. Based on the experimental data and the fitting results of the three simulations, it can be concluded that the copper adsorption mechanism of MCS is dominated by monomolecular chemisorption, while physical adsorption also plays a key role.

Conclusion

In this work, MCS was fabricated via a chemical cross-linking method. The Cu^{2+} adsorption of the MCS composite was tested as 38.7 mg/g. Kinetics model, adsorption activation energy model, and isotherm model fittings were employed to study the mechanism of Cu^{2+} adsorption. Kinetic model fitting indicates that the Cu^{2+} adsorption of MCS is dominated by chemical adsorption. Diffusion simulation suggests that both the boundary layer diffusion and intra-particle diffusion have an important effect on Cu^{2+} adsorption. Adsorption isotherm fitting indicates that the Cu^{2+} adsorption of MCS could be a monomolecular force. While the Ea value obtained by adsorption activation energy fitting (10.1 kJ/mol) implies that physical adsorption plays an important role in Cu^{2+} adsorption. Combined with the results of the three fittings, it could be concluded that the adsorption process of Cu^{2+} by MCS is a combination of chemical adsorption and physical adsorption.

References

[1] Azimi A, Azari A, Rezakazemi M, et al. Removal of Heavy Metals from Industrial Wastewaters: A Review. ChemBioEng Reviews, 2017, 4(1): 37-59.

[2] Brewer G J. Copper toxicity in Alzheimer's disease: Cognitive loss from ingestion of inorganic copper. Journal of Trace Elements in Medicine and Biology, 2012, 26(2): 89-92.

[3] Lai C L, Lin S H. Electrocoagulation of chemical mechanical polishing (CMP) wastewater from semiconductor fabrication. Chemical Engineering Journal, 2003, 95(1): 205-211.

[4] Lai C L, Lin S H. Treatment of chemical mechanical polishing wastewater by electrocoagulation: system performances and sludge settling characteristics. Chemosphere, 2004, 54(3): 235-242.

[5] Hollingsworth J, Sierra-Alvarez R, Zhou M, et al. Anaerobic biodegradability and methanogenic toxicity of key constituents in copper chemical mechanical planarization effluents of the semiconductor industry. Chemosphere, 2005, 59(9): 1219-1228.

[6] Lin S H, Yang C R. Chemical and physical treatments of chemical mechanical polishing wastewater from semiconductor fabrication. Journal of Hazardous Materials, 2004, 108(1): 103-109.

[7] Zou S-W, How C-W, Chen J P. Photocatalytic Treatment of Wastewater Contaminated with Organic Waste and Copper Ions from the Semiconductor Industry. Industrial & Engineering Chemistry Research, 2007, 46(20): 6566-6571.

[8] Su Y-N, Lin W-S, Hou C-H, et al. Performance of integrated membrane filtration and electrodialysis processes for copper recovery from wafer polishing wastewater. Journal of Water Process Engineering, 2014, 4: 149-158.

[9] Razak M R, Yusof N A, Aris A Z, et al. Phosphoric acid modified kenaf fiber (K-PA) as green adsorbent for the removal of copper (II) ions towards industrial waste water effluents. Reactive and Functional Polymers, 2020, 147: 104466.

[10] Wang S, Wang K, Dai C, et al. Adsorption of Pb2+ on amino-functionalized core–shell magnetic mesoporous SBA-15 silica composite. Chemical Engineering Journal, 2015, 262: 897-903.

[11] Qin L, Feng L, Li C, et al. Amination/oxidization dual-modification of waste ginkgo shells as bio-adsorbents for copper ion removal. Journal of Cleaner Production, 2019, 228: 112-123.

[12] Anbinder P S, Macchi C, Amalvy J, et al. A study of the structural changes in a chitosan matrix produced by the adsorption of copper and chromium ions. Carbohydrate Polymers, 2019, 222: 114987.

[13] Li A, Lin R, Lin C, et al. An environment-friendly and multi-functional absorbent from chitosan for organic pollutants and heavy metal ion. Carbohydrate Polymers, 2016, 148: 272-280.

[14] Kandile N G, Mohamed H M, Mohamed M I. New heterocycle modified chitosan adsorbent for metal ions (II) removal from aqueous systems. International Journal of Biological Macromolecules, 2015, 72: 110-116.

[15] Gamal A, Ibrahim A G, Eliwa E M, et al. Synthesis and characterization of a novel benzothiazole functionalized chitosan and its use for effective adsorption of Cu(II). International Journal of Biological Macromolecules, 2021, 183: 1283-1292.

[16] Li J J, Dan H B, Xie W, et al. Synthesis and phosphorus adsorption of coal-fly-ash magnetic adsorbents. Chinese Journal of Inorganic Chemistry, 2018, 34(8): 1455-1462.

[17] Wu X F, Li J J, Zhu J B, et al. Advances in the resource utilization of fly ash magnetic micro-spheres. Materials Review, 2015, 29(23): 103-107.

Facile synthesis of the SrTiO₃/PANI composites with advanced microwave absorption performance

Yan Wang, Chongmei Wu, Guiyang Xian, Zhaolin Zhu, Yin Liu**

School of Materials Science and Engineering, Anhui University of Science and Technology, Huainan 232001, Anhui, China
**Corresponding authors: yinliu@aust.edu.cn (Yin Liu)

Abstract

In this research, Strontium titanate (SrTiO₃) synthesized by hydrothermal method was used as the core, and polyaniline (PANI) as the shell was prepared by simple in-situ oxidative polymerization route. There are two strong absorption peaks when SrTiO₃/ PANI nanocomposite was composed of SrTiO₃ and PANI with a ratio of 1:2, the maximum reflection loss of −54 dB at 12.8 GHz while the thickness of 1.91 mm, another reflection loss was –48.49 dB at 15.84 GHz with 1.59 mm.

Keywords: Strontium titanate; Polyaniline; Compound; Electromagnetic absorption

Introduction

With the increasingly serious problem of electromagnetic pollution originated from the extensive use of electronic equipment and devices, microwave absorbing materials have drawn considerable interests in the field of electromagnetic absorption[1,2]. In the recent past, composites that are electrically conducting and dielectric have been employed for EMI shielding[3]. Therefore, SrTiO₃/PANI compound materials are expected as a new type of microwave absorber.

Experimental

1. Materials

Strontium nitrate ($Sr(NO_3)_2$), Tetrabutyl titanate ($C_{16}H_{36}O_4Ti$), aniline monomer (C_6H_7N), ammonium persulfate (APS), Ethanol, glycol and sodium hydroxide (NaOH) were supplied by Aladdin Chemical Company. All the chemicals and reagents were used directly without any pretreatment. Deionized water was used for all experiments.

2. Synthesis of SrTiO₃ nanocubes

SrTiO₃ was synthesized by a typical hydrothermal method. The calculated amount of $Sr(NO_3)_2$ (2.1163 g) was dissolved in 20 mL deionized water under constant stirring named A solution, $C_{16}H_{36}O_4Ti$ (3.4032 ml) is dissolved in a solvent with a ratio of ethanol to ethylene glycol of 1:3 and named B solution. Slowly added solution A to solution B with proper stirred, the dissolution of NaOH in the solution made the pH value reach 11~12. The reaction mixture

were transferred to a 100mL autoclave and subjected to hydrothermal treatment at 200℃ for 20 h. The SrTiO₃ nanocubes can be obtained.

3. Preparation of SrTiO₃/ PANI Nanocomposite

SrTiO₃/ PANI binary composites were prepared by using typical in-situ oxidative polymerization. Aniline is the monomer, SrTiO₃ is the dispersed core material, and ammonium persulfate (APS) is the catalyst, while HCl was used as the dopant. Prepared with different wt% of SrTiO₃ (3:10, 5:10, 7:10 with PANI) added to Nanocomposites, Dissolve APS according to stoichiometric ratio in dilute hydrochloric acid, added SrTiO₃ in different proportions under the condition of ice bath and proper stirred, then slowly dropped aniline solution. After reaction for 24 h, a dark green thick liquid was obtained, Washed, filtered and dried[4]. The obtained complexes were named SP1, SP2, SP3.

Results and Discussion

SrTiO₃/ PANI nanocomposite were shown in Fig. 1.The characteristic peaks of SrTiO₃ in accordance with JCPDS Card No. 35-0734.There was a steamed bread peak between 20 and 35 degrees, which represents the existence of PANI. In addition, a little amount of strontium sulfate impurities in the complex[5].
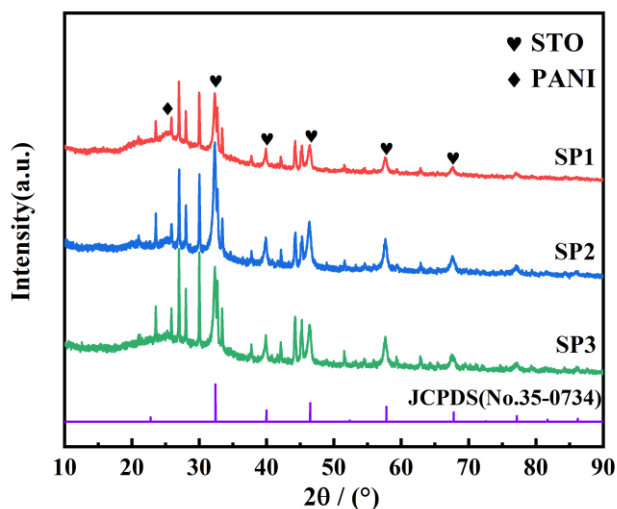
Fig. 1 XRD patterns of SP1, SP2, SP3

Table 1 The microwave absorption performance of the three SrTiO₃/ PANI samples

	SP1	SP2		SP3
Reflection loss(dB)	-57.98	−54	−48.49	-54.6
Thickness(mm)	5.12	1.91	15.84	4.12
Frequency(GHz)	4.49	12.8	1.59	5.28

The strength of the microwave absorption properties of SrTiO₃/ PANI composites is

characterized by the VNA. The reflection loss, frequency and thickness of the three composite samples are shown in Table 1. Fig. 2 shows reflection loss of three samples. It is obliviously that SP1 sample exhibited an optimum RL of -57.98dB at 5.12 GHz with a thickness of 4.49 mm, and SP3 sample has reach -54.6dB at 5.28 GHz with a thickness of 4.12 mm. In comparison, the best performance of microwave absorption was SP2 sample, which has two peaks, the maximum RL was −54 dB at 12.8 GHz and the thickness was 1.91 mm, another was –48.49 dB at 15.84 GHz with 1.59 mm.
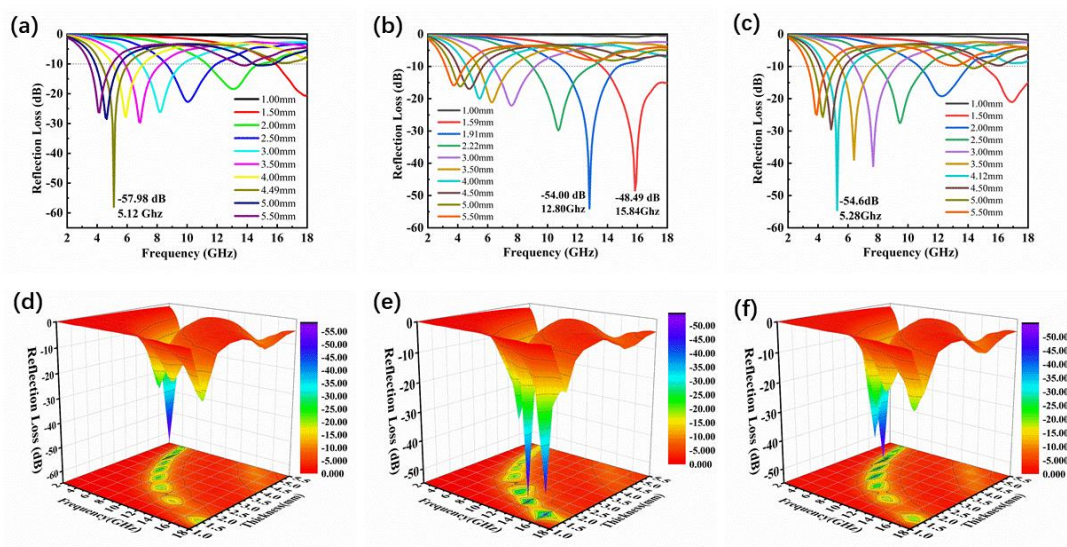
Fig. 2 RL at different thickness: SP1 (a), SP2 (b) and SP3 (c) and 3D reflection loss profiles: SP1 (d), SP2 (e) and SP3 (f)

Conclusions

SrTiO$_3$/ PANI nanocomposites, with strong microwave absorption performances, have been prepared. The SrTiO$_3$ was prepared by using a simple hydrothermal process, while the PANI was synthesized by using in-situ polymerization in ice-bath. Microwave absorption performance of nanocomposites could be optimized by controlling the composition to achieve unique interfaces with enhanced interfacial polarization and polarization relaxation. Specifically, when the ratio of SrTiO$_3$ and PANI was 2:1, the nanocomposite exhibited reflection loss (RL) of −54 dB at 12.8 GHz with a thickness of 1.91 mm and –48.49 dB at 15.84 GHz with 1.59 mm. Therefore, SrTiO$_3$/ PANI nanocomposites could be used as a promising candidate of microwave absorbing materials.

Acknowledgment

References

[1] R. Shu, Y. Wu, Z. Li, J. Zhang, Z. Wan, Y. Liu, M. Zheng, Facile synthesis of cobalt-zinc ferrite microspheres decorated nitrogen-doped multi-walled carbon nanotubes hybrid composites with excellent microwave absorption in the X-band, Compos. Sci. Technol. 184 (2019) 107839.

[2] R. Shu, X. Li, Y. Wu, J. Zhang, Z. Wan, Fabrication of magnesium ferrite microspheres decorated nitrogen-doped reduced graphene oxide hybrid composite toward high-efficiency electromagnetic wave absorption, J. Alloys Compd. 859 (2021) 157865.

[3] P. Sambyal, A.P. Singh, M. Verma, M. Farukh, B.P. Singh, S.K. Dhawan, Tailored polyaniline/barium strontium titanate/expanded graphite multiphase composite for efficient radar absorption, RSC Adv. 4 (2014) 12614–12624.

[4] J. Ma, H. Ren, Z. Liu, J. Zhou, Y. Wang, B. Hu, Y. Liu, L.B. Kong, T. Zhang, Embedded MoS_2-PANI nanocomposites with advanced microwave absorption performance, Compos. Sci. Technol. 198 (2020) 108239.

[5] S. Shahabuddin, A. Numan, M.M. Shahid, R. Khanam, R. Saidur, A.K. Pandey, S. Ramesh, Polyaniline-$SrTiO_3$ nanocube based binary nanocomposite as highly stable electrode material for high performance supercapaterry, Ceram. Int. 45 (2019) 11428–11437.

Development of multi-functional films modified with stearic acid/TiO$_2$ nanoparticles

Yanfen Wang, Yin Liu, Juan Gao, Mengting Li

School of Materials Science and Engineering, Anhui University of Science and Technology, Huainan 232001, PR China

Abstract

A novel multifunctional film was successfully prepared by a simple dip coating approach. The film consisting of TiO$_2$ nanoparticles and stearic acid (SA) exhibited a controlled wettability to water and a good transparency under the visible light. Meanwhile, the coating times had significant effect on the wettability and transmittance of the SA/TiO$_2$ films. Such excellent performance could be contributed to hierarchical micro/nano-sized roughness and low surface energy.

Keywords: stearic acid/TiO$_2$; transparency; wettability; micro/nano-sized roughness

The superhydrophobic surfaces have attracted great attention in scientific research and industrial application because of their excellent water-repellent property. It is well known that artificial superhydrophobic surfaces are mainly obtained by two steps. Firstly, the surfaces with hierarchical micro/nano-sized roughness are created by adopting appropriate means. Subsequently, the low surface energy materials are deposited on the above rough surfaces to attain hydrophobic property. So far, a large number of routes had been designed for the preparation of superhydrophobic surfaces. However, there are still some problems in these routes, including multi-step processes, harsh preparation conditions, high cost of materials. In addition, the low transparency is the key problem to restrain the application of superhydrophobic surfaces. Based on the above considerations, we produced the films surfaces with transparent and superhydrophobic properties by using stearic acid (SA) and TiO$_2$ nanoparticles based on a simple coating process. The structure, optical property and wettability of the surface were examined. Scheme 1 shows preparation diagram of SA/TiO$_2$ films.
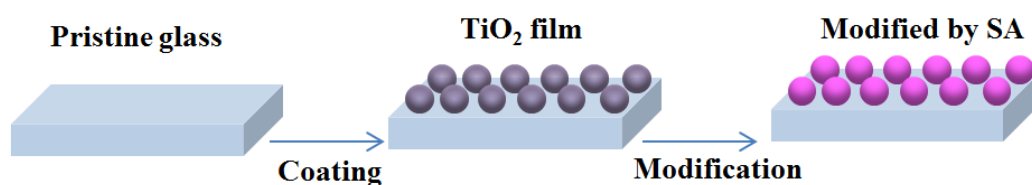
Scheme 1 Preparation diagram of SA/TiO$_2$ films on the glasses

Fig. 1 shows fourier-transform infrared (FT-IR) spectra of TiO$_2$ and SA/TiO$_2$ surface. It is found that the two absorption peaks at the wavelength of 2900 and 2800 cm^{-1} correspond to the antisymmetric and symmetric stretching vibrations of methyl and methylene, respectively.

After the chemical modification of SA, two new absorption peaks appear at the wavelengths of 1750 and 1600 cm^{-1}, which can be attributed to the stretching vibration of carboxyl group. The results indicate that stearic acid has been successfully modified on the surface of TiO$_2$ coating.
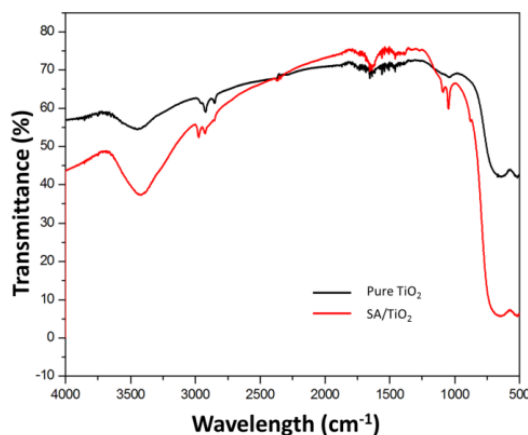
Fig. 1 FT-IR spectra of TiO$_2$ and SA/TiO$_2$ films

The wettability of the as-prepared films is investigated by the water contact angle (CA) on the surface. Static photos with water droplets with different coating times are shown in Fig. 3. The hydrophilic nature of TiO$_2$ nanoparticles is observed, and CA is measured to be 43°. However, the wettability of surfaces is markedly changed after the modification with SA. The SA/TiO$_2$ films with different coating times from 1, 3, 5 and 7 times are 75°, 101°, 119°and 149°, respectively. Water CA depends heavily upon coating times of TiO$_2$ in the coating, which is due to that the surface roughness gradually increases with the increasing coating times. When the coating cycle is 7, CA of the film reaches a maximum, showing an excellent superhydrophobic property.
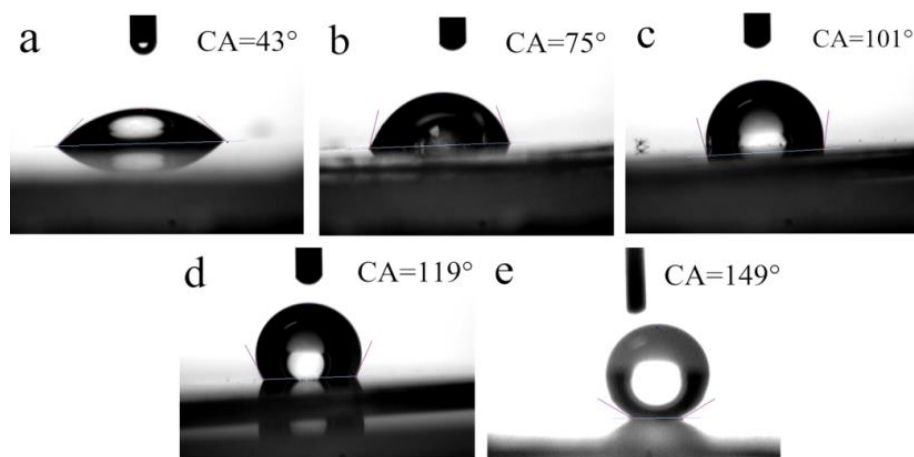
Fig. 2 Satic photos with water droplets on the films: (a) TiO$_2$, (b) SA/TiO$_2$-1, (c) SA/TiO$_2$-3, (d) SA/TiO$_2$-5, (e) SA/TiO$_2$-7

Fig. 3 shows the surface morphology of glass with 7-cycles TiO_2 coating. The glass substrate is covered by the ordered and uniform TiO_2 nanoparticles, and the size of these particles are about 200-500 nm. Interestingly, such a structure creates a fascinating micro/nanoscale hierarchical roughness, which is beneficial for obtaining remarkable superhydrophobicity.
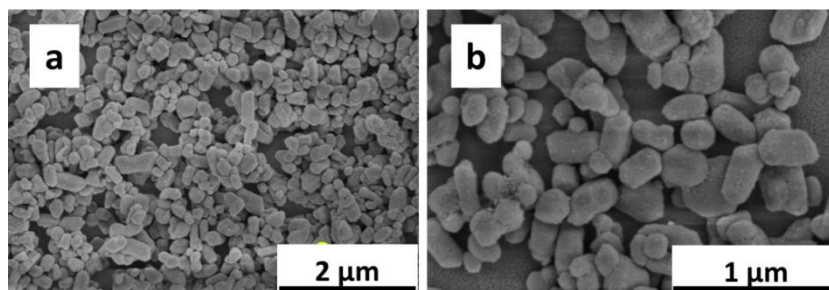
Fig. 3 SEM images of glass with 7-cycles TiO_2 coating.

Fig. 4 displays the transmittance of SA/TiO_2 on glasses. It is found that the coated glasses maintain their optically transparency under the visible light. The transmittance of the glass decreases with increasing coating times. In the curve of superhydrophobic glass impregnated for 7 times, the transmittance is between 40 % and 50 %, showing a good transparency.
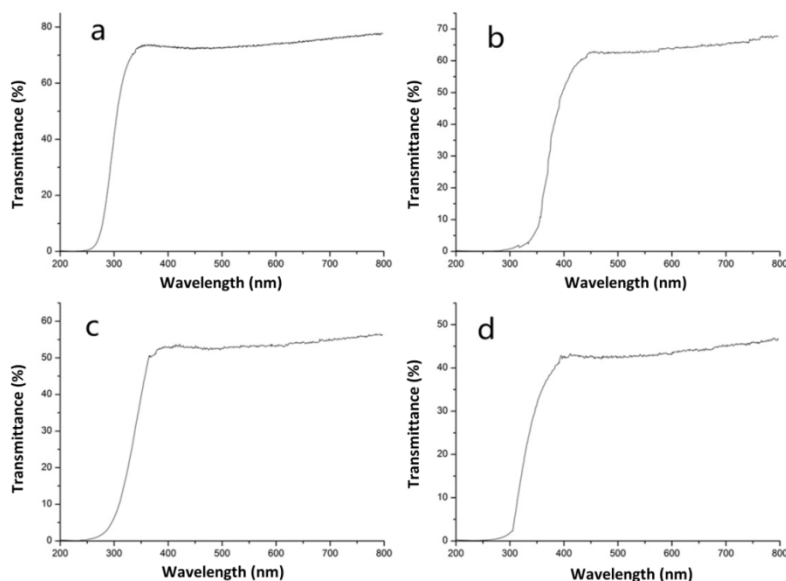
Fig. 4 The transmittance of SA/TiO_2 glasses with different coating times: (a) 1, (b) 3, (c) 5, (d) 7.

In this study, we successfully fabricated a multifunctional film with transparent and superhydrophobic surface by a simple dip coating approach. The film consisting of TiO_2 nanoparticles and SA exhibited a controlled wettability to water and a good transparency under the visible light. Such excellent performance can be contributed to hierarchical micro/nano-sized roughness and low surface energy.

Acknowledgements

References

[1] H.M. Kim, J.W. Choi, J.S. Kwon, et al., J. Nanosci. Nanotechno. 19 (2019) 6452-6457.
[2] Y.F. Wang, Y. Liu, L. Zhang, et al., Appl. Surf. Sci. 496 (2019) 143743.

Coal-based carbon /FeCo composites with excellent microwave absorption performance were prepared from anthracite

Yang Fan, Jingyu Wang, Ximing Zhang, Yin Liu∗

School of Materials Science and Engineering, Anhui University of Science and Technology, Huainan 232001, Anhui, China
∗Corresponding authors: yinliu@aust.edu.cn (Yin Liu)

Abstract

In this study, coal-based carbon/FeCo (CBC/FeCo) magnetic composites were prepared. The CBC/FeCo composites exhibit strong electromagnetic (EM) wave absorption, with minimum reflection loss (RL_{min}) of -60.81 and -49.82 dB at thicknesses of 1.38 and 2.45 mm, respectively. In addition, the effects of activation temperature and the content of FeCO on EM absorption performance of the composites also studied. Specifically, the sample of S-2 EM absorption performance optimized. We believed that the CBC/FeCo composites could be promising candidate for EM absorbers.

Keywords: Coal-based carbon; FeCo alloy; Layered stripes; EM wave absorption

Introduction

Coal is one of the most widely used carbon materials in the world. When coal used as energy, carbon dioxide and other toxic and harmful gases will be produced in the combustion process, resulting in the greenhouse effect. Therefore, efficient and clean use of coal to reduce greenhouse gas emissions and toxic gas emissions is one of the hot spots of carbon materials research. However, there are relatively few studies on the preparation of microwave absorption materials from various types of coal.[1, 2]

Experimental

Anthracite of 0.5 g with particle sizes of 0.20-0.40 mm were washed and dried. Then, mixing with different contents of FeCo, followed by the addition of 10 ml of deionized water. On the other hand, 1 g of KOH added to the mixtures. The mixtures dried in a vacuum oven at 80 °C. The dried samples heated to 800 °C in a tubular furnace under N_2 atmosphere and calcined at this temperature for 2 h. The samples magnetically separated and throughly washed with deionized water and absolute ethanol for five times to remove the free ions and residues. Finally, the samples dried in a vacuum oven at 80 °C for 12 h to obtain the CBC/FeCo composites.

Results and Discussion

Fig. 1 (a) shows XRD patterns of the CBC/FeCo composites. Three diffraction peaks at 44.87°, 65.31° and 82.74°, corresponding to the (110), (200) and (211) crystal planes of FeCo.[3, 4]
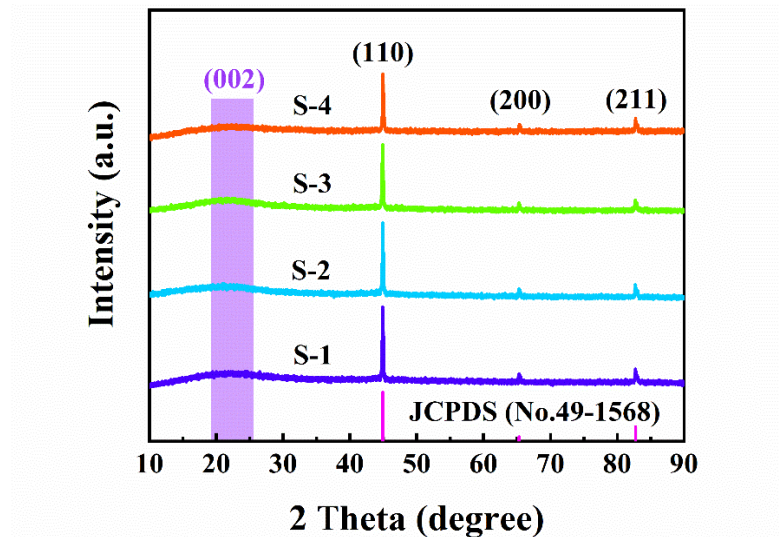
Fig. 1. XRD patterns of the CBC/FeCo composites

Fig. 2 shows SEM images of the S-2. As shown in Fig. 2, obvious layered stripes are observed in the CBC/FeCo samples. The surface loaded with magnetic particles.
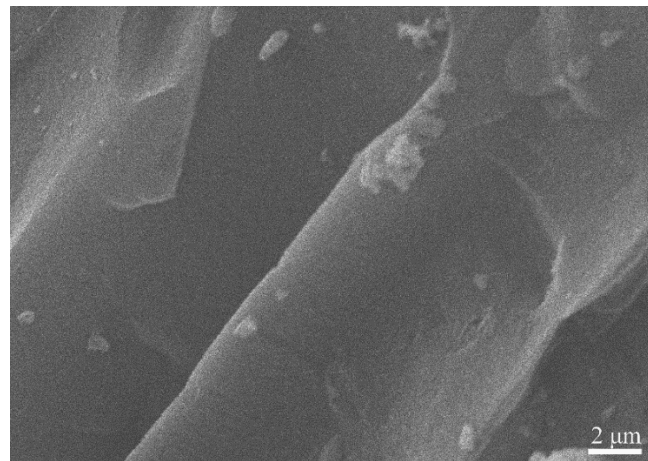
Fig. 2. SEM images of the S-2 with layered stripes structure.

Fig. 3 shows two-dimensional EM absorption curves of the CBC/FeCo composites. EM absorption properties can be reflected by the curves of the reflection loss. The sample exhibits optimum EM absorption performance, with an EAB of 3.12 GHz, the RL_{min} of -60.81 dB at 16.80 GHz and a thickness of 1.38 mm.
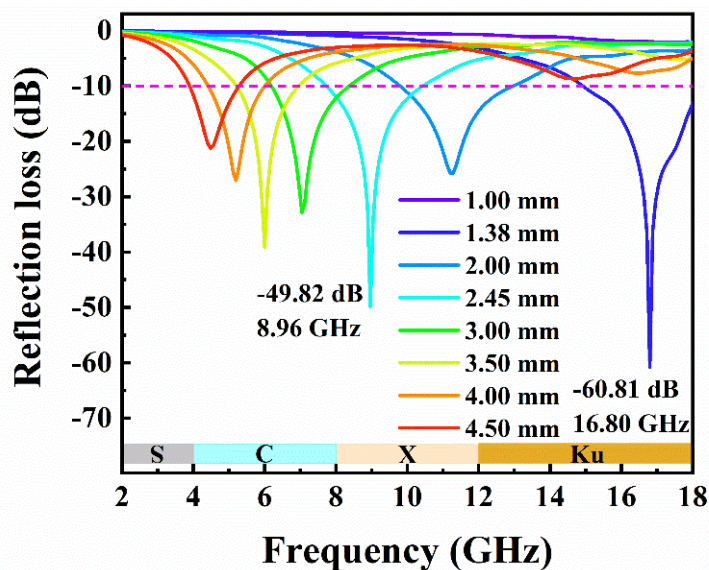
Fig. 3. Reflection loss curves of the sample of S-2.

Conclusions

In summary, CBC/FeCo magnetic composites derived from FeCo alloy and coal-based carbon exhibited excellent EM absorption performances. The EM absorption performance optimized by adjusting the mass loading of FeCo and processing temperature. Specifically, the sample with 0.3 g FeCo alloy after processing at 800 ℃ had an effective abroad bandwidth (EBA) of 3.12 GHz (14.88-18 GHz), as the thickness was only 1.38 mm. Our novel composites could be promising candidates for high performance EM absorption applications.

Acknowledgements

References

[1]   Dmitrienko MA, Strizhak PA. Environmentally and economically efficient utilization of coal processing waste. Science of the Total Environment 2017;598:21-7.

[2]   Mohanty A, Chakladar S, Mallick S, Chakravarty S. Structural characterization of coking component of an Indian coking coal. Fuel 2019;249:411-7.

[3]   Kuo H-C, Liu S-H, Lin Y-G, Chiang C-L, Tsang DCW. Synthesis of FeCo-N@N-doped carbon oxygen reduction catalysts via microwave-assisted ammoxidation. Catalysis Science & Technology 2020;10(12):3949-58.

[4]   Xiong Y, Xu L, Yang C, Sun Q, Xu X. Implanting FeCo/C nanocages with tunable electromagnetic parameters in anisotropic wood carbon aerogels for efficient microwave absorption. Journal of Materials Chemistry A 2020;8(36):18863-71.

A novel ZIF-derived Fe,Co@N–C bifunctional oxygen electrocatalysts for rechargeable liquid/solid Zn-air batteries

Yanyan Zhang, Yang Li*, Kejian Shi, Wenhan Zhou

School of Mechanics and Optoelectronic Physics, Anhui University of Science and Technology, Huainan 232001, P. R. China

Abstract

In view of the practical application of non-noble metal catalysts in industrial production, it is urgent for ZAB to design dual-function electrocatalysts with excellent performance, low price and simple production steps. This paper proposes a novel Fe Co, Zn-Coordinated zeolitic imidazolate framework (FeCo-ZIF), which requires no additional carbon source and reduces environmental pollution. The flake fluffy structure formed after pyrolysis enhanced the dispersion of metal particles. Compared with industrial Pt/C (half-wave potential of 0.837V) and RuO2 (over potential), the newly prepared FeCo N C-900 has better ORR (half-wave potential of 0.858V) and OER (overpotential of 370 mV at 10 mA cm^{-2}) properties because the combination of Fe and Co is favorable for double power characteristic energy. Using FeCo N C-900 as an air cathode, liquid and solid ZABs were prepared. Experimental results show that the liquid ZABs have higher peak power density (91 mW cm^{-2}) and better cycle stability than commercial Pt/C + RuO$_2$. The open circuit potential of rechargeable liquid and flexible solid ZABs reached 1.447V and 1.406V respectively. This simple synthesis strategy will provide a new idea for the preparation of bifunctional catalysts with energy storage and conversion applications.

* To whom correspondence should be addressed. Email: liyang800904@163.com; Post address: School of Mechanics and Optoelectronic Physics, Anhui University of Science and Technology, Huainan 232001, P.R.China.
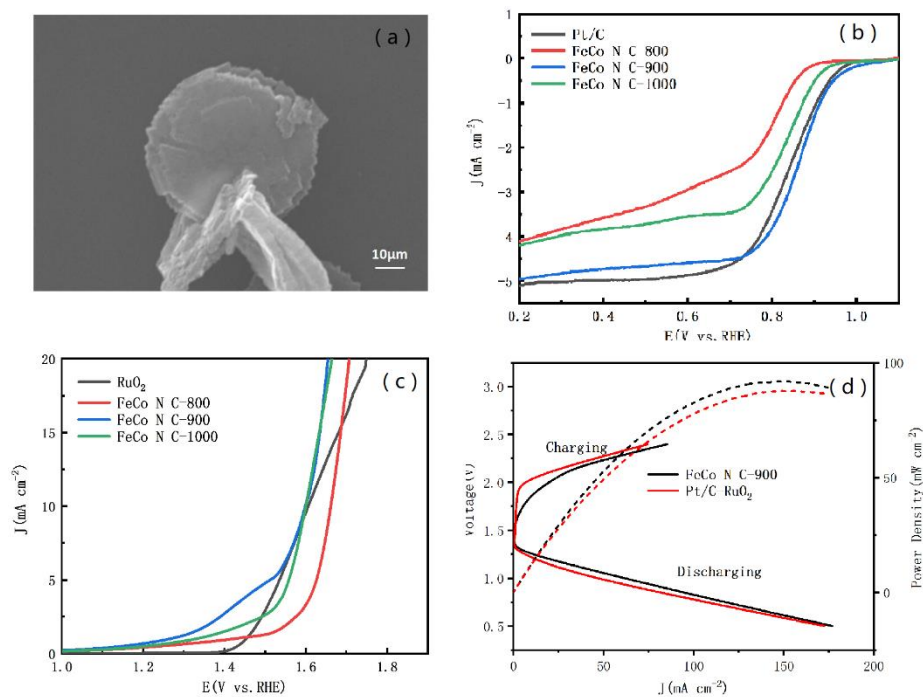
Figure 1 a) SEM images for FeCo N C-900. (b) LSV for the ORR curves of FeCo N C-1000, FeCo N C-900, FeCo N C-800, 20% Pt/C at 1600 rpm.c) LSV for the OER curves of FeCo N C-1000, FeCo N C-900, FeCo N C-800, RuO$_2$ in 1 M KOH solution.d) Discharging-charging and power density polarization curves of commercial Pt/C-RuO$_2$ and FeCo N C-900.

Colymerization of Styrene and Norbornene Using Pyrazolylimine Nickel (II) /Methylaluminoxane (MAO) Catalytic System

WANG Yuan-yuan, GAO Jun-shan

School of Material science and engineering, Anhui University of Science and Technology, Anhui, Huainan, 232001

Abstract

The copolymerization of styrene and norbornene with pyrazolylimine nickel complex: 2, 6-diisopropyl-N-(phenyl-1-3, 5-dimethylpyrazolylmethylene) phenylimine nickel dibromide (complex **1**) in the presence of methylaluminoxane (MAO) was studied. Complex 1/MAO show high catalytic activities towards the copolymerization of styrene and norbornene, up to the magnitude of 10^5g polymer/(mol Ni·h). The NMR results indicated that the chain of copolymers were consisted of short polystyrene segments or styrene units and long polynorbornene segments.

Key words: Pyrazolylimine nickel complexes, Norbornene, Styrene, Copolymeriation

Introduction

Polystyrene is one of the most widely used general polymer materials, with good hardness, transparency and processing properties. As early as in the 1960s, Natta et al. catalyzed styrene to isotactic polystyrene (*i*-PS) with Ziegler-Natta catalyst (TiCl4-AlR3) [1]. Since 1980s, Ishihara et al. catalyzed styrene polymerization with metallocene /MAO system to obtain syndiotactic (*s*-PS) with high melting point, high crystallinity and high intermetric [2-4]. In recent years, the polymerization of styrene catalyzed with late-transition metal catalytic systems has attracted extensive attention. In general, atctic polystyrene (*a*-PS) with narrow molecular weight distribution was obtained using late-transition metal catalysts [5-7]. Recently, the vinyl polymerization of norbornene has been considerably attracted because of the vinyl-typepolynorbornene having unique physical properties, such as high glass transition temperature, optical transparency and low birefringence [8].

In this paper, pyrazolylimide nickel (Figure 1) was used as a late-transition metal catalyst to study the copolymerization of styrene and norbornene in the presence of methylaluminoxane (MAO), and the microstructure of polystyrene was characterized.
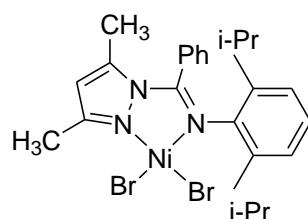
Figure 1 The structure of complex **1**

Experimental

In a typical procedure, the appropriate MAO solid was added into a 50 ml flask, and then freshly distilled toluene was added *via* syringe. Styrene, norbornene and precursor catalyst solution in toluene (2 mmol/L) was injected into the well-stirred solution in order, and the total reaction volume was remained at 20 ml. The polymerization was carried out for the desired time and then quenched with concentrated HCl in ethanol (HCl/ethanol, 5:95, v/v). The resulting precipitated polymer was collected, filtered, and washed with ethanol for several times, and then dried in vacuum at 50 °C to a constant weight.

Results and Discussion

Effect of monomer feed ratio on copolymerization

In the experiments, the total concentration of fixed styrene and norbornene remained the value of $3.0\,mol \cdot L^{-1}$. Different norbornene/styrene copolymers were synthesized by adjusting the feeding ratio of the two monomers. With the consideration of homopolymerization conditions of the two monomers, the copolymerization temperature was 40°C, the Al/Ni ratio value was 600, the catalyst concentration was $2.5 \times 10^{-4}\,mol \cdot L^{-1}$ and the reaction time was 1 hour. The compolymerization results were showed in Table 1. The results indicated that the addition of a small amount of the other monomer would greatly reduce the copolymerization activity, compared with the homopolymerization of the two monomers. For example, For example, the copolymerization activity decreased from 9.25×10^{5}g PS/(mol Ni·h) to 1.56×10^{5}g copolymer /(mol Ni·h) when the feed ratio of norbornene and styrene is 80/20; the copolymerization activity decreased from 6.07×10^{5}g PNBE/(mol Ni·h) to 3.24×10^{5}g copolymer /(mol Ni·h) with norbornene homopolymerization when the feed ratio of norbornene and styrene is 80/20.

Table 1 Influence of various monomer ratios on copolymerization of styrene and norbornene with complex **1**/MAO catalytic system[a]

Entry	Feeding ratio (mol%)		Activity[b]	Insoluble in CHCl$_3$	Soluble in acetone	Insoluble in acetone	St in copolymer
	St	NBE		Wt%	Wt%	Wt%	(mol%)
1	100	0	9.25	0	100	-	-
2	80	20	1.56	0	38.0	62.0	20.2
3	60	40	2.04	0.8	24.0	75.2	9.8
4	40	60	2.76	1.2	22.4	76.4	5.6
5	20	80	3.24	1.8	24.6	73.6	1.8
6	0	100	6.07	100	0	-	-

a) Polymerization condition: solvent: toluene; [Ni]=2.5×10^{-4}mol·L^{-1}; [NBE]+[St]=3.0mol·L^{-1}; Tp=40°C; Al/Ni=600; tp=1h. In units of 10^{5}g polymer/(mol Ni·h).

As can be seen in Table 1, the copolymerization reaction products were separated by continuous extraction of boiling chloroform and boiling acetone, and the insoluble fraction of boiling acetone was more than 60%. Polynorbornene and polystyrene synthesized with the same catalyst were extracted from boiling chloroform and boiling acetone. It was found that polynorbornene was insoluble in boiling chloroform while polystyrene was completely soluble in boiling acetone according to the extraction experiments. Therefore, it can be inferred that the copolymerization reaction products were separated by continuous extraction of boiling chloroform and boiling acetone, and the products of boiling chloroform soluble and boiling acetone insoluble were pure norbornene/styrene copolymer.

Nuclear magnetic resonance (NMR) study of copolymers

^{1}H NMR

Figure 2 showed the ^{1}H NMR spectra of the copolymers obtained by the complex 1/MAO catalytic system at different feed ratios. It can be divided into two regions: one is the aliphatic hydrogen region (0.8~2.5 *ppm*), which are the hydrogen signals of CH_2 and CH of norbornene unit and CH_2 and CHPh of styrene unit; another one is hydrogen region of the aromatic ring, which are the hydrogen signals on the benzene ring. The proportion of styrene chains in copolymers can be calculated, according to the integral area ratio of aliphatic hydrogen and aromatic hydrogen. From ^{1}H NMR of styrene homopolymer, the aromatic ring region is mainly composed of two peaks, that is, 7.2 *ppm* is the meta-position and para-position hydrogens of benzene ring, and 6.5 *ppm* is the ortho-position hydrogen of benzene ring. According to ^{1}H NMR of copolymers, only one resonance peak appeared at about 7.1 *ppm*, when the ratio of styrene to norbornene was less than 80/20, indicating that the chain link of styrene in copolymer was very short, no more than 4 units.
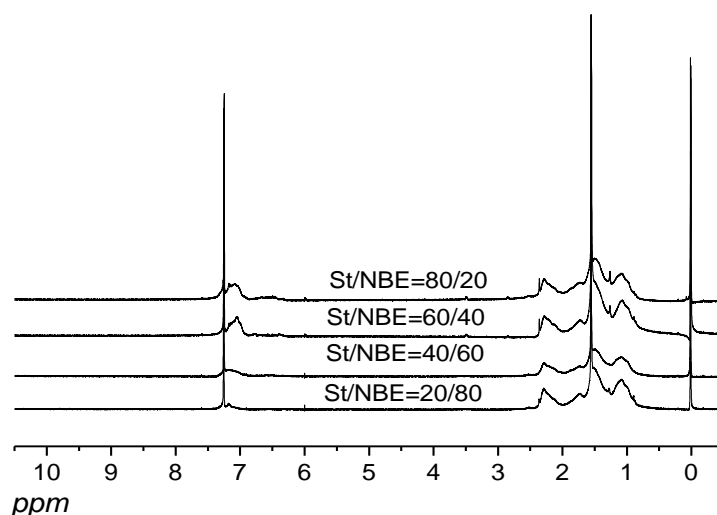
Figure 2 ^{1}H NMR spectra of styrene and norbornene copolymers

3.2.2 ^{13}C NMR

Figure 3 was the ^{13}C NMR spectrum of styrene/norbornene copolymer (Entry 4 in Table 1), which can be divided into two regions: aliphatic carbon region (20-60 *ppm*) and aromatic carbon region (110-150 *ppm*). The specific attribution of each peak were given in Table 2.
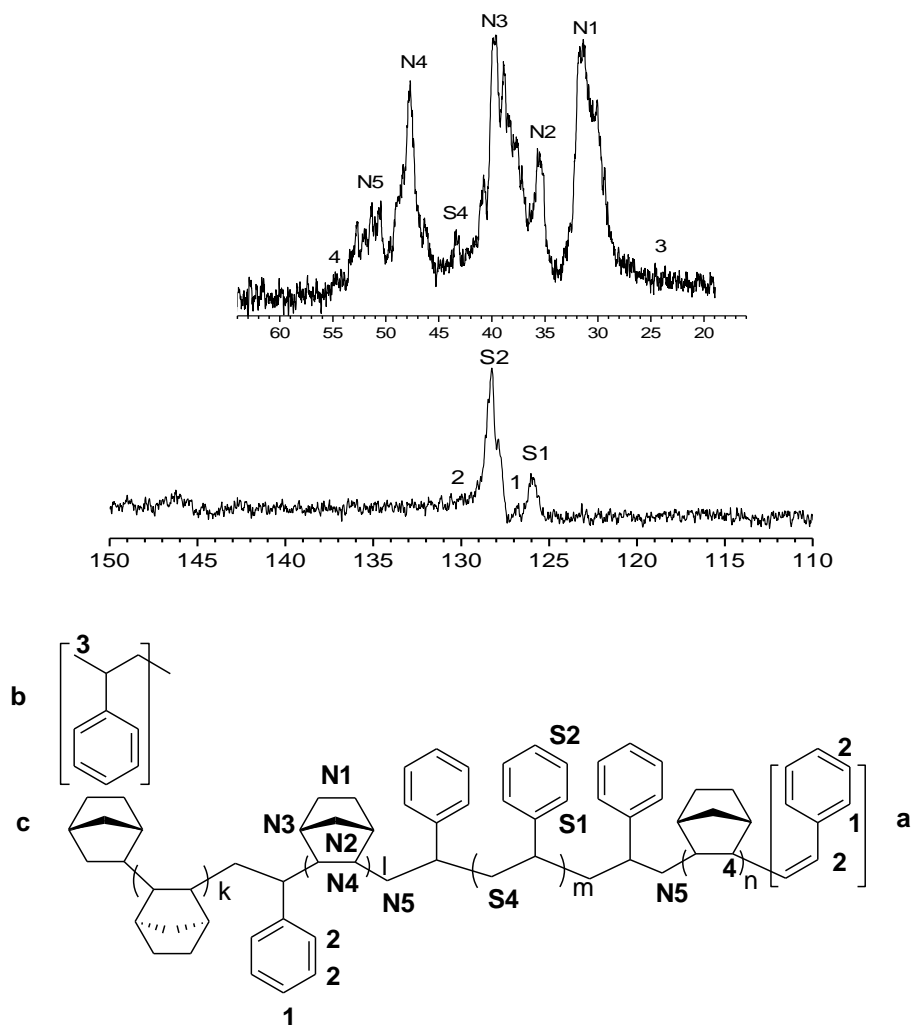
Figure 3 ^{13}C NMR spectrum of styrene/norbornene copolymer (Entry 4 in Table 1)

In the aromatic region, there are two strong vibration peaks S1 (125.9~126.2 *ppm*) and S2 (128.0~128.2 *ppm*), which are respectively assigned to the ortho, meta, and para carbon of the benzene ring on the styrene chain. Peak 2 is the signal of the ortho carbon of the isolated, short styrene chain or chain end of benzene ring.

In the aliphatic carbon region, there is a small peak 3 in the high field, which is considered to the end methyl group obtained by 2, 1 insertion of styrene to initiate polymerization. However, none of the end-group signals generated by the polymerization initiated by styrene 1, 2 insertion were detected. The end-group signals generated during norbornene initiation are overlapped in formant N1.

Table 2 The assignment of ^{13}C NMR spectrum of styrene/norbornene copolymer

Peak	Chemical shifts (*ppm*)	Assignments
		aromatic regions
S1	125.9~126.2	ortho, meta carbon of benzene ring
S2	128.0~128.2	para carbon of benzene ring
1	126.9	ortho carbon atoms of benzene ring of chain end group or para carbons of isolated or very short styrene sequence.
2	130.0	meta carbon atoms of benzene ring of chain end group or doubt bond carbon, -CH$_2$=CHPh, **a** or ortho and meta carbons of isolated or very short styrene sequence.
S3	144.0~150.5	C-1 of benzene ring of long styrene sequence
		aliphatic regions
3	24.4	methyl carbon (CH$_3$CHPh-)
4	54.9	methine carbons of styrene at joints between styrene and norbornene
S4	43.3	methylene carbons of long styrene sequence
N1, N2, N3, N4		C1-C7 signal of norbornene sequence

According to the above analysis results, it can be concluded that the molecular chain of the target copolymer is composed of short polystyrene segments or styrene units and long polynorbornene segments.

Conclusion

The copolymerization of norbornene and styrene was catalyzed by 1/MAO system. The effects of feed ratios of different monomers on the copolymerization activity and copolymer composition were studied, and the copolymer structures were characterized .The results showed that the pyrazolimide nickel catalyst was active for norbornene/styrene copolymerization, whereas the catalytic activity of copolymerization was much lower than that of homopolymerization. The NMR results indicated that the chain of copolymers were consisted of short polystyrene segments or styrene units and long polynorbornene segments.

References

[1] Natta G, Pino P, Mantica E, Danusso F, Mazzanti G, Peraldo M. Stereospecific polymerizat ion of α-olefins. *Chim. Ind.* 1956, 38**,** 124-127.

[2] Ishihara N, Seimiya T, Kuramoto M, et al. Crystalline syndiotactic polystyrene. Macromolecules, 1986, 19: 2464-2465

[3] Pó R, Cardi N. Synthesis of syndiotactic polystyrene: Reaction mechanisms and catalysis. Progress in Polymer Science*,* 1996, 21(1)**:** 47-88.

[4] Wang Y Y, Li B X, Zhu F M, et al. Polymerization of Styrene Using Pyrazolylimine Nickel (II)/Methylaluminoxane Catalytic Systems. Journal of Applied Polymer Science, 2012, 125: 121-125.

[5] Jimenez-Tenorio M, Puert M C, Salcedo I, et al. Cationic Nickel Complexes Containing Bulky Phosphine Ligands: Catalyst Precursors for Styrene Polymerization. Organometallics, 2004, 23: 3139-3146.

[6] Crossetti G L, Bormioli C, Ripa A, et al. Polymerization of styrene to isotactic polymer with MAO-Ni(acac)$_2$. Examination of the factors that influence activity and stereospecificity. Macromol Rapid Commun*,* 1997, 18(9)**:** 801-808.

[7] Pó R, Cardi N, Santi R, et al. Polymerization of styrene with nickel complex/methylalumino- xane catalytic systems. Journal of Polymer Science A: Polymer Chemistry, 1998, 36 (12): 2119-2126

[8] Grove N R, Kohl P A, Allen S A B, Jayaraman S, et al. Functionalized polynorbornene dielectric polymers: Adhesion and mechanical properties. Journal of Polymer Science B : Polymer Physics, 1999, 37 (21): 3003-3010.

Study on surface modification of hollow glass microspheres

Zhaolin Zhu, Guiyang Xian,Chongmei Wu, Yan Wang, Yin Liu. *

School of Materials Science and Engineering, Anhui University of Science and Technology,
Huainan 232001, Anhui, China
*Corresponding authors: yinliu@aust.edu.cn (Yin Liu)

Abstract

In this paper, the surface modification of hollow glass microspheres is introduced. Different surface modifiers are used to modify the hollow glass microspheres to achieve different purposes and improve the scope of application. Four modifiers are mainly used, which are sodium stearate, titanate coupling agent, γ -aminopropyl triethoxysilane(KH550) and cerium nitrate.

Keywords: surface modification; hollow glass microspheres; sodium stearate; titanate coupling agent

Introduction

Hollow glass microspheres are tiny spherical powder containing inert gas and external rigid glass layer. This structure gives it many unique properties, such as light weight, low thermal conductivity, high compressive strength. Because of its unique hollow structure, it has a larger specific surface area, which ensures good dispersion performance in composite materials[1]. If want to fill hollow glass beads into polymer materials, it is necessary to modify their surface, change their original polarity, can be better used as filler, for dispersion. In the study by Yung et al[2], using the silane coupling agent KH-560, the dosage is 5% of hollow glass microspheres, the modified hollow glass microspheres is added to the epoxy resin, forming and curing to obtain the final sample; in the study by Ozmen et al[3], hollow glass microspheres were silanized, activated by silane coupling agent, and finally dried; S.N.Patanker et al[4], the properties of hollow glass microspheres in polyethylene were studied. They chose to graft maleic anhydride with polyethylene, that is, to modify the hollow glass microspheres with maleic anhydride to enhance the compatibility of hollow glass microspheres and polyethylene.

In this work, in order to adapt the hollow glass microspheres to different polymer matrix, a variety of surface modifiers were used to modify the surface of hollow glass microspheres, and the influence of different modifiers on the modification of hollow glass microspheres was studied.

Experiment

Hollow glass microspheres were washed with ethanol and dried at 75°C for 2h in a vacuum, then, hollow glass microspheres were added to 100 milliliter sodium hydroxide solution (0.5mol/L) and stirred at 60°C for 1.5h to form hydroxyl groups on the surface of hollow glass microspheres. Hollow glass microspheres were washed and filtered with water for three times and dried at 80°C for 12h, choosing different surface modifiers: γ-aminopropyl triethoxysilane(KH-550)、sodium stearate, cerium nitrate hexahydrate, CS-201 titanate coupling agent, Kh-550 and titanate coupling agent were hydrolyzed in water for 5min, then hollow glass microspheres eroded by sodium hydroxide were added, and the solution was heated to 80°C and stirred for 2h. Sodium stearate and cerium nitrate hexahydrate are prepared in dilute solution, then hollow glass microspheres are added, heated and stirred, and finally filtered and dried to obtain the final sample.

Results and Discussion
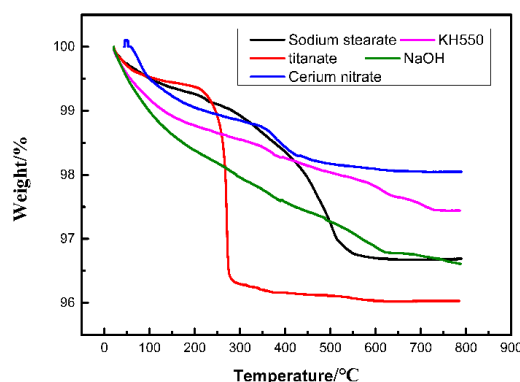
Figure 1 Thermogravimetric curves of hollow glass beads modified with different modifiers

As shown in Figure 1, is the thermogravimetric analysis curve of hollow glass microspheres modified by different modifiers in nitrogen. All hollow glass microspheres were eroded by NaOH before modification, and a large number of hydroxyl groups were formed on the surface of hollow glass microspheres. After being eroded by NaOH, the quality of hollow glass microspheres did not change at higher than 600°C. After modification with sodium stearate, most of the water evaporated at 100°C, and the mass of the hollow glass microspheres changed obviously at 350°C, The boiling point of sodium stearate is about 360°C. With the increase of temperature, sodium stearate attached to the surface of HGM is gradually decomposed and evaporated, resulting in lighter weight. Titanate starts to decompose at about 250°C, which is why the mass drops so quickly.

Conclusions

Hollow glass beads show different properties after surface treatment with different modifiers. The mass of the hollow glass beads treated by NaOH does not change after 630℃, and the loss of burning is about 3%. After KH-550 treatment, the mass does not change after 700℃, and the loss of burning is about 2%. After modification with cerium nitrate, the quality changes slightly after 450℃, indicating that the modification effect is good.

Acknowledgments

References

[1] Li, R., Wang, P., Zhang, P., Fan, G., Wang, G., Ouyang, X., Ma, N., & Wei, H. (2020). Surface modification of hollow glass microsphere and its marine-adaptive composites with epoxy resin. Advanced Composites Letters, 29.

[2] Yung, K., Zhu, B., Yue, T., & Xie, C. (2009). Preparation and properties of hollow glass microsphere-filled epoxy-matrix composites. Composites Science and Technology, 69, 260-264.

[3] Ozmen, M., Can, K., Akın, I., Arslan, G., Tor, A., Çengeloğlu, Y., & Ersoz, M. (2009). Surface modification of glass beads with glutaraldehyde: characterization and their adsorption property for metal ions. Journal of hazardous materials, 171 1-3, 594-600.

[4] Patankar, S., & Kranov, Y. (2010). Hollow glass microsphere HDPE composites for low energy sustainability. Materials Science and Engineering A-structural Materials Properties Microstructure and Processing, 527, 1361-1366.

Preparation and properties of high temperature resistant materials from sanitary porcelain waste

Zhenfei Lv, Yuena Jiang, Xihu Li, Zhenying Liu, Xiulin Shen*

School of Materials Science and Engineering, Anhui University of Science and Technology, Huainan, Anhui, 232001, PR China.
* Corresponding author, E-mail: xlshen@aust.edu.cn

Abstract

In this experiment, waste sanitary ware based high temperature resistant materials were prepared by high temperature sintering with sanitary ware waste, kaolin and white corundum as the main component, and water glass as binder. The effects of raw material ratio on phase composition, micro morphology, densification and mechanical properties were studied by means of XRD (X-ray diffraction analysis), SEM (scanning electron microscope), bulk density, apparent porosity and normal temperature compressive strength. It is found that the main components in the sintered samples are mullite, α-SiO_2 and α-Al_2O_3. The density of green body can be increased by changing the content of white corundum as a result of its phase composition and granularity.

Keywords: sanitary ware waste; high temperature resistant materials; solid state sintering; resource utilization

Introduction

Since ancient times, ceramics are important daily products in China. There are many kinds of ceramics every day. The ceramic manufacturing industry seems to have become one of the mainstays of China's industrial manufacturing industry [1-3]. However, due to the increase of sanitary ceramics output, a large number of waste ceramics have been produced in the process of sanitary ceramics [4]. These wastes not only occupy a lot of space resources and cause a waste of resources, but also cause air, water and ground pollution. Therefore, rational utilization of ceramic waste has caught more and more researchers' interests [5-7].

For the utilization of ceramic waste, there are many utilization directions, such as architectural ceramics, porous ceramics, decorative materials, concrete materials and so on [8-11]. This paper mainly discusses the phase, microstructure and performance analysis of and white corundum with different mass fractions after heat treatment at 1250-1350 °C, where different mesh sanitary porcelain waste and kaolin were used as raw materials, and water glass as binder.

The sintered samples are tested to characterize their various properties. The experimental results show that the sanitary porcelain waste can be recycled again by adopting a reasonable process flow, which greatly reduces the environmental burden and is in line with the current green concept of sustainable development.

Experimental Procedures

Waste sanitary porcelain (200mesh, 0-1mm, 1-3mm; Beijing jingshe Xiangyun Logistics Co., Ltd), kaolin (Jiangxi Province), White corundum (purity: 99%, Henan Yiquan environmental protection Co., Ltd) were used as raw materials. Sodium silicate (modulus 2.5-3; Huainan Sodium silicate factory) was used as binder. The main experimental steps are as follows: firstly, the raw materials were weighed according to the experimental formula (shown in Table 1) and mixed by ball milling. The following step was using a powder pressing machine to compress the primary-processed precursor under 20 MPa into cylindrical samples. Finally, the dried sample was put into the box resistance furnace for sintering. The temperature system is as follows: rise the room temperature from 200 ℃ at the heating rate of 5 ℃ / min, then rise to 1000 ℃ at the heating rate of 10 ℃ / min, and then rise to 1250 ℃, 1300 ℃ and 1350 ℃ respectively at the heating rate of 5 ℃ / min and hold for 3 h.

Table 1 The mass addition of raw materials

Sample number	Waste sanitary porcelain			White corundum	Kaolin	Sodium silicate
	1-3 mm	200 mesh-1 mm	200mesh			
T1	45	20	30	5	10	10
T2	45	15	30	10	10	10
T3	45	10	30	15	10	10
T4	45	5	30	20	10	10
T5	45	0	30	25	10	10

Phases of the acquired products were characterized by X-ray diffractometer (XRD, D8 Advance, Bruker-AXS, Germany). Their morphology and microstructure were identified by field emission scanning electron microscopy (FESEM, Zeiss Supra 55, Germany). Their mechanical properties were obtained using universal testing machine (REGER3010, Shenzhen, China).

Results and discussion

As can be seen from Fig 1 (1), by comparing the PDF standard card, we found that kaolinite raw materials mainly contain kaolinite (PDF No.89-6538) and α- SiO_2 these two phases. For waste sanitary porcelain, the three phases are mullite α- SiO_2 and α- The intensity of the characteristic diffraction peak of Al_2O_3 phase is much greater than that of other kinds of phases. Because it is a ceramic product that has been fired, it contains more mullite phase, in addition to some α- SiO_2 and α- Al_2O_3 phase. However, the intensity and distribution of characteristic peaks of various phases are different between waste sanitary porcelain and white corundum.
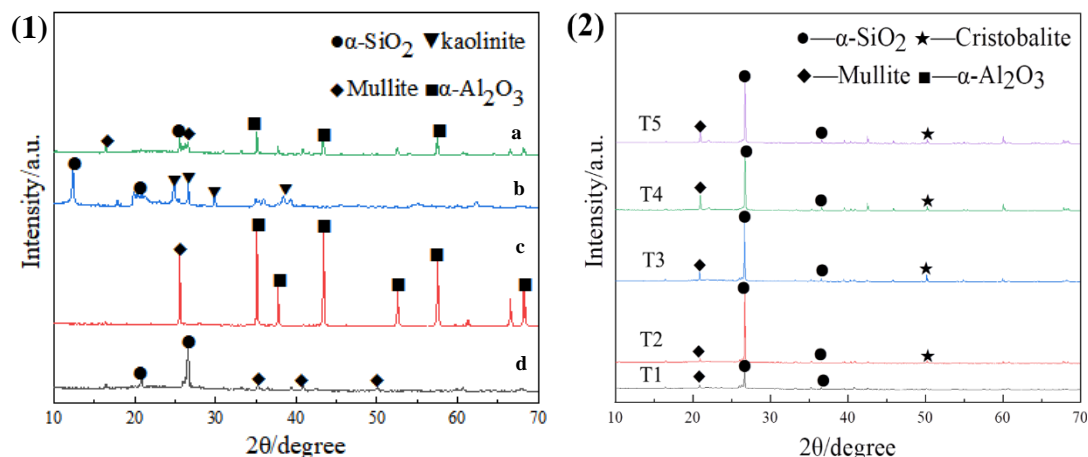
Fig.1 X-ray diffraction patterns: (1) raw materials: a-white corundum, b-kaolin, c-waste 95 porcelain, d-waste sanitary porcelain; (2) prepared samples from T1 to T5.

By observing and analyzing XRD patterns in Fig.1 (2), it is found that the phase composition of waste sanitary porcelain body after high temperature treatment is different from that of waste sanitary porcelain body in addition of α-SiO$_2$, mullite and α-Al$_2$O$_3$. α-cristobalite phase can be found in individual sample of group T. α-quartz can be transformed into α-cristobalite at 1050 °C. Based on the above analysis, the reason for the partial formation of α-cristobalite phase is that the sintering holding temperature of the sample is higher than its transformation temperature (1200 °C) but lower than the conversion temperature (1470 °C). The characteristic diffraction peaks of α-cristobalite with high intensity correspond to its (101) crystal plane, showing the characteristics of preferred growth orientation [12].
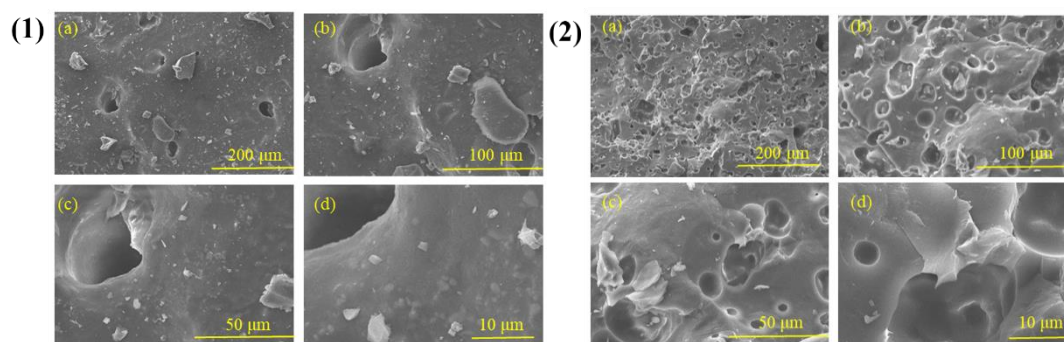
Fig.2 Field emission scanning electron microscopy images of the sample obtained at 1300 °C with different corundum addition: (1) 5%; (2) 10%.

Figure 2 (1) shows the sample sintered at 1300 °C with 5% white corundum added. There are many small pores on the surface, many pits and flat continuous parts. It is speculated that the reason is that continuous products are generated after liquid phase sintering and cooling. Some bubbles will be generated in the melt at high temperature and discharged to the surface, resulting in large holes and pits.

Figure 2(1) shows the sample sintered at 1300 °C with 10% white corundum added. It can be seen from the SEM picture that the sample is flat as a whole, but there are large and deep holes in some areas, and its diameter is much larger than that in Figure 2 (1). The content of

white corundum increases and the whole becomes flat, but there are large and deep holes. The main reason is that high-temperature melting can produce glass phase and fill the gap, but there are not enough molten glass phases to completely fill, resulting in a certain number of holes in some areas. Another reason is that the grading is uneven, and fine powder agglomeration may occur at the holes, Agglomeration is easy to produce pores, or there is too little fine powder in local areas, which can not effectively fill the pores [13].

Conclusions

In this experiment, waste sanitary ceramics, white corundum and kaolin were used to prepare samples with certain strength by solid-state synthesis. The main phase composition is mullite, α-SiO$_2$, α-Al$_2$O$_3$ and α-cristobalite. Among them, mullite, α-SiO$_2$, α-Al$_2$O$_3$ has good high temperature resistance and can be used as a consumption substitute for high-temperature kiln parts, which is conducive to the sustainable and low-carbon development of ceramic industry.

Acknowledgement

Additional information

Competing financial interests: The authors declare no competing financial interests.

References
[1] Ma X D, Han J C, Du W. Preparation and Characterization of Mullite Whiskers from Different Silica Sources via Molten Salt Reaction[J]. Journal of Inorganic Chemistry, 2019, 35(10): 1885-1895.
[2] Xiao G Q, Yang S L, Ding D H, et al. One-step synthesis of in-situ carbon-containing calcium aluminate cement as binders for refractory castables. Ceramics International, 2018, 44(13): 15378-15384.
[3] Yu Z, Yang L, Zhou S, et al. Durability of cement-sodium silicate grouts with a high water to binder ratio in marine environments. Construction & Building Materials, 2018, 189: 550-559.
[4] Tong K T, Raffaele V, Soutsos M N. Use of Vietnamese rice husk ash for the production of sodium silicate as the activator for alkali-activated binders. Journal of Cleaner Production, 2018, 207: 272-286.
[5] O. B. Montes, R. Moreno, M. T. Colomer, et al. Synthesis of mullite powders through a suspension combustion process[J]. J Am Ceram Soc.2006, 89(2): 484-489.
[6] Yue-feng Tang, Ai-dong Li, Hui-qin Ling, et al. Fabrication of ultra-fine mullite powders[J]. Mater Chem Phys. 2002, (75): 301-304.
[7] Yang D, Feng N X, Wang Y W, et al. Preparation of primary Al-Si alloy from bauxite tailings by carbothermal reduction process[J]. Transactions of Nonferrous Metals Society of China. 2010, 20(1): 147-152.

[8] Mileti S, Ili M, Vasi R M. Recycled ceramic waste for the electro-insulators jointing mixture and for other building materials[J]. Key Engineering Materials, 1997, (136): 2252-2255.

[9] Muduli R, Mukharjee B B. Effect of incorporation of metakaolin and recycled coarse aggregate on properties of concrete[J]. Journal of Cleaner Production, 2018, 209: 398-414.

[10] Alhumoud J M. Municipal solid waste recycling in the gulf co-operation council states[J]. Resources Conservation & Recycling, 2005, 45(2): 142-158.

[11] Bučevac D, Dapčević A, Maksimović V. Porous acicular mullite obtained by controlled oxidation of waste molybdenum disilicide[J]. Materials Research Bulletin, 2014, 50: 155-160.

[12] Cui J R, Zhang L F. Metallurgical recovery of metals from electronic waste: A review[J]. Journal of Hazardous Materials, 2008, 158(2-3): 228-256.

[13] Jang Hong-seok, So Seung-young. The properties of cement-based mortar using different particle size of grinding waste insulator powder[J]. Journal of Building Engineering, 2015, 3: 48-57.

Effect of Cobalt Oxide on the properties of Mullite Synthesized by Sol-gel Method

Zhenying Liu[1, *], Shouwu Huang[1], Chongmei Wu[1], Wenjie Wang[1], Nan Xie[1], Zhongde Yang[2], Xin Lin[2]

[1]School of Materials Science and Engineering, Anhui University of Science and Technology, Huainan 232001, China
[2]Anhui CONCH- SCG Refractory Co., Ltd., Wuhu, China
*Corresponding authors: zyliu@aust.edu.cn

Abstract

Mullite precursor powders were prepared by a sol-gel method using aluminum nitrate nonahydrate and ethyl orthosilicate as raw materials. The effect of cobalt oxide addition on the phase compositions and densification of mullite ceramics obtained by sintering of mullite precursor were investigated. The results showed that the formation temperature of mullite was significantly reduced, and it was about 100 °C lower than that of the sample without cobalt oxide addition. And a large number of needle-like mullite grains obtained in the sample. Needle-like mullite grains interweaved with each other to form a dense network structure. The effect of cobalt oxide addition attributed to Al^{3+} ions in mullite $[AlO_6]$ octahedron structure replaced by Co^{2+} ions, which caused its grain lattice distortion and activate its grain lattice.

Keywords: cobalt oxide, mullite, sol-gel method

Introduction

Mullite ($3Al_2O_3 \cdot 2SiO_2$) had achieved outstanding importance as a material for both traditional and adva nced ceramics because of its favourable thermal and mechanical properties[1, 2]. Mullite was wide-spreadly applied in many fields, including thermal insulation materials, thermal storage material, structure material, etc.. Various methods and techniques were used to prepare mullite ceramics, such as particle stacking [3], solid-phase reaction [4, 5], molten salt synthesis[6]. Of these, the solid phase method was simple process with high sintering temperature, molten salt synthesis prepared mullite ceramics at low sintering temperature, but a complex process applied by the method. Therefore, the simple and efficient synthesis method of mullite had attracted much attention. In order to lower temperature for the sintering samples and the abnormal mullite grain growth controlled. Transition metal ions introduced into the reaction medium to increase the diffusion rate of ions and promote the synthesis of mullite.

In this study, mullite precursors were obtained by sol-gel method. The effect of cobalt oxide addition on mullite crystal, as well as the phase compositions and morphology evolution microstructure of mullite ceramics synthesized was studied. Especially, the properties of pretreated materials and further on their sintering mechanism were studied in detail.

Experimental

Al(NO$_3$)$_3$·9H$_2$O (Sinopharm Chemical Reagent Group Co., Ltd., China, >99.5% purity) and TEOS (Sinopharm Chemical Reagent Group Co., Ltd., China) as raw materials, Mullite precursor was prepared by a sol-gel method, and high-purity cobalt oxide (D$_{50}$=1 μm, ≥99.9 wt.%, Macklin Biochemical Co., Ltd., Shanghai, China) was used as sintering aids. The mixtures were uni-axially pressed at 15 MPa to obtain discs of 15 mm in diameter and 5 mm in thickness and square shape samples. The green bodies were dried at 110 ℃ for 24 h and sintered at different temperatures (900 ℃、1 000 ℃、1 150 ℃、1 250 ℃，1 300 ℃) for 2 h at a heating rate of 5 °C/min, and then cooled down naturally.

Results and discussion

Effect of cobalt oxide addition on phase evolution of mullite ceramics sintered at different temperatures

Figure 1 showed the XRD patterns of samples sintered at different temperatures. Compared with the XRD pattern of the sintered sample without cobalt oxide, it was found that with the addition of 5 wt.% (mass fraction) of cobalt oxide, a small amount of mullite peaks appeard in sintered sample at 900 °C. At 1 150 °C, a small amount of cobalt aluminate (CoAl$_2$O$_4$) phase was formed, but the diffraction peak intensity was weak. As the sintering temperature continued to increase, the main crystalline phase of mullite was formed in large quantities. Therefore, the sol-gel method was used to prepare the mullite precursor, mullite was formed at the lower sintering temperature with the addition of cobalt oxide, and promoted the nucleation and growth of mullite phase.
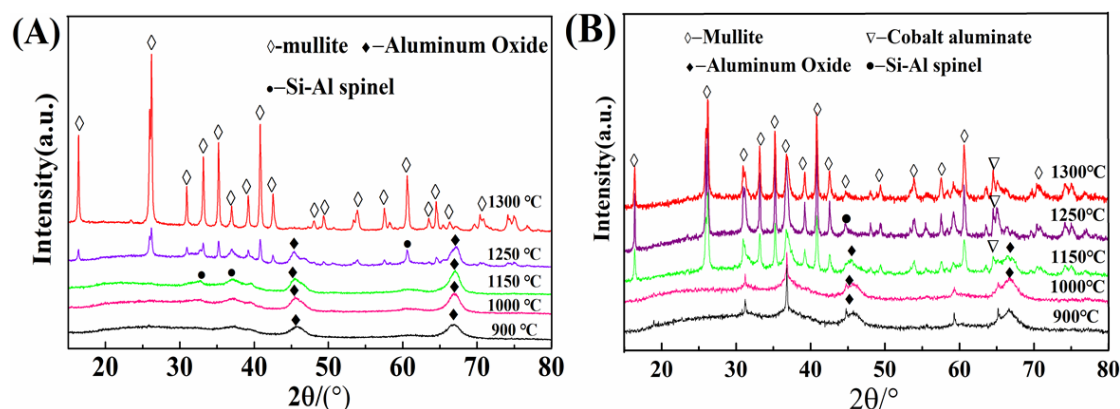
Fig.1 XRD patterns of samples sintered (A- without cobalt oxide, B- with 5% cobalt oxide)

The effect of cobalt oxide addition on the micromorphology of mullite ceramics prepared

Figure 2 showed SEM images of the sintered samples with 5 wt.% cobalt oxide at different temperatures. After sintering at 1150°C, the sample had a large number of large pores and poor crystallization, accompanied by a small amount of columnar mullite (see Fig. 5A). As the sintering temperature increased at 1 250 °C, the number of short columnar mullite increased, and the crystal grains gradually grow (see Fig.5B). The sample sintered at 1 300 °C for 2 hours, mullite grow up along the c-axis direction into fine needle-like or columnar

327

grains (see Fig.5C), and formd the densified structure. This was because the Co^{2+} ions in the sample dissolved in the mullite lattice to promote the formation of liquid phase. In view of solid-liquid diffusion-dominated mass transfer process, mullite grains develop well, and the anisotropic growth was obvious.
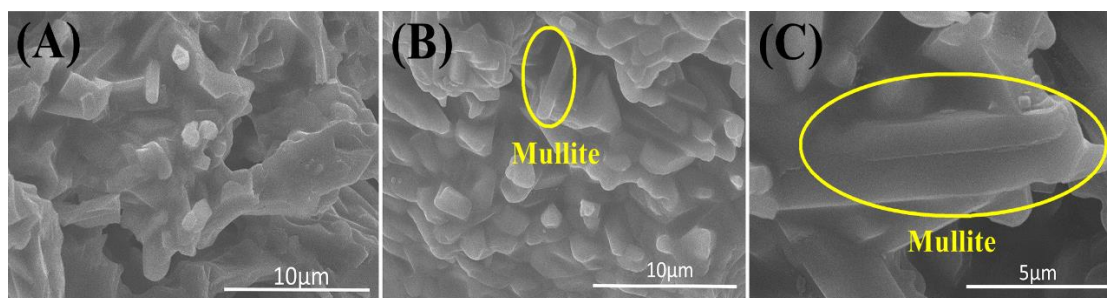
Fig.2 SEM images of the samples with 5 wt.% cobalt oxide sintered at different temperatures: (A) 1150 °C, (B) 1250 °C, (C) 1300 °C

Conclusions

The mullite precursor was prepared by the sol-gel method, and cobalt oxide was added as a sintering aid to realize the formation mullite phase at low temperature. The needle shaped morphology in presence of 5wt.% cobalt oxide additive at a comparatively lower temperature improved the properties of mullite ceramics.

Acknowledgment

References

[1] Gao H, Luo F, Wen Q L, et al. Effect of preparation conditions on mechanical, dielectric and microwave absorption properties of SiC fiber/mullite matrix composite. *Ceramics International*, 2019, (45), 11625-11632.

[2] Li w, Zhang J. Li X C, et al. Synthesis and electromagnetic properties of one-dimensional La^{3+}-doped mullite based on first-principles simulation. *Ceramics International*, 2019, (45), 17325-17335.

[3] Liu Y, Lian W, Su W F, et al. Synthesis and mechanical properties of mullite ceramics with coal gangue and wastes refractory as raw materials. *Applied Ceramic Technology*, 2020, (17): 205–210.

[4] Ye H, Li Y, Sun J L, et al. Novel iron-rich mullite solid solution synthesis using fused-silica and α-Al_2O_3 powders. *Ceramics International*, 2019, (45): 4680-4684.

[5] Deng X G, Zhang W C, Yin J Q. et al. Microstructure and mechanical performance of porous mullite ceramics added with TiO_2. *Ceramics International*, 2020, (46): 8438–8443.

[6] Wang W, Li H, Lai K, Du k. Preparation and characterization of mullite whiskers from silica fume by using a low temperature molten salt method. *Journal of Alloys & Compounds,* 2012; 510: 92-96.

Preparation and Application of g-C$_3$N$_4$/PVDF composite film

Zhou Luzhi, Tan Jiewen, Yuan Xinshun, Li Jialu, Cheng Changhong, Yu qingbo*

School of materials science and engineering, Anhui University of technology, Huainan, Anhui 232001

Abstract

Taking polyvinylidene fluoride (PVDF) as the substrate, graphite carbon nitride was evenly mixed in polyvinylidene fluoride by solution immersion method, and it was made into g-C$_3$N$_4$/PVDF composite film samples with piezoelectric effect and photocatalytic function. The dispersion, absorbance and piezoelectric properties were studied by Fourier infrared spectroscopy, UV spectrophotometer and electrochemical workstation. The results show that carbon nitride is successfully dispersed in polyvinylidene fluoride film. The piezoelectric properties reach the best when the addition amount of g-C$_3$N$_4$ is 0.2g. In the ultrasonic degradation of methylene blue, acidic conditions are more conducive to the degradation of methylene blue. At the same time, the increase of temperature and initial solution concentration will reduce the degradation efficiency. When the addition of g-C$_3$N$_4$ is 0.2g, the photocatalytic degradation efficiency is the highest, up to 55%.
Keywords: Polyvinylidene fluoride; Graphite phase carbon nitride; Solution immersion method; Ultrasonic degradation

Introduction

With the progress and development of society, more and more waste organic dyes are discharged by human beings. At present, the treatment methods of organic dyes include activated carbon adsorption and membrane adsorption, but these methods transfer pollutants in solution, and microbial treatment has high requirements for culture environment [1~2]. Catalytic water purification by catalyst is another way. Its main limitation lies in the catalytic performance of the catalyst. Improving the catalytic efficiency by modifying the catalyst is the main research direction at present. In 2012, Hong [3] et al reported for the first time the study of piezoelectric catalytic degradation of organic compounds while ultrasonic operation. Their view is that in the field of degradation of organic pollutants, piezoelectric catalysis and photocatalysis have similar mechanisms, but there are great differences in the generation of charge. Photocatalysis is based on photoexcitation, and the other is based on piezoelectric effect. As a piezoelectric material, polyvinylidene fluoride film has many good properties, but its surface activity is low. The purpose of this paper is to modify the piezoelectric PVDF membrane and improve its decomposition efficiency of methylene dyes by piezoelectric ultrasonic synergistic catalysis. The specific contents of this paper include the synthesis of g-C$_3$N$_4$/PVDF composite film by solution immersion method with PVDF film as substrate and graphite carbon nitride as modified material, and its properties were studied.[4]

Experimental section

Synthesis of g-C₃N₄

Ten grams of dicyandiamide was put into a quartz boat, then heated to 550°C for 4 h with a heating rate of 2.5°C/min under N_2 gas. The obtained sample was denoted as g-C₃N₄.

1.2 Preparation of g-C₃N₄/PVDF Composites

In this experiment, the composites were prepared based on the preparation of pure PVDF film: 1g PVDF resin powder was dissolved in 9.45g (10ml) DMF, covered with fresh-keeping film, the stirrer was set at 60 ℃ and stirred at constant temperature for 2h. After stirring for one hour, different amounts of carbon nitride were added respectively. In order to ensure that g-C₃N₄ can be evenly dispersed in the membrane preparation solution, g-C₃N₄ is blended with 2ml absolute ethanol and added after ultrasonic. Then stir together for another hour, let it stand for defoaming, wait for it to cool to room temperature, then dip about 5ml of sample with glass rod and apply it on the flat glass sheet, and let 25% of the tetrahedral preparer, press both ends with your hand, scratch the sample at a uniform speed of 150 mm per second, and apply the scraping film. The obtained glass sheet is placed in deionized water at room temperature to exchange solvent. After the membrane automatically falls off from the glass rod, the residual solvent left on the membrane surface is washed and dried in a 60 ℃ oven for 12h to obtain a dry and uniform g-C₃N₄/PVDF composite film sample.

Characterisation

The chemical structure was obtained by Fourier transform infrared spectroscopy (FTIR, Nicolet 380). The concentration of MB was measured by the UV-vis spectrophotometer, and the test wavelength was 664 nm. Piezoelectric property were measured on electrochemical workstation.

Results and discussion

As shown in Figure 1, the composite film made by adding g-C₃N₄ is compared with PVDF pure film. The spectra of composite samples and pure PVDF are roughly the same, and there is no large-area disappearance of characteristic peaks, indicating that the PVDF structural skeleton in the composite is not damaged by the addition of g-C₃N₄. At the same time, in the spectrum of the composite, a C=Nbond representing g-C₃N₄ appears at $1687cm^{-3}$, indicating that g-C₃N₄ is successfully incorporated into the composite.

The effect of pH on g-C₃N₄/PVDF composite films was studied. According to the results shown in Figure 2, the degradation effect of methylene blue is better than that of neutral conditions in both acidic and alkaline environments. When the solution is at pH < 7 or pH > 7, the degradation efficiency of methylene blue in one hour is 56% and 49%, while when the solution is neutral, the degradation efficiency is only 43%.That is, the acid-base environment is more conducive to the improvement of methylene blue degradation efficiency.

It is inferred that the reason for this phenomenon is that when the pH in the initial solution is increased, the piezoelectric material surface will have a negative charge. The hydroxyl

radical in the solution will also increase with the increase of OH- concentration[5]. The oxidation mechanism of hydroxyl radical is usually carried out under alkaline conditions. Therefore, alkaline conditions are beneficial to the ultrasonic degradation of methylene blue. When the pH concentration is low, the main form of organic matter is molecules, which are easy to approach and enter the cavitation bubble by evaporation. Then the pyrolysis effect occurs directly in the cavitation bubble; At the same time, it can undergo oxidation reaction between the surface of the bubble and the liquid, so as to improve the degradation efficiency of the solution.

The effect of temperature on g-C$_3$N$_4$/PVDF composite film is studied. As shown in Figure 3, the experimental data show that the degradation efficiency gradually decreases with the continuous increase of temperature, and the two are negatively correlated. The degradation efficiency reached the maximum at room temperature (20 ℃), and the degradation efficiency was 56%

It is speculated that the reason for this phenomenon is that when the ultrasonic cavitation effect occurs, the degradation reaction of methylene blue is at the interface between the cavitation bubble and the liquid. After the temperature increases, the liquid vaporization increases, affecting the continuous generation of cavitation bubbles [6].At the same time, there is a large amount of water vapor generated by evaporation in the bubble, which weakens the cavitation effect and reduces the catalytic efficiency of the solution.

The effect of methylene blue on the initial concentration was studied. From Figure 4, the solution degradation efficiency decreases rapidly with the gradual increase of the initial methylene blue concentration. When the solution concentration was 30 mg / L, the degradation efficiency was only 4%.

The Figure 5 shows the output current of g-C$_3$N$_4$/PVDF composite films with different doping amounts under the same frequency and mechanical force. The results show that the output current increases gradually when the doping content increases from 0.05g to 0.2g. As shown in Figure 5D, when the doping amount reaches 0.2g, the piezoelectric performance of g-C$_3$N$_4$/PVDF composite film reaches the best, and the maximum positive current output reaches 1.7μA. When he doping amount continues to rises from 0.2 g, the output current decreases and the piezoelectric performance decreases. The change trend is the same as the methylene blue solution catalyzed by g-C$_3$N$_4$/PVDF composite film. It is speculated that this result is related to the conductivity and crystallinity of the film.

Conclusion

Using polyvinylidene fluoride (PVDF) as substrate, the modified graphite phase carbon nitride was evenly mixed in polyvinylidene fluoride (PVDF) by solution immersion method, and it was made into g-C$_3$N$_4$/PVDF composite film samples with piezoelectric effect and photocatalytic function. Based on the full text, the following conclusions are obtained

(1) Through Fourier transform infrared spectroscopy, we determined that the PVDF film was not damaged by the addition of g-C$_3$N$_4$, and successfully prepared a uniform g-C$_3$N$_4$/PVDF composite film.

(2) The catalytic degradation of methylene blue by g-C$_3$N$_4$/PVDF composite film is affected by pH value, temperature and initial concentration of methylene blue. Acidic and alkaline environment are more suitable for the decomposition of methylene blue than neutral environment; When the temperature is 20 ℃, g-C$_3$N$_4$/PVDF composite film has the best catalytic performance; The degradation efficiency of g-C$_3$N$_4$/PVDF composite film to high concentration methylene blue decreased rapidly. For 30mg / L methylene blue solution, the degradation efficiency was only 4%.

(3) The piezoelectric properties of g-C$_3$N$_4$/PVDF composite films with different doping amounts are analyzed. When the doping amount of g-C$_3$N$_4$ is 2g, the piezoelectric properties of the composites are the best.

Reference

[1] Liang Yi research progress on treatment methods of organic dye wastewater [J] modern industrial economic informatization, 2020, 10 (7): 129-130.

[2] Feng Shuxiang, Liu Xia, Zhang Rongrong. Research progress of dye wastewater treatment methods [J]. Journal of Yulin University, 2014, 24 (6): 21 - 25

[3] Shao Dengkui. Research on piezoelectric catalysis for oxygen reduction reaction [D]. University of Chinese Academy of Sciences (Shanghai Institute of silicate, Chinese Academy of Sciences), 2018

[4] Heiji Kawai. The Piezoelectricity of Poly (vinylidene Fluoride)[J]. Japanese Journal of Applied Physics,2014,8(7).

[5] Xia Liangshu, Wang Meng, Li Laibing, Chen Zhongqing. Study on ultrasonic catalytic degradation of methyl orange in US / Fe3 + / H2O2 System [J]. Chemical engineering, 2007 (07): 58-62

[6] Liu Zhenrong, Li Hong, Wang Jun, Zhang Chaohong, Guo Baodong, Zhang Xiangdong, Wu Jing. Ultrasonic degradation of methylene blue solution catalyzed by TiO2 [J]. Chemical research, 2005 (01): 69-71
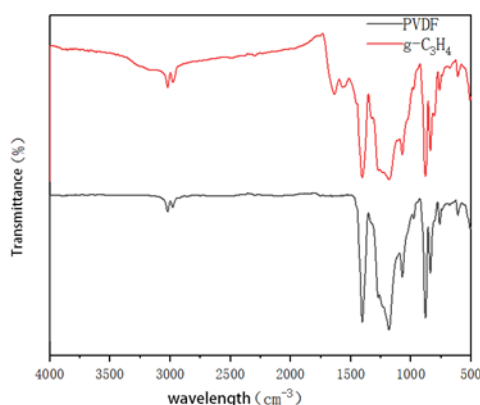
Figure 1 FTIR of g-C$_3$N$_4$/PVDF composite film.
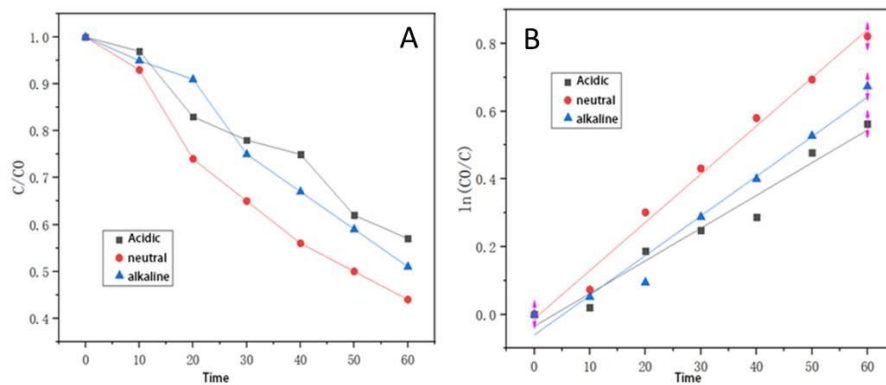
Figure 2 (A) Photocatalytic degradation curves of different initial solution pH; (B) The pseudo-first-order reaction kinetics of samples.
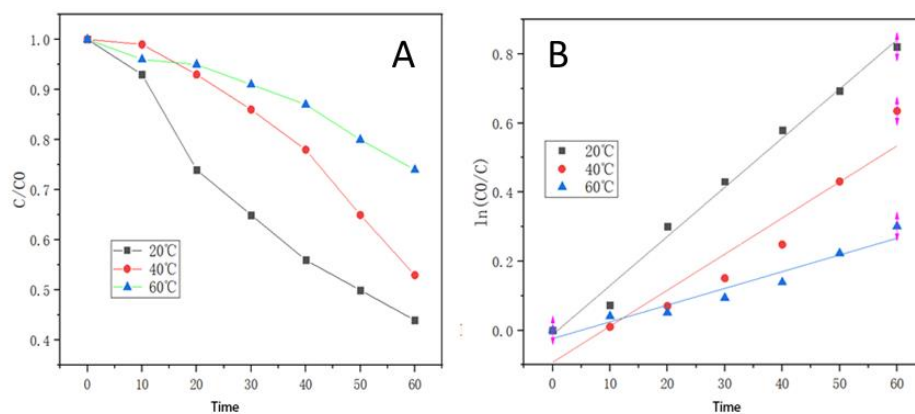
Figure 3 (A) Photocatalytic degradation curves of different temperatures; (B) The pseudo-first-order reaction kinetics of samples.
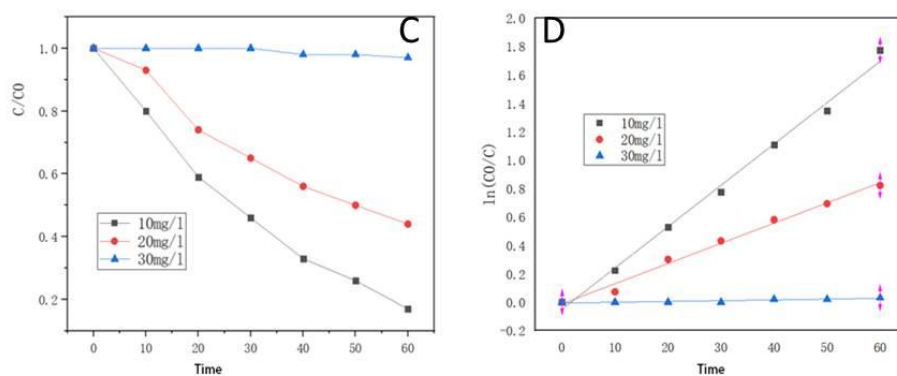
Figure 4 (A) Photocatalytic degradation curves of different initial concentration of methylene blue; (B) The pseudo-first-order reaction kinetics of samples.
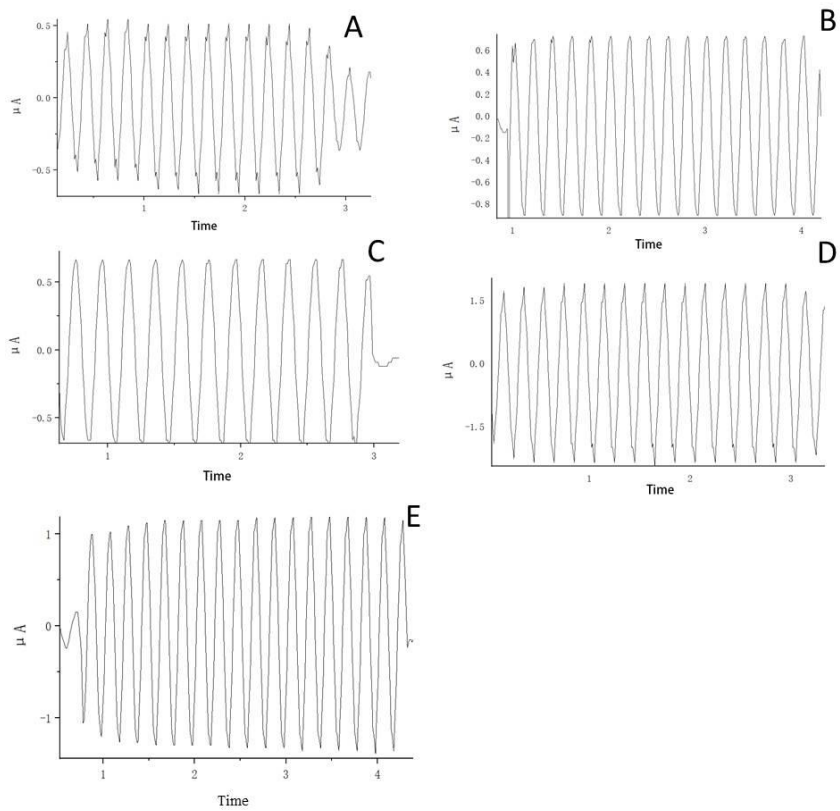
Figure 5 The doping amount is 0.05g (A), 0.1g (B), 0.15g (C), 0.2g (D), 0.25g (E).

A study of effect of alcohol spray on latent fingerprint quality on non-porous forensic evidences on Covid-19 pandemic period

Panattha Buranasiri and Rachadaporn Benchawattananon

[1]Office of Police Forensic Science, Bangkok, 10330, Thailand

[2]Integrated Science Forensic Science Faculty of Science Khon Kaen University, Khon kaen , 40002, Thailand

Corresponding author: rachadaporn@kku.ac.th

Abstract

Actual Covid-19 pandemic situation when any case occurs, takes time to get to collect evidence at the crime scene because sometimes the incident takes about 1 week. The result in unclear fingerprints on witness objects, affect whom collects latent fingerprints and affect the quality of the fingerprints. A study of effect of alcohol spray on fingerprint quality on forensic evidence on Covid-19 pandemic period. To study of effect of different concentrations of alcohol gel on fingerprint quality on glass and plastic. The objective of the research to study the alcohol hand sanitizer with a concentration of 70 %, 75% and 80 %, which will affect the latent fingerprints on glass, plastic and metal witness objects after a period of time 1 , 5, 10, 15, 20, 25, 30, 45 and 60 days. Let the experimenter make a fingerprint stamp on the witness object, divided as follows: 1. The subject must not wash his hands with alcohol spray before stamping his fingerprint on the witness object for 1-2 hours, and then stamp the fingerprint on the witness object 2. The test subjects wash their hands using 70% alcohol spray, leave it for 15 minutes, and then stamp their fingerprints on the witness object. 3. The test subjects wash their hands using 80% alcohol spray, leave it for 15 minutes, and then stamp their fingerprints on the witness object. The force used to imprint fingerprints was approximately 750 -800 g (36,750 -39,250 N/m2), and the experimental temperature was about 29 -32 °C. Take time for study period of time and test minutiae. Finding the alcohol hand sanitizer with a concentration of 70 % keep the fingerprint better than 80 % alcohol hand sanitizer and many factors effect such as temperature, humidity and individual fingerprint conditions.

Keywords : alcohol hand sanitizer, covid-19, fingerprint, forensic evidence

Introduction

From past to present Thailand has always had crime cases. Which proves forensic police is one of the professions in the judicial process. It is responsible for collecting and verifying evidence objects in cases in order to bring about justice in society. This requires knowledge and skills trained in science in order to be effective in diagnosing witness objects that affect the

circumstances of a particular case.Kongsak et al.(2020) If considering the actual situation, when any case occurs, the forensic officer takes a period of time in order to collect the evidence in the crime scene.Doibud et al.(23017) Because sometimes the incident can happen for a while, but the victim is just aware of the incident and may cause the evidence objects to be contaminated or unclear lines of fingerprint. Also, due to the current Covid-19 situation, it continues to occur. The behavior of people living in Thailand has changed. For example, wearing a mask in public, washing hands regularly with alcohol gel and spraying alcohol. or standing 1-2 meters apart, which is a current measure that everyone needs to do. This altered behavior may result in alteration of the fingerprints on the witness object.It affects the forensic officer who collects fingerprints and affects the quality of fingerprints. The research that examined the quality of fingerprints over time in various witnesses gave an example of Nawarat et al.(2016) research that compared the quality of latent fingerprints on the fruit's surface. Using black powder and superglue method the fruits used in the experiment were red apples, green apples, jujube, bananas and ripe mangos. The latent fingerprint samples will be prepared immediately in 1 day and 2 days [1] or the research of Nuchanat (2019). The quality of latent fingerprints on plastic handles and metal knives submerged in different types of water which are brackish water and fresh water, was studied by Small Particle Reagent (SPR) and Super Glue methods. (SG) for a period of 1, 7, 14, 21 and 28 days, respectively [2]. From the information and research that the researcher has mentioned above, the interesting point in this research is the fingers that are washed.Alcohol sprays at a concentration of 70% and 80%, which are the most common concentrations in Thailand. Which has the duration of collecting fingerprints of different witnesses will affect the quality of the fingerprints or not.

Objective

To study the quality of latent fingerprints when using alcohol spray at concentrations of 70 % and 80% on non-porous witness objects which are plastic, glass and metal after a period of time 1 , 5, 10, 15 , 20, 25, 30 ,45 and 60 days

Experimental

Materials

70 %, 75% and 80% alcohol spray, black power with forensic squirrel hair brush, transparent tape, fingerprint pad, non-porous material (plastic, glass and metal) and white paper.

Methodology

compare fingerprint quality after use alcohol spray between 70 % ,75% and 80% alcohol spray on non-porous objects (forensic evidences plastic, glass and metal) for a period of 1 ,5,

10, 15, 20, 25, 30, 45, 60 days ,respectively and fingerprint collection by black power method with forensic squirrel hair brush.

Experiment process

The force used to imprint fingerprints was approximately 750 -800 g (36,750 -39,250 N/m2), and the experimental temperature was about 29 -32 °C. Take time for study period of time and test minutiae

1. Stamping finger with ink for examine quality of latent finger print without alcohol (blank)

- Finger stamping with ink

2. wash hands with 70% and 80% alcohol spray, leave it for 15 minutes and stamping finger on non-porous objects (forensic evidences plastic, glass and metal) for a period of 1 ,5, 10, 15, 20, 25, 30, 45, 60 days ,respectively.

- Alcohol spray 70% (Ubon bio)
- Alcohol spray 80% (CHARIYA)

- Finger stamping after use alcohol spray
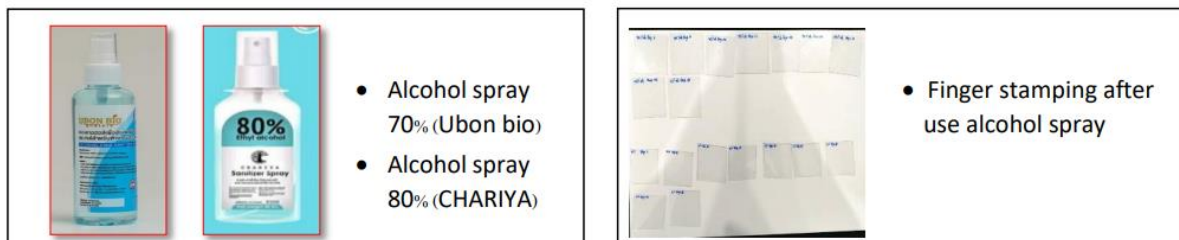
3. Fingerprint collection by black power method with forensic squirrel hair brush for a period of 1, 5, 10, 15, 20, 25, 30, 45, 60 days, respectively.

- black power with forensic squirrel hair brush, transparent tape

4. Verify quality of latent fingerprint for a period of 1, 5, 10, 15, 20, 25, 30, 45, 60 days, respectively.
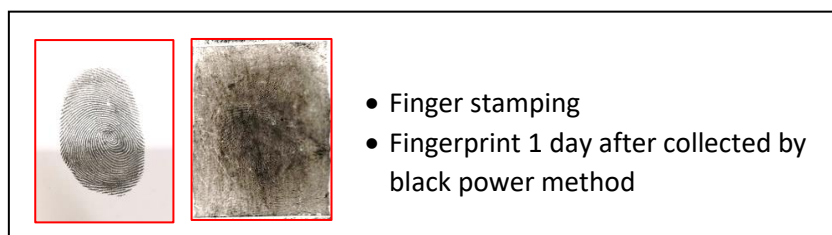
- Finger stamping
- Fingerprint 1 day after collected by black power method

Acknowledgements

References

1. Nawarat Jaiwijit,Supachai Supaluxnaree,Sirirat Choosakunkraing and Pattratip Laohabud.(2017) Comparative latent fingerprint on fruits by dust powder and superglue .The Science journal of Phetchaburi Rajabhat University .14(1) 64-73.

2. Nuchanart Jaruratanawiboon.(2019). Detection of latent fingerprints on submerged knives using Small Particle Reagent and Super Glue. Journal of Criminology and Forensic Science Police Cadet Academy.128-141.

3. Kongsak pattarith and Rachadaporn Benchawattananon. "The Novel Photoluminescence Powder Synthesized from Zinc Carbonate Nanoparticles Associated with Fluorescein Dye for Its Latent Fingerprint Detection". Oriental Journal of Chemistry 2020; 36(2): 237-243.

4. Doibut, T., and Benchawattananon, R.Small particle reagent based on natural dyes for developing latent fingerprints on non-porous wet surfaces (2017) Management and Innovation Technology International Conference, pp. 225-228.

Recovering of Perfluorocarbon from the Spent Decontamination Emulsion using Distillation Method

Naon Chang[1,2], Huijun Won[1], and Seonbyeong Kim[1*]

[1]Decommissioning Technology Research Division, Korea Atomic Energy Research Institute, Daejeon 34057, Korea

[2]Department of Nuclear Engineering, Hanyang University, Seoul 04763, Korea

[*]Corresponding author. Tel: +82-428684681, E-mail: sbkim@kaeri.re.kr

Abstract

In a nuclear facility, the radioactive oxide layers can be generated on the base metal by neutron absorption during operation. It is necessary to remove the radioactive oxide layers for reducing the radiation exposure to workers before decommissioning of nuclear facility. In order to remove the radioactive oxide layer, it is possible to apply the P-BED (perfluorocarbon-based emulsion for oxide layer dissolution) including PFC (perfluorocarbon), inorganic acid, and anionic surfactant. After finishing the decontamination using P-BED, PFC, acid, surfactant, and radioactive metal ion can be existed in the spent P-BED. The purpose of this study are to derive a recovering method of perfluorocarbon from the spent P-BED using distillation. Before distillation experiment, spent P-BED surrogate was prepared by removing the Cr oxide layers on the SUS304 specimen. The distillation test was performed using vacuum distillation unit, and the distillation temperature of spent P-BED was 80 $^{\circ}$C. From the distillation test, about 95 % of PFC was recovered by distillation. A concentration of Cr ion was analyzed using atomic absorption spectroscopy (AAnalysis, Perkin Elmer). From the result of AA analysis, it was verified that the Cr ions were not existed in the recovered PFC. Based on this result, it was confirmed that PFC was effectively recovered by distillation method.

Keywords: Nuclear facility, Decontamination, PFC, Emulsion, Recovery

Evaluation of GlobalFiler™ IQC PCR Amplification Kits using half volume reaction in low template DNA of Forensic samples

Waritsara Chompubai[1*] and Rachadaporn Benchawattananon[2*]

[1*] Scientist , Forensic biology and DNA examinations sub division Police Forensic Science Center4,Khon Kaen ,Thailand 40000

[2*] Integrated Science Forensic Science Faculty of Science Khon Kaen University, Khon kaen , 40002, Thailand

Corresponding author: rachadaporn@kku.ac.th

Abstract

In forensic genetic analysis, Short tandem repeat (STR) markers are widely used for human identification. GlobalFiler™ IQC kit is highly power of discrimination. In this study, DNA samples obtain from forensic casework, several samples were extracted with PrepFiler Automated Forensic DNA Extraction Kit, Quantifiler™ HP for DNA quantification. In PCR amplification, using half volume reaction of GlobalFiler™ IQC. Capillary electrophoresis was performed on the 3500 Genetic Analyzer and DNA profiling has been performed with GeneMapper ID-X Software v1.4. Low amount of DNA samples was divided into two groups by DNA concentration, group1; DNA concentration between 0.0041 ng/µl to 0.0083 ng/µl and group2; DNA concentration between 0.0084 ng/µl to 0.0167 ng/µl. Both concentrations were observed percentage of allele recovery in DNA profile of all casework samples, were classified into 4 types of DNA profile consist of full profile, partial profile, mixture profile and no profile DNA. The analytical thresholds to detect real peak is 175 RFU and the stochastic thresholds that used to detect homozygous peak is 1300 RFU. Reduced reaction volume is challenge in forensic genetic field especially in low amount of template of casework samples.

Keywords: GlobalFiler™ IQC, low template DNA, STR, forensic evidence

Introduction

Short tandem repeat (STR) analysis methods are widely used in forensic DNA analysis. (Hirunya et al., 2016) The GlobalFiler™ IQC kit was designed to amplify 21 autosomal STR loci for human identification. The kit include locus SE33 that provide highly polymorphic allele (E. Almohammed, 2019). In addition, the kit amplifies 2 Internal Quality Control (IQC) markers to assess the PCR reaction (Applied Biosystem, 2019). In forensic field, casework DNA samples were occurred different type of source of DNA such as buccal, blood, hair, cigarette and touch DNA, the quality of DNA depending on environment condition that introduce a complicate for DNA interpretation (K. Elwick, 2018). However, the successful of full profile received from casework samples have several factors. The aim of this study to evaluate the performance of the GlobalFiler™ IQC kit using half volume reaction with low template DNA from casework samples.

Objective

To evaluate the performance of the GlobalFiler™ IQC kit using half volume reaction with low template DNA from casework samples.

Experimental

Materials and methods

1. **Sample collection and extraction**

   The sample from casework were extract using PrepFiler Automated Forensic DNA Extraction Kit, 30µl of DNA elution volume.

2. **Quantification and Amplification**

   Extracted DNA samples were quantified with Quantifiler™ HP and amplified with GlobalFiler™ IQC PCR Amplification Kits using half volume reaction.

3. **DNA analysis and interpretation**

   PCR products were separated and detected via capillary electrophoresis using 3500 Genetic Analyzer. STR DNA sample profiles were analysed using GeneMapper ID-X Software v1.4. Peak were used for analytical threshold and stochastic threshold is 175 RFU and 1300 RFU, respectively.

Experiment process

1. DNA casework samples were divided into 2 groups, group1; concentration between 0.0041 ng/µl to 0.0083 ng/µl and group2; DNA concentration between 0.0084 ng/µl to 0.0167 ng/µl. Both groups were amplified with GlobalFiler™ IQC PCR Amplification Kits using half volume reaction.

2. Evaluate percentage of allele detection of low amount DNA template in DNA profile of casework samples, classify into 4 types, and consist of full profile, partial profile, mixture profile and no profile DNA.

Acknowledgements

References

1. Almohammed, E., & Hadi, S. (2019). Internal validation of GlobalFilerTM kit using reduced reaction volume. Forensic Science International: Genetics Supplement Series, 7(1), 878–883.

2. Applied Biosystem®by Life TechnologiesTM. GlobalFiler™ and GlobalFiler™ IQC PCR Amplification Kits USER GUIDE. 2019.

3. Bogas, V., Carvalho, M., Corte-Real, F., & Porto, M. J. (2015). Testing the behavior of GlobalFiler® PCR amplification kit with degraded and/or inhibited biological samples. Forensic Science International: Genetics Supplement Series, 5, e21–e23.

4. Hirunya Sintusiri and Rachadaporn Benchawattananon.(2016) Spiecies Identification Of Wild Mushroom By Nucleotide Sequence Analysis On ITS Region. National Forensic Science Conference: Beyond Pleace with Forensic Science: 23-24 june 2016, Forensic Science Faculty of Forensic Science,Prince of Songkhla University : 8-9.

Determination of sibutramine compound in slimming supplements using distance-based paper devices

Chanya Punthama[1] and Wijitar Dungchai [1*]

[1] Organic Synthesis, Electrochemistry & Natural Product Research Unit, Department of Chemistry, Faculty of Science, King Mongkut's University of Technology Thonburi, Prachautid Road, Thungkru, Bangkok, 10140, Thailand.
*e-mail: wijitar.dun@kmutt.ac.th

Abstract

Sibutramine was adulterating in slimming supplementary used for lost weight in recent years. We developed microfluidic paper-based analytical devices (μPADs) for the determination of sibutramine by the oxidation reaction of the potassium permanganate and the etching reaction of AgNPs with the permanganate remaining. Potassium permanganate remaining in an alkaline medium can be reacted with AgNPs observed a change of pink to a colorless band length by the ruler. Under the optimal conditions, the calibration curve between the colorless band and sibutramine concentration was in the range of 6.3-158 μmol/L, and the detection limit was found to be 6.3 μmol/L. Our proposed devices can be applied to detect sibutramine in real samples and are instrument-free, portable, and cost-efficiency. For the validation method, our results were no significant distinction in accuracy and precision.

Keywords: Sibutramine hydrochloride, Distance-based paper device, Adulterated products

Introduction

The critical global problem of health is obesity or overweight, leading to the production of a sliming weight supplement. Overweight people require dietary supplements or slimming formulations consisting of natural extraction because of having low harmful side effects from adulterant chemical drugs [1]. Moreover, sliming dietary supplements based on herbal are distributed in the local market or internet online. They have discovered weight control drugs in various brands in the market share of Bangkok, Thailand. As a result, some consumers received dangerous health because of adulterant synthetic chemical drugs in a dietary supplement. The Food and Drug Administration (FAD) has reminded consumers to consume dietary supplement trademarks. The adulterants are frequently created in phototherapeutic formulations, including anorexics, anxiolytics, antidepressants, diuretics, and laxatives [2], [3]. Recently, several dietary supplements in the market were found non-declared synthetic substances in theirs, such as sibutramine. Sibutramine is the most popular adulterant in slimming dietary supplements. It is an anti-obesity drug in the hydrochloride form by serotonin and noradrenaline reuptake inhibitors [2]. Sibutramine is efficient in inducing appetite extinction, increasing the energy-sensing of satiety, and reducing intestinal fat adsorption by changed neurotransmitters in the brain. It also causes several side effects, including headaches, unstable funniness, nervous depression, fretfulness, and chemical dependence [1]. Sibutramine has been removed from the market in many countries because it is a prohibited substance in sliming weight formulations [4].

Several techniques have been used to identify and quantify sibutramine in dietary supplements or herbal products, such as high-performance liquid chromatography with mass

spectrometric (HPLC-MS) [5], liquid chromatography with mass spectrometry (LC-MS) [6], [7], thin-layer chromatography (TLC) [3], capillary electrophoresis (CE) [8], and infrared spectroscopy [9]. These methods have many advantages, such as specification, and high sensitivity, but they required complicated instruments, experienced analysts, and time consumption. Nevertheless, various laboratories and local officers require a low-cost, portable, and simple procedure to determine sibutramine in supplements and beverages [3]. Microfluidic paper-based analytical devices (μPADs), when compared to conventional methods, have advantages, including friendly consumers, lower cost, portable, and environmentally friendly [10]. The μPADs coupled with the colorimetric detection usually read out the change of color shade by the naked eye, but it was different of color shade in each surrounding. The interpretation might misunderstand and needs external software/hardware. Some researchers have developed distance-based paper devices for reducing error measurement and without recorded hardware [11]. Therefore, we aim is to develop an alternative analytical method that is a rapid measurement, on-site portable, simple instrument, and inexpensive cost for the adulterants detection. This method was applied for determining adulterants substances in dietary supplements because their products were available in the local market and easy to consume by consumers. Our proposed device can be used to detect sibutramine in various real samples.

Experimental

Reagents and materials

A stock standard solution of 1000 mg/L sibutramine hydrochloride was purchased from Sigma-Aldrich (Missouri). Boric acid (Merck, Darmstadt, Germany), acetic acid (BDH, England), phosphoric acid (QReC, New Zealand), sodium hydroxide (Merck, Darmstadt, Germany), hydrochloric acid (QReC, New Zealand), silver nitrate (Carlo Erba, France), starch soluble (Merck, Darmstadt, Germany), sodium borohydride (Univar, Canada), hydrogen peroxide (Merck, Darmstadt, Germany), sodium dihydrogen phosphate dihydrate (Univar, Canada), and methanol (Macron fine chemical, India) were received and used for this study. All chemical reagents were analytical-grade substances.

Apparatuses

A scanner (Scx-3405, Samsung) was used to record the experimental results. Transmission electron microscopy (TEM) was analyzed by JEM-2100 Plus Electron Microscope. Reversed-phase HPLC equipment (Agilent Pro star 230 series with column 150*4.6 mm*1/4" Valco Microsorb-MV 100-5 C18) was used to validate the accuracy of our proposed method.

Fabrication of distance-based paper device

Firstly, the pattern of our device was created in the CorelDrawX7 program, including sample zone (circle, diameter 7 mm) and detection zone (length, 40 mm). The black line was the hydrophobic part, and the white space was the hydrophilic part. Then, the pattern was printed on Whatman filter paper No.1 using the solid ink printer (ColorQube, Xerox, Thailand). Next, the paper device was melted an oven at 120 ℃ for 5 minutes. Finally, the paper device was cool down at room temperature and ready to use. A stock solution of 6.5 μL AgNPs were spotted two times onto the detection zone using an autopipette. AgNPs solutions were prepared

according to the previous report synthesis procedure [12]. Forty-five µL of potassium permanganate solution was mixed with the sibutramine solution/sample solution (1:1 v/v) in the microcentrifuge tubes and incubated for 15 minutes. The solution was then adjusted to acidic conditions by hydrochloric solution. The mixture solution was dropped for 20 µL onto the sample zone.

Preparation of slimming supplements samples

Dietary supplements were purchased from the local market Bangkok, Thailand, and online market applications. The sample solution was collected from dietary supplement capsules. The fine powder from the pills was weighed 0.020x g and dissolved with deionized water. Before analysis by distance-based paper devices, the sample solution was filtrated and made the final volume to 25.00 mL with deionized water. For the validation method by HPLC, 0.020x g of sample powder was dissolved in methanol. Then, the solution was filtrated and made the final volume to 25.00 mL with methanol.

Results and Discussion

Potassium permanganate is a powerful oxidizing reagent [13]. Permanganate is the excellent strong oxidation state in the six species oxidation state of manganese metal. Mn (VII) changes different oxidation states in alkaline media. The oxidation reaction is recovered in two steps in a procedure. Firstly, the formation of the rapid intermediary complex generates a green-blue color solution of hypomanganate (V) and manganate (VI). Then, the result of the reaction gives keto and/or keto acid derivatives as the products [14], [15].

Characterization

The important characteristic wavelength band in Fig. 1 is wavelength 525 nm as an absorption maximum of alkaline permanganate. The highest absorption peak of alkaline permanganate was decay when it had sibutramine analyte. Therefore, the solution color changed from purple to green color as the formation of manganate (VI) intermediate [13], [16]. The oxidation occurs manganate (VI) as a wavelength 606 nm band because of the weakness of MnO_4^- absorption. Accordingly, the experiment can detect uncomplicated manganate (VI) [14]. Silver nanoparticles present an absorbance wavelength peak at 520 nm [17]. This peak was disappeared while silver nanoparticles react to permanganate. The absorption of permanganate decreased the oxidation of sibutramine by permanganate and increased the sibutramine derivatives [16]. When silver nanoparticles were combined in solution, the adsorption permanganate was reduced. To confirm the interaction between alkaline permanganate and sibutramine was studied by TEM. The morphology was shown in the TEM pictures. The reducing particle scale caused potassium permanganate to reach silver nanoparticles as shown in Fig. 2 and 3. Silver nanoparticle size accumulated crosslinking by themselves after mixing sibutramine.
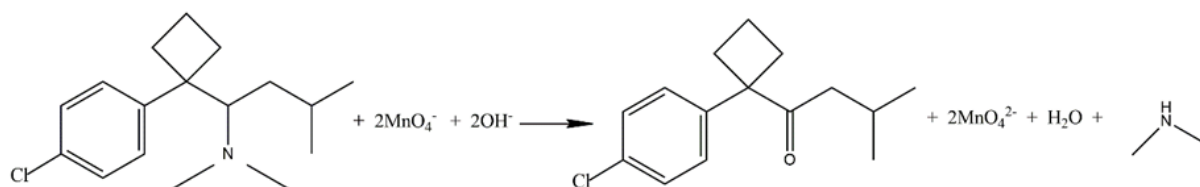
Fig. 1 Diagram shows the prediction of the oxidation reaction of sibutramine by permanganate ion in alkaline solution.
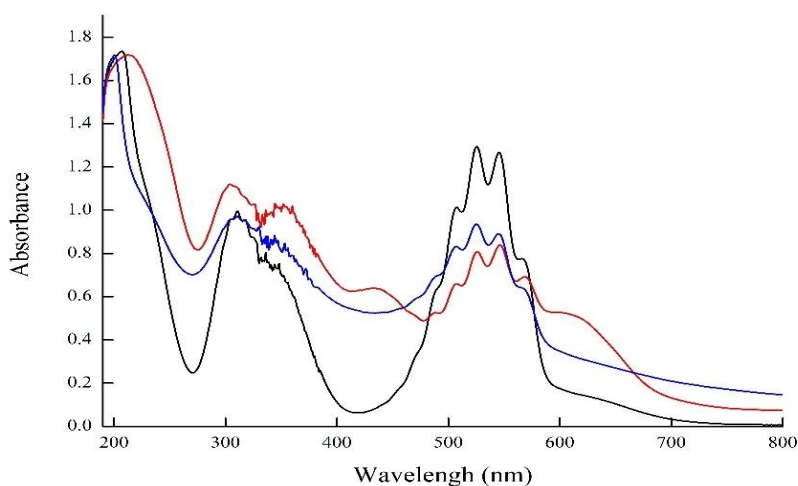
Fig. 2 The ultraviolet-visible spectrum the oxidation of sibutramine by alkaline medium permanganate (black line), the addition of 2 mg/L of sibutramine solution (red line), and the addition of silver nanoparticle solution (blue line).
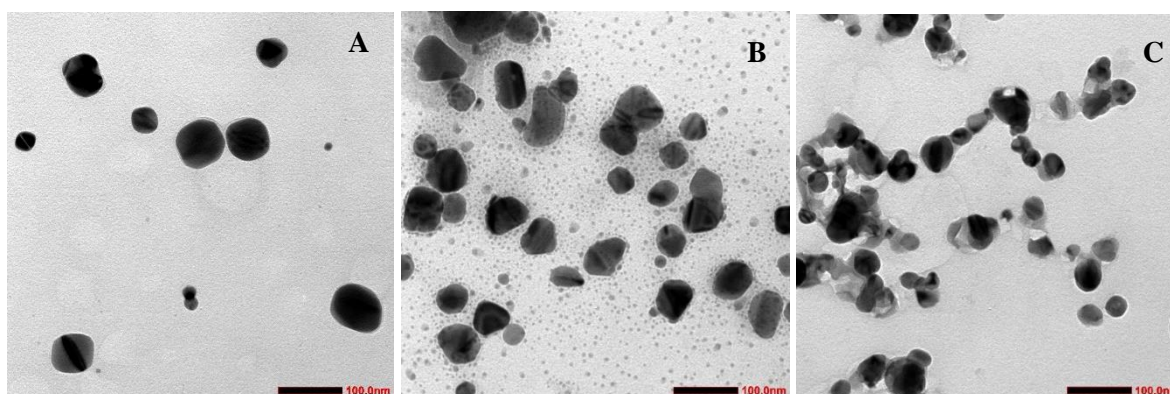
Fig. 3 The TEM picture shows etching of silver nanoparticles with potassium permanganate (A) the TEM picture shows the adding of 5 mg/L sibutramine, silver nanoparticles, and potassium permanganate (B) and the TEM picture shows the adding of 20 mg/L sibutramine, silver nanoparticles, and potassium permanganate (C).

Effect of KMnO₄ concentrations

The sibutramine concentration, time, pH were held constant, when potassium permanganate concentrations were studied in the various range of 2.5, 5, 7.5, 10, and 12.5 mmol/L. The plot of log(concentration of sibutramine, mg/L) between white color band distance (mm) was a linear relationship of reaction as shown in Table 1. Therefore, the optimal condition of potassium permanganate concentrations was 5 mmol/L because it showed a great determination coefficient (R-square = 0.9992). The permanganate remaining was received several sibutramine concentrations reacting permanganate solution onto the microcentrifuge tubes. The excess permanganate can react AgNPs onto the detection zone, so the white color band length decrease. Enough permanganate was related to the best coefficient of determination (good straight line). However, high excess permanganate (7.5 to 12.5 mmol/L) caused band distance unrelated linear relationship.

Table 1 The effect of KMnO₄ concentrations for 2.5 to 12.5 mmol/L

KMnO₄ (mmol/L)	Coefficient of Determination (R^2)
2.5	0.9937
5.0	0.9992
7.5	0.9896
10.0	0.9663
12.50	0.9878

b 2.5 b 5 b 7.5 b 10 b 12.5   mmol/L KMnO₄
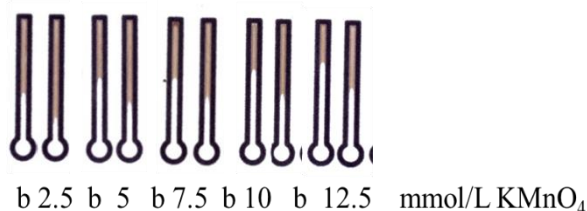
Fig. 4 The white color band length responses of the reaction between blank (b) and 10 mg/L sibutramine hydrochloride with several KMnO₄ concentrations (mmol/L)

Effect of range pH samples

The pH range samples solution was studied for the suitable oxidation reaction. This condition was studied through varying the types of buffer solutions (sodium-citrate buffer, sodium phosphate buffer, Tris-hydrochloride buffer, disodium hydrogen phosphate-sodium hydroxide buffer, and deionized water) in the reaction medium. The pH section was studied 3-12 pH. As the result can be seen pH 3 to 5 there is no white color band length because this condition is not suitable for this reaction [13]. Moreover, increasing pH conditions is an appropriate formation of manganate (VI) transient species [18]. However, deionized water is reasonable to change acidic conditions for permanganate ion and AgNPs onto devices. It was found that pH range affected sibutramine determination as shown in Fig. 5. The suitable condition was chosen deionized water to adjusted medium solution.
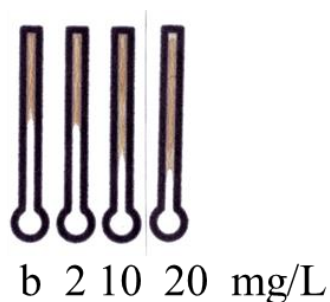
pH	Coefficient of Determination (R^2)
6	0.9896
7	0.9981
8	0.9060
9	0.9921
10	0.9916
11	0.9998
12	0.9995
Deionized water	0.9982

(A)

(B)

Fig. 5 The effect of range pH samples (A) The white color band length responses of blank (b) and 2, 10, and 20 mg/L sibutramine hydrochloride in deionized water sample condition with 5 mmol/L $KMnO_4$ concentrations (B)

Effect of time

The reaction time measured the period between potassium permanganate and sibutramine concentration, including 10 to 45 minutes. The results showed that Fig. 6 was described the relation log(concentration, mg/L) and color band distance (mm) as giving Coefficient of Determination (R^2) and several reaction times. During 15 minutes was observed distinctly distance of etching silver nanoparticles because sibutramine-transient complexes formation is short-lived intermediates. If this reaction time is too long then it is perhaps formation manganese (IV) as the final product [13]. Furthermore, the coefficient of determination at reaction time 15 minutes was acceptable and reduced time consumption of reaction.
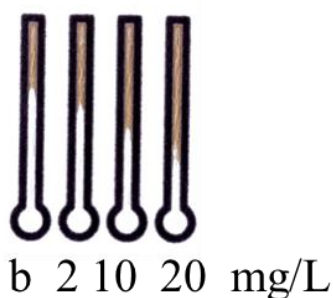
Time (min)	Coefficient of Determination (R^2)
10	0.9257
15	0.9992
20	0.9235
25	0.9887
30	0.9757
35	0.9644
40	0.9448
45	0.9957

(A)

(B)

Fig. 6 The effect of time (A) The white color band length responses of blank (b) and 2, 10, and 20 mg/L sibutramine hydrochloride in deionized water sample condition with 5 mmol/L $KMnO_4$ concentrations for 15 minutes reaction time (B)

Effect of interferences

As a result, indicated that the selectivity effect of sibutramine determination against other compounds: ascorbic acid, l-cysteine, chitosan, gallic acid, caffeine, and quercetin was investigated as ration 1:1 according to Fig. 7. Ascorbic acid and l-cysteine did not affect sibutramine detection because of distance variation less than 10% of the intensity white color band. However, chitosan, gallic acid, caffeine, and quercetin (other compounds mixed sibutramine ratio 1:1) were affect sibutramine determination. Thus, ascorbic acid or l-cysteine mixed sibutramine in ration 1:1 did not impact the reaction. According to Fig. 8, the concentrations of other compounds were researched 10 and 20 mg/L of sibutramine, ascorbic acid, l-cysteine, chitosan, gallic acid, caffeine, and quercetin. Ascorbic acid, l-cysteine, chitosan, gallic acid, caffeine did not impact sibutramine determination because they obtained the white color length equal to the blank solution. Only quercetin was observed effect to the permanganate oxidation and affect to white color length.
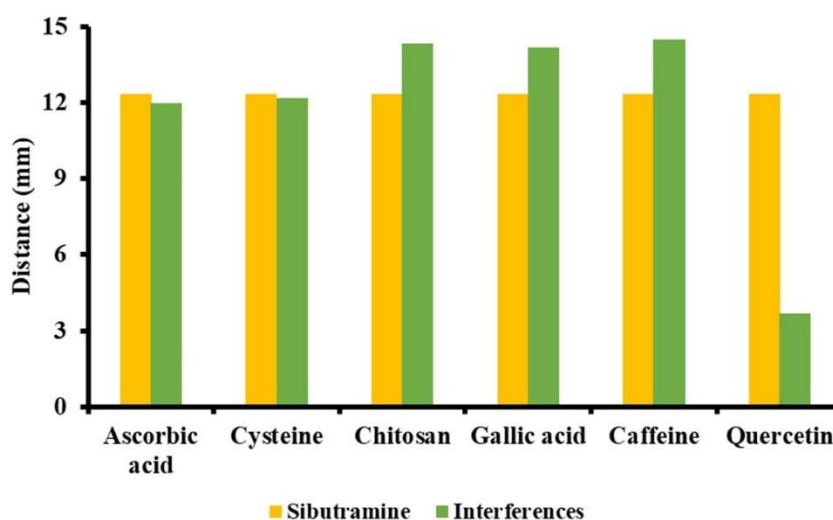
Fig. 7 Selectivity of sibutramine determination against other compounds: ascorbic acid, l-cysteine, chitosan, gallic acid, caffeine, and quercetin ration 10:10 ppm with white color band length (mm)
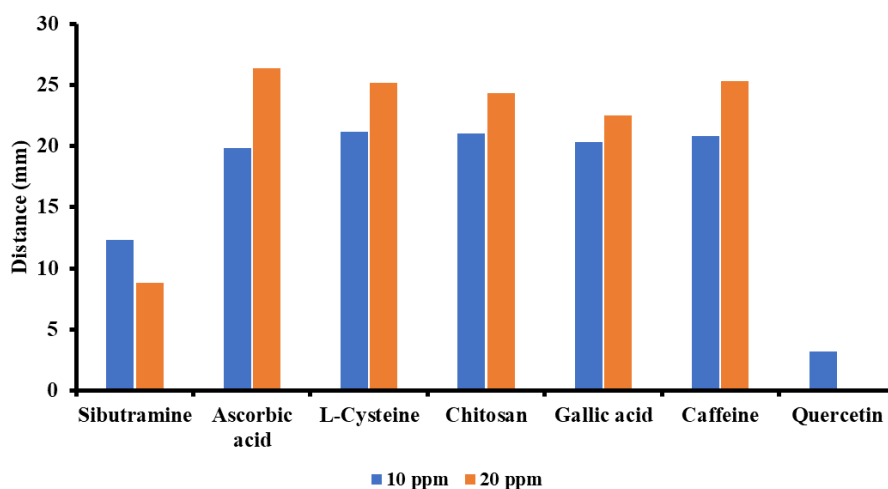
Fig. 8 The effect of sensitivity 10 and 20 mg/L including sibutramine, ascorbic acid, l-cysteine, chitosan, gallic acid, caffeine and quercetin with white color band length (mm)

Analytical validation

The analytical performance of the paper-based devices for sibutramine detection was shown under the best condition. The measurement of sibutramine determination measured etching silver nanoparticle distance by ruler scale. The linear relationship was obtained between logarithmic plot of sibutramine concentrations and distance in the range 2.0-50.0 mg/L. The linear relationship and coefficient of determination were Y= -11.148X + 23.626 and 0.9852, respectively. The limit of quantification (LOQ) and limit of detection (LOD) were 2.0 mg/L with observed the eyes, and researchers can monitor clearly by the naked eye. The relative standard deviation (RSD) of sibutramine determination was 12.66, 6.60 and 11.45% for 5, 20 and 50 mg/L, respectively (n=10). Moreover, the process can practice for the detection of sibutramine in slimming supplement samples. The detection limit and sibutramine detection were predominant comfortable to use the device and apply various samples.
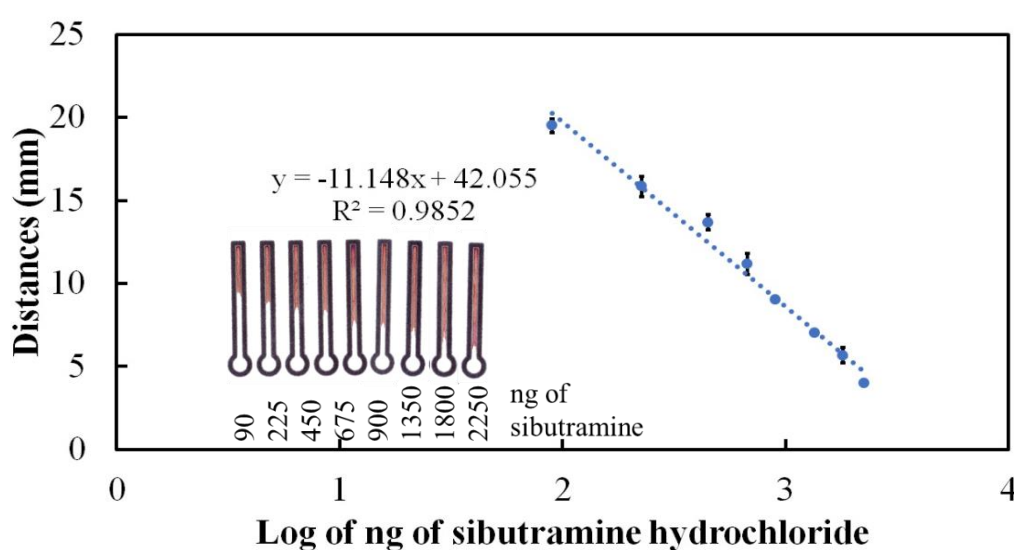
Fig. 9 The calibration curve of sibutramine concentration between 2 to 50 mg/L (90 to 2250 ng) of sibutramine concentration and white color band length (mm)

Application in real samples

Several dietary supplement samples were purchased from the local market and shopping market application online. This work was applied to discover sibutramine quantitative for 8 sliming supplement samples. The device was discovered sibutramine in dietary supplement samples at a range of concentration 3.85-5.74 mg/L (According to Table 4). The spiking levels are added 4 and 8 mg/L and the recovery values were obtained in the range of 89-114% [19]. The conditions were shown that the developed method and HPLC method were determined sibutramine detection by permanganate oxidation. The information two methods were compared by a paired t-test at the 95% confidence level (paired t-test value gave $t_{calculated}$ (-0.068) below $t_{critical}$ (4.303), n=3). This work and validation method were not significant the mean values of sibutramine concentration between the two methods.

Table 2 Sibutramine in real samples was quantitatively determined by comparing our method and the HPLC method.

Samples	Adding (mg/L)	This work		HPLC method	
		Found	%Recovery	Found	%Recovery
1	0	ND	-	ND	-
	4	4.23 ± 0.42	106	3.92 ± 0.39	98
	8	8.68 ± 0.41	109	7.71 ± 0.03	96
2	0	19.25 ± 0.34	-	20.80 ± 0.09	-
	4	23.60 ± 0.51	93	24.10 ± 0.10	103
	8	27.23 ± 0.63	106	28.51 ± 0.05	102
3	0	ND	-	ND	-
	4	4.13 ± 0.21	103	4.09 ± 0.06	102
	8	7.69 ± 0.40	96	7.67 ± 0.12	96
4	0	ND	-	ND	-
	4	4.45 ± 0.23	111	3.79 ± 0.04	95
	8	8.86 ± 0.45	107	7.81 ± 0.05	98
5	0	28.70 ± 0.29	-	29.40 ± 0.03	-
	4	32.60 ± 0.50	105	33.44 ± 0.04	101
	8	37.82 ± 0.77	114	37.32 ± 0.12	99
6	0	ND	-	ND	-
	4	4.28 ± 0.00	107	3.99 ± 0.12	100
	8	8.01 ± 0.85	100	7.93 ± 0.10	100
7	0	ND	-	ND	-
	4	4.14 ± 0.21	103	4.07 ± 0.06	101
	8	7.41 ± 0.00	92	8.10 ± 0.04	101
8	0	20.80 ± 0.21	-	18.60 ± 0.02	-
	4	24.36 ± 0.40	89	22.40 ± 0.14	95
	8	28.04 ± 0.62	103	26.68 ± 0.24	101

ND = Non detectable

Conclusion

The oxidation of sibutramine hydrochloride by potassium permanganate in an alkaline medium has been researched. The amount of sibutramine in dietary supplementary was successfully quantitatively analyzed by naked-eye. Moreover, this work was observed a low detection limit and clearly distinguish experiment results. Consequently, the µPADs were comprehensive for uncomplicated, inexpensive, and on-site analysis.

Acknowledgements

References

[1]   L. M. de Carvalho *et al.*, "Presence of synthetic pharmaceuticals as adulterants in slimming phytotherapeutic formulations and their analytical determination.," *Forensic Sci. Int.*, vol. 204, no. 1–3, pp. 6–12, Jan. 2011, doi: 10.1016/j.forsciint.2010.04.045.

[2]   J. M. Carvalho, A. R. Da Silva, A. L. M. C. Da Cunha, R. Q. Aucélio, M. A. André Luis, and C. L. Katia, "Voltammetric determination of sibutramine in beverages and in pharmaceutical formulations," *Quim. Nova*, vol. 35, no. 5, pp. 988–992, 2012, doi: 10.1590/S0100-40422012000500023.

[3]   P. Phattanawasin, U. Sotanaphun, T. Sukwattanasinit, J. Akkarawaranthorn, and S. Kitchaiya, "Quantitative determination of sibutramine in adulterated herbal slimming formulations by TLC-image analysis method.," *Forensic Sci. Int.*, vol. 219, no. 1–3, pp. 96–100, Jun. 2012, doi: 10.1016/j.forsciint.2011.12.004.

[4]   Y. Guo, Y. Ni, J. Chen, and S. Kokot, "A kinetic spectrofluorometric method, aided by chemometrics, for the analysis of sibutramine, indapamide and hydrochlorothiazide compounds found in weight-reducing tonic samples," *Anal. Methods*, vol. 8, no. 1, pp. 197–204, 2016, doi: 10.1039/C5AY02191J.

[5]   E. Ariburnu, M. F. Uludag, H. Yalcinkaya, and E. Yesilada, "Comparative determination of sibutramine as an adulterant in natural slimming products by HPLC and HPTLC densitometry.," *J. Pharm. Biomed. Anal.*, vol. 64–65, pp. 77–81, May 2012, doi: 10.1016/j.jpba.2012.02.004.

[6]   M. J. Bogusz, H. Hassan, E. Al-Enazi, Z. Ibrahim, and M. Al-Tufail, "Application of LC–ESI–MS–MS for detection of synthetic adulterants in herbal remedies," *J. Pharm. Biomed. Anal.*, vol. 41, no. 2, pp. 554–564, 2006, doi: https://doi.org/10.1016/j.jpba.2005.12.015.

[7]   P. Wilson and C. Masse, "Detection of Synthetic Drugs as Adulterants in Natural and Herbal Slimming Products by LC-ESI-MS/MS with Polarity Switching.," *J. AOAC Int.*, vol. 99, no. 4, pp. 929–940, Jul. 2016, doi: 10.5740/jaoacint.15-0295.

[8]   L. M. de Carvalho, M. Martini, A. P. Moreira, S. C. Garcia, P. C. d. Nascimento, and D. Bohrer, "Determination of synthetic pharmaceuticals in phytotherapeutics by capillary zone electrophoresis with contactless conductivity detection (CZE-C4D)," *Microchem. J.*, vol. 96, no. 1, pp. 114–119, 2010, doi: 10.1016/j.microc.2010.02.006.

[9]   E. Deconinck, T. Cauwenbergh, J. L. Bothy, D. Custers, P. Courselle, and J. O. De Beer, "Detection of sibutramine in adulterated dietary supplements using attenuated total reflectance-infrared spectroscopy.," *J. Pharm. Biomed. Anal.*, vol. 100, pp. 279–283, Nov. 2014, doi: 10.1016/j.jpba.2014.08.009.

[10]   L.-M. Fu and Y.-N. Wang, "Detection methods and applications of microfluidic paper-based analytical devices," *TrAC Trends Anal. Chem.*, vol. 107, pp. 196–211, 2018, doi: https://doi.org/10.1016/j.trac.2018.08.018.

[11]   C. T. Gerold, E. Bakker, and C. S. Henry, "Selective Distance-Based K+ Quantification on Paper-Based Microfluidics," *Anal. Chem.*, vol. 90, no. 7, pp. 4894–4900, Apr. 2018, doi: 10.1021/acs.analchem.8b00559.

[12]   T. Parnklang, C. Lertvachirapaiboon, P. Pienpinijtham, K. Wongravee, C. Thammacharoen, and S. Ekgasit, "H2O2-triggered shape transformation of silver nanospheres to nanoprisms with controllable longitudinal LSPR wavelengths," *RSC Adv.*, vol. 3, no. 31, pp. 12886–12894, 2013, doi: 10.1039/C3RA41486H.

[13]   R. Hassan, A. R. Dahy, S. Ibrahim, I. Zaafarany, and A. Fawzy, "Oxidation of Some Macromolecules. Kinetics and Mechanism of Oxidation of Methyl Cellulose Polysaccharide by Permanganate Ion in Acid Perchlorate Solutions," *Ind. Eng. Chem. Res.*, vol. 51, no. 15, pp. 5424–5432, Apr. 2012, doi: 10.1021/ie200646p.

[14] R. M. Hassan, "Alginate polyelectrolyte ionotropic gels. XIV. Kinetics and mechanism of formation of intermediate complex during the oxidation of alginate polysaccharide by alkaline permanganate with a spectrophotometric evidence of manganate(VI) transient species," *J. Polym. Sci. Part A Polym. Chem.*, vol. 31, no. 1, pp. 51–59, Jan. 1993, doi: https://doi.org/10.1002/pola.1993.080310106.

[15] K. S. Khairou and R. M. Hassan, "Pectate polyelectrolyte ionotropic gels 1. Kinetics and mechanisms of formation of manganate (VI)-pectate intermediate complex during the oxidation of pectate polysaccharide by alkaline permanganate," *Eur. Polym. J.*, vol. 36, no. 9, pp. 2021–2030, 2000, doi: 10.1016/S0014-3057(99)00040-3.

[16] A. Fawzy, S. A. Ahmed, I. I. Althagafi, M. H. Morad, and K. S. Khairou, "Kinetics and Mechanistic Study of Permanganate Oxidation of Fluorenone Hydrazone in Alkaline Medium," *Adv. Phys. Chem.*, vol. 2016, p. 4526578, 2016, doi: 10.1155/2016/4526578.

[17] W. Leesutthiphonchai, W. Dungchai, W. Siangproh, N. Ngamrojnavanich, and O. Chailapakul, "Selective determination of homocysteine levels in human plasma using a silver nanoparticle-based colorimetric assay," *Talanta*, vol. 85, no. 2, pp. 870–876, 2011, doi: https://doi.org/10.1016/j.talanta.2011.04.041.

[18] A. M. Shaker, "Base-catalyzed oxidation of carboxymethyl-cellulose polymer by permanganate," *J. Colloid Interface Sci.*, vol. 233, no. 2, pp. 197–204, 2001, doi: 10.1006/jcis.2000.7246.

[19] AOAC International, "Guidelines for Single Laboratory Validation of Chemical Methods for Dietary Supplements Botanicals," *Assoc. Off. Anal. Chem.*, pp. 1–38, 2002.

DFT Investigations on Depolymerization Mechanism of Lignin Oligomer Catalyzed by Pd/NbOPO$_4$

Jiajia He,[1] Dianyong Tang,[2*] Changwei Hu,[1] Chan Kyung Kim,[3*] Zhishan Su[1*]

[1]Key Laboratory of Green Chemistry and Technology, Ministry of Education, College of Chemistry, Sichuan University, Chengdu, Sichuan 610064, P. R. China.
[2]College of Pharmacy & International Academy of Targeted Therapeutics and Innovation, Chongqing University of Arts and Sciences, Chongqing 402160, China.
[3]Department of Chemistry and Chemical Engineering, Inha University, 100 Inha-ro, Michuhol-gu, Incheon 22212, Korea.

Abstract

With the increasingly serious environmental problems, the development and utilization of new renewable energy have attracted much attention. The catalytic depolymerization of lignin to produce high value-added chemicals and biofuels is of great significance for sustainable development. [1,2] Experimental results indicated that Pd/NbOPO$_4$exhibitedgoodcatalytic performance for efficient degradation of oligomers in pubescens.[2] The aromatic monomers and small molecular weight oligomers are obtained at low temperature. To understand the role of Pd/NbOPO$_4$ in the depolymerization reaction, DFT calculations have been performed using CP2K and LASP programs, with Gaussian Plane Wave method and PBE functional. The calculations indicated that NbO$_x$ species on the catalyst facilitated the breakage of β-O-4bond of oligomer, with the energy barrier of ~0.9 eV. The resulting small molecule fragments were further converted into aromatic monomers by C-C bond breakage in the presence of Pd species. Possible depolymerization pathways for the oligomer fragments (**A** and **B**) were proposed, in which the C$_\beta$-C$_\gamma$ bond breakage, decarboxylation and hydrogenation of side chain unsaturated bonds are involved.
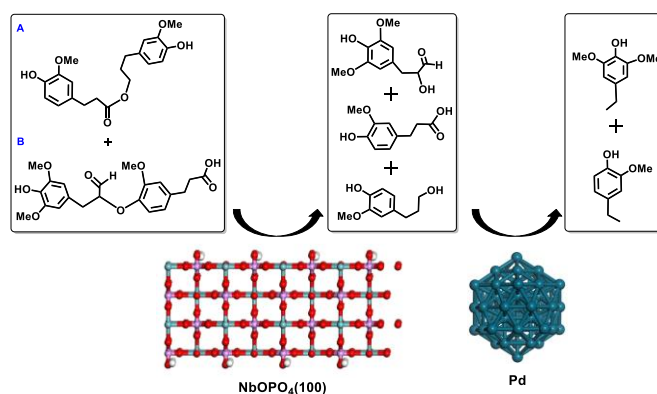
Figure 1. Depolymerization mechanism of oligomers (**A** and **B**) catalyzed by Pd/NbOPO$_4$.

References
[1] Q. N. Xia, Q. Cuan, X. H. Liu, X. Q. Gong, G. Z. Lu, Y. Q. Wang, *Angew. Chem. Int. Ed.* **2014**, *53*, 9755.
[2] Q. Y. Fang, Z. C. Jiang, K. Guo, X. D. Liu, Z. Li, G. Y. Li, C. W. Hu, *Appl. Catal. B-Environ.*, **2020**, *263*, 118325.

Theoretical Research of 2, 3, 5, 6-Tetra(1H-tetrazol-5-yl) pyrazine and 1,1-Diamino-2,2-Dinitroethylene Blending System

Jun Li,[1*] Wendong Liu,[1] Xinhui Zhang,[1] Yueyang Wang,[1]
Zongchang Li,[1] Xinan Chen,[1] Yiqing Zhang,[1] and Chan Kyung Kim[2*]

[1]Department of Chemical Engineering, North University of China, 3#, Xueyuan Road, Taiyuan 030051, China
[2]Department of Chemistry and Chemical Engineering, Inha University, Incheon, 22212, Korea

Abstract

Herein, to study the properties of 2, 3, 5, 6-tetra(1H-tetrazol-5-yl) pyrazine (H_4TTP) and 1,1′-diamino-2,2′-dinitroethylene (FOX-7) blending system, the H_4TTP, FOX-7 monomers and H_4TTP/FOX-7 dimers was optimized using density functional theory (DFT), and the binding energy, mechanical properties and cohesive energy density of H_4TTP/FOX-7 blends with different mass ratios were calculated by molecular dynamics (MD) simulation. The results show that the HOMO of H_4TTP molecule is distributed on the pyrazine ring and the tetrazole ring, while the LUMO are mainly distributed on the pyrazine ring, with a small amount on the tetrazole ring. The HOMO of FOX-7 molecules is mainly located on the C=C bonds, while the LUMO are mainly located on the nitro groups. There exists van der Waals (vdW) interaction between H_4TTP and FOX-7 molecules in the H_4TTP/FOX-7 dimers and O···H-N hydrogen bonds between the nitro-O atoms of FOX-7 and the H atoms of H_4TTP. In H_4TTP molecule, steric hindrance effect exists inside the pyrazine ring in the center, and N···H-N hydrogen bonds exist between the two tetrazole rings, which belong to strong hydrogen bond. In FOX-7 molecule, there are relatively strong O···H-N internal hydrogen bonds between the nitro-O atoms and the amino-H atoms. When the mass ratio of H_4TTP and FOX-7 is 2/1, the H_4TTP/FOX-7 blending system is the most stable. FOX-7 and H_4TTP have stronger rigidity and elasticity, respectively, and the H_4TTP/FOX-7 blending systems with mass ratios of 1/3 and 1/2 show brittleness. In addition, FOX-7 has the best ductility, and H_4TTP has the best toughness. The blending structures of H_4TTP/FOX-7 improve the sensitivity of H_4TTP and the safety of explosives.
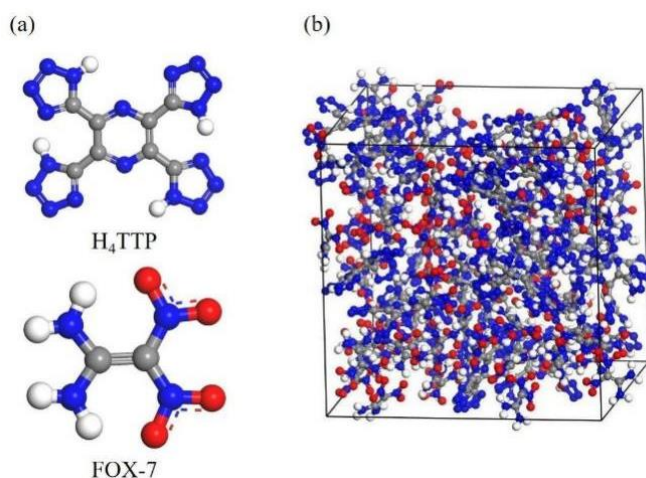
Fig. 1. (a) Molecular structures of H_4TTP and FOX-7; (b) Blending model of H_4TTP/FOX-7 with a mass ratio of 1/1 (C, H, O, N are represented by gray, white, red, and blue colors, respectively)
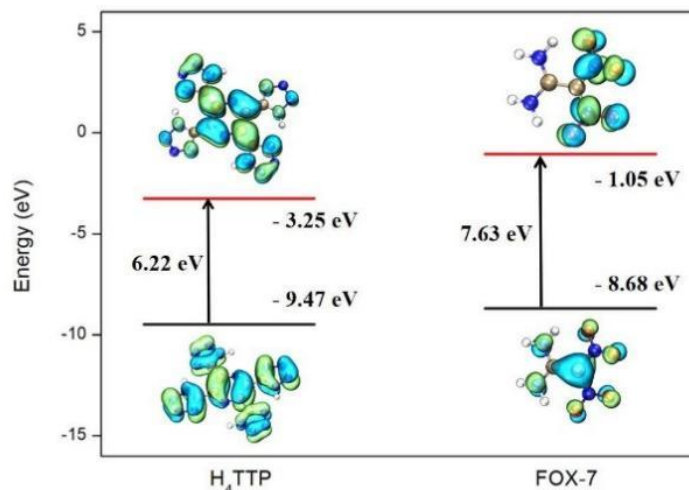
Fig. 2. Frontier molecular orbitals and energy gaps of H₄TTP and FOX-7 molecules
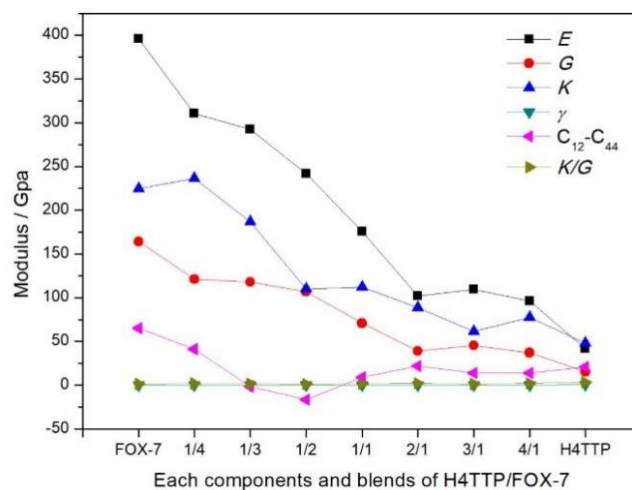
Fig. 3. Mechanical properties of H₄TTP/FOX-7 each component and blends

Acknowledgements

References

1. Lu T, Chen Q. Interaction Region Indicator: A Simple Real Space Function Clearly Revealing Both Chemical Bonds and Weak Interactions[J]. Chemistry-Methods, 2021,1: 231-239.

2. Yang Z J, Tang L, Wen T Q, et al. Effects of Si solute on the glass formation and atomic structure of Pd liquid[J]. Journal of Physics Condensed Matter, 2019, 31, 135701.

3. Tang L, Wen T Q, Wang N, et al. Structural and Chemical Orders in Ni$_{64.5}$Zr$_{35.5}$ Metallic Glass by Molecular Dynamics Simulation[J]. Physical Review Materials, 2018, 2(3).

Single-atom copper anchored on t-BaTiO₃ for piezo-Fenton degradation of tetracycline

Zeda Meng*, Quanzi Pan, Xin Ni

Provincial Key Laboratory of Environmental Science and Engineering, College of Chemistry and Bioengineering, Suzhou University of Science and Technology, Suzhou 215009, China

* Corresponding author. Tel:+86-512-68056461; Fax:+86-512-69209055;
Email: compelitely@163.com

Abstract

In summary, the monoatomic copper nanoparticles anchored on the tetragonal BaTiO₃ were prepared, and their piezoelectric catalytic activity was studied through the degradation of tetracycline solution. Under the larger piezoelectric potential on the surface of the catalyst, the conduction band and valence band move, which accelerates the easier and faster migration of electrons and holes when reacting with dissolved oxygen. The rate of generation of hydrogen peroxide increases, and the concentration of hydroxyl radicals in the solution increases. Cu-BaTiO₃ nanomaterials also showed excellent piezoelectric catalytic activity and stability during four consecutive piezoelectric catalytic processes.

A general in situ deposition strategy for synthesis of porous material with asymmetric wettability

Jingming Wang, Luyang Hu, Yin Liu

School of Materials Science and Engineering, Anhui University of Science and Technology, Huainan, 232001, China.

Abstract

The Janus porous material with asymmetric wettability endows it versatile and promising in many applications. However, it is usually difficult to prepare because of the diffusion of modifiers by the capillary effect in porous structures. In the paper, a general strategy, including surface hydrophobization, oxidation treatment and chemical bath deposition (CBD), is proposed for the preparation of the Janus porous material. The obtained material generally maintains the structure of the substrate, and one side is hydrophilic and the other side is hydrophobic. Especially using the water-wetted Janus fabric as a separation cell, the permeation flux is enhanced by 214.5% for water and by 112.5% for oil, respectively, compared to that in the pristine fabric. Thus, this work provides a new route to develop multifunctional materials for potential application in quick oily wastewater remediation.

Keywords: Janus porous materials; In situ deposition; Wettability; microstructure

In daily production and life, large amounts of oily wastewater are generated. How to effectively treat these polluted water have become a global issue. A better approach is use porous material with special wettability for adsorption removal of oil. It is noted that the adsorption capacity of these materials is mainly dependent on their porous structure, and density and viscosity of oil. Once the adsorption is saturated, there is no extra space for oil storage. In order to recover adsorption function, the absorbed oil need to be removed first by distillation, squeezing or burning. Compared to the indirect route of oil-water separation process, continuous oil-water separation under gravity or pressure displays high flexibility. In these filters used for direct oil/water separation, most of which are obtained by the common porous material, such as stainless steel mesh, copper mesh, sponge, fabric, as a substrate to construct the required microstructure and superwetting property. Due to existence of the postmodification process, the separation medium commonly shows a reduced porosity and pore size relative to the substrate. Therefore, it is a challenge to improve the flux under a high separation efficiency and gravity driven for the filtration material with the fixed framework. In the paper, we develop a general preparation strategy of Janus porous material with asymmetric wettability for the fast fluid transmission. The detailed procedure of our synthesis design is exhibited in scheme 1.
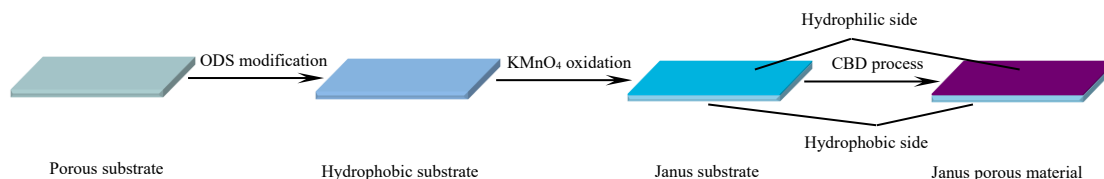
Scheme 1. Schematic illustration of the preparation process of a Janus porous material.

Take cotton fabric as an example, Fig.1a shows the photographs of pristine cotton fabric, Janus cotton fabric and Janus composite fabric. After the KMnO$_4$ oxidation and CBD treatment, the ordered woven structure of fabric is maintained (Fig.1b). The well-established texture structure of the Co(CO$_3$)$_{0.5}$OH·0.11H$_2$O nanoneedle array grows on the cotton fabric to form a large-scale hydrophilic coating. It is note that some bare fibers locate a few tens of microns (about 40 μm) below the surface and parallel to composite fibers can be found. Because the permeation and separation performance of porous material is related to its surface wettability, water contact angles (WCAs) on each surface of the Janus fabric are measured, as shown in Fig.1c and 1d. The hydrophilic side of Janus composite fabric exhibits a smaller initial WCA of about 39°, which continuously decreases to apparent 0° within 30 s. The water droplet on the Janus composite fabric gradually permeates through the fabric pores without obvious spreading on the hydrophobic side, indicating the directional water transport property of the material.
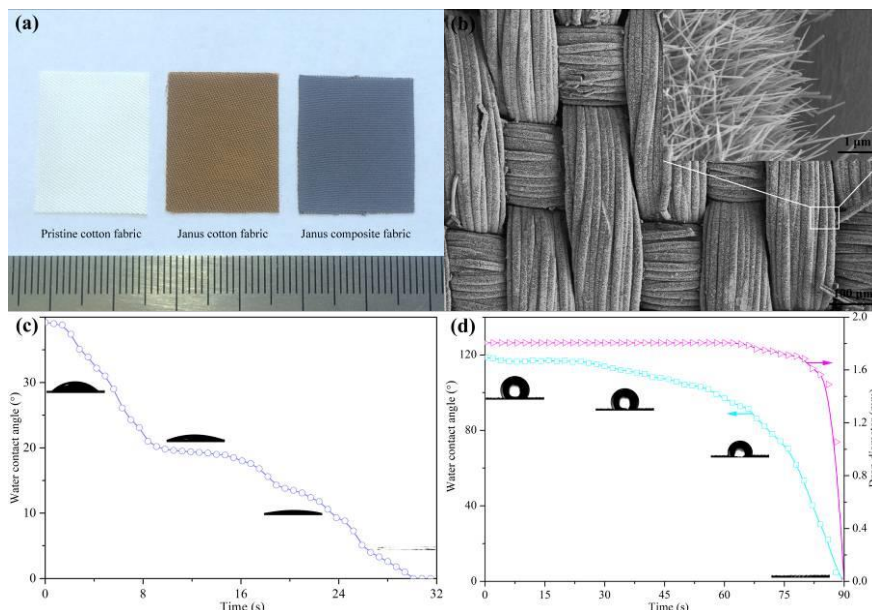
Fig.1 a) Photographs of the samples. b) SEM images of the hydrophilic side of the Janus composite fabric. The insert shows Co(CO$_3$)$_{0.5}$OH·0.11H$_2$O nanoneedle arrays and bare cotton fiber. c) Dynamic water contact angles on the hydrophilic side of Janus composite fabric. d) Water contact angles and drop diameters evolution with time for the hydrophobic side of Janus composite fabric.

Enlightened by the above-mentioned work, it is found that the synthesis of Janus composite fabric with 1D nanostructured $Co(CO_3)_{0.5}OH\cdot0.11H_2O$ arrays is easily extended to other substrates, such as melamine sponge, Ni foam, and cellulose paper. The typical photographs of hydrophilic side (upper row) and hydrophobic side (lower row) of corresponding Janus composite materials are shown in Fig.2a. Both sides with a distinct color difference can be seen. Fig.2b-d exhibit SEM images of hydrophilic side of these materials. It is obviously observed that the $Co(CO_3)_{0.5}OH\cdot0.11H_2O$ nanoneedles also grow only on surface layer of Janus material which is consistent with that on hydrophilic side of Janus fabric (Fig.1b).
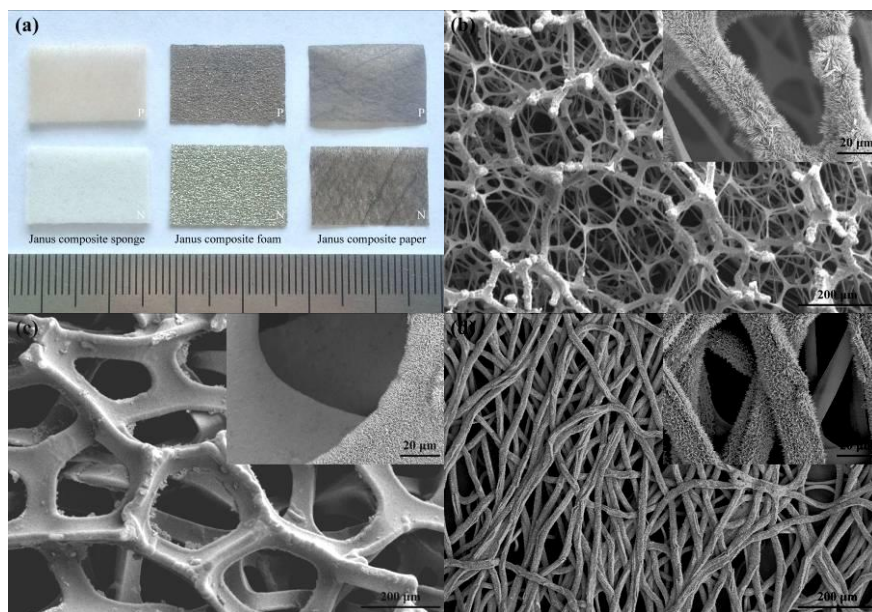
Fig.2. a) Photographs of samples (P: Hydrophilic side, N: Hydrophobic side). SEM images of the hydrophilic side of b) Janus composite sponge, c) Janus composite foam and d) Janus composite paper. The insert shows a magnified image.

In the paper, we use the Janus composite fabric with $Co(CO_3)_{0.5}OH\cdot0.11H_2O$ nanoneedles as an example to demonstrate the application of such material in oil and water separation. It is found that if the composite Janus fabric with water-wetted hydrophilic side is first fixed upward, and then dichloromethane is poured on the fabric, once the water film is completely broken by the oil, the separation time for the Janus fabric will decrease by 12.5% compared to the pristine fabric (Fig.3a). In addition to increasing the flux of the oil, such fabric can also be used to enhance the separation of water by changing the direction of the fabric. For example, when the composite Janus fabric is fixed with hydrophilic side downward, 11.4 mL water is separated in 28.3 s while the pristine cotton fabric takes 60.7 s to complete the penetration (Fig.3b). Thus, it is possible for the filtration material with the fixed framework to obtain an improved flux under gravity driven.
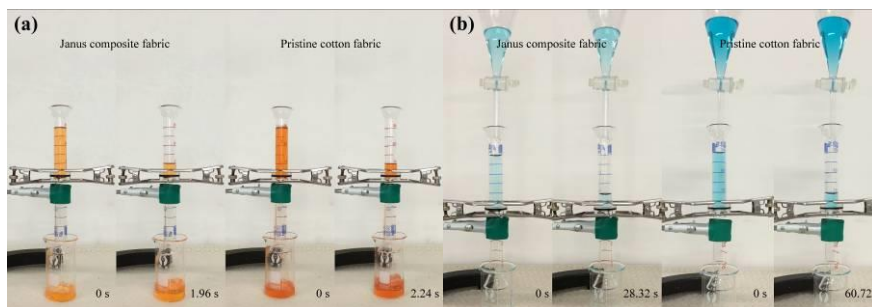
Fig. 3. a) Digital photos of dichloromethane transmission through the Janus composite fabric with oil-broken water channel and the pristine cotton fabric, respectively. b) Digital photos of water transmission through the Janus composite fabric and the pristine cotton fabric, respectively.

In summary, we fabricated a Janus composite fabric with $Co(CO_3)_{0.5}OH \cdot 0.11H_2O$ nanoneedle arrays by combining surface hydrophobization, $KMnO_4$ oxidation and CBD treatment. The facile Janus material synthesis strategy could be extended to various substrates such as melamine sponge, Ni foam, and cellulose paper. Taking the Janus composite fabric with deposited $Co(CO_3)_{0.5}OH \cdot 0.11H_2O$ nanoneedle array as an example, the wetted Janus composite fabric presented a higher permeability than the pristine one. This study opened up a new way towards the rational design and development of advanced and efficient functional materials for selective oil and water separation.

Acknowledgments

References

[1] L. Hu, Y. Liu, Z. Wang, et al., *ACS Appl. Nano Mater.* 3 (2020) 3779-3786.
[2] B. Wang, W. Liang, Z. Guo, et al., *Chem. Soc. Rev.* 44 (2015) 336-361.

Molecular dynamics simulation of mechanical properties of $Fe_{0.5}Ti_{0.5}$-CNT nanocomposites

Xinxin Wang, Chao Zhang*, Jiangwei Xu, Yin Liu，Chuyang Xu

School of Materials Science and Engineering, Anhui University of Science and Technology, Huainan 232001, China

Abstract

$Fe_{0.5}Ti_{0.5}$ alloy is not only a kind of important hydrogen storage material with the advantages of large hydrogen storage capacity and low price, but also has great application potential in the fields of automobile, aerospace and biomechanics due to its high strength and good ductility. In this paper, based on the molecular dynamics simulation method, the functional $Fe_{0.5}Ti_{0.5}$-CNT nanocomposites were prepared by embedding carbon nanotubes into the nanocrystals of polycrystalline $Fe_{0.5}Ti_{0.5}$ alloy. Compared with the polycrystalline $Fe_{0.5}Ti_{0.5}$ alloy, the strength and plasticity of the $Fe_{0.5}Ti_{0.5}$-CNT nanocomposites are significantly improved, and the unique structure of carbon nanotubes also plays a role in other functions of nanocomposites.

Keywords: Nanocomposites; Molecular dynamics simulation; carbon nanotube; FeTi alloys

1. Introduction

With the industrial demand for high melting point, high strength and low density materials, intermetallic compounds NiTi, NiAl and FeTi have gradually attracted extensive attention. As a Ti based alloy, FeTi alloy not only has attractive advantages, but also is widely used in hydrogen storage materials[1]. However, cracks may occur in FeTi alloy during hydrogen absorption, and serious cracks may lead to the decrease of mechanical properties of the alloy, which will hinder its wide application. Based on the above reasons, people gradually have a strong interest in nanocrystalline alloys.

Carbon nanotubes (CNTs) are one of the most promising reinforcement materials in composites with excellent mechanical and thermal properties[2]. In addition, in 2010, Ackland[3] predicted that CNTs with general strengthening properties and inner surfaces could be used as "nanodustbins" for storing defects and gas atoms. nanocrystalline metallic materials rich in GBs have ultra-high strength and hardness. Combined with rich GBs and 3D CNT networks, the overall concept of network nanocomposites can be constructed, which is a strategy with broad application prospects for future high-performance material design.

In this paper, bulk $Fe_{0.5}Ti_{0.5}$-CNT nanocomposites are selected as the research model materials. The bulk $Fe_{0.5}Ti_{0.5}$-CNT nanocomposites with carbon nanotubes were prepared by adding carbon nanotubes into the $Fe_{0.5}Ti_{0.5}$-CNT nanocomposites. This method can greatly reduce brittleness, matrix crack and cavity expansion. At the same time, the thermal conductivity and mechanical integrity of the material can be improved by rapid heat transfer and stress load transfer through the embedded carbon nanotubes.

2. Simulation details

The molecular dynamics simulation of $Fe_{0.5}Ti_{0.5}$-CNT (15,15) nanocomposites system was carried out using large-scale parallel atom/molecule simulator (LAMMPS) [4], and the mechanical properties of $Fe_{0.5}Ti_{0.5}$-CNT (15,15) nanocomposites were calculated. Meam potential [5] was used to describe the interaction of Fe-Fe, Fe-C, Fe-Ti and Ti-C. Through the combination of Atomsk software and Lammps, the $Fe_{0.5}Ti_{0.5}$-CNT (15,15) nanocomposites model with a size of $20\times20\times40$ nm was established, which contains 1015023 atoms (20 grains in total) with an average grain size of 9.283 nm. The model structure is shown in Fig. 1.

Uniaxial tensile simulation was carried out, and the time step of the whole simulation process was 0.001 ps. At 300 K, NPT ensemble equilibrium model was used. After balancing, the model loading process was realized by applying a certain deformation rate to the simulation box under NPT ensemble. Under the constant strain rate of 0.01 ps^{-1}, no pressure was applied in the x- and y-directions, and uniaxial tensile deformation was carried out in the z direction. The simulation results were visualized and statistically analyzed by OVITO software [6]. CNA and dislocation extraction algorithm (DXA) were used to identify the lattice structure and distortion generated during stretching [7].

FeTi alloy   CNT   FeTi-CNT alloy
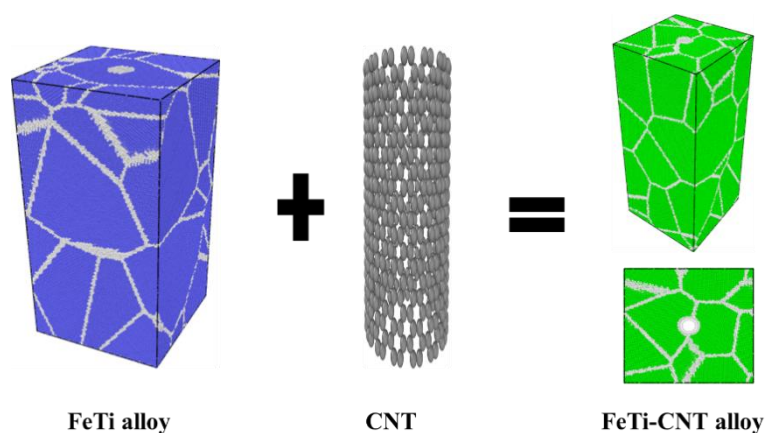
Fig. 1 Common neighbor analysis shows $Fe_{0.5}Ti_{0.5}$-CNT nanocomposites structure

3. Results

Fig. 2 shows the stress-strain curve of $Fe_{0.5}Ti_{0.5}$-CNT nanocomposites under uniaxial tensile load at room temperature (300 K). It can be seen from the figure that the whole system has undergone three stages of deformation under tensile load, namely elastic deformation stage, yield stage and plastic deformation stage. At the beginning of tensile, the stress-strain relationship is linear, obeying Hooke's law, and the stress changes linearly with strain, corresponding to the linear part of the curve in Fig. 2. The deformation is elastic deformation, and it disappears if the loading is stopped at this stage, which is consistent with the elastic deformation in the tensile process of single crystal metal. The yield strength σe and tensile strength σb of the material are 3.464 GPa and 5.273 GPa, respectively. By fitting the slope of the 0-0.03 strain segment of the stress-strain curve, the Young's modulus E of the tensile direction is 115.21 GPa. Compared with $Fe_{0.5}Ti_{0.5}$ alloy, $Fe_{0.5}Ti_{0.5}$-CNT nanocomposites have good ductility.
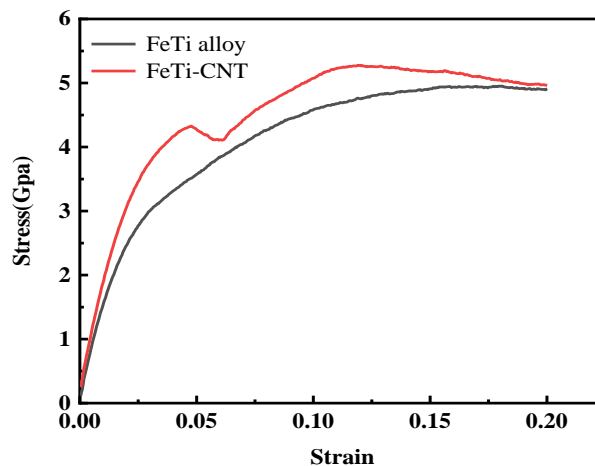
Fig 2. Stress-strain curves of $Fe_{0.5}Ti_{0.5}$-CNT nanocomposites

In order to study the microstructure changes of nanocomposites under tensile loading, the atomic structure diagrams of nanocomposites under different tensile strains at room temperature were extracted, as shown in Fig. 3. Dislocation extraction algorithm (DXA) can be used to observe the generation of dislocation under different tensile strains.

(a)0.03   (b) 0.05   (c) 0.06   (d) 0.12   (e) 0.18
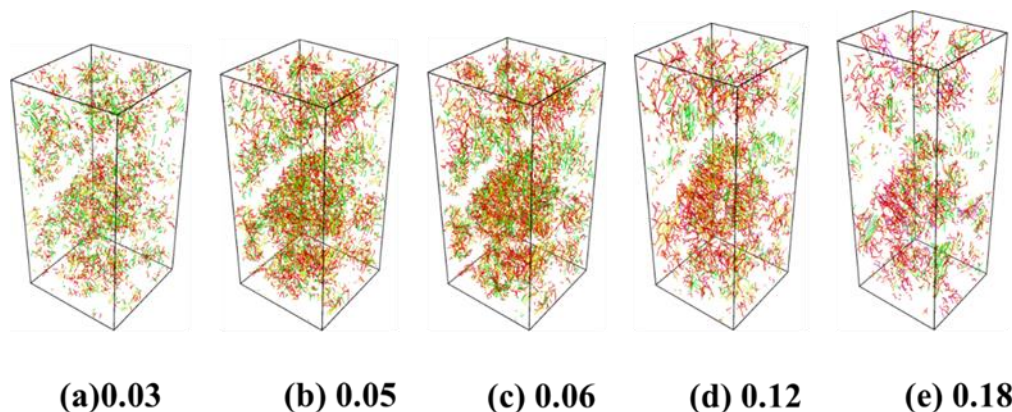
Fig 3. Dislocations of $Fe_{0.5}Ti_{0.5}$-CNT nanocomposites at different strain stages

4. Conclusions

In conclusion, $Fe_{0.5}Ti_{0.5}$-CNT nanocomposites were simulated and designed by molecular dynamics method, and their mechanical properties were explored. The results show that the strength and ductility of polycrystalline $Fe_{0.5}Ti_{0.5}$ alloy can be significantly improved by adding carbon nanotubes. In addition, the network structure of carbon nanotubes can be used as a nanodustbin to contain gas. It is believed that the hydrogen storage capacity of $Fe_{0.5}Ti_{0.5}$ alloy as a hydrogen storage material can also be further improved, which needs further exploration.

Acknowledgments

References

[1] Zhu L F, M Friák, Udyansky A , et al. Ab initio based study of finite-temperature structural, elastic and thermodynamic properties of FeTi[J]. Intermetallics, 2014, 45(2):11-17.

[2] Liang, Yue, Seyed, et al. Epoxy composites with carbon nanotubes and graphene nanoplatelets - Dispersion and synergy effects[J]. Carbon: An International Journal Sponsored by the American Carbon Society, 2014, 78:268-278.

[3] Ackland, Graeme. Controlling Radiation Damage[J]. Science, 2010.

[4] Plimpton S. Fast parallel algorithms for short-range molecular dynamics. 1993.

[5] Hkk A , Wsj B , Bjl A . Modified embedded-atom method interatomic potentials for the Fe–Ti–C and Fe–Ti–N ternary systems - ScienceDirect[J]. Acta Materialia, 2009, 57(11):3140-3147.

[6] Stukowski, Alexander. Visualization and analysis of atomistic simulation data with OVITO–the Open Visualization Tool[J]. Modelling Simul. mater.sci.eng, 2010, 18(1):2154-2162.

[7] Sarkar, Jit. Investigation of mechanical properties and deformation behavior of single-crystal Al-Cu core-shell nanowire generated using non-equilibrium molecular dynamics simulation[J]. Journal of nanoparticle research: An interdisciplinary forum for nanoscale science and technology, 2018, 20(6).

Bct-C$_5$: A new body-centered tetragonal carbon allotrope

Jiangwei Xu, Chao Zhang*, Yu Cao, Yin Liu, Chuyang Xu

School of Materials Science and Engineering, Anhui University of Science and Technology, Huainan 232001, China

Abstract

Based on first-principles calculations, a new carbon allotrope was predicted with a body-centered tetragonal structure. This carbon phase contains five carbon atoms in a primitive cell, thus termed bct-C$_5$. The stability of bct-C$_5$ was verified by calculating the total energy, *ab-initio* molecular dynamics simulation, phonon spectrum and elastic constants. It was found that bct-C$_5$ was thermodynamically stable. Moreover, bct-C$_5$ was an indirect band gap semiconductor with a band gap of 3.17 eV. The Vickers hardness of bct-C$_5$ was calculated to be 31.6 GPa, and the shear strength was up to 55.9 GPa. Furthermore, the computed X-ray diffraction pattern was in a good agreement with the experimental data of the detonation and chimney soot. These results indicate that bct-C$_5$ can be feasibly prepared in the near future and has potential applications in mechanical and electronic devices.

Keywords: Carbon allotropes; First-principles calculations; Semiconductor; Hard material

1. Introduction

Carbon atoms can form three different hybrid orbitals, namely *sp*, *sp^2* and *sp^3* hybridization in terms of molecular orbital theory. Therefore, the carbon element can form various allotropes, which possess widely different physical and chemical properties[1,2]. With the development of high-performance computers and first-principles computation, more and more new carbon allotropes have been predicted theoretically. At the same time, with the development and maturity of experimental synthesis technology, it has been possible to synthesize various carbon allotropes, for example, fullerenes, carbon nanotubes, graphene and T-carbon[3,4].

Due to the wide demand of superhard materials in various fields, the prediction and synthesis of superhard carbon phases have been the particular focus of materials researcher. In recent years, several new carbon allotropes with superhard properties have been predicted theoretically. These newly predicted superhard materials, such as M-carbon, W-carbon, O-carbon and C$_{20}$-T, just like diamond, have *sp^3*-hybridized characters and thus possess a high density and high hardness. These predicted superhard carbon allotropes are expected to play an essential role in future engineering applications.

In this work, a new carbon allotrope was constructed by modifying the structure of T$_5$-carbon, and its mechanical and electrical properties were calculated by using first-principles calculations. The primitive cell of the new carbon phase contains five carbon atoms by forming a body-centered tetragonal structure, thus termed bct-C$_5$. By calculating the total energy, ab-initio molecular dynamics simulations (AIMD), phonon spectra and elastic constants, the

stability of bct-C$_5$ was comprehensively investigated. The calculation results show that bct-C$_5$ is thermodynamically stable, and possesses a Vickers hardness of 31.6 GPa, and an indirect band gap of 3.17 eV. Importantly, the X-ray diffraction (XRD) spectrum of bct-C$_5$ shows that it might appear in detonation and soot. Collectively, these results indicate that it is feasible to fabricate bct-C$_5$ in the near future, and it has a wide application prospect in mechanical and electronic devices.

2. Computational methods

Our simulations were performed using the first-principles theory implemented in the Vienna ab initio simulation package (VASP). The generalized gradient approximation (GGA) with the Perdew-BurkeErnzerhof (PBE) functional was used to describe the exchange of plane waves was 520 eV. The convergence standard of ionic relaxation was 1.0×10^{-3} eV/Å. Importantly, Heyd-Scuseria-Ernzerhof (HSE06) hybrid functional was used to calculate the electronic properties to describe the electronic structure more accurately. In the phonon spectrum calculation, the harmonic (second order) interatomic force constants (IFCs), which were calculated by density functional perturbation (DFPT) method, a 3×3×3 supercell was carried out to calculate the phonon spectrum with a 4×4×4 k-meshes. The phonon dispersion was obtained by the PHONOPY code.

3. Results and discussion

As shown in Figure 1, the carbon atoms of bct-C$_5$ are composed of quasi sp^3-hybridized bonds, forming a triangular structure. The space group of bct-C$_5$ is I-4m2 (No.119). The Wyckoff positions are 2a (0.000, 0.000, 0.000) and 8i (0.208, 0.000, 0.781). The bond lengths between atoms are d_1 = 1.534 Å, d_2 = 1.505 Å, and d_3 = 1.493 Å, respectively. The optimized equilibrium volume of bct-C$_5$ (7.68 Å^3/atom) is larger than that of diamond (5.69 Å^3/atom) but smaller than that of T-carbon (13.25 Å^3/atom). The cohesive energy of bct-C$_5$ is calculated to be about 7.14 eV, which is less than those of diamond (7.84 eV) and graphite (8.04 eV), but greater than those of T$_5$-carbon (6.81 eV) and T-carbon (6.67 eV), suggesting that the stability of the new carbon phase is lower than those of diamond and graphite, but higher than those of T$_5$-carbon and T-carbon.
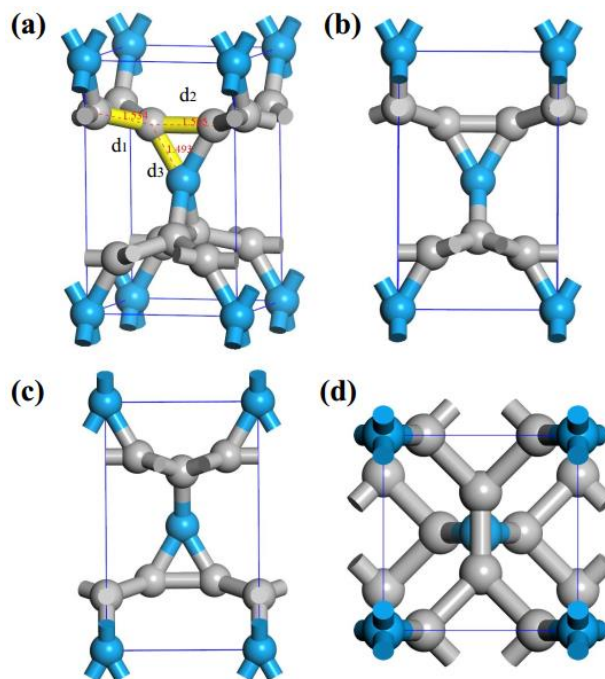
Fig. 1 The crystal structure of bct-C$_5$. (a) There are three different bond lengths in this structure, d$_1$, d$_2$ and d$_3$, respectively. (b)–(d) present the views of three different directions of [100], [010] and [001]. The blue spheres represent identical carbon atoms in the crystal.

In order to check the dynamical and thermal stability of bct-C$_5$, we carried out phonon spectra calculation and *ab-initio* molecular dynamics (AIMD) simulation. As shown in Fig. 2(a), there is no negative frequency in the phonon spectra, which indicates that bct-C$_5$ is dynamically stable. For the AIMD calculation, a 3×3×3 supercell was used, and no structural change was observed for 10 ps at the temperature of 500 K, indicating that bct-C$_5$ is in a thermodynamically metastable state. The energy-volume curve was calculated to test the energy stability of bct-C$_5$, and the results are shown in Fig. 2(b). It can be seen that the potential energy of bct-C$_5$ is lower than those of T-carbon and T$_5$-carbon, indicating that bct-C$_5$ is more stable than T-carbon and T$_5$-carbon. In order to determine the mechanical stability, we also calculated the elastic constants of bct-C$_5$ and found that the independent elastic constants C$_{11}$, C$_{12}$, C$_{13}$, C$_{33}$, C$_{44}$ and C$_{66}$ are 690.169, 91.489, 135.024, 480.719, 206.712, and 189.331 GPa, respectively. These calculated results show that the new carbon allotrope satisfies the Born mechanical stability conditions: C$_{11}$ > |C$_{12}$| and $2 C_{13}^2$ < C$_{33}$ (C$_{11}$ + C$_{12}$) and C$_{44}$ > 0 and C$_{66}$ >

0, confirming the mechanical stability of bct-C$_5$. As can be seen from the above analysis, bct-C$_5$ is a relatively stable carbon phase, which may be potentially synthesized in experiments.

The projected band structure of bct-C$_5$ was calculated by using the PBE functional. It was found that bct-C$_5$ was an indirect band gap semiconductor with a band gap of 3.17 eV, as shown in Figure 3. It is well-known that PBE functional normally underestimates the band gap. To obtain a more accurate band gap, the HSE06 functional was used and the band gap was calculated to be 4.15 eV, which indicates that bct-C$_5$ is a wide band gap semiconductor. The mechanical properties of bct-C$_5$ was also investigated. The Vickers hardness can be calculated

by the empirical formula of Chen's mode. The Vickers hardness of bct-C$_5$ was calculated to be 31.6 GPa based on the formula, which is higher than that of T-carbon (5.6 GPa), and lower than that of diamond (95.7 GPa). In order to further investigate the mechanical behavior and hardness of the material, we calculated the tensile deformation of uniaxial stress and the shear deformation of slip system, in which three typical crystal directions of [100], [001] and [110] and four typical slip systems (100)[010], (100)[001], (110)[$\bar{1}10$] and (110)[001] were selected, respectively.
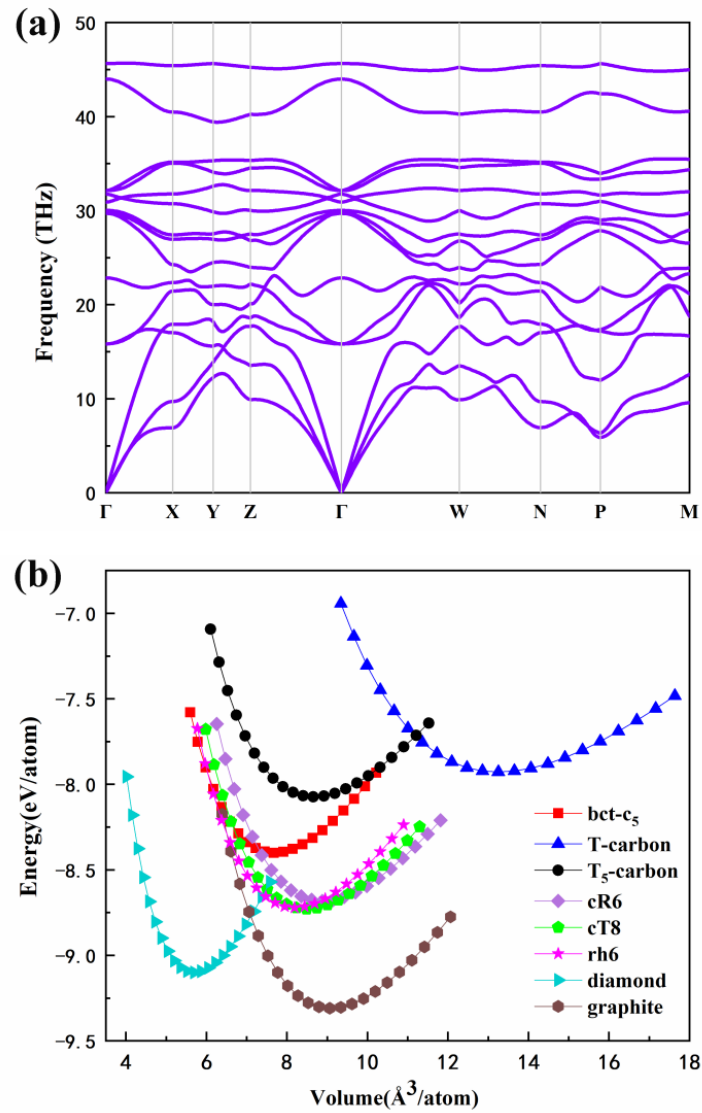
Fig. 2 (a) Phonon spectra of bct-C$_5$. (b) Curves of total energy per atom versus volume of bct-C$_5$, T-carbon, T$_5$-carbon, cR6, cT8, rh6, diamond and graphite.
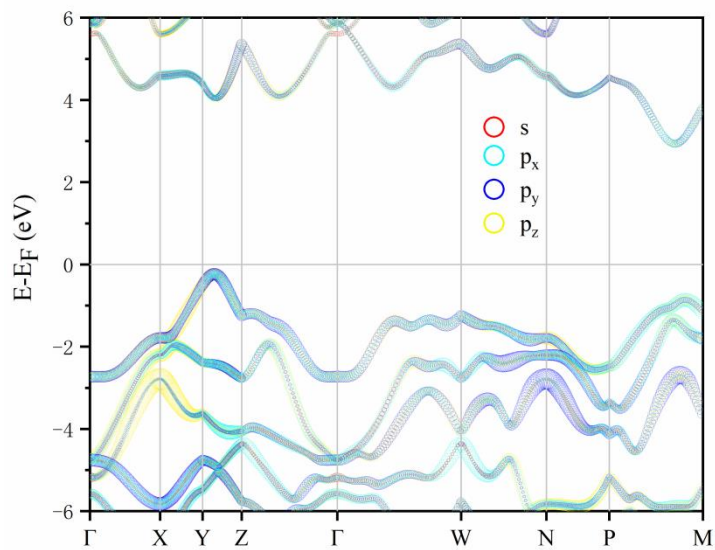
Fig. 3 The projected band structure of bct-C$_5$, in which each orbital is shown in different colors.
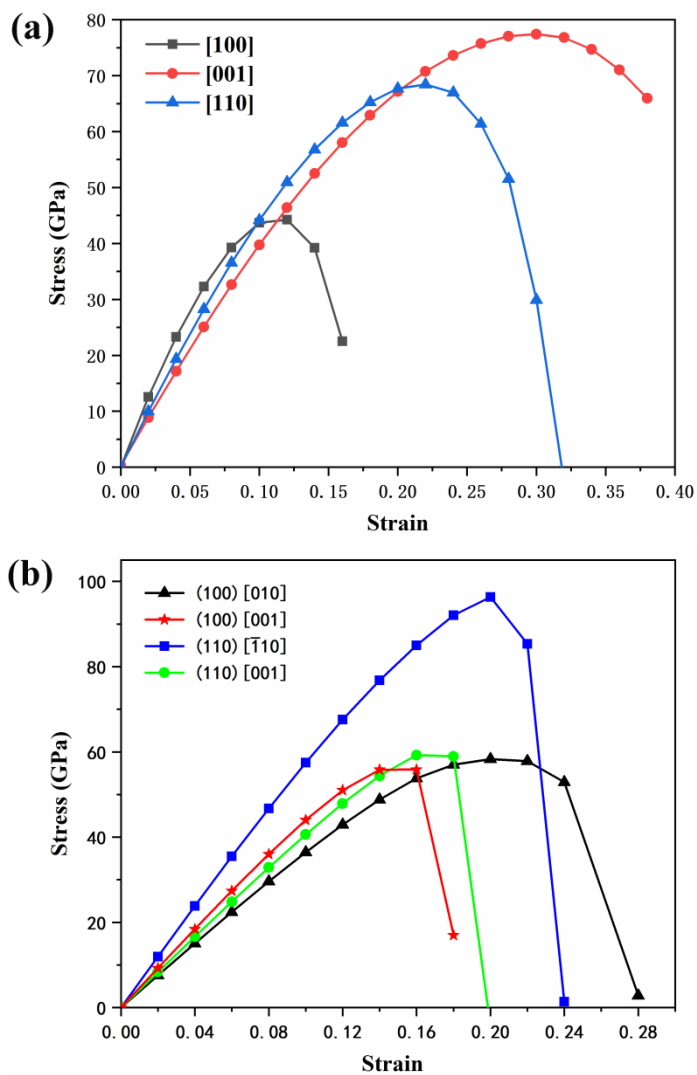
Fig. 4 Stress-strain curves of bct-C$_5$. (a) Tensile deformation and (b) shear deformation.

The calculated tensile and shear deformations are shown in Fig. 4. As can be seen from Fig. 4(a), the tensile strengths of bct-C_5 in the directions of [100], [001] and [110] is 44.2, 77.4, and 68.4 GPa, respectively. It can be concluded that bct-C_5 can endure the tensile strength of 44.2 GPa at least. Compared with other carbon allotropes, although it is lower than that of diamond (91.1 GPa and 82.3 GPa), it is higher than that of T-carbon (40.1 GPa). In Fig. 4(b), the ideal shear strengths for (100)[010], (100)[001], (110)[$\overline{1}10$] and (110)[001] systems are 58.3, 55.9, 96.3, and 59.3 GPa, respectively. It can be concluded that the shear strength is also lower than that of diamond (92.5 GPa and 86.8 GPa), but higher than that of T-carbon (7.3 GPa). It can be seen from the above results that the weakest shear strength (55.9 GPa) of bct-C_5 is much higher than the weakest tensile strength (44.2 GPa), which is about 26%. Therefore, the major damage mode of bct-C_5 is tensile failure, which is the same as diamond, but different from T-carbon. It is well-known that the weakest tensile strength or shear strength at zero pressure is the upper limit of the mechanical strength, therfore, we can infer that the hardness of bct-C_5 should be lower than 44.2 GPa, which is in a good agreement with the calculated results based on Chen's model.

4.Conclusions

In conclusion, a new wide band gap semiconductor bct-C_5 was predicted using first-principles calculations. The dynamic stability, thermodynamic stability, energy stability and mechanical stability were examined by phonon spectrum, AIMD simulation, the energy-volume curve and elastic constants calculations. It is found that bct-C_5 is an indirect band gap semiconductor with a band gap of 4.15 eV. The Vickers hardness of bct-C_5 is 44.2 GPa, which is close to the value obtained from the Chen's model (31.6 GPa) for Vickers hardness calculation. Importantly, the XRD spectrum indicates that bct-C_5 can be obtained from detonation and chimney soot. These results indicate thatbct-C_5 can be feasibly realized in experiments.

Acknowledgments

References

[1] Qingyang Fan, Heng Liu, Li Jiang, Yu. Xinhai, Wei Zhang, Sining Yun, Two orthorhombic superhard carbon allotropes: C16 and C24, Diam. Relat. Mater. 116 (2021), 108426.

[2] Lin Zhou, Changchun Chai, Wei Zhang, Yanxing Song, Zheren Zhang, Yintang Yang, oI20-carbon: a new superhard carbon allotrope, Diam. Relat. Mater. 113 (2021), 108284.

[3] Xian-Lei Sheng, Qing-Bo Yan, Fei Ye, Qing-Rong Zheng, Su. Gang, T-carbon: a novel carbon allotrope, Phys. Rev. Lett. 106 (15) (2011), 155703.

[4] Jinying Zhang, Rui Wang, Xi Zhu, Aifei Pan, Chenxiao Han, Xin Li, Dan Zhao, Chuansheng Ma, Wenjun Wang, Su. Haibin, Chunming Niu, Pseudo-topotactic conversion of carbon nanotubes to t-carbon nanowires under picosecond laser irradiation in methanol, Nat. Commun. 8 (2017) 683.

Irradiation damage mechanism of NiFe alloys based on two-temperature molecular dynamics

Jiangwei Xu, Chao Zhang*, Huajin Hu , Yin Liu, Chuyang Xu

School of Materials Science and Engineering, Anhui University of Science and Technology, Huainan 232001, China

Abstract

In the previous work on radiation damage, the classical molecular dynamics (MD) cascade simulation did not consider the electronic effect. However, according to the recent research of two-temperature molecular dynamics (2T-MD) simulation, the electronic effect will affect the total number of defects and the distribution of defects in clusters. In this paper, taking the equiatomic NiFe alloy as an example, some parameters needed to establish the 2T-MD model are preliminarily calculated.

Keywords: Irradiation damage; Two-temperature; Molecular dynamics; NiFe alloys

1. Introduction

Traditionally, cascade simulation based on MD is generally used to study irradiation events. This simulation method has an important driving force for studying the evolution and distribution of irradiation damage. Classical MD simulation is a widely used method to study irradiation events in the early stage, which follows the energy conservation and does not consider electronic effects. However, in fact, electron excitation will affect the generation and evolution of radiation damage. Recently, in the 2T-MD model described by Duffy and Rutherford[1], not only the electronic effect but also the e-ph coupling effect are considered. The 2T-MD model describes the energy exchange between atomic and electronic subsystems. In high energy irradiation, energy is transferred from atomic system to electronic system due to inelastic electron scattering and e-ph interactions. Depending on the local temperature difference, part of the energy stored in the electronic system returns to the atomic system, while the other part diffuses through the electron. This energy transfer process can be expressed by heat diffusion equation.

Nickel-based concentrated solid solution alloys is composed of two or more metal

elements with almost equal concentration, and forms a single-phase fcc alloy with random position occupation. Due to their chemical complexity, they exhibit excellent thermal, electrical and mechanical properties, which makes them good candidates for nuclear applications. In this paper, we simulate the nickel ion cascade in equiatomic NiFe, in which the energy of primary knock-on atom (PKA) is 30 keV.

2. Theory and calculation methods

In the 2T-MD cascade simulation, not only the electronic stopping effect but also the e-ph interactions are taken into account. In the 2T-MD model described by Duffy and Rutherford, the motion equation used in classical MD simulation is modified[3] (Eq. (1)):

$$m_i \frac{\partial v_i}{\partial t} = F_i(t) - \gamma_i v_i + \tilde{F}(t)$$

(1)

Here v_i and m are the velocity and mass of atom i, respectively, and $F_i(t)$ is the force acting on atom i due to the interaction with surrounding atoms at time t. The energy loss is included via a friction term with coefficient γ_i, where when $v_i > v_c$, the friction term $\gamma_i = \gamma_s + \gamma_p$; when $v_i \leq v_c$, $\gamma_i = \gamma_p$. v_c is the cut-off velocity, which is equivalent to twice the cohesive energy of the system[4]. The energy gain of electron bombardment is included by a stochastic force term $\tilde{F}(t)$ with magnitude and orientation. The e-ph coupling is activated at time t_{eph}, which is determined by the thermalization time in the cascades with electronic stopping only.

The energy transfer between atomic and electronic subsystems is described by the heat diffusion equation[5], which includes electronic specific heat C_e and electronic thermal conductivity k_e.

$$C_e \frac{\partial T_e}{\partial t} = \nabla(k_e \nabla T_e) - g_p(T_e - T_a) + g_s T_a'$$

(2)

where g_s and g_p are electronic stopping constant and e-ph coupling constant, respectively. The second term on the right side of the equation represents the energy exchange due to the temperature difference between the atomic system (T_a) and the electronic system (T_e). The third term on the right side of the equation represents the energy exchange because of the electronic stopping mechanism, where the parameter T_a' has units of temperature, and can be calculated from the average kinetic energy of the subset of atoms subjected to electronic stopping, that is, their velocity is greater than the cut-off value v_c., g_s and g_p are expressed as[6]:

$$g_p = \frac{3Nk_B\gamma_p}{\Delta V m_i} \quad (3)$$

$$g_s = \frac{3N'k_B\gamma_s}{\Delta V m_i} \quad (4)$$

where N is the number of atoms in the coarse-grained cell of volume ΔV, k_B is the Boltzmann constant, and N' is the number of atoms with a velocity greater than v_c.

In the low speed region, the electronic stopping power is proportional to the ion velocity, and the proportional constant (λ) is determined by Lindhard and Scharff [7] model:

$$dE/dx = \lambda E^{1/2} \quad (5)$$
$$m\,dv/dt = \lambda(m/2)^{1/2}v \quad (6)$$

then, from Eq. (1) $\quad \gamma_s = \lambda(m/2)^{1/2} \quad (7)$

the relaxation time corresponding to electronic stopping is

$$\tau_s = m/\gamma_s = (2m)^{1/2}/\lambda \quad (8)$$

the timescale of energy loss caused by electron-ion interactions is

$$\tau_p = m/\gamma_p \quad (9)$$

then, from Eq. (3) $\quad \tau_p = 3nk_B/g_p \quad (10)$

where n is the number of atoms per unit volume.

3. Results and discussion

The total electronic density of states (DOS) of NiFe alloy calculated from the electronic structure results within VASP is shown in Fig. 1, where Fermi energy corresponds to zero energy. The electronic specific heat C_e in a certain electronic temperature range is obtained by the calculated DOS. Using the Stopping and Range of Ions in Matter (SRIM) software, we can calculate that the value of the proportional constant λ in Eq. (5) is 0.0658 eV$^{1/2}$Å^{-1}, and then from Eq. (8), the value of τ_s is 1668 fs .
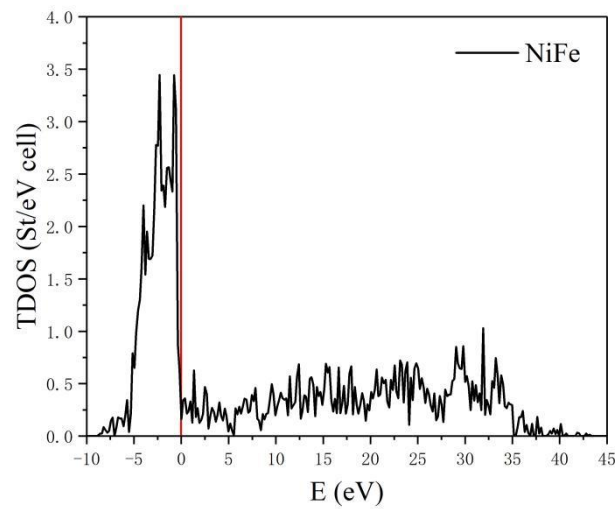
Fig. 1. Calculated total density of states of NiFe alloy. Fermi level corresponds to 0 energy.
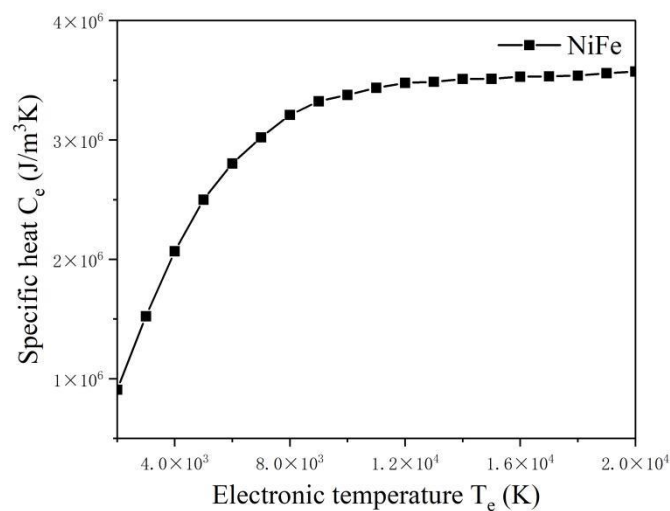
Fig. 2. Electronic specific heat for a range of electron temperatures.

The classical MD cascade simulation ignores the energy dissipation effect of electronic stopping mechanism, while 2T-MD simulation takes into account not only the electron excitation effect, but also the e-ph coupling effect, which has become a new important direction to study radiation damage events. Our research group has only made preliminary calculation on the parameters required to establish 2T-MD model, and the subsequent parts still need to be improved.

Acknowledgments

References

[1]   D M Duffy, A M Rutherford. Including the effects of electronic stopping and electron-ion interactions in radiation damage simulations[J]. Journal of Physics: Condensed Matter, 2007, 19(1): 016207.

[2]   S.G. Ma, Y. Zhang. Effect of Nb addition on the microstructure and properties of AlCoCrFeNi high-entropy alloy[J]. Materials Science and Engineering: A, 2012, 532: 480-486.

[3]   Eva Zarkadoula,, German Samolyuk, William J. Weber. Effects of the electron-phonon coupling activation in collision cascades[J]. Journal of Nuclear Materials, 2017, 490: 317-322.

[4]   Eugeni E Zhurkin, Anton S Kolesnikov. Atomic scale modelling of Al and Ni(111) surface erosion under cluster impact[J].Nuclear Instruments and Methods in Physics Research Section B: Beam Interactions with Materials and Atoms, 2003, 202: 269-277.

[5]   A M Rutherford, D M Duffy. The effect of electron-ion interactions on radiation damage simulations[J]. Journal of Physics: Condensed Matter,2007, 19: 496201.

[6]   Eva Zarkadoula,, German Samolyuk, William J. Weber. Two-temperature model in molecular dynamics simulations of cascades in Ni-based alloys[J]. Journal of Alloys and Compounds, 2017, 700: 106-112.

[7]   J.Lindhard, M.Scharff. Energy Dissipation by Ions in the kev Region[J]. Physical Review, 1961, 124(1): 128-130.

Preparation and adsorption to PM2.5 of PAM/GO aerogel

Jieqi Zhang, Xiuling Lin*, Chao Zhang

School of Materials Science and Engineering, Anhui University of Science and Technology,

Huainan 232001, China

Abstract

In this paper, a solvent exchange method was designed to prepare polyacrylamide/ graphene oxide aerogel. Polyacrylamide/graphene oxide aerogel can effectively adsorb PM2.5, and its adsorption efficiency is higher than that of polyacrylamide/graphene oxide/cellulose aerogel. Moreover, the preparation process is cost-effective and easy to expand without any special drying technology and heating process. This provides an ideal platform for large-scale production of graphene aerogels.

Keywords: aerogel; adsorption; PM2.5; PAM/GO

Introduction

In recent years, the problem of air pollution has become increasingly serious, which has a great impact on human health and living environment[1]. Volatile organic compounds (VOCs), fine particles, especially particles with a diameter less than 2.5μm (PM2.5)[2, 3], are all caused by the linear increase in the number of automobiles.[4]. Researchers have invented various air filters to capture PM2.5 and improve air quality[5].

Graphene oxide(GO) is the oxide of graphene, which was first synthesized by Brodie in the mid-19th century[6]. The generally accepted GO model is that epoxy and alcohol groups are uncorrelated random distribution on the surface, and alcohol and carboxyl groups are around the edge[7]. GO has more oxygen-containing functional groups than graphene, so its properties are more reactive. Its properties can be improved through various reactions with oxygen-containing functional groups. Its surface modification has become a research hotspot at present.

Therefore, GO was chosen to prepare polyacrylamide(PAM)/GO aerogels and PAM/GO/cellulose(CNFs) aerogels by acetone solvent exchange, and tested their adsorption capacity for PM2. 5.

Experimental section

Materials

Acrylamide (AM), Graphene oxide (GO), Potassium persulfate (KPS), *N,N*-methylene bisacrylamide (MBA), Tetramethylethylenediamine (TEMED), Acetone, Graphene oxide (GO) was provided by Turing Evolution Technology Co., Ltd (Shenzhen, China). They were all analytical grade and used directly without further purification.

Preparation of PAM/GO aerogels

The GO solution was prepared by 0.030g in 30 ml deionized water and then ultrasonic treatment 1h. AM, MBA and KPS were taken into GO solution and stirred for 20min, then added 60 μL TEMED to the hydrogel solution. The precursor solution was quickly poured into the mold and formed at room temperature. After molding, the gel was frozen in the fridge for one night (-18 ℃). On the second day, each of the frozen hydrogels was placed in 100ml acetone solution (10% (w/w)) at room temperature for 1h and then exchanged with pure acetone (3 times × 15 minutes, 50mL/ aerogel). All acetone soaked aerogels were subsequently air-dried.

Preparation of PAM/GO/CNFs aerogels

The GO solution was prepared by 0.030g in 20 ml deionized water and then ultrasonic treatment 1h. Meanwhile, CNFs were weighed and stirred with 10 mL deionized water for 1 h. Then mix the graphene oxide solution and cellulose solution evenly. The subsequent test steps are consistent with preparation of PAM/GO aerogels.

Determination of PM2. 5 adsorbed by aerogels

The PM2.5 was simulated by the flue gas ignited from sandalwood. The aerogel blocks were placed in a sealed glove box with known PM2.5 concentration. And the concentration of PM2.5 was measured every 30min.

Results and discussion

Aerogels were prepared by mixing PAM, CNFs and GO solution, with subsequent freezing in a conventional freezer (-18℃), thawing, solvent exchange, and air drying. The prepared aerogels is shown in Fig 1. Obviously, the surface of PAM/GO aerogels is uneven, while aerogel with CNFs is in neat shape. It indicates that CNFs can modify the macroscopic morphology of aerogels.
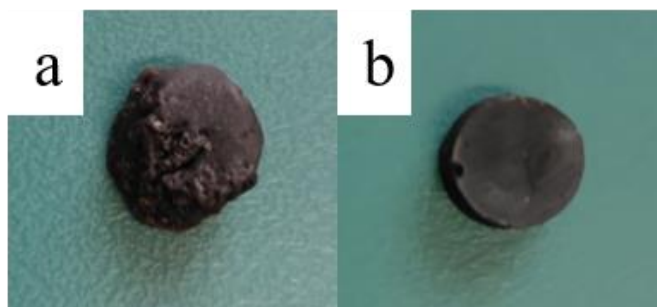
Fig. 1 (a) PAM/GO aerogel (b) PAM/GO/CNFs aerogel micromorphology

The effects of different adsorbent dosage on PM2.5 adsorption capacity of aerogels were measured(Fig2). Among them, 1, 2 and 3 represent different adsorbent dosage, as shown in Table 1.

Table 1 Adsorbent quality represented by different labels

sample	1	2	3
PAM/GO	0.412g	0.620g	0.640g
PAM/GO/CNFs	0.517g	0.640g	0.737g
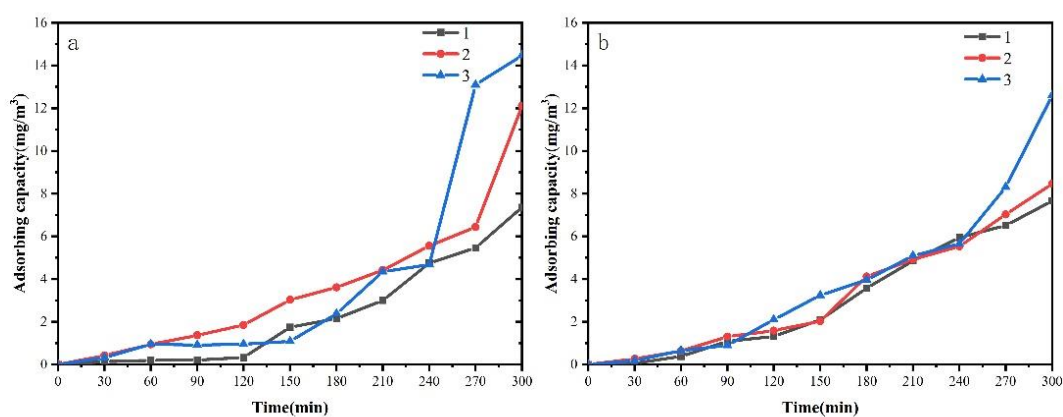
Fig. 2 Adsorption capacity of (a) PAM/GO(b) PAM/GO/CNFs aerogel with different mass for PM2.5

For a certain concentration of PM2.5, because of the limited adsorption sites on aerogels, the aeration of low dose aerogels is easy to reach the saturated adsorption state. However, the number of adsorbed active sites increased with the number of aerogels. Moreover, the active

sites were in an unsaturated state of adsorption, so the adsorption rate of PM2.5 on gel increased. As can be seen from Fig 2, with the increase of adsorbent dosage, the more PM2.5 adsorbed by aerogel. Figure 3 shows the comparison of adsorption of two kinds of aerogel with the same mass. The "no aerogel" indicates that no aerogel has been added.
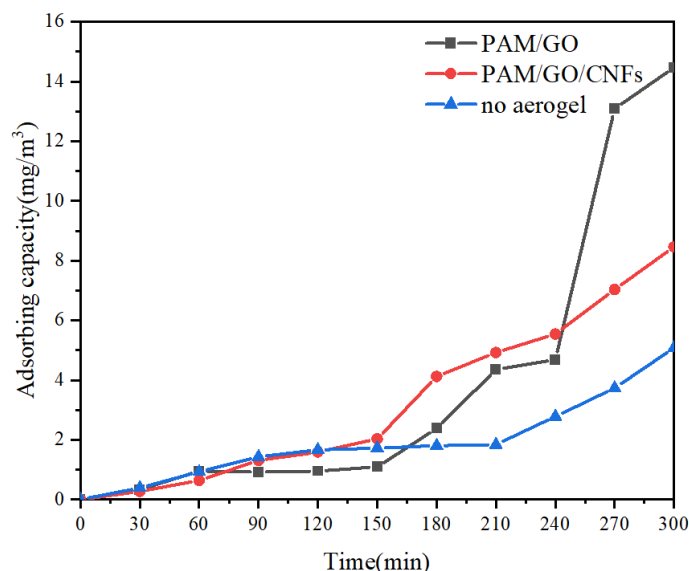
Fig. 3 Comparison of PM2.5 adsorption capacity between PAM/GO and PAM/GO/CNFs

Obviously, although the morphology of PAM/GO/CNFs aerogel is neat, the adsorption capacity of PAM/GO/CNFs with the same quality for PM2.5 is not as strong as that of PAM/GO aerogel. This may be because the presence of CNFs hinders the cross-linking between PAM and GO, thus reducing the adsorption capacity of aerogel. Therefore, although CNFs can play a role in the macroscopic morphology of aerogel, its presence has no effect on the adsorption of PM2.5 by aerogel. Therefore, we chose PAM and GO two-component aerogel as PM2.5 sorbent.

Conclusions

In summary, PAM/GO aerogel was prepared by solvent exchange with acetone, which bypassed the complex steps of freeze drying or supercritical drying. The prepared PAM/GO aerogel is a good PM2.5 adsorbent, and in a certain range, the more aerogels, the better the adsorption effect. Compared with the traditional method, this method is simpler and more suitable for the preparation of PAM/GO aerogel, and has broad application prospects.

Acknowledgments

References

[1]   L. K. Fonken, X. Xu, Z. M. Weil, et al. Air pollution impairs cognition, provokes depressive-like behaviors and alters hippocampal cytokine expression and morphology[J]. Mol Psychiatry, 2011, 16(10): 987-995, 973.

[2]   M. He, T. Ichinose, Y. Yoshida, et al. Urban PM2.5 exacerbates allergic inflammation in the murine lung via a TLR2/TLR4/MyD88-signaling pathway[J]. Sci Rep, 2017, 7(1): 11027.

[3]   M. Mazidi,J. R. Speakman. Ambient particulate air pollution (PM2.5) is associated with the ratio of type 2 diabetes to obesity[J]. Sci Rep, 2017, 7(1): 9144.

[4]   H. Liu, S. Zhang, L. Liu, et al. A Fluffy Dual-Network Structured Nanofiber/Net Filter Enables High-Efficiency Air Filtration[J]. Advanced Functional Materials, 2019, 29(39).

[5]   M. Zhang, Y. Qi,Z. Zhang. AgBr/BiOBr Nano-Heterostructure-Decorated Polyacrylonitrile Nanofibers: A Recyclable High-Performance Photocatalyst for Dye Degradation under Visible-Light Irradiation[J]. Polymers (Basel), 2019, 11(10).

[6]   Brodie, B. C. On the Atomic Weight of Graphite.Philos.Trans. R. Soc. London1859,14, 249–259.

[7]   R. C. Sinclair,P. V. Coveney. Modeling Nanostructure in Graphene Oxide: Inhomogeneity and the Percolation Threshold[J]. J Chem Inf Model, 2019, 59(6): 2741-2745.

Effect of POE-*g*-MAH with reactive groups on micromorphology evolution and mechanical properties of PP/PLA blends

Bingyu Fan[1]; Jin Liu [*1,2]; Zhen Li [1,2];; Ping Wang[1]; Xianbiao Wang[1]; Fengjun Zhang[1]

[1] School of Materials Science and Chemical Engineering, Anhui Jianzhu University, Hefei 230601, P. R. China ; [2]Anhui Key Laboratory of Advanced Building Materials, Anhui Jianzhu University, Hefei 230601, P. R. China

Abstract

In order to improve the interfacial compatibility between polypropylene (PP) and polylactic acid (PLA), PP /PLA/POE-*g*-MAH blends were prepared by melt blending method with POE-g-MAH as the reactive group. The effects of POE-*g*-MAH on the micromorphology and macro-properties of PP/PLA blends were investigated by DSC, SEM, torque rheometer, and tensile test. The SEM and DSC results showed that the high content of POE-*g*-MAH can improve the interfacial adhesion between PP and PLA, which form a micro-crosslinked network structure at the interface. Meanwhile, with the increase of POE-g-MAH content, the micro phase morphology of PP and PLA changed from the initial "island" structure to "similar bi-continuous phase" structure. The mechanical properties test results show that the high content of POE-g-MAH can significantly improve the toughness of PP/PLA blend material, especially when 10% POE-g-MAH was introduced, the elongation at break of the material reached 76.2%, which was 5 times that of PP/PLA blend. PP/PLA/ POE-g-MAH blends have excellent mechanical properties, which was mainly due to the improved interface compatibility between PP and PLA.

Keyword：polypropylene；polylactic acid；micromorphology
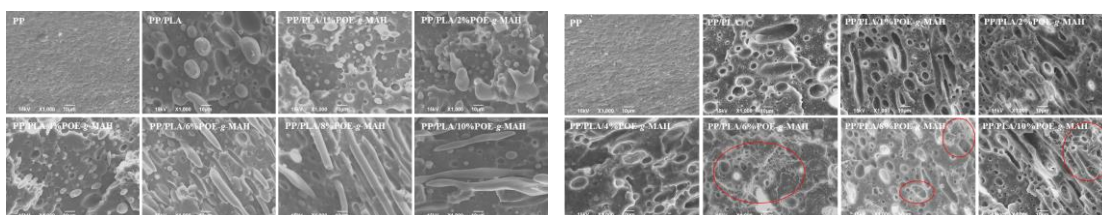
Fig. 1 Micrograph of interfacial morphology of PP/PLA blends
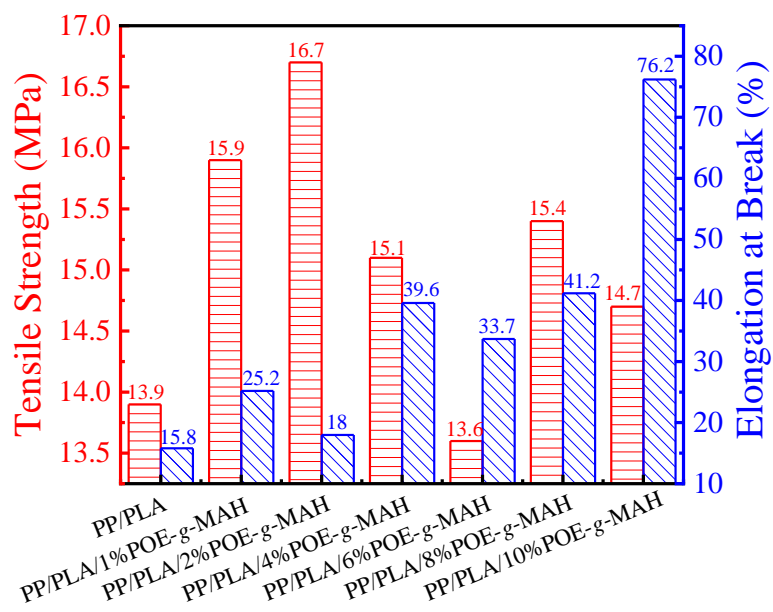
Fig. 2 Tensile tests results of PP/PLA/POE-g-MAH blends

Acknowledgments:

This work was financially supported by University Collaborative Innovation Project of Anhui province (GXXT-2019-017), and Natural Science Research Project of Anhui Jianzhu University（JY2021-C-050）.

Noble I-type 0D/0D ZnS@Cu₃P heterojunction for photocatalytic hydrogen evolution

Weiqin Cai [a,b], Fengjun Zhang [a,b*], Yingrui Wang [b,c] , Dongcai Li [b]

[a] Key Laboratory of Functional Molecule Design and Interface Process, Anhui Jianzhu University, Hefei 230601, Anhui China

[b] Anhui Key Laboratory of Advanced Building Materials, Anhui Jianzhu University, Hefei 230601, Anhui China

[c] Construction economy and real estate management research center, Anhui Jianzhu University, Hefei 230601, Anhui China）

* Corresponding author: Feng-Jun Zhang, E-mail: fjzhang@ahjzu.edu.cn;

Abstract

Developing an efficient and stable photocatalytic hydrogen evolution system is a practical strategy to solve the environmental and energy crisis. Herein, a new noble metal free I-type ZnS/Cu₃P composite was successfully prepared by a hydrothermal-calcination way, and its structure and morphology were characterized. The experimental results demonstrated that the photocatalytic performance of pure ZnS nanoparticles is very weak. However, the addition of Cu₃P greatly improved the photocatalytic performance. The yield of the best sample (2% ZnS/Cu₃P) was 729μmol/g/h, about 17 times than that of ZnS. Photocurrent, photoluminescence and electrochemical impedance spectroscopy confirmed that Cu₃P greatly enhanced the charge separation process. The improvement of photocatalytic performance of ZnS/Cu₃P is mainly due to the addition of Cu₃P nanoparticles, which can not only expand the specific surface area and supply for rich reaction sites, but enhance its photocatalytic performance. Furthermore, the equitable mechanism of improving photocatalytic competence was still discussed. This research also provides a way for the design and synthesis of new noble-metal-free photocatalysts with outstanding hydrogen production activity.

Keywords: ZnS, Cu₃P, nanoparticles, type I heterojunction, photocatalysis

Acknowledgments

The structural guiding and catalysis effects of doping of cobalt ions on ZnCr$_2$O$_4$ oxides for methane combustion

Jia He，Xiao-Qiang Shao，Shao-Jie Feng*

[1] Key Laboratory of Functional Molecule Design and Interface Process, Anhui Jianzhu University, Hefei Anhui, P. R. China, 230601）

[2] Anhui Key Laboratory of Advanced Building Materials, Anhui Jianzhu University, Hefei Anhui, P. R. China, 230022）

∗Corresponding author: Feng Shao-Jie, E-mail: fengshaojie@ahjzu.edu.cn

Abstract

A series of novel cobalt ion doped ZnCr$_{2-x}$Co$_x$O$_4$ (x=0, 0.1, 0.15, 0.2) spinel oxides were synthesized by hydrothermal method. XRD results show that the doping of cobalt promotes the crystallization of spinel oxide significantly, spinel ZnCr$_{2-x}$Co$_x$O$_4$ (x=0.1, 0.15, 0.2) can be formed oxide at 500 ℃. SEM and BET results showed that ZnCr$_{2-x}$Co$_x$O$_4$ (x=0.1, 0.15, 0.2) nanoparticles with high specific surface area and better dispersion were synthesized. Catalytic experiments show that the sample doped with cobalt can effectively improve the catalytic activity. For ZnCr$_{1.85}$Co$_{0.15}$O$_4$ catalyst, the methane conversion temperature T$_{90}$ was 300 °C, while the T$_{90}$ of ZnCr$_2$O$_4$ spinel was 500°C. The oxygen temperature program desorption curve shows that the sample has two obvious oxygen species desorption near the range of 250 ℃ and 700 ℃. XPS analysis shows that the doping of cobalt ions will affect the valence change of spinel, leading to the production of active oxygen in the spinel structure, reducing the desorption temperature of α-O$_2$, and playing an important role in the catalytic reaction. Excessive cobalt ions may form CoO$_x$ species and accelerate the oxygen exchange rate.

Keywords: spinel; ZnCr$_{2-x}$Co$_x$O$_4$; cobalt ion doping; methane combustion
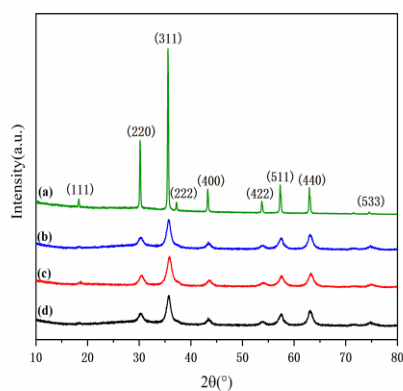
Figure 1. XRD of the ZnCr$_{2-x}$Co$_x$O$_4$

(a) x = 0, (b) x = 0.1, (c) x = 0.15,(d)x=0.2.
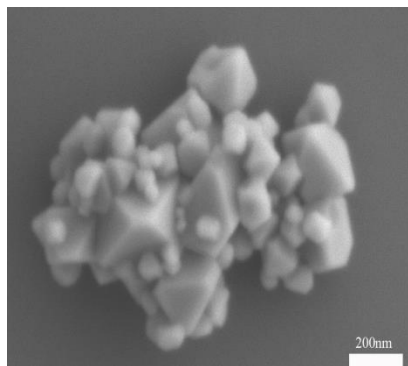
Figure 2. SEM of the ZnCr$_2$O$_4$.

.
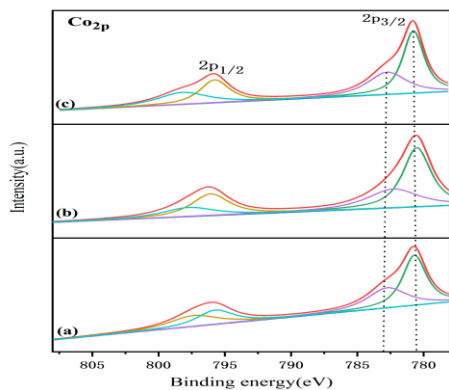
Fig. 3. XPS spectra of ZnCr$_{2-x}$Co$_x$O$_4$
(a)x=0.1,(b)x= 0.15, (c) x = 0.2.
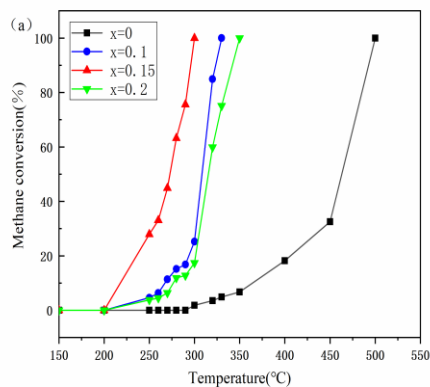
Figure 4. Methane conversion

Synthesis and characterization of noble metal-free semiconductor photocatalyst $Mn_{0.5}Cd_{0.5}S/NiCo_2Se_4$ for hydrogen production

Chao Liu[1], Feng-Jun Zhang[1, 2*]

[1] Key Laboratory of Functional Molecule Design and Interface Process, Anhui Jianzhu University, Hefei Anhui, P. R. China, 230601）

[2] Anhui Key Laboratory of Advanced Building Materials, Anhui Jianzhu University, Hefei Anhui, P. R. China, 230022）

∗Corresponding author: Zhang Feng-Jun, E-mail: fjzhang@ahjzu.edu.cn

Abstract

The $Mn_{0.5}Cd_{0.5}S/NiCo_2Se_4$ photocatalysts were prepared by a two-step synthetic hydrothermal method. The morphology, phase structure, band gap and catalytic properties of the prepared samples were investigated by X-ray diffraction, transmission electron microscopy, scanning electron microscopy and UV-vis spectrophotometer. The hydrogen production efficiency of the prepared catalysts was tested in a mixed solution of Na_2S and Na_2SO_3 under visible light. Among them, $Mn_{0.5}Cd_{0.5}S/NiCo_2Se_4$-4% had the best photocatalytic hydrogen production effect, reaching 19953 μmol-1h-1, which was 1.62 times higher than that of pure $Mn_{0.5}Cd_{0.5}S$. The presence of $NiCo_2Se_4$ photocatalyst enhanced the separation of photogenerated carriers and reduced the electron-hole complexation rate, which was beneficial to enhance the photocatalytic hydrogen production capacity.

Keywords: heterogeneous junction; hydrogen production

Mechanism of thermal activation on granular coal gangue and its impact on the performance of cement mortars

Sun Daosheng*, Liu Peng, Wang Aiguo, Mo Liwu, Liu Kaiwei, Guan Yanmei

Anhui Key Laboratory of Advanced Building Materials, Anhui Jianzhu University, Hefei Anhui, P. R. China, 230022

*Corresponding author: Sun Daosheng, E-mail: sundaosheng@163.com

Abstract

Coal gangue (CG) is a kind of solid waste discharged from the process of coal mining and washing without efficient utilization. Motivated by using the CG as supplementary cementitious materials (SCMs) for the partial substitution of cement, the CG was thermally activated via calcining under high temperature and the corresponding mechanism was discussed. The effect of calcination on the microstructure and pozzolanic reactivity of CG as well as the corresponding influence on the performance of Portland cement mortars were investigated via using TG/DSC, SEM, XRD and NMR. Results showed that, CG mainly consist of kaolinite and quartz. Under 550 °C, the kaolinite in CG was transformed into metakaolin, and the metakaolin was further transformed into mullite when the calcination temperature was elevated to 950°C. Thermally activated CG had a high pozzolanic reactivity, which improved the mechanical of cement mortars. For instance, the flexural and compressive strengths of mortars mixed with 30 wt.% CG calcined at 750 °C were increased by 16.1 % and 46.4 % compared with that of the mortars mixed with CG, respectively. This is attributed to the increased relative contents of Q3 in 29Si NMR and Al[5]+Al[4] in 27Al NMR. The higher the relative contents of [SiO4] with Q3(-100.26 ppm) structure and Al[5]+Al[4] , the higher the reactivity of calcined CG. This study develops a potential approach to recycle CG and develop greener cement materials.

Keywords: Coal gangue, Activation, Microstructure, Nuclear magnetic resonance, Mechanical strengths

The Effect of Epoxy Chain Extender on the Interface State and Performance of PLA/PA1211 Blends

Xinliang Chen[1]; Jin Liu [*1,2]; Ping Wang[1,2]; Zhen Li [1] Di Wang[1]; Xianbiao Wang[1]

[1] School of Materials Science and Chemical Engineering, Anhui Jianzhu University, Hefei 230601, P. R. China ; [2] Anhui Key Laboratory of Advanced Building Materials, Anhui Jianzhu University, Hefei 230601, P. R. China; *Corresponding to: Jin Liu (E-mail address: liujin@ahjzu.edu.cn)

Abstract

The inherent brittleness of polylactic acid (PLA) limits its application. In order to improve toughness, it is usually blended with elastomer. In this paper, nylon 1211 (PA1211) with good toughness was blended with PLA, but the compatibility between PLA and PA1211 was poor. Therefore, based on the previous research, epoxy chain extender (ADR 4468) was introduced to prepare a series of PLA/PA1211/ADR blends by melt blending, so as to enhanced the interaction between the two interfaces through the reaction between the epoxy group of ADR and the hydroxyl end of PLA or the amino end of PA1211 (figure 1), and finally improved the macro properties of the materials. The torque data showed that the melt strength of PLA/PA1211/ADR blends increased by 86% and the hydrolysis in the process of PLA blending was reduced. DSC data showed that ADR reduced the crystallization temperature of PA1211 and limited the chain movement of PA1211, but had little effect on the crystallization properties of PLA. DMA and rheological data showed that ADR could promote a variety of micro crosslinking structures in PLA/PA1211 blends, enhanced the entanglement ability between molecular chains and improved the toughness of the materials. When the addition of ADR was 1.5 wt%, the tensile strength, elongation at break and notch impact strength of the material were 58.55 MPa, 75.01% and 44 kJ/m^2 (figure 2), which were 7%, 22 times and 1.5 times higher than those of PLA/PA1211 blend respectively. The strength and toughness of the material were improved at the same time, and had good balance of stiffness and toughness.
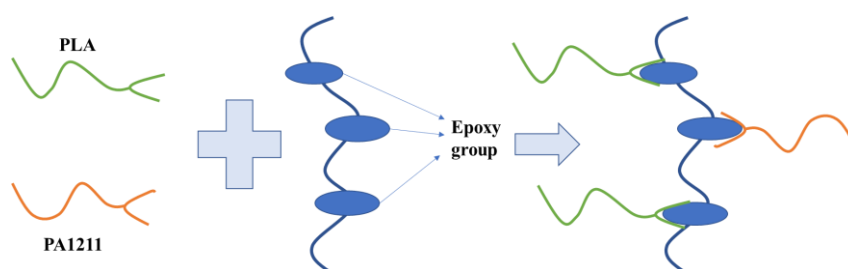
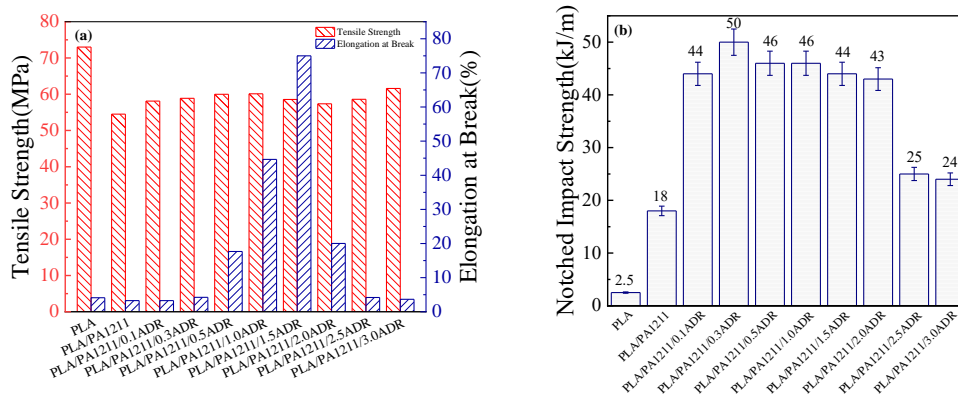Fig. 1. The modified mechanism of PLA/PA1211/ADR blending system

Fig. 2. Graph of tensile strength and elongation at break of PLA/PA1211/ADR blends (a); Graph of notched impact strength of PLA/PA1211/ADR blends (b)

Key words: Epoxy chain extender; Melt blending; Compatibility; Interface state and performance of blends

.

Preparation and properties of surface-modified nano-ZnO light-initiated

UV-curable waterborne polyurethane acrylate composite film

Yun Shen[1]; Jin Liu [*1,2]; Zhen Li [1,2];; Ping Wang[1]; Xianbiao Wang[1]; Fengjun Zhang[1,2]

[1] School of Materials Science and Chemical Engineering, Anhui Jianzhu University, Hefei 230601, P. R. China ; [2]Anhui Key Laboratory of Advanced Building Materials, Anhui Jianzhu University, Hefei 230601, P. R. China

Abstract

In this experiment, a waterborne polyurethane acrylate composite film initiated by ZnO nanoparticles light was prepared by UV curing. In order to improve the dispersibility of ZnO nanoparticles, KH570 was used to modify the surface of the nanoparticles and characterized by infrared spectroscopy. The performance of a series of composite films with different ZnO nanoparticles content was studied. Compared with the unmodified ZnO nanoparticles composite film, a series of modified composite films with different ZnO nanoparticles content have reduced water absorption and increased water contact angle. Among them, the water absorption rate of the composite membrane with the unmodified ZnO nanoparticles content of 0.5wt.% is 17.36%, and the water contact angle is 63.77°, and the water absorption rate of the composite membrane with the modified ZnO nanoparticles content of 1.0wt.% is 10.54%. The water contact angle is 67.07°, which may be due to the enhancement of molecular order and hydrophobicity in the composite film. The results show that the surface modification of ZnO nanoparticles with KH570 improves the dispersion of nanoparticles and the hydrophobicity of the composite film.

Key words: UV-curable; Waterborne polyurethane acrylate; ZnO nanoparticles photoinitiator；Nanocomposite films；Surface modification
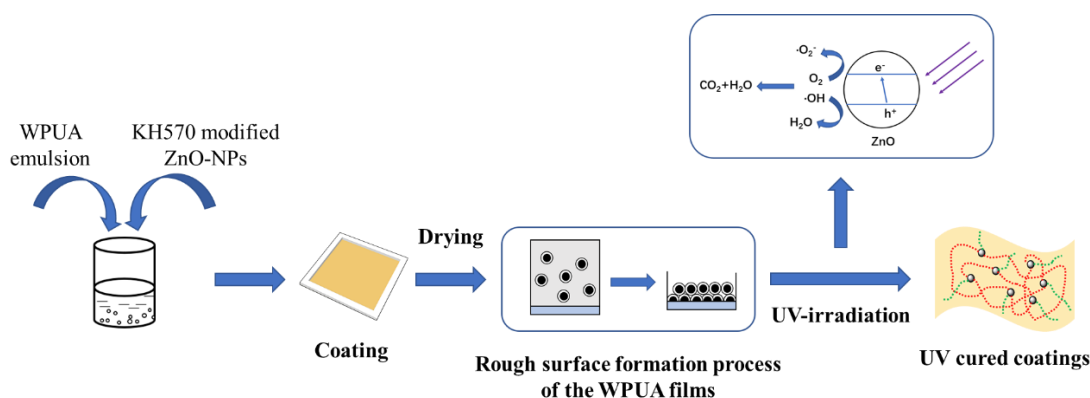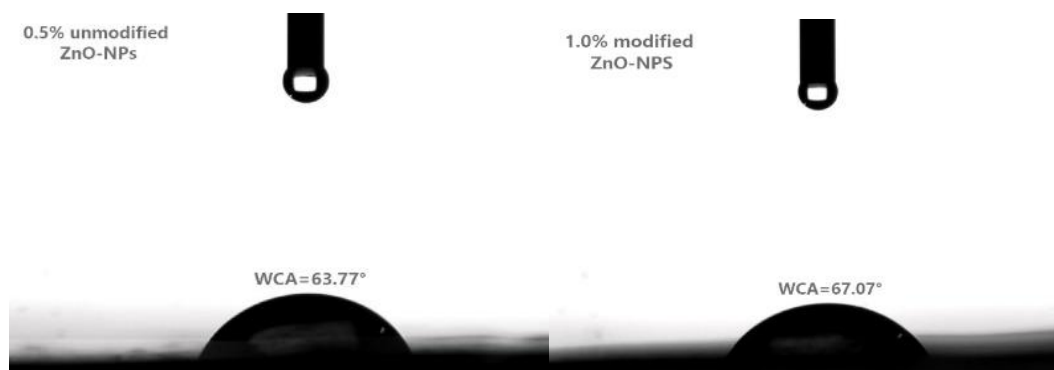

Fig 1. The process of WPUA films by UV cured coating

Fig 2. The water contact angle testing of composite films

Preparation and electrical properties of Co₃O₄ materials

Tianhao Hu，Guotao Dong，Ye Ge，BinQuan Cao，Jing Wang *

College of Materials Science and Engineering, Anhui University of Science And Technology, Huainan, Anhui 232001

*Corresponding author (Phone and WeChat: + 0086 (13855418833); jingwang@aust.edu.cn)

Abstract

Zeolite imidazole ester framework material (ZIF-67) is a porous crystal material. Its excellent chemical stability, high porosity and large specific surface area make it an ideal template. At the same time, the material with this structure can also be used to synthesize high-performance Co₃O₄ electrode materials. Co₃O₄ material with rhombic dodecahedron was synthesized by heat treatment with ZIF-67 as template. Then a three electrode system was constructed to test the electrochemical properties of electrode materials. The results show that the microstructure and surface morphology of Co₃O₄ can be effectively controlled by using ZIF-67 as template; The specific capacitance of Co₃O₄ electrode can reach 820 F/g; After 5000 charge discharge cycles, the specific capacitance retention is about 60%, and the cycle performance is good; The coulomb efficiency of charge and discharge is about 100%; It has high conductivity and excellent rate performance.

Keywords：Electrode；Supercapacitor；Zeolite imidazole ester skeleton；Electrical performance

1. Introduction

Supercapacitor is a new type of energy storage device. It not only has the advantages of rapid charge and discharge, but also has the energy storage performance of battery. It also has the characteristics of long cycle life, strong temperature resistance, high power density and green environmental protection. The excellent electrode materials directly determine the performance of supercapacitors. Carbon materials, conductive polymers and metal oxides can be used as electrode materials. In this paper, the framework with tetrahedral structure is formed by crosslinking organic imidazole ester and transition metal, and then the zeolite imidazole ester framework material (ZIF-67) [1] is further synthesized. The three-dimensional Co₃O₄ material with rhombic dodecahedral structure is synthesized as a template . The surface morphology and microstructure of Co₃O₄ are controlled by template method, which effectively improves the performance of Co₃O₄ in electrode materials[2,5.9].

2. Experimental

2.1. Reagents and instruments

The reagents are cobalt nitrate hexahydrate, absolute ethanol, 2-methylimidazole, hydrochloric acid and sulfuric acid. Nickel foam, N- methyl pyrrolidone, acetylene black and polyvinylidene fluoride(PVDF) were used to prepare electrodes. We need sand core suction filter, ultrasonic cleaner, electronic balance, pH meter, vacuum drying oven, muffle furnace,

constant temperature magnetic stirrer, tablet press, saturated calomel reference electrode, beaker, three electrolytic cells, electrochemical workstation and blue battery test system.

2.2. The preparation methods

First of all, we prepared Co_3O_4 powder, took 0.9 g $Co(NO_3)_2 \cdot 6H_2O$ and 5 mL deionized fully mixed, magnetic stirring for 10min to get a uniformly dispersed red solution. Then 4.9 g of 2-methylimidazole was added to 25 mL of deionized mixture, and a colorless and transparent solution was prepared after magnetic stirring for 10min. The red solution prepared above is added to the colorless solution drop by drop, and the mixed solution is stirred while dropping the solution, and the purple suspension is finally obtained after dropping completely. Then the purple suspension was put into a constant temperature magnetic mixer for 12 h to make it evenly mixed. Then the solution was pumped and filtered by sand core extraction and filtration device, and the purple precipitate obtained was dried in an oven at 60°C for 24 hours. Finally, the purple viscous powder was taken out as the precursor of ZIF-67. The precursor was then put into muffle furnace, set the temperature at 400°C for sintering, and kept at this temperature for 4 hours before natural cooling. Finally, the Co_3O_4 powder transformed by ZIF-67 was obtained.

2.3. Preparation of electrode

The obtained materials can be used to prepare electrode materials and applied to supercapacitors. Mix Co_3O_4 powder (active material), acetylene black (conductive agent) and polyvinylidene fluoride (PVDF) at a mass ratio of 8:1:1, drop an appropriate amount of N-methylpyrrolidone (dispersant), and grind for 30 min until the material is paste. Smear the paste onto the well processed 1*1 cm nickel foam block, then place the nickel strip and press the sheet at 6 MPa to obtain the electrode piece of the working electrode.
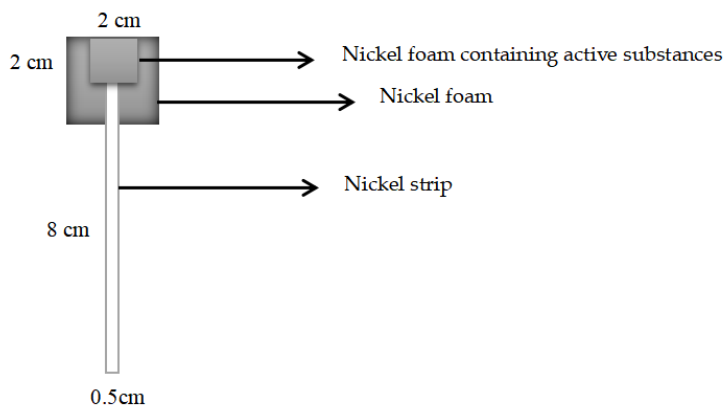
Figure 1. Schematic diagram of nickel strip electrode.

3. Results

3.1. Experimental result

1. The structure, morphology and electrical properties of the samples were analyzed by scanning electron microscope(SEM), diffraction of x-rays(XRD), Thermogravimetric Analysis(TG) and electrochemical workstation.

2. We can conclude that the prepared Co_3O_4 powder maintains the rhombic

dodecahedral structure[3] of the precursor zif-67, with finer particles, more uniform distribution and larger specific surface area.

3. XRD test shows the crystal phase composition and diffraction peak of the product. The crystal phase basically has no impurity peak[6], and the product does not contain other impurities.

4. The electrochemical test shows that the product has large specific capacitance, small internal resistance, excellent charge discharge performance and power storage.

3.2. Data analysis

3.2.1. Electron microscopic analysis

Fig. 2 is a scanning electron microscope photograph of ZIF-67. It can be seen from Fig. a and Fig. b that ZIF-67 is a rhombic dodecahedral structure. It can be seen from the full picture that ZIF-67 particles are evenly distributed, with flat surface and good engraving, and the particle size is about 500-900 nm.
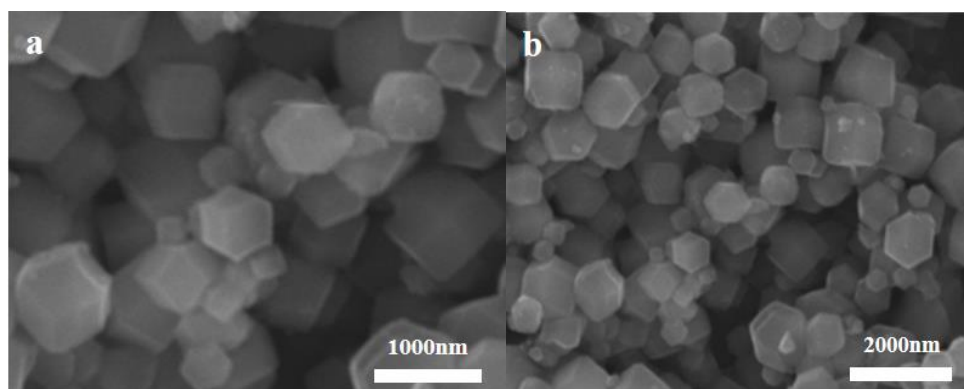
Figure 2. SEM of ZIF-67

As shown in Fig. 3, the scanning electron microscope photograph of Co_3O_4 powder is shown. It can be seen from a that the product strictly maintains the rhombic dodecahedral structure of the precursor. It can be seen from the full picture that the particle size is gradually reduced during the formation of Co_3O_4 powder from ZIF-67, and the particle size distribution is about 300-700 nm.
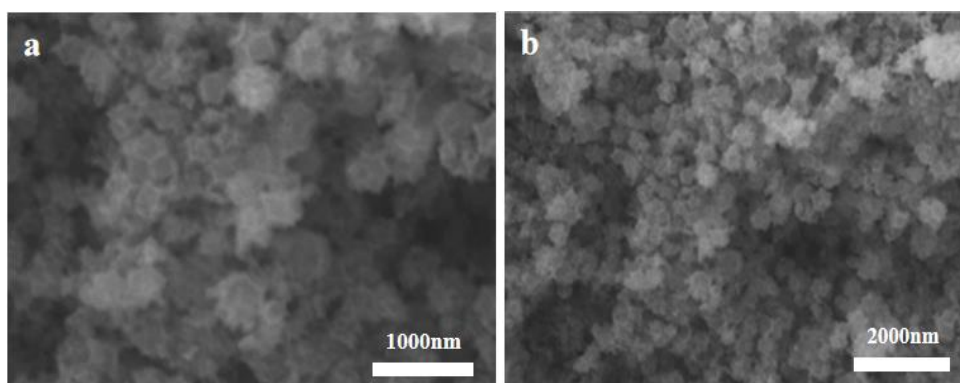
**Figure 3.** SEM of Co_3O_4.

3.2.2. XRD analysis

Figure 4 shows the XRD analysis results of ZIF-67 and Co_3O_4. As can be seen from the figure, there are three groups of strong peaks in both. The three peaks of ZIF-67 were located near 0.6°, 12.5°and 18.0°. The peaks of Co_3O_4 were located around 31.3°, 36.9°and 65.4°, and the corresponding crystal planes were (220), (311) and (440), respectively, which were consistent with the simulated crystal of Co_3O_4, indicating that the product was pure Co_3O_4.
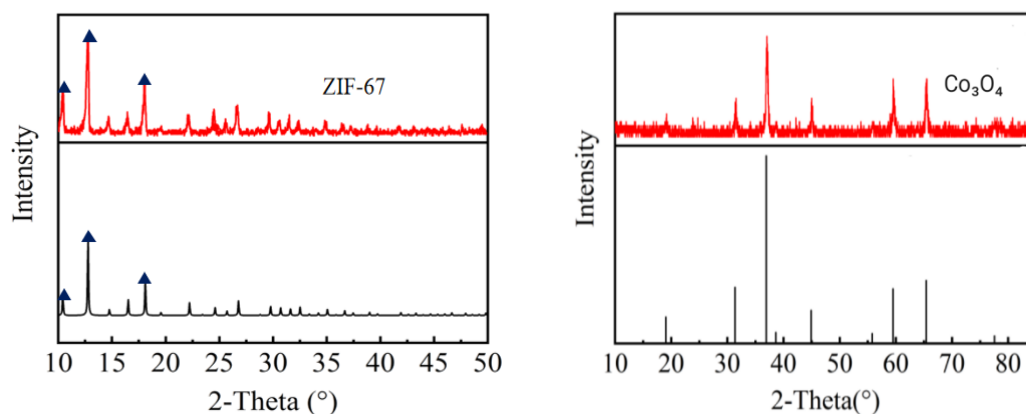
**Fig. 4.** XRD of ZIF-67 and Co_3O_4.

3.2.3. TG analysis

As shown in Figure. 5, the thermogravimetric curve shows slow weight loss at 315 ℃, and severe weight loss at 373 ℃, until the thermogravimetric curve shows a platform at 385 ℃ and tends to be flat. The weight loss during weight loss was 63.9%. Therefore, 400 ℃ is more conducive to the formation of Co_3O_4, which can be used as the best heat treatment temperature in this experiment.
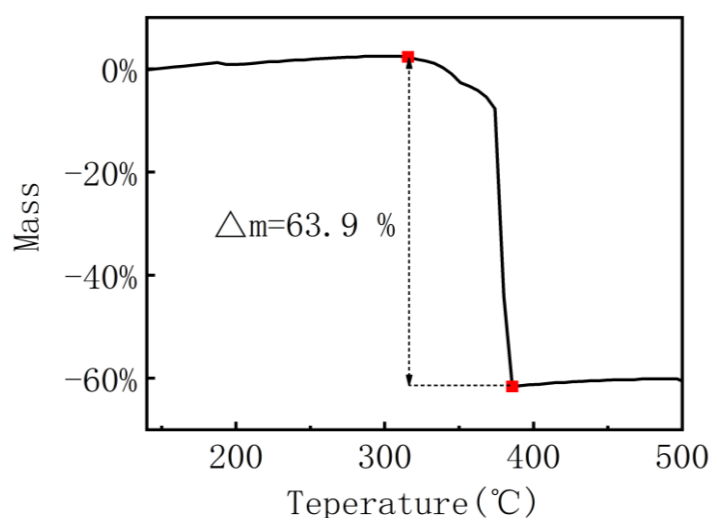
**Fig. 5.** TG curve of ZIF-67

397

3.2.4. CV analysis

Figure 6 shows the CV Curve of Co_3O_4 material at different scanning rates. The figure shows the change of potential. When the scanning speed is increased, the oxidation peak moves to high potential and the reduction peak moves to low potential, which is related to the redox reaction of cobalt ion[4,7,10]. When the scanning rate increases, the curve area and the specific capacitance of the material also increase.
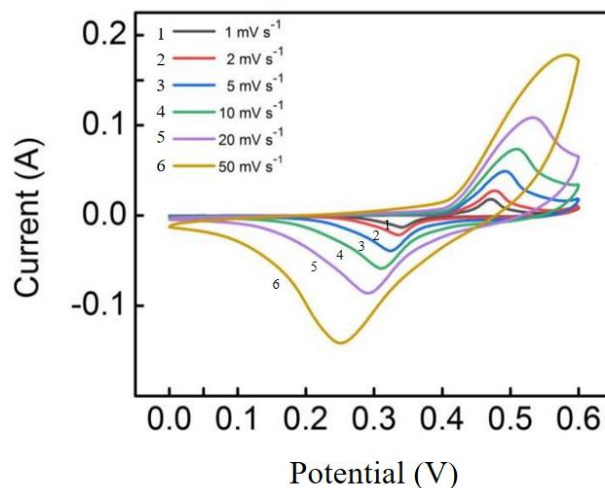
Fig. 6. Cyclic voltammetry curve of Co_3O_4 powder

3.2.5. Capacitance performance analysis

As shown in Fig. 7, specific capacitance of materials at different current densities can be obtained through GCD test.
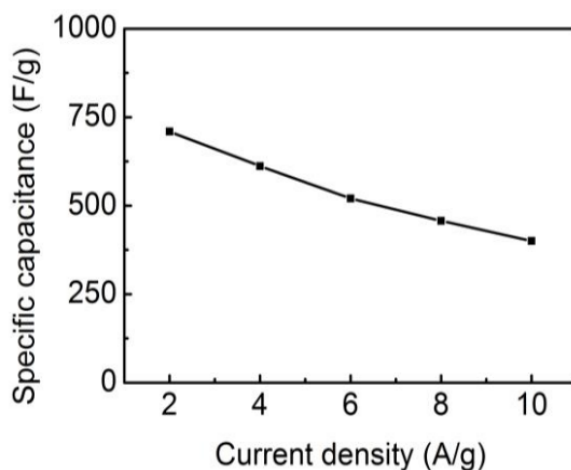
Fig. 7. Specific capacitance of Co_3O_4
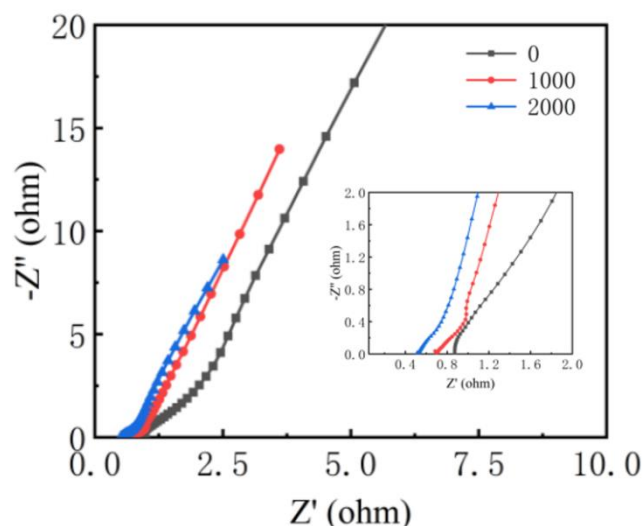
As shown in Table. 1, the specific capacitance of materials under different current densities can be seen. The data peak of Co_3O_4 remains stable, indicating that the Co_3O_4 electrode[4,7,10] has good electrochemical stability and excellent energy storage performance.

Table.1. Specific capacitance at different current densities.

| Current density（A/g）	2	4	6	8	10
Co3O4（F/g）	709.45	612.00	520.76	457.45	400.36

3.2.6. EIS analysis

Fig. 8 shows the EIS test results of the electrode material. The impedance of the material can be estimated from the high frequency region and the transverse axis intercept. It can be seen from the figure that the impedance of the material under 0 cycles is 0.872 Ω; The impedance at 1000 cycles is 0.695 Ω; The impedance at 2000 cycles is 0.508 Ω. It can be seen that the internal resistance of the material is very small and the corresponding conductivity is good.

Fig. 8. EIS plots of Co_3O_4

3.2.7. Cyclic stability analysis

As shown in Fig. 9, set the current density to 4 A/g and conduct charge discharge cycle test on the electrode material. It can be seen from the figure that the specific capacitance of the electrode material in 0 this cycle is about 799 F/g; The specific capacitance at 1000 cycles is 485 F/g; The specific capacitance at 5000 cycles is 465 F/g. After 5000 cycles, the specific capacitance decreased by 40% and the temperature was maintained, showing good cycle stability.
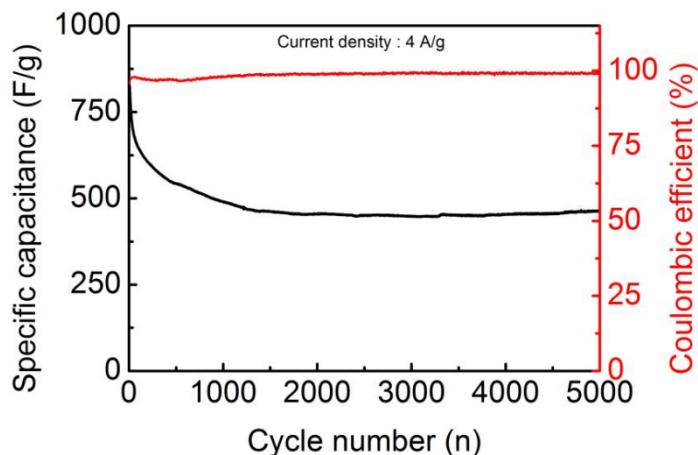
Fig. 8. Cycle performance curve .

4. Discussion

In this paper, high performance Co_3O_4 powder material was synthesized from ZIF-67. The morphology, structure and electrical properties were analyzed by testing. The rhomboid dodecahedron structure of Co_3O_4 can be seen by SEM. XRD analysis showed that the crystal shape of the product was cubic spinel structure. After charge-discharge cycle test, it can be found that the specific capacitance of Co_3O_4 is large and stable, and the charge-discharge coulomb efficiency reaches about 100%. Through GCD test, it can be concluded that Co_3O_4 electrode material has high specific capacitance and good conductivity. According to The EIS test, the curve is close to vertical, indicating that the ion diffusion rate is fast and suitable for the electrode material of supercapacitor.

References

[1] Junfeng, Qian, Fuan, et al. Hydrothermal synthesis of zeolitic imidazolate framework-67 (ZIF-67) nanocrystals - ScienceDirect[J]. Materials Letters, 2012, 82(1):220-223.
[2] Li H , Ma H , Wang X , et al. Efficient oxidation of ethylbenzene catalyzed by cobalt zeolitic imidazolate framework ZIF-67 and NHPI[J]. Journal of Energy Chemistry, 2014, 23(006):742-746.
[3] Guo J , Zhang Y , He Y C , et al. Photocatalytic performance of Co_3O_4/C based on ZIF-67/C composite materials[J]. Polyhedron, 2019, 175:114215.
[4] Yao L A , Jl A , Ying D B , et al. Co_3O_4 @carbon with high Co^{2+}/Co^{3+} ratios derived from ZIF-67 supported on N-doped carbon nanospheres as stable bifunctional oxygen catalysts[J]. Materials Today Energy, 2021(15):100737.
[5] Wang, Hu, Meng, et al. Recent Advance in Co_3O_4 and Co_3O_4-Containing Electrode Materials for High-Performance Supercapacitors[J]. Molecules, 2020, 25(2):269.
[6] Wang Y , Shi Z , Huang Y , et al. Supercapacitor Devices Based on Graphene Materials[J]. Journal of Physical Chemistry C, 2009, 113(30):13103-13107.
[7] Zhou S , Ye Z , Hu S , et al. Designed formation of Co_3O_4/$ZnCo_2O_4$/CuO hollow polyhedral nanocages derived from zeolitic imidazolate framework-67 for high-performance supercapacitors[J]. Nanoscale, 2018, 10:10.1039.C8NR05138K-.
[8] D Yu, Wu B , Ge L , et al. Decorating nanoporous ZIF-67-derived $NiCo_2O_4$ shells on a Co_3O_4 nanowire array core for battery-type electrodes with enhanced energy storage performance[J]. Journal of Materials Chemistry A, 2016:10878-10884.

[9] Kung, ChungWei, Chen, et al. Synthesis of Co_3O_4 nanosheets via electrodeposition followed by ozone treatment and their application to high-performance supercapacitors[J]. Journal of Power Sources, 2012, 214(214):91-99.

[10] Meher K, Sumanta, Rao R. Ultralayered Co_3O_4 for High-Performance Supercapacitor Applications[J]. Journal of Physical Chemistry C, 2011, 115(31):15646-15654.

[11] Wang M X , Zhang J , Fan H L , et al. ZIF-67 derived Co_3O_4/carbon aerogel composite for supercapacitor electrodes[J]. New Journal of Chemistry, 2019, 43.

Novel Preparation of Functional β–SiC Fiber based In₂O₃ Nanocomposite and Controlling of Influence Factors for the Chemical Gas Sensing

Zambaga Otgonbayar [1], Young Jun Joo [3], Kwang Youn Cho [3], Sang Yul Park [4], Kwang Youl Park [4], Won-Chun Oh [1, 2*]

[1] Department of Advanced Materials Science & Engineering, Hanseo University, Seosan-si, Chungnam, Korea, 356-706

[2] College of Materials Science and Engineering, Anhui University of Science & Technology, Huainan 232001, PR China

[3] Korea Institutes of Ceramic Engineering and Technology, Soho-ro, Jinju-Si, Gyeongsangnam-do, South Korea

[4] Daeho I&T, Changwon-si, Gyeongsangnam-do, 51338, Korea; *E-mail: wc_oh@hanseo.ac.kr

Abstract

The gas sensing ability of a pure SiC fiber is limited due to its low-sensitivity and selectivity with poor recovery time during a gas sensing test. The combination of functional β-SiC fibers with metal- oxide (MO) can lead to excellent electronic conductivity, boosted chemical activity, and high reaction activity with the target gas and SiC-In₂O₃ sensor material. Influence factors such as amounts of MO, current collectors, and gas species (CO_2, O_2 and without gas) for the gas sensing ability of SiC-In₂O₃ nanocomposite were determined at standard room temperature (25 °C) and high temperature (350 °C) conditions. The gas sensing ability of the functional β–SiC fiber was significantly enhanced by the loading of In₂O₃ metal-oxide. In addition, the MO junction on the β–SiC fiber was mainly subjected to the Si-C-O-In bond sensor layer with an effective electron-transfer ability. The gas sensing mechanism was based on the transfer of charges, in which the sensing material acted as an absorber or a donor of charges. The sensor material could use different current- collectors to support the electron transfer and gas sensing ability of the material. A 1:0.5M SiC-In₂O₃ coated Ni-foil current collector sensor showed better sensing ability for CO_2 and O_2 gases than other gas sensors at room temperature and high temperature conditions. The sensing result of the electrode was obtained with different current density values without or with gas purging conditions because CO_2 and O_2 gases had electron acceptor properties. During the gas sensing test, the sensor material donated electrons to target gases. The current value on the CV graph then significantly changed. Our obtained sample analysis data and the gas sensing test adequately demonstrated that MO junctions on functional β–SiC fibers could improve the sensitivity of a sensor material and particularly upgrade the sensor material for gas sensing.

Keywords. SiC fiber, hydrothermal, binary nanocomposite, gas sensing

Acknowledgment

Enhancement of Cell Growth by *Mychonastes homosphaera* Extract in HDF Fibroblasts

Jun Hee Kim[1], Ji Woo Hong[1], Da Hye Gam[1], Jae Hyun Park[1], and Jin Woo Kim[1,2*]

[1]Department of Food Science, Sun Moon University, Natural Science 118, 70 Sunmoon-ro 221, Tangjeong-myeon, Asan-si, Chungnam 336-708, Korea
[2]FlexPro Biotechnology, Natural Science 128, 70 Sunmoon-ro 221, Tangjeong-myeon, Asan-si, Chungcheongnam-do, Korea
*Correspondence: kimjw1028@sunmoon.ac.kr; Tel.: +82-41-530-2226

Abstract

The study was performed to investigated the anti-wrinkle effect of *Mychonastes homosphaerai* extract to verify the anti-wrinkle effect and indicated the collagenase activity inhibitory was $67.0\pm1.72\%$. The cytotoxicity, in presence of *M. homosphaera* extract, was measured by using the MTT assay in HDF, confirmed no appearing the cytotoxicity at concentrations less than 1.0 mg/mL. Evaluation of the effect of *M. homosphaerai* extract on HDF migration showed that 0.25 mg/mL *M. homosphaerai* extract enhanced HDF growth by 21.2%. Liquid chromatography with tandem mass spectrometry analyses showed that *M. homosphaerai* extract identify of gallic acid which indicated the phenolic compounds. In this study, we proposed an extraction process for the production of cosmetic materials that have a combination of anti-wrinkle effects from *M. homosphaerai*, which are marine waste.

Keywords: Skin-regeneration, *M. homosphaerai*, Gallic acid, Collagen, Fibroblast

Graphical abstract
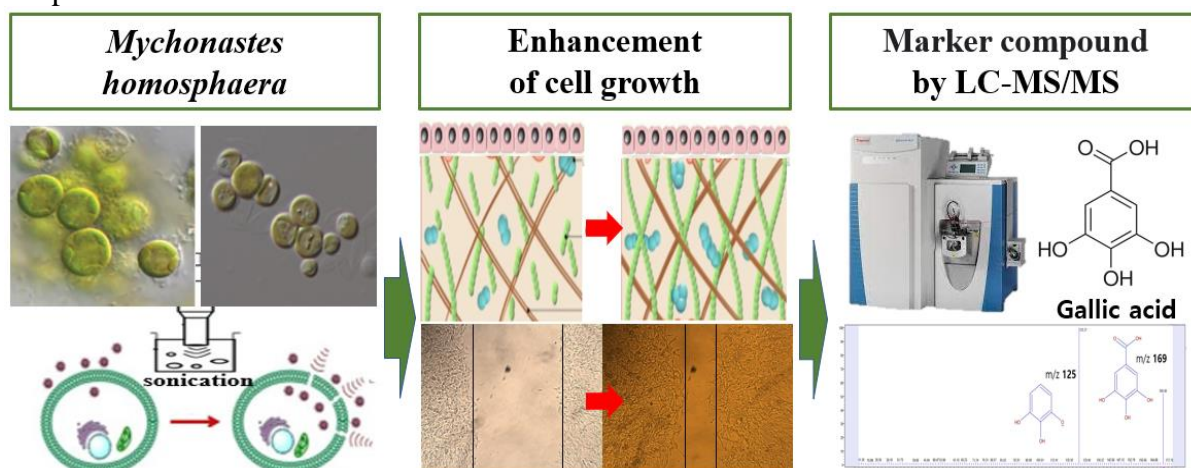
References

[1] Miguel, S. P., Ribeiro, M. P., Otero, A., & Coutinho, P. (2021). Application of microalgae and microalgal bioactive compounds in skin regeneration. *Algal Research*, *58*, 102395.

[2] Wu, J., Gu, X., Yang, D., Xu, S., Wang, S., Chen, X., & Wang, Z. (2021). Bioactive substances and potentiality of marine microalgae. *Food Science & Nutrition*, *9*(9), 5279-5292.

[3] Krienitz, L., Bock, C., Dadheech, P. K., & Pröschold, T. (2011). Taxonomic reassessment of the genus Mychonastes (Chlorophyceae, Chlorophyta) including the description of eight new species. *Phycologia*, *50*(1), 89-106.

[4] Adamczyk-Grochala, J., Wnuk, M., Duda, M., Zuczek, J., & Lewinska, A. (2020). Treatment with Modified Extracts of the Microalga Planktochlorella nurekis Attenuates the Development of Stress-Induced Senescence in Human Skin Cells. *Nutrients*, *12*(4), 1005.

In-situ Synthesis and Electrochemical Properties of High Capacity Silicon-based Composites for Lithium-Ion Batteries

Bo Ding*[a,b,c]

[a]Materials and Chemical Engineering Department, Bengbu College, Anhui, 233030, China
[b]Anhui Provincial Engineering Laboratory of Silicon-based Materials, Anhui, 233030, China
[c]Engineering Technology Research Center of Silicon-based Materials, Anhui, 233030, China

Abstract

Magnesium and silicon monoxide were subjected to an in situ oxidation-reduction reaction by high-energy ball milling to form a composite of silicon and magnesia followed by mixing with graphite . The Si/MgO/G (denoted as SMG) composite powder was then coated with carbon via high-temperature carbonization of pitch to fabricate a carbon-coated composite structure of SMG@C as anode composite material for lithium-ion batteries. X-ray diffraction analysis, scanning electron microscopy, cyclic voltammetry, and electrochemical impedance spectroscopy were carried out to study the phase, morphology, structure, and the electrochemical properties of the silicon-based anode composite materials. It has been found that the prepared SMG@C anode composite material showed a core-shell structure composed of Si, MgO, graphite, and amorphous carbon. Electrochemical testing indicated that SMG@C exhibited good electrochemical performance, including not only a low impedance but also good cycle stability and rate performance. At a current density of 100 mA/g, SMG@C maintained a capacity of 1124 mAh/g at 75 cycles, and the cycle performance remained relatively stable. After cycling at different current density, the capacity of SMG@C was restored to its initial state when it was tested at 100 mA/g current density. The SMG@C anode material prepared by the simple process of HEBM plus high temperature calcination of a carbon coating is promising to replace conventional graphite anode material for high energy density lithium ion batteries.

Keywords: high-energy ball milling; carbon coating; silicon-based anode material; silicon monoxide; lithium ion battery

References:
[1] T. F. Yi, T. T. Wei, Y. Li, et al. Efforts on enhancing the Li-ion diffusion coefficient and electronic conductivity of titanate-based anode materials for advanced Li-ion batteries. Energy Storage Materials, 2020,26:165-197.
[2] P. Li, J. Y. Hwang, Y. K. Sun. Nano/Microstructured Silicon−Graphite Composite Anode for High-Energy-Density LiIon Battery. ACS Nano, 2019, 13: 2624-2633.
[3]   N. Zhou, Y. F. Wu, Q. Zhou; et al. Enhanced cycling performance and rate capacity of SiO anode material by compositing with monoclinic TiO_2 (B). Applied Surface Science, 2019, 486:292–302.

[4] M. Xia, L. Y. Ran, X. Xiong; et al. Enhancing the electrochemical performance of micron-scale SiO@C/CNTs anode via adding piezoelectric material BaTiO$_3$ for high-power lithium ion battery. Journal of Alloys and Compounds, 2019, 800:116-124.

[5] Yu Zhang, Guannan Guo, Chen Chen; et al. An affordable manufacturing method to boost the initial Coulombic efficiency of disproportionated SiO lithium-ion battery anodes. Journal of Power Sources, 2019, 426 :116-123.

[6] M. Xia, Z. Zhou, Y. F. Su; et al. Scalable synthesis SiO@C anode by fluidization thermal chemical vapor deposition in fluidized bed reactor for high-energy lithium-ion battery.

Applied Surface Science, 2019, 467–468:298-308.

[7] Tao Y.; Zeng G.F.; Xiao C.Y.; et al. Porosity controlled synthesis of nanoporous silicon by chemical dealloying as anode for high energy lithium-ion batteries. Journal of Colloid and Interface Science. 2019,554:674-681.

[8] Cai Z, Ma Y., Huang X. et al. High electrochemical stability Al-doped spinel LiMn$_2$O$_4$ cathode material for Li-ion batteries. Journal of Energy Storage. 27 (2020) 101036.

The Synthesis of Copper Thick Film on Alumina Substrates using a Novel Electroplating Method for Power Electronic Devices

Jun Fang*[a,b]

[a]School of Material and Chemical Engineering, Bengbu University, Anhui, 233030, China
[b]Anhui Provincial Engineering Laboratory of Silicon-based Materials, Anhui, 233030, China

Abstract

In this paper, copper metallization layer was prepared on the surface of alumina ceramics by a novel electroplating method. The required Cu metallization film can be obtained by coating a layer of paste system with uniformly dispersed Cu particles on the surface of alumina ceramics, sintering at 1050 °C and reduction at 900 °C. The reduced Cu film is used as the seed layer for subsequent electroplating to improve the thickness and densification of the metal film. The composition and structure of the interface layer between Cu film and alumina substrate are analyzed. XRD results show that Cu and O react at the interface to form $CuAlO_2$ eutectic products, which is the guarantee for the effective bonding between Cu film and alumina substrate. When sintered at 1050 °C and reduced at 900 °C, the surface resistance can be as low as 4.55 mΩ / $\square$, and the bonding strength can reach 94 N. After electroplating, the thickness of Cu film can further reach 70~80 μm. This can meet the requirements of power electronic devices.

Keywords: alumina substrates; copper metallization; copper paste; electroplate; power device

References:

[1] Seager C W, Kokini K, Trumble K and Krane M J M. The influence of $CuAlO_2$ on the strength of eutectically bonded Cu/Al_2O_3 interfaces. Scripta Mater 2002, 46: 395-400.
[2] Wei X, Xu H X, Zhan J, Zhang H, Cao Y. Comparative studies on microstructures, strengths and reliabilities of two types of AlN direct bonding copper substrates. Ceramic International 2018, 44(15): 18935-18941.
[3] Zhao F, Jiao C, Xie D Q, Lu B, Qiu M B. Research on laser-assisted selective metallization of a 3D printed ceramic surface. RSC Advances 2020, 10(72): 44015-44024.
[4] Ning H L, Geng Z T, Ma J S, Huang F X. Research of electroplating Cu on pretreatment ceramic substrates. Rare Metal Materials and Engineering 2004, 33(3): 321-323.

Preparation and Gas Sensing Performance of g-C₃N₄/CuO Composite

Xianfeng Zhang*, Jiale Fang, Lanfang Shao

Anhui Provincial Engineering Laboratory of Silicon-based Materials, School of Material and Chemical Engineering, Bengbu University, Bengbu, 233030, PR China

Abstract

CuO is a typical p-type semiconductor gas sensitive material. Its synthesis method is simple and its performance is good, but it has some defects such as low sensitivity, poor selectivity, zero drift and so on.[1] The g-C₃N₄ structure is a stable planar layer, which enables it to accelerate electron diffusion and provide holes, and it can be combined with semiconductor materials to improve the gas sensitivity of the material.[2] In this paper, CuO and g-C₃N₄/CuO composites were prepared by hydrothermal synthesis method. The chemical composition, crystal structure and microstructure of g-C₃N₄/CuO composites were analyzed and characterized by X-Ray Diffraction(XRD), Fourier Transform Infrared Spectroscopy(FTIR), Scanning Electron Microscopy(SEM) and other means. The research results showed that the CuO nanomaterial is indeed doped with agglomerated spherical g-C₃N₄. The effects of different mass fractions of g-C₃N₄/CuO nanocomposites on the response sensitivity and gas selectivity of acetone were investigated. The experimental results show that the g-C₃N₄/CuO doped with 3% g-C₃N₄ has the best performance. The sensitivity to 100 ppm acetone is 4.7 and the response recovery time is 18 s and 14 s under the optimal working tepmerature at 260 ℃.

Key words：CuO; g-C₃N₄; gas sensing performance; g-C₃N₄/CuO composite

References

[1] Pandey P., Merwyn S., Agarwal G. S., et al. Electrochemical synthesis of multi-armed CuO nanoparticles and their remarkable bactericidal potential against waterborne bacteria. Journal of Nanoparticle Research, 2012, 14(1):1-13.

[2] Zhang W., Xu C., Liu E., et al. Facile strategy to construction Z-scheme ZnCo₂O₄/g-C₃N₄ photocatalyst with efficient H₂ evolution activity. Applied Surface Science, 2020, 515:146-039.

Acknowledgments

_____

* Corresponding author
E-mail: zxf@bbc.edu.cn
Tel: +86-552-317-9368